

---

# Robust $3d$ and $3d-4f$ metallacrowns with chromium(III) ions and anisotropic lanthanide(III) ions

---

## Dissertation

**Anne Lüpke**

geboren am 19.09.1993 in Koblenz

Dissertation zur Erlangung des Grades eines 'Doktor rerum naturalium (Dr. rer. nat.)' des  
Fachbereichs 09 - Chemie, Pharmazie, Geographie und Geowissenschaften  
der Johannes Gutenberg-Universität Mainz

Department Chemie  
Arbeitsgruppe Prof. Dr. Eva Rentschler

JOHANNES GUTENBERG  
UNIVERSITÄT MAINZ



Mainz, August 2022



## **Eigenständigkeitserklärung**

Die vorliegende Arbeit wurde in der Zeit von Mai 2019 bis August 2022 am Department Chemie unter der Betreuung von Prof. Dr. XXXXX und Prof. Dr. XXXXX im Rahmen des Max Planck Graduate Center mit der Johannes Gutenberg-Universität Mainz (MPGC Mainz) angefertigt.

I hereby declare that I wrote the dissertation submitted without any unauthorized external assistance and used only sources acknowledged in the work. All textual passages which are appropriated verbatim or paraphrased from published and unpublished texts as well as all information obtained from oral sources are duly indicated and listed in accordance with bibliographical rules. In carrying out this research, I complied with the rules of standard scientific practice as formulated in the statutes of Johannes Gutenberg-University Mainz to insure standard scientific practice.

Mainz, August 2022

---

Anne Lüpke

Dekanin: Prof. Dr. XXXXX

Erstgutachterin: Prof. Dr. XXXXX

Zweitgutachterin: Prof. Dr. XXXXX

Betreuer im Rahmen des MPGC: Prof. Dr. XXXXX, Prof. Dr. XXXXX

Prüfer: Prof. Dr. XXXXX, Prof. Dr. XXXXX, Prof. Dr. XXXXX



*- Für Mama -*



## Kurzzusammenfassung

Quantencomputer und molekülbasierte Elektronik (engl. *Spintronic devices*) sind bedeutende Anwendungen im Bereich des molekularen Magnetismus, der seit der Entdeckung der langsamen, molekularen magnetischen Relaxation in so genannten Einzelmolekülmagneten (SMMs), intensiv erforscht wird. Zukünftig werden für die digitale Datenverarbeitung sowohl größere Speicherkapazitäten als auch schnellere Leistungen erforderlich sein, die nicht allein durch die weitere Miniaturisierung von Komponenten erreicht werden können. SMMs, die auf Oberflächen aufgebracht werden, können die Dichte von Speichermedien signifikant erhöhen. Eine realistische Anwendung solcher Systeme erfordert die Kontrolle auf molekularer Ebene über eine Schnittstelle zur Außenwelt. Bei Oberflächenauftragung kommt es jedoch häufig zu einer Fragmentierung der fragilen molekularen Koordinationsverbindungen. Dies erklärt, warum es tausende geeignete Moleküle mit SMM Verhalten gibt, jedoch nur ein Bruchteil erfolgreich auf Oberflächen adsorbiert werden konnten und somit für weitere Untersuchungen interessant sind.

Ein spezifisches Liganden-Design ist notwendig, um die Leistungsfähigkeit von lanthanoid-basierten SMMs zu verbessern. Bei der Koordination von Lanthanoiden als Gastionen in Metallakronen (MCs) können hierbei bevorzugte Geometrien ( $D_{4d}$ ,  $C_{5h}$ ) geschaffen werden, die das Quantentunneln als Relaxationsprozess der Magnetisierung unterdrücken. MC-Komplexe gehören zu einer innovativen Verbindungsklasse und weisen robuste Eigenschaften in Bezug auf die Integrität des MC-Motivs in Lösung auf. Außerdem zeigen diese kollektive, kontrollierbare, magnetische Spin-Austauschwechselwirkungen, die zu interessanten elektronischen Grundzuständen führen können.

Im ersten Teil dieser Arbeit wurden kinetisch inerte Chrom(III)-Ionen verwendet, um die Stabilität von MCs weiter zu erhöhen. Solche isotropen  $3d$ -Übergangsmetallionen koordinieren in klar definierten Symmetrien, wodurch die Synthese von großen Clustern erleichtert wird. Weiterhin wurden in dieser Arbeit die magnetischen Austauschwechselwirkungen zwischen benachbarten Metallzentren untersucht. Magnetisierungsmessungen ergaben einen Grundzustand mit hohem Spin für eine [9-MC-3] Kavität. Die erste erfolgreiche Synthese von Chrom(III)-Metallakronen ermöglicht die Entwicklung neuer kinetisch und thermodynamisch stabiler MCs. In dieser Arbeit wird durch die Solvothermalsynthese eine Möglichkeit für die Untersuchung verschiedener MCs mit unterschiedlichen Kavitäten, Gast-Ionen und daraus resultierenden magnetischen Eigenschaften geschaffen. Im zweiten Teil dieser Arbeit werden zusätzlich anisotrope Lanthanoid(III)-Ionen verwendet, die als Gastionen der MCs koordiniert werden. Dazu zählen zum Beispiel Dysprosium(III)- und Terbium(III)-Gastionen die einen großen Spingrundzustand  $S$  in Kombination mit einer großen magnetischen Anisotropie  $D$  aufweisen. Die Synthese von  $3d-4f$ -Komplexen sowie die Einflussfaktoren auf das SMM-Verhalten wurden untersucht. Daher wird in diesem Teil der Arbeit abschließend die Kombination von stabilen Chrom(III)-Ionen mit dem robusten Metallakronen-Netzwerk und anisotropen Lanthanid(III)-Ionen untersucht.





## Abstract

Quantum computing and molecule-based electronics are two of the most desired applications in molecular magnetism since the discovery of slow magnetic relaxation for discrete molecules, so called single-molecule magnets (SMMs). Data processing will require larger storage capacities and faster performance in future applications, which cannot be provided solely by miniaturization of components. In that regard, SMMs that are applied on surfaces could significantly increase the density of storage media. A realistic application of such devices requires the control at a molecular level through the interfaces to the outside world. Often, fragmentation of fragile molecular coordination compounds occurs at the surface during the surface immobilization process. This explains the lack of molecular devices out of thousands of potential molecular candidates. Metallocrown (MC) complexes on the other hand, belong to an emerging class of compounds. They exhibit robust properties with regard to the integrity of the MC motif in solution as well as collective spin interactions which lead to interesting electronic ground states. The characteristic arrangement of spin centers provides a framework for magnetic exchange interactions and represents an important future direction for magneto-chemical research focused on developing useful magnetic molecular devices.

In the first part of this thesis, kinetic inert chromium(III) ions are applied to increase the stability of MCs even further. Such isotropic  $3d$  transition metal ions are coordinated in well-defined geometries which can enhance the formation of large clusters. Furthermore, theoretical models were applied to understand and predict magnetic exchange interactions between neighboring metal centers. Magnetization measurements revealed a high spin ground state for a [9-MC-3] cavity. The first successful chromium(III) metallocrown synthesis paves the way for new kinetically and thermodynamically stable MCs for future applications. In this work, solvothermal synthesis establishes the platform for formation of diverse MCs with different cavities, guest ions, and magnetic properties. Various ligands and co-ligands enhance the crystallization ability of these complexes and can be used to adjust the cavity size.

In the second part of this thesis, anisotropic lanthanide(III) ions (like dysprosium(III) and terbium(III) ions) are additionally implemented in the MC scaffold which is necessary for the application of MC-based SMMs including chromium(III) ions. Therefore, the synthesis of  $3d-4f$  complexes with dysprosium(III) and terbium(III) guest ions that possess a large spin ground state  $S$  combined with large magnetic anisotropy  $D$  provide the requirements for SMM behavior. Specific ligand design is necessary to enhance the SMM performance of the applied lanthanide(III) ions even further. Through the coordination as guest ions in MC frameworks, preferred geometries ( $D_{4d}$ ,  $C_{5h}$ ) can be created which suppress quantum tunneling as a relaxation mechanism of the magnetization. Thus, a combination of stable chromium(III) ions with the robust metallocrown framework and anisotropic lanthanide(III) ions was investigated. Different cavities like a [15-MC-5] and [12-MC-4] create ideal coordination environments for the guest ions.



# Danksagung

XXXXX



## General remarks

This thesis is divided in 6 Chapters.

**Chapter 1** gives an introduction and an overview of the relevant literature and theoretical background of metallocrowns, chromium ions and single-molecule magnets. This is necessary to follow and understand the results presented in this thesis in the following chapters.

**Chapter 2** presents the scope, motivation, and the scientific goal of the thesis by presenting the aim of this work and the motivation for the reported projects.

**Chapter 3** gives an overview of the selected and synthesized ligands and complexes of this thesis. Additionally, the abbreviated names and the schematical structures are shown.

**Chapter 4** starts with the introduction of a novel chromium metallocrown. This metallocrown is the first building block of this work since it shows the potential of solvothermal synthesis in the research area of metallocrown especially with kinetically inert metal ions. Following the already published results a comparison to another chromium metallocrown is drawn. Like the first  $[\text{Cr}_3\text{Cr}]$ -MC a 9-MC-3 cavity was obtained by using a modified ligand. The second part of Chapter 4 covers the addition of lanthanide(III) ions to the synthesis route of chromium metallocrowns. The influence of the size of the lanthanide(III) ions and the anisotropy is presented and discussed. Several different compounds were obtained.

**Chapter 5** summarizes all the obtained results and provides an outlook for future projects in this research field.

Finally, for ease of reading and clarity, the experimental synthesis routes, X-ray parameters, calculations for the geometries and magnetic evaluations and simulations, electrospray ionization and cyclic voltammetry measurements are included chapter by chapter in the appendix in **Chapter 6**. Therefore, Chapter 6.1 summarizes the experimental part and supporting information of Chapter 4.1, while Chapter 6.2 shows the additional information to the corresponding Chapter 4.2. and so on.

# Contents

Kurzzusammenfassung .....	I
Abstract.....	II
Danksagung.....	III
General remarks.....	IV
Contents.....	1
1. Introduction.....	1
1.1. Metallacrowns.....	1
1.1.1. Building blocks of MCs.....	2
1.1.2. Smart choice of the ligands.....	3
1.1.3. Guest and ring metal ions.....	5
1.1.4. Vacant metallacrowns.....	6
1.1.5. Properties and application of metallacrowns.....	7
1.2. Chromium ions.....	10
1.2.1. Multinuclear molecules with chromium(III) ions.....	12
1.3. Solvothermal synthesis.....	15
1.4. Single-molecule magnets - SMMs.....	17
1.4.1. Approach to increase the energy barrier.....	21
1.4.2. Detection of SMM behavior - alternating current measurements.....	24
1.5. References.....	25
2. Motivation and aim of this work.....	31
2.1. References.....	35
3. List of compounds.....	38
4. Results and Discussion.....	41
4.1. Chromium(III) metallacrowns.....	42
4.1.1. [9-MC-3] metallacrown with chromium(III) ions salicylhydroxamic acid.....	42
4.1.1.1. References.....	51
4.1.2. Influencing the metallacrown cavity including iron and chromium ions.....	53
4.1.2.1. $\{\text{Fe}^{\text{III}}(\mu_2\text{-OOCPh})_3[9\text{-MC}_{\text{Fe}(\text{III})\text{N}(\text{tBuShi})\text{-3]}(\text{MeOH})_3\} (\text{tBu}-[\text{Fe}_3\text{Fe}])$ .....	55
4.1.2.2. $\{\text{Cr}^{\text{III}}(\mu_2\text{-piv})_3[9\text{-MC}_{\text{Cr}(\text{III})\text{N}(\text{tBu}^2\text{Shi})\text{-3]}(\text{morph})_3\} \cdot \text{MeOH} ((\text{tBu})_2\text{-}[\text{Cr}_3\text{Cr}])$ .....	67
4.1.3. Vacant metallacrowns with chromium(III) ions.....	79
4.2. <i>3d-4f</i> Metallacrowns with chromium(III) ions.....	97
4.2.1.1. [15-MC-5] Metallacrown.....	99
4.2.1.2. $[\text{Cr}_6\text{Tb}_4]$ Cluster.....	104
4.2.2. $[\text{Cr}_4\text{Ln}_2]$ Clusters.....	109
4.2.2.1. $[\text{Cr}_4\text{Ln}_2]$ Clusters including 3,5-di- <i>tert</i> -butylsalicylate.....	109

4.2.2.2.	<i>In-situ</i> formation of 3,5-di <i>tert</i> -butyl-salicylate (Sal-[Cr <sub>4</sub> Tb <sub>2</sub> ]) .....	111
4.2.2.3.	[Cr <sub>4</sub> Dy <sub>2</sub> ] with salicylhydroxamates .....	113
4.2.3.	[12-MC-4] metallacrown with a ligand bridge .....	118
4.3.	References .....	127
5.	Conclusion and future perspectives .....	131
5.1.	References .....	135
6.	Experimental Part and Supporting Information.....	136
6.1.	Supporting information for Chapter 4.1.....	139
6.1.1.	Structure determination.....	140
6.1.2.	Crystal packing.....	142
6.1.3.	Coordination of ligand.....	143
6.1.4.	Isomers.....	144
6.1.5.	SHAPE calculations.....	146
6.1.6.	Synthesis.....	147
6.1.7.	IR spectroscopy .....	148
6.1.8.	UV-Vis Spectroscopy.....	148
6.1.8.	Powder XRD.....	149
6.1.9.	Simulation of Zeeman splitting .....	150
6.1.10.	Magnetization measurement.....	151
6.1.11.	References.....	151
6.2.1.	Supporting information for Chapter 4.1.2.1.....	152
6.2.1.1.	Synthesis of 5- <i>tert</i> -butylmethyl salicylate.....	152
6.2.1.2.	Synthesis of 5- <i>tert</i> -butylsalicylhydroxamic acid.....	153
6.2.1.3.	Synthesis of Fe(III)( $\mu_2$ -OOCPh) <sub>3</sub> [9-MC <sub>Fe(III)L2-3</sub> ](MeOH) <sub>3</sub> ( <i>t</i> bu-[Fe <sub>3</sub> Fe]).....	154
6.2.1.4.	Structure determination.....	156
6.2.1.5.	Continuous Shape Measurements.....	159
6.2.1.6.	Evaluation of magnetic data .....	160
6.2.1.7.	Cyclic voltammetry.....	161
6.2.1.8.	NMR spectra .....	163
6.2.1.9.	IR spectra.....	164
6.2.2.	Supporting information for Chapter 4.1.2.2.....	164
6.2.2.1.	Synthesis of chromium pivalate (Cr <sub>3</sub> O(O <sub>2</sub> C <i>tert</i> -butyl) <sub>6</sub> (H <sub>2</sub> O) <sub>3</sub> ](O <sub>2</sub> C <i>tert</i> -butyl) HO <sub>2</sub> C <i>tert</i> -butyl) .....	164
6.2.2.2.	Synthesis of 3,5-di- <i>tert</i> -butylsalicylate .....	166
6.2.2.3.	Synthesis of 3,5-di- <i>tert</i> -butylsalicylhydroxamic acid .....	167
6.2.2.4.	Synthesis of [9-MC-3] ( <i>t</i> bu) <sub>2</sub> -[Cr <sub>3</sub> Cr].....	168
6.2.2.5.	Structure determination.....	169

6.2.2.6. Continuous Shape Measurements of (t <sub>bu</sub> ) <sub>2</sub> -[Cr <sub>3</sub> Cr]	173
6.2.2.7. Magnetic evaluation of data	174
6.2.2.8. Electrospray ionization mass spectrometry (ESI)	175
6.2.2.9. Cyclic voltammetry	180
6.2.2.10. NMR spectra	181
6.2.2.11. Infrared spectra	183
6.3. Supporting information for Chapter 4.1.3.	185
6.3.1. Synthesis of vacant ShiH <sub>3</sub> [Cr <sub>4</sub> ]	185
6.3.2. Synthesis of 4-methoxy salicylhydroxamic acid	186
6.3.3. Synthesis of vacant OMe-[Cr <sub>4</sub> ]	187
6.3.4. Synthesis of pic-[Cr <sub>4</sub> ]	188
6.3.5. Synthesis of 3-hydroxy-2-naphtylhydroxamic acid (Nha)	189
6.3.6. Synthesis of Nha-[Cr <sub>4</sub> ]	190
6.3.7. Structure determination of [Cr <sub>4</sub> ]and OMe-[Cr <sub>4</sub> ]	191
6.3.8. Structure determination of pic-[Cr <sub>4</sub> ]	192
6.3.9. Continuous Shape Measurements	194
6.3.10. Evaluation of magnetic data	196
6.3.11. Electrospray Ionization mass spectrometry (ESI)	198
6.3.12. Cyclic voltammetry	205
6.3.13. NMR	207
6.3.14. Infrared spectra	208
6.4. Supporting information for Chapter 4.2.1.	211
6.4.2.1. Synthesis of [Cr <sub>5</sub> Dy] [15-MC-5] metallacrown	211
6.4.2.2. Synthesis of [Cr <sub>6</sub> Tb <sub>4</sub> ]	212
6.4.2.3. Synthesis of Sal-[Cr <sub>2</sub> Dy <sub>4</sub> ] with 3,5-di- <i>tert</i> -butyl salicylhydroxamate	213
6.4.2.4. Synthesis of Sal-[Cr <sub>2</sub> Tb <sub>4</sub> ] with 3,5-di- <i>tert</i> -butyl salicylhydroxamate	214
6.4.2.5. Synthesis of [Cr <sub>2</sub> Dy <sub>4</sub> ] ShiH <sub>3</sub>	215
6.4.2.6. Synthesis of [Cr <sub>2</sub> Dy <sub>4</sub> ] ShiH <sub>3</sub>	216
6.4.2.7. Synthesis of [Cr <sub>4</sub> Dy] [12-MC-4]metallacrown	217
6.4.2.8. Structure determination of [Cr <sub>5</sub> Dy] and [Cr <sub>6</sub> Tb <sub>4</sub> ]	219
6.4.2.9. Structure determination of Sal-[Cr <sub>4</sub> Dy <sub>2</sub> ] and Sal-[Cr <sub>4</sub> Tb <sub>2</sub> ] including 3,5-di- <i>tert</i> -butylsalicylhydroxate and corresponding acid	220
6.4.2.10. Structure determination [Cr <sub>4</sub> Dy <sub>2</sub> ]	222
6.4.2.11. Structure determination [Cr <sub>4</sub> Dy]	224
6.4.2.12. Continuous Shape Measurements	225
6.4.2.13. Evaluation of magnetic data	227
6.4.2.14. Infrared spectra	228



6.5. General procedure of solvothermal synthesis .....	231
7. Instrumental part.....	232
7.1. General.....	232
7.2. Infrared spectroscopy.....	232
7.3. X-Ray analysis .....	232
7.4. Continuous Shape Measurement .....	232
7.5. NMR spectroscopy .....	232
7.6. ESI mass spectrometry.....	232
7.7. Cyclic voltammetry.....	233
7.8. SQUID magnetometry .....	233
7.9. Elemental Analysis .....	233
8. References .....	234

## List of abbreviations

Abbreviation	Explanation
CH <sub>3</sub> OH	methanol
$\chi_m$	molar magnetic susceptibility
Cr(OH) <sub>x</sub>	chromium hydroxides
CShM	Continuous Shape Measurement value
CV	cyclic voltametry
<i>d</i>	distance
<i>D</i>	magnetic anisotropy
<i>E</i> <sub>pa</sub>	anodic peak potential
<i>E</i> <sub>pc</sub>	cathodic peak potential
eq.	equivalents: molar ratios in chemical reactions
ESI	electrospray ionization mass spectrometry
<i>g</i>	Landé factor
<i>g<sub>f</sub></i>	Landé factor for lanthanide ions
$\hat{H}$	total energy operator “Hamiltonian”
<i>i</i> <sub>pa</sub>	anodic peak current
<i>i</i> <sub>pc</sub>	cathodic peak current
IR	infrared
<i>J</i>	exchange coupling constant
<i>k<sub>B</sub></i>	Boltzmann constant
<i>L</i>	total orbit angular momentum
<i>m</i>	mass
<i>M</i>	magnetization
MC	metallacrown
MeOH	methanol
[Mn <sub>12</sub> OAc]	manganese acetate cluster (Mn(III),Mn(IV)) [Mn <sub>12</sub> O <sub>12</sub> (O <sub>2</sub> CMe) <sub>16</sub> (H <sub>2</sub> O) <sub>4</sub> ] · MeCOOH · 3 H <sub>2</sub> O
morph	morpholine
<i>M<sub>s</sub></i>	sublevel
<i>N<sub>A</sub></i>	Avogadro constant: 6.022 10.23 mol <sup>-1</sup>
OAc	acetate
pic	gamma picoline (4-pyridine)
piv	pivalate
pK <sub>a</sub>	acid dissociation constant

Abbreviation	Explanation
py	pyridine
R	gas constant: $8.3144598 \text{ JK}^{-1}\text{mol}^{-1}$
R	residual
$S$	total spin angular momentum
SalH <sub>3</sub>	salicylic acid
Shi <sup>3-</sup>	salicyl hydroxamate
ShiH <sub>3</sub>	salicylhydroxamic acid
SIM	single-ion magnet
SMM	single-molecule magnet
SQUID	Superconducting Quantum Interference Device
$S_T$	total spin ground state
$T$	temperature
TIP	Temperature Independent Paramagnetism
$U_{\text{eff}}$	effective energy barrier
UV	ultra violet (energy range of electromagnetic radiation 100-380 nm)
$V$	volume
Vis	visible (energy range of electromagnetic radiation 380-780 nm)
X-ray	electromagnetic radiation with a wavelength range of 0.01 - 10 nm
ZFS	zero field splitting
$zJ$	intermolecular interaction
$\Delta$	delta
$\Delta E_p$	peak potential difference
$\Lambda$	lambda
$\mu_B$	Bohr magneton: $9.274 \cdot 10^{-24} \text{ J T}^{-1}$
$\mu_{\text{eff}}$	effective magnetic moment
$\tau$	relaxation time
$\nu$	excitation frequency



# 1. Introduction

## 1.1. Metallacrowns

In 1987 Donald J. Cram, Jean-Marie Lehn, and Charles J. Pedersen were jointly awarded the Nobel Prize in chemistry “for their development and use of molecules with structure-specific interactions of high selectivity”.<sup>[1]</sup> In addition, their work contributed significantly to new concepts of host-guest chemistry, molecular recognition, and supramolecular chemistry.<sup>[2–4]</sup> More than 20 years in advance, Pederson discovered dibenzo-18-crown-6 which is an 18-atom heterocycle that contains six oxygen atoms.<sup>[5]</sup> In general, crown ethers are polyoxo-macrocyclic molecules that are well-known to coordinate a large variety of alkali metal cations.<sup>[6]</sup>

In 1989, Pecoraro and Lah categorized and named the metallacrown family accordingly to the compound family of these crown ethers for the first time. They recognized the similarities to crown ether ring structures, replacing two carbon atoms with  $3d$  metal ions and nitrogen ions. In this year they reported three metallacrowns (MCs) including a vacant [9-MC-3] vanadium(V), [9-MC-3] iron(III), and a [12-MC-4] manganese(III/II) compound.<sup>[7–9]</sup> The class of supramolecular substances that started with crown ethers, therefore, opened the path for today's applications of MCs in the field of host-guest chemistry, recognition agents, extended networks, or molecular magnetism.<sup>[10–12]</sup>

However, a crown ether only consists of organic components, whereas in a metallacrown metal ions are also part of the repeating unit. Crown ethers are composed of  $[-(\text{CH}_2)_m\text{-O}]_n$ - repeating units,<sup>[6]</sup> while metallacrowns, mostly form  $[-\text{M-N-O}]_n$ - repeating units in their basic framework. The notation of metallacrowns is based on the naming of organic crown ethers. The abbreviation [X-MC-Y] describes the ring size by X and the number of donor atoms by Y. Thus, a [12-MC 4] consists of twelve ring atoms (with four repeating units  $-\text{[M-N-O]}_4$ -) and four oxygen donor atoms (see Figure 1. 1). The charged metal ions  $\text{M}^{n+}$  and their valences can change, which enables a variety of possible structures.<sup>[13]</sup>

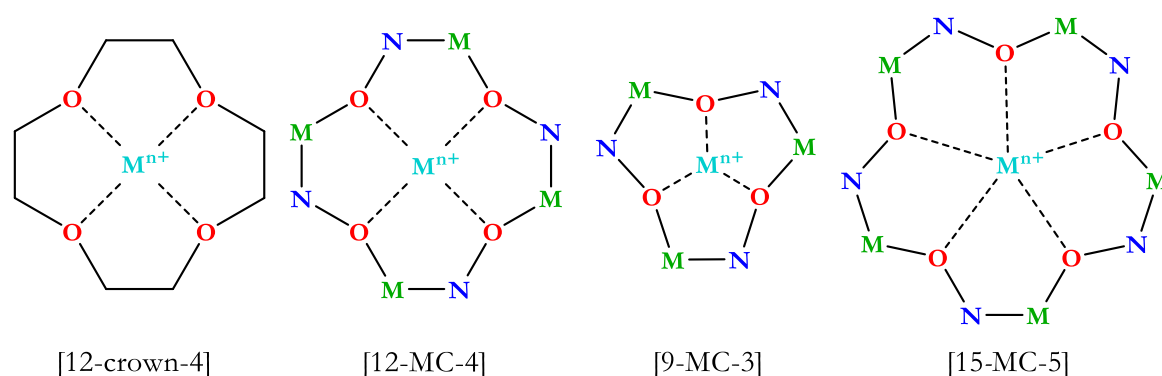
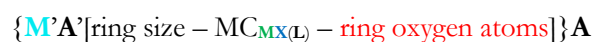


**Figure 1. 1.** Schematical representation of the repeating unit with a coordinated guest ion  $\text{M}^{n+}$  of a [12-crown-4] crown ether and a [12-MC-4], [9-MC-3], and [15-MC-5] metallacrown.

The commonly used sum formula introduced by Pecoraro is shown below:<sup>[13]</sup>



In this sum formula,  $M'$  is assigned to the guest metal ion,  $A'$  represents a bound anion,  $M$  is the subscripted element symbol for the ring metal ion,  $X$  is the abbreviation for the heteroatom coordinating the ring metal ions in the repeating unit from the ligand  $L$ , and  $A$  assigned to non-coordinating anions. At present, many different cavities of metallocrowns exist. These are ranging from 9-MC-3 to 12-MC-4 and 60-MC-20, with a diverse range of ligands enabling these ring sizes to be assembled.<sup>[13,14]</sup>

Furthermore, the coordination of diverse guest ions (e.g. alkali, lanthanide, or transition metal ions) can occur *via* the donor atoms inside the ring, yielding both homo- and heterometallic compounds. The family of metallocrowns also includes metallahelicates, metallacoronates, and metallacryptants.<sup>[15-17]</sup>

### 1.1.1. Building blocks of MCs

The schematic structure of an exemplary [12-MC-4] metallocrown is shown in Figure 1. 2. This includes the ligand (black), which is triply-deprotonated salicylhydroxamic acid in the chosen example, ring metal ions (green), and the guest ion (turquoise). The incorporation of many  $3d$  ions as ring metal and guest ions or  $4f$  ions as guest ions requires the presence of co-ligands. These occupy the vacant coordination sites of an octahedral or square-pyramidal coordination sphere. Co-ligands can either coordinate in a linear fashion to the ring metal ions (orange) or in a bridging fashion from a ring metal ion to a guest ion (yellow). Solvent molecules such as water or methanol, coordinating bases such as morpholine or methanolate, or bridging counterions from the metal precursor compound such as acetates can serve as co-ligands.<sup>[13,14]</sup>

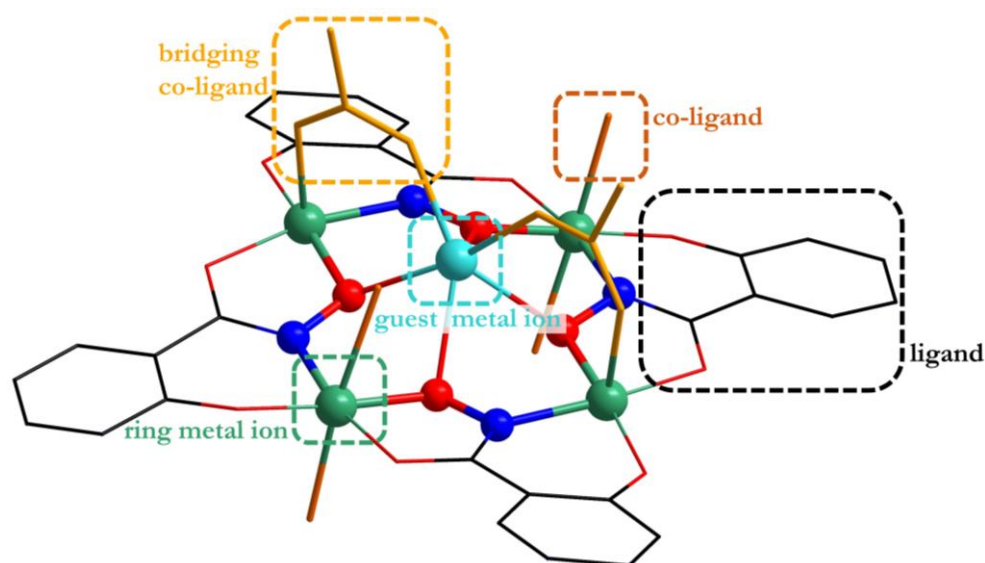


**Figure 1. 2.** Schematic representation of the building blocks of a metallocrown. The boxes outline ligand (black), ring metal ion (green), co-ligand (orange), bridging co-ligand (yellow), and guest ion (turquoise). Color code of atoms: oxygen red, nitrogen blue, carbon black, ring metal ion green, and guest ion (turquoise).

### 1.1.2. Smart choice of the ligands

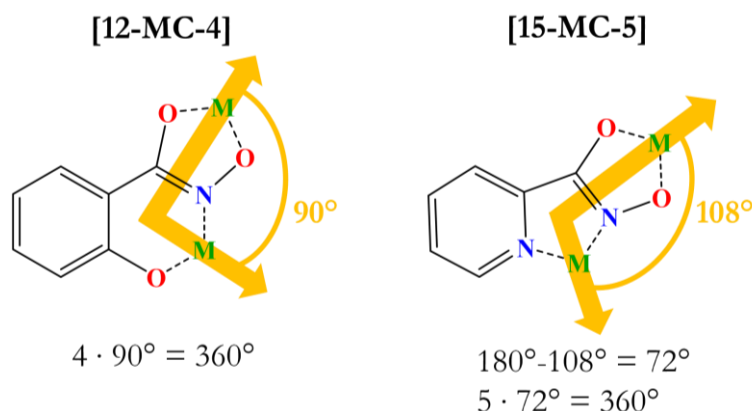
The metallacrown structure is obtained by self-assembly of transition metal ions and appropriate ligands in a controlled fashion.<sup>[18]</sup> In the following, the smart choice of the ligand for this process will be presented. In general, many parameters like the cavity, configuration, connectivity, or magnetic properties of the metallacrown can be tuned by the choice of appropriate ligands. Hydroxamic acids are commonly used ligands for the formation of metallacrowns due to their high affinity towards transition metal ions.<sup>[19]</sup> In nature, especially the iron(III) ion is selectively coordinated by the hydroxamic acid group in siderophores. Here, the water-soluble iron(III) hydroxamic complex is used to seize the limited amount of available iron(III) to the bacteria for bacterial growth. This is necessary because iron(III) ions have low bioavailability because they are often present in the insoluble oxy-hydroxo form at neutral pH values.<sup>[20]</sup>

In particular, salicylhydroxamic acid will be discussed as the ligand of interest for this thesis. This ligand and its derivatives are highly suitable for the purpose to create multinuclear metallacrowns. The  $pK_a$  value of salicylhydroxamic acid for the first deprotonation at the hydroxamic unit is  $pK_{a1} = 7.46$  and the  $pK_s$  value of the deprotonation of the phenolic hydroxide group is  $pK_{a2} = 9.72$ .<sup>[21]</sup> Due to tautomerization mechanism, a hydroxamate is formed. This allows to observe and verify formation of a coordination through the emergence of characteristic bands in the IR spectrum. For this purpose, the energies of the carbonyl band (C=O), the C-N, and the N-O bands are considered, which shift to different energies upon complexation. UV/Vis spectroscopy can also be applied to characterize metallacrown the species based on  $n-\pi^*$  and  $\pi-\pi^*$  transition and can be understood by the change from a carbonyl group (C=O) to an imine (C=N) bond.<sup>[22]</sup>

The presented ligand design also favors the formation and stability of multinuclear complexes by taking advantage of the chelate effect. Through the complexation, two metal ions are forming a five-membered and a six-membered ring (Figure 1. 3). The stability of chelate complexes can be explained both kinetically and thermodynamically. Once the first donor atom of a chelate ligand is coordinated, the second and all next donor atoms are coordinated faster compared to monodentate ligands. This is due to the spatial proximity to the metal center. Besides that, a ligand exchange is kinetically hampered because all bonds between metal and donor atoms of the chelating ligand must be broken before the ligand can dissociate. The thermodynamic stability can be justified by the entropy increase during the formation of the chelate complex.<sup>[23]</sup> Further, the choice of the chelating ligand is particularly important because it can dictate the cavity of the metallacrown in the case of planar *trans*-arrangement.

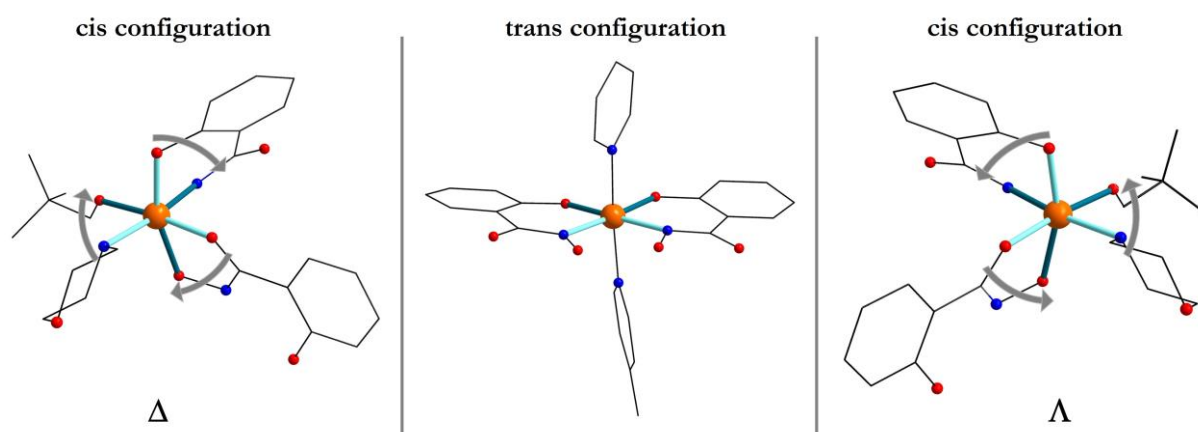
The dependence of the cavity on the binding mode of the ligand is shown in Figure 1. 3 using the examples of salicylhydroxamic acid and 2-pyridinehydroxamic acid. In the case of the triply deprotonated salicylhydroxamic acid, a six-membered ring and a five-membered ring are formed by chelation. When the ligands are arranged in a planar *trans* fashion, the coordination results in an interior angle of  $90^\circ$  between the metal ions as shown in Figure 1. 3 (left).<sup>[13]</sup> If the repeating unit {M-N-O-} is present four times, a closed ring is formed and a [12-MC-4] metallacrown is formed. If the 2-pyridine hydroxamic acid is used two five-membered rings are formed, resulting in an interior angle of  $108^\circ$  between the metal centers. As a result, ring closure does not occur until five repeating units and a [15-MC-5] metallacrown are formed as shown in

Figure 1. 3 (right). Additionally, finetuning of the ligand field is achieved with substituents on the aromatic system which have different electronic and steric properties.<sup>[24]</sup>



**Figure 1. 3.** Representation of the forming of five- and six-membered rings as rationale for planar [12-MC-4] and [15-MC-5] metallacrown formation. Left: A five and a six-membered ring lead to the formation of a [12-MC-4] metallacrown cavity. Right: Two five-membered rings lead to the formation of a [15-MC-5] metallacrown cavity.

A *trans* ligand arrangement in a [12-MC-4] metallacrown is not chiral as shown in Figure 1. 4 (middle). Nevertheless, it is possible to obtain a [9-MC-3] or a [15-MC-5] metallacrown with the salicylhydroxamic acid ligand which is indeed chiral. The stereochemistry of the ring metal ions determines the resulting metallacrown. However, the ligands are not planar in *trans*-position to each other compared to a [12-MC-4] cavity. Therefore, a so-called *cis*-propeller configuration (delta  $\Delta$  in Figure 1. 4 left; or lambda  $\Lambda$  in Figure 1. 4 right) is formed for all or some of the ring metal ions. The coordination of the chelating ligand salicylhydroxamic acid to the metal ion leads to a five-membered chelate ring *via* the iminophenolate moiety and a six-membered chelate ring *via* the hydroxamate group. In the case of a [9-MC-3] cavity, the same chirality for all ring metal ions is a prerequisite. Hence, all ring metal ions must have either  $\Delta\Delta\Delta$  or  $\Lambda\Lambda\Lambda$  chirality.<sup>[25,26]</sup>



**Figure 1. 4.** Schematic representation of the *cis*-propeller configuration of the ligands of a central metal ion (left: delta  $\Delta$ , right: lambda  $\Lambda$ ) and the *trans*-configuration of the ligands of a central metal ion (middle). Color code of atoms: central metal ion orange, oxygen red, nitrogen blue, and carbon black.



### 1.1.3. Guest and ring metal ions

The most commonly used ring metal ions are mid to late first-row  $3d$  transition metal ions including Mn(III),<sup>[9,27–29]</sup> Fe(III),<sup>[8,30,31]</sup> Co(III),<sup>[11,32]</sup> Ni(II),<sup>[33–35]</sup> Cu(II)<sup>[30,36–38]</sup> and Zn(II)<sup>[39–42]</sup>. These different ions account for a variety of properties of metallacrowns in molecular magnetism, catalysis, and luminescence.<sup>[14]</sup> Different numbers of ring metal ions can influence the magnetic behavior of the resulting metallacrown. In most cases, an even number of paramagnetic ring metal ions (e.g. [12-MC-4]) leads to a diamagnetic ground state with antiferromagnetic coupling within the spin centers of the ring metal ions.<sup>[43,44]</sup> However, if metallacrowns consist of an odd number of ring metal ions, a non-zero magnetic moment can be expected (e.g. [15-MC-5]). Complete compensation of the spins is not possible in this case.<sup>[45]</sup>

Furthermore, it is decisive to consider how the ligand coordinates the guest ion. Different possible coordination modes range from in-plane coordination (Figure 1. 5, left) to the formation of half-sandwich (Figure 1. 5, middle) and sandwich metallacrowns (Figure 1. 5, right). The ability to coordinate metal ions out-of-plane can be used to obtain half-sandwich and sandwich compounds.<sup>[9]</sup> Lanthanide ion complexes are commonly used as magnetic resonance imaging contrast agents, luminescent sensors, and for their magnetic properties like single-molecule magnet behavior.<sup>[46]</sup> Combining the properties of  $3d$  transition metal ions in metallacrowns with those of  $4f$  lanthanide ions allows obtaining  $3d-4f$  complex compounds with many exciting characteristics.<sup>[39,47]</sup> The ionic radius of guest ions changes from 73 pm (copper(II), six-coordinated) to 83 pm (manganese(II), high spin.) and 104 pm (terbium(III), eight-coordinated).<sup>[48]</sup> Additionally, lanthanide ions prefer a coordination number  $n > 6$ . Therefore, in a sandwich metallacrown, the two [12-MC-4] ligand units create a distorted antiprismatic coordination sphere and provide eight oxygen donor atoms as coordination partners.<sup>[49,50]</sup> The transition of a [12-MC-4] metallacrown with an in-plane coordination of the copper(II) guest ion to the out-of-plane coordination of manganese(II) and terbium(III) guest ion is shown in Figure 1. 5.

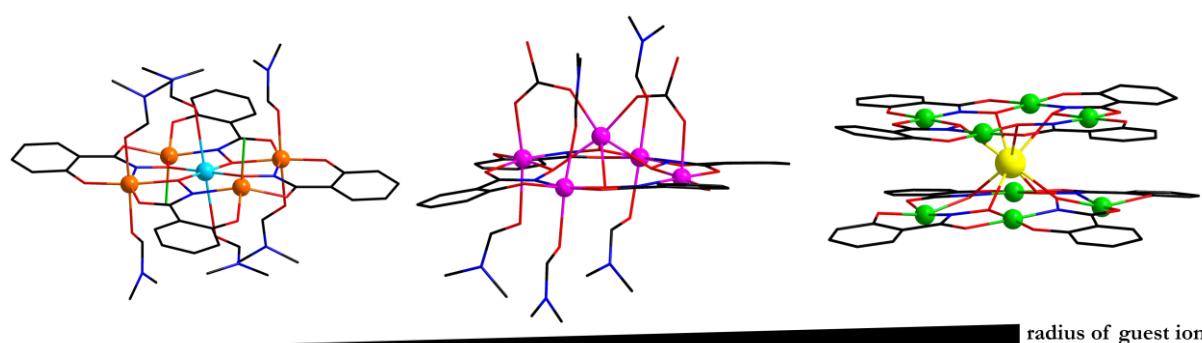


**Figure 1. 5.** Comparison of guest ions in the structural motif for [12-MC-4] metallacrowns. Left: Heterometallic [12-MC-4] metallacrown with copper(II) as guest ion (in-plane) and iron(III) ring metal ions<sup>[50]</sup>. Middle: Mixed valent [12-MC-4] metallacrown with a manganese(II) guest ion (out-of-plane) and manganese(III) ring metal ions. Right: Sandwich [12-MC-4]<sub>2</sub> metallacrown with terbium(III) guest ion (out-of-plane) and nickel(II) as ring metal ions<sup>[50]</sup>. Adapted with changes from reference [30,50]. Color code of atoms: oxygen red, nitrogen blue, carbon black, copper(II) light blue, iron(III) orange, manganese (II/III) purple, nickel(II) light green, and terbium(III) yellow.

In the case of the manganese metallacrown, a half-sandwich structure is achieved while two [12-MC-4] metallacrown units create a sandwich molecule around the terbium(III) ion. Changing from [12-MC-4] to [15-MC-5] cavity the lanthanide ion can be coordinated in-plane again. These different examples show the highly flexible and controllable fashion of the metallacrown formation. One of the first metallacrowns with a [15-MC-5] cavity was reported by Pecoraro and co-workers in 1996.<sup>[35]</sup> This metallacrown contains a neodymium(III) guest ion in an in-plane coordination. In this complex, five copper(II) ring metal ions are coordinated by L- $\alpha$ -amino hydroximates (which is the hydroximate derivative of the corresponding amino acid) ligands to create a chiral cluster.<sup>[35]</sup>

#### 1.1.4. Vacant metallacrowns

Even if no guest ion is coordinated within the metallacrown, a so-called vacant metallacrown can be formed. This class of metal crowns was already reported by the first famous representative, introduced as [VO(salicylhydroximate)(CH<sub>3</sub>OH)]<sub>3</sub> in 1989.<sup>[7]</sup> This metallacrown has a [9-MC-3] cavity containing solely vanadium(V) ions as ring metal ions. Two prominent additional examples are shown in Figure 1. 6. Both metallacrowns do not host a guest ion or molecule in their central cavity. The vacant metallacycle [12-MC<sub>Co(III)N(SH)-4</sub>](py)<sub>8</sub> which was reported by the Rentschler group in 2014 containing cobalt(III) ions shows a tilted orientation of the ligands with different coordination configurations of salicylhydroxamic acid. One cobalt(III) ion shows a planar trans-orientation of the ligands whereas the other three cobalt(III) ions all have a *cis*-propeller configuration. In addition, a reverse of the characteristic metallacrown repeating unit from -N-O- to -O-N- is observed.<sup>[11]</sup> For comparison, the vacant metallacrown containing four copper(II) ions has been reported by Colacio and co-workers in 1999 and is shown in Figure 1. 6 on the right.<sup>[51]</sup>

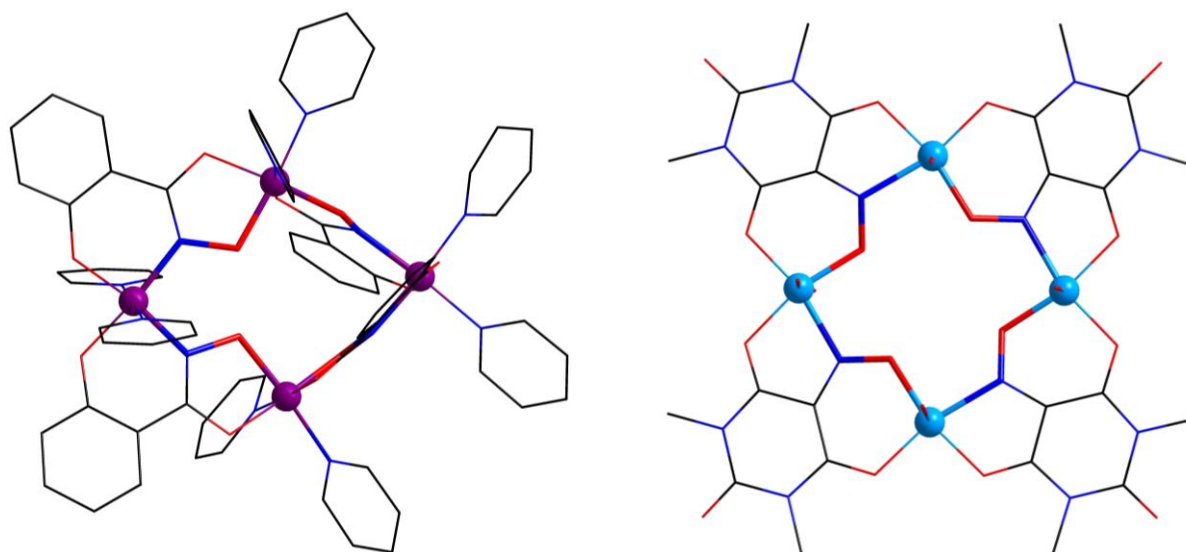


**Figure 1. 6.** Schematic representation of two vacant metallacrowns with a [12-MC-4] cavity. Left: Vacant [12-MC-4] metallacrown with cobalt(II) ions and salicylhydroxamic acid as ligand. Right: Vacant [12-MC-4] metallacrown with copper(II) ions and dimethylvioluric acid as ligand. Adapted with changes from reference [11,51]. Color code of atoms: copper(II) light blue, cobalt(II) purple, oxygen red, nitrogen blue, and carbon black.

The ligand is deprotonated 1,3-dimethylvioluric acid that creates a five and a six-membered ring upon chelating coordination of the copper(II) ions. Strong antiferromagnetic coupling is mediated *via* the N-O-repeating unit. Additionally, a very planar metallacrown is formed due to strict *trans*-orientation of the chelating ligands.

Additionally, azametallacrowns were synthesized containing a repeating unit  $-[M-N-N]_n-$  solely with nitrogen donor atoms.<sup>[52–54]</sup> Multiple examples of homometallic azametallacrowns are reported comprising tetrazole, pyrazole, and triazole ligands have been reported over the past decades.<sup>[55]</sup> Furthermore, if the repeating unit  $-[M-O-N-M-N-O]_n-$  spans the ring of the metallacrown, this is called an inverse metallacrown.<sup>[14]</sup>

### 1.1.5. Properties and application of metallacrowns

The variety of combinable components and the broad range of applicable ligands, co-ligands, ring metal ions, and guest metal ions open a wide field of possible applications for metallacrowns. Possible applications range from catalysis, luminescence to molecular magnetism.<sup>[14]</sup> In the following paragraphs, two representative examples of luminescent metallacrowns will be described to illustrate the manifold applications of metallacrowns. Metallacrowns with a lanthanide(III) ion as the guest ion are preferred candidates to investigate photoemission of lanthanides. At this, chelating ligands such as salicylhydroxamates and co-ligands including bridging benzoates are suitable to serve as energetic antennas for lanthanide ions.<sup>[39,56–58]</sup> Since there is no *f-f* orbital excitation due to the Laporte prohibition, the ligands are utilized to excite a lanthanide(III) ion through an energy transfer.<sup>[49,58,59]</sup> Thus, *3d-4f* metallacrowns containing zinc(II) and various lanthanide(III) ions like lanthanum, terbium, and ytterbium have been reported to show luminescent properties.<sup>[39,60,61]</sup> In 2016, Pecoraro and co-workers reported luminescent metallacrowns containing triply deprotonated salicylhydroxamic acid as ligands and gallium(III) ions.<sup>[57]</sup> In this metallacrown, four gallium(III) ions serve as ring metal ions and lanthanide(III) ions were used as the guest ion. Gallium(III) ions were chosen because they prevent quenching of emission through *d-d* relaxation which is also known from zinc(II) ions. The filled *d*-electron shells of both ions, do not allow *d-d* transitions that are known to quench luminescence of lanthanide ions.<sup>[39]</sup> In 2022, a heterotrimetallic [12-MC-4] metallacrown was reported by Zaleski, Petoud, and co-workers. The metallacrown includes lanthanide(III), aluminum(III), and sodium(I) ions. Here, the same design principles were applied as in the beforementioned metallacrown containing gallium(III) and lanthanide(III) ions. No unpaired electrons in d-orbitals are present. The excitation into ligand-centered orbitals was used to trigger lanthanide emission from the *f-f* transition.<sup>[62,63]</sup> Besides that, the ligand design of the metallacrown is also very suitable to create luminescent complexes, since neither N-H, O-H, or C-H vibrations are present near the luminophoric center, which would also quench the luminescence of the lanthanide(III) ions.<sup>[39]</sup>

Metallacrowns are investigated as building units for coordination polymers, cluster structures, and extended networks. This leads to interesting hybrid materials with large cavities and enlarged reactive surfaces.<sup>[12]</sup>

Intriguing examples are 2D polymers<sup>[36]</sup> or helical structures<sup>[64]</sup>. The connection of multiple metallacrowns was achieved *via* coordination of different guest ions<sup>[37,65]</sup>, linkage of the organic ligands<sup>[66]</sup>, and coordinating groups in the ligand backbone to form a peculiar porous-coordination polymeric architecture.<sup>[67]</sup> This linkage is not the focus of this thesis. For further discussion on this topic, a detailed summary is reported in the chapter “Metallacrown Complexes Reaching the Nanosize Regime” from former group members of the Rentschler group.<sup>[12]</sup>

Metallacrowns are also used in the field of molecular magnetism due to prominent coupling pathways and the versatile exchange of the guest and ring metal ions. The following section gives an overview of metallacrowns with interesting magnetic properties or single-molecule magnet behavior. The first example is the 3*d* heterometallic [12-MC-4] metallacrown which was reported by Happ and Rentschler in 2014.<sup>[30]</sup> It is important to mention that this metallacrown was the only heterometallic metallacrown containing two different 3*d* ions for six years, followed by only one other 3*d* heterometallic metallacrown recently reported by Zaleski and co-workers.<sup>[68]</sup> In the first heterometallic metallacrown, iron(III) ions form the metallacrown framework and deprotonated salicylhydroxamic acid serves as ligand. In addition, a copper(II) guest ion leads to a heterometallic metallacrown. A high spin ground state is observed due to the superior magnetic exchange interactions of the copper(II) ions with the iron(III) ring metal ions compared to the iron(III) ring metal ions among each other. This is called the magnetic director approach. Here, two competing magnetic couplings must be considered. One magnetic coupling is between the guest ion and the ring metal ions. The second coupling describes the magnetic interaction amongst the ring metal ions.<sup>[69]</sup> However, no single-molecule magnet behavior was observed for this metallacrown due to the lack of magnetic anisotropy (see Chapter 1.4.1).

Nevertheless, there are some examples of 3*d* metallacrowns that do show single-molecule magnet (SMM) behavior. Chapter 1.4. gives a detailed overview of compounds and the theoretical background of single-molecule magnet behavior. Therefore, only few examples of metallacrowns with this single-molecule magnet behavior are presented in the following. One of the very first metallacrowns from the year 1989 ([Mn(II)(OAc)<sub>2</sub>[12-MC<sub>Mn(III)N(SH)</sub>-4](DMF)<sub>6</sub>)]<sup>[9]</sup> was magnetically characterized over 20 years later to show single-molecule magnet behavior.<sup>[28]</sup> An example of 3*d* ions with single-molecule magnet behavior was reported by Tong and co-workers by using a [15-MC-5] cavity.<sup>[70]</sup> Here, five copper(II) ions are coordinated by quinaldichydroxamates as ring metal ions while europium(III) acts as a guest ion. Here, spins of the antiferromagnetically coupled copper(II) ions cannot cancel each other out completely. Thus, an  $S = 1/2$  spin ground state is achieved most likely leading to single-molecule magnet properties.<sup>[70]</sup> Europium(III) has an angular momentum quantum number  $J = 0$  as the ground state and therefore, will not show single-ion magnet behavior.<sup>[71]</sup>

The metallacrowns scaffold was also used as a coordination environment for anisotropic lanthanide(III) ions. In the field of single-ion magnets, these metallacrowns were well established as an important research area in recent years.<sup>[50,72,73]</sup> Different cavities already proved to provide an appropriate coordination environment for several lanthanide(III) ions. Most prominent examples are [15-MC-5] and [12-MC-4]

metallacrowns.<sup>[70,74,75]</sup> A [12-MC<sub>Zn(II)</sub>-4] metallacrown with ytterbium(III) guest ions in a half-sandwich structure is reported by Tong and co-workers in 2015.<sup>[72]</sup> This metallacrown showed a single-molecule magnet behavior and an energy barrier of  $U_{\text{eff}} \approx 16 \text{ cm}^{-1}$  under a 600 Oe dc field (see Figure 1. 7 a). Rauguth and Rentschler reported a [12-MC<sub>Ni(II)</sub>-4]<sub>2</sub> sandwich metallacrown containing terbium(III) ions with a much higher energy barrier of  $U_{\text{eff}} \approx 241 \text{ cm}^{-1}$  under zero field and up to  $407 \text{ cm}^{-1}$  under 3200 Oe (see Figure 1. 7 b).<sup>[50]</sup> Both of these metallacrowns create an antiprismatic coordination symmetry for the lanthanide ion suppressing quantum tunneling (see Chapter 1.4.1.). These  $3d-4f$  metallacrown-based complexes impressively demonstrate the importance of the ligand field in the research fields of molecular and single-molecule magnetism.

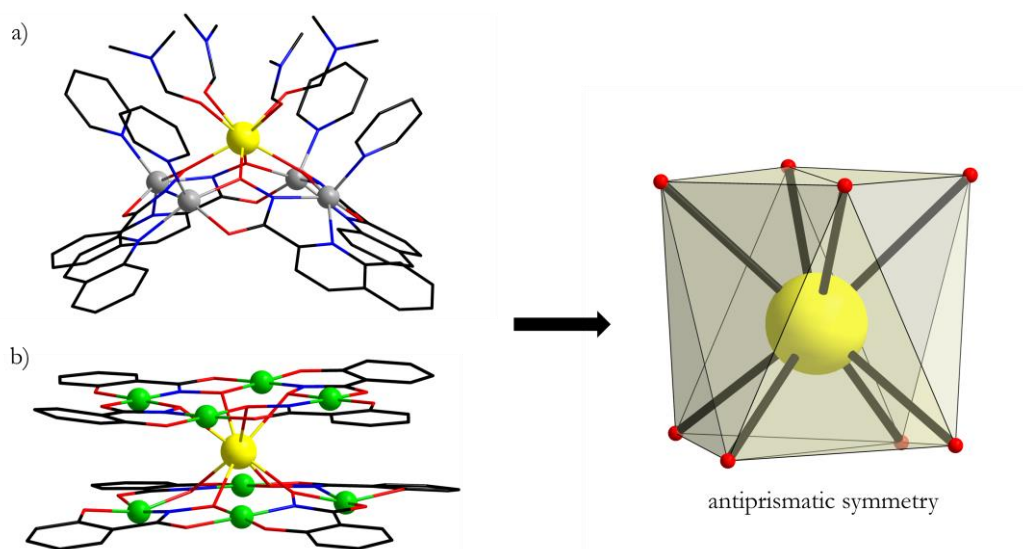


**Figure 1. 7.** Illustration of a) half-sandwich metallacrown; b) sandwich metallacrown and their common antiprismatic coordination symmetry.<sup>[50,72]</sup> Color code of atoms: zinc(II) grey, lanthanide(III) ion yellow, nickel (II) light green, oxygen red, nitrogen blue, and carbon black. The graphics are adapted from references [50] and [72].

In general, metallacrowns can be used for a variety of applications due to the flexibility and variable use of influence parameters. Due to the numerous interesting properties in the fields of molecular magnetism, catalysis, and photoluminescence, metallacrown compounds show a broad application potential.<sup>[14]</sup>

## 1.2. Chromium ions

Chromium and chromium ions have a wide range of applications in lasers, as pigments, catalysts, steel additives, and many more.<sup>[76]</sup> This  $3d$  transition metal is often present in the oxidation states of +II, +III, and +VI.<sup>[76]</sup> Chromium(III) ions have the most stable oxidation state and exhibit a  $3d^3$  electron configuration, which means that all  $t_{2g}$  orbitals are half occupied in an octahedral ligand field.<sup>[48]</sup> Therefore, almost exclusively six-coordinated chromium(III) complexes exist, which prefer an octahedral coordination geometry and thus exhibit a large ligand field stabilization energy. The coordination chemistry of chromium(III) ions exhibits various scientific publications, e.g. on structural characterization or reactivity. To illustrate the potential, two examples of chromium catalysts will be presented in the following.

Chromium oxide complexes, most prominently the Philips catalyst, are used in organic syntheses for example to produce polyethylene.<sup>[77]</sup> Although almost the majority of high-density polyethylene is nowadays produced under use of this catalyst, the nature and the oxidation status of the active chromium species and the catalysis mechanism, have not yet been finally clarified. This chromium oxide catalyst is adsorbed onto wide pore silica and activated *via* calcination and used in industry for almost 70 years.<sup>[78,79]</sup>

The second example of chromium in catalysis is a nickel-catalyzed and chromium-mediated reaction which is called the Nozaki–Hiyama–Kishi reaction.<sup>[80,81]</sup> In this reaction, a secondary allyl or vinyl alcohol is formed by reacting an aldehyde with allyl or vinyl halides under mediation of anhydrous chromium(II) chloride. Nickel salts in small equivalents were found to catalyze the formation of the C–Cr bond. The reaction is well suited for applications in natural product chemistry and total syntheses of complex target molecules due to its high chemoselectivity.<sup>[82]</sup>

Due to the  $3d^3$  electron configuration, chromium(III) ions are relatively kinetically inert concerning substitution and rearrangement of ligands,<sup>[83]</sup> which complicates the stepwise synthesis of polynuclear chromium(III) complexes.<sup>[84]</sup> However, once a complex is formed, this kinetic inertness prevents metal ion exchanges, resulting in a stable metallocrown. These ion exchange processes should be prevented especially for heterometallic multinuclear complexes. Furthermore, chromium(III) ions are paramagnetic due to the three unpaired electrons.<sup>[85]</sup> Thus, magnetic exchange interactions can occur in multinuclear chromium(III) complexes, resulting in antiferromagnetic or ferromagnetic couplings.

Chromium(III) ions are often used as an active component in applications utilizing luminescence. In daily life, luminescence is required for lasers, biological markers, computer screens, or lamps.<sup>[86,87]</sup> In luminescent materials, an absorption of electromagnetic radiation (visible and UV light) through an excitation from the ground state  $S_0$  into an excited singlet state  $S_1^*$  is achieved. The most prominent example is the ruby laser which was developed in 1960 and led to the first milestone in the field of commercial laser applications.<sup>[87]</sup> Ruby is a corundum doped with 0.05 % chromium(III) ions, creating a distorted octahedral environment for chromium(III). However, the ruby laser has lost its importance nowadays, since its efficiency is comparatively low, and the wavelength is also accessible by other lasers. Therefore, much six-coordinate chromium(III) complexes are reported that show near-infrared (NIR) phosphorescence with high quantum

yields.<sup>[88]</sup> The Tanabe-Sugano diagram for  $d^3$  electron configurations shows the possible energy levels in octahedral field, which are described by term symbols. Based on the selection rules, excitation to the  ${}^4T_2$  and  ${}^4T_1$  states occurs in chromium(III) complexes (see Jablonski diagram, Figure 1. 8). From these states, non-radiative relaxation processes like intersystem crossing (ISC) can lead to a very fast population of the doublet states  ${}^2T_1$  and  ${}^2E$ .<sup>[89]</sup> If a back-ISC occurs a delayed fluorescence is observed. From the doublet states  ${}^2T_1$  and  ${}^2E$  phosphorescence occurs with sharp dual emission due to the spin reversal to the  ${}^4A_2$  ground state.<sup>[90]</sup> Sharp emission bands of chromium(III) complexes are present because the  ${}^2E$  state and the  ${}^4A_2$  ground state belong to the same  $(t_{2g})^3(e_g)^0$  configuration and have the same dependence on ligand field strength, as shown in a Tanabe-Sugano diagram by the parallel states. Therefore, only one spin has to “flip” its orientation. When rigid ligands are used, the energy from the excited  ${}^4T_2$  state of chromium(III) ions is less likely to transfer to the ground state by nonradiative molecular vibration, and the quantum efficiency increases.<sup>[88]</sup>

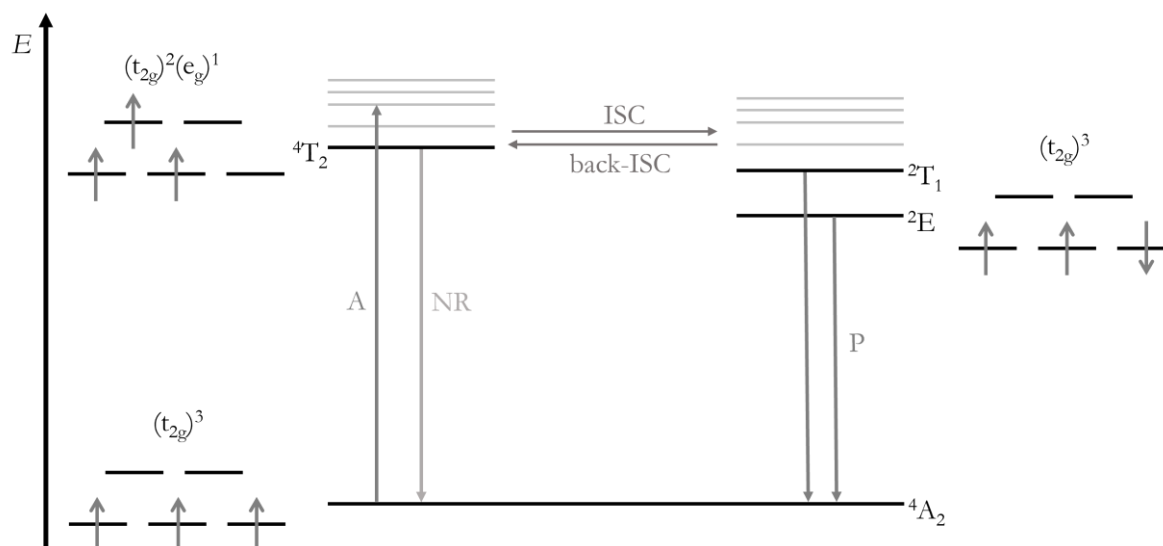


**Figure 1. 8.** Jablonski diagram of the electron configurations of chromium(III) ions in an octahedral coordination sphere including microstates.

According to the Laporte rule, only electron transitions of compounds with inversion centers are allowed while changing the parity. Thus, ligand field transitions such as  $d-d$  or  $f-f$ -transitions are generally forbidden. Due to the spin selection rule, the change of spin multiplicity is forbidden during a transition.<sup>[91]</sup> However, deviations from ideal geometries and spin-orbit coupling in transition metals lead to a partial overruling.<sup>[83]</sup> Besides that, another possible relaxation process can occur under certain circumstances: If a so-called sensitizer is present at a suitable distance from the acceptor, an energy transfer can occur. This energy transfer is a non-radiative process from an excited state of the sensitizer  $S_1$  to an excited state of the acceptor  $A_1^*$ . From the excited state of the acceptor, the process follows the same path of relaxation as mentioned above.<sup>[92]</sup>

Nowadays, chromium(III) ions still serve as sensitizers in YAG solid-state lasers (abbreviation of neodymium-doped Yttrium-Aluminum-Garnet laser), where chromium ions absorb energy and transfer it to the neodymium(III) ions. Here, the energy transfer is occurring from an excited state of the chromium(III) ion to an excited state of the neodymium(III) ions. Subsequently, laser emission from the excited state of the neodymium(III) ions to the ground state of the neodymium(III) ions can be observed.<sup>[93]</sup> The use of chromium(III) ions as sensitizers has been reported in the literature not only for neodymium(III) ions but also for erbium(III) and thulium(III) ions in solid-state devices to produce near-infrared emission.<sup>[94]</sup>

### 1.2.1. Multinuclear molecules with chromium(III) ions

In 1908, the multinuclear compound class of trinuclear chromium clusters with bridging acetate unit was described for the first time.<sup>[95]</sup> Later, the structure of the  $\mu_3$ -oxo-bridged trinuclear metal carboxylates containing chromium ions  $[\text{Cr}_3(\text{III})(\mu_3\text{-O})(\text{RCOO})_6\text{L}_3]^+$  was revealed by X-ray diffraction and extensively characterized in literature since the 1980s.<sup>[96]</sup> In this structural motive mostly oxides occur as the central bridging anions. Various bridging ligands RCOO extend the versatile application range of these molecules. The organic group R can be modified e.g., with H-,  $\text{CH}_3$ -, *tert*-butyl- or aromatic substituents. Additionally, the peripheral bond ligands L are usually coordinating solvent molecules like water, alcohols, pyridine, or bond counter ions like fluorides as shown in Figure 1. <sup>9[96]</sup>

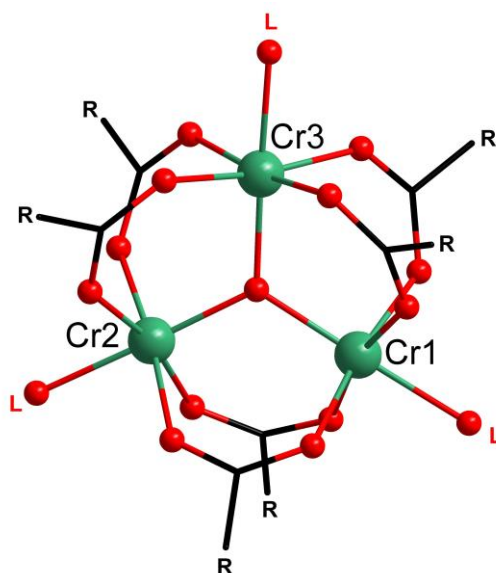


**Figure 1. 9.** Schematic representation of  $\mu_3$ -oxo-bridged trinuclear metal carboxylate containing chromium(III) ions  $[\text{Cr}_3(\text{III})(\mu_3\text{-O})(\text{RCOO})_6\text{L}_3]^+$  (where R = organic group, L = peripheral bond ligand).<sup>[97]</sup> Hydrogen atoms counter ions and solvent molecules are omitted for clarity. Adapted from source [97].



These molecules are perfect candidates to study magnetic metal-metal interactions in clusters with spin frustration due to the triangle-orientation of chromium ions.<sup>[98–100]</sup> The antiferromagnetic exchange interactions *via* a superexchange highly depend on the Cr-O-Cr angles. By definition, one would apply the following Equation 1 of the Hamiltonian  $\hat{H}$  to determine the exchange interactions  $J$  of the chromium ions with the spin  $S$ .

$$\hat{H} = -2J(S_1 \cdot S_2 + S_2 \cdot S_3 + S_3 \cdot S_1) \quad (1)$$

However, a model with two or three different coupling constants  $J$  is applied to determine the strength of magnetic exchange interactions in many cases due to distortion of the molecules.<sup>[101]</sup> Such clusters are often used as homogenous catalysts for oxidation reactions or as reactants for higher nuclearity clusters.<sup>[102]</sup>

Another very prominent representative of multinuclear chromium complexes is the eight-membered and ring-shaped chromium(III) complex  $\{\text{Cr}_8\}$ .<sup>[103]</sup> This so-called chromium wheel has the stoichiometric composition of  $[\text{Cr}_8\text{F}_8(\text{piv})_{16}]\cdot\text{Bu}_2\text{NH}$  and is shown in Figure 1. 10 on the left side.<sup>[104]</sup> Chromic wheels can be synthesized by the conventional method of refluxing boiling solvents or solvothermal synthesis. The metal ions are  $\mu_2$ -bridged by multiple pivalate ligands and are additionally coordinated and connected by fluoride ions.<sup>[105]</sup> Altering the reaction conditions allow different reaction pathways, which enables targeted manipulation of the reaction kinetics, and thus the ring size of the synthesized complex. The spin ground state of these chromic wheels is  $S = 0$  due to antiferromagnetic coupling of the even number of eight chromium(III) ions.<sup>[105]</sup> However, heterometallic compounds  $\{\text{Cr}_7\text{M}\}$  can be synthesized to modify the magnetic spin ground state. The stoichiometric addition of a metal ion M with the oxidation state +II allows the substitution of one chromium(III) ion in the ring. Some examples of heterometallic chromium wheels with Mn, Fe, Co, Ni, and Zn ions have been reported previously. Despite antiferromagnetic coupling, the spins of different transition metals cannot compensate each other completely. To achieve a spin frustration with interesting magnetic properties, a chromium wheel with an odd number of chromium(III) ions was reported by Winpenny and co-workers in 2016.<sup>[45]</sup> In this case, the complete canceling of the spin  $S$  is also not possible. These complexes can be synthesized by templating the ammonium cation and addition of diisopropylamine. As expected, then, a spin ground state of  $S = 3/2$  is detected.

Another example of a ring-shaped molecule with antiferromagnetic exchange interactions of chromium(III) ions was reported by Liao and co-workers in 2011. This aza-[18-MC-6] shows a spin ground state of  $S = 0$  and was synthesized by hydrothermal synthesis. The antiferromagnetic exchange occurs *via* the Cr-N-N-Cr torsion angle of almost  $180^\circ$  (see Figure 1. 10, right side).<sup>[53]</sup>

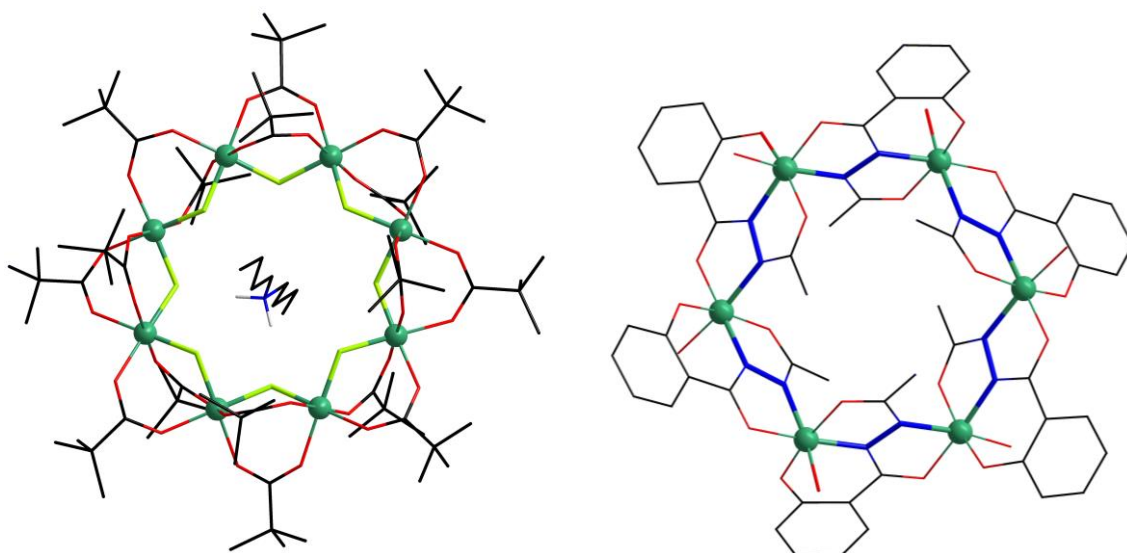


**Figure 1.10.** Left: Structure of the chromic wheel  $\{Cr_8\}$  adapted from source [104]; Right: Aza-[18-MC-6] metallacrown adapted from source [53]. Color code of atoms: chromium(III) ions green, oxygen red, nitrogen blue, carbon black, and fluoride light green.

Both examples show that chromium(III) complexes are not suitable for single-molecule magnet behavior and corresponding applications because of the following reasons: Chromium(III) ions have an isotropic electron distribution and show strong antiferromagnetic couplings in multinuclear complexes. If an application as a single-molecule magnet is desired, an anisotropic ion has to be added. Thus, only clusters with both chromium(III) and dysprosium(III) ions have been described in literature where single-molecule magnetic behavior has been observed.<sup>[106–108]</sup> Murray and co-workers reported in 2013 a dysprosium(III) dimer in which the lanthanide(III) ions are bridged *via* organic ligands and chromium(III) ions. Ferromagnetic exchange interactions take place between the lanthanide(III) ions as they interact antiferromagnetically with the chromium(III) ions. The chromium(III) ions in these complexes enable ferromagnetic exchange interactions of the dysprosium(III) ions and enhance the single-molecule magnetic behavior.<sup>[109]</sup>

However, post-synthetic modification of the  $\{Cr_7Ni\}$  wheels was reported to create entangled pairs of qubits that are connected *via* a gate. This gate is a redox switchable  $\{Ru_2Co\}$  triangle and connects two of the pyridine functionalized heterometallic  $\{Cr_7Ni-O_2C-py\}$  wheels which represent the qubits. The pyridine functionalized  $\{Ru_2Co\}$  triangle shows a similar structure to the famous  $Cr_3O$  triangle family which was previously discussed. The addition of terminal pyridine groups to both compounds allows a linkage of  $[\{Cr_7Ni-O_2C-py\} \rightarrow [Ru^{III}_2Co^{II}O(tert-BuCO_2)_6(py)]^? \leftarrow \{Cr_7Ni-O_2C-py\}]$ .<sup>[110]</sup> This supramolecular design strategy for the construction of two-qubits assemblies represents another step towards the application of molecular compounds for tunable spintronic devices.

### 1.3. Solvothermal synthesis

The large majority of paramagnetic polynuclear complexes are synthesized by so-called conventional methods of coordination chemistry. Thereby, metal salts and bridging and/or terminal ligands react in a common solvent at temperatures dictated by the boiling point of this solvent at atmospheric pressure. Although this method has been very successful in synthesizing an astonishing number of molecular compounds it can hardly be applied to kinetic inert metal ions.<sup>[111]</sup>

Generally, in solvothermal synthesis, the reaction solution is heated in sealed vessels. The used temperatures are higher than the boiling points of the used solvents under autogenous pressure. Under these conditions, enhanced diffusion of the chemical components is achieved due to the lower viscosity of the solvents. Additionally, the solubility of the reactants can be altered. This is the case in the hydrothermal synthesis using water as the solvent which leads to a change in the dielectric constant at different temperatures. Therefore, compounds can dissolve and react that are insoluble under ambient conditions.<sup>[111]</sup> In addition, this method enables the variation of different kinds of reaction parameters e.g. solvents, metal precursor salts, temperatures, and time of the reaction can be changed and adjusted very easily.<sup>[112]</sup> Another advantage is the possibility to grow single crystals under elevated pressure and temperature regimes with slow cooling rates. This method of hydrothermal growth is used in production of SiO<sub>2</sub> crystals on an industrial scale.<sup>[113]</sup>

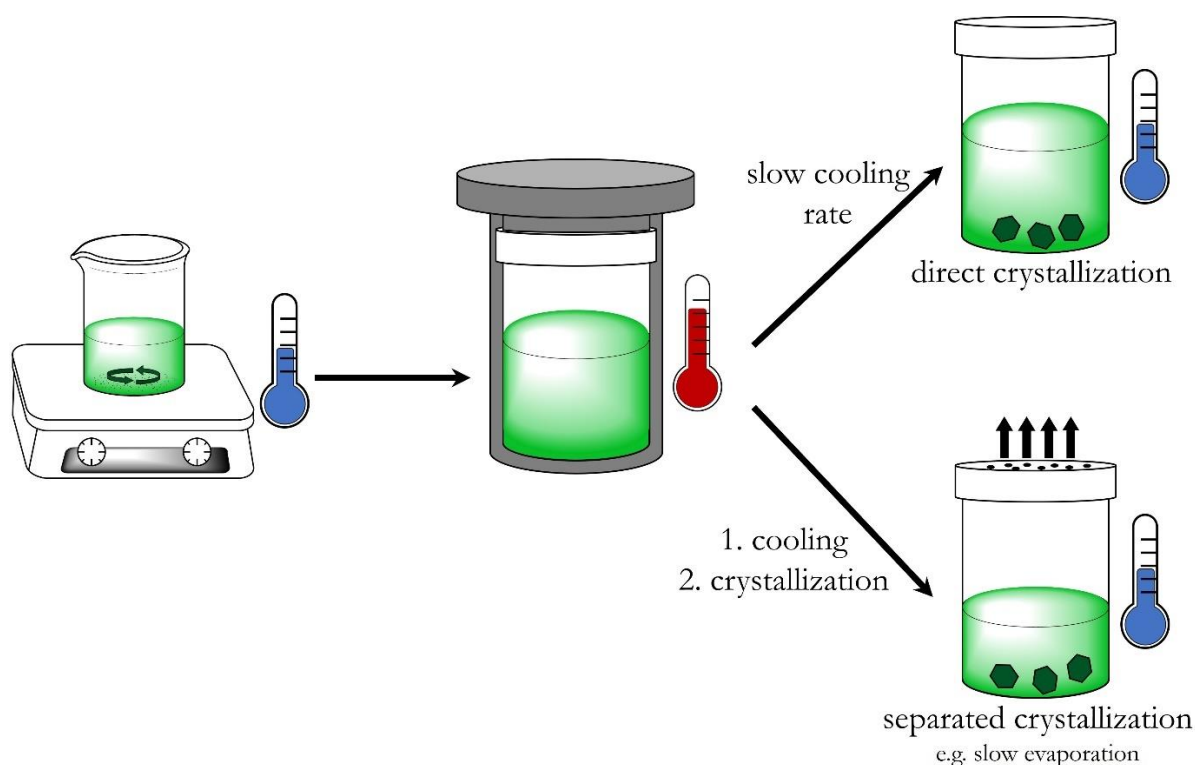


**Figure 1. 11.** Schematic representation of the synthesis steps utilizing the solvothermal route. Left: All reactants are dissolved or suspended in an appropriate solvent at room temperature; Middle: The reaction in an autoclave with sealed vessels is performed at high temperatures; Right: Slow cooling rate leads directly to crystallization of the product (top), cooling of the reaction solution and separated crystallization step of the product (bottom).

The synthesis steps utilizing the solvothermal synthesis route are schematically shown in Figure 1. 11. Firstly, all reactants are dissolved or suspended in an appropriate solvent at room temperature (left). Then,

the reaction is transferred and heated in an autoclave with a sealed vessel. Afterwards, two possible ways to grow crystals are depicted. In the top of Figure 1. 11, a slow cooling rate leads directly to the crystallization of the product. In the lower part of Figure 1. 11, the cooling of the reaction solution is the first step followed by a separated crystallization step of the product. This method can be used if no crystals are obtained *via* the route. Typical crystallization methods include slow evaporation of the solvent and layering or diffusion of solvents with different polarities.

Solvothermal syntheses are often used to prepare inorganic compounds with microporous networks and low-dimensional chalcogenide-based substructures or metal nanocrystals.<sup>[112]</sup> Recently, an increasing number of examples of solvothermal synthesis for preparation of molecular compounds is reported.<sup>[114–116]</sup> Especially, chromium(III) or cobalt(II) ions require much harsher synthetic conditions to form multinuclear complexes due to the kinetic inertness. Further, solvothermal synthesis is often used to directly crystallize the product by applying very low cooling rates.<sup>[114,115]</sup> The heterometallic complex  $[\text{Ni}(\text{II})_6\text{Cr}(\text{HL}_{zw})_6(\text{HL})_6]\text{Cl}_3$  was reported by Milios and co-workers in 2018 with an amidoxime ligand HL, in which six bridged nickel(II) ions form a ring and a chromium(III) ion is coordinated by six oxygen atoms in the center of the ring. Here, separation of crystallization after cooling of the reaction solution is used to obtain single crystals.<sup>[116]</sup> The chromium(III) compounds prepared in this work and discussed in Chapter 4 will use solvothermal synthesis preparation and crystallization methods.

## 1.4. Single-molecule magnets - SMMs

In 1993, Sessoli and co-workers described the magnetic properties of the first single-molecule magnet with the sum formula  $[\text{Mn}_{12}\text{O}_{12}(\text{O}_2\text{CMe})_{16}(\text{H}_2\text{O})_4]$ .<sup>[117]</sup> The structure of the twelve-core manganese acetate complex (abbreviated as  $[\text{Mn}_{12}\text{OAc}]$ ) exhibits slow relaxation of magnetization, shows hysteretic behavior at low temperatures and features a spin ground state of  $S = 10$ . Thus, this complex can be identified as a single-molecule magnet. This breakthrough led to many publications of complexes containing transition metal ions or lanthanide ions that exhibited single-molecule magnetic behavior. A new field of coordination chemistry containing single-molecule magnet ions was established.<sup>[118]</sup>

Then, the possibility to develop a new kind of storage and data devices was quickly identified by utilizing the bistability of single-molecule magnets.<sup>[119]</sup> Due to this behavior, high density data storages, quantum computing and spintronic devices are potential future areas of application.<sup>[120–122]</sup> These devices with the same memory effect could drastically evoke a change from solid-state data storage to molecules that are applied on a processable surface. Therefore, these molecules have to be able to maintain their magnetization for a very long time combined with a slow relaxation of the magnetization.<sup>[123]</sup> In the optimal case, the relaxation of the magnetization occurs in a practical time scale of several years. In contrast to the solid-state devices used nowadays, single molecules are magnetized and therefore do not possess several magnetic domains with a significant number of magnetic moments. The stored information in the binary code is corresponding to the direction of the magnetization in these domains of the solid-state devices.<sup>[119]</sup> In comparison, SMMs could represent binary number switches with a single molecule enhancing drastically data storage density and computing power. For future data storage options, one has to consider a vast amount of electronic data. Miniaturization of data storage is necessary and seen in the development of devices like smartphones. This intriguing magnetic behavior and potential applications in high-density data storage makes single-molecule magnets excellent building blocks for this purpose. This multi-disciplinary area of research includes the discovery of new synthesis strategies to enhance the SMM behavior, magnetic characterization methods of bulk and surface properties, and surface deposition techniques.<sup>[124]</sup>

The subject of current research is the improvement and development of new coordination compounds that enable the miniaturization of data storage through their properties as single-molecule magnets. Spin orientations must be specifically induced for this purpose by an applied magnetic field. For processing and storing data, suitable technology for data processing (to read them out) must be developed. At a temperature of 2 K, the magnetization of the  $[\text{Mn}_{12}\text{OAc}]$  complex can be maintained for several months. The cluster contains four manganese(IV) and eight manganese(III) ions which are ferromagnetically coupled within the same oxidation state. A dominant antiferromagnetic coupling between manganese(IV) and manganese(III) ions leads to a spin ground state  $S = 10$ . Zero field splitting (ZFS) is causing 21 separated sublevels ( $M_S = 2S + 1$ ). This splitting of the ground state is crucially dependent on axial anisotropy  $D$  and the rhombic/transverse parameter  $E$ . The Hamiltonian  $\hat{H}_{\text{ZFS}}$  for the zero-field splitting is shown in Equation 2 with regards to the cartesian spin projection operators  $\hat{S}_{xyz}$ .

$$\hat{H}_{\text{ZFS}} = D \left[ \hat{S}_z^2 - \frac{S(S+1)}{3} \right] + E(\hat{S}_x^2 - \hat{S}_y^2) \quad (2)$$

Then, two energetically degenerate spin ground states with a preferred magnetic orientation of the spins are obtained.<sup>[124]</sup>

There are several ways to evaluate the SMM properties of a compound. The blocking temperature  $T_B$  specifies the temperature below the magnetization is maintained for at least 100s. More popular, however, is the specification of the effective energy barrier  $U$ , which must be exceeded to reverse the magnetization.<sup>[125]</sup> A high value of  $U$  promises long preservation of magnetization even at higher operating temperatures. Maximizing the energy barrier is therefore a central goal of the research community. The magnitude of the energy barrier  $U$  depends on the absolute value of magnetic anisotropy  $|D|$  and the total spin  $S$  of the molecule.

$$U = |D| \cdot S^2 \quad (3)$$

Equation 4 is used for half integer spin systems.

$$U = |D| \cdot \left( S^2 - \frac{1}{4} \right) \quad (4)$$

The double-well potential for the  $[\text{Mn}_{12}\text{OAc}]$  complex is shown in Figure 1. 12 and the possible relaxation processes for a classic SMM are discussed in the following.

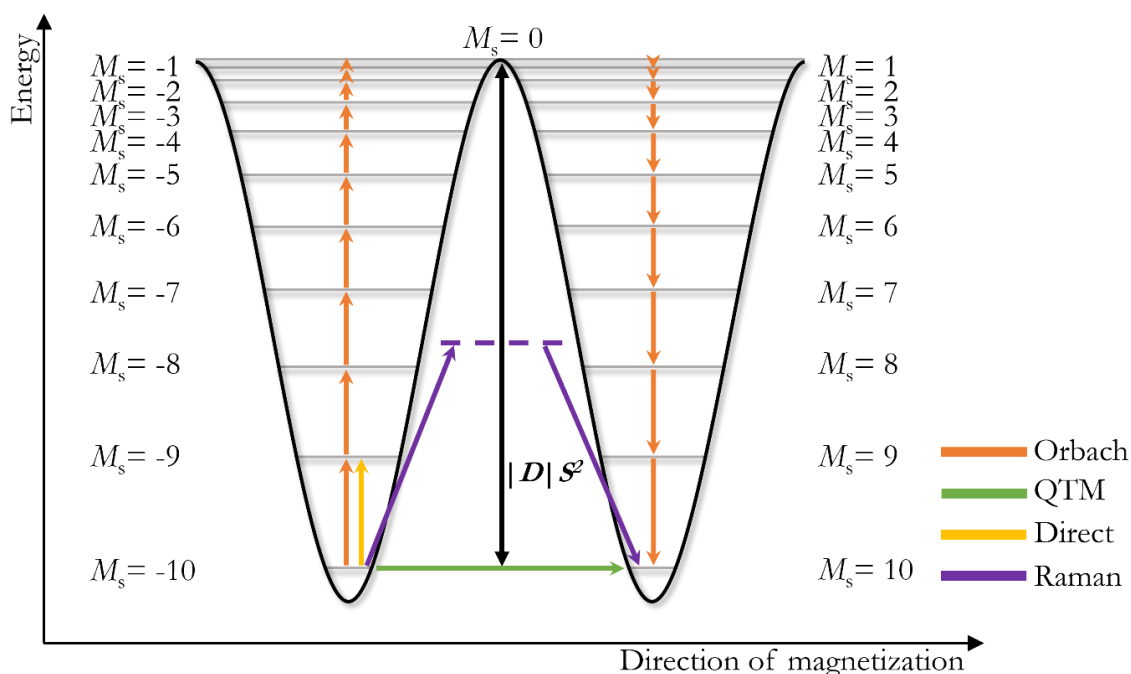


**Figure 1. 12.** Energy levels from  $M_s = \pm 10$  to  $M_s = 0$  in dependence on the direction of magnetization creating the double-well potential. Different relaxation mechanisms are shown: Orbach relaxation orange, quantum tunneling (QTM) green, direct relaxation yellow, and Raman relaxation purple.

If the axial anisotropy is much higher than the rhombic anisotropy ( $|D| \gg |E|$ ), a molecule can favor the orientation of the magnetic moment in two ways. If the axial anisotropy along a single axis is preferred, then  $D < 0$ , and the high  $|M_S|$  level has the lowest energy. In this regard, an easy z-axis is present. This case is observed for the  $[\text{Mn}_{12}\text{OAc}]$  cluster in Figure 1. 12. At the lowest energy  $M_S = 10$  most magnetic moment is ordered along the z-axis, while an easy xy-plane orientation is occurring in the  $M_S = 0$  state. An inversed oriented double-well potential is observed if  $D > 0$ . Conventionally an easy xy-plane is given. Then, the ground state would be  $M_S = 0$ .

In the following, the different relaxation processes are separately discussed. In general, these relaxations are caused by an interaction of the molecule with the surrounding environment. In this interaction, a phonon with the energy of the difference between two  $M_S$  states is absorbed or emitted by the molecule. Phonons are quantized lattice vibrations that lead to a distortion of the molecular geometry. This relaxation pathway does not apply to the quantum tunneling of magnetization (QTM), since it is a purely quantum mechanical effect.

### Orbach relaxation

In an Orbach relaxation, all the excited higher energy levels must be thermally overcome. An excitation to a higher energy state is caused by the absorption of a phonon. Only a spin-phonon transition of  $\Delta M_S = \pm 1$  will occur. Once the  $M_S = 0$  state is reached, the system relaxes to a lower  $M_S$  state by releasing a phonon to the crystal lattice. This process is strongly dependent on temperature but not on the applied field. This process primarily takes place as the relaxation pathway  $\tau_{\text{Or}}^{-1}$  when only a very small energy barrier is obtained. In contrast, for compounds with a very high energy barrier, this process occurs only at high temperatures.<sup>[126]</sup>

$$\tau_{\text{Or}}^{-1} = \tau_0^{-1} \cdot e^{\frac{-U_{\text{eff}}}{k_B T}} \quad (5)$$

### Quantum tunneling (QTM)

At very low temperatures, most of the SMMs show a temperature-independent relaxation time  $\tau_{\text{QT}}^{-1}$ . However, this cannot be explained by the absorption of phonons since no suitable amount of energy is available. The relaxation processes at these temperatures can be explained by the concept of quantum mechanics. Here, a reversal of the magnetization is achieved by tunneling between two energetically degenerated  $M_S$  states. The energy levels of the  $M_S$  states can be manipulated, by applying a small magnetic field  $H$ . Therefore, this relaxation path can be suppressed.<sup>[126]</sup> In Kramers ions, a transition of this type is forbidden. Though, quantum tunneling can be caused by dipolar interactions or transverse anisotropy which results in the removal of the degeneracy.<sup>[71]</sup> The variables  $B$  and  $F$  are empirical.

$$\tau_{\text{QT}}^{-1} = \frac{B}{1 + F \cdot H^2} \quad (6)$$

### Direct relaxation

In this mechanism, a phonon from the crystal lattice is absorbed by the metal ion. Then a transition to a new  $M_S$  state takes place. This transition occurs without the occupation of a transition state i.e., a direct path. This process depends on the temperature  $T$  and an applied magnetic field  $H$ . Without an additional applied magnetic field, this process does not occur. Often, only a small magnetic field is applied to suppress quantum tunneling of the magnetization, which however may be already too high to ignore a direct process. Similar to the relaxation of the Raman mechanism, this mechanism also allows bypassing the energy barrier  $U$  where no real intermediate state is occupied.

$$\tau_D^{-1} = A_1 \cdot H^4 \cdot T + A_2 \cdot H^4 \cdot T \quad (7)$$

### Raman relaxation

In the Raman process, a phonon of higher energy is absorbed, leading to excitation from the  $M_S$  state to a virtual state. By emitting this phonon, the respective spin state of the other side of the double-well potential can be reached. The absorbed energy does not correspond to a real state, but a superposition of multiple lattice oscillations. This virtual state can lie below the  $M_S$  state with the highest energy. In the above-shown example in Figure 1. 12, this would be the  $M_S = 0$  state. Thus, the relaxation does not have to overcome the energy barrier. Therefore, phonons of lower energies can be absorbed or emitted. In comparison to the Orbach process, no  $M_S$  state is occupied in this process. The variable  $C$  corresponds to the probability of excitation.

$$\tau_R^{-1} = C \cdot T^n \quad (8)$$

The following Equation 9 summarizes the four relaxation processes of the relaxation rate  $\tau^{-1}$ :

$$\tau^{-1} = \tau_0^{-1} \cdot e^{-\frac{U_{\text{eff}}}{kT}} + \frac{B}{1 + F \cdot H^2} + A_1 \cdot H^4 \cdot T + A_2 \cdot H^4 \cdot T + C \cdot T^n \quad (9)$$

The important influence parameters on the relaxation rate  $\tau^{-1}$  and therefore the performance as a single-molecule magnet are again shown in Equation 9. It is important to note that at low temperatures quantum tunneling can be suppressed by applying a small, applied field. However, thereby, the relaxation is increased via a direct mechanism. Therefore, a compromise needs to be found to achieve the best evaluation of the magnetic data. With a large applied magnetic field, the relaxation becomes faster by the direct mechanism. However, with increasing temperature, the Raman mechanism becomes more important. Orbach relaxation is dominant at very high temperatures. This relaxation is important for the determination of the effective energy barrier.



### 1.4.1. Approach to increase the energy barrier

After the discovery of the single-molecule magnet behavior in the  $[\text{Mn}_{12}\text{OAc}]$  cluster, a lot of clusters with high nuclearities were published.<sup>[127]</sup> The  $[\text{Mn}_{12}\text{OAc}]$  cluster has a spin ground state of  $S = 10$  resulting from the mixed-valence manganese(III/IV) interaction. The feature of a large number of unpaired electrons has drawn intense attention towards creating high spin ground states and therefore enhancing single-molecule magnet performance.<sup>[128]</sup> The large spin-ground states arise from the magnetic exchange interaction of multiple spin-carrying ions. These clusters showed record-breaking spin ground states like the twenty-five-core manganese cluster  $\text{Mn}_{25}$  with a spin ground state of  $S = 51/2$ <sup>[129]</sup>, the  $\text{Mn}_{19}$  cluster with a spin ground state of  $S = 83/2$ <sup>[130]</sup> or the  $\text{Fe}_{42}$  cluster with a spin ground state of  $S = 45$ <sup>[131]</sup>. Nevertheless, only in the first-mentioned example, the cluster  $\text{Mn}_{25}$  showed a very low energy barrier of  $14 \text{ cm}^{-1}$  at all.<sup>[129]</sup> The other examples were not single-molecule magnets. The main reason for this magnetic behavior is that  $D$  is inversely proportional to  $S^2$ . Thus, Equation 3 incorrectly suggests here that the height of the energy barrier  $U$  is a function of  $S$ .<sup>[128]</sup> Therefore, the main challenge in the field of molecular magnetism remained the synthesis of new cluster molecules with high energy barriers.

In 2003, Ishikawa and co-workers presented a single-molecule magnet based on a single lanthanide ion. The term single-ion magnet is used for this compound's properties because the single-molecule magnet behavior of the whole molecule is caused by the single-ion anisotropy of only one ion. In this structure, a terbium(III) and dysprosium(III) ion is coordinated by two phthalocyanate ligands (Pc) to form a monometallic sandwich-like structure with the molecular formula  $[\text{N}(\text{tBu})_4][\text{Tb}(\text{Pc})_2]$ .<sup>[132]</sup> The lanthanoid(III) ion is therefore surrounded by a square-antiprismatic coordination environment. This results in a coordination polyhedron with a  $D_{4d}$  symmetry. The energy barrier  $U_{\text{eff}} = 230 \text{ cm}^{-1}$  was reported and in 2013 even improved to  $U_{\text{eff}} = 653 \text{ cm}^{-1}$  by modification of the ligand.<sup>[133,134]</sup> Especially since the discovery of these lanthanide-based single-ion magnets (SIM), research has moved beyond  $3d$  metal clusters as single-molecule magnets and focused on  $4f$ - and mixed  $3d$ - and  $4f$ - metal complexes and clusters.

When lanthanide ions are used, the  $M_J$  states are considered instead of the  $M_S$  states. Analogous to the double-well potential in Figure 1. 12,  $2J+1$   $M_J$  microstates can split if the design of the molecule and crystal field are appropriate. This results in an  $M_J$  ground state with the most magnetic microstates lowest in energy. Based on Sievers' calculations from 1981 (Figure 1. 13 a), Rinehart and Long showed in 2011 again that the variation of the electron density can be used as a simple concept to approximately choose the coordination environment for different lanthanide(III) ions due to electronic repulsion (Figure 1. 13 b). This repulsion arises from the Coulomb interactions between the electrons of the lanthanide(III) ion and the coordinating ligands. The trivalent lanthanide(III) ions have different orientations of the total electron densities. A classification can be made between equatorial elongated (Ce(III), Pr(III), Nd(III), Tb(III), Dy(III), and Ho(III) = oblate), axially elongated (Pm(III), Sm(III), Er(III), Tm(III) and Yb(III) = prolate) and isotropic (Gd(III) and Lu(III)) electron density distributions.<sup>[74]</sup> A large crystal field splitting can only be achieved considering the shape of the electron density. This requires different ligand fields to be used depending on the lanthanide(III) ions. Looking at the dysprosium(III) ion in Figure 1. 13 c, the  $M_J = \pm 15/2$  microstate of

shows an oblate, and the  $M_J = \pm 1/2$  states a prolate electron density distribution. This can be used to determine which  $M_J$  state is the ground state. For example, if four point charges are positioned above and below the central atom by coordination of ligands on an axis, the  $M_J = \pm 15/2$  state will have a weak Coulomb repulsion, and the  $M_J = \pm 1/2$  state will have a strong Coulomb repulsion (Figure 1. 13 b). Thus, in the case of dysprosium(III), a stabilization of the large  $M_J$  states can be provoked. Comparing the shapes of the electron density distribution of the transitions for the lanthanide(III) ions, one notices that dysprosium exhibits a monotonic transition from a flattened to an elongated shape. Therefore, relaxation *via* an Orbach mechanism is favored compared to other relaxation mechanisms.

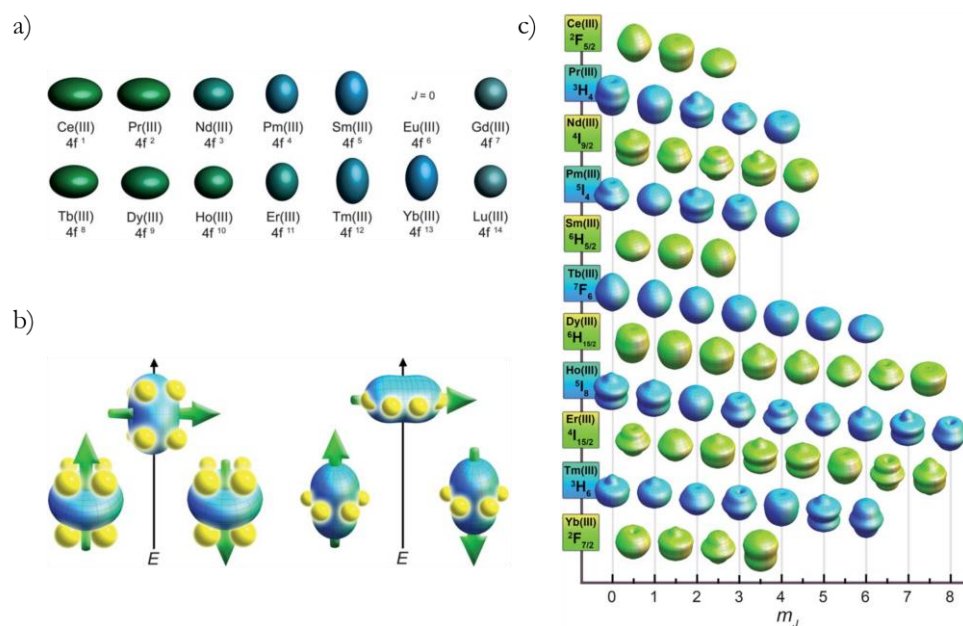


**Figure 1. 13.** a) Total electron density distribution of the 4f/electrons of all trivalent lanthanide(III) ions. Europium(III) is not shown due to a  $J = 0$  ground state; b) energy of configurations of the electron density concerning the crystal field environment for lanthanide ion, oblate (left), and prolate (right); c) quadrupole moments of the  $2J+1$  ground states.<sup>[71]</sup> Images from J. D. Rinehart and Long reference [71] (License Agreement with rightsholder Royal Society of Chemistry with order license ID 1256479-1).

QTM predominates at low temperatures because Orbach and Raman processes are temperature-dependent. The QTM is dependent on the external magnetic field, thus even a weak applied magnetic field can minimize quantum tunneling. Furthermore, several geometries are preferred to suppress quantum tunneling as a relaxation pathway of the magnetization of lanthanide(III) ions.<sup>[135]</sup> Tong and co-workers showed in theoretical calculations that this tunneling in lanthanide complexes can be inhibited by certain symmetries of the central metal ion of the QTM. These symmetries are  $C_n$   $n > 6$ ,  $C_{5h}/D_{5h}$ ,  $S_8/D_{4d}$ , and  $S_{12}/D_{6d}$ .<sup>[135]</sup> Two of the presented symmetries can be easily achieved by the implementation of lanthanide(III) ions in the metallocrown framework.<sup>[50,74]</sup> The ligand field of the lanthanide(III) ion as guest ions in metallocrowns can be influenced by the coordination geometries of the different cavities. In a [12-MC-4] metallocrown, a square antiprismatic geometry<sup>[50,72]</sup> can be achieved while in a [15-MC-5] metallocrown a pentagonal bipyramidal geometry<sup>[70,74]</sup> can occur. If these geometries are achieved, a lower amount of quantum tunneling should take place.

The latest record holder of the blocking temperature was reported by Layfield and co-workers in 2018 (Figure 1.14).<sup>[136]</sup> In this complex, the dysprosium(III) ion is coordinated by two derivatives of cyclopentadienyl ligands ( $\text{Cp}^*$  and  $\text{Cp}^{\text{tr5}}$ ) to form a sandwich-type coordination cluster  $[\text{Dy}(\text{Cp}^{\text{tr5}})\text{Cp}^*][\text{B}(\text{C}_6\text{F}_5)_4]$ . A wide Cp-Dy-Cp angle is obtained, leading to a strong axial ligand field of this cation.<sup>[137]</sup> The blocking temperature of  $T_B = 80$  K above the boiling temperature of liquid nitrogen removes a crucial barrier to the development of single-molecule magnets that function at practical temperatures towards room temperature devices.

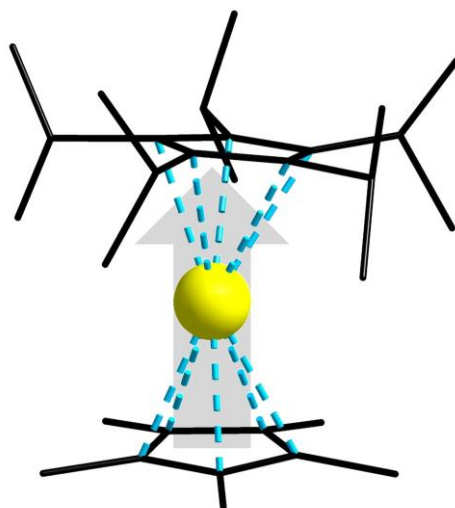


**Figure 1.14.** Schematic structure of the  $\text{Dy}(\text{Cp}^{\text{tr5}})\text{Cp}^*$  cation with highlighted anisotropy axis (grey arrow). Hydrogen atoms and counter ion are omitted for clarity. Color code of atoms: dysprosium(III) ion yellow, carbon black, Dy-C bond dashed light blue.

### 1.4.2. Detection of SMM behavior - alternating current measurements

Frequency-dependent alternating current (ac) magnetic susceptibility measurements are performed to investigate the SMM behavior of a compound and determine the energy barrier  $U_{\text{eff}}$ . These measurements are either carried out at zero-field or with a small applied direct current (dc) field. A SQUID magnetometer (abbreviation for superconducting quantum interference device) is used for this purpose.

The magnetic ac susceptibility  $\chi$  depends on the angular frequency  $\omega$  of the magnetic field and is equal to the sum of the real in-phase susceptibility  $\chi'$  and the imaginary out-of-phase susceptibility  $\chi''$ . The magnetic ac susceptibility  $\chi$  with the generalized Debye model is described in Equation 10. [124]

$$\chi(\omega) = \chi' + i\chi'' = \chi_s + \frac{\chi_T - \chi_s}{1 + (i\omega\tau)^{1-\alpha}} \quad (10)$$

In Equation 10,  $\chi_s$  and  $\chi_T$  correspond to the isothermal and the adiabatic susceptibility respectively. The plot of  $\chi''$  against  $\chi'$  is called a Cole-Cole plot (Figure 1. 15). The semicircles show a temperature and frequency dependency. The correction factor  $\alpha$  is also included in Equation 10. This factor can range between 0 to 1 and describes the distribution of different relaxation times. If  $\alpha$  is zero, only one relaxation process takes place. The semicircle in the Cole-Cole plot flattens as  $\alpha$  increases. At the maximum of the semicircle in the Cole-Cole plot  $\omega = \tau^{-1}$  applies. Therefore, the relaxation time  $\tau$  can be obtained from this plot. In combination with Equation 9, the different relaxation pathways can be used to obtain the effective energy barrier  $U_{\text{eff}}$ . [124]

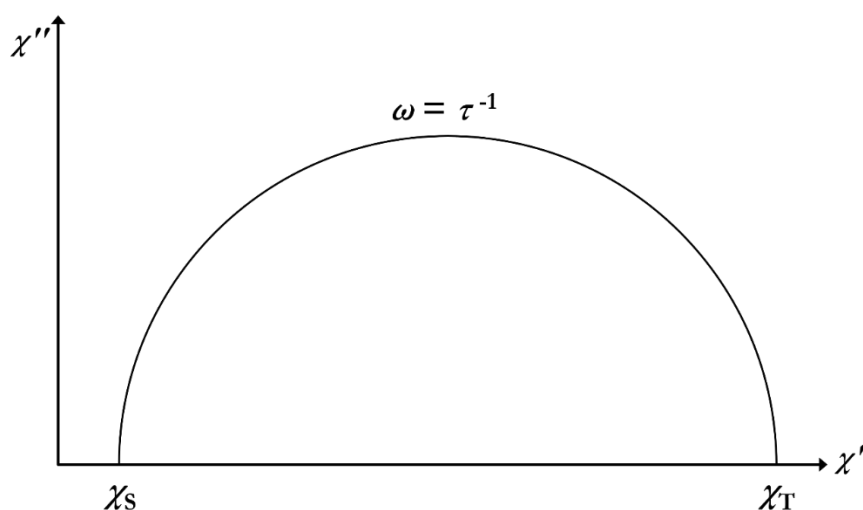


**Figure 1. 15.** Illustration of a Cole-Cole plot for  $\chi''$  against  $\chi'$  showing the isothermal susceptibility  $\chi_s$  and the adiabatic susceptibility  $\chi_T$ .

In Chapter 4.2 alternating current (ac) magnetic susceptibility measurements will be used to investigate single-molecule magnet behavior and to determine the effective energy barriers  $U_{\text{eff}}$ .

## 1.5. References

- [1] Nobel Prize Outreach AB, "The Nobel Prize in Chemistry 1987," retrieved from <https://www.nobelprize.org/prizes/chemistry/1987/summary/>, **2022**. (access Wednesday, 17<sup>th</sup> August 2022)
- [2] D. J. Cram, *Angew. Chem. Int. Ed. Engl.* **1988**, *27*, 1009–1020.
- [3] J.-M. Lehn, *Angew. Chem. Int. Ed. Engl.* **1988**, *27*, 89–112.
- [4] C. J. Pedersen, *Angew. Chem. Int. Ed. Engl.* **1988**, *27*, 1021–1027.
- [5] C. J. Pedersen, *Science* **1988**, *241*, 536–540.
- [6] G. W. Gokel, H. D. Durst, *Synthesis* **1976**, *1976*, 168–184.
- [7] V. L. Pecoraro, *Inorganica Chim. Acta* **1989**, *155*, 171–173.
- [8] M. Soo Lah, M. L. Kirk, W. Hatfield, V. L. Pecoraro, *J. Chem. Soc. Chem. Commun.* **1989**, *0*, 1606–1608.
- [9] M. S. Lah, V. L. Pecoraro, *J. Am. Chem. Soc.* **1989**, *111*, 7258–7259.
- [10] J. J. Bodwin, A. D. Cutland, R. G. Malkani, V. L. Pecoraro, *Coord. Chem. Rev.* **2001**, *216–217*, 489–512.
- [11] P. Happ, C. Plenk, E. Rentschler, *Coord. Chem. Rev.* **2015**, *289–290*, 238–260.
- [12] A. A. Athanasopoulou, C. Gamer, L. Völker, E. Rentschler, in *Nov. Magn. Nanostructures* (Eds.: N. Domracheva, M. Caporali, E. Rentschler), Elsevier, **2018**, pp. 51–96.
- [13] G. Mezei, C. M. Zaleski, V. L. Pecoraro, *Chem. Rev.* **2007**, *107*, 4933–5003.
- [14] M. Ostrowska, I. O. Fritsky, E. Gumienna-Kontecka, A. V. Pavlishchuk, *Coord. Chem. Rev.* **2016**, *327–328*, 304–332.
- [15] J. A. Johnson, J. W. Kampf, V. L. Pecoraro, *Angew. Chem.* **2003**, *115*, 564–567.
- [16] C. T. Pham, H. H. Nguyen, U. Abram, *Eur. J. Inorg. Chem.* **2018**, *2018*, 951–957.
- [17] A. A. Athanasopoulou, L. M. Carrella, E. Rentschler, *Dalton Trans.* **2019**, *48*, 4779–4783.
- [18] M. Tegoni, M. Remelli, *Coord. Chem. Rev.* **2012**, *256*, 289–315.
- [19] R. Codd, *Coord. Chem. Rev.* **2008**, *252*, 1387–1408.
- [20] J. B. Neilands, *J. Biol. Chem.* **1995**, *270*, 26723–26726.
- [21] N. K. Dutt, T. Seshadri, *Bull. Chem. Soc. Jpn.* **1967**, *40*, 2280–2283.
- [22] Sheetal, K. Nehra, R. Kaushal, S. Arora, D. Kaur, R. Kaushal, *Russ. J. Gen. Chem.* **2016**, *86*, 154–160.
- [23] B. Weber, *Koordinationschemie: Grundlagen und aktuelle Trends*, Springer-Verlag, **2014**.
- [24] L. J. Völker, *Molekularer Magnetismus Metallakronen-basierter Komplexverbindungen*, Johannes Gutenberg-Universität Mainz, **2018**.
- [25] C. Dendrinou-Samara, A. N. Papadopoulos, D. A. Malamataris, A. Tarushi, C. P. Raptopoulou, A. Terzis, E. Samaras, D. P. Kessissoglou, *J. Inorg. Biochem.* **2005**, *99*, 864–875.
- [26] A. Lüpke, L. M. Carrella, E. Rentschler, *Chem. – Eur. J.* **2021**, *27*, 4283–4286.
- [27] C. Dendrinou-Samara, A. N. Papadopoulos, D. A. Malamataris, A. Tarushi, C. P. Raptopoulou, A. Terzis, E. Samaras, D. P. Kessissoglou, *J. Inorg. Biochem.* **2005**, *99*, 864–875.
- [28] C. M. Zaleski, S. Tricard, E. C. Depperman, W. Wernsdorfer, T. Mallah, M. L. Kirk, V. L. Pecoraro, *Inorg. Chem.* **2011**, *50*, 11348–11352.
- [29] A. Tarushi, G. D. Geromichalos, K. Lafazanis, C. P. Raptopoulou, V. Psycharis, N. Lalioti, A. A. Pantazaki, D. P. Kessissoglou, V. Tangoulis, G. Psomas, *New J. Chem.* **2018**, *42*, 6955–6967.
- [30] P. Happ, E. Rentschler, *Dalton Trans.* **2014**, *43*, 15308–15312.

- [31] T. Lou, H. Yang, S. Zeng, D. Li, J. Dou, T. Lou, H. Yang, S. Zeng, D. Li, J. Dou, *Crystals* **2018**, *8*, 229.
- [32] M. Woźniczka, M. Świątek, M. Pająk, J. Gądek-Sobczyńska, M. Chmiela, W. Gonciarz, P. Lisiecki, B. Pasternak, A. Kufelnicki, *J. Inorg. Biochem.* **2018**, *187*, 62–72.
- [33] C. McDonald, S. Sanz, E. K. Brechin, M. K. Singh, G. Rajaraman, D. Gaynor, L. F. Jones, *RSC Adv.* **2014**, *4*, 38182–38191.
- [34] S. H. Seda, J. Janczak, J. Lisowski, *Inorg. Chem. Commun.* **2006**, *9*, 792–796.
- [35] A. J. Stemmler, A. Barwinski, M. J. Baldwin, V. Young, V. L. Pecoraro, *J. Am. Chem. Soc.* **1996**, *118*, 11962–11963.
- [36] C. Atzeri, L. Marchiò, C. Y. Chow, J. W. Kampf, V. L. Pecoraro, M. Tegoni, *Chem. – Eur. J.* **2016**, *22*, 6482–6486.
- [37] A. V. Pavlishchuk, S. V. Kolotilov, M. Zeller, L. K. Thompson, I. O. Fritsky, A. W. Addison, A. D. Hunter, *Eur. J. Inorg. Chem.* **2010**, *2010*, 4851–4858.
- [38] M. A. Katkova, G. S. Zabrodina, E. V. Baranov, M. S. Muravyeva, E. A. Kluev, A. S. Shavyrin, G. Y. Zhigulin, S. Y. Ketkov, *Appl. Organomet. Chem.* **2018**, *32*, e4389.
- [39] J. Jankolovits, C. M. Andolina, J. W. Kampf, K. N. Raymond, V. L. Pecoraro, *Angew. Chem. Int. Ed.* **2011**, *50*, 9660–9664.
- [40] J. Jankolovits, J. W. Kampf, V. L. Pecoraro, *Polyhedron* **2013**, *52*, 491–499.
- [41] M. Alexiou, C. Dendrinou-Samara, C. P. Raptopoulou, A. Terzis, D. P. Kessissoglou, *Inorg. Chem.* **2002**, *41*, 4732–4738.
- [42] C. Y. Chow, E. R. Trivedi, V. Pecoraro, C. M. Zaleski, *Comments Inorg. Chem.* **2015**, *35*, 214–253.
- [43] Z. Chen, M. Jia, Z. Zhang, F. Liang, *Cryst. Growth Des.* **2010**, *10*, 4806–4814.
- [44] A. B. Lago, J. Pasán, L. Cañadillas-Delgado, O. Fabelo, F. J. M. Casado, M. Julve, F. Lloret, C. Ruiz-Pérez, *New J. Chem.* **2011**, *35*, 1817–1822.
- [45] R. J. Woolfson, G. A. Timco, A. Chiesa, I. J. Vitorica-Yrezabal, F. Tuna, T. Guidi, E. Pavarini, P. Santini, S. Carretta, R. E. P. Winpenny, *Angew. Chem. Int. Ed.* **2016**, *55*, 8856–8859.
- [46] C. M. Zaleski, E. C. Depperman, J. W. Kampf, M. L. Kirk, V. L. Pecoraro, *Angew. Chem. Int. Ed.* **2004**, *43*, 3912–3914.
- [47] W.-W. Chang, H. Yang, H.-Q. Tian, D.-C. Li, J.-M. Dou, *New J. Chem.* **2020**, *44*, 14145–14150.
- [48] C. E. Housecroft, A. G. Sharpe, *Inorganic Chemistry*, Prentice Hall, Harlow, **2002**.
- [49] C. Y. Chow, E. R. Trivedi, V. Pecoraro, C. M. Zaleski, *Comments Inorg. Chem.* **2015**, *35*, 214–253.
- [50] A. Rauguth, A. Kredel, L. M. Carrella, E. Rentschler, *Inorg. Chem.* **2021**, *60*, 14031–14037.
- [51] E. Colacio, C. López-Magaña, V. McKee, A. Romerosa, *J. Chem. Soc. Dalton Trans.* **1999**, 2923–2926.
- [52] S. Lin, S.-X. Liu, Z. Chen, B.-Z. Lin, S. Gao, *Inorg. Chem.* **2004**, *43*, 2222–2224.
- [53] G.-J. Chen, C.-Y. Gao, W. Gu, X. Liu, S.-P. Yan, J.-L. Tian, D.-Z. Liao, *Z. Für Anorg. Allg. Chem.* **2011**, *637*, 374–376.
- [54] H. Yang, F. Cao, D. Li, S. Zeng, Y. Song, J. Dou, *Chem. – Eur. J.* **2015**, *21*, 14478–14485.
- [55] M. Sutradhar, M. F. C. Guedes da Silva, A. J. L. Pombeiro, *Inorg. Chem. Commun.* **2013**, *30*, 42–45.
- [56] S. V. Eliseeva, T. N. Nguyen, J. W. Kampf, E. R. Trivedi, V. L. Pecoraro, S. Petoud, *Chem. Sci.* **2022**, *13*, 2919–2931.
- [57] C. Y. Chow, S. V. Eliseeva, E. R. Trivedi, T. N. Nguyen, J. W. Kampf, S. Petoud, V. L. Pecoraro, *J. Am. Chem. Soc.* **2016**, *138*, 5100–5109.
- [58] J. C. Lutter, S. V. Eliseeva, J. W. Kampf, S. Petoud, V. L. Pecoraro, *Chem. – Eur. J.* **2018**, *24*, 10773–10783.

- [59] T. N. Nguyen, C. Y. Chow, S. V. Eliseeva, E. R. Trivedi, J. W. Kampf, I. Martinić, S. Petoud, V. L. Pecoraro, *Chem. – Eur. J.* **2018**, *24*, 1031–1035.
- [60] J. Jankolovits, J. W. Kampf, V. L. Pecoraro, *Chin. Chem. Lett.* **2015**, *26*, 444–448.
- [61] J. P. Karns, S. V. Eliseeva, C. L. Ward, M. J. Allen, S. Petoud, J. C. Lutter, *Inorg. Chem.* **2022**, *61*, 5691–5695.
- [62] J. R. Travis, A. M. Smihosky, A. C. Kauffman, S. E. Ramstrom, A. J. Lewis, S. G. Nagy, R. E. Rheam, M. Zeller, C. M. Zaleski, *J. Chem. Crystallogr.* **2021**, *51*, 372–393.
- [63] S. V. Eliseeva, J. R. Travis, S. G. Nagy, A. M. Smihosky, C. M. Foley, A. C. Kauffman, C. M. Zaleski, S. Petoud, *Dalton Trans.* **2022**, *51*, 5989–5996.
- [64] A. D. Cutland-Van Noord, J. W. Kampf, V. L. Pecoraro, *Angew. Chem.* **2002**, *114*, 4861–4864.
- [65] J. Jankolovits, A. D. C. Van-Noord, J. W. Kampf, V. L. Pecoraro, *Dalton Trans.* **2013**, *42*, 9803–9808.
- [66] C. Plenk, J. Krause, M. Beck, E. Rentschler, *Chem. Commun.* **2015**, *51*, 6524–6527.
- [67] V. Marzaroli, G. Spigolon, G. Lococciolo, M. Quaretti, C. Salviati, J. W. Kampf, G. Licini, L. Marchiò, V. L. Pecoraro, M. Tegoni, *Cryst. Growth Des.* **2019**, *19*, 1954–1964.
- [68] A. J. Lewis, E. Garlatti, F. Cugini, M. Solzi, M. Zeller, S. Carretta, C. M. Zaleski, *Inorg. Chem.* **2020**, *59*, 11894–11900.
- [69] P. Happ, A. Sapozhnik, J. Klanke, P. Czaja, A. Chernenkaya, K. Medjanik, S. Schuppler, P. Nagel, M. Merz, E. Rentschler, H. J. Elmers, *Phys. Rev. B* **2016**, *93*, 174404.
- [70] J. Wang, Z.-Y. Ruan, Q.-W. Li, Y.-C. Chen, G.-Z. Huang, J.-L. Liu, D. Reta, N. F. Chilton, Z.-X. Wang, M.-L. Tong, *Dalton Trans.* **2019**, *48*, 1686–1692.
- [71] J. D. Rinehart, J. R. Long, *Chem. Sci.* **2011**, *2*, 2078.
- [72] Q.-W. Li, J.-L. Liu, J.-H. Jia, Y.-C. Chen, J. Liu, L.-F. Wang, M.-L. Tong, *Chem. Commun.* **2015**, *51*, 10291–10294.
- [73] A. Alhassanat, C. Gamer, A. Rauguth, A. A. Athanasopoulou, J. Sutter, C. Luo, H. Ryll, F. Radu, A. A. Sapozhnik, T. Mashoff, E. Rentschler, H. J. Elmers, *Phys. Rev. B* **2018**, *98*, 064428.
- [74] J. Wang, Q.-W. Li, S.-G. Wu, Y.-C. Chen, R.-C. Wan, G.-Z. Huang, Y. Liu, J.-L. Liu, D. Reta, M. J. Giansiracusa, Z.-X. Wang, N. F. Chilton, M.-L. Tong, *Angew. Chem.* **2021**, *133*, 5359–5366.
- [75] J. Liu, Y.-C. Chen, J.-L. Liu, V. Vieru, L. Ungur, J.-H. Jia, L. F. Chibotaru, Y. Lan, W. Wernsdorfer, S. Gao, X.-M. Chen, M.-L. Tong, *J. Am. Chem. Soc.* **2016**, *138*, 5441–5450.
- [76] N. Wiberg, A. F. Holleman, E. Wiberg, G. Fischer, *Lehrbuch der Anorganischen Chemie*, De Gruyter, Berlin New York, **2007**.
- [77] J. P. Hogan, R. L. Banks, in *Hist. Polyolefins World's Most Widely Used Polym.* (Eds.: R.B. Seymour, T. Cheng), Springer Netherlands, Dordrecht, **1986**, pp. 103–115.
- [78] M. P. McDaniel, in *Adv. Catal.* (Eds.: D.D. Eley, H. Pines, P.B. Weisz), Academic Press, **1985**, pp. 47–98.
- [79] J. P. Hogan, *J. Polym. Sci. [A1]* **1970**, *8*, 2637–2652.
- [80] Y. Okude, S. Hirano, T. Hiyama, H. Nozaki, *J. Am. Chem. Soc.* **1977**, *99*, 3179–3181.
- [81] Haolun. Jin, Junichi. Uenishi, W. J. Christ, Yoshito. Kishi, *J. Am. Chem. Soc.* **1986**, *108*, 5644–5646.
- [82] A. Fürstner, N. Shi, *J. Am. Chem. Soc.* **1996**, *118*, 12349–12357.
- [83] E. Riedel, R. Alsasser, C. Janiak, T. M. Klapötke, *Moderne Anorganische Chemie*, Gruyter, Berlin, **2007**.
- [84] M. Murrie, S. Parsons, R. E. P. Winpenny, I. M. Atkinson, C. Benelli, *Chem. Commun.* **1999**, 285–286.
- [85] Erwin Riedel, *Allgemeine Und Anorganische Chemie*, Walter De Gruyter, **2008**.

- [86] V. S. Letokhov, *Nature* **1985**, *316*, 325–330.
- [87] W. Radloff, *Laser in Wissenschaft und Technik*, Spektrum Akademischer Verlag Heidelberg, **2010**.
- [88] C. Wang, S. Otto, M. Dorn, E. Kreidt, J. Lebon, L. Sršan, P. Di Martino-Fumo, M. Gerhards, U. Resch-Genger, M. Seitz, K. Heinze, *Angew. Chem.* **2018**, *130*, 1125–1130.
- [89] L. H. Gade, *Koordinationschemie*, Wiley, Weinheim, **2010**.
- [90] S. Otto, C. Förster, C. Wang, U. Resch-Genger, K. Heinze, *Chem. – Eur. J.* **2018**, *24*, 12555–12563.
- [91] M. A. Halcrow, *Spin-Crossover Materials: Properties and Applications*, Wiley, Chichester, West Sussex, United Kingdom, **2013**.
- [92] J.-C. G. Bünzli, C. Piguet, *Chem. Soc. Rev.* **2005**, *34*, 1048.
- [93] M. D. Seltzer, *J. Chem. Educ.* **1995**, *72*, 886.
- [94] Y. Shen, T. Riedener, K. L. Bray, *Phys. Rev. B* **2000**, *61*, 11460–11471.
- [95] R. F. Weinland, *Berichte Dtsch. Chem. Ges.* **1908**, *41*, 3236–3245.
- [96] R. D. Cannon, R. P. White, in *Prog. Inorg. Chem.*, John Wiley & Sons, Ltd, **1988**, pp. 195–298.
- [97] C. E. Anson, J. P. Bourke, R. D. Cannon, U. A. Jayasooriya, M. Molinier, A. K. Powell, *Inorg. Chem.* **1997**, *36*, 1265–1267.
- [98] A. Vlachos, V. Psycharis, C. P. Raptopoulou, N. Lalioti, Y. Sanakis, G. Diamantopoulos, M. Fardis, M. Karayanni, G. Papavassiliou, A. Terzis, *Inorganica Chim. Acta* **2004**, *357*, 3162–3172.
- [99] A. Figuerola, V. Tangoulis, J. Ribas, H. Hartl, I. Brüdgam, M. Maestro, C. Diaz, *Inorg. Chem.* **2007**, *46*, 11017–11024.
- [100] A. Ghirri, J. van Tol, I. Vitorica-Yrezabal, G. A. Timco, R. E. P. Winpenny, *Dalton Trans.* **2015**, *44*, 14027–14033.
- [101] P. Chaudhuri, M. Hess, E. Rentschler, T. Weyhermüller, U. Flörke, *New J. Chem.* **1998**, *22*, 553–555.
- [102] S. P. Pali, D. E. Richardson, M. L. Hansen, B. B. Iversen, F. K. Larsen, L. Sîngorean, G. A. Timco, N. V. Gerbeleu, K. R. Jennings, J. R. Eyler, *Inorganica Chim. Acta* **2001**, *319*, 23–42.
- [103] E. J. L. McInnes, G. A. Timco, G. F. S. Whitehead, R. E. P. Winpenny, *Angew. Chem. Int. Ed.* **2015**, *54*, 14244–14269.
- [104] F. K. Larsen, E. J. L. McInnes, H. E. Mkami, J. Overgaard, S. Piligkos, G. Rajaraman, E. Rentschler, A. A. Smith, G. M. Smith, V. Boote, M. Jennings, G. A. Timco, R. E. P. Winpenny, *Angew. Chem. Int. Ed.* **2003**, *42*, 101–105.
- [105] J. van Slageren, R. Sessoli, D. Gatteschi, A. A. Smith, M. Helliwell, R. E. P. Winpenny, A. Cornia, A.-L. Barra, A. G. M. Jansen, E. Rentschler, G. A. Timco, *Chem. – Eur. J.* **2002**, *8*, 277–285.
- [106] J. Rinck, G. Novitchi, W. Van den Heuvel, L. Ungur, Y. Lan, W. Wernsdorfer, C. E. Anson, L. F. Chibotaru, A. K. Powell, *Angew. Chem. Int. Ed.* **2010**, *49*, 7583–7587.
- [107] K. R. Vignesh, A. Soncini, S. K. Langley, W. Wernsdorfer, K. S. Murray, G. Rajaraman, *Nat. Commun.* **2017**, *8*, 1023.
- [108] K. R. Vignesh, S. K. Langley, A. Swain, B. Moubaraki, M. Damjanović, W. Wernsdorfer, G. Rajaraman, K. S. Murray, *Angew. Chem. Int. Ed.* **2018**, *57*, 779–784.
- [109] S. K. Langley, D. P. Wielechowski, V. Vieru, N. F. Chilton, B. Moubaraki, B. F. Abrahams, L. F. Chibotaru, K. S. Murray, *Angew. Chem. Int. Ed.* **2013**, *52*, 12014–12019.
- [110] J. Ferrando-Soria, E. Moreno Pineda, A. Chiesa, A. Fernandez, S. A. Magee, S. Carretta, P. Santini, I. J. Vitorica-Yrezabal, F. Tuna, G. A. Timco, E. J. L. McInnes, R. E. P. Winpenny, *Nat. Commun.* **2016**, *7*, 11377.
- [111] R. H. Laye, E. J. L. McInnes, *Eur. J. Inorg. Chem.* **2004**, *2004*, 2811–2818.
- [112] J. Lai, W. Niu, R. Luque, G. Xu, *Nano Today* **2015**, *10*, 240–267.



- [113] Y. Fujikawa, K. Nakajima, T. Sakurai, Eds., *Frontiers in Materials Research*, Springer, Berlin ; London, **2008**.
- [114] S. O. H. Gutschke, D. J. Price, A. K. Powell, P. T. Wood, *Angew. Chem. Int. Ed.* **1999**, *38*, 1088–1090.
- [115] E. J. L. McInnes, C. Anson, A. K. Powell, A. J. Thomson, S. Poussereau, R. Sessoli, *Chem. Commun.* **2001**, 89–90.
- [116] F. E. Kakaroni, A. Collet, E. Sakellari, D. I. Tzimopoulos, M. Siczek, T. Lis, M. Murrie, C. J. Milios, *Dalton Trans.* **2018**, *47*, 58–61.
- [117] R. Sessoli, D. Gatteschi, A. Caneschi, M. A. Novak, *Nature* **1993**, *365*, 141–143.
- [118] G. Christou, D. Gatteschi, D. N. Hendrickson, R. Sessoli, *MRS Bull.* **2000**, *25*, 66–71.
- [119] A. Zabala-Lekuona, J. M. Seco, E. Colacio, *Coord. Chem. Rev.* **2021**, *441*, 213984.
- [120] K. Katoh, H. Isshiki, T. Komeda, M. Yamashita, *Coord. Chem. Rev.* **2011**, *255*, 2124–2148.
- [121] L. Bogani, W. Wernsdorfer, *Nat. Mater.* **2008**, *7*, 179–186.
- [122] J. Camarero, E. Coronado, *J. Mater. Chem.* **2009**, *19*, 1678–1684.
- [123] R. Winpenny, G. Aromí, Eds., *Single-Molecule Magnets and Related Phenomena*, Springer, Berlin ; New York, **2006**.
- [124] D. Gatteschi, R. Sessoli, J. Villain, *Molecular Nanomagnets*, OUP Oxford, **2006**.
- [125] D. N. Woodruff, R. E. P. Winpenny, R. A. Layfield, *Chem. Rev.* **2013**, *113*, 5110–5148.
- [126] M. J. Giansiracusa, G. K. Gransbury, N. F. Chilton, D. P. Mills, in *Encycl. Inorg. Bioinorg. Chem.*, John Wiley & Sons, Ltd, **2021**, pp. 1–21.
- [127] D. Shao, X.-Y. Wang, *Chin. J. Chem.* **2020**, *38*, 1005–1018.
- [128] F. Neese, D. A. Pantazis, *Faraday Discuss* **2011**, *148*, 229–238.
- [129] M. Murugesu, M. Habrych, W. Wernsdorfer, K. A. Abboud, G. Christou, *J. Am. Chem. Soc.* **2004**, *126*, 4766–4767.
- [130] A. M. Ako, I. J. Hewitt, V. Mereacre, R. Clérac, W. Wernsdorfer, C. E. Anson, A. K. Powell, *Angew. Chem. Int. Ed.* **2006**, *45*, 4926–4929.
- [131] S. Kang, H. Zheng, T. Liu, K. Hamachi, S. Kanegawa, K. Sugimoto, Y. Shiota, S. Hayami, M. Mito, T. Nakamura, M. Nakano, M. L. Baker, H. Nojiri, K. Yoshizawa, C. Duan, O. Sato, *Nat. Commun.* **2015**, *6*, 5955.
- [132] N. Ishikawa, M. Sugita, T. Ishikawa, S. Koshihara, Y. Kaizu, *J. Am. Chem. Soc.* **2003**, *125*, 8694–8695.
- [133] C. R. Ganiwet, B. Ballesteros, G. de la Torre, J. M. Clemente-Juan, E. Coronado, T. Torres, *Chem. Weinh. Bergstr. Ger.* **2013**, *19*, 1457–1465.
- [134] Y. Chen, F. Ma, X. Chen, B. Dong, K. Wang, S. Jiang, C. Wang, X. Chen, D. Qi, H. Sun, B. Wang, S. Gao, J. Jiang, *Inorg. Chem.* **2017**, *56*, 13889–13896.
- [135] J.-L. Liu, Y.-C. Chen, M.-L. Tong, *Chem. Soc. Rev.* **2018**, *47*, 2431–2453.
- [136] F.-S. Guo, B. M. Day, Y.-C. Chen, M.-L. Tong, A. Mansikkamäki, R. A. Layfield, *Science* **2018**, *362*, 1400–1403.
- [137] D. Reta, J. G. C. Kragoskow, N. F. Chilton, *J. Am. Chem. Soc.* **2021**, *143*, 5943–5950.



## 2. Motivation and aim of this work

In 1956, IBM sold the first commercially successful computer (305 RAMAC), using magnetic iron oxide materials for data storage.<sup>[1]</sup> The computer, which weighed several tons, could store five megabytes of data, whereas today, every smartphone has several gigabytes of memory.<sup>[2]</sup> This drastic development of miniaturization shows the changing demands of today's data processing. Less than ten years later, Gordon Moore predicted a doubling of transistor density in computer chips (integrated circuits) every second year.<sup>[3]</sup> In the future, data processing will require even larger storage capacities and faster performance, which cannot be provided solely by miniaturization of components. One limiting factor is the thickness of the magnetic metal oxide layer as electron tunneling and overheating is caused by the decrease of this layer.<sup>[4]</sup> Single-molecule magnets (SMMs) are among the most promising candidates to significantly increase density and efficiency of storage devices.<sup>[5]</sup> The field of rationally designing these molecular building blocks is subject of current multidisciplinary research and has developed a lot since the discovery of magnetic bistability in the  $3d$  metal ion cluster by Sessoli and co-workers in 1993.<sup>[6]</sup> Research continues to have great potential and importance for enabling practical use of these molecules that should be capable to receive, store and process information.

Two major challenges must be overcome for the facilitation of SMMs: First, the compounds should exhibit SMM behavior at elevated temperatures. In 2000, Sessoli and co-workers stated that the next most important goal is to synthesize a complex with SMM behavior above the boiling point of liquid nitrogen at 77 K to ensure feasible conditions for their application.<sup>[7]</sup> At that time the focus was on the synthesis of large clusters with large numbers of spin centers of  $3d$  metal ions.<sup>[8-10]</sup> However, lanthanide-based SMMs could clearly surpass their  $3d$  counterparts with their high blocking temperatures and energy barriers. Their strong spin-orbit coupling, and large anisotropy enabled a significant increase in the energy barrier. In 2018, Layfield and co-workers published a SMM exhibiting magnetic hysteresis behavior at a new record blocking temperature of  $T_B = 80$  K.<sup>[11]</sup> This dysprosium metallocene cation has an effective energy barrier of  $U_{\text{eff}} = 1541$  cm<sup>-1</sup>, which represents another major accomplishment in the search for SMMs that are applicable under reasonable conditions.

Secondly, adsorption onto surfaces and the processability of the molecular storage media must be developed.<sup>[12]</sup> The example of the SMM  $[\text{Dy}(\text{O}^i\text{Bu})_2(\text{py})_5][\text{BPh}_4]$  with a high energy barrier  $U_{\text{eff}} = 1815(1)$  K<sup>[13]</sup> shows the potential of rising energy barriers. However, since this SMM is air sensitive, it is not suitable for commercial applications,<sup>[14]</sup> thus requiring the synthesis of air-stable compounds.

One approach to realize devices on a molecular level are molecular spintronics where the injection, manipulation, and detection of spins is investigated.<sup>[15,16]</sup> This field of research focusses on controlling and addressing single molecules and spin systems through interactions on interfaces which is a crucial step for communication to the outside world. However, fragmentation of fragile molecular complexes or a change in the oxidation state<sup>[17]</sup> often prevents their successful adsorption on surfaces. Additionally, their magnetic

behavior on surfaces must be controlled. The organization of complexes that maintain SMM properties on surfaces is not straightforward and requires a study of their individual behavior by utilizing a local probe.<sup>[18]</sup> Thus, due to the chemical instability of most SMM complexes, only few examples have been successfully deposited on surfaces.<sup>[19]</sup>

Numerous surface immobilization attempts have been successfully realized on several surfaces with the famous SMM-prototype molecule  $[\text{Mn}_{12}\text{OAc}]$ .<sup>[6,20]</sup> Veciana *and co-workers* have reported a biphenyl-carboxylate derivative that was deposited onto a thin film surface. Here, a polymeric matrix stabilized the SMM and enhanced mechanical strength of the film.<sup>[21]</sup> However, most attempts were performed using chemisorption techniques to deposit  $[\text{Mn}_{12}\text{OAc}]$  onto conducting gold surfaces. Chemisorption is based on the formation of a chemical bond between the surface and the corresponding functional groups of the molecules. Ligand exchange with sulfur-containing groups in the backbone was used to exploit the thiophilic properties of gold surfaces, while the SMM behavior of the bulk molecule was retained.<sup>[22,23]</sup> Cornia and co-workers showed the successful deposition of such thioacetyl-protected derivatives of  $[\text{Mn}_{12}\text{OAc}]$  on a gold film for the first time in 2003. They accomplished the *in-situ* deprotection of the thiol groups to form Au-thiolate anchors (Au(111)).<sup>[24]</sup> Here, scanning tunneling microscopy (STM) was used to study the surface coverage, which was further established as an important analysis tool in the following years.<sup>[25]</sup> This was followed by the work of Heersche and co-workers who inserted single  $[\text{Mn}_{12}\text{OAc}]$  molecules between gold nano-electrodes to investigate transport phenomena in a single-molecule transistor geometry.<sup>[26]</sup>

Gaining control over the orientation of molecules and therefore their anisotropy axis on surfaces is another crucial step. This challenge was addressed by Mannini and Cornia with co-workers by altering the chain length of the thioacetyl terminated alkyl and investigating the chemisorption of the corresponding tetra iron(III) complex  $[\text{Fe}_4]$ <sup>[27]</sup> onto gold.<sup>[28]</sup> The famous double decker terbium(III) phthalocyanine complex  $[\text{TbPc}_2]$  (SIM) was also successfully applied on various surfaces firstly reported by Ishikawa in 2003.<sup>[29,30]</sup> Physisorption of this complex was achieved by deposition of molecules by thermal evaporation in ultrahigh vacuum. Physisorption utilizes physical interactions of the surface with molecules to enable immobilization of molecules on the respective surface. This is undoubtedly the most adequate process to achieve clean surface coverage.<sup>[31]</sup> Klar and co-workers thermally evaporated  $[\text{TbPc}_2]$  molecules on highly ordered pyrolytic graphite (HOPG) and proved a hysteretic loop of the magnetization.<sup>[32]</sup> However,  $[\text{TbPc}_2]$  is rather the exception among SMM examples in terms of the high thermal stability required for the technique.<sup>[33]</sup>

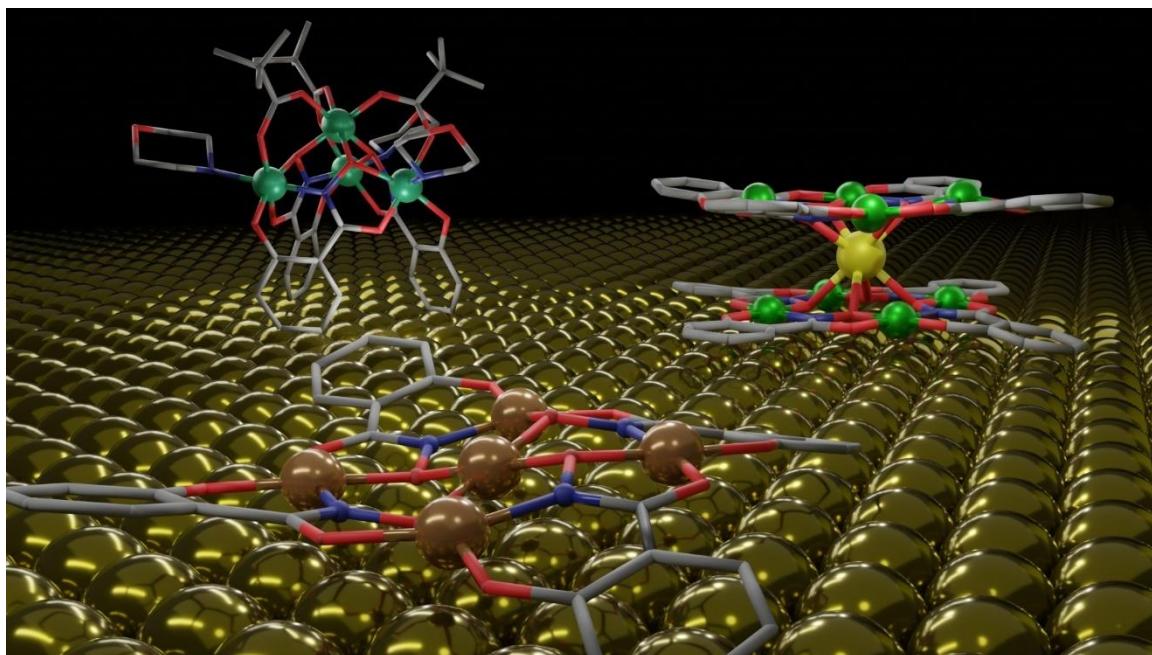


**Figure 2. 1.** Schematic representation of possible arrangement of metallacrowns on a gold surface. Color code: chromium(III) ions green, dysprosium(III) ion yellow, oxygen red, nickel(II) ions light green, nitrogen blue, carbon grey (prepared with *Blender 3.1.0*).

Accordingly, air stable molecules, that stay intact during surface preparation are required to leverage the potential of SMMs in molecular spintronics and information storage. Thus, in this thesis, kinetically inert chromium(III) ions are used to build multinuclear metallacrowns. Kinetic inert chromium(III) ions have been studied with regard to their robustness<sup>[34,35]</sup> in complexes for many decades but they have never been implemented into metallacrowns.<sup>[36–38]</sup> *3d* Metal ions with isotropic electron configurations offer two additional important advantages: (1) Their well-defined coordination geometries enhance the construction of large clusters and (2) theoretical models can be applied to investigate and predict magnetic exchange interactions between neighboring metal centers in these isotropic systems.<sup>[39]</sup> Metallacrowns offer a reliable coordination scaffold with discrete and stable oxidation states that can be tuned *via* the cavity size and a variety of metal ions. This property offers the desired robust preliminary conditions required to face the challenges of surface immobilization of such complexes. The combination of kinetic inert chromium(III) ions and metallacrowns containing chelating ligands is expected to create very stable coordination compounds.

Additionally, the second part of this thesis focuses on the implementation of lanthanide(III) ions as guest ions within chromium(III) metallacrowns. Dysprosium(III) and terbium(III) ions possess large ground spin states  $S$  combined with large magnetic anisotropies  $D$  which provide the essential requirements for SMM behavior. A targeted ligand design is then applied to further optimize the SMM properties. Coordination of the guest ion in metallacrown scaffolds can create symmetries which enhance the SMM performance.<sup>[40]</sup> Thus, metallacrowns have been established as a promising complex ligand for the preparation of SMMs.

The wide range of established and new ligands offers a variety of possible metallacrown frameworks. Furthermore, a variation of co-ligands and solvents can be employed to alter the structural properties.

It was been demonstrated that the incorporation of highly anisotropic lanthanide(III) ions into highly isotropic  $3d$  ion matrices can enhance the SMM properties.<sup>[41–43]</sup> Thus, the following examples of clusters in which both, chromium(III) and dysprosium(III) ions, are implemented will show the potential of the addition of chromium(III) ions.

Two categories have been established. Firstly, fluoride bridges are connecting the polynuclear complexes  $\{\text{Cr}^{\text{III}}\text{-F-Ln}^{\text{III}}\}$ .<sup>[44,45]</sup> Bendix and coworkers showed that polynuclear  $\{\text{Cr}^{\text{III}}\text{-F-Ln}^{\text{III}}\}$  clusters exhibit slow relaxation of magnetization, and that the topology of this cluster strongly depends on the structure of the chromium(III) precursor.<sup>[45]</sup> This offers an easily accessible handle to influence the self-assembly process and the geometry of the resulting complex: the chromium(III) ion source. Secondly, several  $\mu_3$ - and  $\mu_2$ -oxo bridged  $\{\text{Cr}(\text{III})\text{-O-Ln}(\text{III})\}$  complexes have been reported to show SMM behavior. In 2015, Car and coworkers demonstrated that the almost ideal coordination of the chromium(III) ion enhanced the distortion of the square-anti-prismatic geometry of the lanthanide(III) ions within the complex *via* these bridges.<sup>[46]</sup> Thus, a favorable coordination to suppress quantum tunneling (QTM)<sup>[40]</sup> led to detection of an out-of-phase signal at zero applied field.

Another important control is magnetic exchange mechanism. Murray and coworkers published a dysprosium(III) dimer in 2013, in which the lanthanide(III) ions are bridged *via* organic ligands and chromium(III) ions.<sup>[47]</sup> Ferromagnetic exchange interactions take place between the lanthanide(III) ions as they interact antiferromagnetically with chromium(III) ions. The chromium(III) ions in these complexes enable ferromagnetic exchange interactions of the dysprosium(III) ions and enhance SMM behavior. Compounds with competing Dy–Cr, Dy–Dy, and Cr–Cr exchange interaction that dominate the obtained spin structure were also obtained by Powell and co-workers.<sup>[41]</sup>

In summary, the stability of coordination compounds must be enhanced to realistically enable their processing for surface applications. The combination of kinetic inert chromium(III) ions with robust metallacrown scaffolds will therefore be investigated in this thesis. The structural analysis and implementation of a magnetic exchange model will be implemented to understand the magnetic behavior in the bulk. Additionally, anisotropic lanthanide(III) ions will be introduced to achieve a slow relaxation of magnetization

## 2.1. References

- [1] “IBM Archives: IBM 305 RAMAC,” can be found under [//www.ibm.com/ibm/history/exhibits/storage/storage\\_PH0305.html](http://www.ibm.com/ibm/history/exhibits/storage/storage_PH0305.html), **2003**.
- [2] M. Affronte, *J. Mater. Chem.* **2009**, *19*, 1731–1737.
- [3] M. Lundstrom, *Science* **2003**, *299*, 210–211.
- [4] V. I. Minkin, *Russ. Chem. Bull.* **2008**, *57*, 687–717.
- [5] M. N. Leuenberger, D. Loss, *Nature* **2001**, *410*, 789–793.
- [6] R. Sessoli, D. Gatteschi, A. Caneschi, M. A. Novak, *Nature* **1993**, *365*, 141–143.
- [7] G. Christou, D. Gatteschi, D. N. Hendrickson, R. Sessoli, *MRS Bull.* **2000**, *25*, 66–71.
- [8] M. Murugesu, M. Habrych, W. Wernsdorfer, K. A. Abboud, G. Christou, *J. Am. Chem. Soc.* **2004**, *126*, 4766–4767.
- [9] A. M. Ako, I. J. Hewitt, V. Mereacre, R. Clérac, W. Wernsdorfer, C. E. Anson, A. K. Powell, *Angew. Chem. Int. Ed.* **2006**, *45*, 4926–4929.
- [10] S. Kang, H. Zheng, T. Liu, K. Hamachi, S. Kanegawa, K. Sugimoto, Y. Shiota, S. Hayami, M. Mito, T. Nakamura, M. Nakano, M. L. Baker, H. Nojiri, K. Yoshizawa, C. Duan, O. Sato, *Nat. Commun.* **2015**, *6*, 5955.
- [11] F.-S. Guo, B. M. Day, Y.-C. Chen, M.-L. Tong, A. Mansikkamäki, R. A. Layfield, *Science* **2018**, *362*, 1400–1403.
- [12] D. N. Woodruff, R. E. P. Winpenny, R. A. Layfield, *Chem. Rev.* **2013**, *113*, 5110–5148.
- [13] Y.-S. Ding, N. F. Chilton, R. E. P. Winpenny, Y.-Z. Zheng, *Angew. Chem. Int. Ed.* **2016**, *55*, 16071–16074.
- [14] A. Zabala-Lekuona, J. M. Seco, E. Colacio, *Coord. Chem. Rev.* **2021**, *441*, 213984.
- [15] S. Sanvito, *Chem. Soc. Rev.* **2011**, *40*, 3336–3355.
- [16] M. Moors, J. Warneke, X. López, C. de Graaf, B. Abel, K. Yu. Monakhov, *Acc. Chem. Res.* **2021**, *54*, 3377–3389.
- [17] M. Mannini, P. Sainctavit, R. Sessoli, C. Cartier dit Moulin, F. Pineider, M.-A. Arrio, A. Cornia, D. Gatteschi, *Chem. – Eur. J.* **2008**, *14*, 7530–7535.
- [18] A. Cornia, M. Mannini, P. Sainctavit, R. Sessoli, *Chem. Soc. Rev.* **2011**, *40*, 3076.
- [19] E. Moreno Pineda, T. Komeda, K. Katoh, M. Yamashita, M. Ruben, *Dalton Trans.* **2016**, *45*, 18417–18433.
- [20] R. Bagai, G. Christou, *Chem. Soc. Rev.* **2009**, *38*, 1011–1026.
- [21] D. Ruiz-Molina, M. Mas-Torrent, J. Gómez, A. i. Balana, N. Domingo, J. Tejada, M. t. Martínez, C. Rovira, J. Veciana, *Adv. Mater.* **2003**, *15*, 42–45.
- [22] R. G. Nuzzo, D. L. Allara, *J. Am. Chem. Soc.* **1983**, *105*, 4481–4483.
- [23] M. Pacchioni, A. Cornia, A. C. Fabretti, L. Zobbi, D. Bonacchi, A. Caneschi, G. Chastanet, D. Gatteschi, R. Sessoli, *Chem. Commun.* **2004**, 2604–2605.
- [24] A. Cornia, A. C. Fabretti, M. Pacchioni, L. Zobbi, D. Bonacchi, A. Caneschi, D. Gatteschi, R. Biagi, U. Del Pennino, V. De Renzi, L. Gurevich, H. S. J. Van der Zant, *Angew. Chem. Int. Ed.* **2003**, *42*, 1645–1648.
- [25] M. Burgert, S. Voss, S. Herr, M. Fonin, U. Groth, U. Rüdiger, *J. Am. Chem. Soc.* **2007**, *129*, 14362–14366.
- [26] H. B. Heersche, Z. de Groot, J. A. Folk, H. S. J. van der Zant, C. Romeike, M. R. Wegewijs, L. Zobbi, D. Barreca, E. Tondello, A. Cornia, *Phys. Rev. Lett.* **2006**, *96*, 206801.

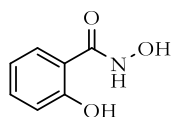
- [27] S. Accorsi, A.-L. Barra, A. Caneschi, G. Chastanet, A. Cornia, A. C. Fabretti, D. Gatteschi, C. Mortalò, E. Olivieri, F. Parenti, P. Rosa, R. Sessoli, L. Sorace, W. Wernsdorfer, L. Zobbi, *J. Am. Chem. Soc.* **2006**, *128*, 4742–4755.
- [28] L. Poggini, E. Tancini, C. Danieli, A. L. Sorrentino, G. Serrano, A. Lunghi, L. Malavolti, G. Cucinotta, A.-L. Barra, A. Juhin, M.-A. Arrio, W. Li, E. Otero, P. Ohresser, L. Joly, J. P. Kappler, F. Totti, P. Saintavit, A. Caneschi, R. Sessoli, A. Cornia, M. Mannini, *Adv. Mater. Interfaces* **2021**, *8*, 2101182.
- [29] N. Ishikawa, M. Sugita, T. Ishikawa, S. Koshihara, Y. Kaizu, *J. Am. Chem. Soc.* **2003**, *125*, 8694–8695.
- [30] M. Mannini, F. Bertani, C. Tudisco, L. Malavolti, L. Poggini, K. Misztal, D. Menozzi, A. Motta, E. Otero, P. Ohresser, P. Saintavit, G. G. Condorelli, E. Dalcanale, R. Sessoli, *Nat. Commun.* **2014**, *5*, 4582.
- [31] G. Rogez, B. Donnio, E. Terazzi, J.-L. Gallani, J.-P. Kappler, J.-P. Bucher, M. Drillon, *Adv. Mater.* **2009**, *21*, 4323–4333.
- [32] D. Klar, A. Candini, L. Joly, S. Klyatskaya, B. Krumme, P. Ohresser, J.-P. Kappler, M. Ruben, H. Wende, *Dalton Trans.* **2014**, *43*, 10686–10689.
- [33] Z. Zhu, C. Zhao, T. Feng, X. Liu, X. Ying, X.-L. Li, Y.-Q. Zhang, J. Tang, *J. Am. Chem. Soc.* **2021**, *143*, 10077–10082.
- [34] S. I. Shupack, *Environ. Health Perspect.* **1991**, *92*, 7–11.
- [35] G. Marx, K. G. Heumann, *Fresenius J. Anal. Chem.* **1999**, *364*, 489–494.
- [36] M. Murrie, S. Parsons, R. E. P. Winpenny, I. M. Atkinson, C. Benelli, *Chem. Commun.* **1999**, 285–286.
- [37] E. Houton, P. Comar, M. B. Pitak, S. J. Coles, A. G. Ryder, S. Piligkos, E. K. Brechin, L. F. Jones, *RSC Adv.* **2016**, *6*, 73668–73676.
- [38] F. K. Larsen, J. Overgaard, S. Parsons, E. Rentschler, A. A. Smith, G. A. Timco, R. E. P. Winpenny, *Angew. Chem. Int. Ed.* **2003**, *42*, 5978–5981.
- [39] F. E. Kakaroni, A. Collet, E. Sakellari, D. I. Tzimopoulos, M. Siczek, T. Lis, M. Murrie, C. J. Milios, *Dalton Trans.* **2018**, *47*, 58–61.
- [40] J.-L. Liu, Y.-C. Chen, M.-L. Tong, *Chem. Soc. Rev.* **2018**, *47*, 2431–2453.
- [41] J. Rinck, G. Novitchi, W. Van den Heuvel, L. Ungur, Y. Lan, W. Wernsdorfer, C. E. Anson, L. F. Chibotaru, A. K. Powell, *Angew. Chem. Int. Ed.* **2010**, *49*, 7583–7587.
- [42] K. R. Vignesh, S. K. Langley, A. Swain, B. Moubaraki, M. Damjanović, W. Wernsdorfer, G. Rajaraman, K. S. Murray, *Angew. Chem. Int. Ed.* **2018**, *57*, 779–784.
- [43] C. Cui, J.-P. Cao, X.-M. Luo, Q.-F. Lin, Y. Xu, *Chem. – Eur. J.* **2018**, *24*, 15295–15302.
- [44] A. McRobbie, A. R. Sarwar, S. Yeninas, H. Nowell, M. L. Baker, D. Allan, M. Luban, C. A. Muryn, R. G. Pritchard, R. Prozorov, G. A. Timco, F. Tuna, G. F. S. Whitehead, R. E. P. Winpenny, *Chem. Commun.* **2011**, *47*, 6251–6253.
- [45] C. A. Thuesen, K. S. Pedersen, M. Schau-Magnussen, M. Evangelisti, J. Vibenholt, S. Piligkos, H. Weihe, J. Bendix, *Dalton Trans.* **2012**, *41*, 11284–11292.
- [46] P.-E. Car, A. Favre, A. Caneschi, R. Sessoli, *Dalton Trans.* **2015**, *44*, 15769–15773.
- [47] S. K. Langley, D. P. Wielechowski, V. Vieru, N. F. Chilton, B. Moubaraki, B. F. Abrahams, L. F. Chibotaru, K. S. Murray, *Angew. Chem. Int. Ed.* **2013**, *52*, 12014–12019.



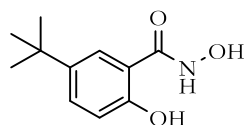
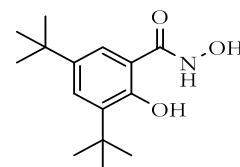
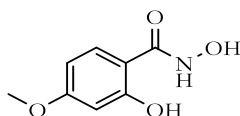


### 3. List of compounds

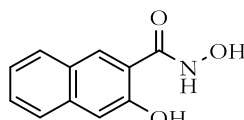
#### Ligands



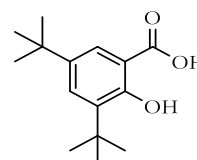
salicylhydroxamic acid

**ShiH<sub>3</sub>**5-*tert*-butyl-salicylhydroxamic acid**4bu-ShiH<sub>3</sub>**3,5-di-*tert*-butyl-salicylhydroxamic acid**(4bu)<sub>2</sub>-ShiH<sub>3</sub>**

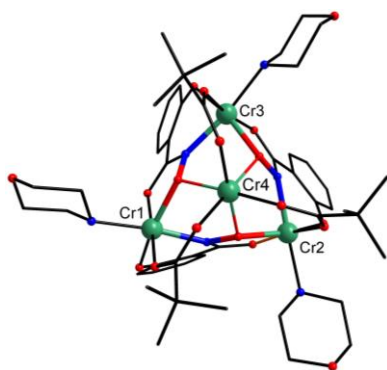
4-methoxy-salicylhydroxamic acid

**OMeShiH<sub>3</sub>**

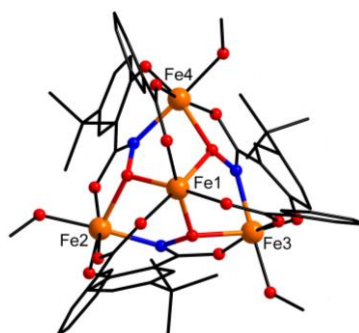
3-hydroxy-2-naphthylhydroxamic acid

**Nha**3,5-di-*tert*-butyl-salicylic acid**(4bu)<sub>2</sub>-SalH<sub>2</sub>**

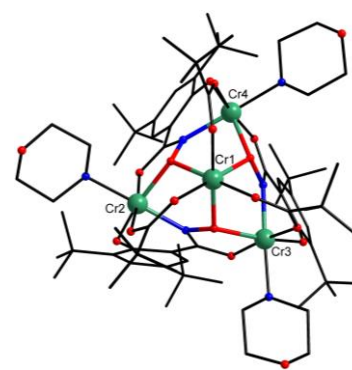
#### Homometallic complexes



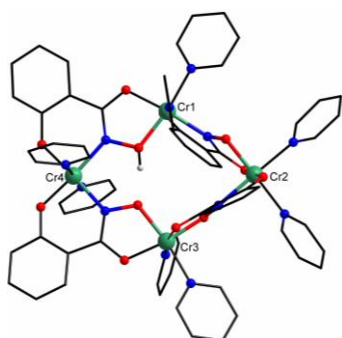
{Cr<sup>III</sup>( $\mu_2$ -piv)<sub>3</sub>  
[9-MCCr(III)N(Shi)-3](morph)<sub>3</sub>]  
· MeOH  
[Cr<sub>3</sub>Cr]



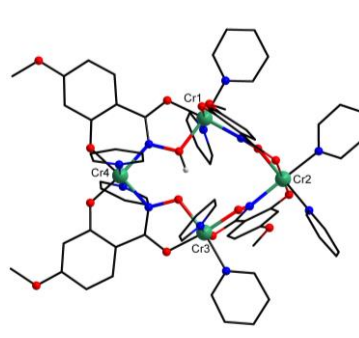
{Fe<sup>III</sup>( $\mu_2$ -OOCPh)<sub>3</sub>  
[9-MCFe(III)N(4buShi)-3](MeOH)<sub>3</sub>]  
· x MeOH  
4bu-[Fe<sub>3</sub>Fe]



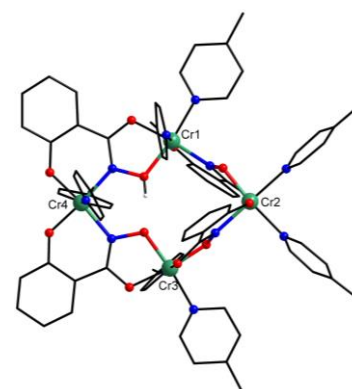
{Cr<sup>III</sup>( $\mu_2$ -piv)<sub>3</sub>  
[9-MCCr(III)N(4bu<sub>2</sub>Shi)-3](morph)<sub>3</sub>]  
· MeOH  
(4bu)<sub>2</sub>-[Cr<sub>3</sub>Cr]



{[12-MCCr(III)N(ShiH)(Shi)<sub>3</sub>-  
4](py)<sub>8</sub>Cl} 5 MeOH  
[Cr<sub>4</sub>]

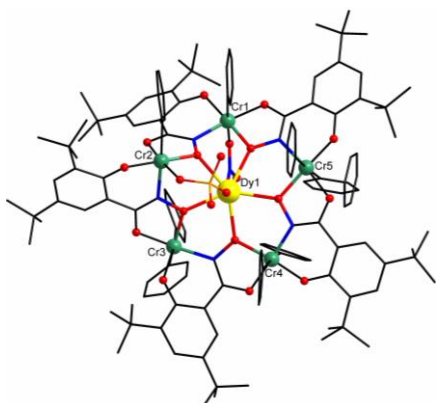


{[12-MCCr(III)N(OMeShiH)(OMeShi)<sub>3</sub>-  
4](py)<sub>8</sub>Cl} x H<sub>2</sub>O  
OMe-[Cr<sub>4</sub>]

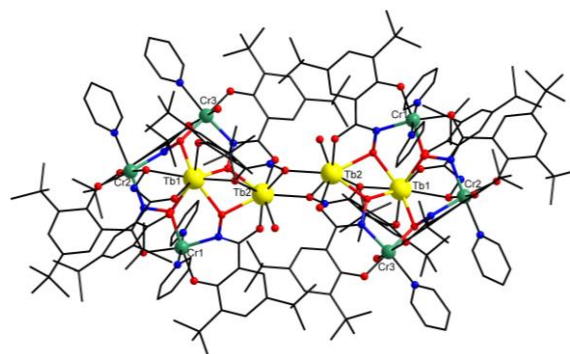


{[12-MCCr(III)N(ShiH)(Shi)<sub>3</sub>-4]( $\gamma$ -  
py)<sub>8</sub>Cl} · 3.75 H<sub>2</sub>O · 0.5 O  
pic-[Cr<sub>4</sub>]

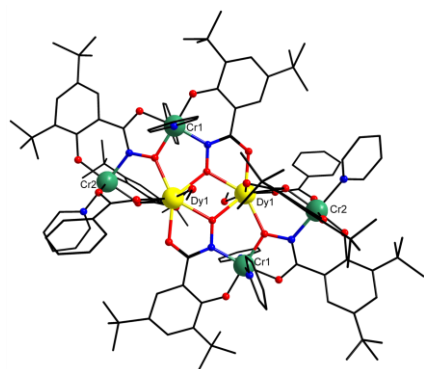
## 3d-4f Complexes



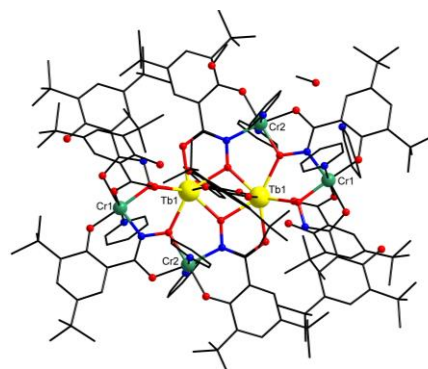
$\{\text{Dy}^{\text{III}}(\mu_2\text{-NO}_3)(\mu_2\text{-SO}_4)[15\text{-MC}_{\text{Cr}(\text{III})\text{N}((\text{t}\text{bu})_2\text{Shi})_5\text{-5]}(\text{py})_3\}$   
 $\cdot 2 \text{ py} \cdot \text{MeOH}$   
**[Cr<sub>5</sub>Dy]**



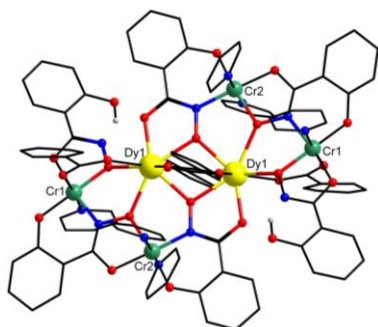
$[(\text{Cr}^{\text{III}})_6(\text{Tb}^{\text{III}})_4(\text{MeOH})_2(\text{py})_6((\text{t}\text{bu})_2\text{Shi})_4$   
 $((\text{t}\text{bu})_2\text{ShiH}_2)_2] \cdot 4 \text{ py} \cdot 2 \text{ MeOH}$   
**[Cr<sub>6</sub>Tb<sub>4</sub>]**



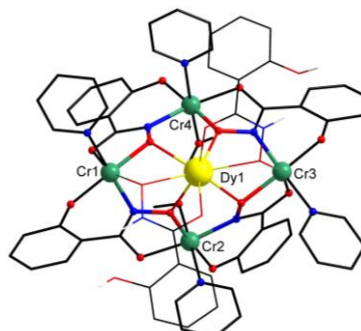
$[\text{Cr}^{\text{III}}_4\text{Dy}^{\text{III}}_2(\mu_2\text{-OOCPh})_2(\text{MeOH})_2(\text{py})_6((\text{t}\text{bu})_2\text{Shi})_4((\text{t}\text{bu})_2\text{Sal})_2]$   
 $\cdot 3 \text{ MeOH}$   
**Sal-[Cr<sub>4</sub>Dy<sub>2</sub>]**



$(\text{Hpy})_2[\text{Cr}^{\text{III}}_4\text{Tb}^{\text{III}}_2(\mu_2\text{-OOCPh})_{0.5}(\text{py})_6$   
 $((\text{t}\text{bu})_2\text{Shi})_4((\text{t}\text{bu})_2\text{ShiH}_2)_2((\text{t}\text{bu})_2\text{SalH})_{3.5}] \cdot 3 \text{ MeOH}$   
**Sal-[Cr<sub>4</sub>Tb<sub>2</sub>]**



$(\text{Hpy})_2[\text{Cr}^{\text{III}}_4\text{Dy}^{\text{III}}_2(\mu_2\text{-OOCPh})_4(\text{py})_6(\text{Shi})_4(\text{ShiH}_2)_2] \cdot 2 \text{ MeOH}$   
**[Cr<sub>4</sub>Dy<sub>2</sub>]**



$\{\text{Dy}^{\text{III}}(\mu_2\text{-}\eta^3\text{-ShiH}_2)_2[12\text{-MC}_{\text{Cr}(\text{III})\text{N}(\text{Shi})_4\text{-4]}(\text{MeOH})(\text{py})_4(\text{MeO})]\}$   
 $\cdot 2 \text{ MeOH} \cdot 2 \text{ py} \cdot 2 \text{ H}_2\text{O}$   
**[Cr<sub>4</sub>Dy]**



## 4. Results and Discussion

The following discussion of the results is separated into two parts. In the first Chapter 4.1, the obtained MCs with chromium(III) ions<sup>[1]</sup> are discussed and their physical properties are compared to the analog iron(III) complex when possible. It is reported that different ligands and co-ligands can influence the size of the MC cavity, the composition of the structure and the crystallization ability.<sup>[2]</sup> The selected triple deprotonated salicylhydroxamate ligands coordinate the triple positively charged metal(III) ions to compensate their mutual charge (see **Fehler! Verweisquelle konnte nicht gefunden werden.**). The coordination of a chromium(III) guest ion requires charge balance *via* coordination of counterions. If the resulting MC is overall charged, suitable counterions balance this charge in the lattice sites of the crystal. The focus lays on the discussion of the structure obtained by single-crystal X-ray structure analysis, susceptibility, and magnetization measurements as well as the stability under electrochemical and ionization conditions. Chapter 4.1. represents a major part of this thesis.

In Chapter 4.2, the investigation on combination of chromium(III) and lanthanide(III) ions in forming heterometallic *3d-4f* MC complexes is discussed. Even though, a wide range of *3d-4f* complexes are already known no MCs with chromium(III) and lanthanide(III) ions are reported in the literature so far. The addition of anisotropic lanthanide(III) ions is necessary to obtain the desired SMM behavior moreover it influences the size of the MC cavity (see Chapter 1.1). The Chapter focuses on the obtained structures investigated by single-crystal X-ray structure analysis, emphasizing especially the distortion of the symmetry of lanthanide(III) ions in the cavity of MCs and their influence on the resulting magnetic properties.

### Chromium Complexes

Due to the low reactivity of chromium(III) ions under ambient conditions, the synthesis strategy must be adjusted accordingly. This is contrary to the known reaction conditions for more frequently used *3d* transition metal ions. In all cases, the pH value was carefully monitored since chromium(III) hydroxide ( $\text{Cr}(\text{OH})_3 \cdot n \text{H}_2\text{O}$ ) easily precipitates under basic conditions, making chromium(III) ions inaccessible for further reactions.<sup>[3]</sup> Additionally, at higher temperatures or basic pH values polymeric chromium networks containing hydroxide -OH- bridges are often observed.<sup>[4]</sup>

The results in Chapter 4.1.1. were already published in Chemistry - A European Journal in the course of the Ph.D.<sup>[1]</sup> In the following chapters 4.1.2 and 4.1.3, this paper will be classified as the first building block of Chapter 4 "Results and Discussion" of this dissertation. It is refrained from rewriting these chapter to minimize the risk of self-plagiarism by such rewriting. Furthermore, connections and comparisons to the paper will be made in the following chapters.

## 4.1. Chromium(III) metallacrowns

### 4.1.1. [9-MC-3] metallacrown with chromium(III) ions salicylhydroxamic acid

#### Filling the Gap in the Metallacrown Family: The 9-MC-3 Chromium Metallacrown

[1] A. Lüpke, L.M. Carrella, E. Rentschler, *Chem. – Eur. J.* **2021**, *27*, 4283-4286.

([doi.org/10.1002/chem.202004947](https://doi.org/10.1002/chem.202004947))

The results presented in the following chapter (p. 5-13) were first published on January 14<sup>th</sup>, 2021 (issue online March 1<sup>st</sup>, 2021) and are adapted from the communication<sup>[1]</sup>

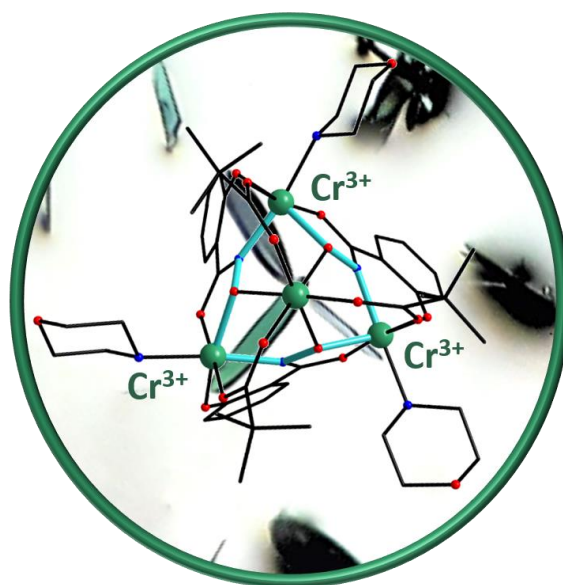
Further supporting information can be found in the appendix, **Chapter 6.1**.

The labelling of the Figure numbers and the numbers of the references were changed accordingly to the format of this thesis.

© 2020 The Authors. Chemistry - A European Journal published by Wiley-VCH GmbH - (This is an open access article under the terms of the [Creative Commons Attribution-NonCommercial-NoDerivs License](https://creativecommons.org/licenses/by-nc-nd/4.0/), which permits use and distribution in any medium, provided the original work is properly cited, the use is non-commercial and no modifications or adaptations are made)

#### Abstract:

In this work, we report on a long-sought missing complex in the metallacrown family. We synthesized and characterized the novel chromium metallacrown (MC) complex  $\{\text{Cr}^{\text{III}}(\mu_2\text{-piv})_3[9\text{-MC}_{\text{Cr}(\text{III})\text{N}(\text{shi})\text{-3}}](\text{morph})_3\} \cdot \text{MeOH}$  (in which  $\text{shi}^{3-}$  = salicyl hydroxamate,  $\text{piv}$  = pivalate, and  $\text{morph}$  = morpholine). The MC with a 9-MC-3 cavity of kinetically inert chromium(III) ions was synthesized by a solvothermal reaction. Magnetization measurements reveal a high spin ground state.



**Graphical Abstract Metalacycles:** In this work, we report on the synthesis and characterization of the long sought chromium metallacrown (MC) complex  $\{\text{Cr}^{\text{III}}(\mu_2\text{-piv})_3[9\text{-MC}_{\text{Cr}(\text{III})\text{N}(\text{shi})\text{-3}}](\text{morph})_3\} \cdot \text{MeOH}$ . The MC with a 9-MC-3 cavity of kinetically inert chromium(III) ions was finally successfully synthesized by a solvothermal reaction (see figure).

#### Summary:

The earth-abundant  $3d$  metal chromium is often used to build clusters. The electron configuration of chromium(III) ions is  $d^3$  (paramagnetic) and can lead to interesting magnetic properties. The preferred well-defined octahedral geometry of chromium(III) ions in complexes makes it a promising candidate to design metallacrowns. Chromium wheels and bridged chromium clusters exist but there was no metallacrown MC with chromium ions known until now.

This chapter describes the synthesis and characterization of a novel chromium(III) metallacrown **[Cr<sub>3</sub>Cr]-MC**. Over 30 years ago the very first metallacrowns were reported and a chromium(III) metallacrown was already predicted. The first metallacrowns included two metallacrowns with a 9-MC-3 structural motif. In this thesis, this prediction is finally achieved by the synthesis of  $\{\text{Cr}^{\text{III}}(\mu_2\text{-piv})_3[9\text{-MC}_{\text{Cr}(\text{III})\text{N}(\text{sh})\text{-}3](\text{morph})_3]\cdot\text{MeOH}$  with a similar 9-MC-3 cavity. The properties of this metallacrown were especially investigated by single-crystal X-ray structure analysis, magnetic susceptibility, and magnetization measurements. As expected, preferred octahedral ligand field around the chromium(III) ions are ideally realized in the scaffold and the cavity of the metallacrown. The structure showed a *cis*-propeller orientation of the chelating ligand leading to a 9-MC-3 cavity. Interesting magnetic properties with a spin ground state  $S_{\text{T}} \neq 0$  could be obtained. Due to two competing antiferromagnetic exchange interactions, a high spin ground state of  $S_{\text{T}} = 3$  was detected and confirmed by the susceptibility and magnetization data. The synthesis approach of solvothermal synthesis in the field of metallacrown chemistry is newly used to obtain chromium(III) metallacrowns.

This first successful synthesis of a metallacrown with chromium(III) ions paves the way for new kinetically and thermodynamically stable MCs for future applications. The kinetic inertness of chromium(III) ions makes the building of high nuclearity complexes challenging. Nevertheless, the stability allows the treatment under harsh conditions that are used for surface applications of this magnetic molecules and excludes ion exchange reactions.

#### Author Contributions:

- Anne Lüpke: Concept development, complex synthesis and characterizations, collection of magnetic measurements and evaluation, figure and cover preparation, manuscript preparation.
- Luca M. Carrella: X-ray structure refinements, scientific supervision, and manuscript correction.
- Eva Rentschler: Scientific supervision and manuscript correction.

All authors have read and agreed to the published version of the manuscript.

#### General remarks:

The cited references, figures, equations and schemes are analog to the pictures and citation in the publication. However, the reference numbers are changed accordingly to this thesis. The first source [1] of this thesis is referring to the paper itself.

**Acknowledgements:**

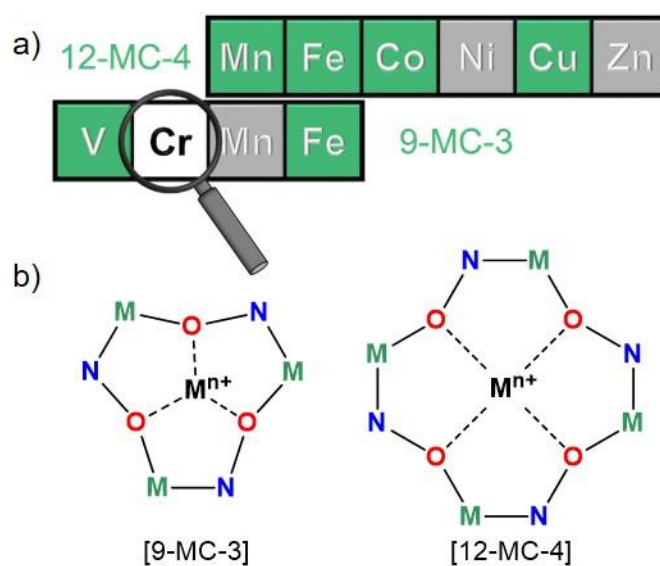
We are very grateful to Dr. Dieter Schollmeyer for the collection of the X-ray diffraction data. Funded by the Deutsche Forschungsgemeinschaft (DFG, German Research Foundation)—TRR 173-268565370 (project A09). This work was supported by the Max Planck Graduate Center with the Johannes Gutenberg-Universität Mainz (MPGC). Open access funding enabled and organized by Projekt DEAL.



## Introduction and Discussion

Metallacrowns (MCs) belong to a continuously developing class of compounds in the field of molecular recognition,<sup>[5–8]</sup> catalysis,<sup>[9]</sup> and magneto chemistry.<sup>[10–14]</sup> Like their organic crown ether analogs, MCs contain oxygen donor atoms in their repeating units,  $-[M-N-O]_n-$ , allowing them to coordinate metal guest ions. This makes them perfect candidates for molecular recognition.<sup>[5]</sup>

The very first metallacrowns, which were reported by V. Pecoraro in 1989, included the complexes  $[(VVO)_3(shi^{3-})_3(CH_3OH)_3]$ <sup>[15]</sup> and  $[Fe_4(shi^{3-})_3(MeOH)_3(OAc)_3]$ .<sup>[16]</sup> Both showed a 9-MC-3 structural motif. While vanadium 9-MC-3 was vacant and therefore had no guest ion,<sup>[15]</sup> the iron complex contained iron(III) as the central guest ion (Scheme 4.1). Thus, Pecoraro et al. forecasted more than 30 years ago that „[...] it should be possible to form [...] metallacrown ethers through synthesis of the kinetically inert  $Co^{III}$  or  $Cr^{III}$  analogues. We expect that these exchange inert clusters will form the 9-C-3 structure since the metals should be octahedral.“<sup>[16]</sup> While we reported the first cobalt MC with a 12-MC-4 cavity in 2015,<sup>[13]</sup> no chromium metallacrown with either a classical 12-MC-4 or a 9-MC-3 motif has been reported in the last 30 years. Now, we have filled this gap in the metallacrown family by synthesizing the first 9-MC-3 chromium(III) complex.



**Scheme 4. 1.** a) Color code: green: elements for which classical MCs with shi are reported;<sup>[5,13]</sup> gray: For Ni,<sup>[17,18]</sup> Zn,<sup>[19]</sup> and Mn<sup>[20,21]</sup> ions (the latter in 9-MC-3), MCs with various other ligands are reported; b) schematic representation of the repetition units for a [12-MC-4] and a [9-MC-3] cavity with guest metal ions (black color).

The likely reason for the absence of Cr-MCs is due to the challenging chemistry of chromium(III).  $Cr^{3+}$  is a kinetically inert metal ion that requires thermodynamically well-suited reaction conditions.<sup>[22]</sup> One possibility is working under basic conditions to deprotonate the desired ligands and facilitate their ligation. However, oxido-complexes are easily formed, even if the precipitation of  $Cr(OH)_3$  is avoided by controlling the pH.<sup>[23,24]</sup> Indeed,  $\mu_3$ -oxo-bridged trinuclear metal carboxylates  $[Cr^{III}(\mu_3-O)(RCOO)_6 L_3]^+$  are well known in literature.<sup>[25]</sup> Although few complexes with additional bridging  $\mu_2$ -oxime ligands are found in literature,

no reports on Cr-based MCs exist.<sup>[26,27]</sup> We attribute this lack to synthetic challenges. Fortunately, solvothermal reaction conditions have now paved the way for the synthesis of chromium(III) MCs. By applying moderate pressure and high temperatures, we were able to obtain the 9-Cr-3 MC.

Our research focuses on the magneto chemistry of MCs. In recent years, MCs have proven that they can behave as Single-Molecule Magnets, SMMs.<sup>[11,20,28]</sup> The use of kinetically inert metal ions can increase the stability of MCs which is necessary to enable the processing of MC-based SMMs.<sup>[29]</sup> We herein report the first step towards this goal. The enhanced stability will open the field for heterometallic MCs using kinetic inert ring-building  $\text{Cr}^{3+}$  on the one hand and embed magnetic anisotropic guest ions achieving SMM behavior on the other hand.

$\{\text{Cr}^{\text{III}}(\mu_2\text{-piv})_3[9\text{-MC}_{\text{Cr}(\text{III})\text{N}(\text{shi})\text{-3}}](\text{morph})_3\} \cdot \text{MeOH}$ , hereafter referred to as **[Cr<sub>3</sub>Cr]-MC** crystallizes in the monoclinic space group  $P2_1/n$  with four molecules per unit cell. The crystallographic data as well as selected bond lengths and angles are summarized in the SI (Table S1-S4, Deposition numbers [2047296](#) contains the supplementary crystallographic data for this paper. These data are provided free of charge by the joint Cambridge Crystallographic Data Centre and Fachinformationszentrum Karlsruhe [Access Structures service](#)). As the basic reaction conditions facilitate the full deprotonation of the ligand, three salicylhydroxamtes,  $\text{shi}^{3-}$ , coordinate the chromium(III) ring metal ions Cr1, Cr2, and Cr3, and form a 9-MC-3 cavity with the characteristic repetition unit [Cr-N-O] (see Figure 4.1).

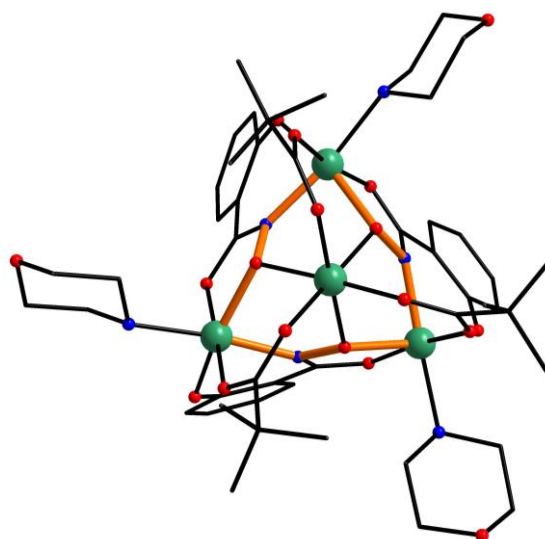


**Figure 4. 1.** Schematic representation of the molecular structure of  $\text{Cr}^{\text{III}}(\mu_2\text{-piv})_3[9\text{-MC}_{\text{Cr}(\text{III})\text{N}(\text{shi})\text{-3}}](\text{morph})_3$ . Hydrogen atoms are omitted for clarity. Color code: chromium(III) ions green, oxygen red, nitrogen blue, carbon black.

All chromium (III) ions are octahedrally coordinated, as expected based on their  $d^3$  electronic configuration (see Figure S5). For the ring-forming metal ions, this means that the  $\text{shi}^{3-}$  ligands are coordinated, providing four donor atoms (three O-donor atoms and one N-donor atom). An N-donor atom from a morpholine co-ligand and an O-donor atom from a pivalate complete the octahedral coordination (Figure 4. 2 b).

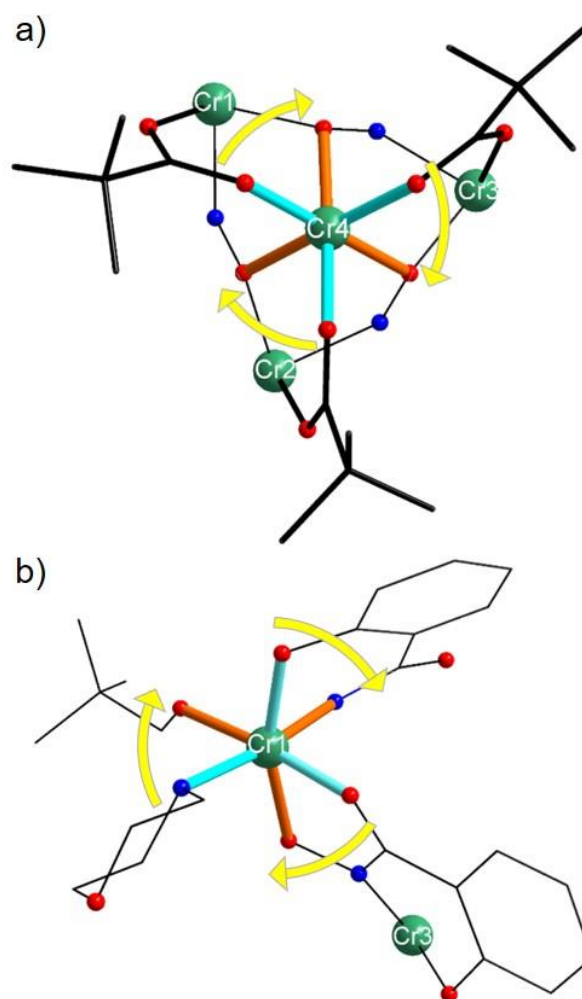


**Figure 4. 2.** Schematic representation of  $\Delta$  isomers of a) central chromium(III) ion Cr4 and b) ring metal ion Cr1. Color code: chromium(III) ions green, oxygen red, nitrogen blue, carbon black.

As the ligands are oriented *cis* to each other, the metal ions adopt an asymmetric *cis*-propeller configuration. This chiral arrangement can lead to two different isomers. Only the right-handed  $\Delta$ -isomer is shown in Figure 4. 2. It is important to note that the same chirality for all ring metal ions is a prerequisite for forming a 9-MC-3 with the repetition unit [Cr-N-O]. Hence, all ring metal ions must have either  $\Delta\Delta\Delta$  or  $\Lambda\Lambda\Lambda$  chirality (Figure 2 and S4). Figure 1 depicts the  $\Delta\Delta\Delta$ - $\Delta$  isomer of the [Cr<sub>3</sub>Cr]-MC. Due to the centrosymmetric space group, a racemate with the  $\Delta$ -isomer and  $\Lambda$ -isomer naturally results in a solid-state, as shown in Figures S4 and S5. For detailed information on the determination of chirality, see Supporting Information.

Finally, it is worth noting that the small cavity of the 9-MC-3 ring does not allow coordination of the central chromium ion in the center. This leads to considerable out-of-plane coordination of Cr4. The guest ion is located 1.89 Å above the Cr1, Cr2, and Cr3 plane and 1.11 Å above the O3, O6, and O9 plane (see Figure S7–S8) and is additionally held by three pivalate ligands coordinated in a  $\mu^2$ - $\eta^1$ : $\eta^2$  mode.

The  $[\text{Cr}_3\text{Cr}]$ -MC was spectroscopically characterized in bulk using IR and UV/Vis spectroscopy (see SI with Figures S10 and S11). The UV/Vis spectrum of  $[\text{Cr}_3\text{Cr}]$ -MC in methanol shows absorption bands at 256 nm and 356 nm which can be assigned to ligand-based  $\pi$ - $\pi^*$  and  $n$ - $\pi^*$  excitations.<sup>[30]</sup> Two bands at higher wavelengths, 425 nm and 577 nm, can be assigned to the spin-allowed ligand field transitions from the  ${}^4A_{2g} \rightarrow {}^4T_{2g}$  (F) and  ${}^4A_{2g} \rightarrow {}^4T_{1g}$  (F),<sup>[31]</sup> respectively, confirming the  $t_{2g}^3$  electron configuration.

To further elucidate the magnetic properties of the  $[\text{Cr}_3\text{Cr}]$ -MC, we performed variable temperature magnetic susceptibility measurements. Figure 4.3 shows that the  $\chi_m T$  product steadily decreases when cooling, from  $5.9 \text{ cm}^3 \text{ K mol}^{-1}$  at 300 K to a minimum of  $3.3 \text{ cm}^3 \text{ K mol}^{-1}$  at about 40 K. Further lowering of the temperature leads to the  $\chi_m T$  product increasing again, until a value of  $4.4 \text{ cm}^3 \text{ K mol}^{-1}$  is reached at 4 K. The experimental  $\chi_m T$  value at 300 K is well below the theoretical value for four uncoupled  $S=3/2$  spin centers calculated using the spin-only formula ( $7.5 \text{ cm}^3 \text{ K mol}^{-1}$ ) indicating significant antiferromagnetic exchange interactions. The shape of the  $\chi_m T$  vs.  $T$  curve further suggests the presence of competing antiferromagnetic exchange interactions.

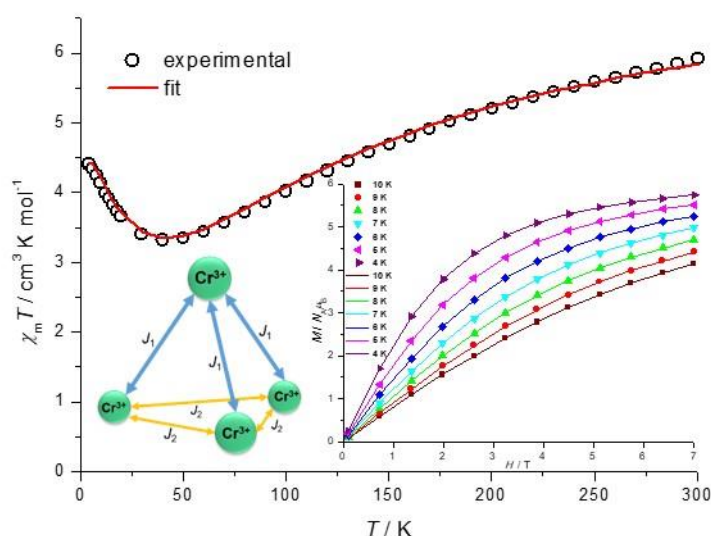


**Figure 4.3.** Temperature-dependence of magnetic susceptibility for  $[\text{Cr}_3\text{Cr}]$ -MC. The solid line represents the best fit of the data. Inset a) Idealized coupling scheme for metallacrown with coupling constant  $J_1$  between guest ion (Cr4) and ring metal ions (Cr1, Cr2, Cr3) and coupling constant  $J_2$  between neighboring ions (ring metal ions Cr1, Cr2, Cr3); b) field-dependent magnetization (4–10 K). Solid lines represent the best fit of the data.

The program PHI<sup>[32]</sup> was used to fit the susceptibility and magnetization data simultaneously using the Hamiltonian  $\hat{H}$  exchange (Equation 11) with the coupling Scheme depicted in the inset in Figure 4.3. In this equation,  $J_1$  describes the coupling constant between the guest and ring metal ions, while  $J_2$  describes the coupling between the neighboring ring metal ions.

$$\hat{H} = -2J_1(\hat{S}_{\text{Cr4}} \cdot \hat{S}_{\text{Cr1}} + \hat{S}_{\text{Cr4}} \cdot \hat{S}_{\text{Cr2}} + \hat{S}_{\text{Cr4}} \cdot \hat{S}_{\text{Cr3}}) - 2J_2(\hat{S}_{\text{Cr1}} \cdot \hat{S}_{\text{Cr2}} + \hat{S}_{\text{Cr2}} \cdot \hat{S}_{\text{Cr3}} + \hat{S}_{\text{Cr1}} \cdot \hat{S}_{\text{Cr3}}) \quad (11)$$

The best fit was obtained for the exchange coupling constants  $J_1 = -11.2 \text{ cm}^{-1}$  and  $J_2 = -3.2 \text{ cm}^{-1}$  with the  $g$  factor for the chromium(III) ions fixed at  $g_{\text{Cr}^{3+}} = 2.00$ . The residual  $R$  was calculated to be  $0.10 \times 10^{-9}$ . We included a very small intermolecular antiferromagnetic interaction, implemented as mean field interaction  $zJ = -0.045 \text{ cm}^{-1}$ . Although this value is very low, its inclusion is necessary to obtain a satisfactory simulation of the data. Such a small intermolecular antiferromagnetic coupling is easily explained by weak dipole-dipole interactions between the chromium(III) ions of neighboring MCs ( $d = 5.5 \text{ \AA}$ , see Figure S1). The value of the higher antiferromagnetic interaction between the ring metal ions and the guest ion,  $J_1 = -11.2 \text{ cm}^{-1}$ , is in accordance with the observed average angles  $\text{Cr}_{\text{ring}}\text{-O-Cr}_{\text{guest}}$  of  $\approx 113^\circ$ . The exchange between neighboring ring metal ions occurs exclusively via NO moieties with average torsion angles  $\text{Cr}_{\text{ring}}\text{-O-N-Cr}_{\text{ring}}$  of  $\approx 154^\circ$ , which explains the lower value of  $J_2 = -3.2 \text{ cm}^{-1}$ .

Similar Cr-O-Cr bond angles as in our  $[\text{Cr}_3\text{Cr}]\text{-MC}$  are reported for the above-mentioned carboxylates,  $[\text{Cr}_3(\mu_3\text{-O})(\text{RCOO})_6]$  with  $110\text{--}120^\circ$ . For these  $\mu_3\text{-oxo}$  complexes coupling constants between  $-9.5 \text{ cm}^{-1}$  and  $-14 \text{ cm}^{-1}$  are reported.<sup>[26,33,34]</sup> However, the comparison with the iron(III) metallacrown,  $\text{Fe}^{\text{III}}[\text{9-MC}_{\text{Fe(III)N}(\text{sh})\text{-3}}]$ , seems more appropriate as it shows the same  $\mu_2\text{-O}$  mode with an angle of  $115^\circ$ .<sup>[35]</sup> The reported coupling constant is  $-14 \text{ cm}^{-1}$  which matches the value obtained in our study perfectly. It is less easy to compare the antiferromagnetic exchange interaction  $J_2$  via the  $\text{Cr}^{3+}\text{-N-O-Cr}^{3+}$  coordination with examples from the literature. To the best of our knowledge, all complexes with  $\text{Cr}^{3+}\text{-N-O-Cr}^{3+}$  coordination have additional bridging oxygen ligands, and the  $\text{Cr}^{3+}\text{-O-Cr}^{3+}$  exchange process is considered to dominate. Moreover, the  $\mu_3\text{-oxo}$ -bridged complexes with  $\text{Cr}^{3+}\text{-N-O-Cr}^{3+}$  bridges have much smaller torsion angles and are thus not comparable with the torsion angles in our  $[\text{Cr}_3\text{Cr}]\text{-MC}$ .<sup>[26,27]</sup> Again, the above-mentioned iron(III) metallacrown has a comparable large torsion angle of  $150^\circ$ .<sup>[35]</sup> The coupling constant within the ring for this MC was also determined as  $J_2 = -3.2 \text{ cm}^{-1}$ . Taking into account a dominant  $\pi$ -contribution for the exchange interaction via the hydroxamate group, the comparable coupling strength is easily explained by the analog electron configuration for the  $d^5$  and  $d^6$  metal ions regarding the  $t_{2g}$ -orbitals with  $\pi$ -character.

For MC complexes with competing exchange interactions,  $J_1$  and  $J_2$ , previous research has shown that the relative energies of the spin states are functions of the ratio between the coupling constants  $J_1/J_2$ .<sup>[12,36]</sup> At a ratio of  $J_1/J_2$  close to 1, the  $S_{\text{T}}$  ground state with the lowest multiplicity occurs as a result of an alternating spin alignment in the cyclic scaffold. On the contrary, if  $J_1$  coupling constants dominate, the peripheral spins align antiparallel to the central spin. In our study, we extracted a  $J_1/J_2$  ratio of 3.5 and showed that the antiferromagnetic coupling  $J_1$  of the guest ion with the ring metal ions is slightly dominant, thus forcing the coordination cluster into a high spin ground state of  $S_{\text{T}} = 3$ .

To confirm this ground state, we performed field-dependent magnetization measurements between 4 K and 10 K in an applied field of 0 to 7 T (see insert Figure 4. 3 and S15). Although the magnetization increases rapidly, it does not reach saturation. However, extrapolation of the saturation value in higher fields is consistent with six unpaired electrons, indicating a spin ground state of  $S_{\text{T}} = 3$ . (For the simulation of the Zeeman splitting see Figures S13 and S14)

In conclusion, we synthesized the long-sought missing chromium metallacrown  $\{\text{Cr}^{\text{III}}(\mu_2\text{-piv})_3[9\text{-MC}_{\text{Cr}(\text{III})\text{N}(\text{shi})\text{-3}}](\text{morph})_3\} \cdot \text{MeOH}$ , which was predicted over 30 years ago.<sup>[16]</sup> The structure corresponds to predictions made based on the iron(III) metallacrown. The magnetic analysis revealed two competing antiferromagnetic exchange interactions, resulting in a spin ground state of  $S_T=3$ . This first successful chromium(III) MC synthesis paves the way for new kinetically and thermodynamically stable MCs which can be used in multiple applications. We will continue this line of research with the aim of implementing other ions in chromium metallacrown cavities.

Published in “Chemistry – A European Journal” with the cover prepared by Anne Lüpke (Volume 27, Issue 13, March 1, 2021, Pages 4283-4286).<sup>[37,38]</sup>

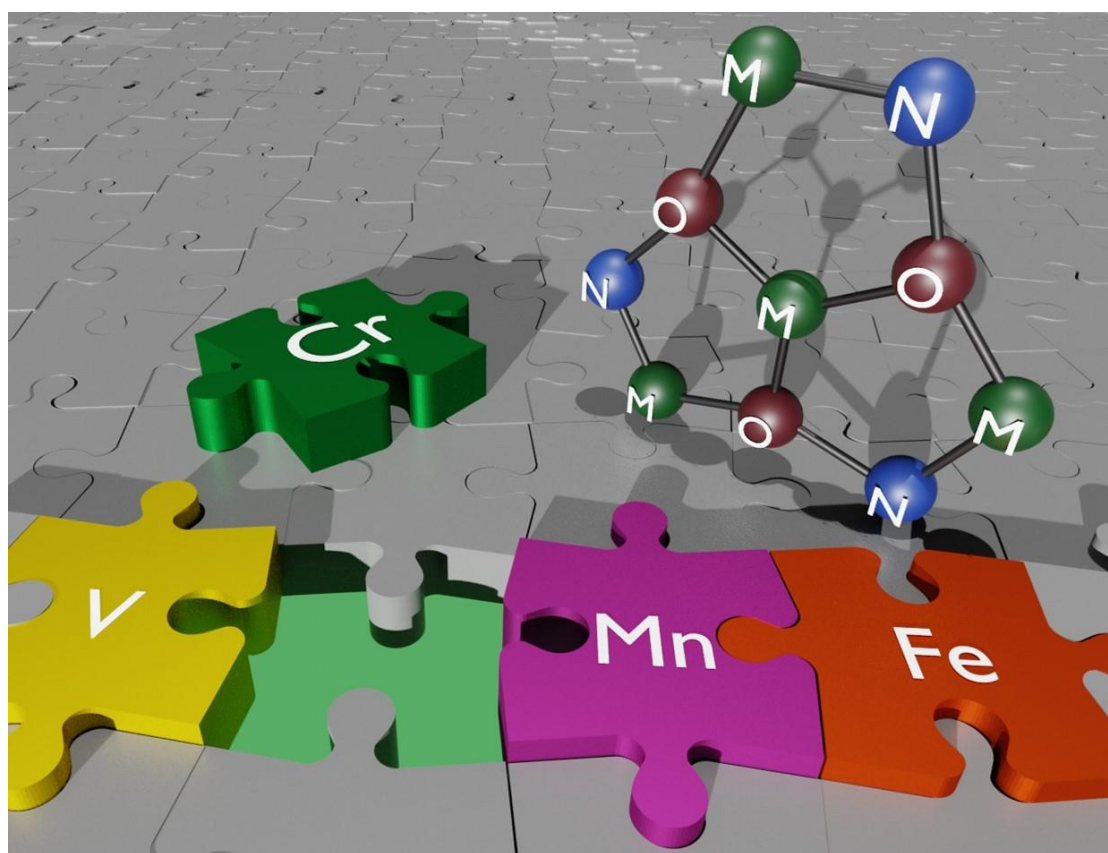


**Figure 4. 4.** Front Cover: Filling the Gap in the Metallacrown Family: The 9-MC-3 Chromium Metallacrown (Chem. Eur. J. 13/2021), prepared by Anne Lüpke with *Blender*.<sup>[38]</sup>

#### 4.1.1.1. References

- [1] A. Lüpke, L. M. Carrella, E. Rentschler, *Chem. – Eur. J.* **2021**, *27*, 4283–4286.
- [2] G. Mezei, C. M. Zaleski, V. L. Pecoraro, *Chem. Rev.* **2007**, *107*, 4933–5003.
- [3] L. Spiccia, W. Marty, *Inorg. Chem.* **1986**, *25*, 266–271.
- [4] S. I. Shupack, *Environ. Health Perspect.* **1991**, *92*, 7–11.
- [5] G. Mezei, C. M. Zaleski, V. L. Pecoraro, *Chem. Rev.* **2007**, *107*, 4933–5003.
- [6] V. L. Pecoraro, A. J. Stemmler, B. R. Gibney, J. J. Bodwin, H. Wang, J. W. Kampf, A. Barwinski, in *Prog. Inorg. Chem.*, Wiley-Blackwell, **2007**, pp. 83–177.
- [7] J. J. Bodwin, A. D. Cutland, R. G. Malkani, V. L. Pecoraro, *Coord. Chem. Rev.* **2001**, *216–217*, 489–512.
- [8] L. F. Jones, C. A. Kilner, M. A. Halcrow, *Chem. – Eur. J.* **2009**, *15*, 4667–4675.
- [9] M. Ostrowska, I. O. Fritsky, E. Gumienna-Kontecka, A. V. Pavlishchuk, *Coord. Chem. Rev.* **2016**, *327–328*, 304–332.
- [10] C. J. Milios, A. Vinslava, W. Wernsdorfer, S. Moggach, S. Parsons, S. P. Perlepes, G. Christou, E. K. Brechin, *J. Am. Chem. Soc.* **2007**, *129*, 2754–2755.
- [11] C. M. Zaleski, S. Tricard, E. C. Depperman, W. Wernsdorfer, T. Mallah, M. L. Kirk, V. L. Pecoraro, *Inorg. Chem.* **2011**, *50*, 11348–11352.
- [12] P. Happ, E. Rentschler, *Dalton Trans. Camb. Engl. 2003* **2014**, *43*, 15308–15312.
- [13] P. Happ, C. Plenck, E. Rentschler, *Coord. Chem. Rev.* **2015**, *289–290*, 238–260.
- [14] C. Plenck, J. Krause, M. Beck, E. Rentschler, *Chem. Commun.* **2015**, *51*, 6524–6527.
- [15] V. L. Pecoraro, *Inorganica Chim. Acta* **1989**, *155*, 171–173.
- [16] M. Soo Lah, M. L. Kirk, W. Hatfield, V. L. Pecoraro, *J. Chem. Soc. Chem. Commun.* **1989**, *0*, 1606–1608.
- [17] A. J. S. George Psomas Catherine Dendrinou-Samara, Jeffrey J. Bodwin, Manuela Schneider, Maria Alexiou, Jeff W. Kampf, Dimitris P. Kessissoglu, Vincent L. Pecoraro, *Inorg. Chem.* **2001**, 1562–1570.
- [18] C. McDonald, S. Sanz, E. K. Brechin, M. K. Singh, G. Rajaraman, D. Gaynor, L. F. Jones, *RSC Adv.* **2014**, *4*, 38182–38191.
- [19] M. Alexiou, C. Dendrinou-Samara, C. P. Raptopoulou, A. Terzis, D. P. Kessissoglou, *Inorg. Chem.* **2002**, *41*, 4732–4738.
- [20] S. Wang, L. Kong, H. Yang, Z. He, Z. Jiang, D. Li, S. Zeng, M. Niu, Y. Song, J. Dou, *Inorg. Chem.* **2011**, *50*, 2705–2707.
- [21] A. Tarushi, A. G. Hatzidimitriou, M. Estrader, D. P. Kessissoglou, V. Tangoulis, G. Psomas, *Inorg. Chem.* **2017**, *56*, 7048–7057.
- [22] M. Murrie, S. Parsons, R. E. P. Winpenny, I. M. Atkinson, C. Benelli, *Chem. Commun.* **1999**, 285–286.
- [23] F. Y. Salem, T. F. Parkerton, R. V. Lewis, J. H. Huang, K. L. Dickson, *Sci. Total Environ.* **1989**, *86*, 25–41.
- [24] D. Rai, L. E. Eary, J. M. Zachara, *Sci. Total Environ.* **1989**, *86*, 15–23.

- [25] R. D. Cannon, R. P. White, in *Prog. Inorg. Chem.*, John Wiley & Sons, Ltd, **1988**, pp. 195–298.
- [26] K. V. Pringouri, C. P. Raptopoulou, A. Escuer, T. C. Stamatatos, *Inorganica Chim. Acta* **2007**, *360*, 69–83.
- [27] A.-R. Tomsa, Y. Li, S. Blanchard, P. Herson, K. Boubekeur, P. Gouzerh, A. Proust, *J. Clust. Sci.* **2014**, *25*, 825–838.
- [28] A. J. Lewis, E. Garlatti, F. Cugini, M. Solzi, M. Zeller, S. Carretta, C. M. Zaleski, *Inorg. Chem.* **2020**, *59*, 11894–11900.
- [29] C. Dendrinou-Samara, A. N. Papadopoulos, D. A. Malamataris, A. Tarushi, C. P. Raptopoulou, A. Terzis, E. Samaras, D. P. Kessissoglou, *J. Inorg. Biochem.* **2005**, *99*, 864–875.
- [30] Sheetal, K. Nehra, R. Kaushal, S. Arora, D. Kaur, R. Kaushal, *Russ. J. Gen. Chem.* **2016**, *86*, 154–160.
- [31] C. D. Beard, L. Carr, M. F. Davis, J. Evans, W. Levason, L. D. Norman, G. Reid, M. Webster, *Eur. J. Inorg. Chem.* **2006**, *2006*, 4399–4406.
- [32] N. F. Chilton, R. P. Anderson, L. D. Turner, A. Soncini, K. S. Murray, *J. Comput. Chem.* **2013**, *34*, 1164–1175.
- [33] C. E. Anson, J. P. Bourke, R. D. Cannon, U. A. Jayasooriya, M. Molinier, A. K. Powell, *Inorg. Chem.* **1997**, *36*, 1265–1267.
- [34] P. Chaudhuri, M. Hess, E. Rentschler, T. Weyhermüller, U. Flörke, *New J. Chem.* **1998**, *22*, 553–555.
- [35] C. Y. Chow, R. Guillot, E. Rivière, J. W. Kampf, T. Mallah, V. L. Pecoraro, *Inorg. Chem.* **2016**, *55*, 10238–10247.
- [36] A. B. Lago, J. Pasán, L. Cañadillas-Delgado, O. Fabelo, F. J. M. Casado, M. Julve, F. Lloret, C. Ruiz-Pérez, *New J. Chem.* **2011**, *35*, 1817–1822.
- [37] A. Lüpke, L. M. Carrella, E. Rentschler, *Chem. – Eur. J.* **2021**, *27*, 4215–4215.
- [38] A. Lüpke, L. M. Carrella, E. Rentschler, *Chem. – Eur. J.* **2021**, *27*, 4211–4211.



#### 4.1.2. Influencing the metallacrown cavity including iron and chromium ions

In this chapter, firstly, the choice of the ligands and their synthesis will be discussed. Further, it will be discussed how the formation of different cavities of MCs is influenced by varying the used ligands. Secondly, the crystal structure with the data obtained from the X-ray structure analysis, the analysis of the magnetic properties, and studies of electrochemical and/or electrospray ionization mass spectrometry stability were investigated.

In 1993, Pecoraro and co-workers already showed that the ligand design in the backbone influences the torsion angles of the repetition unit. For the vacant  $[9\text{-MC-(VO}_3^+)_3\text{N(nha)}_3]$  metallacrown the substitution of salicylhydroxamic acid to 3-hydroxy-2-naphthylhydroxamic acid (= **Nha**) was reported.<sup>[39]</sup> It was suggested that an extension of the aromatic system should lead to a higher hydrophobic repulsion of these rings and thus, a larger cavity should form. Surprisingly, the opposite effect was observed. Instead, quadrupolar interactions between the hydrogen atoms of the aromatic rings resulted in a significant twisting of the naphthyl rings and a shorter distance of the naphthoic rings. Therefore, it was refrained from to use this ligand for further studies of a chromium metallacrown in this thesis.

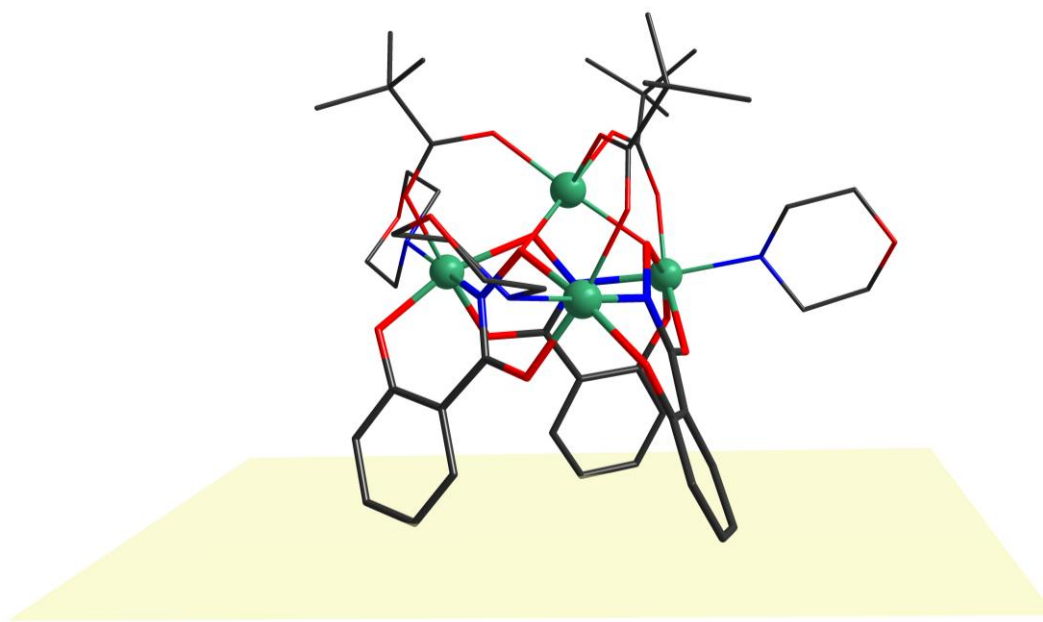
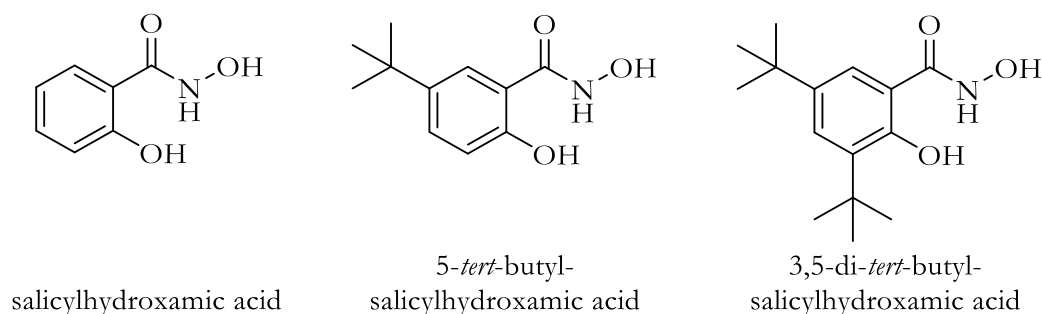


**Figure 4. 5.** Side view of  $[\text{Cr}_3\text{Cr}]$  with a plane (yellow) created through the lowest aromatic carbon atoms of the ligand backbone (thick bonds). Hydrogen atoms are omitted for clarity.

All in all, it is very intriguing to understand the influence of the ligand in the aromatic backbone. In this work, the  $[\text{Cr}_3\text{Cr}]$  MC (see Chapter 4.1.1), will be considered in order to influence the cavity. A flat MC is desirable to form effective interactions with surfaces for surface applications through physisorption. Compared to the synthesized  $[\text{Cr}_3\text{Cr}]$  in this thesis (see Chapter 4.1), a few differences to the vacant  $[9\text{-MC-(VO}_3^+)_3\text{N(Nha)}_3]$  vanadium metallacrown must be considered. Vanadium possesses other co-ligands such as the terminal oxygen ligand which coordinates *via* a double bond. This leads to insufficient space in the coordination for bridging co-ligands present for a potential guest ion. Thus, the two major differences

are the change in bond type and the lack of guest ion coordination. However, the cavity, the ligand, and geometry are similar to each other. Again, **Nha** ligands are arranged in a *cis*-propeller configuration with either a  $\Delta\Delta\Delta$ - $\Delta$  or  $\Lambda\Lambda\Lambda$ - $\Lambda$  chirality. In this study, two ligands were synthesized and analyzed in the context of the MC cavity. An overview of the ligands that are used in the Chapters 4.1.2.1 and Chapter 4.1.2.2 is illustrated in Scheme 4.2.



**Scheme 4. 2.** Overview of ligands used in this chapter: salicylhydroxamic acid ( $\text{shiH}_3$ ), 5-*tert*-butylsalicylhydroxamic acid ( $\text{t}^{\text{bu}}\text{ShiH}_3$ ); 3,5-di-*tert*-butylsalicylhydroxamic acid ( $\text{t}^{\text{bu}}_2\text{ShiH}_3$ ).

Salicylhydroxamic acid is commercially available and can be used for synthesis without further processing. 5-*tert*-Butylsalicylhydroxamic acid and 3,5-di-*tert*-butylsalicylhydroxamic acid were synthesized and their synthetic routes are explained in the following: The ligand 5-*tert*-butylsalicylhydroxamic acid was prepared in a two-step procedure starting from methyl salicylate. First, a Friedel-Crafts alkylation was carried out using aluminum chloride and *tert*-butyl chloride. Aluminum trichloride acts as Lewis acid leading to a heterolytic cleavage of the C-Cl-bond in *tert*-butyl chloride. The resulting *tert*-butyl cation is attacked in the following by the nucleophilic salicylic methyl ester. The alkylation occurs *para*-position due to its +M-effect of the hydroxide group. In addition, the ester group is directing in *meta*-position, since the -M-effect reduces the electron density in the *para*- and *ortho*-positions. By rearomatization, the 5-*tert*-butylmethyl salicylate is obtained. In the second step, the hydroxylamine is prepared *in situ* by using a methanolic potassium hydroxide solution and a methanolic hydroxylamine hydrochloride solution. Hydroxylamine<sup>[40]</sup> attacks the carbonyl carbon of the 5-*tert*-butylsalicyl methyl ester and forms 5-*tert*-butylsalicylhydroxamic acid *via* an addition-elimination mechanism finally releasing methanol. The product was crystallized from methanol.

3,5-di-*tert*-butylsalicylhydroxamic acid was synthesized in a two-step reaction. First, 3,5-di-*tert*-butylsalicylic acid is converted into the corresponding methyl ester by an acid catalyzed esterification reaction in methanol in the presence of sulfuric acid. The transformation is necessary to provide a better leaving group enabling a subsequent aminolysis. For this step, hydroxylamine is prepared *in situ* by using a methanolic potassium hydroxide solution and a methanolic hydroxylamine hydrochloride solution. Again, hydroxylamine<sup>[40]</sup> attacks the carbonyl carbon of the 3,5-di-*tert*-butylsalicyl methyl ester and forms 3,5-di-*tert*-butylsalicylhydroxamic acid upon elimination of methanol. The product was purified by column chromatography.

#### 4.1.2.1. $\{\text{Fe}^{\text{III}}(\mu_2\text{-OOCPh})_3[9\text{-MC}_{\text{Fe}(\text{III})\text{N}(\text{tBuShi})\text{-3]}(\text{MeOH})_3]\} \cdot x \text{MeOH}$ (**tBu-[Fe<sub>3</sub>Fe]**)

Iron(III) and chromium(III) ions are often compared due to the analog half-occupied  $t_{2g}$ -orbitals with  $\pi$ -character in the  $d^3$  and  $d^5$  electron configuration.<sup>[1,41,42]</sup> Preliminary studies were performed using iron(III) compounds to synthesize MCs. This study was carried out under my supervision by undergraduate student Tristan Fischer for his Bachelor thesis. The synthesis was performed under ambient conditions since no additional solvothermal conditions were required. Iron(III) chloride ( $\text{FeCl}_3 \cdot 6\text{H}_2\text{O}$ ), 5-*tert*-butylsalicylhydroxamic acid (**tBuShiH<sub>3</sub>**), sodium benzoate, and tetrabutylammonium perchlorate were dissolved in methanol and stirred for 40 minutes. The solution was filtered and allowed to crystallize under ambient conditions by slow evaporation of the solvent. Brown plates were obtained after 10 days as single crystals of  $\{\text{Fe}^{\text{III}}(\mu_2\text{-OOCPh})_3[9\text{-MC}_{\text{Fe}(\text{III})\text{N}(\text{tBuShi})\text{-3]}(\text{MeOH})_3]\} \cdot x \text{MeOH}$  hereafter named as **tBu-[Fe<sub>3</sub>Fe]**. The structure is shown in Figure 4. 6 and is comparable to the reported **[Cr<sub>3</sub>Cr]** MC with a [9-MC-3] cavity (Chapter 4.1.1.).

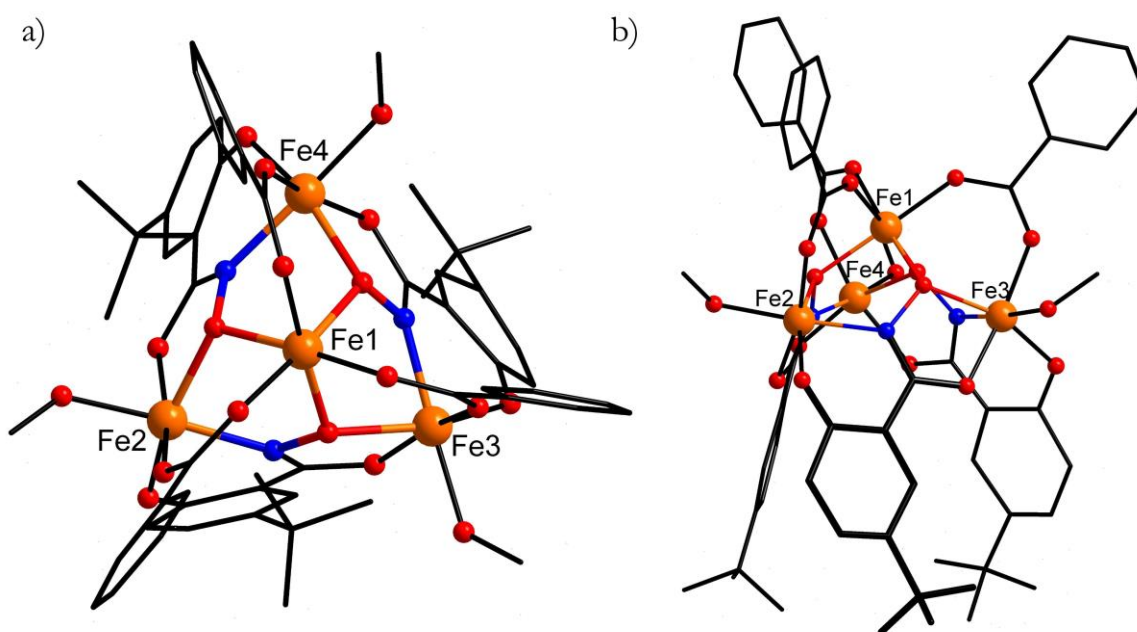


**Figure 4. 6.** Schematic representation of the molecular structure of  $\{\text{Fe}^{\text{III}}(\mu_2\text{-OOCPh})_3[9\text{-MC}_{\text{Fe}(\text{III})\text{N}(\text{tBuShi})\text{-3]}(\text{MeOH})_3]\}$ ; a) with emphasized repetition unit (top view); b) with emphasized coordinated ligand (side view). Hydrogen atoms are omitted for clarity. Color code: iron(III) ions orange, oxygen red, nitrogen blue, carbon black.

The MC crystallizes in a triclinic crystal system with the space group P-1. The lattice parameters are  $a = 17.5521(3) \text{ \AA}$ ,  $b = 17.5490(3) \text{ \AA}$ ,  $c = 48.6297(9) \text{ \AA}$ ,  $\alpha = 84.1970(10)^\circ$ ,  $\beta = 81.07730(10)^\circ$ , and  $\gamma = 59.9330(10)^\circ$ . Three MC molecules (a (Fe1-F4), b (Fe5-Fe8) and c(Fe9-Fe12)) are found in the asymmetric unit and six MC molecules in the unit cell (see Figure 4. 8 and Figure S17). The number of non-coordinating solvent molecules could not be determined completely due to the small crystal size and poor crystal quality only low angle data could be collected. The triply deprotonated 5-*tert*-butylsalicylhydroxamic acid coordinates three iron(III) ions to form a five- and six-membered ring, thus forming the [9-MC-3] cavity of a MC. Each iron(III) ring metal ion is linked to the iron(III) guest ion by a  $\mu_2$ -bridging benzoate

co-ligand. The iron(III) guest ion is octahedrally coordinated by three donor oxygen atoms of the ligand and by three oxygen atoms of the benzoate. The 5-*tert*-butylsalicylhydroxamate ligand occupies four of the six coordination sites to form an octahedral geometry of the iron(III) ring ions. The remaining two coordination sites are occupied by one oxygen atom of the benzoate, and one oxygen atom of the coordinating peripheral methanol creating the octahedral environment. The additive tetrabutylammonium perchlorate is not included in the crystal, but it promotes the crystallization of **tbu-[Fe<sub>3</sub>Fe]** single-crystals.

The coordination of the iron(III) guest ion is similar to the chromium(III) ions in **[Cr<sub>3</sub>Cr]** out-of-plane due to the iron(III) ion size (see Figure S16). The coordination environment of metal ion surrounded by six ligands can be assigned to five different polyhedra (Table 4. 1, Table 4. 2).<sup>[43–47]</sup>

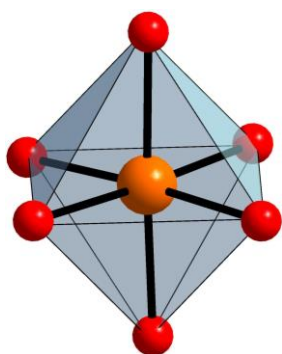


**Figure 4. 7.** Schematic representation of the ideal coordination polyhedron (grey) of the Fe1 of **tbu-[Fe<sub>3</sub>Fe]** for an octahedral symmetry. Color code of atoms: oxygen red, iron(III) ion orange.

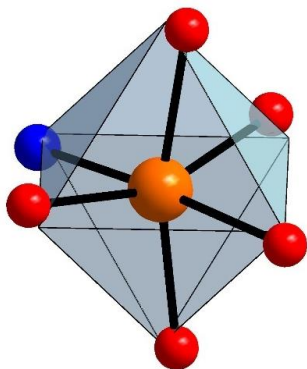


**Figure 4. 8.** Schematic representation of the ideal coordination polyhedron (grey) of the Fe4 of **tbu-[Fe<sub>3</sub>Fe]** for an octahedral symmetry. Color code of atoms: oxygen red, nitrogen blue, iron(III) ion orange.

**Table 4. 1.** Calculated deviations from ideal polyhedra for guest ion Fe1 *via* Continuous Shape Measurements.

Polyhedra	CShM
Hexagon $D_{6h}$	32.576
Pentagonal pyramid $C_{5v}$	28.366
<b>Octahedron <math>O_h</math></b>	<b>0.113</b>
Trigonal prism $D_{3h}$	14.422
Johnson pentagonal pyramid $C_{5v}$	32.071

**Table 4. 2.** Calculated deviations from ideal polyhedra for ring metal ion Fe4 *via* Continuous Shape Measurements.

Polyhedra	CShM
Hexagon $D_{6h}$	32.839
Pentagonal pyramid $C_{5v}$	21.879
<b>Octahedron <math>O_h</math></b>	<b>1.539</b>
Trigonal prism $D_{3h}$	10.036
Johnson pentagonal pyramid $C_{5v}$	25.577

Using the SHAPE-program a value of 0.11 is calculated for the iron(III) guest ion. This value describes the deviation from the ideal octahedral coordination environment. Regarding the iron(III) ring ions, the SHAPE value CShM is 1.48 on average (see Tables S9-12). In general, the SHAPE values specify the deviation of the coordination environment of the iron(III) ion from the ideal coordination geometry. If a small deviation from the ideal geometry is achieved, a small calculated SHAPE value close to zero is obtained. The SHAPE values clearly indicate a nearly perfect octahedral coordination geometry for the iron(III) guest ion. In the case of the iron(III) ring metal ions, a minor distortion of the octahedral coordination geometry occurs

because one coordination site is occupied by a nitrogen atom. In contrast, the iron(III) guest ion is coordinated exclusively by oxygen atoms. These octahedral polyeder of the guest ion Fe1 and one ring metal ions Fe4 are also shown in Figure 4. 7 and Figure 4. 8. The thin black lines define the vertices of the ideal octahedral geometry while the ideal faces are highlighted in gray. The distortion from the ideal geometry of the ring metal ion is clearly evident. This is also due to the bridging co-ligand. Compared to **[Cr<sub>3</sub>Cr]** the deviations are slightly higher but due to the uniform occupation of the antibonding  $e_g^*$  orbitals only small deviation of the ideal geometry can be observed.

**Table 4. 3.** Selected bond lengths of each iron(III) ion of **bu-[Fe<sub>3</sub>Fe]**.

ion	Fe1	Fe2	Fe3	Fe4
bond length / Å	O3 2.006(11)	O1 1.933(14)	O2 1.996(13)	O5 1.998(14)
	O6 2.008(12)	O8 2.012(14)	O3 2.075(11)	O6 2.062(11)
	O9 2.013(12)	O9 2.082(11)	O4 1.931(15)	O7 1.899(15)
	O10 2.011(12)	O11 1.993(15)	O13 1.971(13)	O15 1.974(13)
	O12 1.984(13)	O16 2.022(15)	O17 2.042(15)	O18 2.067(15)
	O14 1.998(12)	N1 2.039(14)	N2 2.042(14)	N3 2.046(14)
ion	Fe5	Fe6	Fe7	Fe8
bond length / Å	O21 2.019(10)	O19 1.913(12)	O20 1.972(12)	O23 1.993(11)
	O24 2.049(10)	O26 2.014(11)	O21 2.077(10)	O24 2.047(11)
	O27 2.028(11)	O27 2.042(10)	O22 1.938(11)	O25 1.886(12)
	O28 2.033(11)	O29 2.007(12)	O31 2.008(13)	O33 1.977(12)
	O30 2.021(12)	O34 2.062(11)	O35 2.038(11)	O36 2.091(11)
	O32 2.049(11)	N6 2.057(13)	N5 2.078(13)	N4 2.063(13)
ion	Fe9	Fe10	Fe11	Fe12
bond length / Å	O39 2.002(11)	O37 1.919(12)	O38 1.977(12)	O41 1.994(12)
	O42 2.027(10)	O44 1.975(11)	O39 2.070(11)	O42 2.063(10)
	O45 1.997(10)	O45 2.079(10)	O40 1.933(11)	O43 1.912(11)
	O46 2.001(11)	O47 1.952(12)	O49 1.991(13)	O51 1.987(12)
	O48 2.038(11)	O52 2.033(12)	O53 2.053(10)	O54 2.021(12)
	O50 2.005(12)	N7 2.064(13)	N8 2.067(13)	N9 2.057(13)

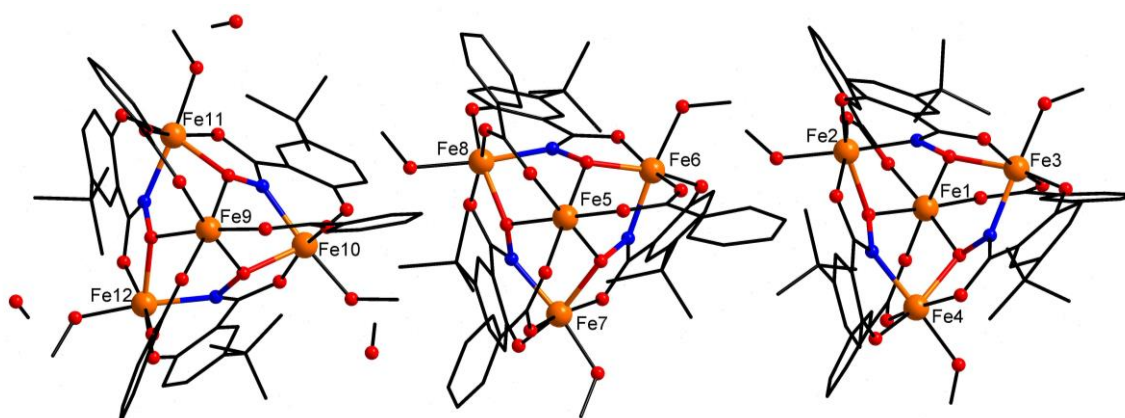


**Figure 4. 9.** Asymmetric unit containing three MC molecules (a,b,c) of **bu-[Fe<sub>3</sub>Fe]**. Hydrogen atoms are omitted for clarity. Color code: iron(III) ions orange, oxygen red, nitrogen blue, carbon black.

A selection of bond and torsion angles for the three independent cluster molecules in the asymmetric unit is shown in Table 4.4. These are important to examine the magnetic exchange interactions of the ring metal ion Fe1 to the ring metal ions Fe2, Fe3, and Fe4. It is shown that for the three different MC molecules, the bond angles and torsion are very similar. Therefore, one “average” molecule was considered with a mean value for bond angle of  $113.9^\circ$  between the guest and ring metal ions and a torsion angle of  $155.3^\circ$  for the intramolecular interaction of the iron(III) ions for the evaluation of the magnetic data.

**Table 4.4.** Selected bond angles and torsion angles for the MC molecules a, b, and c in the asymmetric unit for **4bu-[Fe<sub>3</sub>Fe]**.

	bond angles		torsion angles	
<b>4bu-[Fe<sub>3</sub>Fe] (a)</b>	Fe1-O9-Fe2	$113.5(5)^\circ$	Fe2-O9-N3-Fe4	$155.1(6)^\circ$
	Fe1-O3-Fe3	$113.7(5)^\circ$	Fe2-O3-N1-Fe3	$154.8(7)^\circ$
	Fe1-O6-Fe4	$113.8(5)^\circ$	Fe4-O6-N2-Fe3	$155.4(7)^\circ$
<b>4bu-[Fe<sub>3</sub>Fe] (b)</b>	Fe5-O27-Fe6	$114.1(5)^\circ$	Fe7-O21-N6-Fe6	$156.0(6)^\circ$
	Fe5-O21-Fe7	$113.6(5)^\circ$	Fe6-O27-N4-Fe8	$156.2(6)^\circ$
	Fe8-O24-Fe5	$113.2(5)^\circ$	Fe8-O24-N5-Fe7	$155.3(6)^\circ$
<b>4bu-[Fe<sub>3</sub>Fe] (c)</b>	Fe9-O45-Fe10	$114.3(5)^\circ$	Fe10-O39-N7-Fe11	$154.2(6)^\circ$
	Fe9-O42-Fe12	$114.0(5)^\circ$	Fe10-O45-N9-Fe12	$154.6(6)^\circ$
	Fe9-O39-Fe11	$114.5(5)^\circ$	Fe12-O42-N8-Fe11	$155.7(7)^\circ$
<b>average</b>	Fe <sub>guest</sub> -O-Fe <sub>ring</sub>	$113.9^\circ$	Fe <sub>guest</sub> -O-N-Fe <sub>ring</sub>	$155.3^\circ$

### Evaluation of magnetic data

The magnetic properties of **4bu-[Fe<sub>3</sub>Fe]** were investigated and are discussed in the following. The temperature-dependent molar magnetic susceptibility  $\chi_m T$  is plotted against the temperature  $T$  in the range of 2K - 300K in Figure 4. 10 a including the fit of the susceptibility using the coupling scheme in Figure 4. 10 b and the Hamiltonian in Equation 14.

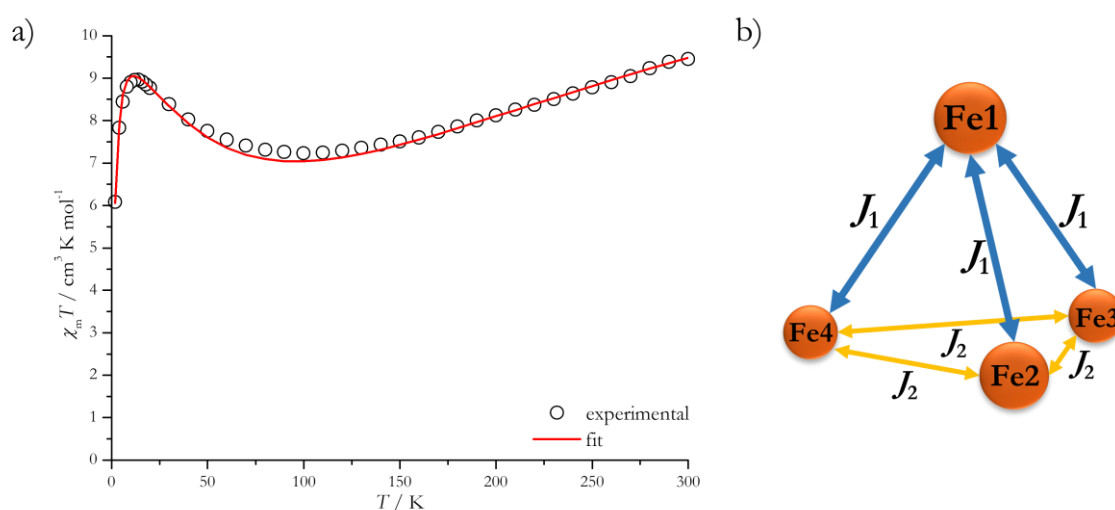


**Figure 4. 10.** a) Temperature-dependence of magnetic susceptibility for [Fe<sub>3</sub>Fe]-MC. The solid red line represents the best fit of the data; b) Idealized coupling scheme for MC with coupling constant  $J_1$  between guest ion (Fe1) and ring metal ions (Fe2, Fe3, Fe4) and coupling constant  $J_2$  between neighboring ions (ring metal ions Fe2, Fe3, Fe4).

The spin-only formula in equation 12 is used to calculate the theoretical  $\chi_m T$  value at 300 K with Equation 13 for the  $3d$  metal ions if the orbital momentum can be neglected.

$$\mu_{\text{eff}} = g \cdot \sqrt{S(S+1)}\mu_B \quad (12)$$

$$\chi_M T \approx \frac{N_A \mu_B^2}{3k_B} \cdot (\mu_{\text{eff}})^2 \approx \frac{g^2 \cdot S(S+1)}{8} \quad (13)$$

In this case, each iron(III) ion should contribute with  $\chi_m T = 4.375 \text{ cm}^3 \text{ K mol}^{-1}$  with  $g = 2$  and  $S = 5/2$ . Thus, the expected  $\chi_m T$  value for **bu-[Fe<sub>3</sub>Fe]** with four iron(III) ions is  $\chi_m T = 17.5 \text{ cm}^3 \text{ K mol}^{-1}$ . The measured value of  $9.44 \text{ cm}^3 \text{ K mol}^{-1}$  at 300 K is way below this expectation and is thus suggesting significant antiferromagnetic coupling. The  $\chi_m T$  product gradually decreases to  $7.23 \text{ cm}^3 \text{ K mol}^{-1}$  at 100 K. For lower temperatures, an upswing to a maximum  $\chi_m T$  product of  $8.96 \text{ cm}^3 \text{ K mol}^{-1}$  at 14 K is followed by a sharp decrease to  $6.08 \text{ cm}^3 \text{ K mol}^{-1}$  at 2 K. This behavior agrees with the trend of the magnetic data of **[Cr<sub>3</sub>Cr]** (Chapter 4.1.1).<sup>[1]</sup> Therefore, competing antiferromagnetic exchange interactions seem to be present as well. The program PHI 3.1.5.<sup>[32]</sup> was used to achieve the best fit of the susceptibility using the Hamiltonian  $\hat{H}$  with a  $2J$  model shown in Equation 14 referring to the coupling Scheme in Figure 4. 10 b. Similar to **[Cr<sub>3</sub>Cr]** two competing antiferromagnetic coupling pathways are present in this [9-MC-3] cavity.  $J_1$  describes the strength of the coupling between the guest Fe1 and ring metal ions Fe2, Fe3, and Fe4 while  $J_2$  describes the coupling within the neighboring ring metal ions as summarized in Equation 14.

$$\hat{H} = -2J_1(\hat{S}_{\text{Fe1}} \cdot \hat{S}_{\text{Fe2}} + \hat{S}_{\text{Fe1}} \cdot \hat{S}_{\text{Fe3}} + \hat{S}_{\text{Fe1}} \cdot \hat{S}_{\text{Fe4}}) - 2J_2(\hat{S}_{\text{Fe2}} \cdot \hat{S}_{\text{Fe3}} + \hat{S}_{\text{Fe3}} \cdot \hat{S}_{\text{Fe4}} + \hat{S}_{\text{Fe2}} \cdot \hat{S}_{\text{Fe4}}) \quad (14)$$

The best fit of the susceptibility data was obtained with exchange coupling constants  $J_1 = -13.3 \text{ cm}^{-1}$  and  $J_2 = -4.4 \text{ cm}^{-1}$  with the  $g$  fixed factor at  $g = 1.98$ . The residual  $R$  was calculated to be 0.44. The fit implemented an intermolecular exchange as mean field interaction  $zJ = -0.04 \text{ cm}^{-1}$ . Dipole-dipole interaction can occur for example between Fe8 and Fe10 with an intermolecular distance of  $5.55 \text{ \AA}$  (Figure 4. 9). The dominant antiferromagnetic exchange constant  $J_1$  is almost three times higher than the magnetic exchange within the repetition unit  $J_2$  indicating a high-spin ground state with  $S \neq 0$ .

**Table 4. 5** Summary of the fitting parameters of the susceptibility data from the program PHI for **bu-[Fe<sub>3</sub>Fe]**. The  $g$  value of 1.98 was fixed during this calculation.<sup>[35]</sup>

	<b><math>g</math> (fixed)</b>	<b><math>J_1 / \text{cm}^{-1}</math></b>	<b><math>J_2 / \text{cm}^{-1}</math></b>	<b><math>R</math></b>
<b>parameters</b>	1.98	$-13.26 \pm 0.07$	$-4.44 \pm 0.02$	0.44

These fit parameters and magnetic measurements are in good consistency with the reported results of Pecoraro and co-workers in 2016.<sup>[35]</sup> They report the magnetic properties of iron(III) [9-MC-3] metallacrowns with benzoate and acetate bridging co-ligands and the non-functionalized salicylhydroxamic

acid as the ligand. In their calculations a Hamiltonian that equals the sum of the simply multiplied coupling constants  $J$  ( $\hat{H} = -J_1(\hat{S}_{\text{Fe1}} \cdot \hat{S}_{\text{Fe2}} + \hat{S}_{\text{Fe1}} \cdot \hat{S}_{\text{Fe3}} + \hat{S}_{\text{Fe1}} \cdot \hat{S}_{\text{Fe4}}) - J_2(\hat{S}_{\text{Fe2}} \cdot \hat{S}_{\text{Fe3}} + \hat{S}_{\text{Fe3}} \cdot \hat{S}_{\text{Fe4}} + \hat{S}_{\text{Fe2}} \cdot \hat{S}_{\text{Fe4}})$ ) for a  $2J$  model was used including two coupling constants with  $J_1 = -24.9 \text{ cm}^{-1}$ ,  $J_2 = -4.5 \text{ cm}^{-1}$ ,  $g = 1.98$ , and  $\lambda J = -0.69 \text{ cm}^{-1}$  were obtained for the best fit of the data when benzoate is used as the bridging co-ligand. For the acetate bridging co-ligand the evaluation of the data gave values of  $J_1 = -28.0 \text{ cm}^{-1}$ ,  $J_2 = -6.4 \text{ cm}^{-1}$ ,  $g = 1.97$  with a  $D = -0.3 \text{ cm}^{-1}$ .<sup>[35]</sup> Which, if converted to the  $2J$  model, agrees well and is in the same order of magnitude in both cases. Compared to **[Cr<sub>3</sub>Cr]** the ratio  $J_1/J_2$  of 2.99 is very similar ( $J_1/J_2$  ratio = 3.5).

### Electrochemical stability

In the following section, the electrochemical stability of the **4bu-[Fe<sub>3</sub>Fe]** MC will be discussed in detail. In general, the electrochemical stability of MCs is not commonly discussed in literature. However, this stability of MCs is crucial for further processing e.g., in surface immobilization. As already described in Chapter 2, redox reactions between the surface and an applied molecule can occur.<sup>[48]</sup> Therefore, it is crucial to investigate the redox behavior of the molecule prior to surface deposition to understand the redox sensitivity of the sample. If cyclic voltammetry (CV) measurements are performed at all they are especially used to further examine the host-guest relationship of MCs as described in the following. In 2010, the binding affinity with ferrocene carboxylate with  $\text{Ln}^{\text{III}}15\text{-MC}_{\text{Cu}(\text{I})\text{N}(\text{L-phcHA})-5}$  was measured *via* CV by Pecoraro and co-workers.<sup>[49]</sup> Additionally, a vacant [12-MC-6] aza-metallacrown with the cavitand structure  $[\text{Co}_6(\mu\text{-OH})_6(\mu\text{-L})_6]^{m+}$  (HL=3{5}-(pyrid-2-yl)-5{3}-tert-butylpyrazole,  $m = 2$  or  $3$ ) showed different redox properties depending on the counter anion that was used.<sup>[8]</sup> Different anions like perchlorate or tetrafluorophosphate bind in the cavity *via* hydrogen bonds and stabilize different oxidation states due to the different strength of this in-cavity anion binding. Consequently, the isolation of the different oxidation states reflects the different binding preferences of the MC unit for these guest anions.<sup>[8]</sup>

There are only few electrochemical studies of MCs performed in solution.<sup>[50,51]</sup> These preliminary tests will serve as a foundation within the interdisciplinary Ph.D. program (MPGC) to enable a surface application of these complexes.

The CV measuring electrode was a glassy-carbon electrode with a platinum counter electrode. A silver wire was used as a quasi-reference electrode (Ag QRE) to measure the experimental potentials and all potentials were referenced to ferrocene. Since the measurement is highly sensitive to the corrosion of silver resulting in a shift of the peak values, a high effort in cleaning the silver surface is required. A platinum vessel was used as working electrode. All experiments were conducted under argon atmosphere.

All measurements were performed using an approximately 1 mM solution of **4bu-[Fe<sub>3</sub>Fe]** in dimethylformamide with a concentration of 100 mM of the conducting salt tetrabutylammonium hexafluorophosphate. It was referenced against the respective measurement of the ferrocene/ferrocenium



redox species. The cyclic voltammogram shows three oxidation peaks OI, OII and OIII and three reduction peaks RI, RII and RIII (Figure 4. 11). The obtained values for the peak potentials  $E_p$ , half-step potentials  $E_{1/2}$ , and potential difference of the peak currents of the oxidation and reduction wave  $\Delta E_p$  are summarized in Table 4. 6 and discussed in the following.

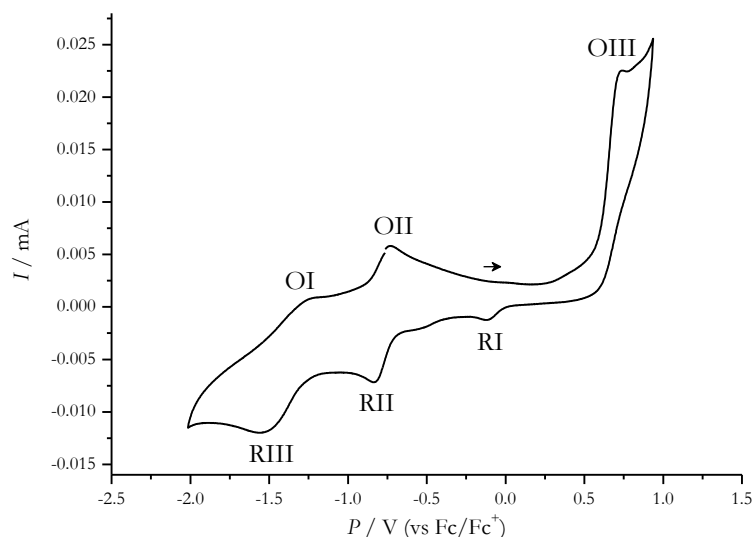


**Figure 4. 11.** Cyclic voltammogram of an approximately 1 mM solution of **tBu-[Fe<sub>3</sub>Fe]** in dimethylformamide with a concentration of 100 mM of the conducting salt tetrabutylammonium hexafluorophosphate. Referenced against ferrocene/ferrocenium.

**Table 4. 6.** Summarized peak potentials  $E_p$ , half-step potentials  $E_{1/2}$ , and potential difference of the peak currents of the oxidation and reduction waves  $\Delta E_p$  for the cyclic voltammogram of **tBu-[Fe<sub>3</sub>Fe]** with a scan rate of 100 mV/s.

$E_{1/2}$	peaks	$E_{pa} / V$	$E_{pc} / V$	$\Delta E_p / mV$
-1.38	OI-RIII	-1.21	-1.55	340
-0.79	OII-RII	-0.74	-0.84	100
	OIII	0.72		
	RI	-0.13		

The cyclic voltammogram of **tBu-[Fe<sub>3</sub>Fe]** displays an irreversible oxidation OIII at a potential of  $E_{pa} = 0.72 V$  referenced to ferrocene/ferrocenium (Figure 4. 12). This oxidation peak most probably represents the oxidation of the 5-*tert*-butylsalicylhydroxamic acid ligand. In comparison, the oxidation of iron(III) to iron(IV) ions is very unlikely in this case, since synthetically obtained complexes require higher potentials, or even a hydrogen-atom transfer or a proton-coupled electron transfer for this oxidation.<sup>[52,53]</sup> The scan rate study of oxidation process OIII and the reduction process RI followed by the oxidation OIV in more detail is shown in Figure 4. 12.

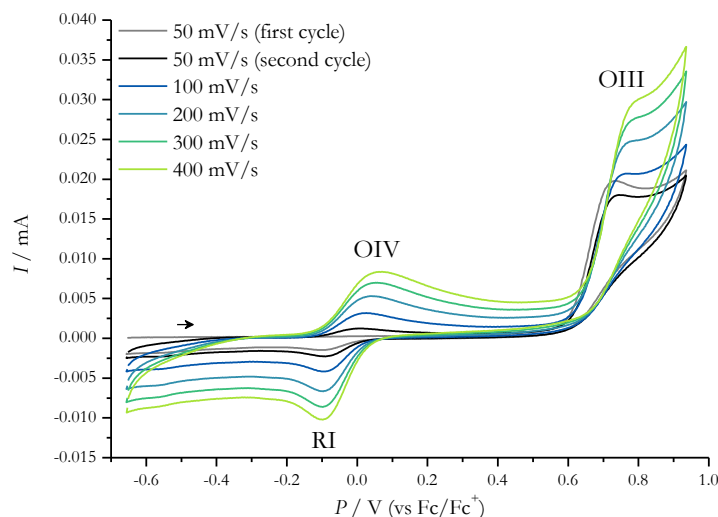


**Figure 4. 12.** Scan rate study of the irreversible oxidation process OIII and the reduction of the daughter product RI including the oxidation OIV.

The reduction RI at  $E_p = -0.13$  V most probably arises from a daughter product of the oxidation OIII at  $E_p = 0.72$  V because no oxidation exists at the potential of approximately 0 V in the first cycle with the scan rate of 50 mV/s. However, in the second and following cycles, there is the oxidation OIV occurring. Thus, this suggests a subsequent chemical reaction coupled to the electron transfer after the oxidation OIII causing the formation of the daughter product.

The peak potentials, peak currents, and ratio of peak currents of the redox pair RI and OIV at  $E_{1/2} = 0.03$  V for the different scan rates are summarized in Table 4. 7. RI and OIV show the half-step potential of  $E_{1/2} = -0.03$  V and exhibit a separation of the peak potential of 66 mV at a scan rate of 100 mV/s. This indicates an electrochemical quasi-reversible reduction and oxidation. Theoretically, a reversible electron transfer would be expected to result within a peak separation of  $\Delta E_p = 59$  mV at a temperature of 25 °C for a one-electron transition. This value is obtained from the Nernst equation, as shown in Equation 14 below. Here,  $R$  is the molar gas constant,  $F$  is the Faraday constant, and  $n$  is the number of electrons transferred.

$$\Delta E_p = \frac{2.3 \cdot R \cdot T}{n \cdot F} = \frac{2.3 \cdot R \cdot 298.15 \text{ K}}{1 \cdot F} = 59 \text{ mV} \quad (14)$$

However, the separation of the peak potentials also depends on many other factors, including the separation of the working and reference electrodes and the uncompensated cell resistance. Thus, in general, a slightly higher separation can be considered for reversible electron transfers as well.

The potentials of the oxidation and reduction waves are dependent on the rate of a potential change (see Table 4. 7). This also suggests that the process is electrochemical quasi-reversible. In the CV of the whole potential range, no oxidation of the daughter product occurs (Figure 4. 11). A second reduction of the daughter product with a following irreversible chemical reaction could explain this behavior. Secondly, a diffusion of the species away from the working electrode could be possible.<sup>[54]</sup>

The peak currents were calculated by subtracting a zero line to compensate for the charging of an electrochemical double layer. Significant errors are expected to arise in determining the baseline. For a pure E-mechanism, the ratio of the peak potentials is  $i_{pa}/i_{pc} = 1$ . Then, the same amount of molecules is reduced and oxidized again. The significant deviation of the ratios of the peak potentials from  $i_{pa}/i_{pc} = 1$ , could be explained by an EC-mechanism. In this mechanism, an electron transfer occurs that is followed by an irreversible homogeneous chemical reaction.<sup>[54]</sup> In addition, it is necessary to note that a peak current ratio deviating from the literature value was also obtained for ferrocene/ferrocene in referencing CVs.<sup>[55]</sup>

Plotting the peak currents for different scan rates against the root of the respective scan rate shows a linear progression (Figure S23). This would indicate a reversible redox process.<sup>[56]</sup> The potentials of the oxidation and reduction waves show a slight dependence on the rate of potential change which indicates an electrochemical quasi-reversible process.

**Table 4. 7.** Summarized peak potentials  $E_{pa}$ ,  $E_{pc}$  and ratios of the peak potentials for RI and OIV of the cyclic voltammogram **bu-[Fe<sub>3</sub>Fe]**.

scan rate	$E_{pa} / \text{V}$	$E_{pc} / \text{V}$	$i_{pa} / \text{mA}$	$i_{pc} / \text{mA}$	$i_{pa}/i_{pc}$
50 mV/s	-0.09	0.00	$1.0 \cdot 10^{-3}$	$2.0 \cdot 10^{-3}$	0.49
100 mV/s	-0.09	0.03	$3.0 \cdot 10^{-3}$	$4.0 \cdot 10^{-3}$	0.75
200 mV/s	-0.10	0.04	$4.9 \cdot 10^{-3}$	$6.5 \cdot 10^{-3}$	0.76
300 mV/s	-0.10	0.05	$6.3 \cdot 10^{-3}$	$8.5 \cdot 10^{-3}$	0.74
400 mV/s	-0.10	0.06	$7.2 \cdot 10^{-3}$	$10.2 \cdot 10^{-3}$	0.70

Another measurement was performed at different scan rates in the cathodic region of RII, RIII, OI and OII (Figure 4. 13, left) In addition, the redox pair RII-OII was investigated in more detail, which is shown in Figure 4. 13 on the right. Peak currents, as well as the corresponding potentials of RII and OII are summarized in Table 4. 8.

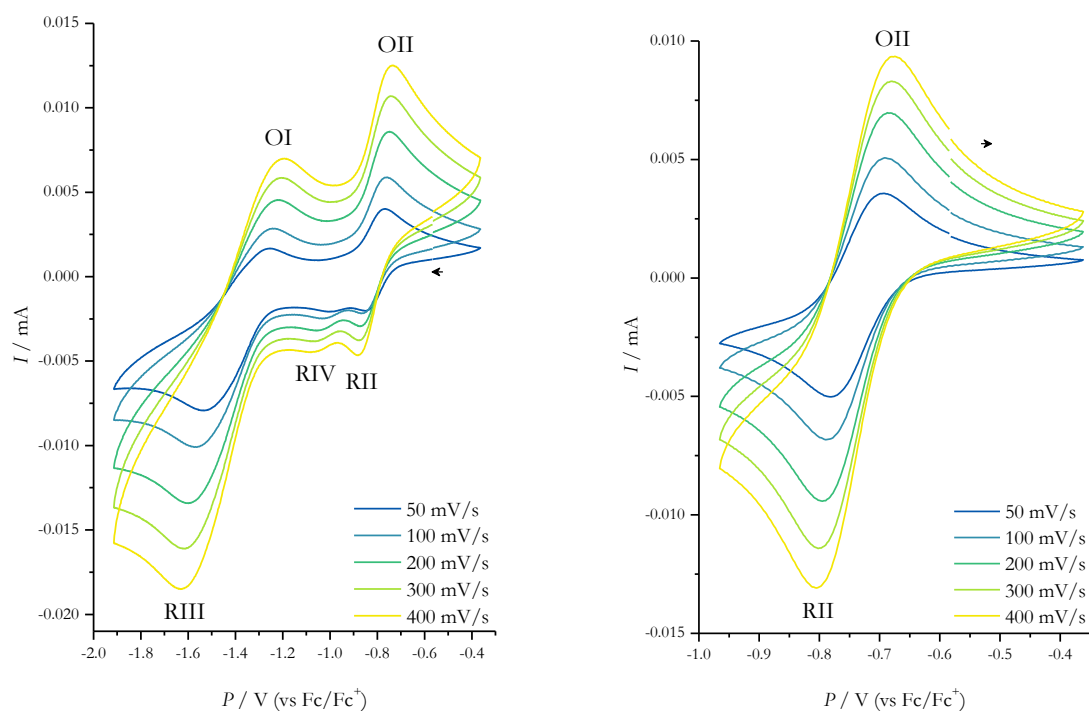


**Figure 4.13.** a) Scan rate study of the redox pair RII-OII, b) scan rate study of the cathodic region of the reduction processes RII, RIII, OI, OII and RIV of  $t\text{Bu-}[\text{Fe}_3\text{Fe}]$ .

**Table 4.8.** Summarized peak potentials  $E_{\text{pa}}$ ,  $E_{\text{pc}}$  and ratios of the peak potentials for the cyclic voltammogram  $t\text{Bu-}[\text{Fe}_3\text{Fe}]$  for different scan rates.

scan rate	$E_{\text{pa}} / \text{V}$	$E_{\text{pc}} / \text{V}$	$i_{\text{pa}} / \text{mA}$	$i_{\text{pc}} / \text{mA}$	$i_{\text{pa}}/i_{\text{pc}}$
50 mV/s	-0.70	-0.78	$3.1 \cdot 10^{-3}$	$4.5 \cdot 10^{-3}$	0.70
100 mV/s	-0.70	-0.78	$4.8 \cdot 10^{-3}$	$6.1 \cdot 10^{-3}$	0.78
200 mV/s	-0.69	-0.79	$6.5 \cdot 10^{-3}$	$8.9 \cdot 10^{-3}$	0.73
300 mV/s	-0.69	-0.80	$7.0 \cdot 10^{-3}$	$10.8 \cdot 10^{-3}$	0.65
400 mV/s	-0.69	-0.80	$8.8 \cdot 10^{-3}$	$11.0 \cdot 10^{-3}$	0.79

The separation of the peak potentials for redox pair RII-OII at  $E_{1/2} = -0.79 \text{ V}$  is 100 mV for a scan rate of 100 mV/s. A reduction of an iron(III) ion of the MC to iron(II) is possible. The significantly lower redox potential compared to the free ion<sup>[41]</sup> is due to the different electronic structure in the complex. The  $t_{2g}$  orbitals are energetically raised by the  $\pi$ -donor function of the 5-*tert*-butyl salicylhydroxamate ligand, thus reduction of the iron(III) ion occurs only at more negative potentials.

The spacing of the peak potentials is slightly smaller at 80 mV for a scan rate of 100 mV/s. The position of the peak potentials changes only slightly with the scan rate, suggesting mainly diffusion control and only incidentally a contribution of heterogeneous electron transfer to the reaction kinetics. Thus, quasi-reversible electron transfer can be assumed for the redox couple at  $E_{1/2} = -0.79 \text{ V}$ .

By changing the scan rate a strong shift of the peak potentials for the redox pair RIII-OI at the half-step potential of  $E_{1/2} = -1.38 \text{ V}$  is observed which indicates a slow electron transfer. Thus, in comparison, a slow

heterogeneous electron transfer is occurring. This third reduction is possibly also attributable to a reduction of an iron(III) atom of the MC to iron(II).

The presence of two reductions, is the result of interactions between the three ring metal ions and the guest ion. Thus, the reduction of an iron(III) ion to iron(II) changes the field of the neighboring iron ions, associated with a change in the redox potential of these neighbors. Electronic coupling via the *-O-N-* bridge for the iron(III) ions in the ring and coupling *via* an oxygen bridge between the iron(III) guest ion and the iron(III) ring ions is expected as shown by the magnetic analysis.

For measurements in the cathodic potential range, the splitting of the second reduction peak into two peaks occurs after the second cycle another reduction process RIV at 1.00 V (see Figure 4. 14). This can be explained by a subsequent irreversible chemical reaction connected to the reduction RII. An ECE mechanism involving electron transfer followed by a rapid chemical reaction and another electron transfer seems feasible.<sup>[57]</sup> After the first reduction of the MC (Figure 4. 14, 1. cycle), a chemical reaction follows. Here, a change in coordination geometry under loss of a peripheral methanol co-ligand could occur. The corresponding oxidations seems to be not influenced by this process. Thus, after the first cycle, the reduction of an iron(III) of this daughter product has a different coordination geometry at a slightly different reduction potential (RIV).

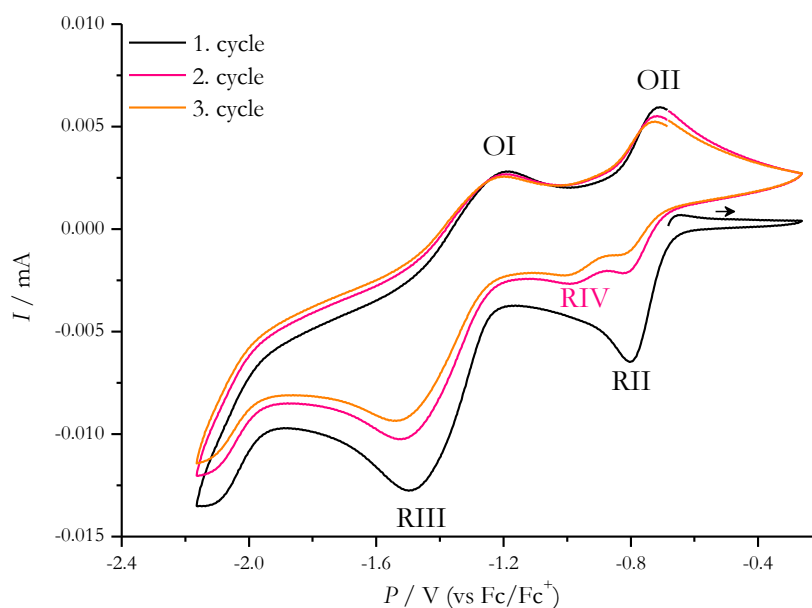


**Figure 4. 14.** Cyclic voltammogram of an approximately 1 mM solution of  $\text{̡bu-}[\text{Fe}_3\text{Fe}]$  in dimethylformamide with a concentration of 100 mM of the conducting salt tetrabutylammonium hexafluorophosphate for the cathodic region. Referenced against ferrocene/ferrocenium; first circle of measurements.

Concluding, the  $\text{̡bu-}[\text{Fe}_3\text{Fe}]$  shows several oxidation and reduction processes. The observed reduction process of iron(III) ions to iron(II) ions is particularly interesting to study in the context of this work. The change in oxidation state should also cause a change in spin state which might lead to different magnetic exchange interactions. A switch from the redox pair iron(III)/iron(II) to the redox pair chromium(III)/chromium(II) will be discussed in the following Chapter 4.2.2.

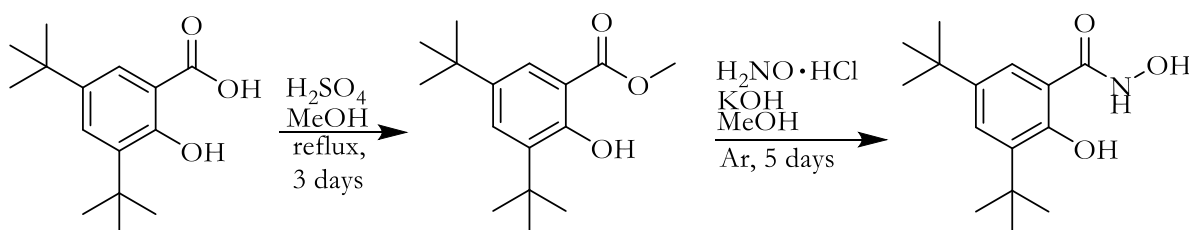
To summarize, the iron(III) MC  $\{\text{Fe}^{\text{III}}(\mu_2\text{-OOCPh})_3[9\text{-MC}_{\text{Fe(III)N}(\text{buShi})\text{-3]}(\text{MeOH})_3\} \cdot x \text{MeOH}$  was synthesized, magnetically characterized, and examined for electrochemical stability. The structure is analogous to the reported chromium(III) **[Cr<sub>3</sub>Cr]** MC from Chapter 4.1.1. The magnetic analysis revealed two competing antiferromagnetic exchange interactions  $J_1 = -24.9 \text{ cm}^{-1}$  and  $J_2 = -4.5 \text{ cm}^{-1}$  which are alike to the chromium analog. This preliminary results for changing the cavity size revealed the synthetic challenges of affecting the cavity. Thus, the next Chapter 4.1.2.2 focuses on the chromium analog with the ligand 3,5-di-*tert*-butyl salicylhydroxamic acid in more detail, because the iron example has two significant disadvantages.

Firstly, it cannot be assumed that an analogous structure is obtained with 5-*tert*-butylsalicylhydroxamic acid and chromium(III) ions. The crystallization of such a compound in combination with solvothermal synthesis is more complex and for each system the conditions have to be adjusted. No suitable crystals for X-ray analysis were obtained for the chromium(III) analogous structure under various crystallization conditions. Secondly, the iron complex is not stable with respect to electron ionization spray mass spectrometry. It was not possible to detect this molecule or fragments of **bu-[Fe<sub>3</sub>Fe]** in the electron spray ionization method (ESI). Chromium(III), on the other hand, is kinetically inert and therefore more suitable to maintain the structure under such harsh conditions. In addition, the ligand 3,5-di-*tert*-butylsalicylhydroxamic acid with additional steric demand is used for better crystallization results.

#### 4.1.2.2. $\{\text{Cr}^{\text{III}}(\mu_2\text{-piv})_3[9\text{-MC}_{\text{Cr}(\text{III})\text{N}((t\text{bu})_2\text{Shi})\text{-3]}(\text{morph})_3]\cdot\text{MeOH} ((t\text{bu})_2\text{-[Cr}_3\text{Cr])}$

Based on the results of  $t\text{bu}\text{-[Fe}_3\text{Fe]}$ , another *tert*-butyl group on the aromatic backbone of salicylhydroxamic acid is introduced in this Chapter. This additional functional group will also serve as further proof whether the cavity of the MC can be influenced. Further, this ligand enhances the crystallization probability due to the sterically demanding functional groups. It has often been observed that *tert*-butyl groups which are attached to aromatic molecular scaffolds significantly increase the solubility of the organic backbone in adequate polar solvents. Thus, the sterically demanding *tert*-butyl groups show a repulsion which lowers the  $\pi\text{-}\pi$  interaction of the aromatic backbone. This should prevent a piling of insoluble molecular accumulations and enhance the crystallization of single-crystals or lead to higher yields of crystals.<sup>[58]</sup>

The crystal structure is essential for further investigations, since structurally very different complexes can be obtained in the self-assembly process. In the case of the  $[\text{Cr}_3\text{Cr}]$  MC presented in Chapter 4.1.1., a very low yield of only 4% of crystals was obtained. An improvement of the crystallization properties, with the same structural composition of e.g., the torsion angles of the metal ions, therefore, represents a very significant advantage for further analysis and utilization of the obtained compound. Higher yields are also important for further surface deposition experiments. Thus, the ligand 3,5-di-*tert*-butylsalicylhydroxamic acid was reacted with chromium(III) ions in solvothermal reactions.



**Scheme 4. 3.** Overview of synthesis steps of 3,5-di-*tert*-butylsalicylhydroxamic acid.

In the first step of this ligand synthesis reaction, an esterification with 3,5-di-*tert*-butylsalicylic acid in methanol and sulfuric acid was carried out under reflux of the solvent (Scheme 4. 3). In the second step, the hydroxylamine is prepared *in situ* by using a methanolic potassium hydroxide solution and a methanolic hydroxylamine hydrochloride solution. Then, hydroxylamine<sup>[40]</sup> attacks the carbonyl carbon of the 5-*tert*-butylsalicylmethyl ester and forms 3,5-di-*tert*-butylsalicylhydroxamic acid with an elimination of methanol.

One equivalent of chromium(III) pivalate, one equivalent of 3,5-di-*tert*-butylsalicylhydroxamic acid, and five equivalents of morpholine were dissolved in methanol under ambient conditions. The solution was transferred in a Teflon vial and heated for 11 hours at 120 °C in autoclave reactor in an oven, cooled to room temperature, and filtered. The reaction solution was allowed to stand in air for slowly concentrating in air to obtain measurable single crystals of  $\text{Cr}^{\text{III}}(\mu_2\text{-piv})_3[9\text{-MC}_{\text{Cr}(\text{III})\text{N}((t\text{bu})_2\text{Shi})\text{-3]}(\text{morph})_3]\cdot\text{MeOH}$  after three weeks. The compound will be referred hereafter as  $(t\text{bu})_2\text{-[Cr}_3\text{Cr]}$ . The pivalate salt of chromium(III) ions was used in this reaction, due to its excellent solubility in methanol. Furthermore, the pivalate anion as a

bridging co-ligand is already incorporated. Including coordinating co-ligands is important to achieve an octahedral coordination geometry for the chromium(III) ions since the ligand is occupying only four coordination sites.  $\{\text{Cr}^{\text{III}}(\mu_2\text{-piv})_3[9\text{-MC}_{\text{Cr}^{\text{III}}\text{N}(3,5\text{-di-}t\text{-butyl sh})\text{-3]}(\text{morph})_3]\cdot\text{MeOH}\}$  crystallizes in the triclinic space group  $P\bar{1}$  with two molecules in the asymmetric unit and four molecules per unit cell. Similar to the  $[\text{Cr}_3\text{Cr}]$  MC, basic reaction conditions facilitate the full deprotonation of the ligand (Chapter 2.1.1.). Here, three 3,5-di-*tert*-butyl salicylhydroxamtes can coordinate the chromium(III) ring metal ions Cr2, Cr3 and Cr4 or Cr6, Cr7 and Cr8 in the other MC respectively (see Figure 4. 15, Figure S 28). For simplicity, only one of the molecules is discussed in detail. The structures are very analogous in their composition, bond and torsion angles (see Table 4. 11, Figure S 28). The [9-MC-3] cavity with the characteristic repeating unit [Cr-N-O] and the *cis*-propeller configuration of the ligand is formed. All chromium(III) ions are surrounded by an octahedral ligand field. The ring metal ions are coordinated by two 3,5-di-*tert*-butylsalicylhydroxamate ligands, providing three O-donor atoms and one N-donor atom. One morpholine co-ligand is coordinated with an N-donor atom and an O-donor atom from a pivalate complete the octahedral coordination. The guest ions are coordinated by three oxygen donor atoms from the 3,5-di-*tert*-butylsalicylhydroxamate ligands and the three bridging pivalate ligands. Thus, an almost perfect octahedral geometry is obtained (Figure 4. 16, Table 4. 9). The average bond length of Cr1 to the oxygen donor atoms is 1.97 Å while the average bond length of the ring metal ions Cr2, Cr3, Cr4 are extremely similar with 2.00 Å due bonding of two types of oxygen and nitrogen donor atoms. Compared to the guest ion, the ring metal ions have a slightly higher deviation from the ideal octahedral geometry shown by the SHAPE values (Figure 4. 17, Table 4. 10). Nevertheless, as expected, only small deviations occur in both cases due to the  $d^3$  electron configuration in the octahedral field.

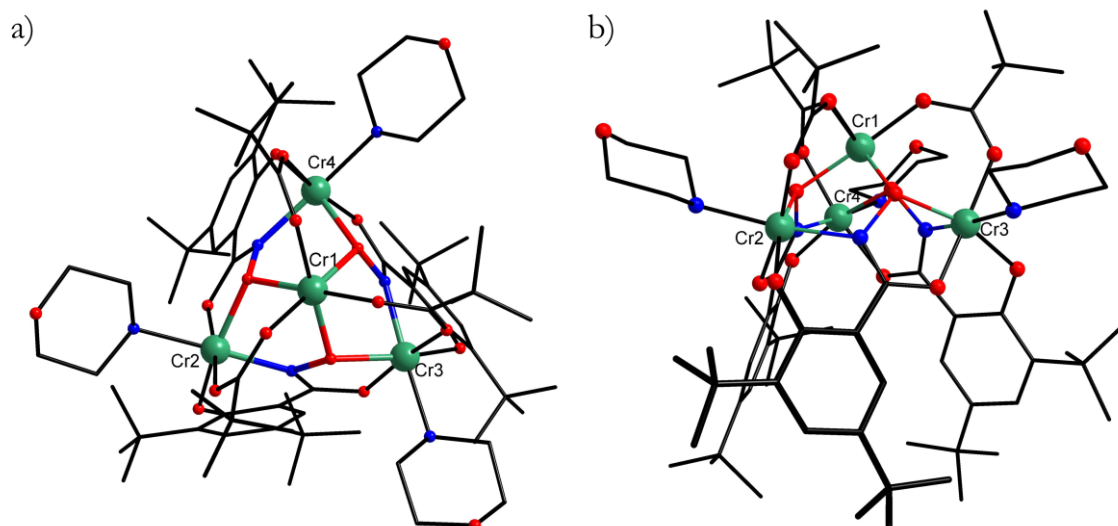


**Figure 4. 15.** a) Top view with highlighted repeating unit b) Side view with highlighted coordinating ligand 3,5-di-*tert*-butylsalicylhydroxamate of the [9-MC-3] MC structure of  $(t\text{bu})_2\text{-}[\text{Cr}_3\text{Cr}]$ . Hydrogen atoms are omitted for clarity. Color code of atoms: oxygen red, nitrogen blue, carbon black, chromium(III) ion green.



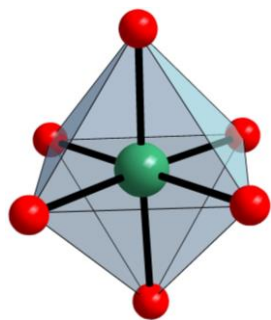


**Figure 4.16.** Schematic representation of the ideal coordination polyhedron of the Cr1 of  $(\text{tbu})_2\text{-}[\text{Cr}_3\text{Cr}]$  for an octahedral symmetry. Color code of atoms: oxygen red, chromium(III) ion green.

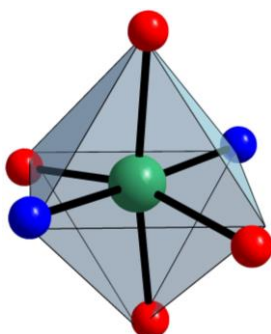


**Figure 4.17.** Schematic representation of the ideal coordination polyhedron of the Cr4 of  $(\text{tbu})_2\text{-}[\text{Cr}_3\text{Cr}]$  for an octahedral symmetry. Color code of atoms: oxygen red, nitrogen blue, chromium(III) ion green.

**Table 4.9.** Calculated deviations from ideal polyhedra for guest ion Cr1 *via* Continuous Shape Measurements.

Polyhedra	CShM
Hexagon $D_{6h}$	33.115
Pentagonal pyramid $C_{5v}$	30.013
<b>Octahedron <math>O_h</math></b>	<b>0.015</b>
Trigonal prism $D_{3h}$	16.343
Johnson pentagonal pyramid $C_{5v}$	33.525

<sup>a</sup>abbreviations: HP-6 hexagon ( $D_{6h}$ ); PPY-6 pentagonal pyramid ( $C_{5v}$ ); OC-6 octahedron ( $O_h$ ); TPR-6 trigonal prism ( $D_{3h}$ ); JPPY-6 Johnson pentagonal pyramid J2 ( $C_{5v}$ )

**Table 4.10.** Calculated deviations from ideal polyhedra for guest ion Cr4 *via* Continuous Shape Measurements.

Polyhedra <sup>a</sup>	CShM
Hexagon $D_{6h}$	31.936
Pentagonal pyramid $C_{5v}$	23.072
<b>Octahedron <math>O_h</math></b>	<b>0.967</b>
Trigonal prism $D_{3h}$	11.925
Johnson pentagonal pyramid $C_{5v}$	26.662

<sup>a</sup>abbreviations: HP-6 hexagon ( $D_{6h}$ ); PPY-6 pentagonal pyramid ( $C_{5v}$ ); OC-6 octahedron ( $O_h$ ); TPR-6 trigonal prism ( $D_{3h}$ ); JPPY-6 Johnson pentagonal pyramid J2 ( $C_{5v}$ )

For each molecule, a non-coordinating methanol solvent molecule is connected *via* hydrogen bonds, as shown in Figure 4.18 (2.40 Å between O5...H19, 2.05 Å between H6...O19). The methanol solvent molecules do not show additional hydrogen bonds or interactions with other molecules in the cell. The two *tert*-butyl groups helped compound  $(\text{tbu})_2\text{-}[\text{Cr}_3\text{Cr}]$  to crystallize faster and the quality of the crystals obtained are much higher in comparison to the unsubstituted ligand-based system.

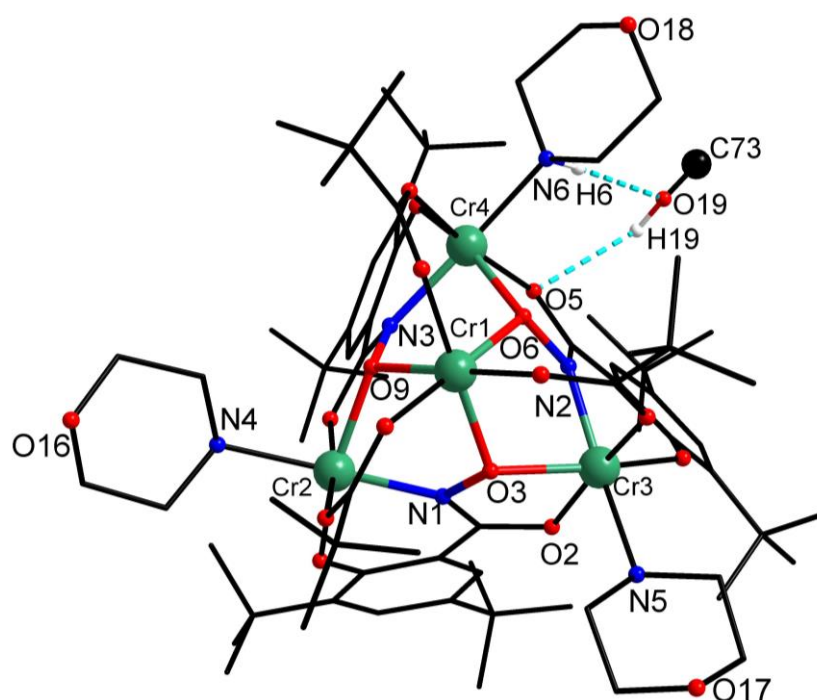


**Figure 4. 18.** Top view with highlighted repeating unit and methanol solvent molecule with hydrogen bonds (light blue) of  $(\text{tbu})_2\text{-}[\text{Cr}_3\text{Cr}]$ . Color code of atoms: oxygen red, nitrogen blue, carbon black, chromium(III) ion green. Hydrogen atoms are omitted for clarity except for H19.

**Table 4. 11.** Selected bond lengths of each chromium(III) ion of  $(\text{tbu})_2\text{-}[\text{Cr}_3\text{Cr}]$  (see Figure S 28 for comparison of structures).

ion	Cr1	Cr2	Cr3	Cr4
bond length / Å	O3 1.9727(12)	O1 1.9095(13)	O2 1.9492(12)	O5 1.9499(13)
	O6 1.9669(12)	O8 1.9461(12)	O3 2.0256(12)	O6 2.0174(12)
	O9 1.9629(13)	O9 2.0252(13)	O4 1.9135(12)	O7 1.9064(13)
	O10 1.9739(13)	O11 1.9959(13)	O13 2.0063(13)	O15 2.0034(14)
	O12 1.9687(13)	N1 1.9805(15)	N2 1.9843(14)	N3 1.9920(16)
	O14 1.9741(13)	N4 2.1255(17)	N5 2.1222(15)	N6 2.1154(17)
ion	Cr5	Cr6	Cr7	Cr8
bond length / Å	O23 1.9664(12)	O21 1.9063(12)	O22 1.9549(13)	O25 1.9456(13)
	O26 1.9671(12)	O28 1.9483(13)	O23 2.0178(13)	O26 2.0319(13)
	O29 1.9687(12)	O29 2.0313(12)	O24 1.9075(13)	O27 1.9111(13)
	O30 1.9615(13)	O31 2.0102(13)	O33 1.9971(13)	O35 1.9954(13)
	O32 1.9656(13)	N7 1.9794(15)	N8 1.9941(15)	N9 1.9853(15)
	O34 1.9690(13)	N10 2.1325(16)	N11 2.1219(16)	N12 2.1312(15)

Upon changing the ligand system from 5-*tert*-butylsalicylhydroxamic acid to 3,5-di-*tert*-butylsalicylhydroxamic acid the angles between guest and ring metal ion  $\text{Cr}_{\text{guest}}\text{-O-Cr}_{\text{ring}}$  and the torsion angles  $\text{Cr}_{\text{ring}}\text{-N-O-Cr}_{\text{ring}}$  within the repeating unit did not change due to the introduction of the two *tert*-butyl groups, as shown in Table 4.12. Therefore, a similar magnetic behavior was expected since the magnetic interactions *via* the donor atoms should be similar.

**Table 4. 12.** Selected torsion angles of each chromium(III) ion guest and ring metal ions for  $(\text{tbu})_2\text{-}[\text{Cr}_3\text{Cr}]$  in comparison to  $[\text{Cr}_3\text{Cr}]$ .

	$(\text{tbu})_2\text{-}[\text{Cr}_3\text{Cr}]$		$[\text{Cr}_3\text{Cr}]$	
<b>Cr<sub>guest</sub>-O-Cr<sub>ring</sub></b>	Cr1-O9-Cr2	112.06(6)°	Cr4-O9-Cr1	113.001(2)°
	Cr1-O3-Cr3	112.51(6)°	Cr4-O3-Cr2	113.672(3)°
	Cr1-O6-Cr4	112.77(6)°	Cr4-O6-Cr3	111.887(3)°
	average	112.45°	average	112.853°
	Cr5-O23-Cr7	112.72(6)°		
	Cr6-O29-Cr5	112.38(6)°		
	Cr8-O26-Cr5	111.42(6)°		
	average	112.17°		
<b>torsion angle Cr<sub>ring</sub>-N-O-Cr<sub>ring</sub></b>	Cr3-O3-N1-Cr2	156.97(7)°	Cr1-N1-O3-Cr2	158.775(3)°
	Cr4-O6-N2-Cr3	155.37(7)°	Cr2-N2-O6-Cr3	147.071(3)°
	Cr2-O9-N3-Cr4	152.44(8)°	Cr3-N3-O9-Cr1	156.925(3)°
	average	154.93°	average	154.257°
	Cr8-O26-N8-Cr7	153.19(7)°		
	Cr7-O23-N7-Cr6	156.32(7)°		
	Cr6-O29-N9-Cr8	157.76(7)°		
	average	155.76°		

### Evaluation of magnetic data

To investigate magnetic properties of  $(\text{tbu})_2\text{-}[\text{Cr}_3\text{Cr}]$ , magnetic susceptibility measurements were performed with an applied magnetic field of 1000 Oe in the range 2-300 K (Figure 4. 19 a). Additionally, magnetization measurements were performed with magnetic fields ranging from 0.1 T to 7 T at 2-10 K (Figure 4. 19 b). The theoretically expected values of the  $\chi_m T$  product can be calculated using Equations 12 and 13 (Chapter 4.1.3). Each of the four chromium(III) ions should therefore contribute to the  $\chi_m T$  product  $1.875 \text{ cm}^3 \text{ K mol}^{-1}$  with  $g = 2$  and  $S = 3/2$ .

Similar to  $[\text{Cr}_3\text{Cr}]$ , the experimental  $\chi_m T$  value at 300 K with  $6.55 \text{ cm}^3 \text{ K mol}^{-1}$  is below the theoretical value of  $7.5 \text{ cm}^3 \text{ K mol}^{-1}$  for four uncoupled  $S = 3/2$  spin centers using the spin-only formula. This is indicating the significant antiferromagnetic exchange interactions as discussed for  $[\text{Cr}_3\text{Cr}]$  (Chapter 4.1.1). Furthermore, a saturation at 300 K is not seen yet. The shape of the curves shows the same trend and indicates the presence of competing antiferromagnetic exchange interactions. In general, the antiferromagnetic coupling is lower than in the case of  $[\text{Cr}_3\text{Cr}]$ . The magnetization measurements suggest a spin ground state  $S_T = 3$  similar to  $[\text{Cr}_3\text{Cr}]$ .

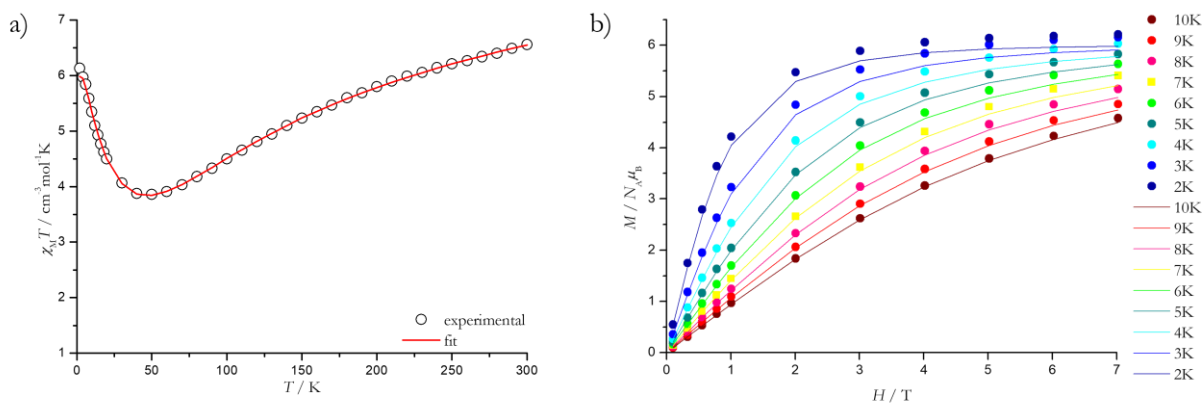


**Figure 4. 19.** a) Temperature-dependence of magnetic susceptibility of  $(\text{fbu})_2\text{-}[\text{Cr}_3\text{Cr}]$ ; b) magnetization measurement of  $(\text{fbu})_2\text{-}[\text{Cr}_3\text{Cr}]$ . The solid red line represents the best fit of the data.

The program PHI<sup>[32]</sup> was used to fit the susceptibility and magnetization data simultaneously using the Hamiltonian exchange. The same coupling scheme as for  $[\text{Cr}_3\text{Cr}]$  can be used in this case (inset Figure 4. 3, Chapter 4.1.1).

$$\hat{H} = -2J_1(\hat{S}_{\text{Cr1}} \cdot \hat{S}_{\text{Cr2}} + \hat{S}_{\text{Cr1}} \cdot \hat{S}_{\text{Cr3}} + \hat{S}_{\text{Cr1}} \cdot \hat{S}_{\text{Cr4}}) - 2J_2(\hat{S}_{\text{Cr2}} \cdot \hat{S}_{\text{Cr3}} + \hat{S}_{\text{Cr3}} \cdot \hat{S}_{\text{Cr4}} + \hat{S}_{\text{Cr2}} \cdot \hat{S}_{\text{Cr4}}) \quad (15)$$

The best fit was obtained for the exchange coupling constants  $J_1 = -10.88 \text{ cm}^{-1}$  and  $J_2 = -2.280 \text{ cm}^{-1}$ . The  $g$  factor for the chromium(III) ions was fixed at  $g_{\text{Cr}^{3+}} = 2.00$ . Here, the residual  $R$  was calculated to be 0.05. A small temperature independent component TIP 0.0019 had to be included in this fit. A TIP can be added to the calculated magnetic susceptibility (see Equation S2, Chapter 6.1.2.6). No intermolecular interaction was included *via* the mean-field approximation because the chromium(III) ions are even more separated from each other compared to  $[\text{Cr}_3\text{Cr}]$  (see Equation S1, Chapter 6.1.2.6). The closest distance for a dipole-dipole interaction is 8.66 Å between the Cr3 and Cr6. Additionally, no interaction *via* hydrogen bonds are facilitated through the non-coordinating methanol molecules.

**Table 4. 13.** Summarized fitting parameters for  $(\text{fbu})_2\text{-}[\text{Cr}_3\text{Cr}]$ .

	$g$ (fix)	$J_1 / \text{cm}^{-1}$	$J_2 / \text{cm}^{-1}$	$R$
<b>parameters</b>	2.0	$-10.88 \pm 0.01$	$-2.28 \pm 0.01$	0.05

Furthermore, the simulation of Zeeman splitting was performed. The obtained Figure 4. 20 and Figure S30 rely on the Hamiltonian with a  $2J$  model (Equation 15) for the best fit of the susceptibility and magnetization data. At zero field the septet ( $2S+1$ ) for the spin ground state of  $S_T = 3$  is energetically only 12  $\text{cm}^{-1}$  lower than the next excited state of  $S_T = 2$ . Comparable to  $[\text{Cr}_3\text{Cr}]$ , the spin ground state is not well separated from the first excited state. In the case of  $[\text{Cr}_3\text{Cr}]$  the separation is only 5  $\text{cm}^{-1}$ . Thus, the Zeeman splitting is more pronounced for the  $S_T = 3$  septet than for the excited states if a field is applied. This leads to a stronger energetic lowering of the ground state at higher magnetic fields. This shows that the ground state

of  $S_T = 3$  is highly populated at higher fields and lower temperatures. In zero-field the spin ground state of  $S_T = 0$  is approximately  $50 \text{ cm}^{-1}$  separated from the  $S_T = 3$ . The ratio  $J_1/J_2$  of 4.8 is slightly higher compared to the ratio of **[Cr<sub>3</sub>Cr]** ( $J_1/J_2$  ratio = 3.5) but the values are still comparable and as expected in the same order of magnitude.

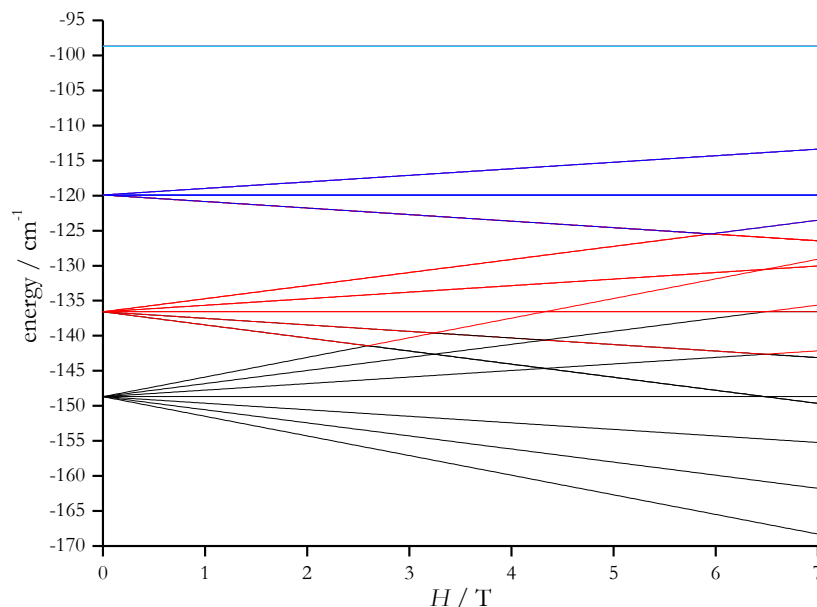


**Figure 4. 20.** Zoom-in of Zeeman splitting simulation of the four lowest spin states of **(fbu)<sub>2</sub>-[Cr<sub>3</sub>Cr]**.

### Electrospray ionization (ESI) mass spectrometry

Electrospray ionization mass spectrometry (ESI) is a commonly used technique to analyze and solve structural problems in the chemistry of organometallic and coordination compounds. However, obtaining appropriate ESI mass spectra and assigning fragments to multinuclear compounds correctly can be difficult. Especially, the mass spectra of self-assembled complexes with high molar masses, many *3d* metal ions and additional coordinated ligands and co-ligands differ a lot from the mass spectra of purely organic samples. It is challenging to obtain an ESI spectrum of the desired multinuclear compounds because the metal complexes can show completely different spectra depending on the conditions of the ESI mass. The labile ligands may be lost, the metal ions possess variable redox states, or they may react with oxygen or moisture. The concentration, injected volume, and the temperature at which the device operates can also influence the obtained spectra.<sup>[59]</sup>

This part of the thesis addresses the stability of the synthesized MCs under these ESI conditions. Within the interdisciplinary research council *Spin+X*, attempts will be made for surface immobilization experiments of the kinetically inert chromium(III) MCs which then will be investigated regarding their magnetic properties. In collaboration with the group of Prof. Ziegler of the TU Kaiserslautern, it has been clarified that the application of the MCs on the surface works very similar to ESI mass spectrometry. Here, the dissolved

MCs get sprayed on a surface by using the electrospray ionization method. Therefore, the high-resolution positive-mode ESI spectrum of **(*t*bu)<sub>2</sub>-[Cr<sub>3</sub>Cr]** was obtained in a methanol/acetonitrile solution which is shown in Figure 4. 21.

Chromium has three stable isotopes (<sup>52</sup>Cr (83.79%), <sup>53</sup>Cr (9.50%), <sup>54</sup>Cr (2.365%))<sup>[41]</sup> that result in characteristic distributions in ESI mass spectrometry. The isotopes of carbon can also contribute to the overall isotope pattern due to the organic ligand in the backbone (<sup>12</sup>C (98.9%), <sup>13</sup>C (1.1%))<sup>[41]</sup>.

In order to assign the measured signals in a spectrum, a match between the expected isotope pattern for chromium was used to identify the signals that contain that certain metal isotope pattern. An estimation of an isotope pattern was performed by the prediction tool of the mass analysis program MestReNova 14.0.1.

The mass spectra of the two chromium MCs **(*t*bu)<sub>2</sub>-[Cr<sub>3</sub>Cr]** and **[Cr<sub>3</sub>Cr]** are shown in Figure 4. 21 and Figure 4. 22. For both molecules the proton [M+H]<sup>+</sup>, sodium [M+Na]<sup>+</sup> and potassium [M+K]<sup>+</sup> adduct were detected. Additionally, all signals show the same characteristic isotope pattern for each molecule. A prediction of isotope pattern for the experimentally obtained complexes with the sum formula C<sub>72</sub>H<sub>114</sub>Cr<sub>4</sub>N<sub>6</sub>O<sub>18</sub> of **(*t*bu)<sub>2</sub>-[Cr<sub>3</sub>Cr]** and C<sub>48</sub>H<sub>66</sub>Cr<sub>4</sub>N<sub>6</sub>O<sub>18</sub> of **[Cr<sub>3</sub>Cr]** was performed. The positive match for both molecules for the proton adduct (see also Figure S 21-36, Tables S 19-20) is shown in Figure 4. 23. This shows again the extraordinary stability of these chromium(III) MCs even at harsh conditions with high temperatures of 275 °C that was used for these measurements.

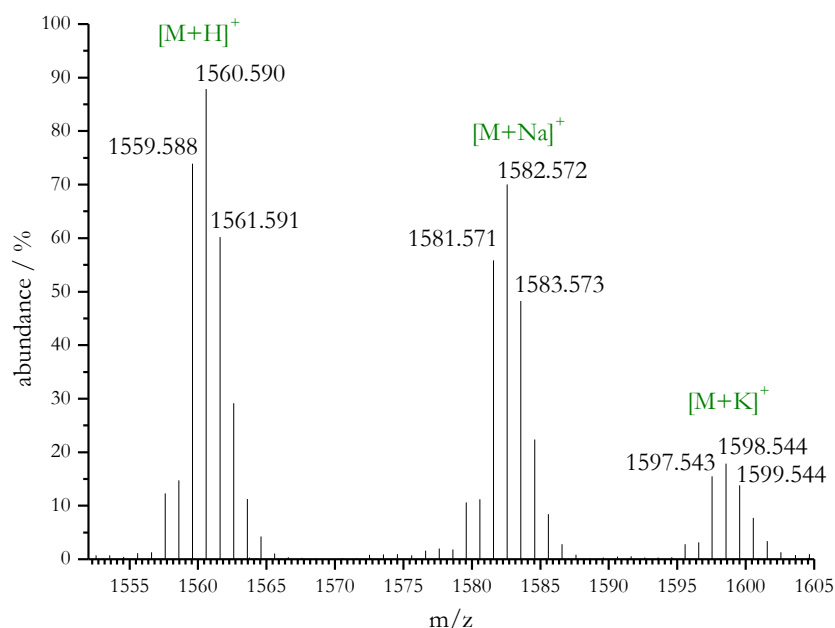


**Figure 4. 21** Positive ion electrospray ionization mass spectrum (zoom-in) of a methanol/acetonitrile solution of **(*t*bu)<sub>2</sub>-[Cr<sub>3</sub>Cr]** for the measured adduct with proton, sodium cation and potassium cation. For each fragment, the three strongest signals are labelled.

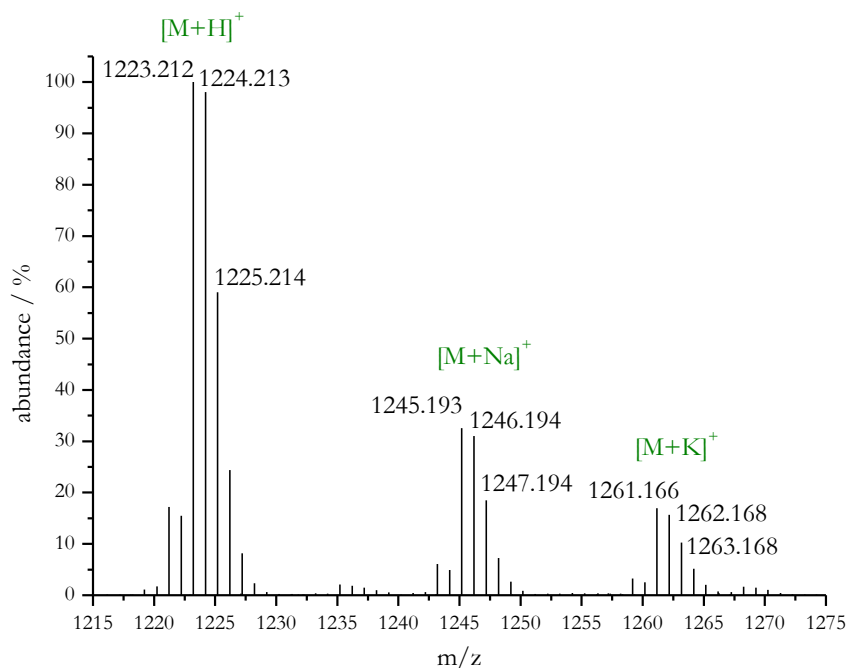


**Figure 4.22.** Positive ion electrospray ionization mass spectrum (zoom-in) of a methanol/acetonitrile solution of  $[\text{Cr}_3\text{Cr}]$  for the measured adduct with proton, sodium cation and potassium cation. For each fragment, the three strongest signals are labelled.

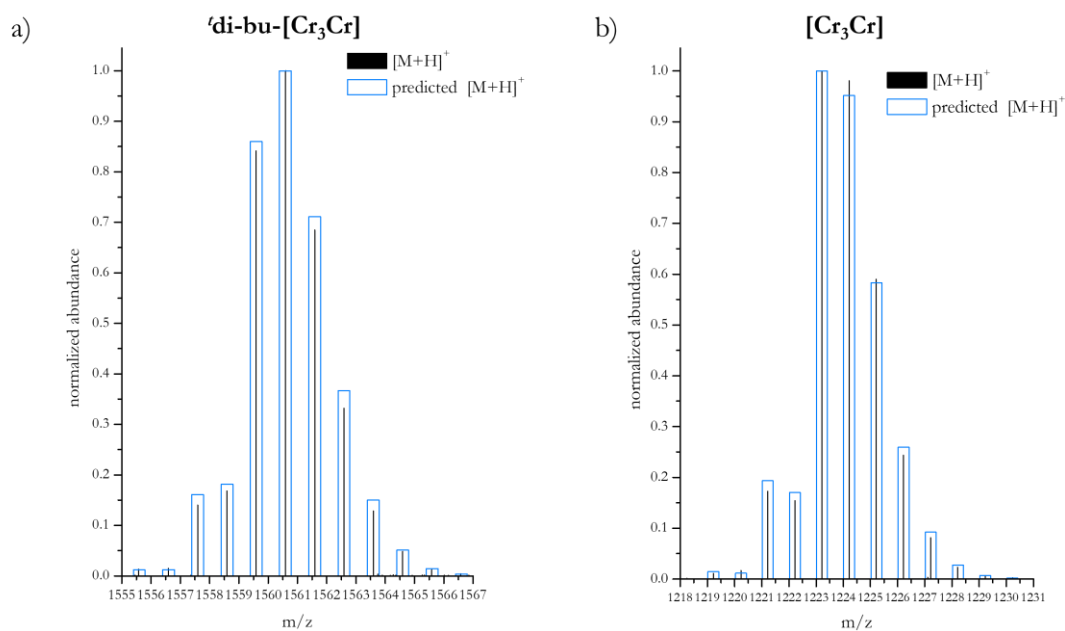


**Figure 4.23.** Normalized abundance from electrospray ionization mass spectrum with zoom-in of isotope pattern of a)  $(\text{tBu})_2\text{-}[\text{Cr}_3\text{Cr}]+\text{H}^+$ , b)  $[\text{Cr}_3\text{Cr}]+\text{H}^+$ . Measurement black bar, prediction blue box.

It was not possible to obtain ESI mass spectra of the analogous iron(III)  $\text{tBu-}[\text{Fe}_3\text{Fe}]$  MC even at higher concentrations or by using milder ionization temperatures of 100 °C. This highlights the kinetic robustness of the two chromium(III) MC  $(\text{tBu})_2\text{-}[\text{Cr}_3\text{Cr}]$  and  $[\text{Cr}_3\text{Cr}]$  due to the half occupied  $t_{2g}$ -orbitals ( $d^3$  electron configuration). All of these compounds have bridging co-ligands, but the monodentate coordinated second

co-ligand is morpholine for the chromium(III) MCs and methanol in case of the iron(III) MC. Therefore, it is likely that the morpholine ligand can easily be protonated and remain coordinated, whereas this was not the case for the methanol co-ligand of **bu-[Fe<sub>3</sub>Fe]**. In addition, antibonding  $e_g^*$  orbitals are occupied in iron(III) complexes, which weakens the strength of the bonds

### Cyclic Voltammetry

To investigate the stability with respect to electrochemical reactions, an approx. 1 mM solution of **bu-[Cr<sub>3</sub>Cr]** in tetrahydrofuran was analyzed by cyclovoltammetry. These measurements provide preliminary information for further processing of surface immobilization of **(bu)<sub>2</sub>-[Cr<sub>3</sub>Cr]**. A 100 mM solution of the conducting salt tetrabutylammonium hexafluorophosphate was used for this purpose. The cyclic voltammogram of **(bu)<sub>2</sub>-[Cr<sub>3</sub>Cr]** shown in Figure 4. 24 indicates no reduction in the cathodic region.



**Table 4. 14** summarizes the obtained values of the anodic peak potential  $E_{pa}$ , cathodic peak potential  $E_{pc}$ , half-step potentials  $E_{1/2}$ , and the potential difference of the peak currents of the oxidation and reduction waves  $\Delta E$ .

In the anodic region, two oxidation OI and OII are observed, along with the corresponding reductions RII and RI. This differs significantly from the behavior of the analogous iron(III) [9-MC-3] MC. In contrast, the ***t*-bu-[Fe<sub>3</sub>Fe]** MC has variable easily accessible redox processes and shows many redox reactions.

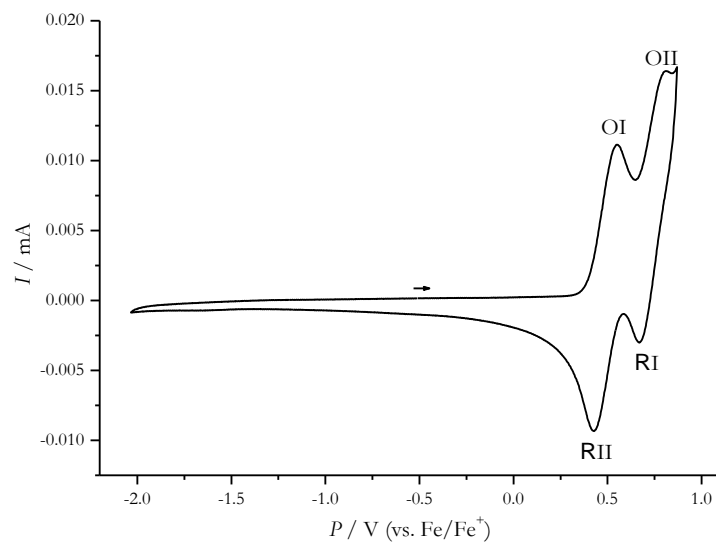


**Figure 4. 24.** Cyclic voltammogram of an approx. 1 mM solution of **(*t*-bu)<sub>2</sub>-[Cr<sub>3</sub>Cr]** in tetrahydrofuran with a concentration of 100 mM of the conducting salt tetrabutylammonium hexafluorophosphate. Referenced against ferrocene/ferrocenium.

**Table 4. 14** Values of peak potentials  $E_p$  (anodic, index a; cathodic, index c), half-step potentials  $E_{1/2}$ , and potential difference of the peak currents of the oxidation and reduction waves  $\Delta E$  for the cyclic voltammogram of  $(t\text{bu})_2\text{-[Cr}_3\text{Cr]}$ .

$E_{pa} / \text{V}$	$E_{pc} / \text{V}$	$E_{1/2} / \text{V}$	$\Delta E / \text{V}$
0.55 (OI)	0.43 (RII)	0.49	120
0.81 (OII)	0.67 (RI)	0.55	140

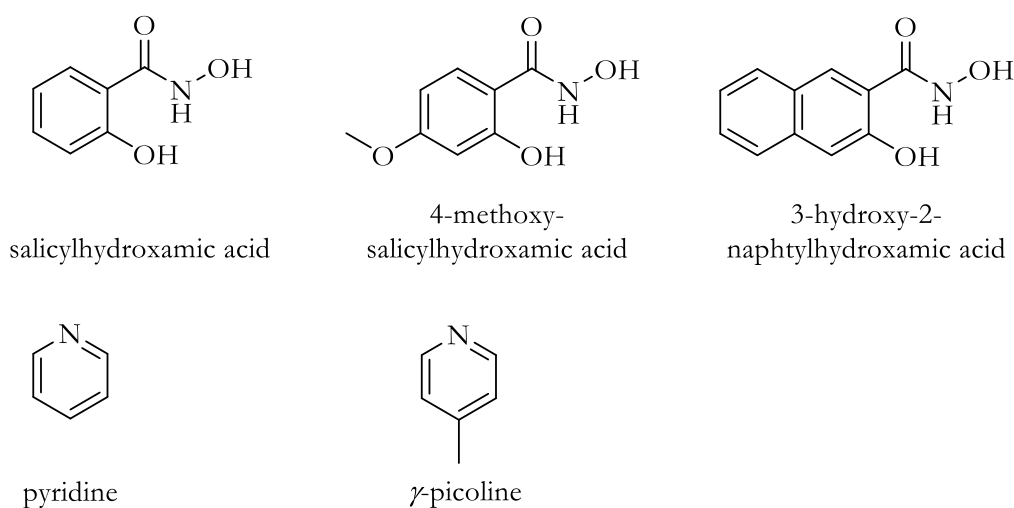
The redox properties of the morpholine co-ligand are already highly studied in literature with morpholine substituted compounds for electrochemical applications. Demirbař and co-workers, for example, showed that the morpholine substituent on a 4-(4-((4-morpholinophenylimino)methyl)phenoxy) phthalonitrile complex with various  $3d$  ions shows oxidation at  $E_{1/2} = 0.94 \text{ V}$  and  $E_{1/2} = 1.15 \text{ V}$  (DCM solutions, referenced versus  $\text{Ag}/\text{AgCl}$ , scan rate  $100 \text{ mV/s}$ ).<sup>[60]</sup> Due to the well-studied polymerization of the morpholine during the oxidation reaction, the redox pairs OI-RII and OII-RI are also assigned to this reaction type.<sup>[61,62]</sup>

In conclusion, in Chapter 4.1.2. two new MCs  $t\text{bu-[Fe}_3\text{Fe]}$  (Chapter 4.1.2.1) and  $(t\text{bu})_2\text{-[Cr}_3\text{Cr]}$  (Chapter 4.1.2.2) with a [9-MC-3] cavity were synthesized and thoroughly investigated for their structural, magnetic and electrochemical properties. Both structures correspond to the  $[\text{Cr}_3\text{Cr}]$  MC. The two ligands 5-*tert*-butylsalicylhydroxamic acid and 3,5-di-*tert*-butylsalicylhydroxamic acid were used to build the repeating unit of these MCs.

To the best of our knowledge, 3,5-di-*tert*-butylsalicylhydroxamic acid is a new synthesized ligand for building MC scaffolds. The choice of ligand with additional *tert*-butyl substituent enhanced to crystallization properties compared to  $[\text{Cr}_3\text{Cr}]$ . It was shown that the cavity is not influenced by the additional *tert*-butyl groups on the aromatic system. In particular, comparison of  $[\text{Cr}_3\text{Cr}]$  with of  $(t\text{bu})_2\text{-[Cr}_3\text{Cr]}$  showed that the octahedral ligand field of chromium(III) ions does not distort further and also the ligand in the repeating unit of the MC does not allow the torsion angles to change. In both MC molecules, bridging co-ligands were used to complete the octahedral coordination environment of the coordinated triply charged guest ion. The stability of chromium MCs was investigated by mass spectrometry and CV. The magnetic analysis revealed two competing antiferromagnetic exchange interactions, resulting in high spin ground state of  $S_T \neq 0$ . This first successful addition to the family of [9-MC-3] MCs shows the robustness of the formation of certain cavities.

#### 4.1.3. Vacant metallacrowns with chromium(III) ions

Another strategy was followed pursued by synthesizing new cavities of metallacrowns that preserve chromium(III) ions. A wide range of co-ligand and bases were used. The monodentate chloride ligand was used to avoid bridging of co-ligands to a central chromium(III) guest ion. Moreover, the negatively charged chloride ions can compensate the overall charge of the MC additionally, either by a direct binding of the chromium(III) ions or as a counterion in the crystal lattice. Triethylamine was chosen as a non-coordinating base. Two vacant coordination sites can be saturated by pyridine co-ligands to provide the preferred octahedral coordination sphere for the chromium(III) ions after the main ligand is coordinated. This approach substantially differs from the strategies of Chapters 4.1.1 and 4.1.2.. The following ligands and co-ligands were utilized in the following to synthesize a chromium MC with good crystallization abilities (see Scheme 4. 4).



**Scheme 4. 4.** Overview of ligands and co-ligands used in this chapter: salicylhydroxamic acid, 4-methoxy-salicylhydroxamic acid, 3-hydroxy-2-naphthylhydroxamic acid and co-ligands: pyridine,  $\gamma$ -picoline.

The reaction of the ligand salicylhydroxamic acid with chromium(III) chloride and triethylamine in a methanol-pyridine solution (15:2 v/v) forms the complex  $\{[12\text{-MC}_{\text{Cr(III)N}(\text{shiH})(\text{Sh})3-4}](\text{py})_8\text{Cl}\} \cdot 5 \text{ MeOH}$ . In the following referred as **[Cr<sub>4</sub>]**. The solvothermal reaction for 11 h at 120 °C followed by the slow evaporation of the solvent was applied for the synthesis and crystallization. The complex crystallizes in the triclinic crystal system in the space group P-1. The lattice parameters are  $a = 14.6096(11) \text{ \AA}$ ,  $b = 15.0827(12) \text{ \AA}$ ,  $c = 17.6266(14) \text{ \AA}$ ,  $\alpha = 79.775(6)^\circ$ ,  $\beta = 84.519(6)^\circ$ ,  $\gamma = 76.005(6)^\circ$ . **[Cr<sub>4</sub>]** represents a vacant reverse [12-MC-4] metallacrown. This twelve-membered metallacycle has two of the classical repeating units [Cr-N-O] which are reversed to [Cr-O-N] for the next two repeating units. No guest ion is coordinated in the central cavity. Four chromium(III) ring metal ions are connected by four salicylhydroxamate ligands and are coordinated by eight pyridine co-ligands as shown in Figure 4. 25. The additional two coordination sites are occupied by two pyridine co-ligands for each chromium(III) ion. Four salicylhydroxamic acid ligands are coordinating the four chromium(III) ions. Three of these ligands are triply

deprotonated while one of the hydroxamate oxygen atoms is protonated leading to a positively charged MC. One uncoordinated chloride counter ion per molecule is compensating this charge.

Next to the desired complex **[Cr<sub>4</sub>]**, a high amount of chromium(III) hydroxide formed as an amorphous precipitate under these reaction conditions. Varying the order of component addition, the speed of base dropping or the amount of base did not influence the amount of precipitate during the reaction. After the solvothermal synthesis, the suspension needed to be centrifuged, and the supernatant was filtered and used for the crystallization of the product. Different crystallization methods, such as very slow cooling of the reaction autoclave, changing the polarity of the solvent, addition of sterically demanding counter ions as well as layering or diffusion of different non-polar solvents into the reaction solution did not lead to the formation of single crystals at all. Only slow evaporation of the solvent led to the above-mentioned small amount of crystals. Therefore, various derivatives of salicylhydroxamic acid were tested for the coordination of the chromium(III) ions. These ligands should positively influence the crystallization behavior due to their different electronic properties and steric demands. Therefore, 4-methoxysalicylhydroxamic acid was prepared *via* a one-step synthesis.

The addition of an aqueous sodium hydroxide solution to an aqueous hydroxylamine hydrochloride solution resulted in the formation of the hydroxylamine free base. The nitrogen attacks the carbonyl carbon of the 4-methoxysalicylic acid methyl ester giving 4-methoxysalicylhydroxamic acid after elimination of methanol. The reaction of chromium(III) chloride, pyridine, triethylamine and 4-methoxy-salicylhydroxamic acid yielded single crystals of  $\{[12\text{-MC}_{\text{Cr(III)N(OMeShiH)(OMeShi)3-4}](\text{py})_8\text{Cl}]\cdot x\text{H}_2\text{O}\}$ . In the following referred as **OMe-[Cr<sub>4</sub>]**. A higher yield of the desired complex was achieved compared to **[Cr<sub>4</sub>]**. Nevertheless, the precipitation of amorphous chromium(III) hydroxide could not be fully prevented. **OMe-[Cr<sub>4</sub>]** crystallizes in the triclinic crystal system in the space group P-1 like **[Cr<sub>4</sub>]**. In both cases, two molecules are present in the unit cell. The lattice parameters are  $a = 11.8438(4) \text{ \AA}$ ,  $b = 18.0784(7) \text{ \AA}$ ,  $c = 21.1735(7) \text{ \AA}$ ,  $\alpha = 105.364(3)^\circ$ ,  $\beta = 94.898(3)^\circ$ ,  $\gamma = 100.516(3)^\circ$ . X-ray analysis revealed the following structures for **[Cr<sub>4</sub>]** and **OMe-[Cr<sub>4</sub>]** with the ligands salicylhydroxamic acid (Figure 4. 25 a, Figure 4. 26 a) and 4-methoxy salicylhydroxamic acid (Figure 4. 25 b, Figure 4. 26 b).

In both complexes, three fully deprotonated salicylhydroxamates, one doubly deprotonated salicylhydroxamic acid and 4-methoxy salicylhydroxamic acid, respectively, coordinate as chelating ligands for four chromium(III) ions. In each empty cavity a hydrogen bond is found between H12 and O9 of 1.57 Å for **[Cr<sub>4</sub>]** as well as H15 and O10 of 1.60 Å for **OMe-[Cr<sub>4</sub>]** due to the protonated oxygen donor atoms O12 and O15 for each MC as shown in Figure 4. 25 and Figure 4. 26 (additionally in Figure 4. 27 and Figure 4. 28).

Both structures consist of two molecules in the unit cell. The separations of these molecules in the unit cell are shown in Figure 4. 27 and Figure 4. 28 as well. The shortest intermolecular interaction within the unit cell is 8.67 Å is for Cr1-Cr2 in **[Cr<sub>4</sub>]**. In case of **OMe-[Cr<sub>4</sub>]** the shortest distance between two chromium(III) ions is 12.31 Å between Cr1 and Cr4 within the unit cell. No hydrogen bonds are connecting these two molecules in both cases. A hydrogen bond per molecule between H11A and O10 for **[Cr<sub>4</sub>]** and

between H23B and O13 **OMe-[Cr<sub>4</sub>]** from an uncoordinated methanol molecule can be recognized (see Figure 4. 27 and Figure 4. 28). These interactions are occurring at the oxygen donor atoms that are included in the *trans*-coordinated ligands (Cr4). The shortest intermolecular distance between Cr1-Cr1 is 6.73 Å for **[Cr<sub>4</sub>]** and 6.61 Å for **OMe-[Cr<sub>4</sub>]** for neighboring molecules along the *c*-axis. Thus, intermolecular magnetic dipole-dipole interactions can be neglected.

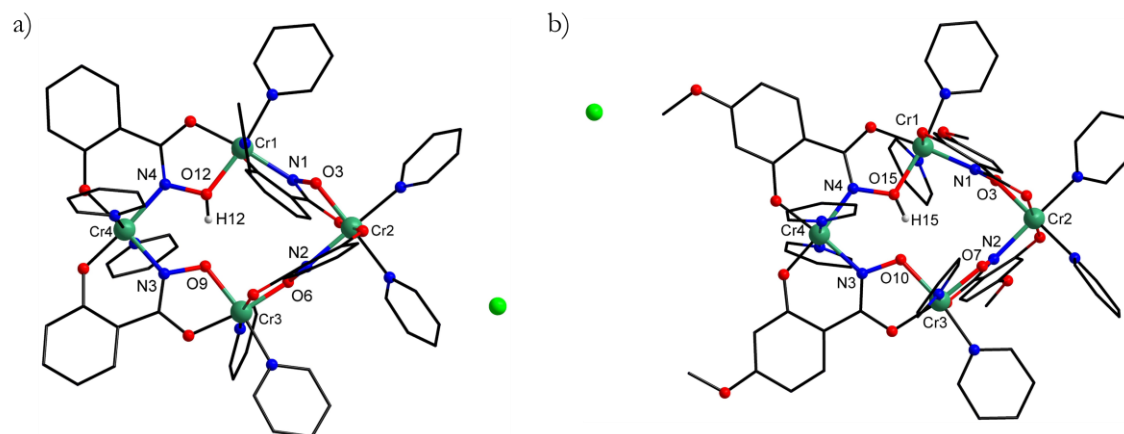


**Figure 4. 25.** Schematic representation of the molecular structure of a) **[Cr<sub>4</sub>]** and b) **OMe-[Cr<sub>4</sub>]** (top-down view). Hydrogen atoms and distorted solvent molecules are omitted for clarity except of H12 and H15 (protonation within repeating unit). Color code: chromium(III) ions green, chloride anion light green, oxygen red, nitrogen blue, hydrogen white, carbon black.

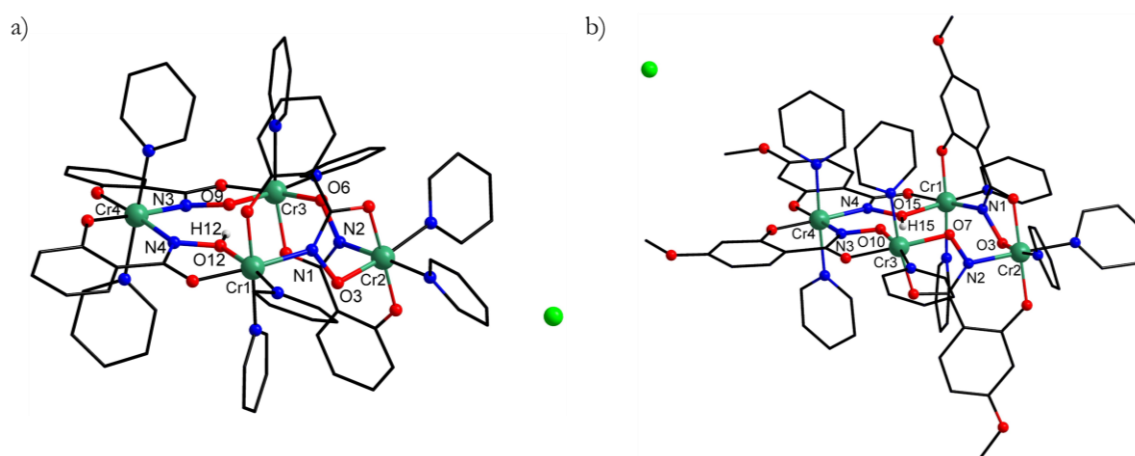


**Figure 4. 26.** Schematic representation of structure of a) **[Cr<sub>4</sub>]** and b) **OMe-[Cr<sub>4</sub>]** (side-on view). Hydrogen atoms and distorted solvent molecules are omitted for clarity except of H12 and H15 (protonation within repeating unit). Color code: chromium(III) ions green, chloride anion light green, oxygen red, nitrogen blue, hydrogen white, carbon black.

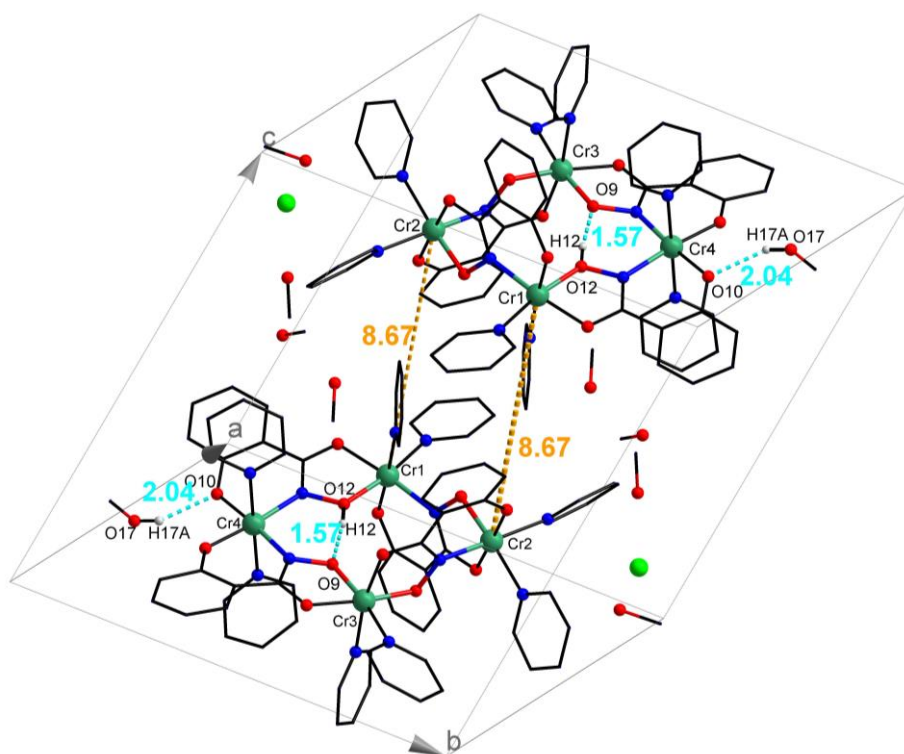


**Figure 4. 27.** Schematic representation of the molecular structure of **[Cr<sub>4</sub>]** in unit cell with highlighted intermolecular interactions. Cr1-Cr2 distance 8.67 Å (orange); hydrogen bonds of Hydrogen atoms are omitted for clarity except of H17A. Color code: chromium(III) ions green, chloride anion light green, oxygen red, nitrogen blue, hydrogen white, carbon black.

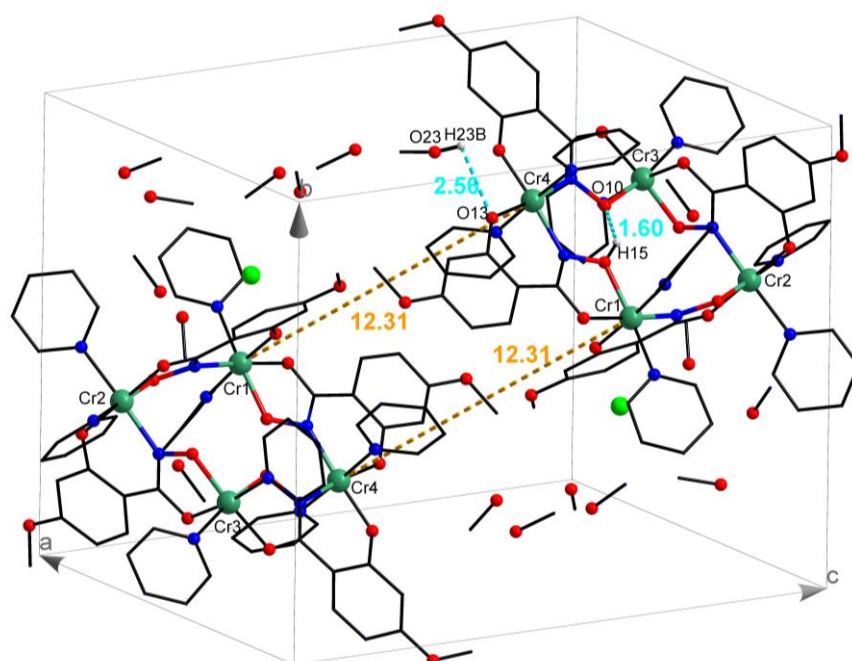


**Figure 4. 28.** Schematic representation of the molecular structure of **OMe-[Cr<sub>4</sub>]** in unit cell with highlighted intermolecular interactions. Cr1-Cr4 distance 12.31 Å (orange); hydrogen bonds of Hydrogen atoms are omitted for clarity except of H23B. Color code: chromium(III) ions green, chloride anion light green, oxygen red, nitrogen blue, hydrogen white, carbon black.

Since no satisfactory crystallization improvements were achieved by changing the ligands, the co-ligand was also varied. The exchange of pyridine to  $\gamma$ -picoline as a co-ligand using the same reaction conditions as for **[Cr<sub>4</sub>]**, led to the formation of  $\{[12\text{-MC}_{\text{Cr(III)N}(\text{shH})(\text{Sh})}_3\text{-4}](\gamma\text{ py})_8\text{Cl}\} \cdot 3.75\text{ H}_2\text{O} \cdot 0.5\text{ O}$ . Hereafter referred as **pic-[Cr<sub>4</sub>]**. The reaction led to the formation of two different sorts of crystals that co-crystallized together and were not separable. Both species crystallized in the triclinic crystal system in the space group P1. The morphology of the first crystal species is block-shaped while the other crystal species has a plate shape morphology. The block shaped crystal has the cell parameters  $a = 12.5299(3)\text{ \AA}$ ,  $b = 13.1913(3)\text{ \AA}$ ,  $c = 13.6818(3)\text{ \AA}$  and  $\alpha = 94.113(2)^\circ$ ,  $\beta = 90.648(2)$  and  $\gamma = 109.111(2)^\circ$ . These parameters are comparable to the plate shaped crystals with an approximately doubled c axis. The parameters are  $a = 12.1574(4)\text{ \AA}$ ,  $b = 13.2654(5)\text{ \AA}$ ,  $c = 26.2873(9)\text{ \AA}$  and  $\alpha = 92.281(3)^\circ$ ,  $\beta = 91.104(3)^\circ$  and  $\gamma = 110.758(3)^\circ$ . Thus, two molecules of **pic-[Cr<sub>4</sub>]** are in the asymmetric unit for the crystal with a plate morphology while only one molecule is present in the block shaped crystal.

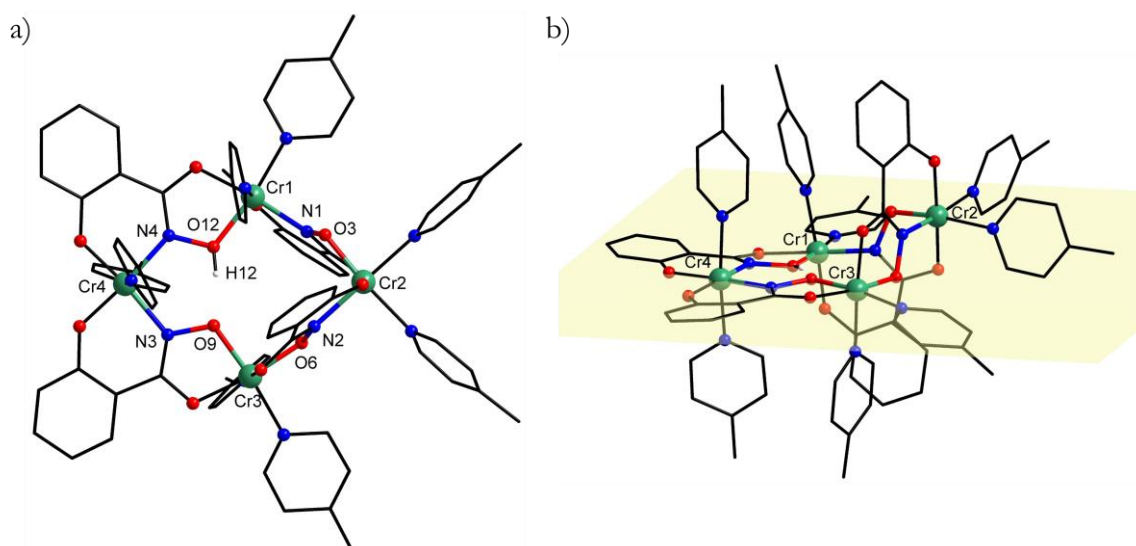


**Figure 4. 29.** Schematic representation of the molecular structure of **pic-[Cr<sub>4</sub>]** a) “top-down view”; b) “side-on” view with out-of-plane coordination of Cr2 ion of plane through Cr1-Cr3-Cr4 (yellow). Uncoordinated solvent molecules, counter ion and hydrogen atoms are omitted for clarity except of H12. Color code: chromium(III) ions green, oxygen red, nitrogen blue, hydrogen white, carbon black.

Similar to **[Cr<sub>4</sub>]** and **OMe-[Cr<sub>4</sub>]** and in contrast to the alignment of a classical [12-MC-4] metallocrown with salicylhydroxamate ligands, for **pic-[Cr<sub>4</sub>]** not all ions are coordinated by the ligand creating a five- and six-membered ring due to the reversed repetition unit. The different coordination environments of the four chromium(III) ions are highlighted in Figure 4. 30. For clarity, only the coordination environment of the first molecule a with Cr1-Cr4 are shown. The chromium(III) ions Cr5-8 show the same coordination modes. Two of the salicylhydroxamate ligands bind with the same bidentate moiety to each of the chromium(III) ions. Thus, Cr3 is involved in two five-membered chelate rings with the hydroxamate moieties, while Cr4 is each coordinated by two iminophenolate groups forming six-membered chelate rings. Cr1 and Cr2 on the other hand have the characteristic five- and six-membered ring, that is characteristic for building of MCs (see Chapter 1.1.2). Additionally, three of the four chromium(III) ions (Cr1, Cr2, Cr3) are coordinated in a

*cis*-configuration and Cr4 shows an in-plane *trans*-configuration of the chelating ligand. Thus, three different coordination environments are formed. Cr1 and Cr2 exhibit a *cis*- N<sub>3</sub>O<sub>3</sub>, Cr3 a *cis*- N<sub>2</sub>O<sub>4</sub> and Cr4 a *trans*-coordinated N<sub>4</sub>O<sub>2</sub> environment as shown in Figure 4. 30.

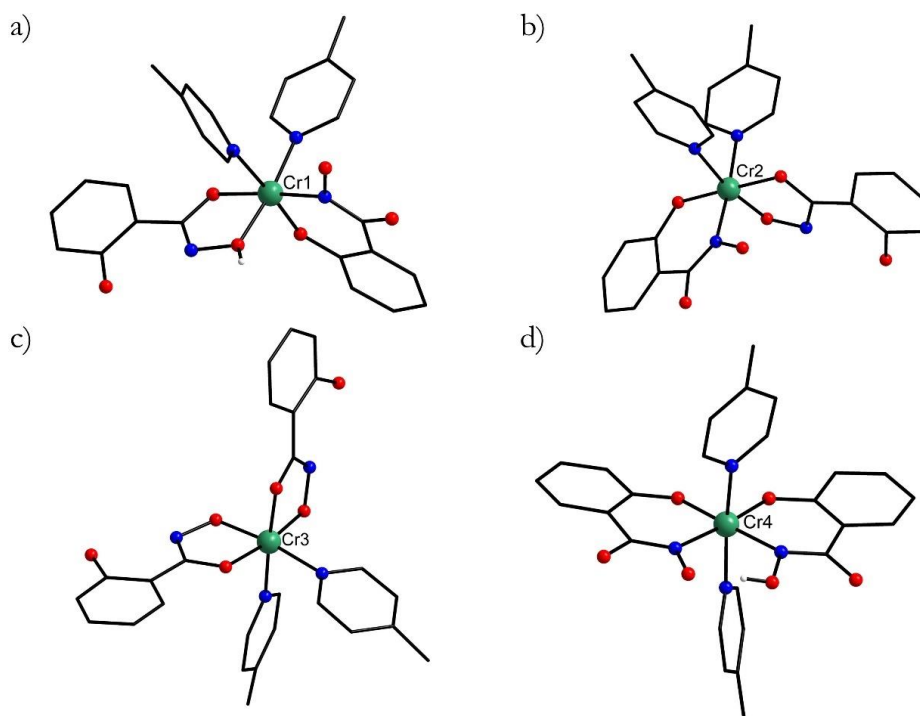


**Figure 4. 30.** Schematic representation of the different coordination environments for **pic-[Cr<sub>4</sub>]** of a) Cr1, b) Cr2, c) Cr3, d) Cr4. Color code: chromium(III) ions green, oxygen red, nitrogen blue, carbon black. Hydrogen atoms (except of H12), chloride anion and non-coordinated solvent molecules are omitted for clarity.

Continuous Shape Measurements (CShMs) have been calculated for each of the chromium(III) ions in **pic-[Cr<sub>4</sub>]** and are summarized in Table 4. 15 and Table 4. 16, for the crystals showing **plate** and **block** morphology, respectively, with an octahedral geometry  $O_h$ . The deviation from the ideal octahedral geometry is very small. The obtained values are slightly smaller than the values of the ring metal ions for the chromium(III) complexes **[Cr<sub>3</sub>Cr]** and **(*bu*)<sub>2</sub>-[Cr<sub>3</sub>Cr]** with [9-MC-3] cavity described before. The fact that the deviation is smaller compared to the ring metal ions in the [9-MC-3] ions caused by the lower ring tension and the possibility of the ligands distorting easier since there is no guest ion.

**Table 4. 15.** Calculated deviations from ideal polyhedra (octahedron  $O_h$ ) for ring metal ions *via* Continuous Shape measurements of **pic-[Cr<sub>4</sub>]** (crystal species with shape of **plate**).

ion	Cr1	Cr2	Cr3	Cr4	Cr5	Cr6	Cr7	Cr8
CShM	0.376	0.606	0.663	0.527	0.495	0.494	0.674	0.413

**Table 4. 16.** Calculated deviations from ideal polyhedra (octahedron  $O_h$ ) for ring metal ions *via* Continuous Shape Measurements of **pic-[Cr<sub>4</sub>]** (crystal species with shape of **block**).

ion	Cr1	Cr2	Cr3	Cr4
CShM	0.438	0.503	0.611	0.491



The separation distance of the molecules in the unit cell of the **plate**-like crystals is 7.47 Å as shown in Figure 4. 31. Compared vacant MCs [**Cr**<sub>4</sub>] and **OMe**-[**Cr**<sub>4</sub>] described above, a hydrogen bond within the ring atoms between H12-O9 of 1.60 Å and between H24A-O21 of 1.58 Å exists. Two differences to these described vacant MCs can be noticed. No additional hydrogen bonds occur between the solvent molecules and the MC. However, there is a T-shaped  $\pi$ -interaction found between the methyl group of the  $\gamma$ -picoline co-ligand and an aromatic ring of a salicylhydroxamate ligand of another MC molecule, which is highlighted in purple in Figure 4. 31.

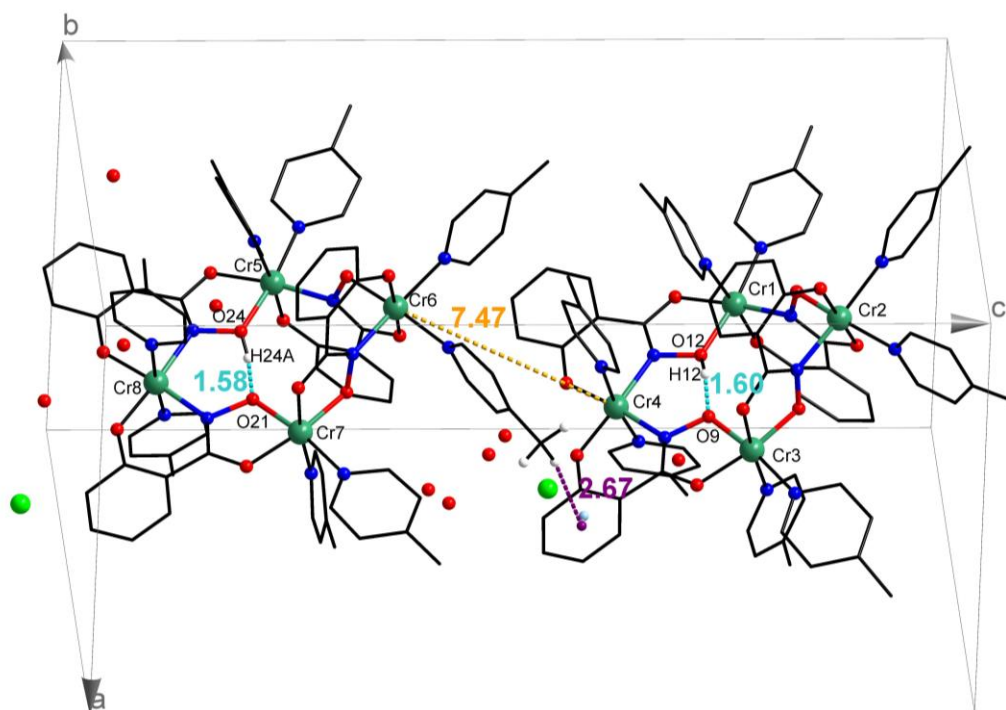


**Figure 4. 31.** Schematic representation of **pic**-[**Cr**<sub>4</sub>] of **plate**-like shaped crystals with molecule a (Cr1,Cr2,Cr3,Cr4) and molecule b (Cr5,Cr6,Cr7,Cr8) in unit cell with highlighted, smallest intermolecular distance for Cr4 and Cr6, Hydrogen bonds within the repeating unit and T-shaped  $\pi$  interaction between  $\gamma$ -picoline and aromatic ring of salicylhydroxamate ligand. Hydrogen atom are omitted for clarity (except of H12,H24A). Each non-coordinated oxygen atom is referring to a water molecule (hydrogen atoms are omitted). Color code: chromium(III) ions green, oxygen red, nitrogen blue, carbon black. Hydrogen atoms (except of H12,H12G, H12E, H12F,H24A) are omitted for clarity.

This T-shaped  $\pi$ -interaction often occur for polarized O–H, N–H, N–H<sup>+</sup>,  $sp^2$  C–H,  $sp^1$  C–H, and S–H groups.<sup>[63]</sup> Malone and co-workers categorized this T-shaped interaction in categories I–VI based on the following parameters which are shown in Figure 4. 32.<sup>[64]</sup> The center of the aromatic ring Q (purple) is separated from the orthogonal intersection P of the interacting H onto the plane through the aromatic ring (light blue) with the offset  $r$  (magenta). The interaction distance  $d_{QH}$  between the center of the aromatic ring Q and the H of the methyl group of the  $\gamma$ -picoline here, is 2.67 Å. The angle  $\alpha$  between the carbon of the methylgroup and Q is 168.19° and the angle between P–Q–H  $\beta$  is 82.1°. These parameters are used to categorize the interaction in accordance to Table 17. The interaction fits in category I. These kind of interactions with a  $sp^3$  hybridized C–H bond in a C–H $\cdots\pi$  interactions is a van-der Waals type. The dominant dispersion influence is also the

dominant attractive interaction.<sup>[65,66]</sup> This difference in the  $\pi$ -interaction could explain the enhanced crystallization ability of **pic-[Cr<sub>4</sub>]** compared to **[Cr<sub>4</sub>]** and **OMe-[Cr<sub>4</sub>]**.

Within the unit cell the molecules are closely packed, but there is no other closer Cr-Cr interaction than 7.47 Å. Thus, an intermolecular magnetic interaction should not occur.

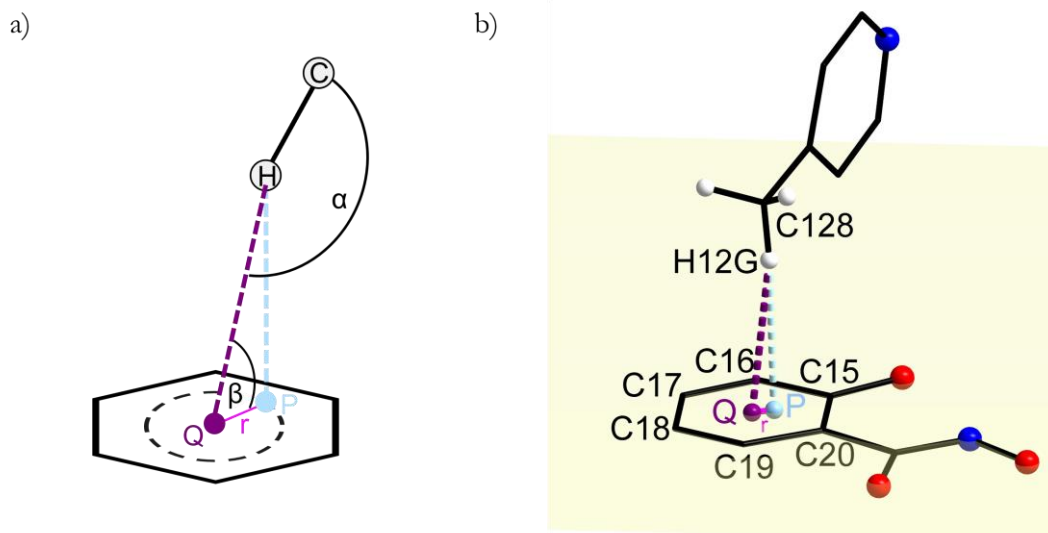


**Figure 4. 32.** a) Schematic representation of C-H $\cdots\pi$  (T-shaped) interaction of **pic-[Cr<sub>4</sub>]** with all parameters of description. b) C-H $\cdots\pi$  interaction of **pic-[Cr<sub>4</sub>]**. Interacting C-H fragment of CH<sub>3</sub> group of to  $\gamma$ -picoline as a co-ligand of next molecule is labeled as C128-H12G. Center of the aromatic ring Q (purple). Orthogonal intersection of H12G onto plane P through aromatic ring (light blue). Offset  $r = 0.367$  Å, interaction distance  $d_{QH} = 2.67$  Å,  $\alpha = 168.19^\circ$  and  $\beta = 82.1^\circ$ .

**Table 4. 17.** Categorization of T-shaped donor atom-H $\cdots\pi$  hydrogen bonds with  $\pi$  systems of Type I – V by Malone and co-workers.<sup>[64]</sup> All mentioned parameters are described in detail and shown in Figure 4. 32.

Type	$d_{QH}$	$\beta$	$\alpha$	$r$
I	$\leq 3.05$ Å	$\geq 53^\circ$	$150^\circ - 180^\circ$	$\leq 0.5$ Å
II	$\leq 3.05$ Å	$\geq 53^\circ$	$150^\circ - 180^\circ$	$0.5$ Å - $1.4$ Å
III	$\leq 3.05$ Å	$\geq 53^\circ$	$< 150^\circ$	$\leq 1.4$ Å
IV	$\leq 3.05$ Å	$40^\circ - 60^\circ$	$130^\circ - 150^\circ$	$\leq 1.4$ Å
V	$\leq 4.00$ Å	$\leq 90^\circ$	$90^\circ - 180^\circ$	$> 1.4$ Å
VI	$\leq 4.00$ Å	$\leq 90^\circ$	$\geq 90^\circ$	$> 1.4$ Å

The average torsion angle between the chromium(III) ring metal ions is  $171.56^\circ$ . However, for all molecules, one of the torsion angles diverges from the other torsion angles by up to  $17^\circ$  degrees as shown in Table 4. 18.

**Table 4. 18.** Selected torsion angles of each chromium(III) ring metal ions for **pic-[Cr<sub>4</sub>]**.

	torsion angles	
<b>pic-[Cr<sub>4</sub>]</b> (plate, molecule a)	Cr2-O3-N1-Cr1	161.1(4)°
	Cr3-O6-N2-Cr2	170.5(3)°
	Cr3-O9-N3-Cr4	178.4(4)°
	Cr1-O12-N4-Cr4	177.4(4)°
<b>pic-[Cr<sub>4</sub>]</b> (plate, molecule b)	Cr6-O15-N13-Cr5	162.6(3)°
	Cr5-O24-N16-Cr8	175.0(4)°
	Cr7-O18-N14-Cr6	173.3(3)°
	Cr7-O21-N15-Cr8	171.6(4)°
<b>pic-[Cr<sub>4</sub>]</b> (block)	Cr2-O3-N1-Cr1	161.33(12)°
	Cr1-O12-N4-Cr4	175.72(12)°
	Cr3-O6-N2-Cr2	173.98(11)°
	Cr3-O9-N3-Cr4	177.81(12)°
average	Cr <sub>ring</sub> -O-N-Cr <sub>ring</sub>	171.56°

No additional amorphous precipitate was formed during the crystallization and higher yields of single crystals compared to **[Cr<sub>4</sub>]** and **OMe-[Cr<sub>4</sub>]** were achieved. This is a very important improvement of the crystallization process and allows further analysis regarding the magnetochemistry and stability of **pic-[Cr<sub>4</sub>]**.

### Evaluation of magnetic data

The magnetic properties of **pic-[Cr<sub>4</sub>]** were investigated and the susceptibility and magnetization data are presented in Figure 4. 33. The crystal morphologies could not be separated for the bulk sample in the following measurements (**plate** and **block**). The magnetic susceptibility measurements were performed with an applied magnetic field of 1000 Oe in the range 2-300 K (Figure 4.33 a). Additionally, magnetization measurements were performed with magnetic fields ranging from 0.1 T to 7 T at 2-10 K (Figure 4.33 b). The theoretically expected value of the  $\chi_m T$  product was calculated using Equations 12 and 13 (Chapter 4.1.2.). The theoretical value of 7.5 cm<sup>3</sup> K mol<sup>-1</sup> with  $g = 2$  and  $S = 3/2$  almost equals the measured value of 7.02 cm<sup>3</sup> K mol<sup>-1</sup> at 300 K indicating already significant lower antiferromagnetic exchange interactions compared to **[Cr<sub>3</sub>Cr]**. With decreasing temperatures, the  $\chi_m T$  product is slowly decreasing until approximately 80 K and then more pronounced, steadily approaching a value of 0.01 cm<sup>3</sup> K mol<sup>-1</sup> at 2 K. Thus, a complete compensation of the spins of the chromium(III) ions is achieved by antiferromagnetic exchange interactions.

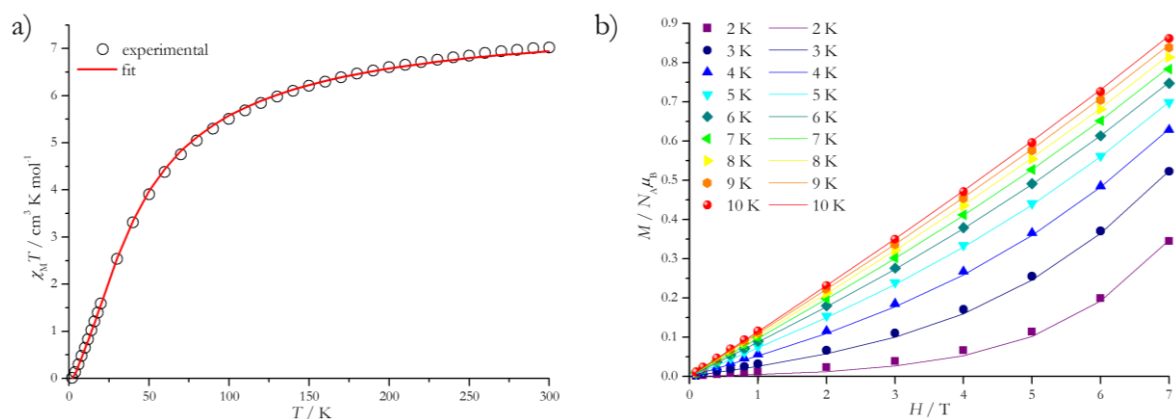


**Figure 4.33.** a) Temperature-dependence of magnetic susceptibility of **pic-[Cr<sub>4</sub>]**; b) magnetization measurement of **pic-[Cr<sub>4</sub>]**. The solid red lines represent the best fit of the data.

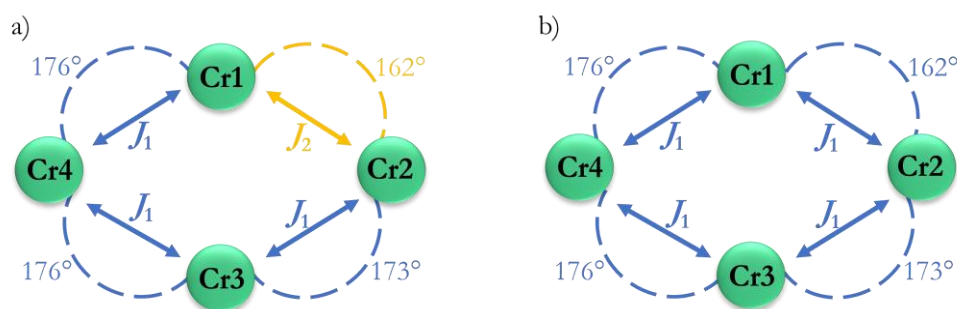


**Figure 4.34.** Idealized coupling scheme of **pic-[Cr<sub>4</sub>]** with averaged angles between ring metal ions; a) with coupling constant  $J_1$  between ring metal ions (Cr2,Cr3,Cr4,Cr1) and coupling constant  $J_2$  between neighboring ring metal ions (Cr1,Cr2); b) with coupling constant  $J_1$  between all ring metal ions (Cr1,Cr2,Cr3,Cr4).

The program PHI<sup>[32]</sup> was used to fit the susceptibility and magnetization data simultaneously using the Hamiltonian for the coupling scheme depicted in Figure 4.34. It would be legitimate to fit the susceptibility and magnetization data with two coupling  $J_1$  and  $J_2$  constants. The average torsion angles differ slightly between Cr1-N-O-Cr2 in comparison to the average torsion angles between Cr2-N-O-Cr3, Cr3-N-O-Cr4 and Cr4-N-O-Cr1 as shown in Figure 4.34 a (see Table 4.18). However, a satisfactory simulation of the data was obtained with one coupling constant only as shown in Figure 4.34 b. Therefore, the magnetic data was fitted according to the coupling scheme using the exchange Hamiltonian  $\hat{H}$  in Equation 16 with one exchange coupling parameter  $J_1$  and one  $g$  value to avoid overparameterization yielding  $J_1 = -4.41 \text{ cm}^{-1}$  and  $g = 2.03$ . The residual  $R$  was calculated to be  $0.2 \cdot 10^{-3}$ . Cr4 and Cr2 are approximately  $7.5 \text{ \AA}$  separated in average. Thus, no intermolecular interaction was considered in this fit.

$$\hat{H} = -2J_1(\hat{S}_{\text{Cr1}} \cdot \hat{S}_{\text{Cr2}} + \hat{S}_{\text{Cr2}} \cdot \hat{S}_{\text{Cr3}} + \hat{S}_{\text{Cr3}} \cdot \hat{S}_{\text{Cr4}} + \hat{S}_{\text{Cr4}} \cdot \hat{S}_{\text{Cr1}}) \quad (16)$$

**Table 4.19.** Summarized fitting parameters of **pic-[Cr<sub>4</sub>]**.

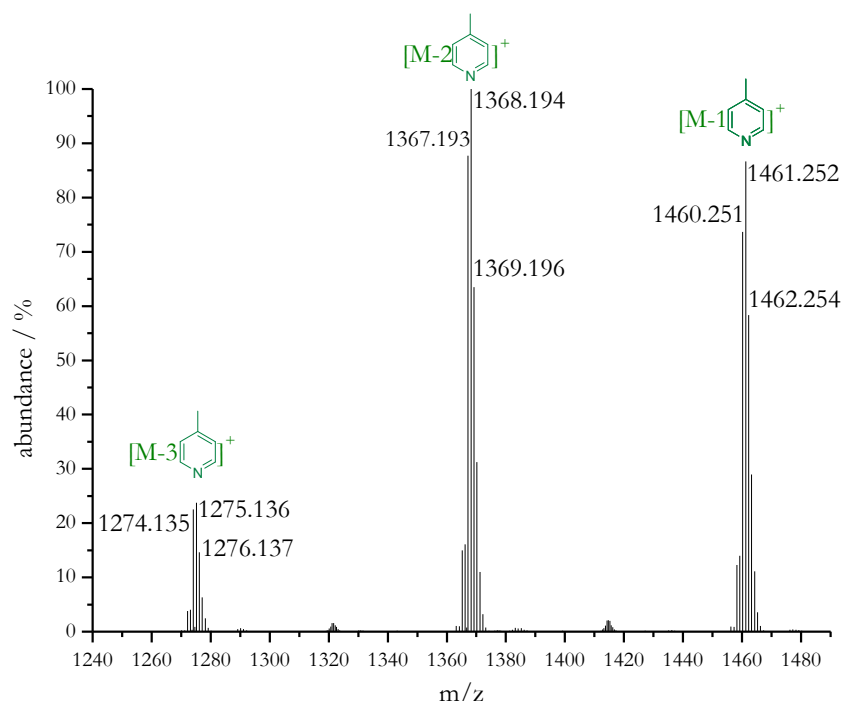
	$g$	$J_1$	$R$
<b>parameters</b>	$2.03 \pm 0.01$	$-4.41 \pm 0.01$	$0.2 \cdot 10^{-3}$

### Electrospray ionization (ESI) mass spectrometry

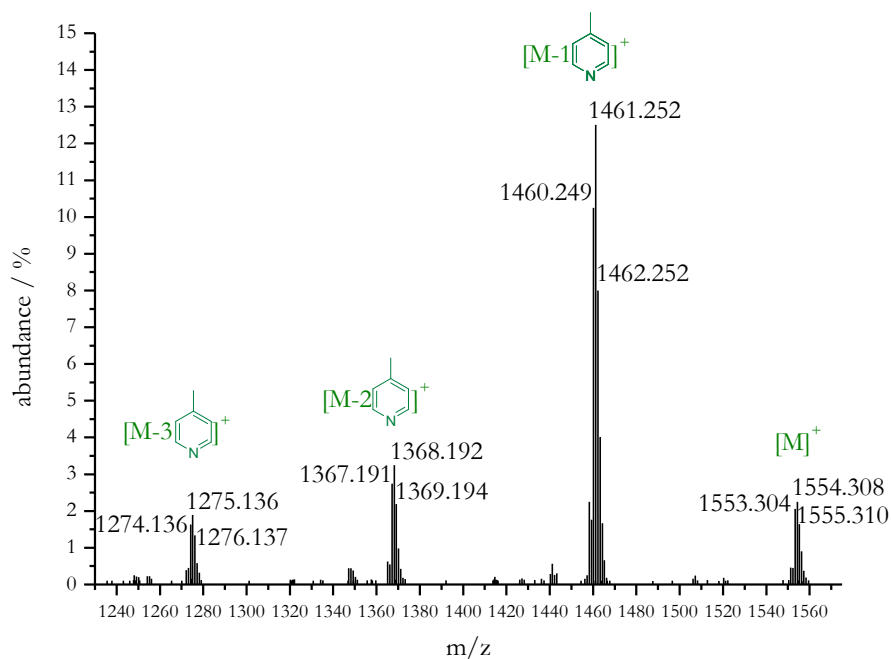
The ESI mass spectra for the ionization of the intact large **[Cr<sub>3</sub>Cr]** and **(*t*-bu)<sub>2</sub>-[Cr<sub>3</sub>Cr]** MCs were already shown in the previous Chapter 4.1.2. The vacant structure of **pic-[Cr4]** differs from these two compounds mainly in the absence of bridging co-ligands. While in the former complexes, the chelating pivalate ligands are coordinated to a ring metal ion and a guest ion and are negatively charged, this is not the case for **pic-[Cr4]** due to the monodentate bound, neutral  $\gamma$ -picoline co-ligands. Thus, the molecule is more fragile towards ligand exchange or ligand loss. However, the molecule is already positively charged, which should enhance the detection of **pic-[Cr4]** in the ESI positive mode.

The prediction tool of MestReNova was used to analyze the spectra with isotope pattern of the predicted sum formula (C<sub>76</sub>H<sub>72</sub>Cr<sub>4</sub>N<sub>12</sub>O<sub>12</sub>). The sum formula contains one proton less as only neutral compound can be predicted while the program adds charged ions (e.g., H<sup>+</sup>) to obtain a positively charged adduct. The measured spectra are shown in Figure 4. 35 for 275 °C and in Figure 4. 36 for 100 °C. **pic-[Cr4]** contains eight linear coordinated  $\gamma$ -picoline co-ligands. The obtained signals show fragments of **pic-[Cr4]** that contain seven ([M-1  $\gamma$ -picoline]<sup>+</sup>1460.251 m/z), six ([M-2  $\gamma$ -picoline]<sup>+</sup> 1367.193 m/z) and five ([M-3  $\gamma$ -picoline]<sup>+</sup> 1274.135 m/z) coordinated  $\gamma$ -picoline co-ligands at a temperature of 275 °C. All signals contain the same characteristic isotope pattern which is in very good agreement with the calculated isotope patterns for each fragment (see Figures 47-52). At milder conditions with a temperature of 100 °C the intact molecule ([M]<sup>+</sup> 1553.304 m/z) can be detected additionally. The measured signal assigned to a fragment with seven  $\gamma$ -picoline is exemplarily illustrated in a zoom-in with the predicted isotope pattern in Figure 4. 37 for 275 °C. These are in very good agreement with each other. As expected, no adducts with sodium [M+Na]<sup>+</sup> or potassium [M+K]<sup>+</sup> can be found because **pic-[Cr4]** is already positively charged.

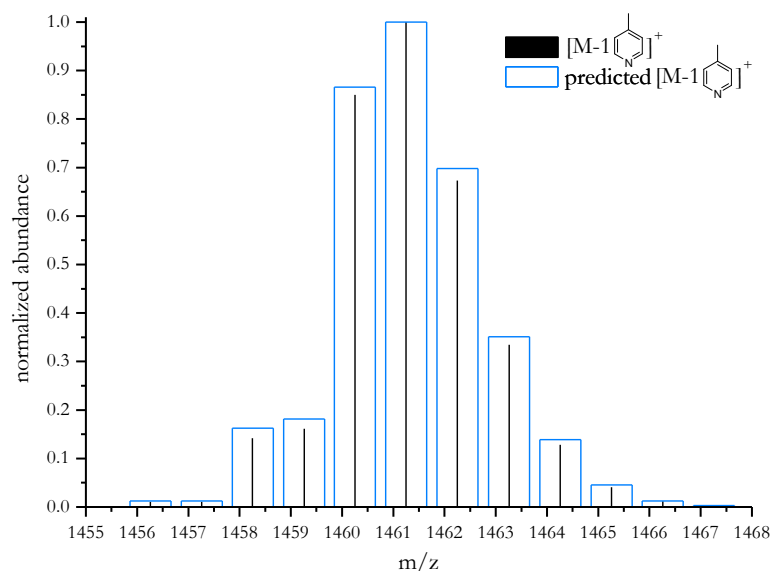
These results highlight the stability of **[Cr<sub>3</sub>Cr]** and **(*t*-bu)<sub>2</sub>-[Cr<sub>3</sub>Cr]** which is most probably also enhanced by the chelating, bridging pivalate co-ligands. For potential surface application attempts the loss of the co-ligands **pic-[Cr4]** in the gas phase can be controlled by applying lower temperatures. Furthermore, coordinating solvent molecules could replace the  $\gamma$ -picoline on a surface. The fragmentation also creates a structure that should be flatter compared to **pic-[Cr4]**.



**Figure 4.35.** Positive ion electrospray ionization mass spectrum (zoom-in) of a methanol/acetonitrile solution of **pic-[Cr<sub>4</sub>]** for the measured adduct with loss of the co-ligand  $\gamma$ -picoline ( $T = 275$  °C). The three highest signals are labelled for each fragment.



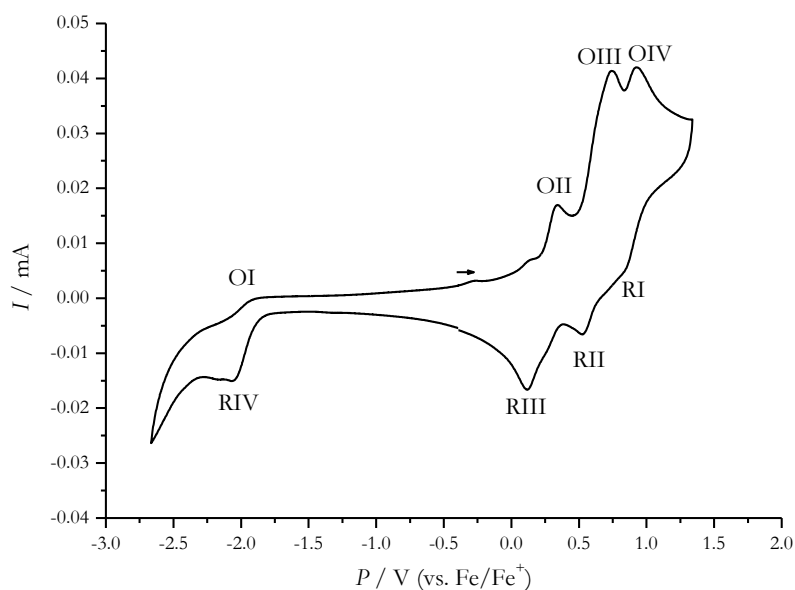
**Figure 4.36.** Positive ion electrospray ionization mass spectrum (zoom-in) of a methanol/acetonitrile solution of **pic-[Cr<sub>4</sub>]** for the measured adduct with loss of the co-ligand  $\gamma$ -picoline ( $T = 100$  °C). The three highest signals are labelled for each fragment.



**Figure 4. 37.** Normalized abundance from electrospray ionization mass spectrum with zoom-in of isotope pattern of **pic-[Cr<sub>4</sub>]<sup>+</sup>** at 275 °C. Measurement black bar, prediction blue box.

### Cyclic Voltammetry

In the following, the electrochemical stability of **pic-[Cr<sub>4</sub>]** will be discussed in detail. The measurements were performed in a 1 mM solution of **pic-[Cr<sub>4</sub>]** in acetonitrile with a concentration of 100 mM of the conducting salt tetrabutylammonium hexafluorophosphate. Again, the spectrum is referenced against ferrocene/ferrocenium. The cyclic voltammogram shows four oxidation peaks and four reduction peaks. The small shoulders of the peaks could not be assigned due to low intensity in Figure 4. 38.

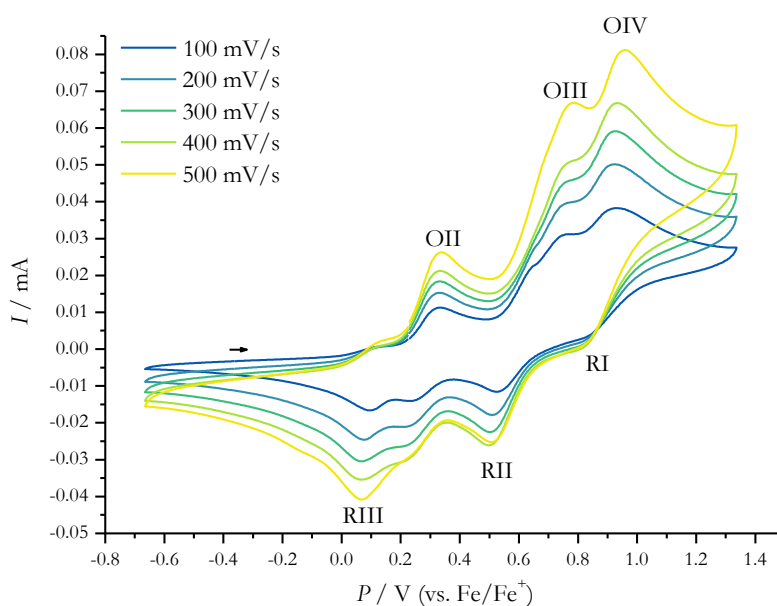


**Figure 4. 38.** Cyclic voltammogram of an approximately 1 mM solution of **pic-[Cr<sub>4</sub>]** in acetonitrile with a concentration of 100 mM of the conducting salt tetrabutylammonium hexafluorophosphate. Referenced against ferrocene/ferrocenium.

**Table 4. 20.** Values of peak potentials  $E_p$  for the cyclic voltammogram of **pic-[Cr<sub>3</sub>Cr]**.

peak	$E_p$ / V	peak	$E_p$ / V
OII	0.34	RI	0.85
OIII	0.73	RII	0.53
OIV	0.93	RIII	0.12
		RIV	-2.06

There are three oxidation peaks in the anodic potential range, which can be roughly assigned to the oxidation of the ligands salicylhydroxamic acid and  $\gamma$ -picoline. Oxidation of chromium(III) to a higher oxidation number is very unlikely at this potential region. The oxidation appears to be chemically reversible for several oxidations, but the assignment is not possible for all redox pairs due to overlapping peaks. Redox-active secondary products of a chemical reaction are not observed. Moreover, two shoulders before the oxidation OII are too low in intensity to be determined. Further experiments using EPR spectroscopy may provide further insight into the nature of redox processes in the anodic region here. These experiments are still pending.

**Figure 4. 39.** Scan rate study of the irreversible oxidation process OIII and the reduction of the daughter product RI including the oxidation OIV.

In the cathodic potential range, there is an irreversible reduction peak (RIV) at -2.06 V, as well as another very small shoulder of this irreversible reduction around -2.17 V. This loses shape at higher scan rates. Thus, the underlying reduction process is slow. The mononuclear chromium(III)-bipyridine(bpy) complex  $[\text{Cr}^{\text{III}}(\text{bpy})_2(\text{H}_2\text{O})_2]^{3+}$ , with a similar octahedral N<sub>4</sub>O<sub>2</sub> coordination, is reduced from chromium(III) to chromium(II) at about -0.5 V in water against Ag/AgCl (Pt electrode, 50 mV/s scan rate, 0.01M Na<sub>2</sub>SO<sub>4</sub>, 0.49 mM complex)<sup>[67]</sup> and -0.7 V against the standard hydrogen electrode (SHE) respectively (glassy carbon electrode, 50 mV/s scan rate)<sup>[68]</sup>. This reduction potential of chromium(III) to chromium(II) depends on the electronic structure of the complex caused by the ligands. Thus, the reduction of a chromium(III) ring



ion of the MC to chromium(II) is possible. A second chromium(III) reduction within the ring could explain the broad reduction RIV. The broad reduction RIV could be the overlay of two reductions. The reduction of the first chromium(III) into chromium(II) changes the field around its neighbors, altering the potential of those neighboring ring metal ions. For these chromium(III) ions, electronic coupling *via* the bridging -O-N- unit is expected which leads to a stepwise reduction of the chromium(III) ions.

Additionally, the irreversibility of the reduction suggests a subsequent chemical process after the reaction. Since chromium(II) ions are exhibiting a  $d^4$  electron configuration, a distorted octahedral coordination geometry is obtained due to the Jahn-Teller effect. The coordination environment contributes significantly to the kinetics of decomposition reactions. For a flexible coordination environment that can coordinate the distorted chromium(II) ion without tension, quasi-reversible reduction of chromium can be expected. In this case of rigid ligands, which cannot adapt to the distortion, decomposition of the complex and thus irreversible reduction should occur.<sup>[56,69]</sup> Depending on the configuration of the chelating ligands in *cis*- or *trans*-configuration, differences in the reversibility of the electron transfer were already found by Speiser and coworkers in 1996.<sup>[69]</sup> Chromium(III) complexes with tri- and hexadentate amino carboxylate ligands ( $N_2O_4$  coordination environment) showed reversible reduction for the *cis*-configuration and a quasi-reversible reduction for the *trans*-configuration. The authors attributed this behavior to differences in the Jahn-Teller distortion axes for the reduced chromium(III) species. The *trans*-configuration allows a simultaneous N-Cr-N bond elongation which leads to greater strain in the facially coordinated *N*-alkyliminodiacetate ligand. Thus, a bond cleavage of the chromium-carboxylate bond is facilitated instead of a reversible electron transfer. Therefore, a quasi-reversible reduction is observed. The coordination of the chromium(III) ions in **pic-[Cr<sub>4</sub>]** is more complex. There are three different coordination environments for the chromium(III) ions. As already described, Cr1 and Cr2 have a  $N_3O_3$  *cis*-configuration, Cr3 a  $N_2O_4$  *cis*-configuration and Cr4 a  $N_4O_2$  *trans*-configuration. Therefore, for Cr4, reduction to chromium(II) could well result in Jahn-Teller elongation. In contrast, for the other chromium(III) ions, high strain would have to be assumed within the chelating ligands.

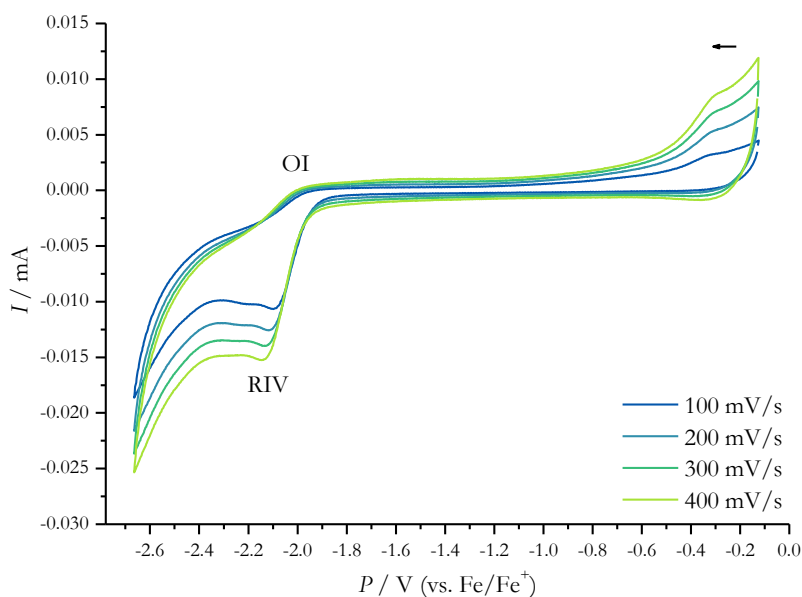


**Figure 4. 40.** Scan rate study of the cathodic region of the reduction processes RIV and OI of **pic-[Cr<sub>4</sub>]**.

### Additional synthesis

Furthermore, 3-hydroxy-2-naphthylhydroxamic acid was used as ligand to obtain better crystallization properties by making use of  $\pi$ - $\pi$  interactions between the extended aromatic motifs.<sup>[70–72]</sup> Thus, the ligand 3-hydroxy-2-naphthylhydroxamic acid (= **Nha**) was prepared in a one-step synthesis. The reaction of hydroxylamine hydrochloride and potassium hydroxide forms hydroxylamine *in-situ*. Then, hydroxylamine<sup>[40]</sup> attacks the carbonyl carbon of methyl 3-hydroxy-2-naphthoate resulting in the potassium salt of 3-hydroxy-2-naphthylhydroxamic acid. The product was crystallized from 1.25 M acetic acid/water solution.

The reaction of the ligand with chromium(III) chloride and triethylamine in a methanol-pyridine solution (15:2 v/v) was performed under solvothermal conditions at 120°C for 11 h, followed by slow evaporation of the solvent. However, only very small microcrystalline needles were obtained. These could not be examined by X-ray analysis due to their size and shape. Other crystallization conditions did not improve the size and shape of the needles. The needles were collected and signals matching the structure of a vacant metallocrown **Nha-[Cr<sub>4</sub>]** were detected by ESI mass spectrometry. In analogy to the structure **pic-[Cr<sub>4</sub>]**, a loss of gamma-picoline can be detected. In addition, this molecule also appears to be charged, as it was detected without further protons (Figure 4. 41). This ESI measurement indicates an analog MC structure to the discussed vacant **[Cr<sub>4</sub>]**, **OMe-[Cr<sub>4</sub>]**, and **pic-[Cr<sub>4</sub>]**.

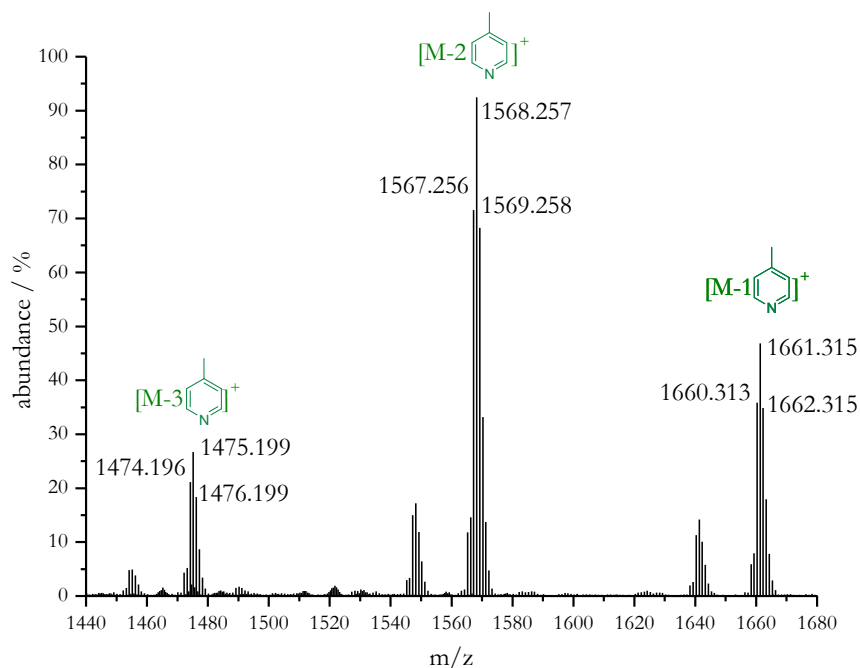


**Figure 4. 41.** Positive ion electrospray ionization mass spectrum (zoom-in) of a methanol/acetonitrile solution of **Nha-[Cr<sub>4</sub>]** for the measured adduct with loss of the co-ligand  $\gamma$ -picoline. The three highest signals are labelled for each fragment.

In general, the vacant MCs described in Chapter 4.1.3, represent the first of their kind containing chromium ions. A structurally related compound was obtained by Peter Happ with diamagnetic cobalt(III) ions.<sup>[73]</sup> In this compound, all ions are in an octahedral ligand field as well. Moreover, only one of the four ring metal ions is coordinated in the *trans*-configuration of the ligands, whereas the other three ring metal ions exhibit a *cis*-propeller configuration. The change in the order of the repeating unit, as well as the coordination of eight co-ligands (pyridine in this case) is analogous. Only minor differences are present here. Two cobalt(III) ions on opposite sides are coordinated by two five-membered chelate rings (hydroximate moieties) while the other two cobalt(III) ions are coordinated by two six-membered chelate rings (iminophenolate groups). Thus, a pseudo-C<sub>2</sub> symmetry is created.

Concluding, a series of new chromium(III) and iron(III) complexes showing a [9-MC-3] metallacrown cavity, have been synthesized by self-assembled reactions at room temperature for the iron(III) and by solvothermal synthesis for the chromium(III) ions. These complexes constitute the first examples of classical MCs incorporating chromium ions in general. Especially the comparison of the three presented compounds **[Cr<sub>3</sub>Cr]**, **†bu-[Fe<sub>3</sub>Fe]** and **(†bu)<sub>2</sub>-[Cr<sub>3</sub>Cr]**, shows that the [9-MC-3] metallacrown cavity leads to two competing magnetic exchange interactions. This results in high spin ground states  $S_T \neq 0$ . Although an even number of ions of the same oxidation state are present, no complete compensation of their spins by antiferromagnetic exchange interactions was observed.

Furthermore, vacant chromium(III) MCs **[Cr<sub>4</sub>]**, **OMe-[Cr<sub>4</sub>]**, **Nha-[Cr<sub>4</sub>]** and **pic-[Cr<sub>4</sub>]** were successfully synthesized using chromium(III) chloride as starting material. In this case a spin ground state of  $S_T = 0$  is obtained. This highlights again the various compositions of MCs. Depending on the cavity and coordination of a guest ion, the magnetic exchange interactions lead to completely different magnetic ground states. The MCs were investigated regarding their electrochemical properties and stability under the conditions of ESI mass spectrometry. The compound **pic-[Cr<sub>4</sub>]** could be detected in this method. Additionally, fragmentation under the loss of co-ligands was observed. The chromium compounds **(†bu)<sub>2</sub>-[Cr<sub>3</sub>Cr]** and **[Cr<sub>3</sub>Cr]** showed an extraordinary stability which is a good basis for further surface immobilization attempts using ultra high vacuum and electrospray methods.

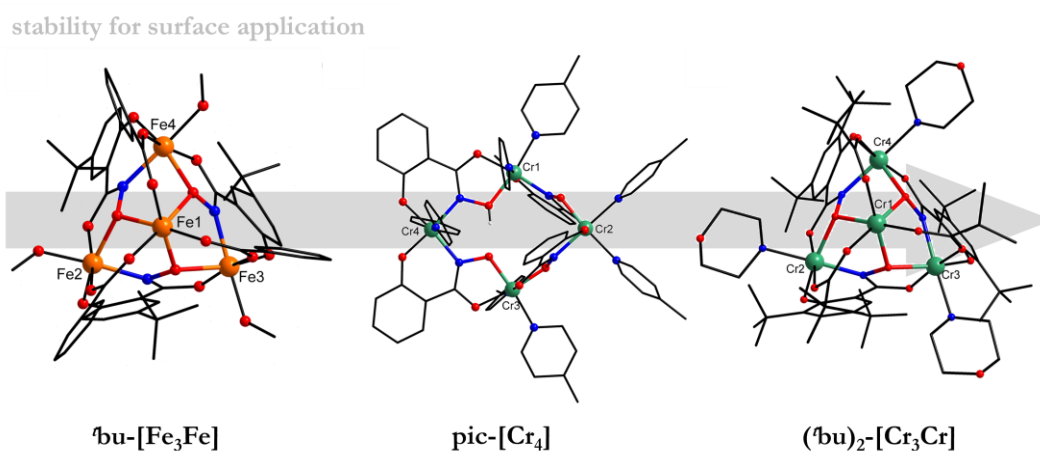


**Figure 4.42** Overview of **†bu-[Fe<sub>3</sub>Fe]**, **pic-[Cr<sub>4</sub>]**, and **(†bu)<sub>2</sub>-[Cr<sub>3</sub>Cr]** with regard to the electrochemical properties and fragmentation und ESI mass spectrometry conditions.

Spin ground states of  $S_T = 0$  and use of isotropic chromium(III) ions most properly will not lead to single-molecule magnet properties.<sup>[74,75]</sup> Thus, in the next Chapter 4.2 additional anisotropic 4f ions are implemented in the chromium(III) metallacrown scaffold as guest ions. Lanthanide(III) ions exhibit a larger ionic radius, facilitating a larger cavity size to synthesize flat metallacrowns.<sup>[76–78]</sup>

## 4.2. 3d-4f Metallocrowns with chromium(III) ions

In the second part of the thesis, the combination between the kinetically inert chromium(III) ions and the anisotropy of lanthanide(III) ions was investigated to achieve a slow relaxation of magnetization of single-molecule magnets.

In this work, the primarily focus is the utilization of dysprosium(III) guest ions because it is categorized as a Kramers-ion. Kramers-ions have an odd number of unpaired electrons which leads to rigorously doubly-degenerate microstates  $M_J$  in all coordination polyheders even without additional applied magnetic field. In case of non-Kramers ions, a higher symmetry environment is required to obtain degenerate ground states in zero-field. It is therefore crucial to design a targeted ligand field to generate the prerequisite bistable ground state and detect single-molecule magnets behavior.<sup>[79]</sup>

MCs have been established as a promising complex ligand for the preparation of single-molecule magnets.<sup>[80]</sup> They allow a variation of the ligand field due to their structural diversity. Thus, in this part of the thesis, MCs with anisotropic dysprosium(III) ions in ideal coordination environments for the development of new single-molecule magnets will be combined with kinetically inert chromium(III) ions.

Furthermore, the influence of the guest ion on the cavity of the MC should be further investigated. In the first part of the thesis, various [9-MC-3] MCs as well as vacant [12-MC-4] MCs were synthesized and characterized. A further extension of these chromium(III) family will be achieved by the implementation of larger lanthanide(III) ions which prefer higher coordination numbers of seven to twelve.

In contrast to 3d metal ions, spin-orbit coupling is more important than crystal field splitting for lanthanide ions. This spin-orbit coupling splits the  $^{2S+1}L$  state into multiplets including different  $J$  values.<sup>[81]</sup> The value of total angular momentum  $J$  for the ground state is given by  $(L - S)$  for  $f$ -shells that are less than half-filled, and by  $(L + S)$  for  $f$ -shells that is more than half-filled (Hund's third rule). The Landé g factor  $g_J$  can be calculated using Equation 17 and depends on the spin  $S$ , angular momentum  $L$  and the total angular momentum  $J$ .<sup>[41]</sup> Similar to Equation 12 and 13, the theoretical value of the susceptibility at room temperature can be obtained by using Equation 18 and 19.

$$g_J = 1 + \frac{S(S + 1) - L(L + 1) + J(J + 1)}{2J(J + 1)} \quad (17)$$

$$\mu_{\text{eff},J} = g_J \cdot \sqrt{S(S + 1)} \mu_B \quad (18)$$

$$\chi_{\text{MT}} \approx \frac{N_A \mu_B^2}{3k_B} \cdot (\mu_{\text{eff},J})^2 \approx \frac{g_J^2 \cdot S(S + 1)}{8} \quad (19)$$

Magnetization  $M$  can be calculated using Equation 20 in  $N_A \mu_B$

$$M = m_J \cdot g_J \quad (20)$$

An overview of relevant parameters for determining theoretical parameters of magnetic susceptibility and magnetization are given in Table 4. 21.

**Table 4. 21.** Theoretical parameters to determine magnetic susceptibility and magnetization.

	<i>S</i>	<i>L</i>	<i>J</i>	<i>g</i>	$\chi T / \text{cm}^3 \text{ K mol}^{-1}$	$M / N_A \mu_B$
<b>Cr(III)</b>	3/2	0	0	2	1.875	3
<b>Tb(III)</b>	3	3	6	3/2	11.81	9
<b>Dy(III)</b>	5/2	5	15/2	4/3	14.17	10

#### 4.2.1.1. [15-MC-5] Metallacrown

The reaction of 3,5-di-*tert*-butylsalicylhydroxamic acid, dysprosium(III)nitrate, potassium chromium(III) sulfate, and triethylamine in a methanol/pyridine solution (15:2 v/v) resulted in the formation of  $\{\text{Dy}^{\text{III}}(\mu_2\text{-NO}_3)(\mu_2\text{-SO}_4)[15\text{-MC}_{\text{Cr}(\text{III})\text{N}((\text{tBu})_2\text{Sh})_5\text{-5]}(\text{py})_8]\} \cdot \text{MeOH} \cdot 2 \text{ py}$  after solvothermal synthesis and slow evaporation of the solvent as brown needles.  $\{\text{Dy}^{\text{III}}(\mu_2\text{-NO}_3)(\mu_2\text{-SO}_4)[15\text{-MC}_{\text{Cr}(\text{III})\text{N}((\text{tBu})_2\text{Sh})_5\text{-5]}(\text{py})_8]\} \cdot \text{MeOH} \cdot 2 \text{ py}$  is hereafter referred to as **[Cr<sub>5</sub>Dy]** and crystallizes in the monoclinic space group C12/c1. The lattice parameters are  $a = 42.2769(12) \text{ \AA}$ ,  $b = 24.2813(5) \text{ \AA}$ ,  $c = 39.7212(12) \text{ \AA}$ ,  $\alpha = 90^\circ$ ,  $\beta = 130.888(2)^\circ$ , and  $\gamma = 90^\circ$ . Five chromium(III) ions form a [15-MC<sub>Cr(III)N((tBu)<sub>2</sub>Sh)<sub>5</sub>-5] metallacrown along with the triply deprotonated 3,5-di-*tert*-butylsalicylhydroxamate ligands (Figure 4. 43). One dysprosium(III) ion serves as a guest ion. The nitrogen and oxygen atoms of the hydroxamate group from 3,5-di-*tert*-butylsalicyl hydroxamate and five chromium(III) ions form the typical of MCs [Cr-N-O-] repeating unit. The charge of the ring metal ions is compensated by the charge of the deprotonated ligand. The charge of the central dysprosium(III) ion is compensated by the bridging ions nitrate and sulfate, which act as co-ligands.</sub>

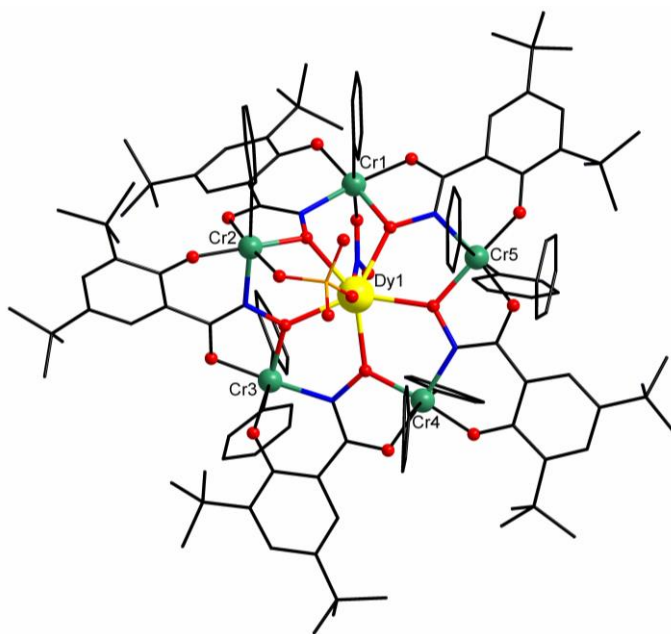


**Figure 4. 43.** Schematic representation of the molecular structure of **[Cr<sub>5</sub>Dy]** including highlighted repeating unit. Uncoordinated solvent molecules and hydrogen atoms are omitted for clarity. Color code: dysprosium(III) yellow, chromium(III) ions green, oxygen red, nitrogen blue, sulfur orange, carbon black.

The MC ring is not planar which is typically expected for a [15-MC-5] cavity with  $3d$  and  $4f$  ions (Figure 4. 44, “side-on” view) and the commonly used picoline hydroxamic acid and its derivatives. However, in this case, 3,5-di-*tert*-butylsalicyl hydroxamate is coordinated as the ligand. The ring metal ions Cr1, Cr3, Cr4 and Cr5 form one plane while both the Dy1 and Cr2 are coordinated out-of-plane (Figure 4. 44, yellow plane). The coordination of Cr2 is particularly notable in this case since the ligands occur in *cis*-configuration exclusively at this site. Therefore, a flat MC where all ring metal ions and the guest ion are forming a planar structure is not achieved. As already mentioned in Chapter 1.1.2, an ideal angle of coordination to form five- and six-

membered rings with salicylhydroxamic acid is achieved in a [12-MC-4] cavity with an angle of  $90^\circ$  between the coordinated ions. This explains the non-planar arrangement of  $[\text{Cr}_5\text{Dy}]$ . However, these kind of bent structures are also reported in literature with salicylhydroxamic acids.<sup>[82–84]</sup> The first MC that was reported with a [15-MC-5] cavity was a manganese(II/III) compound with salicylhydroxamic acid as the ligand by Pecoraro in 1994.<sup>[82]</sup> A very similar bent structure with five manganese(III) ring metal ions and a seven-coordinated manganese(II) guest ion was obtained. Compared to  $[\text{Cr}_5\text{Dy}]$ , three ligands of the manganese(III) ring metal ions are coordinated in *cis*- and two in planar *trans*-configuration.

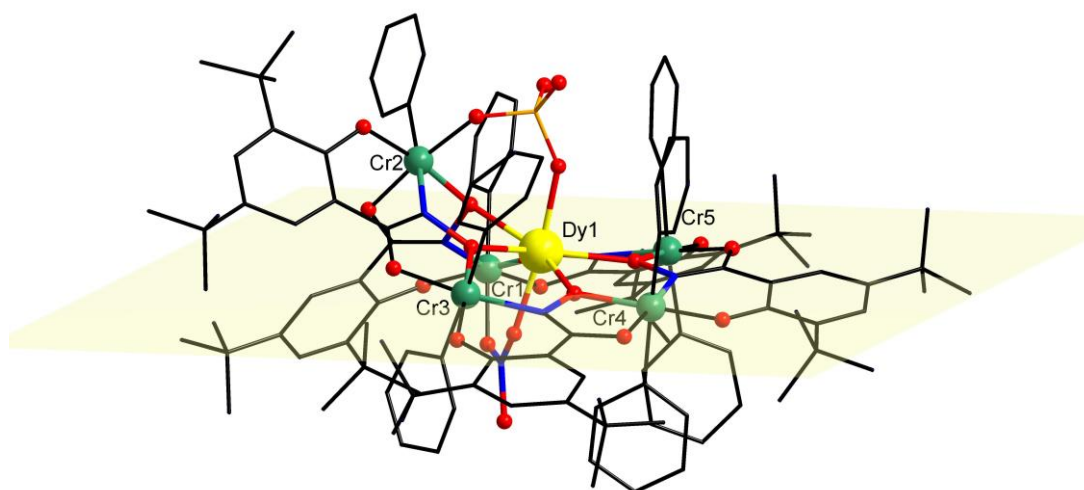


**Figure 4. 44.** Schematic representation of the molecular structure of  $[\text{Cr}_5\text{Dy}]$  in “side-on” view with out-of-plane coordination of Cr2 ion of plane through Cr1-Cr3-Cr4-Cr5 (yellow). Uncoordinated solvent molecules and hydrogen atoms are omitted for clarity. Color code: dysprosium(III) yellow, chromium(III) ions green, oxygen red, nitrogen blue, sulfur orange, carbon black.

Four sites of the coordination sphere of the chromium(III) ring metal ions are occupied by the donor atoms of two salicylhydroxamates ligands. The remaining sites are filled with nitrogen or oxygen atoms of pyridine and bridging nitrate as well as sulfate co-ligands, respectively. Three diverse coordination geometries for Cr1, Cr2 and Cr3-5 have been observed as shown in Figure 4. 45. Three chromium(III) ions Cr3, Cr4 and Cr5 exhibit a *trans*-configuration including two chelating salicylhydroxamates ligands and two pyridine co-ligands. Cr1 shows a *trans*-configuration as well but is additionally coordinated by a pyridine and a nitrate co-ligand instead. In contrast, Cr2 adopts a *cis*-propeller configuration of the ligand with additional a pyridine and a sulfate co-ligand to complete the octahedral coordination sphere.



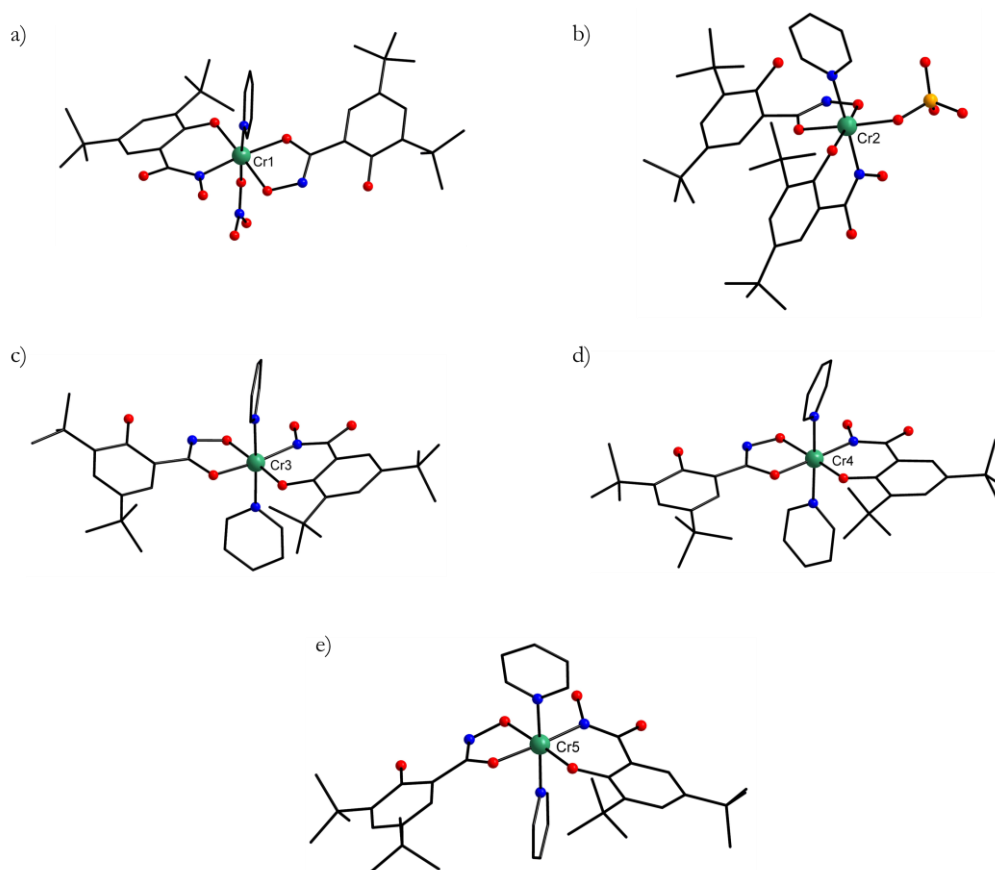


**Figure 4.45.** Schematic representation of the different coordination environments of a) Cr1, b) Cr2, c) Cr3, d) Cr4, e) Cr5. Uncoordinated solvent molecules and hydrogen atoms are omitted for clarity. Color code: dysprosium(III) yellow, chromium(III) ions green, oxygen red, nitrogen blue, sulfur orange, carbon black.

Continuous Shape values given in Table 4.22 are very similar to each other and confirm an almost ideal octahedral symmetry for all chromium(III) ring metal ions.

**Table 4.22.** Calculated deviations from ideal polyhedra (octahedron  $O_h$ ) for ring metal ions *via* Continuous Shape measurements of  $[Cr_5Dy]$ .

ion	Cr1	Cr2	Cr3	Cr4	Cr5
CShM	0.430	0.388	0.366	0.383	0.429

The encapsulated dysprosium(III) ion is seven-coordinate and bound to the five oxygen donor atoms from the ligand. Two additional oxygen atoms are coordinated by bridging Cr1 *via* a nitrate and Cr2 *via* a sulfate ion to Dy1. The cavity of the [15-MC-5] enables a coordination geometry of  $D_{5h}$  symmetry for the central dysprosium(III) ion. This geometry may suppress the relaxation process of quantum tunneling of the magnetization (QTM) (see Chapter 1.4).<sup>[85,86]</sup> Preventing the QTM phenomenon is essential for increasing both the effective energy barrier  $U_{\text{eff}}$  and the blocking temperature  $T_B$ , thereby improving the SMM behavior. The pentagonal bipyramid is obtained as the  $D_{5h}$  coordination environment of the Dysprosium(III) ion. Continuous Shape Measurements confirm the lowest deviation from the ideal geometry of this pentagonal bipyramid with  $D_{5h}$  symmetry (Table 4.23).

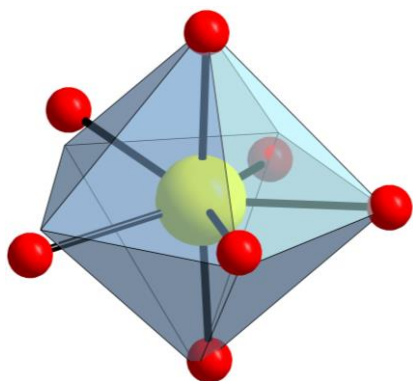


**Figure 4.46.** Schematic representation of the ideal coordination polyhedron (grey) of the Dy1 of  $[\text{Cr}_5\text{Dy}]$  for pentagonal bipyramidal symmetry. Color code of atoms: oxygen red, dysprosium(III) ion yellow.

**Table 4.23.** Calculated deviations from ideal polyhedra for guest ion Dy1 *via* Continuous Shape Measurements.

Polyhedra	CShM
Heptagon $D_{7h}$	33.462
Hexagonal pyramid $C_{6v}$	21.816
<b>Pentagonal bipyramid <math>D_{5h}</math></b>	<b>1.735</b>
Capped octahedron $C_{3v}$	4.011
Capped trigonal prism $C_{2v}$	3.114
Johnson pentagonal bipyramid J13 $D_{5h}$	4.519
Johnson elongated triangular pyramid J7 $C_{3v}$	20.933

The average torsion angle of the chromium(III) ring ions within the repeating unit  $169^\circ$  (Table 4.25) supports the larger cavity size compared to the [9-MC-3] metallacrown  $(\text{bu})_2\text{-}[\text{Cr}_3\text{Cr}]$  with an average torsion angle of  $156^\circ$  (Table 4.12).

**Table 4.24.** Selected bond lengths of each chromium(III) ring metal ions Cr1-Cr5 and the guest ion Dy1 of  $[\text{Cr}_5\text{Dy}]$ .

ion	Cr1	Cr2	Cr3
bond length /Å	O1 1.911(5)	O2 1.979(5)	O5 1.925(5)
	O14 1.957(5)	O3 1.970(5)	O6 1.947(5)
	O15 1.965(5)	O4 1.901(5)	O7 1.890(5)
	O16 2.000(5)	O18 1.997(5)	N3 1.996(6)
	N1 1.963(6)	N2 1.996(6)	N8 2.105(7)
	N6 2.091(6)	N7 2.140(6)	N9 2.083(7)
ion	Cr4	Cr5	Dy1
bond length /Å	O8 1.933(5)	O11 1.956(5)	O3 2.352(5)
	O9 1.978(5)	O12 1.994(5)	O6 2.356(5)
	O10 1.878(5)	O13 1.895(5)	O9 2.387(4)
	N4 1.978(6)	N5 1.984(6)	O12 2.403(5)
	N10 2.097(7)	N12 2.096(7)	O15 2.345(5)
	N11 2.095(7)	N13 2.097(6)	O17 2.255(6)
			O19 2.226(5)
			O1 1.911(5)

**Table 4. 25.** Selected bond angles and torsion angles of **[Cr<sub>5</sub>Dy]**.

bond angles		torsion angles	
Cr1-O15-Dy1	115.0(2)°	Cr2-O3-N1-Cr1	158.9(2)°
Cr2-O3-Dy1	123.3(2)°	Cr3-O6-N2-Cr2	179.9(3)°
Cr3-O6-Dy1	124.2(2)°	Cr4-O9-N3-Cr3	171.3(3)°
Cr4-O9-Dy1	122.6(2)°	Cr5-O12-N4-Cr4	164.2(3)°
Cr5-O12-Dy1	123.3(2)°	Cr1-O15-N5-Cr5	172.4(3)°
average Cr <sub>ring</sub> -O-Dy <sub>guest</sub>	121.7°	average Cr <sub>ring</sub> -O-N-Cr <sub>ring</sub>	169.3°

The obtained sulfate bridge in the MC is well-known in chromic wheels where chromium(III) ions are connected *via* this co-ligand.<sup>[87]</sup> In the research field of MCs, sulfate salts of the starting substances are commonly used.<sup>[88]</sup> Then, sulfate ions act as counter ion, coordinate only the guest ion<sup>[89,90]</sup> or provide a linkage between two MCs<sup>[91,7]</sup>.

The first MC that was reported with a [15-MC-5] cavity was a manganese(II/III) compound with salicylhydroxamic acid as ligand by Pecoraro in 1994.<sup>[82]</sup> A very similar bent structure with five manganese(III) ring metal ions and seven-coordinated manganese(II) guest ion was obtained. Compared to **[Cr<sub>5</sub>Dy]**, three ligands of the manganese(III) ring metal ions are coordinated in *cis*- and two in planar *trans*-configuration. This structural motif containing manganese ions are highly investigated afterwards concerning their configurations and bioactivity.<sup>[84,92,93]</sup> Additionally, the encapsulation of gadolinium(III) and dysprosium(III) was achieved in a [15-MC-5] metallocrown by the complex {Ln<sup>III</sup>[15-MC<sub>Fe(III)N(shi)-5</sub>](OAc)<sub>2</sub>Cl} with salicylhydroxamic acid as ligand by Lutter and co-workers in 2022.<sup>[94]</sup>

The corresponding, isostructural compound with terbium(III) ions was supposed to be synthesized to investigate changes in anisotropy in this symmetry for the guest ion. Terbium(III) ions offer comparable magnetic properties due to analog oblate electron density with an even greater electronic anisotropy.<sup>[95]</sup> It is important to consider that an axial symmetry is required to form a bistable ground state because a non-Kramers ion is present.<sup>[96]</sup> However, when the analogous MC should be synthesized with terbium(III) nitrate under analog conditions the compound [(Cr<sup>III</sup>)<sub>6</sub>(Tb<sup>III</sup>)<sub>4</sub>(MeOH)<sub>2</sub>(py)<sub>6</sub>((*t*bu)<sub>2</sub>Shi)<sub>4</sub>((*t*bu)<sub>2</sub>ShiH)<sub>2</sub>] · 4 py · 2 MeOH was obtained that is hereafter referred as **[Cr<sub>6</sub>Tb<sub>4</sub>]**. **[Cr<sub>6</sub>Tb<sub>4</sub>]** crystallizes similar to **[Cr<sub>5</sub>Dy]** as brown needles.

#### 4.2.1.2. [Cr<sub>6</sub>Tb<sub>4</sub>] Cluster

Complex [Cr<sub>6</sub>Tb<sub>4</sub>] crystallizes in the monoclinic crystal system in the same monoclinic space group C2/c. The lattice parameters differ from [Cr<sub>5</sub>Dy] and show four instead of eight molecules in the unit cell ( $a = 28.1757(10)$  Å,  $b = 35.6765(9)$  Å,  $c = 26.2075(9)$  Å,  $\alpha = 90^\circ$ ,  $\beta = 93.755(3)^\circ$ ,  $\gamma = 90^\circ$ ). This molecular structure does not show a [15-MC-5] metallacrown structure as shown in Figure 4. 47. In the asymmetric unit, three chromium(III) ions are coordinated by four triply deprotonated 3,5-di-*tert*-butylsalicylhydroxamate ligands like a MC repeating unit. However, a change in the order of the repeating unit at Cr2 and the additional coordination of Tb2 as a ring metal ion, changes the structural composition of the molecule. Tb2 is additionally coordinated by an oxygen donor atom of a water molecule. Four oxygen donor atoms of the 3,5-di-*tert*-butylsalicylhydroxamate ligands coordinate Tb1 similar to a guest ion. The coordination sphere of Tb1 is completed by two bridging 3,5-di-*tert*-butylsalicylhydroxamate ligands to Cr2 and Tb2 respectively as shown in Figure 4. 48. Thus, Tb1 and Tb2 are linked *via* three  $\mu_3$ -oxo bridges with angles of approximately  $100^\circ$  (Table 4. 29). The absence of the bridging nitrate and sulfate co-ligands can be clearly noticed. Additionally, there are neither nitrate nor sulfate ions in the crystal structure.

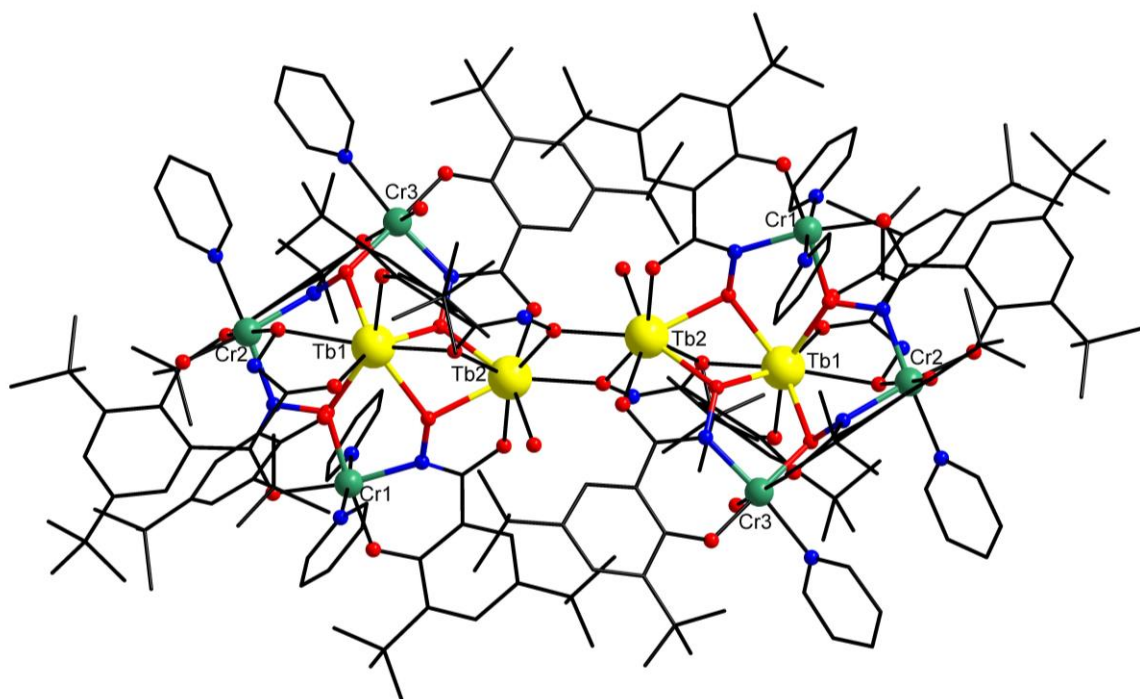


**Figure 4. 47.** Schematic representation of the molecular structure of [Cr<sub>6</sub>Tb<sub>4</sub>] including highlighted repeating unit. Uncoordinated solvent molecules and hydrogen atoms are omitted for clarity. Color code: terbium(III) yellow, chromium(III) ions green, oxygen red, nitrogen blue, carbon black.

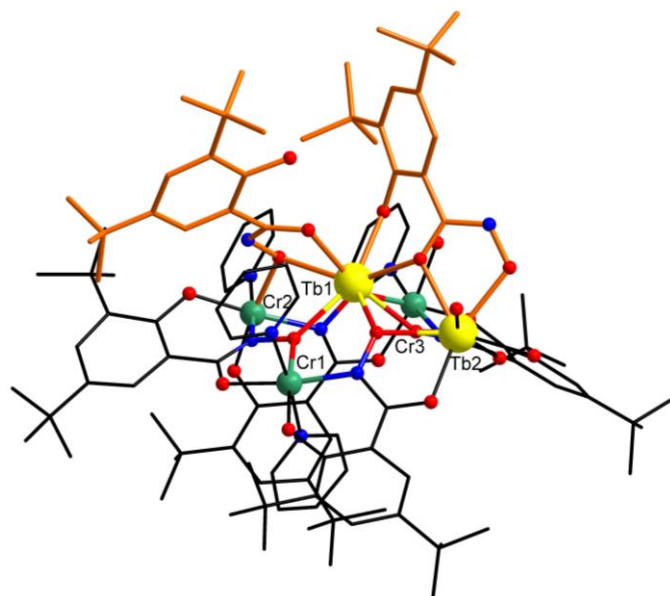


**Figure 4. 48.** Schematic representation of asymmetric unit of  $[\text{Cr}_6\text{Tb}_2]$  with emphasized coordination mode of co-ligand (side view). Hydrogen atoms non-coordinated solvent molecules are omitted for clarity. Color code: chromium(III) ions green, dysprosium(III) ion yellow, oxygen red, nitrogen blue, carbon black.

All chromium(III) ions exhibit an octahedral coordination symmetry with additional pyridine co-ligands. Cr1 is coordinated in a *trans*-configuration while Cr2 and Cr3 are coordinated in a *cis*-propeller configuration.

**Table 4. 26.** Calculated deviations from ideal polyhedra (octahedron  $O_h$ ) for Cr1, Cr2, Cr3 ring metal ions *via* Continuous Shape Measurements of  $[\text{Cr}_6\text{Tb}_2]$ .

ion	Cr1	Cr2	Cr3
CShM	0.537	0.532	0.536

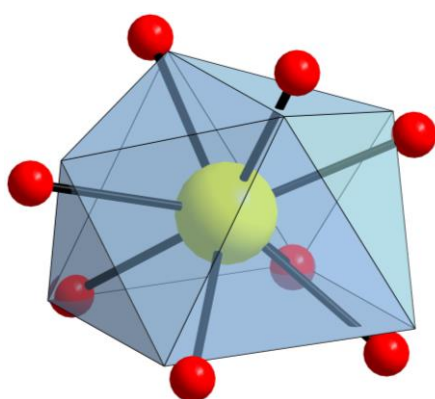


**Figure 4. 49.** Schematic representation of the ideal coordination polyhedron (grey) of the Tb2 of  $[\text{Cr}_6\text{Tb}_4]$  for a pentagonal bipyramidal symmetry. Color code of atoms: oxygen red, terbium(III) ion yellow.

**Table 4. 27.** Calculated deviations from ideal polyhedra for guest ion Tb2 *via* Continuous Shape Measurements.

Polyhedra	CShM
Octagon	33.043
Heptagonal pyramid	21.508
Hexagonal bipyramid	16.514
Cube	14.242
Square antiprism	5.267
Triangular dodecahedron	3.579
Johnson gyrobifastigium J26	13.614
Johnson elongated triangular bipyramid J14	23.801
Biaugmented trigonal prism J50	3.553
<b>Biaugmented trigonal prism</b>	<b>2.846</b>
Snub diphonoid J84	5.205
Triakis tetrahedron	14.878
Elongated trigonal bipyramid	20.443

In contrast to **[Cr<sub>3</sub>Dy]**, Tb1 and Tb2 are coordinated by eight ligands with the small deviation of a biaugmented trigonal prism. The corresponding Shape values and schematical deviation from the ideal geometry are shown in Table 4. 27 and Figure 4. 49. This geometry change is a crucial degradation regarding the axial anisotropy. Therefore, the charge distribution around the two terbium(III) ions seems to be rather homogeneous. Consequently, this is not favorable if SMM behavior is desired for a non-Kramers ion.

Antiferromagnetic exchange interaction between Cr1 and Cr2 as well as Cr2 and Cr3 is expected due an average torsion angle of 165°. This value is in the range between [9-MC-3] metallacrown (e.g. **(t<sub>bu</sub>)<sub>2</sub>-[Cr<sub>3</sub>Cr]**) and [15-MC-5] metallacrown (e.g. **[Cr<sub>3</sub>Dy]**) cavity with antiferromagnetic exchange.

**Table 4. 28.** Selected bond lengths of each chromium(III) ring metal ions Cr1, Cr2, Cr3 and the guest ions Tb1 and Tb2 of **[Cr<sub>6</sub>Tb<sub>4</sub>]**.

ion	Cr1	Cr2	Cr3
bond length /Å	O1 1.916(5)	O4 1.937(5)	O8 1.943(5)
	O5 1.969(5)	O7 1.925(5)	O9 1.976(4)
	O6 1.973(5)	O12 2.004(4)	O13 1.912(5)
	N1 1.978(6)	N2 1.972(6)	O20 2.013(5)
	N7 2.095(7)	N3 2.059(6)	N5 1.963(6)
	N8 2.097(6)	N9 2.128(6)	N10 2.151(7)
ion	Tb1	Tb2	
bond length /Å	O3 2.388(5)	O2 2.274(5)	
	O6 2.399(5)	O3 2.336(5)	
	O9 2.343(5)	O14 2.320(5)	
	O11 2.385(4)	O15 2.347(5)	
	O12 2.486(4)	O17 2.397(5)	
	O15 2.306(4)	O17 2.373(5)	
	O16 2.348(5)	O18 2.380(5)	
	O18 2.356(5)	O19 2.403(5)	

**Table 4. 29.** Selected bond angles and torsion angles of **[Cr<sub>6</sub>Tb<sub>4</sub>]**.

bond angles		torsion angles	
Tb1-O18-Tb2	100.49(19)	Cr1-O6-N2-Cr2	163.3(2)°
Tb1-O15-Tb2	102.97(19)°	Cr3-O9-N3-Cr2	165.8(2)°
Tb2-O3-Tb1	100.84(19)°	Tb1-O3-N1-Cr1	22.4(7)°
Cr1-O6-Tb1	130.3(2)°	Tb1-O6-N2-Cr2	22.4(5)°
Cr2-O12-Tb1	107.24(19)°	Tb1-O15-N5-Cr3	12.0(7)°
Cr3-O9-Tb1	120.8(2)°	Tb2-O3-N1-Cr1	160.7(2)°
		Tb2-O15-N5-Cr3	150.7(3)°

### Evaluation of magnetic data

To further investigate magnetic properties of **[Cr<sub>5</sub>Dy]** magnetic susceptibility measurements were performed with an applied magnetic field of 1000 Oe in the range 2-300 K (Figure 4. 50). The theoretical  $\chi_M T$  product of **[Cr<sub>5</sub>Dy]** should be at 23.55 cm<sup>3</sup> K mol<sup>-1</sup> but the  $\chi_M T$  product reaches a value of 30.5 cm<sup>3</sup> K mol<sup>-1</sup>.

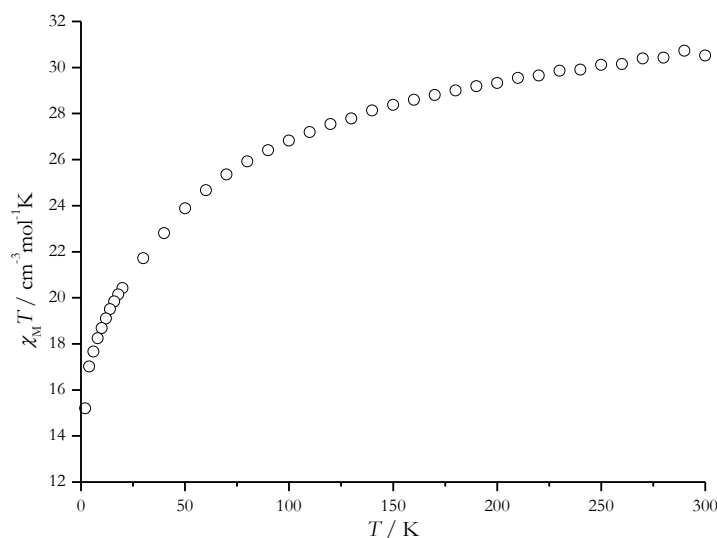


**Figure 4. 50.** Temperature-dependence of magnetic susceptibility of **[Cr<sub>5</sub>Dy]** with possible byproduct **[Cr<sub>6</sub>Dy<sub>4</sub>]** in a temperature range of 2 – 300 K with an external field of 1000 Oe.

Thus, the possible formation of a complex **[Cr<sub>6</sub>Dy<sub>4</sub>]** as byproduct could be the explanation of the susceptibility data: Similar to the structure of **[Cr<sub>6</sub>Tb<sub>4</sub>]**, it is very likely that the cluster **[Cr<sub>6</sub>Dy<sub>4</sub>]** also formed as a byproduct in crystallization of **[Cr<sub>5</sub>Dy]**. **[Cr<sub>6</sub>Tb<sub>4</sub>]** formed under the same conditions as the corresponding **[Cr<sub>5</sub>Dy]**. The incorporation of lanthanide(III) ions in MCs or MC-like clusters, are comparable in their composition of the compounds and are often crystallized isostructural.

However, the theoretical  $\chi_M T$  product of “[Cr<sub>3</sub>Dy<sub>2</sub>]” is expected to be 33.97 cm<sup>3</sup> K mol<sup>-1</sup>. The experimental  $\chi_M T$  susceptibility product is strongly dependent on the molar mass of the compounds. Only the asymmetric unit “[Cr<sub>3</sub>Dy<sub>2</sub>]” of **[Cr<sub>6</sub>Dy<sub>4</sub>]** was included in the calculation of the theoretical value to determine a comparable theoretical value, since the molar masses here are comparable with **[Cr<sub>5</sub>Dy]** ( $M_w(\text{[Cr}_5\text{Dy]}) = 2525 \text{ g/mol}$ ,  $M_w(\text{[Cr}_3\text{Dy}_2]) = 2423 \text{ g/mol}$ ). In order to estimate approximately the ratio of the two compounds using the experimental magnetic susceptibility, the following Equation 21 was solved. The variable  $x$  corresponds to the amount of the biproduct “[Cr<sub>3</sub>Dy<sub>2</sub>]”.

$$\chi_M T_{\text{exp}} \approx (1 - x) \cdot \chi_M T_{\text{theo}}(\text{[Cr}_5\text{Dy]}) + x \cdot \chi_M T_{\text{theo}}(\text{[Cr}_3\text{Dy}_2]) \quad (21)$$

$$30.5 \approx (1 - x) \cdot 23.55 + x \cdot 33.97 \quad (22)$$

$$x \approx 0.67$$

This shows that approximately 2/3 of the measurement susceptibility could be attributed to a potential byproduct [**Cr<sub>6</sub>Dy<sub>4</sub>**]. Simulation of susceptibility data ( $\chi_M T$  product) and magnetization curves is non-trivial and highly computationally demanding due to the large contribution of spin-orbit coupling, including higher orders, and the symmetry of the crystal field, which requires consideration of higher order terms depending on the degree of symmetry. Additional unpaired spins of chromium(III) ions increase the computational complexity even further. Therefore, no simulation of the  $\chi_M T$  product or magnetization data could be performed in this Chapter 4.2.

To avoid the formation of such byproducts less strong bases can be used to achieve more control of the deprotonation process of the ligands. Thus, sodium benzoate was used as a base and co-ligand in the next Chapter 4.2.2.



## 4.2.2. [Cr<sub>4</sub>Ln<sub>2</sub>] Clusters

### 4.2.2.1. [Cr<sub>4</sub>Ln<sub>2</sub>] Clusters including 3,5-di-*tert*-butylsalicylate

It was already shown in [Cr<sub>5</sub>Dy] that a MC with bridging co-ligands between the ring metal to the guest ions can be formed with chromium(III) and dysprosium(III) ions. In this case, nitrate, and sulfate ions, which serve as counterions, were responsible for this coordination. Here, sodium benzoate is used as a base which can also serve as a bridging co-ligand. This approach is comparable with the homometallic structures [Cr<sub>3</sub>Cr] and (t<sub>bu</sub>)<sub>2</sub>-[Cr<sub>3</sub>Cr] in which pivalate ions were used as bridging co-ligands.

Likewise, [12-MC-4] metallocrowns have also been reported with a benzoate bridge between the ring metal ions and the central guest ion. For instance, a family of luminescent MCs including gallium(III) and lanthanide(III) ions were reported by Pecoraro and co-workers.<sup>[97]</sup> The MC {Ln<sup>III</sup>(μ<sub>2</sub>-benzoate)<sub>4</sub>[12-MC<sub>Ga(III)N(shi)-4</sub>]}<sup>-</sup> (Ln = Sm(III) – Yb(III)) contains four benzoate co-ligands that complete (together with the four oxygen donor atoms of the repeating unit) the antiprismatic coordination geometry for several lanthanide(III) ions. Additionally, a [12-MC-4] 3*d*-4*f* metallocrown with the same coordination for the guest ions was reported in 2021 by Zaleski and co-workers ({Ho<sup>III</sup>Na<sup>I</sup>(μ<sub>2</sub>-benzoate)<sub>4</sub>[12-MC<sub>Al(III)N(shi)-4</sub>]}).<sup>[98,99]</sup> Here, all aluminum(III) ring metal ions are octahedrally coordinated. This coordination environment would be ideal for chromium(III) ions too, thus supporting the planned approach of choosing bridging co-ligands.

As the optimization of the purification of the salicylhydroxamic acid derivative (3,5-di-*tert*-butylsalicylhydroxamic acid) turned out to be challenging, preliminary reaction tests were carried out in the meantime with a not purified batch. In addition to the desired ligand, it contained about 30% 3,5-di-*tert*-butylsalicylic acid. Therefore, the incorporation of this corresponding salicylic acid was observed. This conclusion was also drawn in the dissertation of Lara Völker from Rentschler research group.<sup>[100]</sup> The reaction of the crude product of 3,5-di-*tert*-butylsalicylhydroxamic acid, dysprosium(III)nitrate, chromium(III) nitrate nonahydrate and sodium benzoate under solvothermal conditions led to the complex with the general formula [Cr<sup>III</sup><sub>4</sub>Dy<sup>III</sup><sub>2</sub>(μ<sub>2</sub>-OOCPh)<sub>2</sub>(MeOH)<sub>2</sub>(py)<sub>6</sub>((t<sub>bu</sub>)<sub>2</sub>Shi)<sub>4</sub>((t<sub>bu</sub>)<sub>2</sub>Sal)<sub>2</sub>] after slow evaporation of the solvent. This compound will be structurally described, as it could not be reproduced in measurable amounts during this work for further studies. [Cr<sup>III</sup><sub>4</sub>Dy<sup>III</sup><sub>2</sub>(μ<sub>2</sub>-OOCPh)<sub>2</sub>(MeOH)<sub>2</sub>(py)<sub>6</sub>((t<sub>bu</sub>)<sub>2</sub>Shi)<sub>4</sub>((t<sub>bu</sub>)<sub>2</sub>Sal)<sub>2</sub>] will be referred as **Sal-[Cr<sub>4</sub>Dy<sub>2</sub>]** shows some similarities to [Cr<sub>6</sub>Tb<sub>4</sub>] (see Figure 4. 51). Four chromium(III) ions are coordinated by four triply deprotonated 3,5-di-*tert*-butylsalicylhydroxamate ligands. Cr1 is chelated by two 3,5-di-*tert*-butylsalicylhydroxamates in a *trans*-configuration. Two additional pyridine co-ligands complete the coordination sphere. Cr2 is coordinated by one 3,5-di-*tert*-butylsalicylhydroxamate, one benzoate and a deprotonated 3,5-di-*tert*-butylsalicylic acid as well as a pyridine co-ligand. The chelating ligands benzoate and 3,5-di-*tert*-butylsalicylate bridge Cr2 to Dy1. Therefore, one oxygen donor atom of the carboxylate group of 3,5-di-*tert*-butylsalicylate is also bound to the Cr2. Dy1 is additionally coordinated by an oxygen donor atom of a methanol molecule and four oxygen donor atoms of the 3,5-di-*tert*-butylsalicylhydroxamate ligand. This leads to an eightfold coordination. The two dysprosium(III) ions are linked with each other *via* two μ<sub>3</sub>-oxo bridges of the iminophenolate moiety of two 3,5-di-*tert*-butylsalicylhydroxamates.

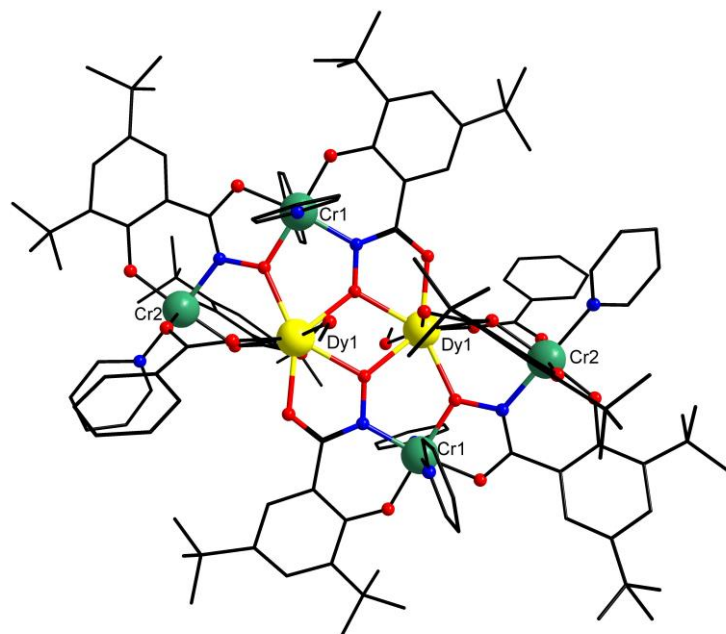


**Figure 4. 51.** Schematic representation of the molecular structure of **Sal-[Cr<sub>4</sub>Dy<sub>2</sub>]** including highlighted repeating unit. Uncoordinated solvent molecules and hydrogen atoms are omitted for clarity. Color code: terbium(III) yellow, chromium(III) ions green, oxygen red, nitrogen blue, carbon black.

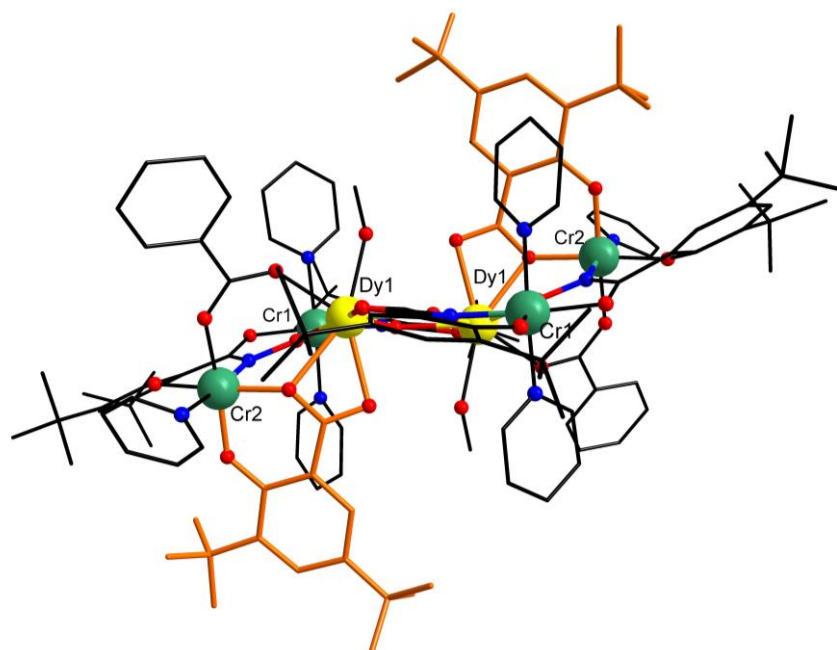


**Figure 4. 52.** Schematic representation of the molecular structure of **Sal-[Cr<sub>4</sub>Dy<sub>2</sub>]** with emphasized coordination mode of deprotonated 3,5-di-*tert*-butylsalicylic acid (orange, side view) Hydrogen atoms non-coordinated solvent molecules are omitted for clarity. Color code: chromium(III) ions green, dysprosium(III) ion yellow, hydrogen atom white, oxygen red, nitrogen blue, carbon black.

#### 4.2.2.2. *In-situ* formation of 3,5-di-*tert*-butyl-salicylate (Sal-[Cr<sub>4</sub>Tb<sub>2</sub>])

After successful optimization of the purification of 3,5-di-*tert*-butyl-salicylhydroxamic acid, the ligand was again reacted with various chromium(III) salts and lanthanide(III) nitrate (see Chapter 6.2.2.3.). The reaction of terbium(III) nitrate, chromium(III) nitrate, 3,5-di-*tert*-butyl-salicylhydroxamic acid and sodium benzoate in a methanol/pyridine suspension yielded the structure with the molecular formula (Hpy)<sub>2</sub>[Cr<sup>III</sup><sub>4</sub>Dy<sup>III</sup><sub>2</sub>( $\mu$ -OOCPh)<sub>0.5</sub>(py)<sub>6</sub>((*tert*-bu)<sub>2</sub>Shi)<sub>4</sub>((*tert*-bu)<sub>2</sub>ShiH)<sub>2</sub>(*tert*-bu)<sub>2</sub>SalH)<sub>3.5</sub>] · 3 MeOH shown in Figure 4. 53 (Sal-[Cr<sub>4</sub>Tb<sub>2</sub>]). However, the *in-situ* formation of 3,5-di-*tert*-butyl-salicylate was seen again. The obtained structure is very similar to the previously discussed complex Sal-[Cr<sub>4</sub>Dy<sub>2</sub>]. There are four chromium(III) ions and two lanthanide(III) ions similar coordinated by the ligand 3,5-di-*tert*-butyl salicylhydroxamic acid. In this case, however, the coordination mode of the bridging co-ligands differs from Sal-[Cr<sub>4</sub>Dy<sub>2</sub>] from the coordination mode shown in Figure 4. 52. Sal-[Cr<sub>4</sub>Tb<sub>2</sub>] shows a direct connection of the terbium(III) ions *via* two ligands in  $\mu$ <sub>2</sub>-coordination mode.

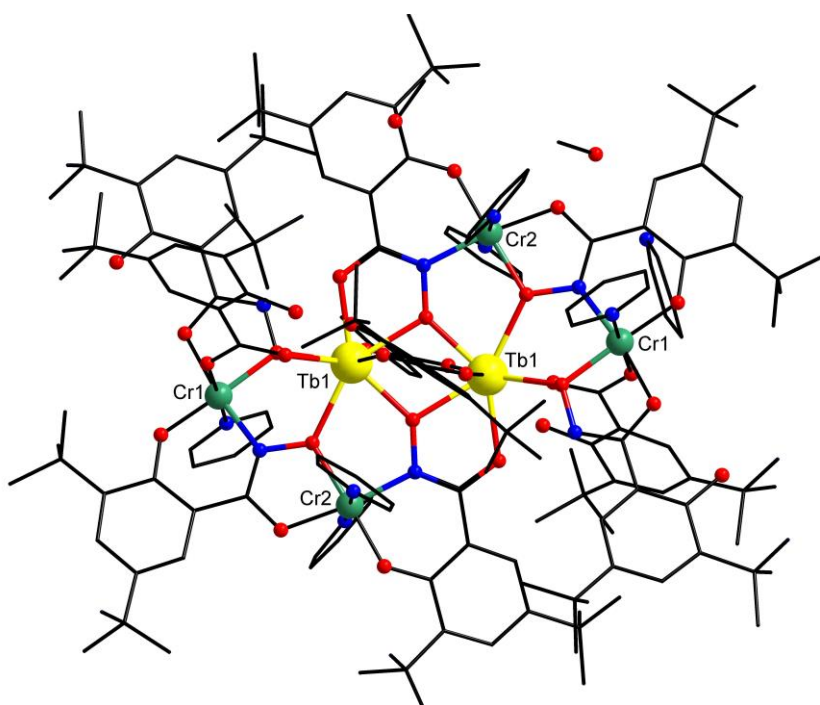


**Figure 4. 53.** Schematic representation of the molecular structure of Sal-[Cr<sub>4</sub>Tb<sub>2</sub>] with emphasized repetition unit (top view). Hydrogen atoms are omitted for clarity. Color code: chromium(III) ions green, terbium(III) ion yellow, oxygen red, nitrogen blue, carbon black.

The coordination of a bridging benzoate co-ligand and a 3,5-di-*tert*-butylsalicylate occurs above the plane of the repeating unit as illustrated in Figure 4. 54. The benzoate ligand is disordered with another 3,5-di-*tert*-butylsalicylate (occupancies 0.5:0.5). The *in-situ* formation of 3,5-di-*tert*-butylsalicylate could not be prevented but in this complex, the acid is bridging the two terbium(III) ions in a different coordination mode instead. Additionally, Cr1 and Tb1 are bridged *via* another 3,5-di-*tert*-butylsalicylic acid (Figure 4. 55).

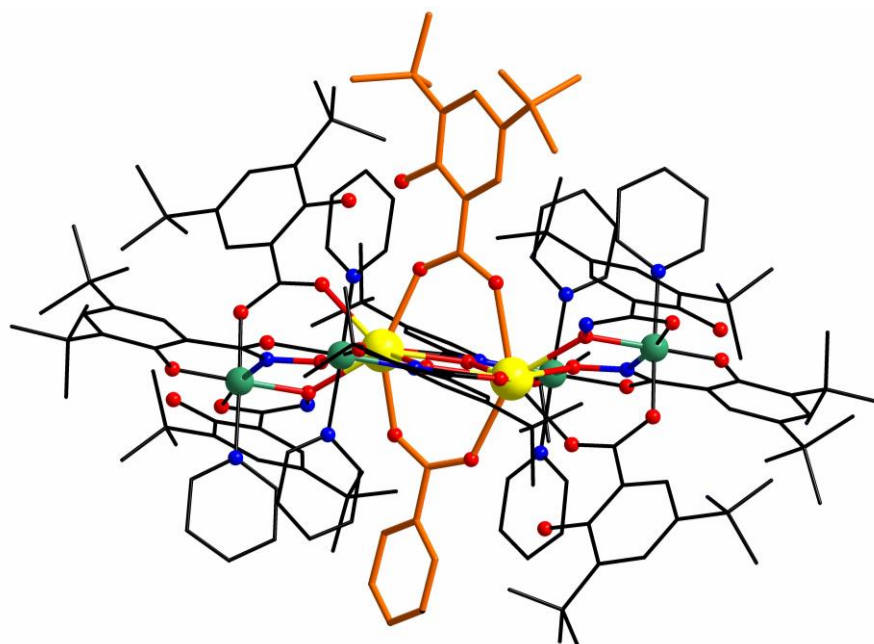


**Figure 4. 54.** Schematic representation of the molecular structure of  $\text{Sal-}[\text{Cr}_4\text{Tb}_2]$  with emphasized bridging between terbium(III) ions *via* benzoate and 3,5-di-*tert*-butylsalicylic acid. These ions are disordered with each other in the crystal structure.

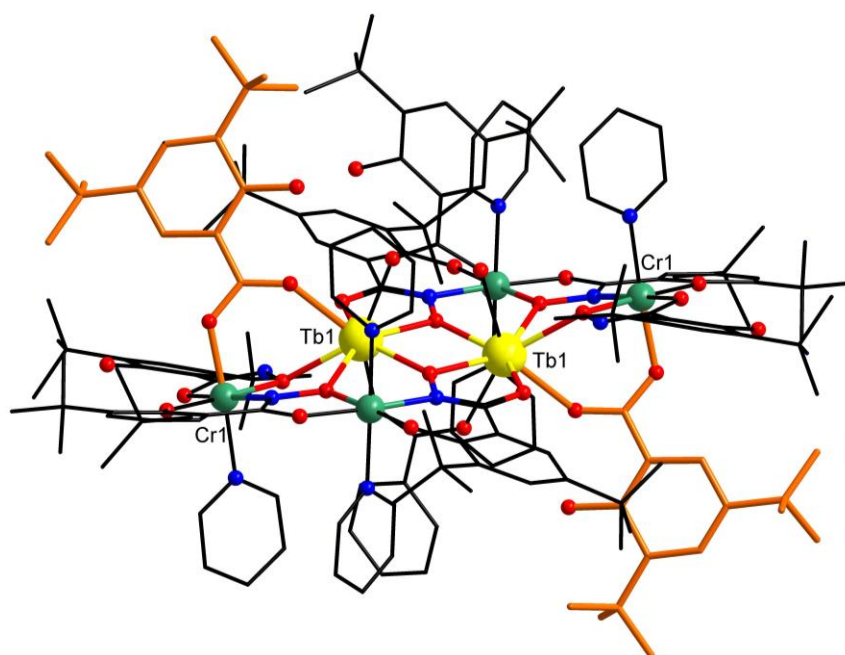


**Figure 4. 55.** Schematic representation of the molecular structure of  $\text{Sal-}[\text{Cr}_4\text{Tb}_2]$  with emphasized coordination mode of bridging 3,5-di-*tert*-butylsalicylate (orange, side view) Hydrogen atoms non-coordinated solvent molecules are omitted for clarity. Color code: chromium(III) ions green, terbium(III) ion yellow, hydrogen atom white, oxygen red, nitrogen blue, carbon black.

This *in-situ* formation of the corresponding 3,5-di-*tert*-butylsalicylate could not be avoided. The variable coordination possibilities of this ligand that are already evident in the two obtained structures makes the targeted synthesis *via* self-assembly processes very challenging. It was therefore switched to unsubstituted salicylhydroxamic acid as preferred ligand to investigate whether the corresponding acid is always formed under these reaction conditions. These results will be described in the next Chapter 4.2.2.2.

#### 4.2.2.3. [Cr<sub>4</sub>Dy<sub>2</sub>] with salicylhydroxamates

Salicylhydroxamic acid, dysprosium(III)nitrate, chromium(III) nitrate nonahydrate and sodium benzoate in a methanol/pyridine solution (15:2 v/v) resulted after solvothermal synthesis and slow evaporation of the solvent in (Hpy)<sub>2</sub>[Cr<sup>III</sup><sub>4</sub>Dy<sup>III</sup><sub>2</sub>(μ<sub>2</sub>-OOCPh)<sub>4</sub>(py)<sub>6</sub>(Shi<sup>3-</sup>)<sub>4</sub>((ShiH<sup>2-</sup>)<sub>2</sub>)] · 2 MeOH. The same structure was also obtained when chromium(III) acetylacetonate was used instead of chromium(III) nitrate as starting material. Thus, neither nitrate ions nor acetylacetonate was incorporated in the structure or as counter ions. Two pyridinium ions balance the negative charge. The crystallographic data are listed in Table S 9. [Cr<sub>4</sub>Dy<sub>2</sub>] crystallizes in the monoclinic crystal system in the space group C2/c. The lattice parameters are  $a = 35.008(2)$  Å,  $b = 19.3804(7)$  Å,  $c = 17.9218(8)$  Å,  $\alpha = 90^\circ$ ,  $\beta = 92.106(4)^\circ$ ,  $\gamma = 90^\circ$ . No decomposition of salicylhydroxamic acid was observed. In [Cr<sub>4</sub>Dy<sub>2</sub>] two of the six salicylhydroxamate ligands are doubly deprotonated, while the other four thus are triply deprotonated and coordinate equal to **Sal**-[Cr<sub>4</sub>Dy<sub>2</sub>] and **Sal**-[Cr<sub>4</sub>Tb<sub>2</sub>]. The additional two coordination sites are occupied by two pyridine co-ligands for Cr2. In the case of Cr1, only one coordination site is occupied by the pyridine co-ligand while the sixth coordination site is occupied by benzoate. These benzoates are coordinated as bridging co-ligands and connect Cr1 and Dy1 as well as Dy1 and Dy1 as shown in Figure 4. 57. One reason that no classical MC was formed is due to this protonated position, which does not allow any further coordination. Thus, no conventional [Cr-N-O] repeating unit can form within a closed ring structure. More addition of base or subsequent deprotonation did not lead to any change in the composition or to any different crystals for X-Ray analysis. However, Cr1 and Cr2 are chelated by the triply and doubly deprotonated salicylhydroxamates ligands creating a five-membered ring *via* the iminophenolate moiety and a six-membered ring *via* the hydroxamate group.

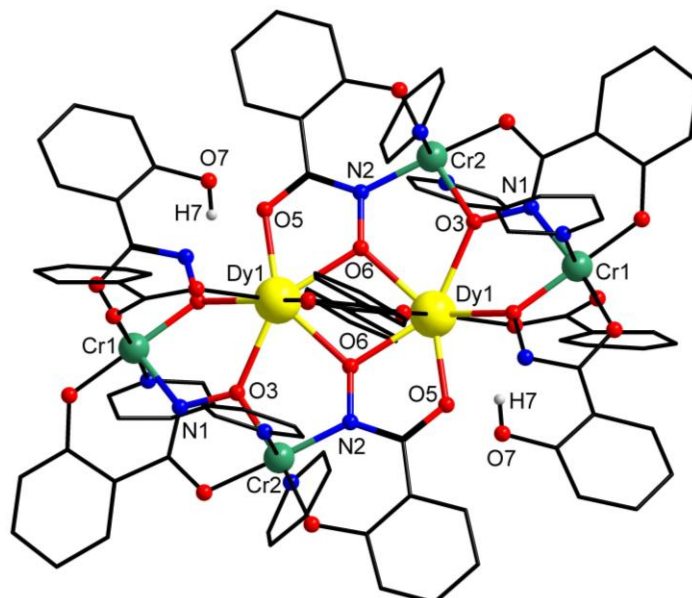


**Figure 4. 56.** Schematic representation of the molecular structure of [Cr<sub>4</sub>Dy<sub>2</sub>] with emphasized repetition unit (top view). Hydrogen atoms non-coordinated solvent molecules are omitted for clarity (except of H7). Color code: chromium(III) ions green, dysprosium(III) ion yellow, hydrogen atom white, oxygen red, nitrogen blue, carbon black.

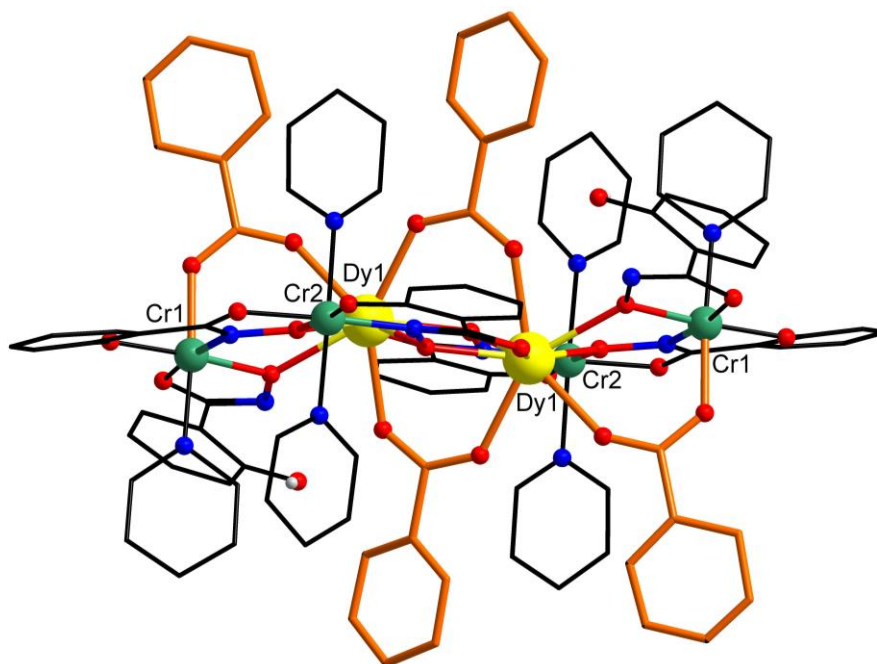


**Figure 4. 57.** Schematic representation of the molecular structure of  $[\text{Cr}_4\text{Dy}_2]$  with emphasized bridging coordination mode of benzoate co-ligand (orange, side view). Hydrogen atoms non-coordinated solvent molecules are omitted for clarity (except of H7). Color code: chromium(III) ions green, dysprosium(III) ion yellow, hydrogen atom white, oxygen red, nitrogen blue, carbon black.

Cr1 and Cr2 show different coordination environments. While Cr1 is coordinated by two nitrogen and four oxygen donor atoms, Cr2 has a coordination environment that include three oxygen and three nitrogen donor atoms. Dy1 is coordinated by eight ligands and shows a distorted triangular dodecahedron polyeder (see Figure 4. 58, Table 4. 30).

The protonated pyridinium ion interacts *via* a hydrogen bond between H7A and O7 (1.8 Å) and an uncoordinated methanol molecule *via* H012 and O4 (2.14 Å)(see Figure 4. 59). Furthermore, an intramolecular hydrogen bond between H7 and N3 (2.12 Å) is observed. Dy1 and Dy1 are separated by a distance of 12.10 Å between two molecules and 9.18 Å separate two Cr2 ions of two molecules.

$[\text{Cr}_4\text{Dy}_2]$  could be reproduced and even the usage of different chromium(III) ion salts led to the same compound with a reliable structural composition. This is a major advantage compared to complexes  $\text{Sal-}[\text{Cr}_4\text{Dy}_2]$  and  $\text{Sal-}[\text{Cr}_4\text{Tb}_2]$ .

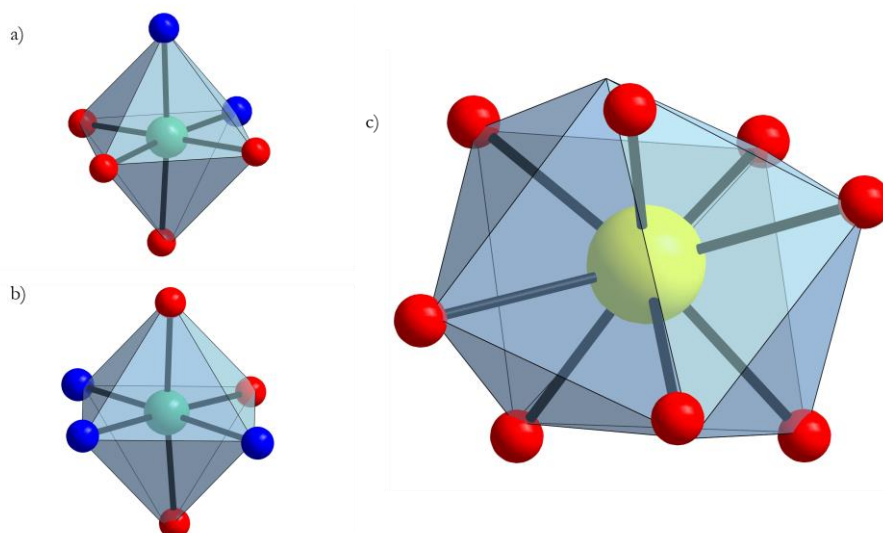


**Figure 4. 58.** Schematic representation of the different coordination environments of a) Cr1, b) Cr2, c) Dy1. Uncoordinated solvent molecules and hydrogen atoms are omitted for clarity. Color code: dysprosium(III) yellow, chromium(III) ions green, oxygen red, nitrogen blue, carbon black.

**Table 4. 30.** Calculated deviations from ideal polyhedra of metal ions *via* Continuous Shape Measurements of  $[\text{Cr}_4\text{Dy}_2]$ .

ion	Cr1	Cr2	ion	Dy1
<b>CShM</b>			<b>CShM</b>	
Octahedron $O_h$	0.321	0.359	Triangular dodecahedron $D_{2d}$	0.767

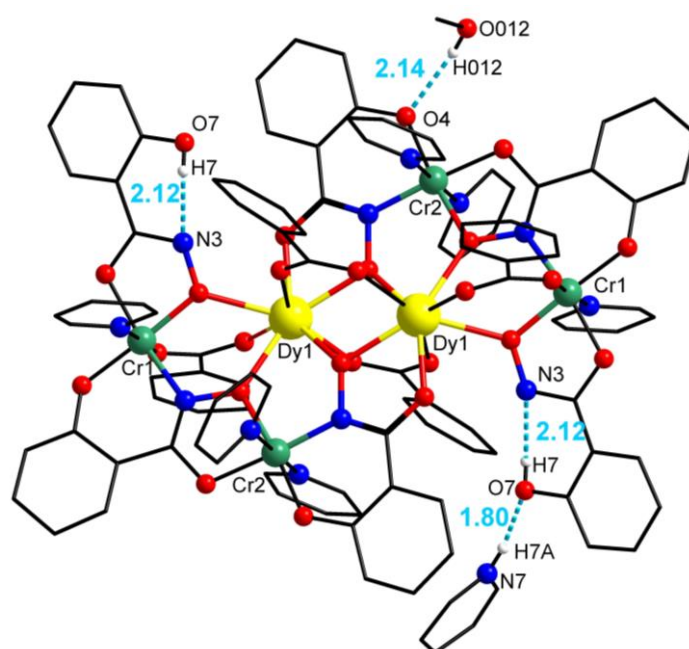


**Figure 4. 59.** Schematic representation of the molecular structure of  $[\text{Cr}_4\text{Dy}_2]$  in unit cell with highlighted intermolecular interactions. Cr1-Cr2 distance 8.67 Å (orange); hydrogen bonds of H7A and H012. Hydrogen atoms are omitted for clarity except of H7A and H012. Color code: chromium(III) ions green, chloride anion light green, oxygen red, nitrogen blue, hydrogen white, carbon black.

**Table 4. 31.** Selected bond lengths of Cr1 and Cr2 as well as Dy1 of [Cr<sub>4</sub>Dy<sub>2</sub>].

ion	Cr1	Cr2	Dy1
bond length /Å	O1 1.924(16)	O2 1.976(15)	O3 2.419(15)
	O8 1.984(15)	O3 1.960(15)	O5 2.246(17)
	O9 1.911(16)	O4 1.888(14)	O6 2.343(13)
	O10 1.996(14)	N2 1.905(14)	O6 2.351(14)
	N1 1.98(2)	N5 2.122(15)	O9 2.461(16)
	N4 2.02(2)	N6 2.106(18)	O11 2.365(13)
			O12 2.360(13)
		O13 2.387(14)	

**Table 4. 32.** Selected bond angles and torsion angles of [Cr<sub>4</sub>Dy<sub>2</sub>].

bond angles		torsion angles	
Cr1-O9-Dy1	123.0(7)°	Cr2-O3-N1-Cr1	173.6(6)°
Cr2-O3-Dy1	120.1(6)°	Dy1-O6-N2-Cr2	177.7(5)°
Dy1-O6-Dy1	105.5(6)°		
average Cr <sub>ring</sub> -O-Dy <sub>guest</sub>	121.6°	average Cr <sub>ring</sub> -O-N-Cr <sub>ring</sub>	175.7°

The structure resembles a so-called "collapsed" MC observed in 2012 by Fritsky and coworkers during the formation of copper(II) MCs.<sup>[101]</sup> In this case, picoline hydroxamic acid was used as ligand and resulted in a collapse of the metallamacrocyclic cavity while forming tetranuclear compounds with copper(II) ions. They attribute this structure to degradation of copper(II) pentanuclear [12-MC-4] metallacrowns into the collapsed complex.

Pecoraro, Mallah and co-workers showed in 2015 the magnetic behavior of several [Ga(III)<sub>4</sub>Ln(III)<sub>2</sub>] (Ln = Gd(III), Tb(III), Dy(III), Er(III), Y(III), Y(III)<sub>0.9</sub>Dy(III)<sub>0.1</sub>) clusters.<sup>[80]</sup> In general, two lanthanide(III) and four gallium(III) ions are coordinated in a comparable manner. No benzoate was used as base and bridging co-ligand. Thus, the dysprosium(III) ions are solely bridged *via* the oxygen donor atoms of salicylhydroxamic acid. The additional bridge to a gallium(III) ion is created by a doubly deprotonated salicylhydroxamic acid. Antiferromagnetic exchange coupling leading to a diamagnetic ground state was detected. Single crystal measurements below 2 K (including 3 using a micro-squid arrays) lead to a magnetic hysteresis cycle at zero field (except for Er(III)).<sup>[80]</sup>

Additionally, a butterfly complex [Cr(III)<sub>2</sub>Dy(III)<sub>2</sub>] was reported with an effective energy barrier  $U_{\text{eff}} = 77$  K (54 cm<sup>-1</sup>) by Murray and co-workers highlights the importance of magnetic exchange within multinuclear lanthanide(III)-based SMMs.<sup>[102]</sup> Here,  $\mu_3$ -oxo and  $\mu_2$ -benzoate bridged chromium(III) and dysprosium(III) ions are present. In contrast to the diamagnetic, low spin analogous cobalt(III) complex [Co(III)<sub>2</sub>Dy(III)<sub>2</sub>] a magnetic hysteresis with large coercive magnetic fields were observed.<sup>[103]</sup> This is due to antiferromagnetic exchange interaction between the chromium(III) and dysprosium(III) ions that reduced QTM. These results were supported by theoretical calculation of the relaxation pathways of magnetization.



### Evaluation of magnetic data

The magnetic properties of  $[\text{Cr}_4\text{Dy}_2]$  were investigated and magnetic susceptibility measurements were performed with an applied magnetic field of 100 Oe in a temperature range of 2-300 K (Figure 4. 60).

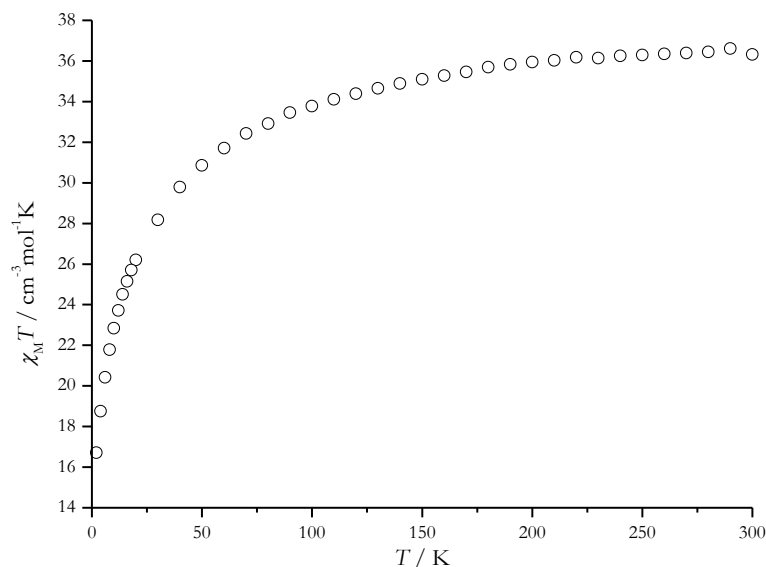


**Figure 4. 60.** Temperature-dependence of magnetic susceptibility of  $[\text{Cr}_4\text{Dy}_2]$  in a temperature range of 2 - 300 K with an external field of 1000 Oe.

The theoretical value of the  $\chi_m T$  product of  $35.84 \text{ cm}^3 \text{ K mol}^{-1}$  can be calculated according to Equation 19. Each dysprosium contributes a value of  $14.17 \text{ cm}^3 \text{ K mol}^{-1}$  and each chromium(III) ion contributes a value of  $1.875 \text{ cm}^3 \text{ K mol}^{-1}$  to the  $\chi_m T$  product of  $[\text{Cr}_4\text{Dy}_2]$ . No out-of-phase signal as observed for the alternating current measurements. These lack of the detection of the slow relaxation of magnetization can be attributed to the coordination environment of Dy1. The triangular dodecahedron does not suppress QTM and is not creating an easy axis for an orientation of the anisotropy.<sup>[81]</sup> However, an appropriate ligand design is crucial to create a preferably easy axis orientation of the magnetization to enhance the SMM performance.

Incomplete deprotonation of salicylhydroxamic acid and the bridging benzoate co-ligand between dysprosium(III) ions prevented the formation of a metallacrown with [12-MC-4] cavity. Evidently, the base strength of sodium benzoate is not sufficient to ensure complete deprotonation of the ligand. Only a completely deprotonated ligand can lead to the formation a MC *via* the iminophenolate moiety which will create a five-membered chelate ring. Therefore, a non-bridging stronger base is used in the next Chapter 4.2.3.

### 4.2.3. [12-MC-4] metallacrown with a ligand bridge

Based on the results of the  $[\text{Cr}_4\text{Dy}_2]$  clusters, a different strategy was chosen for synthesizing MCs with lanthanide(III) and chromium(III) ions. Here, sodium benzoate was omitted as base and bridging co-ligand. Excess of salicylhydroxamic acid was utilized to saturate the coordination sphere of the central guest ion, which can coordinate in mono-, bi- or tridentate fashion. Pyridine was used as a linear coordinating co-ligand to complete the octahedral geometry of the chromium(III) ions.

The reaction of an excess of salicylhydroxamic acid with dysprosium(III) nitrate, chromium(III) potassium sulfate, and triethylamine in a methanol/pyridine solution (15:2 v/v) yielded another lanthanide-chromium MC  $\{\text{Dy}^{\text{III}}(\mu_2\text{-}\eta^3\text{-ShiH}_2)_2[12\text{-MC}_{\text{Cr}(\text{III})\text{N}(\text{Shi})_4\text{-}4]}(\text{MeOH})(\text{py})_4(\text{MeO})\} \cdot \text{H}_2\text{O} \cdot \text{MeOH} \cdot \text{py}$  ( $[\text{Cr}_4\text{Dy}]$ ).  $[\text{Cr}_4\text{Dy}]$  crystallizes in the monoclinic space group  $\text{P}2_1/\text{n}$  with four molecules per unit cell. The cell dimensions are  $a = 15.2611(6)$ ,  $b = 22.2129(6)$ ,  $c = 22.9307(9)$ , and  $\alpha = 90^\circ$ ,  $\beta = 101.387^\circ(3)$ ,  $\gamma = 90^\circ$ . Remarkably, this molecular structure does not contain any additional bridging co-ligands, but two single deprotonated salicylhydroxamic acid molecules complete the coordination sphere of the lanthanide(III) ion instead (see Figure 4. 61). The nitrogen of the hydroxamic unit is protonated. There are neither nitrate nor sulfate ions in the crystal structure. All four salicylhydroxamate ligand molecules are fully deprotonated forming a [12-MC-4] structure with four chromium(III) ions and the characteristic [Cr-N-O] repeating unit. A dysprosium(III) ion acts as the guest ion and is coordinated by four oxygen donor atoms from the repeating unit and two additional doubly deprotonated salicylhydroxamate co-ligands in a  $\mu_2\text{-}\eta^3$ -mode.

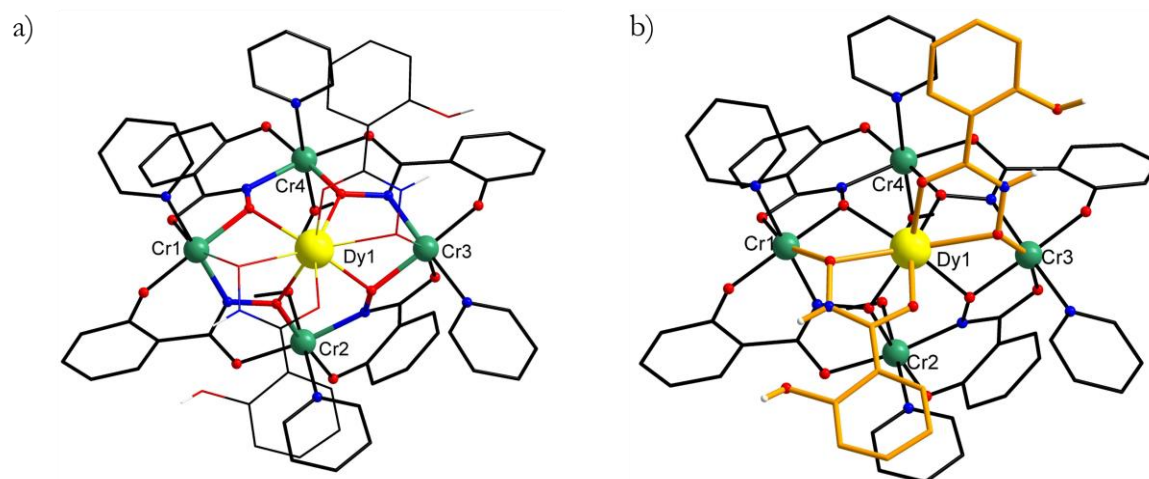


**Figure 4. 61.** Schematic representation of the molecular structure of  $\{\text{Dy}^{\text{III}}(\mu_2\text{-}\eta^3\text{-ShiH}_2)_2[12\text{-MC}_{\text{Cr}(\text{III})\text{N}(\text{Shi})_4\text{-}4]}(\text{MeOH})(\text{py})_4(\text{MeO})\} \cdot \text{H}_2\text{O} \cdot \text{MeOH} \cdot \text{py}$ ; a) with emphasized repetition unit (top view); b) with emphasized  $\mu_2\text{-}\eta^3$ -coordination mode of co-ligand (top view). Hydrogen atoms non-coordinated solvent molecules are omitted for clarity (except of  $\text{H}_2\text{O}$ ). Color code: chromium(III) ions green, dysprosium(III) ion yellow, hydrogen white, oxygen red, nitrogen blue, carbon black.

All chromium(III) ions are octahedrally coordinated and the chelating salicylhydroxamate ligands coordinate in different configurations (see Figure 4. 62, *cis*- and *trans*-configuration). For all four chromium(III) ions, this coordination leads to a five-membered chelate ring *via* the iminophenolate moiety and a six-membered

chelate ring *via* the hydroxamate group. The coordination sphere of ring metal ions Cr1 and Cr3 is accomplished by a *cis*-propeller configuration of the two salicylhydroxamate ligands as well as a pyridine co-ligand and a linear coordinated doubly deprotonated salicylhydroxamic acid co-ligand. In contrast, for Cr2 and Cr4 the ligands are oriented planar in *trans*-position to each other. Here a pyridine and a methanol (Cr4) or methanolate (Cr2) ligand complete the coordination sphere.

A planar [12-MC-4] metallacrown did not form due to the *cis*-propeller configuration of two out of four salicylhydroxamate ligands that coordinate the chromium(III) ring metal ions. Particularly in the side view, the inwardly bent structure of the MC is demonstrated (Figure 4. 64 a). The nearly perfect octahedral coordination of the ring metal ions is retained.

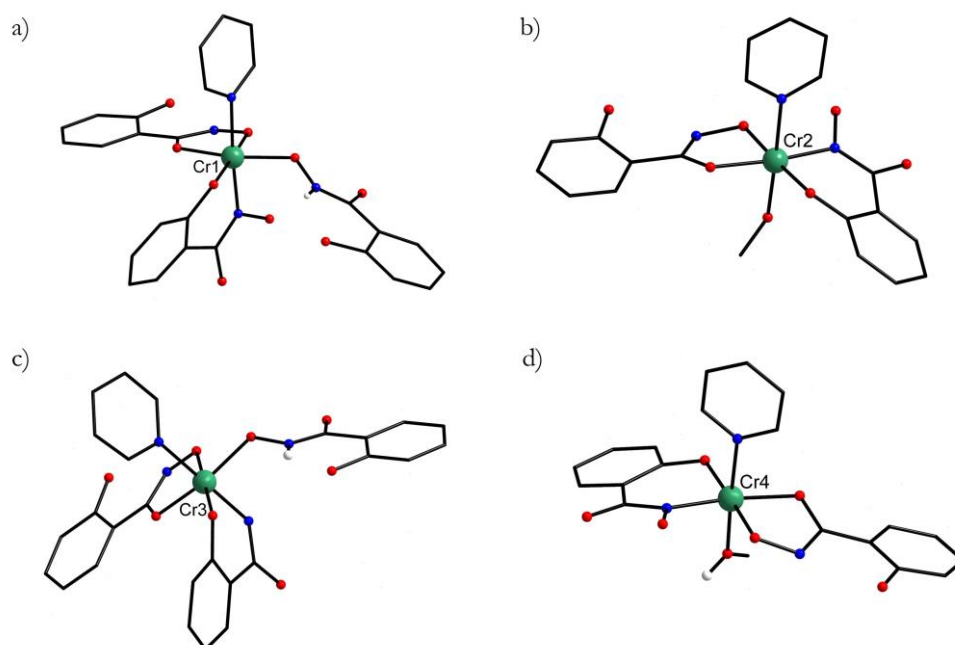


**Figure 4. 62.** Schematic representation of the different octahedral coordination environments of a) Cr1, b) Cr2, c) Cr3, d) Cr4. Color code: chromium(III) ions green, oxygen red, hydrogen white, nitrogen blue, carbon black. Hydrogen atoms (except of H2O), and non-coordinated solvent molecules are omitted for clarity.

Continuous Shape Measurements confirm the small deviation from the ideal octahedron for all four chromium(III) ions (Table 4. 33).

**Table 4. 33.** Calculated deviations from ideal polyhedra (octahedron  $O_h$ ) for ring metal ions *via* Continuous Shape Measurements CShM of  $[Cr_4Dy]$ .

ion	Cr1	Cr2	Cr3	Cr4
CShM	0.882	0.482	0.954	0.471

The Continuous Shape Measurements for Dy1 reveal a triangular dodecahedral symmetry with a Shape value of 2.389. An antiprismatic  $D_{4d}$  would suppress quantum tunneling and enhances single-molecule magnet performance.<sup>[85]</sup> As the symmetry strategies for lanthanide(III) complexes to enhance their performance SMMs was reported in 2018 by Tong and co-workers,<sup>[85]</sup> square antiprismatic symmetries for

the lanthanide(III) guest ions in MCs with small zenithal angles are well-studied in the Rentschler group.<sup>196,104</sup> In these sandwich-type MC complexes distorted antiprismatic symmetries with small zenithal angles lead to an increase of the axiality in the systems which is required for high-anisotropy barriers in SMMs. In the case of **[Cr<sub>4</sub>Dy]**, the distortion of antiprismatic symmetry with a Shape value of 3.673 is much higher as shown in Figure 4. 63 b.

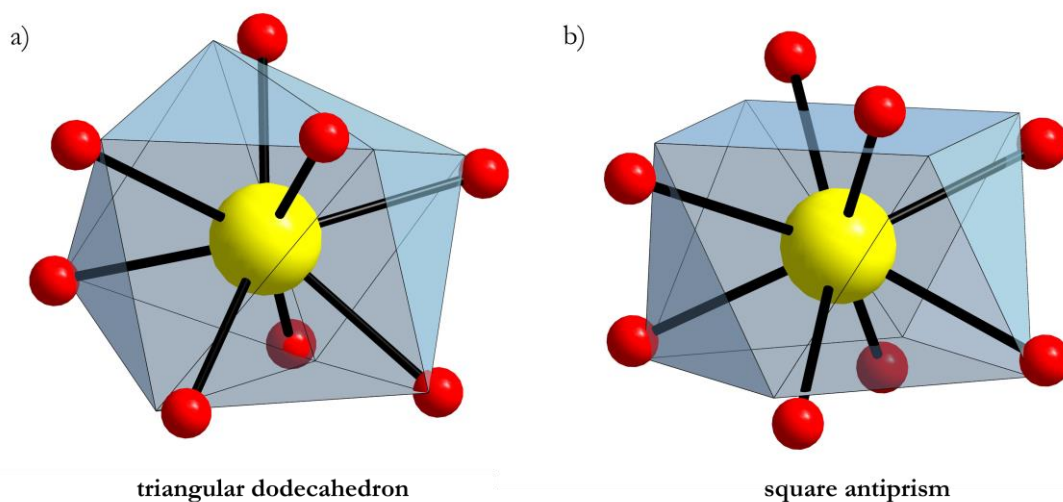


**Figure 4. 63.** Schematic representation of the ideal coordination polyhedron (grey) of Dy1 of **[Cr<sub>4</sub>Dy]** for a) triangular dodecahedral symmetry with CShM = 2.389; b) square antiprismatic symmetry with CShM = 3.673. Color code of atoms: oxygen red, dysprosium(III) ion yellow. Color code: dysprosium(III) ion yellow, oxygen red.

Several intramolecular hydrogen bonds are shown in Figure 4. 64. The short distance between O16 to H6 (1.91 Å) as well as O13 to H5 (1.98 Å) is forming a six-membered ring within the single deprotonated salicylhydroxamic acid that acts as bridging co-ligand. Additionally, a hydrogen bond occurs between O19 to H20 (1.58 Å) of the methanol and methanolate co-ligands of the chromium(III) ring metal ions. One polarized hydrogen H23A of a non-coordinated methanol solvent molecule interacts with the oxygen atom O7 (2.38 Å). Additionally, another non-coordinated pyridine molecule interacts through H16 (1.9 Å)

The dysprosium(III) and chromium(III) ions from two different molecules are widely separated from each other in the unit cell by 15.22 Å (Dy1-Dy1) and 10.49 Å (Cr1-Cr2) (see Figure 4. 65). Hydrogen bonds within the molecule **[Cr<sub>4</sub>Dy]** are not present between different molecules. Therefore, intermolecular dipole interactions can be neglected.

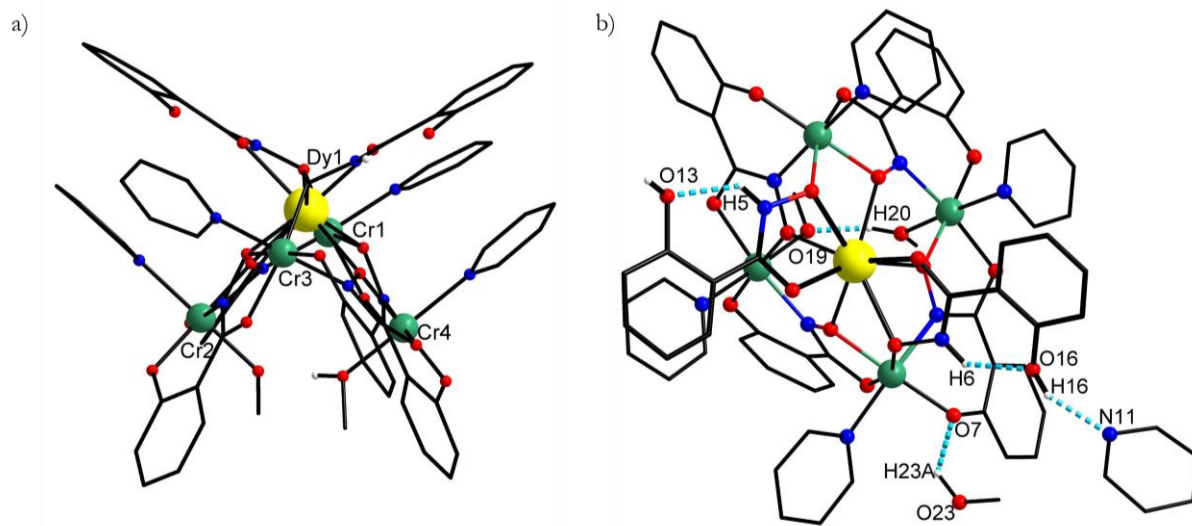


**Figure 4. 64.** Schematic representation of the molecular structure of  $\{\text{Dy}^{\text{III}}(\mu_2\text{-}\eta^3\text{-ShiH}_2)_2[12\text{-MC}_{\text{Cr}(\text{III})\text{N}(\text{Shi})_4\text{-4]}(\text{MeOH})(\text{py})_4(\text{MeO})\} \cdot \text{H}_2\text{O} \cdot \text{MeOH} \cdot \text{py}$ ; a) with emphasized bent structure (side view); b) with emphasized hydrogen bonds within the molecule and to non-coordinated solvent molecules. Hydrogen atoms are omitted for clarity (except for H5, H16, H20, H23A). Color code: dysprosium(III) ions yellow, chromium(III) ions green, oxygen red, hydrogen white, nitrogen blue, carbon black.

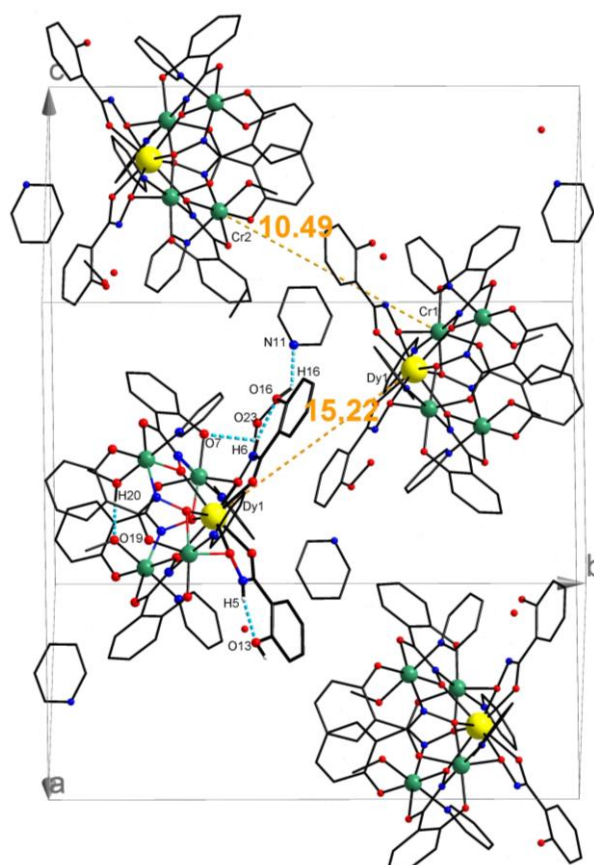


**Figure 4. 65.** Schematic representation of the molecular structure of  $[\text{Cr}_4\text{Dy}]$  in unit cell with highlighted intermolecular interactions. Dy1-Dy1 distance 15.22 Å (orange); Cr1-Cr2 (to second molecule) distance 10.49 Å (orange). Hydrogen atoms are omitted for clarity except of H5, H6, H20. Color code: dysprosium(III) ions yellow, chromium(III) ions green, oxygen red, nitrogen blue, hydrogen white, carbon black.

The average torsion angle that is separating the chromium(III) ring metal ions in the repeating unit [Cr-N-O-Cr] of 161.71° is comparable to the other [12-MC-4] cavities like in the heterometallic MC by Happ and Rentschler (172.44°) or in the 3d-4f sandwich MC for one of the MC units by Rauguth and Rentschler (162.92°).<sup>[105,96]</sup> Moreover, the [DyFe<sub>4</sub>(Shi)<sub>4</sub>(C<sub>6</sub>H<sub>5</sub>COO)<sub>4</sub>(py)<sub>4</sub>] metallocrown represents a comparable example reported by Dou and co-workers in 2018.<sup>[106]</sup> The average torsion angle of 166.97° led to antiferromagnetic exchange interactions of the iron(III) ions in the repeating unit.

**Table 4. 34.** Selected bond lengths of each chromium(III) ring metal ion and the guest ion Dy1 of [Cr<sub>4</sub>Dy].

ion	Dy1	Cr1	Cr2	Cr3	Cr4
bond length /Å	O3 2.334(4)	O1 1.942(4)	O2 1.994(4)	O5 1.970(4)	O8 2.015(4)
	O6 2.338(3)	O11 1.947(4)	O3 1.948(3)	O6 1.957(4)	O9 1.942(4)
	O9 2.338(4)	O12 1.950(4)	O4 1.926(3)	O7 1.932(4)	O10 1.914(4)
	O12 2.345(3)	O15 2.003(4)	O19 1.969(4)	O18 2.011(4)	O20 1.951(4)
	O14 2.325(4)	N1 1.981(4)	N2 1.986(4)	N3 1.994(4)	N4 1.980(5)
	O15 2.446(4)	N7 2.093(4)	N8 2.125(5)	N9 2.083(4)	N10 2.139(5)
	O17 2.312(4)				
	O18 2.445(4)				

**Table 4. 35.** Selected bond angles and torsion angles of [Cr<sub>4</sub>Dy].

bond angles		torsion angles	
Cr1-O12-Dy1	103.92(15)°	Cr1-O12-N4-Cr4	165.02(17)°
Cr1-O15-Dy1	98.86(16)°	Cr2-O3-N1-Cr1	161.5(2)°
Cr2-O3-Dy1	128.48(17)°	Cr3-O6-N2-Cr2	164.40(18)°
Cr3-O6-Dy1	103.65(14)°	Cr4-O9-N3-Cr3	155.9(2)°
Cr3-O18-Dy1	98.38(15)°		
Cr4-O9-Dy1	128.14(18)°		

### Evaluation of magnetic data

To investigate the magnetic properties of [Cr<sub>4</sub>Dy] magnetic susceptibility measurements were performed with an applied magnetic field of 1000 Oe in the temperature range of 2-300 K (Figure 4. 66). In addition, magnetization measurements were performed with magnetic fields ranging from 0.1 T to 7 T at 2-10 K (Figure 4. 19 b). The theoretically expected values of the  $\chi_m T$  product can be calculated using Equations 18 and 19. Each of the four chromium(III) ions should contribute to the  $\chi_m T$  product by 1.875 cm<sup>3</sup> K mol<sup>-1</sup> with  $g = 2$  and  $S = 3/2$ . The contribution of the dysprosium(III) ion is 14.17 cm<sup>3</sup> K mol<sup>-1</sup>. Thus, the experimental value of 20.47 cm<sup>3</sup> K mol<sup>-1</sup> is in very good agreement with the theoretical value of 21.64 cm<sup>3</sup> K mol<sup>-1</sup>. Upon cooling, a decrease in the  $\chi_m T$  product is observed at the entire temperature range. This indicates antiferromagnetic exchange interactions, strong zero-field splitting and most importantly depopulation of excited crystal field states of the dysprosium(III) ion.

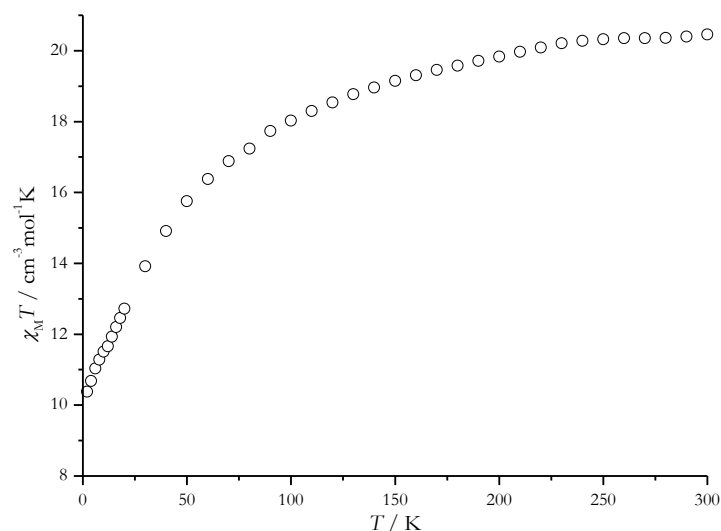


**Figure 4. 66.** Temperature-dependence of magnetic susceptibility of **[Cr<sub>4</sub>Dy]** with applied magnetic field of 1000 Oe in temperature range 2-300 K.

Additionally, the field-dependent magnetization  $M$  was measured at a temperature range of 4 K to 10 K with an applied field  $H$  of 0.1 to 7 T which is shown in Figure 4. 67. As the strength of the magnetic field increases, a pronounced increase in magnetization occurs up to 1 T, followed by a more gradual increase up to 7 T. At a temperature of 4 K and an applied field of 7 T, the magnetization reaches a value of  $6.15 N_A \mu_B$ . The fast decrease at low temperatures and low fields is a sign of an isolated ground state and/or the existence of anisotropy, which prevents the alignment of the magnetic moment along the magnetic field. This results in a lower magnetization value than a theoretically calculated value of  $10 N_A \mu_B$ .<sup>[86]</sup>

Furthermore, the non-superposition of the temperature-dependent reduced magnetization confirms the presence of significant magnetic anisotropy as illustrated in Figure 4. 68. Therefore, AC-susceptibility measurements were performed.

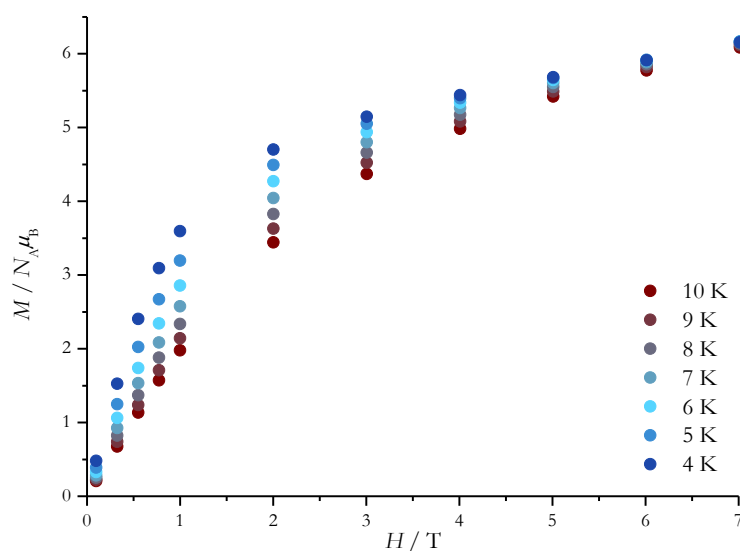


**Figure 4. 67.** Field-dependent magnetization measurement of **[Cr<sub>4</sub>Dy]** in form of  $M$  against  $H$  plot (circles) at a temperature range of 4-10 K.

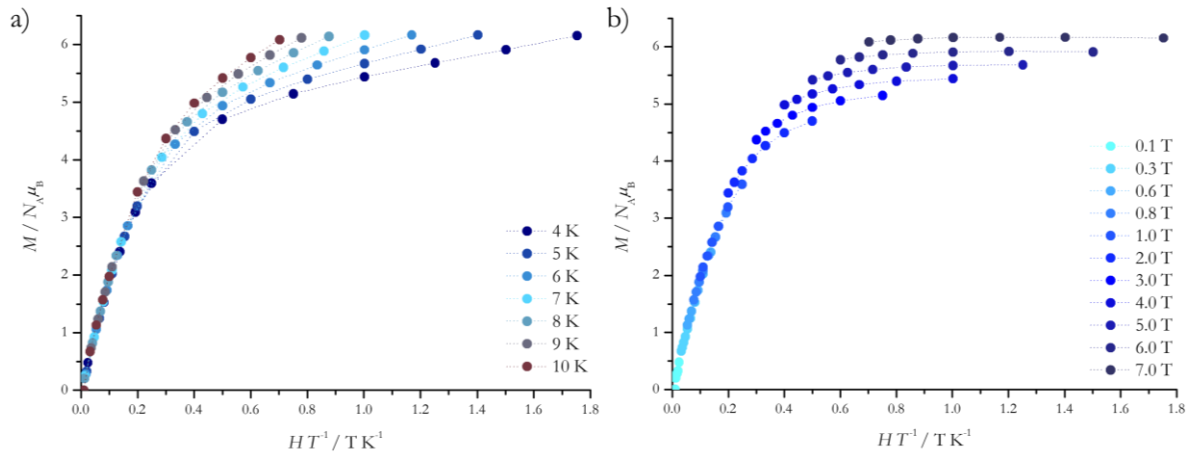


**Figure 4.68.** Temperature and field dependent magnetization measurement of **[Cr<sub>4</sub>Dy]** in form of  $M$  against  $H/T$  plots (circles). Dashed lines are guidelines for the eyes.

When no external field was applied field  $H_{dc} = 0$ , no out-of-phase signal was observed at 2 K. However, by applying an additional field of  $H_{dc} = 1000$  Oe, the highest signal of the out of phase signal was received. The temperature-dependent measurements were performed from 2.2 K to 3.0 K. In common cases, the energy barrier  $U_{eff}$  is determined by using the Cole-Cole plots (see Chapter 1. 4.2). As no maxima are observed, here fitting of the semicircles does not allow to extract a reasonable energy barrier. Therefore, the following Equation 21 is used to get an estimation of  $U_{eff}$ .<sup>[107]</sup> This method was first reported in 2009 by Turta and co-workers and is often used to approximately estimate small energy barriers.<sup>[108]</sup>

$$\ln\left(\frac{\chi''}{\chi'}\right) = \ln(2\pi\nu\tau_0) + \frac{U_{eff}}{k_B} \cdot \frac{1}{T} \quad (21)$$

The following assumptions are made in this approximation method to derive Equation 21:<sup>[109]</sup>

- A very small value of  $\chi_s$  is present and can be neglected.
- An Arrhenius behavior for the relaxation time  $\tau$  is followed. Therefore, no tunneling relaxation processes are considered.
- A homogeneous sample is measured. There is no distribution of different relaxation times, which equals  $\alpha = 0$ . Only one relaxation process takes place.

Then, the quantity  $\ln(\chi''/\chi')$  linearly depends on the inverse temperature  $1/T$ . To obtain a reliable indication of the energy barrier, several excitation frequencies were considered and fitted linearly according to Equation 21. Experimental data of the excitation frequencies 1400 Hz, 893 Hz, 565 Hz, 361 Hz and 229 Hz were fitted with the program Origin7.5 and plotted in Figure 4. 69. As expected, a parallel trend of the fit curves is observed. The linear fits lead to a reasonably estimated effective average energy barrier of  $U_{eff} = 9.3$  cm<sup>-1</sup> (13.4 K) with an average relaxation time  $\tau_0 = 7.8 \cdot 10^{-8}$  s. The parameters of the best fits are



listed in Table 4. 36. The results show a small energy barrier compared to other MCs that contain dysprosium(III) ions. Therefore, tunneling effects cannot be neglected for sure despite of the applied dc field. These tunnel effects can be attributed to the triangular dodecahedral geometry of Dy1 guest ion which is already shown in Figure 4. 63. However, evaluation of these magnetic data confirms that **[Cr<sub>4</sub>Dy]** belongs to the single-molecule magnet family.

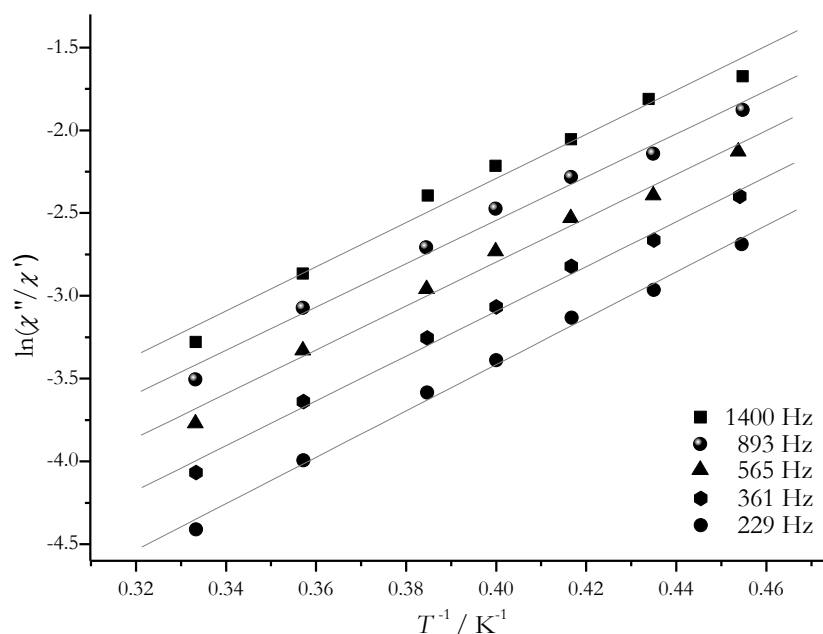


**Figure 4. 69.** Plot of  $\ln(\chi''/\chi')$  vs.  $1/T$  of **[Cr<sub>4</sub>Dy]** with an applied field of  $H_{dc} = 1000$  Oe.

**Table 4. 36.** Values of the linear fit ( $Y = A + BX$ ) for the different excitation frequencies.

excitation frequency	$A = \ln(2\pi\nu\tau_0)$	$\tau_0$ / s	$B = U_{eff} / k_B$ / K	$U_{eff} / \text{cm}^{-1}$	$R$
1400 Hz	$-7.6 \pm 0.3$	$5.7 \cdot 10^{-8}$	$13.3 \pm 0.9$	9.2	0.990
893 Hz	$-7.8 \pm 0.3$	$7.3 \cdot 10^{-8}$	$13.1 \pm 0.6$	9.1	0.994
565 Hz	$-8.1 \pm 0.3$	$8.6 \cdot 10^{-8}$	$13.3 \pm 0.7$	9.2	0.994
361 Hz	$-8.5 \pm 0.2$	$9.0 \cdot 10^{-8}$	$13.5 \pm 0.5$	9.4	0.996
229 Hz	$-9.0 \pm 0.2$	$8.6 \cdot 10^{-8}$	$14.0 \pm 0.5$	9.7	0.997
average	-8.2	$7.8 \cdot 10^{-8}$	13.4	9.3	-

In general, non-planar [12-MC-4] metallacrowns are reported by Pecoraro and co-workers e.g. including gallium(III) ring metal ions and several lanthanide(III) guest ions.<sup>[110]</sup> Here, luminescent lanthanide(III) MCs were synthesized and contributions of crystal packing and non-radiative deactivations through vibronic coupling oscillators were considered to influence the emission properties. In this case, no investigation concerning the magnetic properties were reported although anisotropic lanthanide(III) ions were incorporated. Another non-planar arrangement in a [12-MC-4] cavity was reported by Happ and Rentschler in 2015.<sup>[73]</sup> This MC contains a cobalt(II) guest ion and four cobalt(III) ring metal ions. One salicylhydroxamate ligand is tilted towards the downside of the molecule, while other ligands are in a planar arrangement.

**[Cr<sub>4</sub>Dy]** represents the first example of a [12-MC-4] metallocrown containing both chromium(III) and lanthanide(III) ions. The intended prevention of bridging co-ligands led to a **[Cr<sub>4</sub>Dy]** MC which shows single-molecule magnet behavior. Chapter 4.2. shows parameters that influence the composition and cavity size of chromium MCs in combination with lanthanide(III) ions. Similar to the complexes described in Chapter 4.1, the coordination geometries of the chelating ligands highly influence the cavity size of the formed MCs. Therefore, a [15-MC-5] cavity of **[Cr<sub>5</sub>Dy]** and a [12-MC-4] cavity in **[Cr<sub>4</sub>Dy]** as well as several cluster structures **[Cr<sub>4</sub>Ln<sub>2</sub>]** could be obtained including chromium(III) and lanthanide(III) ions.

### 4.3. References

- [1] A. Lüpke, L. M. Carrella, E. Rentschler, *Chem. – Eur. J.* 2021, 27, 4283–4286.
- [2] G. Mezei, C. M. Zaleski, V. L. Pecoraro, *Chem. Rev.* 2007, 107, 4933–5003.
- [3] L. Spiccia, W. Marty, *Inorg. Chem.* 1986, 25, 266–271.
- [4] S. I. Shupack, *Environ. Health Perspect.* 1991, 92, 7–11.
- [5] G. Mezei, C. M. Zaleski, V. L. Pecoraro, *Chem. Rev.* 2007, 107, 4933–5003.
- [6] V. L. Pecoraro, A. J. Stemmler, B. R. Gibney, J. J. Bodwin, H. Wang, J. W. Kampf, A. Barwinski, in *Prog. Inorg. Chem.*, Wiley-Blackwell, 2007, pp. 83–177.
- [7] J. J. Bodwin, A. D. Cutland, R. G. Malkani, V. L. Pecoraro, *Coord. Chem. Rev.* 2001, 216–217, 489–512.
- [8] L. F. Jones, C. A. Kilner, M. A. Halcrow, *Chem. – Eur. J.* 2009, 15, 4667–4675.
- [9] M. Ostrowska, I. O. Fritsky, E. Gumienna-Kontecka, A. V. Pavlishchuk, *Coord. Chem. Rev.* 2016, 327–328, 304–332.
- [10] C. J. Milios, A. Vinslava, W. Wernsdorfer, S. Moggach, S. Parsons, S. P. Perlepes, G. Christou, E. K. Brechin, *J. Am. Chem. Soc.* 2007, 129, 2754–2755.
- [11] C. M. Zaleski, S. Tricard, E. C. Depperman, W. Wernsdorfer, T. Mallah, M. L. Kirk, V. L. Pecoraro, *Inorg. Chem.* 2011, 50, 11348–11352.
- [12] P. Happ, E. Rentschler, *Dalton Trans. Camb. Engl.* 2003 2014, 43, 15308–15312.
- [13] P. Happ, C. Plenk, E. Rentschler, *Coord. Chem. Rev.* 2015, 289–290, 238–260.
- [14] C. Plenk, J. Krause, M. Beck, E. Rentschler, *Chem. Commun.* 2015, 51, 6524–6527.
- [15] V. L. Pecoraro, *Inorganica Chim. Acta* 1989, 155, 171–173.
- [16] M. Soo Lah, M. L. Kirk, W. Hatfield, V. L. Pecoraro, *J. Chem. Soc. Chem. Commun.* 1989, 0, 1606–1608.
- [17] A. J. S. George Psomas Catherine Dendrinou-Samara, Jeffrey J. Bodwin, Manuela Schneider, Maria Alexiou, Jeff W. Kampf, Dimitris P. Kessissoglou, Vincent L. Pecoraro, *Inorg. Chem.* 2001, 1562–1570.
- [18] C. McDonald, S. Sanz, E. K. Brechin, M. K. Singh, G. Rajaraman, D. Gaynor, L. F. Jones, *RSC Adv.* 2014, 4, 38182–38191.
- [19] M. Alexiou, C. Dendrinou-Samara, C. P. Raptopoulou, A. Terzis, D. P. Kessissoglou, *Inorg. Chem.* 2002, 41, 4732–4738.
- [20] S. Wang, L. Kong, H. Yang, Z. He, Z. Jiang, D. Li, S. Zeng, M. Niu, Y. Song, J. Dou, *Inorg. Chem.* 2011, 50, 2705–2707.
- [21] A. Tarushi, A. G. Hatzidimitriou, M. Estrader, D. P. Kessissoglou, V. Tangoulis, G. Psomas, *Inorg. Chem.* 2017, 56, 7048–7057.
- [22] M. Murrie, S. Parsons, R. E. P. Winpenny, I. M. Atkinson, C. Benelli, *Chem. Commun.* 1999, 285–286.
- [23] F. Y. Salem, T. F. Parkerton, R. V. Lewis, J. H. Huang, K. L. Dickson, *Sci. Total Environ.* 1989, 86, 25–41.
- [24] D. Rai, L. E. Eary, J. M. Zachara, *Sci. Total Environ.* 1989, 86, 15–23.
- [25] R. D. Cannon, R. P. White, in *Prog. Inorg. Chem.*, John Wiley & Sons, Ltd, 1988, pp. 195–298.
- [26] K. V. Pringouri, C. P. Raptopoulou, A. Escuer, T. C. Stamatatos, *Inorganica Chim. Acta* 2007, 360, 69–83.
- [27] A.-R. Tomsa, Y. Li, S. Blanchard, P. Herson, K. Boubekeur, P. Gouzerh, A. Proust, *J. Clust. Sci.* 2014, 25, 825–838.

- [28] A. J. Lewis, E. Garlatti, F. Cugini, M. Solzi, M. Zeller, S. Carretta, C. M. Zaleski, *Inorg. Chem.* 2020, 59, 11894–11900.
- [29] C. Dendrinou-Samara, A. N. Papadopoulos, D. A. Malamataris, A. Tarushi, C. P. Raptopoulou, A. Terzis, E. Samaras, D. P. Kessissoglou, *J. Inorg. Biochem.* 2005, 99, 864–875.
- [30] Sheetal, K. Nehra, R. Kaushal, S. Arora, D. Kaur, R. Kaushal, *Russ. J. Gen. Chem.* 2016, 86, 154–160.
- [31] C. D. Beard, L. Carr, M. F. Davis, J. Evans, W. Levason, L. D. Norman, G. Reid, M. Webster, *Eur. J. Inorg. Chem.* 2006, 2006, 4399–4406.
- [32] N. F. Chilton, R. P. Anderson, L. D. Turner, A. Soncini, K. S. Murray, *J. Comput. Chem.* 2013, 34, 1164–1175.
- [33] C. E. Anson, J. P. Bourke, R. D. Cannon, U. A. Jayasooriya, M. Molinier, A. K. Powell, *Inorg. Chem.* 1997, 36, 1265–1267.
- [34] P. Chaudhuri, M. Hess, E. Rentschler, T. Weyhermüller, U. Flörke, *New J. Chem.* 1998, 22, 553–555.
- [35] C. Y. Chow, R. Guillot, E. Rivière, J. W. Kampf, T. Mallah, V. L. Pecoraro, *Inorg. Chem.* 2016, 55, 10238–10247.
- [36] A. B. Lago, J. Pasán, L. Cañadillas-Delgado, O. Fabelo, F. J. M. Casado, M. Julve, F. Lloret, C. Ruiz-Pérez, *New J. Chem.* 2011, 35, 1817–1822.
- [37] A. Lüpke, L. M. Carrella, E. Rentschler, *Chem. – Eur. J.* 2021, 27, 4215–4215.
- [38] A. Lüpke, L. M. Carrella, E. Rentschler, *Chem. – Eur. J.* 2021, 27, 4211–4211.
- [39] B. R. Gibney, A. J. Stemmler, S. Pilotek, J. W. Kampf, V. L. Pecoraro, *Inorg. Chem.* 1993, 32, 6008–6015.
- [40] E. Ebler, E. Schott, *J. Für Prakt. Chem.* 1908, 78, 289–342.
- [41] C. E. Housecroft, A. G. Sharpe, *Inorganic Chemistry*, Prentice Hall, Harlow, 2002.
- [42] M. Soo Lah, M. L. Kirk, W. Hatfield, V. L. Pecoraro, *J. Chem. Soc. Chem. Commun.* 1989, 0, 1606–1608.
- [43] D. Casanova, P. Alemany, *Phys. Chem. Chem. Phys.* 2010, 12, 15523–15529.
- [44] A. Ruiz-Martínez, D. Casanova, S. Alvarez, *Dalton Trans.* 2008, 0, 2583–2591.
- [45] J. Cirera, E. Ruiz, S. Alvarez, *Chem. – Eur. J.* 2006, 12, 3162–3167.
- [46] D. Casanova, J. Cirera, M. Llunell, P. Alemany, D. Avnir, S. Alvarez, *J. Am. Chem. Soc.* 2004, 126, 1755–1763.
- [47] M. Pinsky, D. Avnir, *Inorg. Chem.* 1998, 37, 5575–5582.
- [48] M. Mannini, P. Sainctavit, R. Sessoli, C. Cartier dit Moulin, F. Pineider, M.-A. Arrio, A. Cornia, D. Gatteschi, *Chem. – Eur. J.* 2008, 14, 7530–7535.
- [49] J. Jankolovits, J. W. Kampf, S. Maldonado, V. L. Pecoraro, *Chem. - Eur. J.* 2010, 16, 6786–6796.
- [50] E. Gouré, B. Gerey, C. N. Astudillo, J. Pécaut, S. Sirach, F. Molton, J. Fortage, M.-N. Collomb, *Inorg. Chem.* 2021, 60, 7922–7936.
- [51] B. J. Sirovets, N. E. Walters, C. N. Bender, C. M. Lenivy, A. S. Troup, D. P. Predecki, J. N. Richardson, C. M. Zaleski, *J. Chem. Educ.* 2013, 90, 782–785.
- [52] S. Tomy, S. I. Shylin, D. Bykov, V. Ksenofontov, E. Gumienna-Kontecka, V. Bon, I. O. Fritsky, *Nat. Commun.* 2017, 8, 14099.
- [53] Z. Wang, W. Qiu, S. Pang, Q. Guo, C. Guan, J. Jiang, *Environ. Sci. Technol.* 2022, 56, 1492–1509.
- [54] N. Elgrishi, K. J. Rountree, B. D. McCarthy, E. S. Rountree, T. T. Eisenhart, J. L. Dempsey, *J. Chem. Educ.* 2018, 95, 197–206.

- [55] N. G. Tsierkezos, *J. Solut. Chem.* 2007, 36, 289–302.
- [56] P. Zanello, C. Nervi, F. F. de Biani, *Inorganic Electrochemistry: Theory, Practice and Application*, Royal Society Of Chemistry, 2019.
- [57] S. W. Feldberg, L. Jetic, *J. Phys. Chem.* 1972, 76, 2439–2446.
- [58] B. Kohl, M. V. Bohnwagner, F. Rominger, H. Wadepohl, A. Dreuw, M. Mastalerz, *Chem. – Eur. J.* 2016, 22, 646–655.
- [59] J. S. McIndoe, K. L. Vikse, *J. Mass Spectrom.* 2019, 54, 466–479.
- [60] D. Akyüz, Ü. Demirbaş, A. Koca, F. Çelik, H. Kantekin, *J. Mol. Struct.* 2020, 1206, 127674.
- [61] D. Akyüz, Ü. Demirbaş, H. T. Akçay, A. Koca, H. Kantekin, *J. Organomet. Chem.* 2020, 924, 121420.
- [62] T. Keleş, D. Akyüz, Z. Biyiklioglu, A. Koca, *Electroanalysis* 2017, 29, 2125–2137.
- [63] M. J. Calhorda, *Chem. Commun.* 2000, 801–809.
- [64] J. F. Malone, C. M. Murray, M. H. Charlton, R. Docherty, A. J. Lavery, *J. Chem. Soc. Faraday Trans.* 1997, 93, 3429–3436.
- [65] S. Tsuzuki, *Annu. Rep. Sect. C Phys. Chem.* 2012, 108, 69–95.
- [66] S. Tsuzuki, K. Honda, T. Uchimaru, M. Mikami, A. Fujii, *J. Phys. Chem. A* 2006, 110, 10163–10168.
- [67] A. Fitch, A. Lavy-Feder, S. A. Lee, M. T. Kirsh, *J. Phys. Chem.* 1988, 92, 6665–6670.
- [68] W. Ruan, J. Mao, S. Yang, C. Shi, G. Jia, Q. Chen, *Chem. Commun.* 2020, 56, 3171–3174.
- [69] M. Hecht, F. A. Schultz, B. Speiser, *Inorg. Chem.* 1996, 35, 5555–5563.
- [70] C. A. Hunter, K. R. Lawson, J. Perkins, C. J. Urch, *J. Chem. Soc. Perkin Trans. 2* 2001, 651–669.
- [71] A. Gehlhaar, E. Schiavo, C. Wölper, Y. Schulte, A. A. Auer, S. Schulz, *Dalton Trans.* 2022, 51, 5016–5023.
- [72] J. Kiehl, T. Hochdörffer, L. M. Carrella, V. Schünemann, M. H. Nygaard, J. Overgaard, E. Rentschler, *Inorg. Chem.* 2022, 61, 3141–3151.
- [73] P. Happ, C. Plenck, E. Rentschler, *Coord. Chem. Rev.* 2015, 289–290, 238–260.
- [74] Y.-Q. Zhai, N. Ge, Z.-H. Li, W.-P. Chen, T. Han, Z.-W. Ouyang, Z. Wang, Y.-Z. Zheng, *Inorg. Chem.* 2021, DOI 10.1021/acs.inorgchem.0c02065.
- [75] M. Darawsheh, L. A. Barrios, O. Roubeau, S. J. Teat, G. Aromí, *Angew. Chem. Int. Ed.* 2018, 57, 13509–13513.
- [76] M. Ostrowska, Y. Toporivska, I. A. Golenya, S. Shova, I. O. Fritsky, V. L. Pecoraro, E. Gumienna-Kontecka, *Inorg. Chem.* 2019, DOI 10.1021/acs.inorgchem.9b02724.
- [77] T. N. Parac-Vogt, A. Pacco, P. Nockemann, Y.-F. Yuan, C. Görlner-Walrand, K. Binnemans, *Eur. J. Inorg. Chem.* 2006, 2006, 1466–1474.
- [78] R. Hoss, F. Vögtle, *Angew. Chem. Int. Ed. Engl.* 1994, 33, 375–384.
- [79] M. J. Giansiracusa, G. K. Gransbury, N. F. Chilton, D. P. Mills, in *Encycl. Inorg. Bioinorg. Chem.*, John Wiley & Sons, Ltd, 2021, pp. 1–21.
- [80] C. Y. Chow, H. Bolvin, V. E. Campbell, R. Guillot, J. W. Kampf, W. Wernsdorfer, F. Gendron, J. Autschbach, V. L. Pecoraro, T. Mallah, *Chem. Sci.* 2015, 6, 4148–4159.
- [81] H. L. C. Feltham, S. Brooker, *Coord. Chem. Rev.* 2014, 276, 1–33.
- [82] D. P. Kessissoglou, J. Kampf, V. L. Pecoraro, *Polyhedron* 1994, 13, 1379–1391.
- [83] C. Dendrinou-Samara, L. Alevizopoulou, L. Iordanidis, E. Samaras, D. P. Kessissoglou, *J. Inorg. Biochem.* 2002, 89, 89–96.

- [84] J. C. Lutter, J. W. Kampf, M. Zeller, C. M. Zaleski, *Acta Crystallogr. Sect. E Struct. Rep. Online* 2013, 69, m483–m484.
- [85] J.-L. Liu, Y.-C. Chen, M.-L. Tong, *Chem. Soc. Rev.* 2018, 47, 2431–2453.
- [86] A. Alhassanat, C. Gamer, A. Rauguth, A. A. Athanasopoulou, J. Sutter, C. Luo, H. Ryll, F. Radu, A. A. Sapozhnik, T. Mashoff, E. Rentschler, H. J. Elmers, *Phys. Rev. B* 2018, 98, 064428.
- [87] M. G. Sorolla, X. Wang, T. Makarenko, A. J. Jacobson, *Inorg. Chem.* 2019, 58, 9935–9940.
- [88] Y. Wang, W.-S. Wu, M.-L. Huang, *Chin. Chem. Lett.* 2016, 27, 423–427.
- [89] A. V. Pavlishchuk, S. V. Kolotilov, I. O. Fritsky, M. Zeller, A. W. Addison, A. D. Hunter, *Acta Crystallogr. C* 2011, 67, m255–m265.
- [90] A. V. Pavlishchuk, S. V. Kolotilov, M. Zeller, S. E. Lofland, L. K. Thompson, A. W. Addison, A. D. Hunter, *Inorg. Chem.* 2017, 56, 13152–13165.
- [91] D. Gaynor, Z. A. Starikova, W. Haase, K. B. Nolan, *J. Chem. Soc. Dalton Trans.* 2001, 1578–1581.
- [92] C. Dendrinou-Samara, G. Psomas, L. Iordanidis, V. Tangoulis, D. P. Kessissoglou, *Chem. – Eur. J.* 2001, 7, 5041–5051.
- [93] C. Dendrinou-Samara, A. N. Papadopoulos, D. A. Malamataris, A. Tarushi, C. P. Raptopoulou, A. Terzis, E. Samaras, D. P. Kessissoglou, *J. Inorg. Biochem.* 2005, 99, 864–875.
- [94] E. S. Biro, C. L. Ward, M. J. Allen, J. C. Lutter, *J. Chem. Crystallogr.* 2022, 52, 152–160.
- [95] J. D. Rinehart, J. R. Long, *Chem. Sci.* 2011, 2, 2078.
- [96] A. Rauguth, A. Kredel, L. M. Carrella, E. Rentschler, *Inorg. Chem.* 2021, [acs.inorgchem.1c01356](https://doi.org/10.1039/c1in1356a).
- [97] C. Y. Chow, S. V. Eliseeva, E. R. Trivedi, T. N. Nguyen, J. W. Kampf, S. Petoud, V. L. Pecoraro, *J. Am. Chem. Soc.* 2016, 138, 5100–5109.
- [98] J. R. Travis, A. M. Smihosky, A. C. Kauffman, S. E. Ramstrom, A. J. Lewis, S. G. Nagy, R. E. Rheam, M. Zeller, C. M. Zaleski, *J. Chem. Crystallogr.* 2021, 51, 372–393.
- [99] S. V. Eliseeva, J. R. Travis, S. G. Nagy, A. M. Smihosky, C. M. Foley, A. C. Kauffman, C. M. Zaleski, S. Petoud, *Dalton Trans.* 2022, 51, 5989–5996.
- [100] L. J. Völker, *Molekularer Magnetismus Metallakronen-basierter Komplexverbindungen*, Johannes Gutenberg-Universität Mainz, 2018.
- [101] I. A. Golenya, E. Gumienna-Kontecka, A. N. Boyko, M. Haukka, I. O. Fritsky, *Inorg. Chem.* 2012, 51, 6221–6227.
- [102] S. K. Langley, D. P. Wielechowski, V. Vieru, N. F. Chilton, B. Moubaraki, B. F. Abrahams, L. F. Chibotaru, K. S. Murray, *Angew. Chem. Int. Ed.* 2013, 52, 12014–12019.
- [103] S. K. Langley, N. F. Chilton, L. Ungur, B. Moubaraki, L. F. Chibotaru, K. S. Murray, *Inorg. Chem.* 2012, 51, 11873–11881.
- [104] A. A. Athanasopoulou, J. J. Baldoví, L. M. Carrella, E. Rentschler, *Dalton Trans.* 2019, DOI 10.1039/C9DT02432H.
- [105] P. Happ, E. Rentschler, *Dalton Trans.* 2014, 43, 15308–15312.
- [106] T. Lou, H. Yang, S. Zeng, D. Li, J. Dou, T. Lou, H. Yang, S. Zeng, D. Li, J. Dou, *Crystals* 2018, 8, 229.
- [107] M. Holynska, *Single-Molecule Magnets - Molecular Architectures and Building Blocks for Spintronics*, John Wiley & Sons, Ltd, 2019.
- [108] J. Bartolomé, G. Filoti, V. Kuncser, G. Schinteie, V. Mereacre, C. E. Anson, A. K. Powell, D. Prodius, C. Turta, *Phys. Rev. B* 2009, 80, 014430.
- [109] C. V. Topping, S. J. Blundell, *J. Phys. Condens. Matter* 2019, 31, 013001.
- [110] T. N. Nguyen, S. V. Eliseeva, C. Y. Chow, J. W. Kampf, S. Petoud, V. L. Pecoraro, *Inorg. Chem. Front.* 2020, DOI 10.1039/C9QI01647C.

## 5. Conclusion and future perspectives

The aim of this work was the synthesis of novel metallacrowns containing kinetic inert chromium(III) ions as well as the investigation of the structure, stability, and magnetic behavior. Metallacrowns belong to the compound class of macrocycles and are capable of coordinating guest and ring metal ions with the general repeating unit [M-N-O]. Due to their structural versatility, a wide variety of cavities and properties can be obtained. These complexes are used in the field of molecular magnetism due to prominent coupling pathways and the versatile magnetic exchange of the guest and ring metal ions. Furthermore, with their reliable coordination scaffold metallacrowns offer the desired robust preliminary conditions which are required for the challenges of surface immobilization of such complexes. The thesis provides an insight into the investigations of the stability of the kinetic inert chromium(III) metallacrowns regarding their stability under ESI mass spectrometry and electrochemical conditions. For any further processing of these metallacrowns e.g., immobilization onto surfaces, air stable molecules must be developed that stay intact during the application conditions.

The combination of the classical robust metallacrowns scaffold including chromium(III) ions was synthesized and investigated for the first time. Two different cavities were obtained *via* solvothermal synthesis for these new homometallic metallacrowns containing  $\{\text{Cr}^{\text{III}}(\mu_2\text{-piv})_3[9\text{-MC}_{\text{Cr}(\text{III})\text{N}(\text{shi})\text{-}3](\text{morph})_3]\cdot\text{MeOH}$  (**[Cr<sub>3</sub>Cr]**),  $\{\text{Cr}^{\text{III}}(\mu_2\text{-piv})_3[9\text{-MC}_{\text{Cr}(\text{III})\text{N}(\text{tribute})\text{-}3](\text{morph})_3]\cdot\text{MeOH}$  (**(*fbu*)<sub>2</sub>-[Cr<sub>3</sub>Cr]**)  $\{[12\text{-MC}_{\text{Cr}(\text{III})\text{N}(\text{shiH})(\text{Shi})\text{-}4](\text{py})_8]\text{Cl}\cdot 5\text{ MeOH}$  (**[Cr<sub>4</sub>]**),  $\{[12\text{-MC}_{\text{Cr}(\text{III})\text{N}(\text{OMeShiH})(\text{OMeShi})\text{-}4](\text{py})_8]\text{Cl}\cdot \text{CH}_{3.75}\text{O}_{0.75}6.75\cdot(\text{MeOH})0.25\cdot(\text{H}_2\text{O})$  (**OMe-[Cr<sub>4</sub>]**) and  $\{[12\text{-MC}_{\text{Cr}(\text{III})\text{N}(\text{shiH})(\text{Shi})\text{-}4](\gamma\text{-py})_8]\text{Cl}\cdot 3.75\text{ H}_2\text{O}\cdot 0.5\text{ O}$  (**pic-[Cr<sub>4</sub>]**). Additionally, an iron(III) analog structure  $\{\text{Fe}^{\text{III}}(\mu_2\text{-OOCPh})_3[9\text{-MC}_{\text{Fe}(\text{III})\text{N}(\text{buShi})\text{-}3](\text{MeOH})_3]\cdot(\text{fbu})_2$  (**[Fe<sub>3</sub>Fe]**) was synthesized to compare the electrochemical properties and ESI mass spectra to **(*fbu*)<sub>2</sub>-[Cr<sub>3</sub>Cr]**.

The [9-MC-3] structure containing chromium(III) ions that was already predicted over 30 years ago was now synthesized and investigated (**[Cr<sub>3</sub>Cr]**). This compound represents the first classical metallacrown that contains kinetic inert chromium(III) ions. In contrast to common synthesis of metallacrowns at ambient conditions, a solvothermal reaction was utilized for this synthesis. All chromium(III) ions adopt an asymmetric *cis*-propeller configuration leading to the [9-MC-3] metallacrown with the [Cr-N-O] repeating unit. ESI mass spectrometry confirms the expected stability compared to other metallacrown complexes of the Rentschler group with various 3*d* metal ions. However, a bulky and not flat metallacrown was obtained. For a surface adsorption *via* physisorption a flat metallacrown could align easier on a flat surface. Therefore, in the following the influence on a metallacrown cavity was investigated.

In this context, an approach was pursued to synthesize metallacrowns with iron(III) as well as chromium(III) ions. The ligands chosen for this study were 5-*tert*-butylsalicylhydroxamic acid and 3,5-di-*tert*-butylsalicylhydroxamic acid as the sterically demanding *tert*-butyl groups could lead to flat metallacrowns. The metallacrowns **(*fbu*)<sub>2</sub>-[Fe<sub>3</sub>Fe]** and **(*fbu*)<sub>2</sub>-[Cr<sub>3</sub>Cr]** were obtained and characterized by utilizing 5-*tert*-

butylsalicylhydroxamic acid and 3,5-di-*tert*-butylsalicylhydroxamic acid respectively. The analog [9-MC-3] cavity was obtained and no change in the torsion angles of the repeating unit was observed in comparison to **[Cr<sub>3</sub>Cr]**. All ring metal ions and guest ions are coordinated in a *cis*-propeller configuration which led to the [9-MC-3] cavity. Additionally, the stability of **(*t*bu)<sub>2</sub>-[Cr<sub>3</sub>Cr]** was proven under ESI mass spectrometry conditions. Thus, the combination of kinetic inert chromium(III) ions and metallacrowns created a very stable coordination compound. Furthermore, the cyclic voltammogram of **(*t*bu)<sub>2</sub>-[Cr<sub>3</sub>Cr]** did not suggest any reduction processes of the chromium(III) ions. **tbu-[Fe<sub>3</sub>Fe]** could not be detected by ESI mass spectrometry and showed redox sensitivity in comparison to **(*t*bu)<sub>2</sub>-[Cr<sub>3</sub>Cr]**. In all cases of the [9-MC-3] cavity, two competing antiferromagnetic exchange interactions resulted in a spin ground state of  $S_T \neq 0$ . As expected, the coupling constants for chromium(III) ( $J_1 = -10.88 \text{ cm}^{-1}$  and  $J_2 = -2.280 \text{ cm}^{-1}$ ) and for iron(III) are in the same range ( $J_1 = -13.3 \text{ cm}^{-1}$ ,  $J_2 = -4.4 \text{ cm}^{-1}$ ).

A larger cavity could be synthesized in a series of vacant metallacrowns  $\{[12\text{-MC}_{\text{Cr(III)N}(\text{ShiH})(\text{Shi})_3\text{-4}}](\text{py})_8\text{Cl}\} \cdot 5 \text{ MeOH}$  (**[Cr<sub>4</sub>]**),  $\{[12\text{-MC}_{\text{Cr(III)N}(\text{OMeShiH})(\text{OMeShi})_3\text{-4}}](\text{py})_8\text{Cl}\} \cdot x\text{H}_2\text{O}$  (**OMe-[Cr<sub>4</sub>]**) and  $\{[12\text{-MC}_{\text{Cr(III)N}(\text{ShiH})(\text{Shi})_3\text{-4}}](\gamma\text{-py})_8\text{Cl}\} \cdot 3.75 \text{ H}_2\text{O} \cdot 0.5 \text{ O}$  (**pic-[Cr<sub>4</sub>]**). These molecules exhibit a [12-MC-4] cavity with a reversed repeating unit. The cavity is not occupied by a guest ion and does not show bridging co-ligands. The crystallization ability of the complexes was optimized from **[Cr<sub>4</sub>]** to **pic-[Cr<sub>4</sub>]** by changing the co-ligand. The larger cavity could be obtained due to a change of the ligand orientation. Three of the four chromium(III) ions are coordinated a *cis*-propeller configuration while one chromium(III) ion shows a *trans*-configuration of the chelating ligand. Thus, Cr<sub>4</sub> is in-plane *trans*-arranged by the two chelating ligands which cannot lead to a [9-MC-3] cavity. Further investigations in ESI mass spectrometry reveal a pattern with less coordinated co-ligands of **pic-[Cr<sub>4</sub>]**. However, at 100°C the intact **pic-[Cr<sub>4</sub>]** molecule could be detected. In contrast to the [9-MC-3] cavity, the vacant metallacrown **pic-[Cr<sub>4</sub>]** all chromium(III) ions are antiferromagnetically coupled which leads to a spin ground state of  $S_T = 0$ . An electrochemical reduction of the chromium(III) ions was detected at potentials lower than 2 V leading to a wide electrochemical window of reduction stability for further applications e.g., surface deposition.

In the second part of this thesis, anisotropic lanthanide(III) ions were implemented to study SMM behavior. Six different *3d-4f* complexes were synthesized. The presented dysprosium(III) and terbium(III) guest ions possess a large spin ground state which is combined with large magnetic anisotropies  $D$ . Thus, these essential requirements for SMM behavior should lead to slow relaxation of magnetization. The targeted ligand design within the metallacrown was used to further optimize the SMM properties as the symmetry and packing of the ligands play a crucial role in the development of such compounds. A variation of co-ligands and bases was employed to alter the structural properties. The complexes  $\{\text{Dy}^{\text{III}}(\mu_2\text{-NO}_3)(\mu_2\text{-SO}_4)[15\text{-MC}_{\text{Cr(III)N}((\text{t}bu)_2\text{Shi})_5\text{-5}}](\text{py})_8\} \cdot 2 \text{ py} \cdot \text{MeOH}$  (**[Cr<sub>5</sub>Dy]**),  $[(\text{Cr}^{\text{III}})_6(\text{Tb}^{\text{III}})_4(\text{MeOH})_2(\text{py})_6(\text{t}bu)_2\text{Shi})_4((\text{t}bu)_2\text{ShiH})_2] \cdot 4 \text{ py} \cdot 2 \text{ MeOH}$  (**[Cr<sub>6</sub>Tb<sub>4</sub>]**),  $[\text{Cr}^{\text{III}}_4\text{Dy}^{\text{III}}_2(\mu_2\text{-OOCPh})_2(\text{MeOH})_2(\text{py})_6((\text{t}bu)_2\text{Shi})_4((\text{t}bu)_2\text{Sal})_2] \cdot 3 \text{ MeOH}$  (**Sal-[Cr<sub>4</sub>Dy<sub>2</sub>]**),  $(\text{Hpy})_2[\text{Cr}^{\text{III}}_4\text{Tb}^{\text{III}}_2(\mu_2\text{-OOCPh})_{0.5}(\text{py})_6((\text{t}bu)_2\text{Shi})_4((\text{t}bu)_2\text{ShiH})_2((\text{t}bu)_2\text{SalH})_{3.5}] \cdot 3 \text{ MeOH}$  (**Sal-[Cr<sub>4</sub>Tb<sub>2</sub>]**),  $(\text{Hpy})_2[\text{Cr}^{\text{III}}_4\text{Dy}^{\text{III}}_2(\mu_2\text{-OOCPh})_4(\text{py})_6(\text{Shi})_4(\text{ShiH})_2] \cdot 2 \text{ MeOH}$  (**[Cr<sub>4</sub>Dy<sub>2</sub>]**), and



$\{\text{Dy}^{\text{III}}(\mu_2\text{-}\eta^3\text{-ShiH}_2)_2[12\text{-MCCr}(\text{III})\text{N}(\text{Shi})_4\text{-4}](\text{MeOH})(\text{py})_4(\text{MeO})\} \cdot 2 \text{ MeOH} \cdot 2 \text{ py} \cdot 2 \text{ H}_2\text{O}$  (**[Cr<sub>4</sub>Dy]**) were obtained and investigated.

Firstly, a [15-MC-5] metallacrown with 3,5-di-*tert*-butylsalicylhydroxamic acid was synthesized (**[Cr<sub>5</sub>Dy]**). The unusual angle of coordination of the salicylhydroxamic acid derivate leads to a bent structure of the metallacrown. In this structure, only one chromium(III) ring metal ion is coordinated in a *cis*-propeller configuration while the other four chromium(III) ions exhibit a planar *trans*-coordination, leading to a large cavity. A dysprosium(III) guest ion was coordinated, which leads (together with two bridging co-ligands) to a pentagonal bipyramidal geometry ( $D_{5h}$ ). This complex would be the ideal candidate to study the SMM performance. However, most likely, a byproduct formed, which was shown by the magnetic data and revealed by the crystallization of the analog terbium(III) containing complex **[Cr<sub>6</sub>Tb<sub>4</sub>]**.

Secondly, two clusters **Sal-[Cr<sub>4</sub>Dy<sub>2</sub>]** and **Sal-[Cr<sub>4</sub>Tb<sub>2</sub>]** with bridging 3,5-di-*tert*-butylsalicylic acid co-ligands and 3,5-di-*tert*-butylsalicylhydroxamic acid as ligand were synthesized. However, this coordination did not lead to the formation of metallacrowns but clusters containing two lanthanide(III) and four chromium(III) ions. Especially **Sal-[Cr<sub>4</sub>Tb<sub>2</sub>]** showed the *in-situ* formation of 3,5-di-*tert*-butylsalicylic acid which should be avoided to obtain a metallacrown. Furthermore, in both complexes 3,5-di-*tert*-butylsalicylic acid coordinates in different flexible bridging coordination modes which cannot lead to heterometallic clusters in a controlled way.

Thus, the exchange of 3,5-di-*tert*-butylsalicylhydroxamic acid to salicylhydroxamic acid led to the complex **[Cr<sub>4</sub>Dy<sub>2</sub>]**. In this complex, only the used benzoate is bridging the two dysprosium(III) ions with each other and to a chromium(III) ion in a reliable coordination. The two dysprosium(III) ions are coordinated by eight ligands and show a distorted triangular dodecahedron geometry. This symmetry is not suppressing QTM leading to no detected AC signal. The four chromium(III) ions are all coordinated in a *trans*-coordination which leads to a partly [12-MC-4] cavity. However, incomplete deprotonation of salicylhydroxamic acid prevented a further coordination of chromium(III) ions that would lead to a [Cr-N-O] repeating unit.

For the first time a [12-MC-4] metallacrown containing both chromium(III) and lanthanide(III) ion is obtained by the synthesis of complex **[Cr<sub>4</sub>Dy]**. **[Cr<sub>4</sub>Dy]** shows slow relaxation of magnetization and an energy barrier of  $U_{\text{eff}} = 9.3 \text{ cm}^{-1}$  (13.4 K) was estimated. In this complex equivalent mixture of *trans*- and *cis*-configurations of the chelating ligands of the four chromium(III) ring metal ions leads to a bent [12-MC-4] cavity. Additionally, the coordination of the larger dysprosium(III) guest ion may have influenced the composition and cavity size of **[Cr<sub>4</sub>Dy]**.

A completely new family of homo- and heterometallic chromium(III) containing metallacrowns has been established in this thesis. In the following, two future perspectives for applications of the obtained complexes are presented. Overall, the stability of the homometallic chromium(III) compounds under ESI conditions was proved to enable further processing for surface preparations. This thesis is an important milestone to achieve deposition of metallacrowns onto surfaces.

Therefore, an exemplary project with the group of Prof Ziegler from the collaborative research center *Spin+X* was initiated. Here, the molecules are dissolved and sprayed onto a surface with comparable conditions to the ESI mass spectrometry method. Essential information, such as the temperature stability or the potential range of a stable oxidation state are now available and show a feasible chance for the adsorption conditions. A method will be developed to analyze the surface with IR spectroscopy. Thus, the IR spectra of the bulk can be compared to changes of the vibration bands after the immobilization process. Additional analysis tools like scanning tunneling microscopy should be used to investigate the surface coverage. Furthermore, deposition of **[Cr<sub>4</sub>Dy]** would be very interesting to follow because of the slow relaxation of magnetization. A comparison of the SMM performance in the bulk and on the surface would be very intriguing to investigate.

Additionally, another approach can be pursued regarding these magnetic compounds by using the magnetocaloric effect (MCE). This MCE is a change of the magnetic materials' temperature  $\Delta T_{ad}$  by altering an applied magnetic field. Applications of MCE for molecule-based material involve so called "magnetic coolers". In this molecule-based MCE materials an adiabatic demagnetization results in a temperature decrease of the material.<sup>[1]</sup> This effect can be utilized in cryogenic magnetic refrigeration on a molecular level.<sup>[2]</sup> Although this phenomena is known since the 1930s, only in the last decade molecular building blocks were investigated on MCE. Therefore, despite the fact that every paramagnetic compound shows MCE in small amounts, a few complexes exhibit large entropy changes  $\Delta S_m$  or temperatures changes  $\Delta T_{ad}$  to realistically replace expensive <sup>3</sup>He cooling.<sup>[2]</sup> Manganese(II) ions are often used in MCE compounds due to the isotropic electron configuration with a spin  $S = 5/2$ .<sup>[3]</sup> However, oxidation to anisotropic manganese(III) ions is a major challenge. The thermodynamic origin of MCE is the change of the magnetic entropy  $S_m$  per mole ( $R = N_A k_B$ ) since  $2S+1$  magnetic levels are present for a compound with spin  $S$ . Thus, by changing the magnetization of a compound by an external magnetic field, magnetic entropy is altered due to the change in the magnetic order. If the total entropy of a compound must be constant while altering the magnetic field (= adiabatic condition), a temperature change of the compound is observed. This can be explained by the compensation of this change in the magnetic entropy by the entropy associated within the lattice. To obtain a correlation between the magnetization  $M$ , the applied magnetic field  $H$ , the temperature  $T$ , and the change in entropy  $\Delta S_m$ , the Maxwell equation for the magnetic entropy must be considered.<sup>[4]</sup>

Prerequisite for a large effect in MCE are large spin ground states, weak exchange coupling, no magnetic anisotropy and therefore low lying close spin states.<sup>[4,5]</sup> Then, altering the temperature or external magnetic field in very small steps, many energy levels can be populated. By using the metallocrown scaffold, the magnetic exchange interaction of the metal ions can be influenced to generate high-spin ground states.<sup>[5]</sup> This was observed for the [9-MC-3] cavity of **[Cr<sub>3</sub>Cr]** and **(*tbu*)<sub>2</sub>-[Cr<sub>3</sub>Cr]**. The importance of the two competing exchange interactions is shown once more because this leads to a high spin ground state. The Zeeman simulation for **[Cr<sub>3</sub>Cr]** and **(*tbu*)<sub>2</sub>-[Cr<sub>3</sub>Cr]** showed exactly the high density of spin states which are separated only by a few wavenumbers. Furthermore, the chromium(III) ions do not exhibit anisotropy and relatively weak exchange interactions for e.g., compared to the copper(II) metallocrowns.

Additionally, isotropic gadolinium(III) ions are used for their MCE performance.<sup>[6–9]</sup> Already in 1926, Debye reported the temperature properties of gadolinium(III) sulfate in relation to the magnetic field.<sup>[10]</sup> In this case the spin ground state of  $S = 7/2$  and the weak magnetic coupling of the shielded  $4f$  orbitals is facilitated. **[Cr<sub>4</sub>Dy<sub>2</sub>]** and **[Cr<sub>4</sub>Dy]** would be ideal candidates for the exchange of dysprosium(III) ions by implementing gadolinium(III) ions in these complexes and investigating their MCE properties. Therefore, heat capacity measurements of the analog **[Cr<sub>4</sub>Gd<sub>2</sub>]** and **[Cr<sub>4</sub>Gd]** heterometallic metallacrowns as well as of for **[Cr<sub>3</sub>Cr]** and **(t<sup>bu</sup>)<sub>2</sub>-[Cr<sub>3</sub>Cr]** would be a promising future perspective of this thesis.

In conclusion, an interesting variety of possible influence factors on molecular structures has been shown in the field of  $3d$  and  $3d$ - $4f$ -based metallacrowns that contain kinetic inert chromium(III) ions. Promising future applications at this very fascinating field of coordination and magnetochemistry were outlined and should be pursued in future work.

## 5.1. References

- [1] M. Fitta, R. Pelka, P. Konieczny, M. Balanda, *Crystals* **2019**, *9*, 9.
- [2] V. K. Pecharsky, K. A. Gschneidner Jr, *J. Magn. Magn. Mater.* 1999, *200*, 44–56.
- [3] Y.-C. Chen, F.-S. Guo, J.-L. Liu, J.-D. Leng, P. Vrábel, M. Orendáč, J. Prokleška, V. Sechovský, M.-L. Tong, *Chem. – Eur. J.* 2014, *20*, 3029–3035.
- [4] M. Evangelisti, E. K. Brechin, *Dalton Trans.* 2010, *39*, 4672–4676.
- [5] C. Y. Chow, R. Guillot, E. Rivière, J. W. Kampf, T. Mallah, V. L. Pecoraro, *Inorg. Chem.* 2016, *55*, 10238–10247.
- [6] C. Cui, J.-P. Cao, X.-M. Luo, Q.-F. Lin, Y. Xu, *Chem. – Eur. J.* n.d., *0*, DOI 10.1002/chem.201802804.
- [7] A. K. Mondal, H. S. Jena, A. Malviya, S. Konar, *Inorg. Chem.* 2016, DOI 10.1021/acs.inorgchem.6b00177.
- [8] Y.-Z. Zheng, M. Evangelisti, R. E. P. Winpenny, *Angew. Chem. Int. Ed Engl.* 2011, *50*, 3692–3695.
- [9] E. V. Salerno, J. W. Kampf, V. L. Pecoraro, T. Mallah, *Inorg. Chem. Front.* 2021, *8*, 2611–2623.
- [10] P. Debye, *Ann. Phys.* 1926, *386*, 1154–1160.

## 6. Experimental Part and Supporting Information

This Chapter is divided according to the order of the parts in Chapter 4 “Results and discussions”.

### Overview of content

6. Experimental part and supporting information .....	136
6.1. Supporting information for Chapter 4.1.....	139
6.1.1. Structure determination .....	140
6.1.2. Crystal packing.....	142
6.1.3. Coordination of ligand.....	143
6.1.4. Isomers .....	144
6.1.5. SHAPE calculations .....	146
6.1.6. Synthesis.....	147
6.1.7. IR spectroscopy .....	148
6.1.8. UV-Vis Spectroscopy.....	148
6.1.8. Powder XRD.....	149
6.1.9. Simulation of Zeeman splitting .....	150
6.1.10. Magnetization measurement.....	151
6.1.11. References.....	151
6.2.1. Supporting information for Chapter 4.1.2.1.....	152
6.2.1.1. Synthesis of 5- <i>tert</i> -butylmethyl salicylate.....	152
6.2.1.2. Synthesis of 5- <i>tert</i> -butylsalicylhydroxamic acid.....	153
6.2.1.3. Synthesis of Fe(III)( $\mu_2$ -OOCPh) <sub>3</sub> [9-MC <sub>Fe(III)L2</sub> -3](MeOH) <sub>3</sub> ( <sup>t</sup> bu-[Fe <sub>3</sub> Fe]).....	154
6.2.1.4. Structure determination.....	156
6.2.1.5. Continuous Shape Measurements.....	159
6.2.1.6. Evaluation of magnetic data .....	160
6.2.1.7. Cyclic voltammetry.....	161
6.2.1.8. NMR spectra .....	163
6.2.1.9. IR spectra.....	164
6.2.2. Supporting information for Chapter 4.1.2.2.....	164
6.2.2.1. Synthesis of chromium pivalate (Cr <sub>3</sub> O(O <sub>2</sub> <i>Ctert</i> -butyl) <sub>6</sub> (H <sub>2</sub> O) <sub>3</sub> )(O <sub>2</sub> <i>Ctert</i> -butyl) HO <sub>2</sub> <i>Ctert</i> -butyl).....	164
6.2.2.2. Synthesis of 3,5-di- <i>tert</i> -butylsalicylate .....	166
6.2.2.3. Synthesis of 3,5-di- <i>tert</i> -butylsalicylhydroxamic acid .....	167
6.2.2.4. Synthesis of [9-MC-3] ( <sup>t</sup> bu) <sub>2</sub> -[Cr <sub>3</sub> Cr].....	168
6.2.2.5. Structure determination.....	169
6.2.2.6. Continuous Shape Measurements of ( <sup>t</sup> bu) <sub>2</sub> -[Cr <sub>3</sub> Cr].....	173
6.2.2.7. Magnetic evaluation of data.....	174

---

6.2.2.8. Electrospray ionization mass spectrometry (ESI) .....	175
6.2.2.9. Cyclic voltammetry.....	180
6.2.2.10. NMR spectra.....	181
6.2.2.11. Infrared spectra.....	183
6.3. Supporting information for Chapter 4.1.3. ....	185
6.3.1. Synthesis of vacant ShiH <sub>3</sub> .....	185
6.3.2. Synthesis of 4-methoxy salicylhydroxamic acid.....	186
6.3.3. Synthesis of vacant OMe Shi.....	187
6.3.4. Synthesis of pic-[Cr <sub>4</sub> ].....	188
6.3.5. Synthesis of 3-hydroxy-2-naphtylhydroxamic acid (Nha).....	189
6.3.6. Synthesis of Nha-[Cr <sub>4</sub> ] .....	190
6.3.7. Structure determination of [Cr <sub>4</sub> ]and OMe-[Cr <sub>4</sub> ] .....	191
6.3.8. Structure determination of pic-[Cr <sub>4</sub> ] .....	192
6.3.9. Continuous Shape Measurements.....	194
6.3.10. Evaluation of magnetic data .....	196
6.3.11. Electrospray Ionization mass spectrometry (ESI) .....	198
6.3.12. Cyclic voltammetry.....	205
6.3.13. NMR.....	207
6.3.14. Infrared spectra.....	208
6.4. Supporting information for Chapter 4.2.1. ....	211
6.4.2.1. Synthesis of [Cr <sub>5</sub> Dy] [15-MC-5] metallocrown .....	211
6.4.2.2. Synthesis of [Cr <sub>6</sub> Tb <sub>4</sub> ].....	212
6.4.2.3. Synthesis of [Cr <sub>2</sub> Dy <sub>4</sub> ] with 3,5-di- <i>tert</i> -butyl salicylhydroxamate .....	213
6.4.2.4. Synthesis of [Cr <sub>2</sub> Tb <sub>4</sub> ] with 3,5-di- <i>tert</i> -butyl salicylhydroxamate .....	214
6.4.2.5. Synthesis of [Cr <sub>2</sub> Dy <sub>4</sub> ] ShiH <sub>3</sub> .....	215
6.4.2.6. Synthesis of [Cr <sub>2</sub> Dy <sub>4</sub> ] ShiH <sub>3</sub> .....	216
6.4.2.7. Synthesis of [Cr <sub>4</sub> Dy] [12-MC-4]metallocrown .....	217
6.4.2.8. Structure determination of [Cr <sub>5</sub> Dy] and [Cr <sub>6</sub> Tb <sub>4</sub> ] .....	219
6.4.2.9. Structure determination of Sal-[Cr <sub>4</sub> Dy <sub>2</sub> ] and Sal-[Cr <sub>4</sub> Tb <sub>2</sub> ] including 3,5-di- <i>tert</i> -butylsalicylhydroxate and corresponding acid .....	220
6.4.2.10. Structure determination [Cr <sub>4</sub> Dy <sub>2</sub> ].....	222
6.4.2.11. Structure determination [Cr <sub>4</sub> Dy].....	224
6.4.2.12. Continuous Shape Measurements .....	225
6.4.2.13. Evaluation of magnetic data .....	227
6.4.2.14. Infrared spectra.....	228
6.5. General procedure of solvothermal synthesis .....	231
7. Instrumental part.....	232

---

7.1. General.....	232
7.2. Infrared spectroscopy.....	232
7.3. X-Ray analysis.....	232
7.4. Continuous Shape Measurement.....	232
7.5. NMR spectroscopy.....	232
7.6. ESI mass spectrometry.....	232
7.7. Cyclic voltammetry.....	233
7.8. SQUID magnetometry.....	233
7.9. Elemental Analysis.....	233
8. References.....	234

## 6.1. Supporting information for Chapter 4.1.

### Materials and Methods

All chemicals were used without further purification and were purchased from Alfa Aesar, Acros Organics and Fisher Chemicals. The starting material Cr<sub>3</sub>piv was synthesized using literature procedure.<sup>[1]</sup>

C, H and N elemental analyses were carried out on a Foss Heraeus Vario EL (Elementar Analysensysteme GmbH, Langenselbold, Germany) at the microanalytical laboratories of the Department of Chemistry at the Johannes Gutenberg University Mainz. The infrared absorption spectrum was collected at room temperature in a range of 3000–450 cm<sup>-1</sup> on a Thermo Fischer NICOLET Nexus FT/IR-5700 spectrometer (Thermo Fischer Scientific, Waltham, MA, USA) equipped with Smart Orbit ATR Diamond cell (Thermo Fischer Scientific, Waltham, MA, USA). UV–Vis absorption measurements were performed in MeOH between 200 nm and 990 nm on a JASCO V-570 UV/Vis/NIR spectrophotometer (JASCO Inc, Easton, MD, USA). Powder XRD data were collected on a D2PHASER (Bruker, Karlsruhe, Germany).

X-ray diffraction data for the structure analysis were collected from suitable single crystals at 173 K with a STOE IPDS 2T at the Johannes Gutenberg University Mainz. The structures were solved with ShelXT<sup>[2]</sup> and refined with ShelXL<sup>[3]</sup> implemented in the program Olex2<sup>[4]</sup>.

Magnetic data of a microcrystalline sample were collected using a Quantum Design SQUID magnetometer MPMSXL in a temperature range between 4–300 K with an applied field of 1 kOe (0.1 T). The magnetic contribution from the holder were experimentally determined and subtracted from the measured susceptibility data. The contribution from underlying diamagnetism was corrected using the estimation in equation  $\chi^{\text{dia}} = kM \cdot 10^{-6} \text{ cm}^3 \text{ mol}^{-1}$ .<sup>[5]</sup> In this equation,  $M$  is the molecular weight of the compound and  $k$  is equal to 0.5. The fit program PHI was used to fit and simulate the magnetic data.<sup>[6]</sup>

**6.1.1. Structure determination**

CCDC 2047296 contains the supplementary crystallographic data for this molecule. These data can be obtained free of charge via [www.ccdc.cam.ac.uk/data\\_request/cif](http://www.ccdc.cam.ac.uk/data_request/cif), or by emailing [data\\_request@ccdc.cam.ac.uk](mailto:data_request@ccdc.cam.ac.uk), or by contacting The Cambridge Crystallographic Data Centre, 12 Union Road, Cambridge CB2 1EZ, UK; fax: +441223 336033.

**Table S 1.** Crystallographic data of complex.

empirical formula	C <sub>49</sub> H <sub>70</sub> Cr <sub>4</sub> N <sub>6</sub> O <sub>19</sub>
formula weight g/mol	1255.11
color	Blue
crystal size / mm	0.04 x 0.213 x 0.52
crystal system	Monoclinic
space group	P2 <sub>1</sub> /n
a/ Å	12.5478(7)
b/ Å	18.4387(8)
c/ Å	25.5018(13)
α/°	90
β/°	95.325(4)
γ/°	90
Z	4
temperature / K	193
volume/ Å <sup>3</sup>	5874.8(5)
radiation	Mo-Kα (λ = 0.71073)
range for data collection /°	2.35 to 26.00
measured reflexes	11481
independent reflexes	6274
F(000)	2616
index ranges	-15 ≤ h ≤ 15 -22 ≤ k ≤ 22 -31 ≤ l ≤ 25
completeness	0.994
max. and min. transmission	0.9638 / 0.7845
R <sub>int</sub>	0.0764
R <sub>sigma</sub>	0.1034
data/restraints/parameters	11481 / 164 / 790
goodness-of-fit on F <sup>2</sup>	1.043
<sup>a</sup> R <sub>1</sub> [I > 2σ (I)]	0.0837
<sup>b</sup> wR <sub>2</sub> [I > 2σ (I)]	0.1929
R <sub>1</sub> [all data]	0.1623
wR <sub>2</sub> [all data]	0.2391

<sup>a</sup>R<sub>1</sub> = Σ(|F<sub>o</sub> - F<sub>c</sub>|) / Σ|F<sub>o</sub>|, <sup>b</sup>wR<sub>2</sub> = [Σ[w(F<sub>o</sub><sup>2</sup> - F<sub>c</sub><sup>2</sup>)<sup>2</sup>] / Σ[w(F<sub>o</sub><sup>2</sup>)<sup>2</sup>]<sup>1/2</sup>, w = 1/[σ<sup>2</sup>(F<sub>o</sub><sup>2</sup>) + (ap)<sup>2</sup> + bp], p = [max(F<sub>o</sub><sup>2</sup>, 0) + 2F<sub>c</sub><sup>2</sup>]/3.



**Table S 2.** Selected bond distances of complex.

Atom 1	Atom 2	Distance/ Å	Atom 1	Atom 2	Distance/ Å
Cr1	N4	2.0984(1)	Cr3	O7	1.9076(1)
Cr1	O10	2.0276(1)	Cr3	O14	1.9874(1)
Cr1	N1	1.9936(1)	Cr3	N6	2.1240(1)
Cr1	O9	2.0390(1)	Cr3	O6	1.9942(1)
Cr1	O8	1.9536(1)	Cr3	O5	1.9413(1)
Cr1	O1	1.9188(1)	Cr3	N3	1.9963(1)
Cr2	O1	1.9939(1)	Cr4	O3	1.9725(1)
Cr2	N2	2.0033(1)	Cr4	O11	1.9472(1)
Cr2	O3	1.9912(1)	Cr4	O9	1.9644(1)
Cr2	O2	1.9700(1)	Cr4	O15	1.9751(1)
Cr2	N5	2.1140(1)	Cr4	O6	1.9679(1)
Cr2	O4	1.8876(1)	Cr4	O13	1.9594(1)

**Table S 3.** Selected angles of ring ions Cr1, Cr2, Cr3 to central guest ion Cr4.

Atom 1	Atom 2	Atom 3	Angle /°
Cr1	O9	CR4	113.001(2)
Cr2	O3	CR4	113.672(3)
Cr3	O6	CR4	111.887(3)

**Table S 4.** Selected torsion Angles of neighboring ring ions Cr1, Cr2 and Cr3.

Atom 1	Atom 2	Atom 3	Atom 4	Angle /°
Cr1	N1	O3	Cr2	-158.775(3)
Cr2	N2	O6	Cr3	-147.071(3)
Cr3	N3	O9	Cr1	-156.925(3)

### 6.1.2. Crystal packing

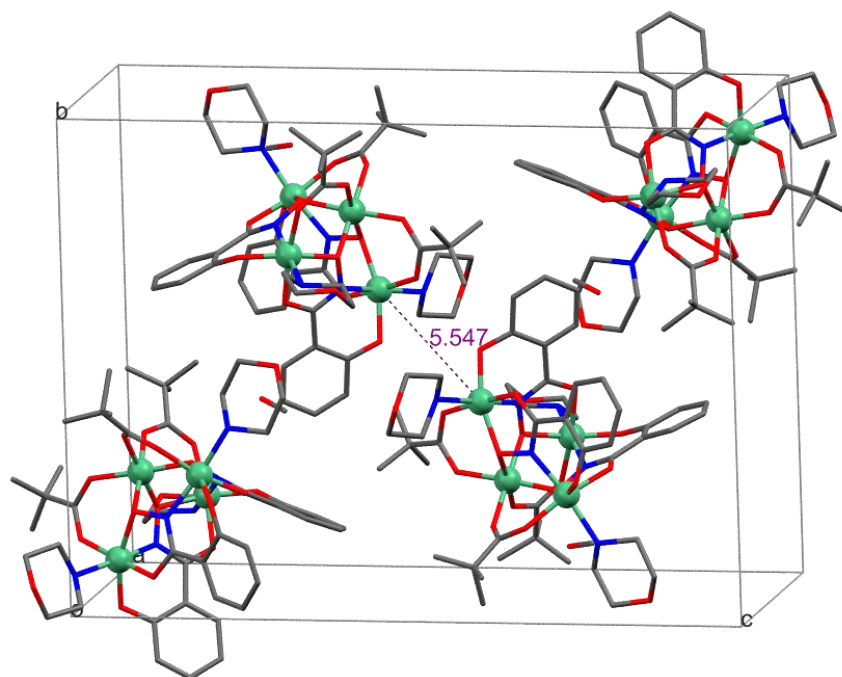


**Figure S 1.** Crystal packing of complex including solvent molecules (MeOH) from crystal structure. Color code: chromium(III) ions green, oxygen red, nitrogen blue, carbon grey.

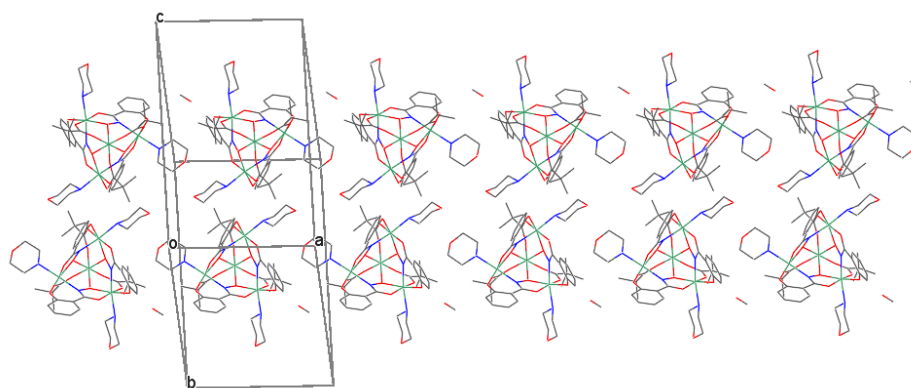
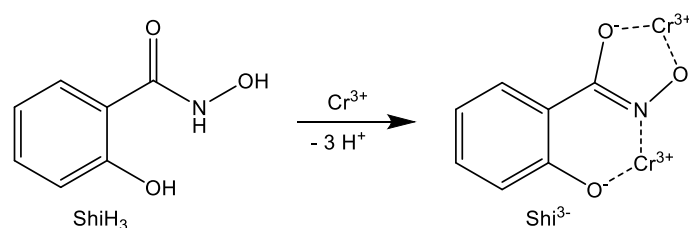


**Figure S 2.** Chain-like packing of molecules along the *a* axis from crystal structure. Color code: chromium(III) ions green, oxygen red, nitrogen blue, carbon grey.

### 6.1.3. Coordination of ligand



**Scheme S 1.** Deprotonation of ligand  $\text{shiH}_3$  and complexation of two chromium(III) ions to form a six and a five membered ring.

#### Inner core

The average angle of  $\text{N-Cr}^{3+}\text{-O}$ , which is part of the repeating unit, is  $84^\circ$  (figure S3) and slightly smaller than the ideal octahedral angle of  $90^\circ$ . Worth mentioning here is the non-planarity of the inner core due to the small cavity.

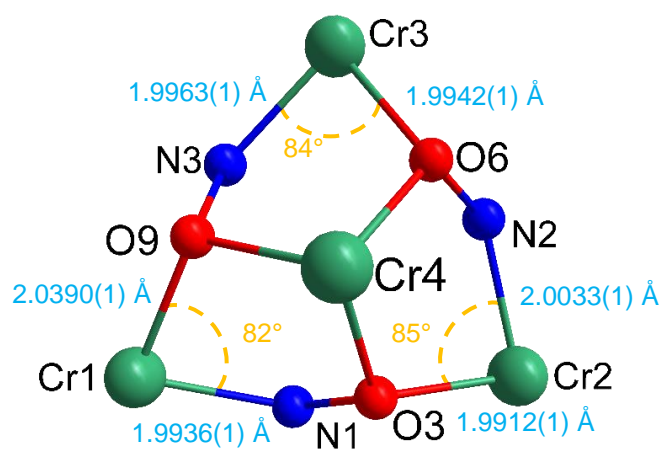


**Figure S 3.** Schematic representation of inner core, bond lengths and angles of  $\text{N-Cr}^{3+}\text{-O}$  within this core. Color code: chromium(III) ions green, oxygen red, nitrogen blue.

## 6.1.4. Isomers

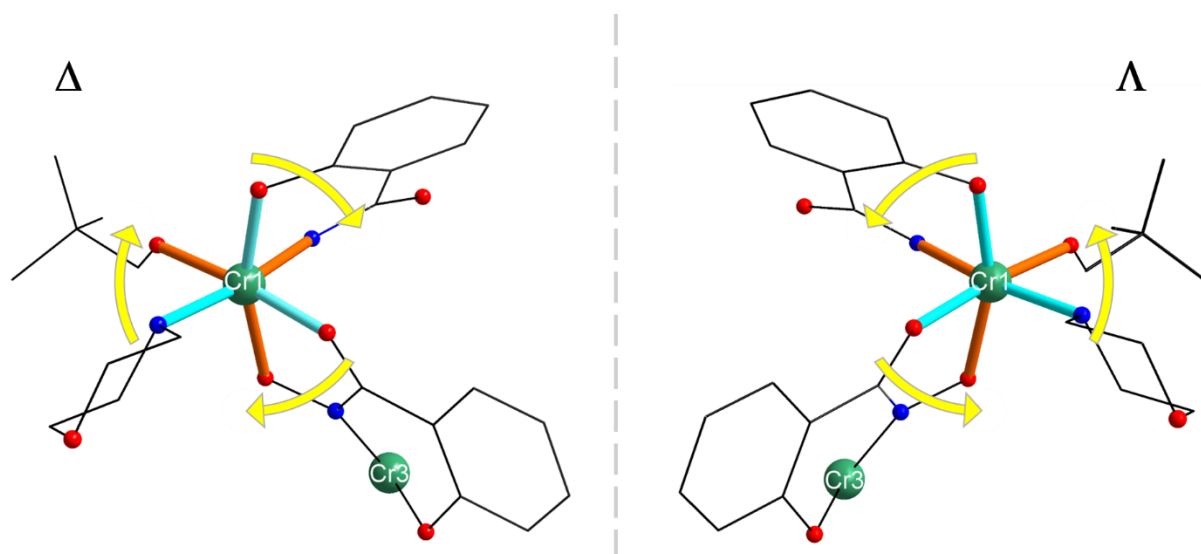


**Figure S 4.** Schematic representation of  $\Delta$  isomer (left) and  $\Lambda$  isomer (right) of the ring metal ion Cr1. Color code: chromium(III) ions green, oxygen red, nitrogen blue, carbon black.

To determine the chirality of the central Cr4 ion, only the chelate rings with the smallest number of atoms have to be taken into account. The rings are formed from the pivalate group bridging to a ring metal ion and the oxygen donor of the NO ligand bridging to the same ring metal ion. All other chelating rings that coordinate the central Cr4 ion contain more atoms. The central guest ion, Cr4, shows the same chirality as the ring metal ions resulting in a pseudo-C<sub>3</sub>-axis.

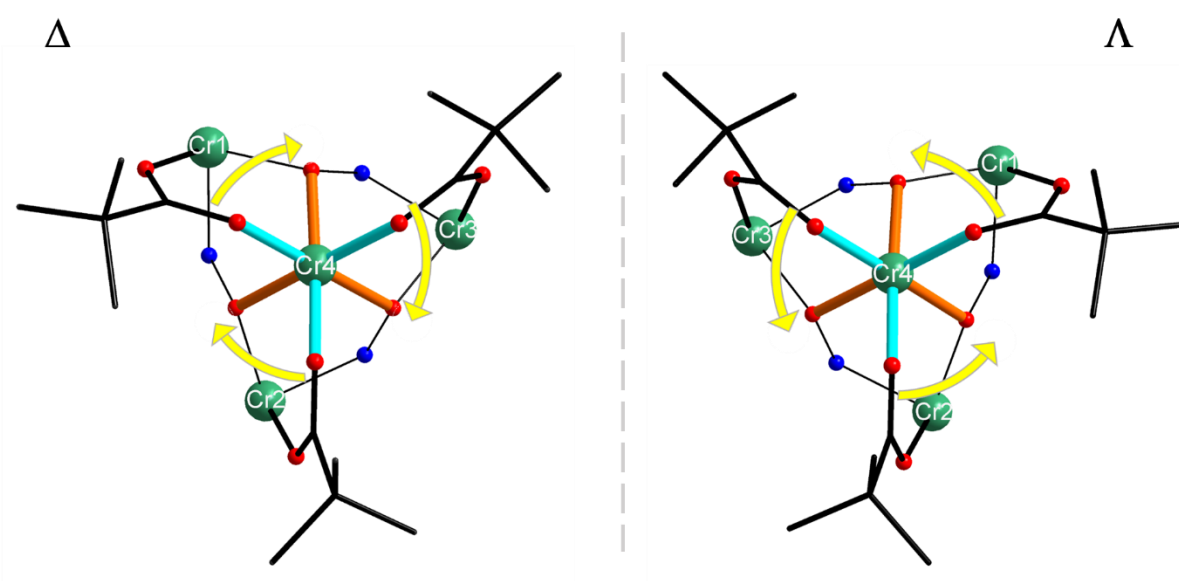


**Figure S 5.** Schematic representation of  $\Delta$  isomer (left) and  $\Lambda$  isomer (right) of the central ion Cr4. Color code: chromium(III) ions green, oxygen red, nitrogen blue, carbon black.

**Cis configuration**

Upon coordination of the shi3- ligands to the chromium ions, a five-membered chelate ring is forming via the iminophenolate moiety and a six-membered chelate ring *via* the hydroximate group. As the ligands are oriented *cis* to each other the metal ions adopt an asymmetric *cis*-propeller configuration.

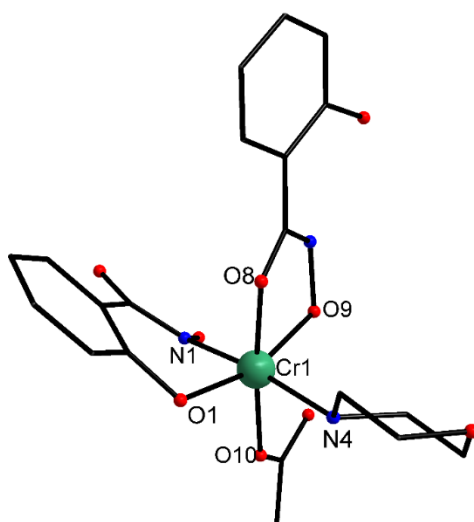


**Figure S 6.** Labeled schematic representation of the *cis* propeller configuration of the ring metal ion Cr1 with two shi3- and two co-ligands. Color code: chromium(III) ions green, oxygen red, nitrogen blue, carbon black.

#### Out of plane coordination

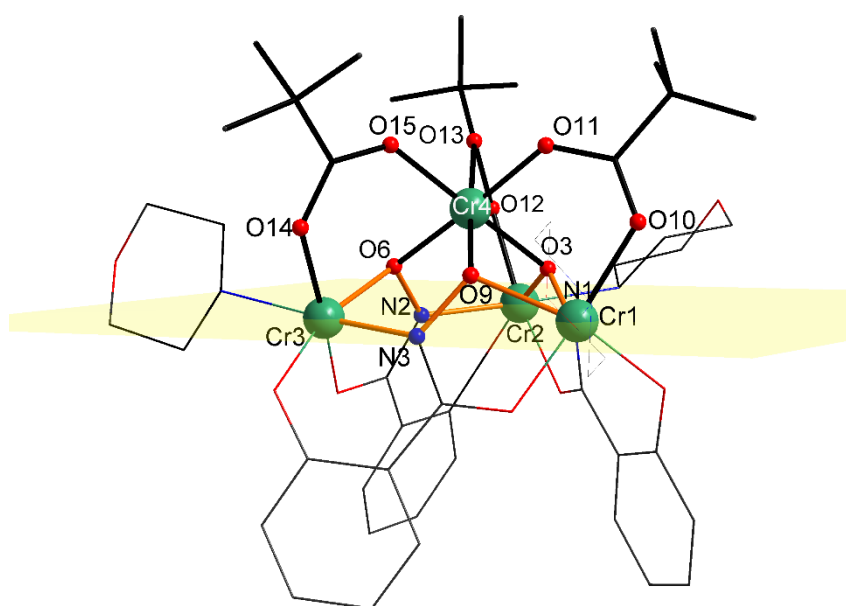


**Figure S 7.** Schematic representation of structure as a “side-on” view with out of plane coordination of chromium(III) guest ion in [Cr<sub>3</sub>Cr]-MC and Cr1-Cr2-Cr3 plane (yellow). Hydrogen atoms are omitted for clarity. Color code: chromium(III) ions green, oxygen red, nitrogen blue, carbon black.

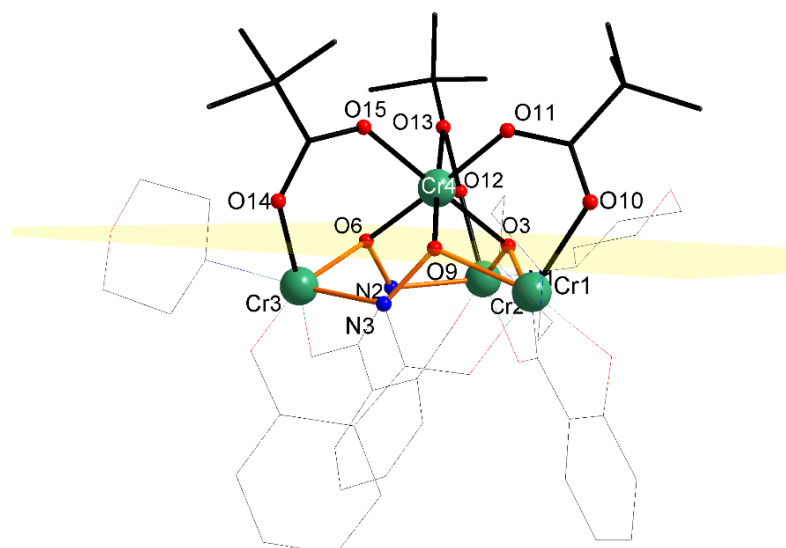


**Figure S 8.** Schematic representation of O3-O6-O9 plane (yellow). Hydrogen atoms are omitted for clarity. Color code: chromium(III) ions green, oxygen red, nitrogen blue, carbon black.

### 6.1.5. SHAPE calculations

**Table S 5.** Calculated deviations from ideal polyhedra for Cr1, Cr2, Cr3 and Cr4 *via* continuous shape measurements.

Polyhedron <sup>c</sup>	Cr1	Cr2	Cr3	Cr4
<b>HP-6</b>	31.085	31.422	31.272	32.953
<b>PPY-6</b>	22.321	23.969	22.059	29.296
<b>OC-6</b>	<b>1.176</b>	<b>0.732</b>	<b>1.275</b>	<b>0.043</b>
<b>TPR-6</b>	11.399	12.342	10.715	15.959
<b>JPPY-6</b>	25.667	27.341	25.389	32.792

<sup>c</sup> abbreviations: HP-6 hexagon ( $D_{6h}$ ); PPY-6 pentagonal pyramid ( $C_{5v}$ ); OC-6 octahedron ( $O_h$ ); TPR-6 trigonal prism ( $D_{3h}$ ); JPPY-6 Johnson pentagonal pyramid J2 ( $C_{5v}$ )

## Ideal octahedral coordination

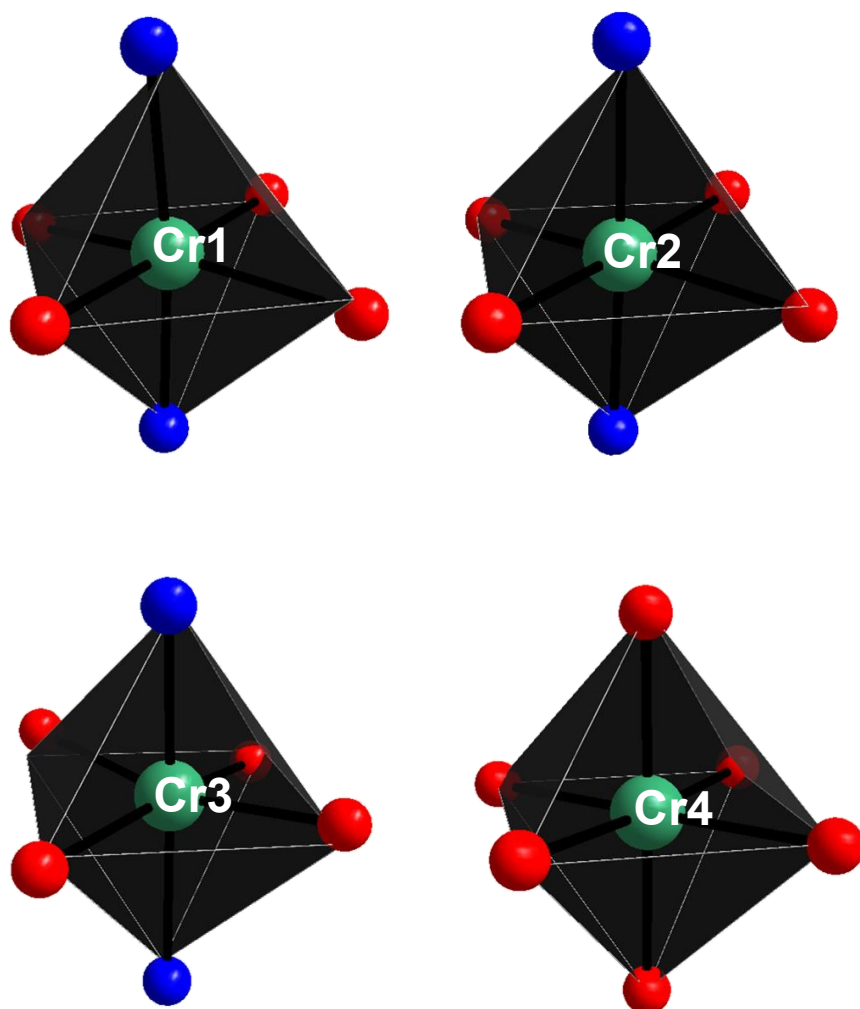


**Figure S 9.** Schematic representation of the octahedral polyheders of Cr1, Cr2, Cr3 and Cr4. The light-gray lines define the vertices of the ideal octahedral polyeder. Color code: chromium(III) ions green, oxygen red, nitrogen blue.

### 6.1.6. Synthesis

Cr<sub>3</sub>piv (0.33 mmol, 313 mg), shiH<sub>3</sub> (1 mmol, 153 mg) and morpholine (5 mmol) were dissolved in MeOH (15 ml) and heated at 120 °C in a Teflon-lined autoclave for 12 hours. The solution was allowed to cool slowly to room temperature and crystals were collected after 4 weeks *via* slow evaporation in yield of 4%. The dried sample was analyzed C<sub>48</sub>H<sub>66</sub>Cr<sub>4</sub>N<sub>6</sub>O<sub>18</sub>: C 47.14, H 5.44, N 6.87. Found: C 47.24, H 5.47, N 6.41. Selected ATR IR data ( $\tilde{\nu}$  /cm<sup>-1</sup>) = 3215 w, 2958 s, 2907 m, 2864 m, 1601 m, 1576 s, 1541 s, 1533 s, 1519 m, 1485 m, 1427 s, 1402 m, 1358 s, 1382 m, 1363 m, 1306 m, 1255 m, 1237 m, 1227 m, 1193 m, 1160 s, 919 m, 898 m, 879 m, 849 m, 825 s, 785 m, 758 s, 702 m, 618 m, 580 s, 552 m.

### 6.1.7. IR spectroscopy

The IR spectrum shows all expected characteristic vibration modes of the coordinated pivalate, salicylhydroxamate, and morpholine ligands.

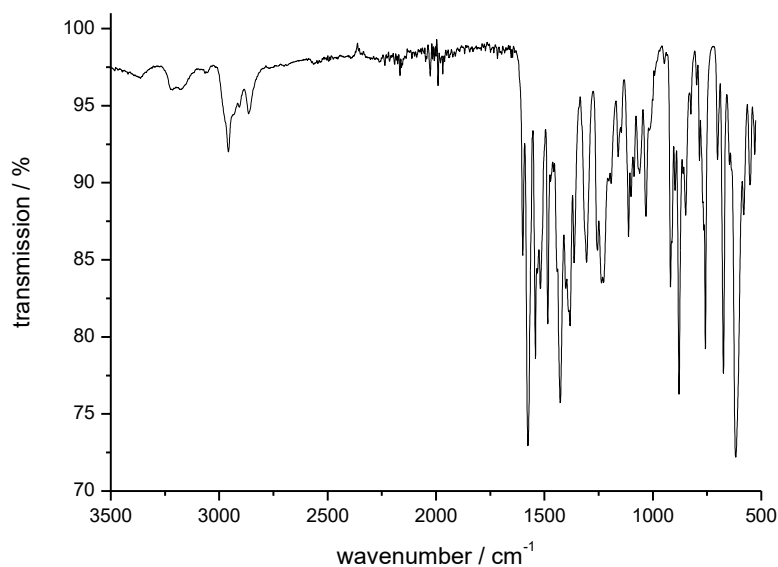


Figure S 10. IR spectrum of complex.

### 6.1.8. UV-Vis Spectroscopy

The UV/VIS spectrum for salicylhydroxamic acid reveals two bands at 237 nm and 300 nm in a methanol solution, which can be assigned to  $\pi-\pi^*$  and  $n-\pi^*$  excitations<sup>[7]</sup>. Upon coordination, these ligand-centered transitions are shifted to 256 nm and 356 nm in the MC. We expect a band in the UV region at higher energy for the third spin-allowed transition  ${}^4A_{2g} \rightarrow {}^4T_{1g} (P)$ , which cannot be detected for this metallacrown in a methanol solution.

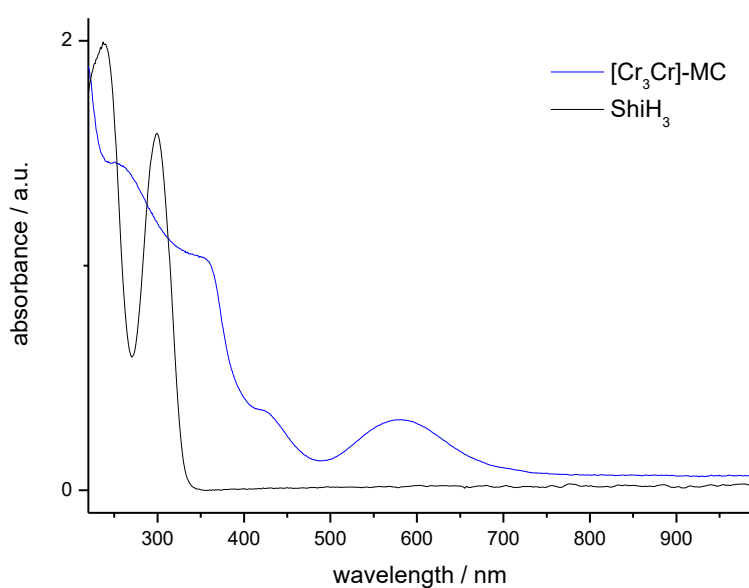
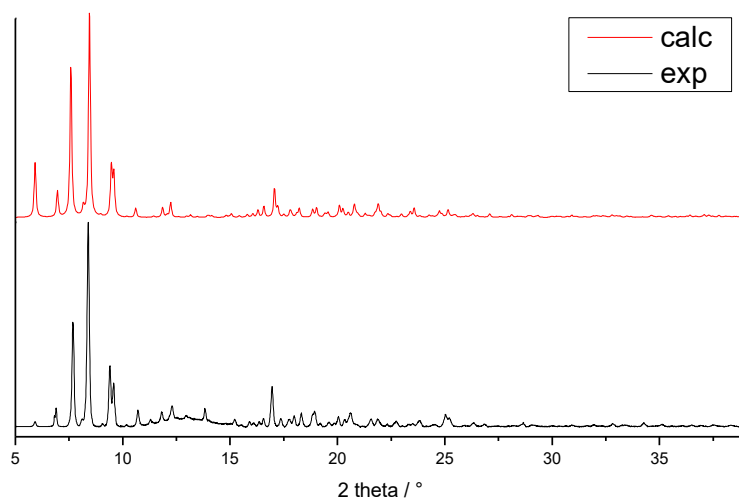


Figure S 11. UV/Vis spectrum of [Cr<sub>3</sub>Cr]-MC (blue) and ShiH<sub>3</sub> (black) in methanol.



**6.1.8. Powder XRD**

**Figure S 12.** Powder XRD of calculated (red) and measured (black) complex.

### 6.1.9. Simulation of Zeeman splitting

Figures S11 and S12 show the simulation of the Zeeman splitting for the  $[\text{Cr}_3\text{Cr}]$ -MC obtained from  $2J$  model (eq. 4) with the values for the best fit of the susceptibility data. At zero field the septet for the spin ground state of  $S_T = 3$  is energetically only  $5 \text{ cm}^{-1}$  lower than the next excited state of  $S_T = 2$ . Thus, the spin ground state is not well separated from the first excited state. In an applied field, the Zeeman splitting is more pronounced for the  $S = 3$  septet than for the excited states, which leads to a stronger energetic lowering of the ground state of higher magnetic fields. This means that the ground state of  $S_T = 3$  is more populated at higher fields and lower temperatures.

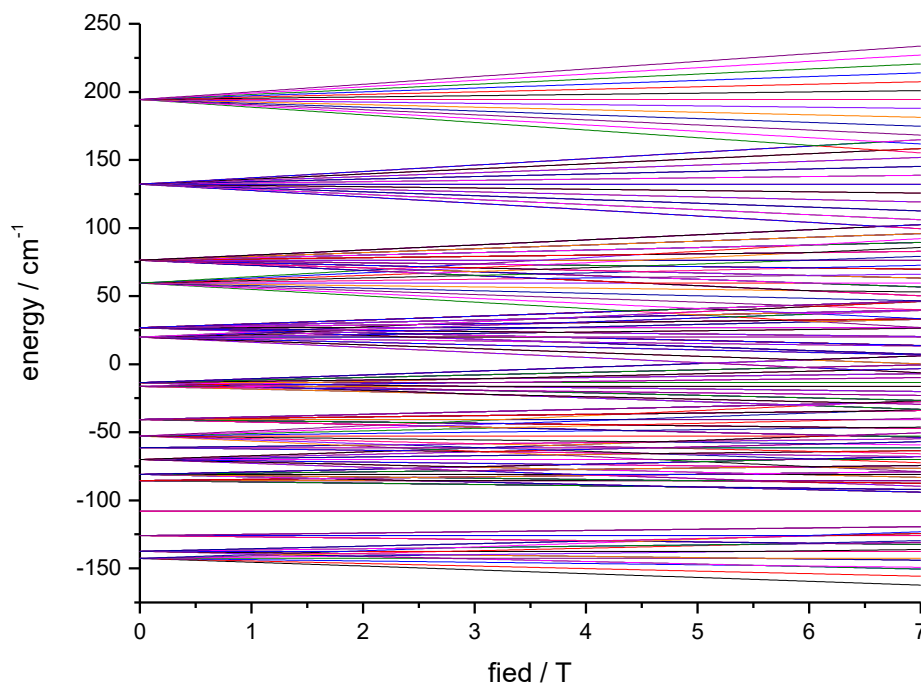


Figure S 13. Zeeman splitting field dependence of the different spin states of  $[\text{Cr}_3\text{Cr}]$ -MC.

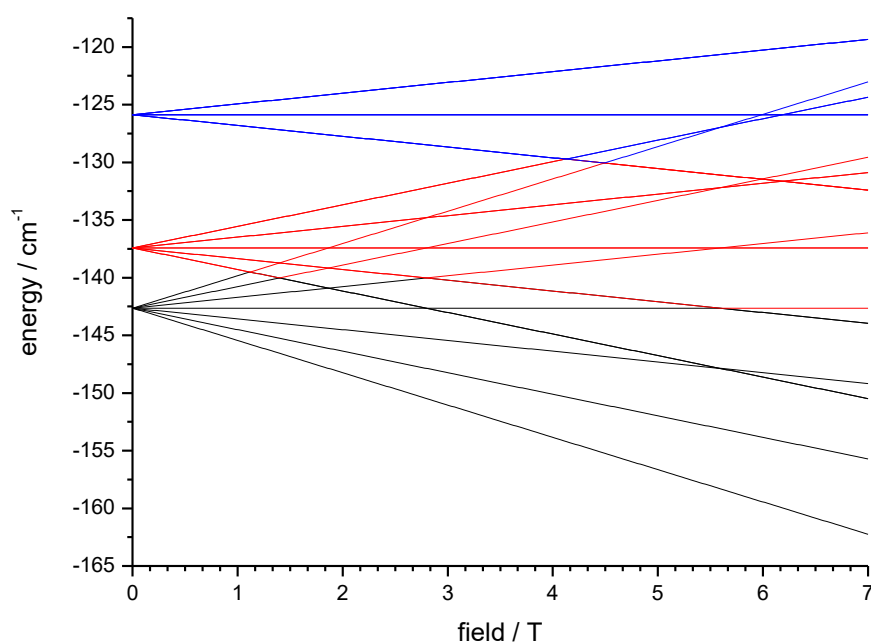
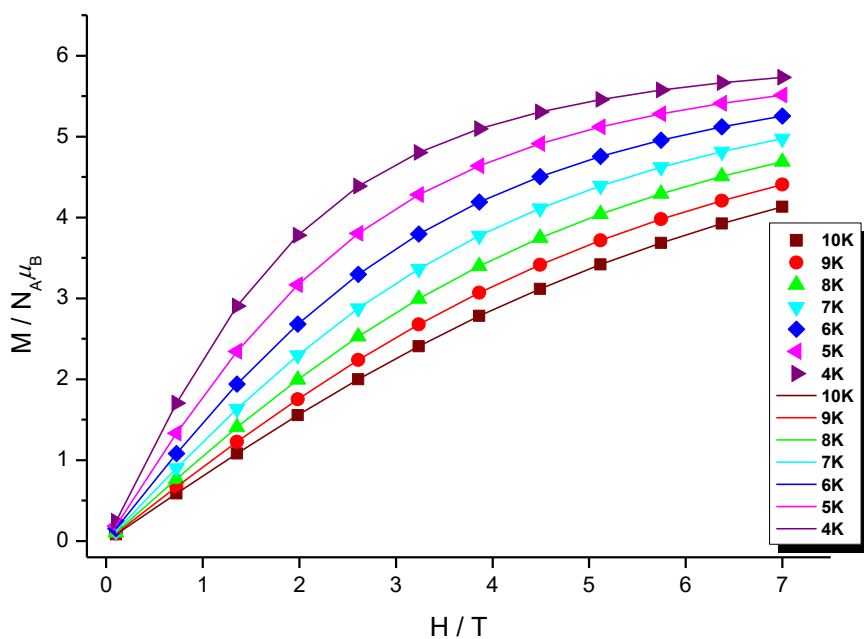


Figure S 14. Zoom-in of Zeeman splitting simulation of different the three lowest spin states.

## 6.1.10. Magnetization measurement

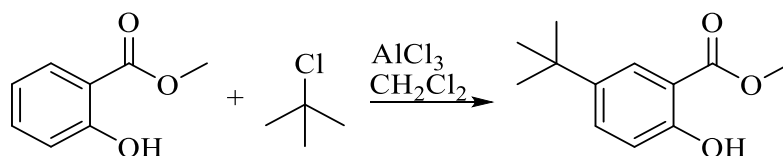


**Figure S 15.** Magnetization  $M$  vs field  $H$  plots in fields of 0.1–7 T and temperatures 4–10 K. Solid lines represent the fit of data.

## 6.1.11. References

- [1] A. Ghirri, J. van Tol, I. Vitorica-Yrezabal, G. A. Timco, R. E. P. Winpenny, *Dalton Trans.* **2015**, 44, 14027–14033.
- [2] G. M. Sheldrick, *Acta Crystallogr. Sect. Found. Adv.* **2015**, 71, 3–8.
- [3] G. M. Sheldrick, *Acta Crystallogr. Sect. C Struct. Chem.* **2015**, 71, 3–8.
- [4] O. V. Dolomanov, L. J. Bourhis, R. J. Gildea, J. a. K. Howard, H. Puschmann, *J. Appl. Crystallogr.* **2009**, 42, 339–341.
- [5] O. Kahn, *Molecular Magnetism*, VCH, New York, NY, **1993**.
- [6] N. F. Chilton, R. P. Anderson, L. D. Turner, A. Soncini, K. S. Murray, *J. Comput. Chem.* **2013**, 34, 1164–1175.
- [7] Sheetal, K. Nehra, R. Kaushal, S. Arora, D. Kaur, R. Kaushal, *Russ. J. Gen. Chem.* **2016**, 86, 154–160.

## 6.2.1. Supporting information for Chapter 4.1.2.1.

6.2.1.1. Synthesis of 5-*tert*-butylmethyl salicylate

## REN-TF-002:

Compound	$M / \frac{\text{g}}{\text{mol}}$	$m / \text{g}$	$n / \text{mol}$	$V / \text{mL}$	eq.
methyl salicylate	152.15	25.0	0.16	-	1.0
aluminium trichloride	133.34	31.4	0.24		1.4
<i>tert</i> -butyl chloride	92.57	16.7	0.18	20	1.1
dichloromethane	84.93	-	-	150	-

Procedure<sup>[8,9]</sup>

Methyl salicylic acid ester (25.0 g, 0.16 mol, 1.0 eq.) was dissolved in 150 mL dichloromethane. Aluminum trichloride (31.4 g, 0.24 mol, 1.4 eq.) was added under cooling of ice. After cooling the solution to room temperature, *tert*-butyl chloride (16.7 g, 0.18 mol, 1.1 eq.) was added dropwise over a period of 30 minutes. The reaction mixture was heated for 3 h under reflux of the solvent. Dichloromethane was removed by distillation under reduced pressure. The resulting red solid was dissolved in diethyl ether. The pH was adjusted to a value of 5 with 1 M HCl. The ethereal phase was separated from the aqueous phase *via* a separating funnel and extracted three times with 50 mL each of 1 M HCl and twice with 50 mL with brine. The aqueous phases were extracted twice with 50 mL of diethyl ether. The combined organic phases were dried over sodium sulfate. Diethyl ether was removed by distillation under reduced pressure. The residue was fractionally distilled under reduced pressure (product at 19 mbar, 135 °C).

## Analytic

yield  $m = 5.17 \text{ g}$  (2.4 mmol, 15% of theory)

IR ( $\tilde{\nu} / \text{cm}^{-1}$ ) = 3196  $\nu(\text{O-H})$ , 2955  $\nu(\text{CH}_3)$ , 2907, 2868, 1674  $\nu(\text{C=O})$ , 1614  $\nu(\text{C=C}_{\text{arom.}})$ , 1248  $\nu(\text{C-O-C})$ , 1194  $\delta(\text{O-CH}_3)$ , 1117  $\delta(\text{C-H}_{\text{arom.}})$ , 1084  $\nu(\text{C-O-C})$ , 904  $\delta(\text{C-H}_{\text{arom.}})$ .

<sup>1</sup>H-NMR (400 MHz, DMSO-*d*<sub>6</sub>,  $\delta$  / ppm): 10.36 (s, 1H, OH), 7.72 (d, 1H,  $J = 2.5 \text{ Hz}$  H-6), 7.60-7.59 (dd, 1H,  $J = 8.7, \text{H-2}$ ), 6.93 (d, 1H,  $J = 8.6 \text{ Hz}$ , H-3), 3.89 (s, 3H, H-15), 1.25 (s, 9H, H-11, H-12, H-13).

6.2.1.2. Synthesis of 5-*tert*-butylsalicylhydroxamic acid

## REN-TF-003:

compound	$M / \frac{\text{g}}{\text{mol}}$	$m / \text{g}$	$n / \text{mmol}$	$V / \text{mL}$	eq.
5- <i>tert</i> -butylmethyl salicylate	208.25	5.00	24	-	1.0
NH <sub>2</sub> OH·HCl	69.49	2.50	36	-	1.5
KOH	56.11	4.72	84	-	3.5
Methanol	32.04	-	-	60	-

Procedure<sup>[10]</sup>

Under argon atmosphere potassium hydroxide (4.72 g, 84 mmol, 1.5 eq.) and hydroxylamine hydrochloride (2.50 g, 36 mmol, 3.5 eq.) were dissolved separately in 30 mL of degassed methanol each. The potassium hydroxide solution was added to the hydroxylamine hydrochloride solution under argon atmosphere, while colorless potassium chloride precipitated. The potassium chloride was filtered under argon atmosphere. To the filtrate, 5-*tert*-butylsalicylic acid methyl ester (5.00 g, 24 mmol, 1.0 eq.) was added under stirring. The yellow reaction solution was stirred under argon atmosphere overnight at room temperature. The solvent was removed by distillation under reduced pressure. The resulting yellow oil was dissolved in water and adjusted to pH 6 with 1M HCl, a brown residue formed. The brown residue was dissolved in methanol and adjusted to a pH of 5 with 1M HCl. Yellow brownish crystals were obtained from the methanolic solution after storing in refrigerator after 10-14 days.

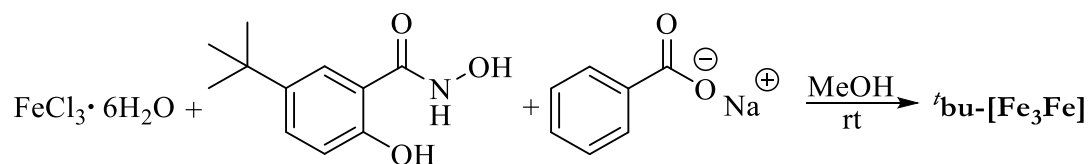
## Analytic

yield  $m = 2.36 \text{ g}$  (11 mmol, 47% of theory)

IR ( $\tilde{\nu} / \text{cm}^{-1}$ ) = 3302 (w), 3104 (m, br), 2958 (s), 2869 (m), 1624 (m), 1609 (s), 1566 (m), 1525 (s), 1499 (s), 1463 (m), 1414 (m), 1377 (m), 1361 (s), 1298 (m), 1265 (s), 1240 (s), 1201 (m), 1168 (s), 1125 (s), 1102 (s), 1048 (s), 938 (m), 921 (m), 908 (m), 845 (m), 821 (s), 782 (m), 708 (s), 660 (s), 607 (s), 583 (s), 546 (s), 468 (m).

<sup>1</sup>H-NMR (400 MHz, DMSO-d<sub>6</sub>,  $\delta$  /ppm): 12.09 (s, 1H, N-OH), 11.50 (s, 1H, NH), 9.30 (s, 1H, C-OH), 7.66 (s, 1H, H-6), 7.41 (d, 1H,  $J = 8.7$ , Hz H-2), 6.82 (d, 1H,  $J = 8.4$  Hz, H-3), 1.25 (s, 9H, H11, H12, H13).

ESI-MS  $m/z = \text{theo: } [M+H]^+ 210.1125, \text{exp: } 210.1126.$

6.2.1.3. Synthesis of Fe(III)( $\mu_2$ -OOCPh)<sub>3</sub>[9-MC<sub>Fe(III)L2</sub>-3](MeOH)<sub>3</sub> (bu-[Fe<sub>3</sub>Fe])

## REN-TF-033d:

compound	$M / \frac{\text{g}}{\text{mol}}$	$m / \text{mg}$	$n / \text{mmol}$	$V / \text{mL}$	eq.
$\text{FeCl}_3 \cdot 6\text{H}_2\text{O}$	270.29	73	0.27	-	1.3
5- <i>tert</i> -butyl salicylhydroxamic acid	209.24	42	0.20	-	1.0
methanol	32.04	-	-	10	-
$\text{NaOBz}$	144.11	86	0.60	-	3.0
$\text{Bu}_4\text{NClO}_4$	341.92	26	0.08	-	-

## Procedure

5-*tert*-butyl salicylhydroxamic acid (42 mg, 0.20 mmol, 1.0 eq.) and sodium benzoate (86 mg, 0.60 mmol, 3.0 eq.) were dissolved in 10 mL methanol under stirring. Iron(III) chloride hexahydrate (73 mg, 0.27 mmol, 1.3 eq.) was added to this solution while the solution was turning dark red immediately. After 5 minutes, tetrabutylammonium perchlorate (TBAP) (26 mg, 0.08 mmol) was added, the solution was stirred 40 minutes and then filtered. By slow evaporation of the solvent black hexagonal single crystals were obtained after 11 days.

## Analytics

yield  $m = 5$  mg (0.004 mmol per Fe, 6% of theory)

X-ray analysis (see Table S 6)

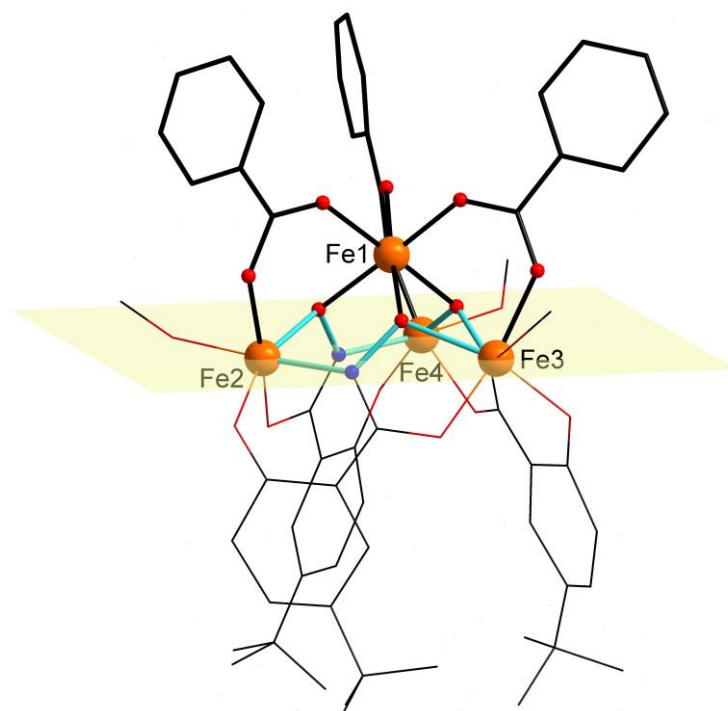


**Figure S 16** Schematic representation of structure as a “side-on” view with out of plane coordination of iron(III) guest ion Fe1 of 'bu-[Fe<sub>3</sub>Fe] and Fe2-Fe3-Fe4 plane (yellow). Hydrogen atoms are omitted for clarity. Color code: iron(III) ions orange, oxygen red, nitrogen blue, carbon black.

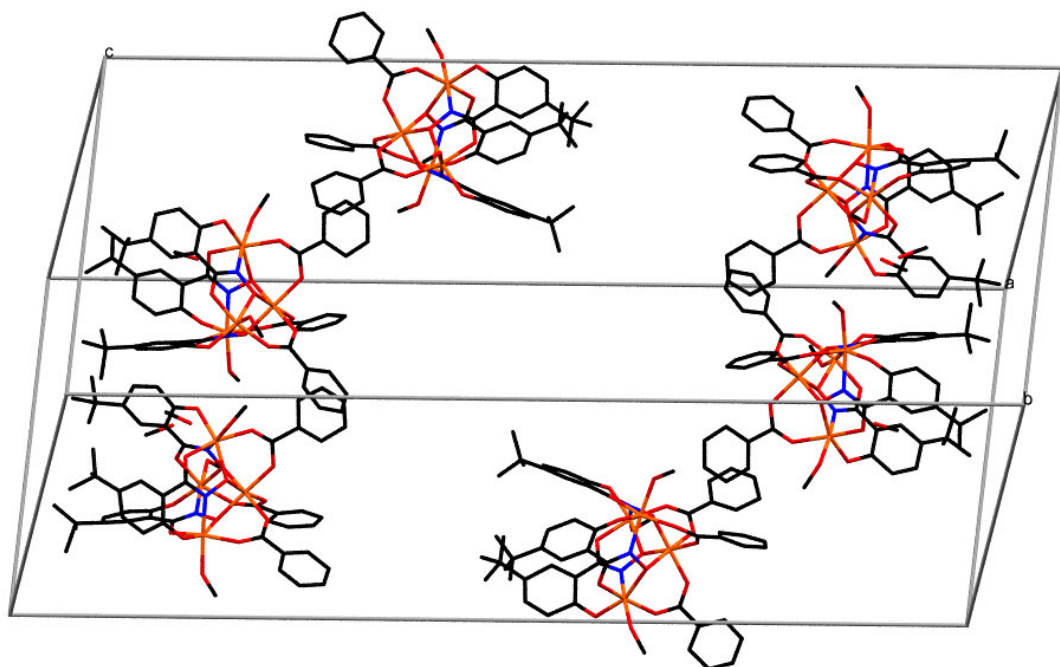


**Figure S 17** Schematic representation of the six molecules in the unit cell. Hydrogen atoms are omitted for clarity. Color code: iron(III) ions orange, oxygen red, nitrogen blue, carbon black. Solvent molecules are not shown.

## 6.2.1.4. Structure determination

Table S 6. Crystallographic data of complex **bu**-[Fe<sub>3</sub>Fe].

	<b>bu</b> -[Fe <sub>3</sub> Fe]
	REN-TF-033d
empirical formula	C <sub>57</sub> H <sub>60</sub> Fe <sub>4</sub> N <sub>3</sub> O <sub>18</sub>
formula weight g/mol	1298.490
overall formula	C <sub>174</sub> H <sub>188</sub> Fe <sub>12</sub> N <sub>9</sub> O <sub>57</sub>
overall formula g/mol	3987.52
crystal size / mm	0.22 x 0.163 x 0.05
crystal system	triclinic
space group	P-1
unit cell dimensions	
<i>a</i> / Å	17.5521(3)
<i>b</i> / Å	17.5490(3)
<i>c</i> / Å	48.6297(9)
$\alpha$ / °	84.1970(10)
$\beta$ / °	81.0730(10)
$\gamma$ / °	59.9330(10)
volume / Å <sup>3</sup>	12801.6(4)
cell formula units <i>Z</i>	2
density $\rho_{\text{calc}}$ / g cm <sup>-3</sup>	1.034
$\mu$ / mm <sup>-1</sup>	0.719
F(000)	4126
temperature / K	173
device type	STOE STADIVARI
radiation	Mo-K $\alpha$
independent reflexes	1.478 < $\theta$ < 28.827
index ranges	-18 < <i>h</i> < 19
	-18 < <i>k</i> < 17
	-50 < <i>l</i> < 56
collected reflections	54777
independent reflections	54777
completeness	0.371
max. and min. transmission	0.9852 and 0.2301
$R_{\text{int}}$	0.0628
$R_{\text{sigma}}$	
data/restraints/parameters	24825 / 6 / 1071
goodness-of-fit on $F^2$	1.469
$^a R_1$ [ $I > 2\sigma(I)$ ]	0.1462
$^b wR_2$ [ $I > 2\sigma(I)$ ]	0.4159
$R_1$ [all data]	0.1982
$wR_2$ [all data]	0.4387

$$^a R_1 = \Sigma(|F_o| - |F_c|) / \Sigma|F_o|, ^b wR_2 = [\Sigma[w(F_o^2 - F_c^2)^2] / \Sigma[w(F_o^2)^2]]^{1/2}, w = 1 / [\sigma^2(F_o^2) + (ap)^2 + bp], p = [\max(F_o^2, 0) + 2F_c^2] / 3.$$

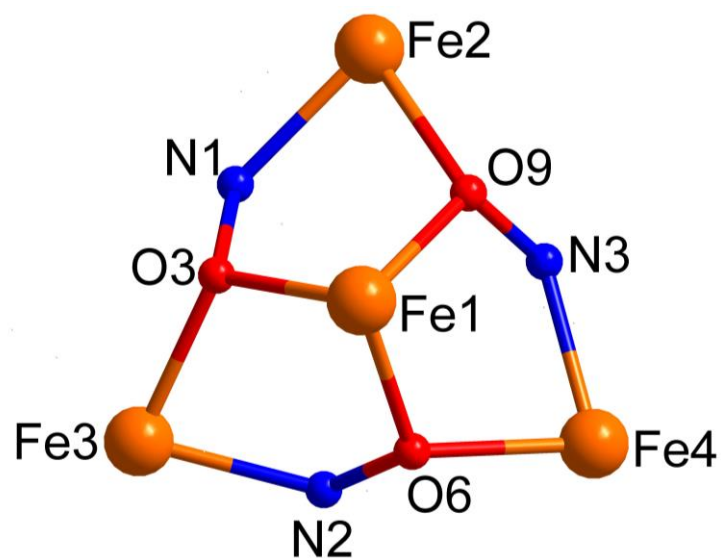
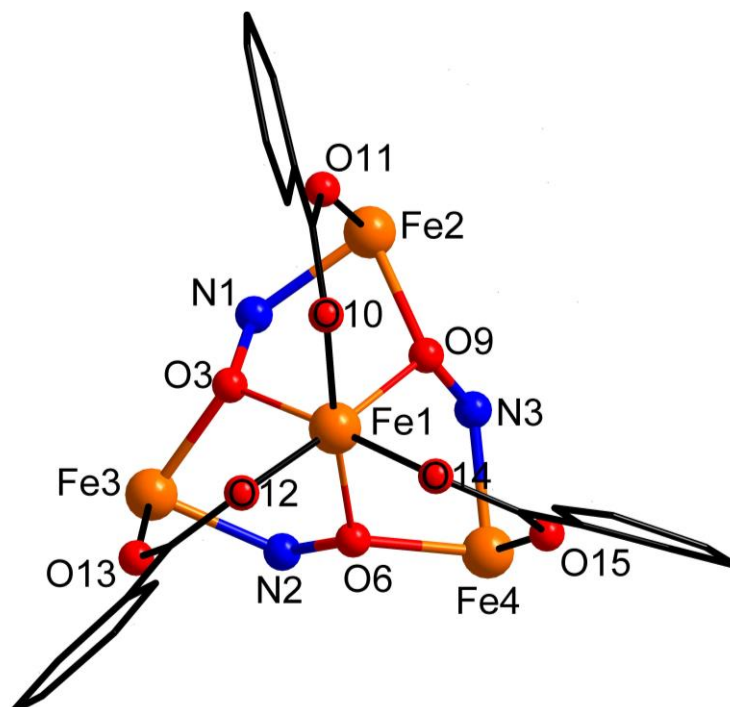


Table S 7. Selected bond length of **bu**-[Fe<sub>3</sub>Fe].

iron(III) ion	donor atom	bond length / Å	iron(III) ion	donor atom	bond length / Å
<b>Fe1</b>	O3	2.006(11)	<b>Fe5</b>	O21	2.019(10)
	O6	2.008(12)		O24	2.049(10)
	O9	2.013(12)		O27	2.028(11)
	O10	2.011(12)		O28	2.033(11)
	O12	1.984(13)		O30	2.021(12)
<b>Fe2</b>	O14	1.998(12)	O32	2.049(11)	
	O1	1.933(14)	<b>Fe6</b>	O19	1.913(12)
	O8	2.012(14)		O26	2.014(11)
	O9	2.082(11)		O27	2.042(10)
	O11	1.993(15)		O29	2.007(12)
O16	2.022(15)	O34		2.062(11)	
<b>Fe3</b>	N1	2.039(14)	N6	2.057(13)	
	O2	1.996(13)	<b>Fe7</b>	O20	1.972(12)
	O3	2.075(11)		O21	2.077(10)
	O4	1.931(15)		O22	1.938(11)
	O13	1.971(13)		O31	2.008(13)
O17	2.042(15)	O35		2.038(11)	
<b>Fe4</b>	N2	2.042(14)	N5	2.078(13)	
	O5	1.998(14)	<b>Fe8</b>	O23	1.993(11)
	O6	2.062(11)		O24	2.047(11)
	O7	1.899(15)		O25	1.886(12)
	O15	1.974(13)		O33	1.977(12)
O18	2.067(15)	O36		2.091(11)	
N3	2.046(14)	N4	2.063(13)		
iron(III) ion	donor atom	bond length			
<b>Fe9</b>	O39	2.002(11)			
	O42	2.027(10)			
	O45	1.997(10)			
	O46	2.001(11)			
	O48	2.038(11)			
<b>Fe10</b>	O50	2.005(12)			
	O37	1.919(12)			
	O44	1.975(11)			
	O45	2.079(10)			
	O47	1.952(12)			
<b>Fe11</b>	O52	2.033(12)			
	O52	2.033(12)			
	N7	2.064(13)			
	O38	1.977(12)			
	O39	2.070(11)			
<b>Fe12</b>	O40	1.933(11)			
	O49	1.991(13)			
	O53	2.053(10)			
	N8	2.067(13)			
	O41	1.994(12)			
O42	2.063(10)				
O43	1.912(11)				
O51	1.987(12)				
O54	2.021(12)				
N9	2.057(13)				

**Table S 8.** Selected angles of ring ions Fe2, Fe3 and Fe4 of **bu-[Fe<sub>3</sub>Fe]** for molecule a).

atoms	angles
N1 Fe2 O9	82.8(5)°
N2 Fe3 O3	81.4(5)°
N3 Fe4 O6	81.9(5)°

**Figure S 18.** Schematic repeating unit of **bu-[Fe<sub>3</sub>Fe]** for molecule a).**Figure S 19.** Schematic repeating unit including bridging benzoate ligands of **bu-[Fe<sub>3</sub>Fe]** for molecule a).

## 6.2.1.5. Continuous Shape Measurements

**Table S 9.** Calculated values for Continuous Shape Measurements for Fe1 of **4bu-[Fe<sub>3</sub>Fe]**.

abbreviation	symmetry	polyeder	CShM
HP-6	D <sub>6h</sub>	Hexagon	32.576
PPY-6	C <sub>5v</sub>	pentagonale Pyramide	28.366
OC-6	O <sub>h</sub>	Oktaeder	0.113
TPR-6	D <sub>3h</sub>	trigonales Prisma	14.422
JPPY-6	C <sub>5v</sub>	Johnson pentagonale Pyramide J2	32.71

**Table S 10.** Calculated values for Continuous Shape Measurements for Fe2 of **4bu-[Fe<sub>3</sub>Fe]**.

abbreviation	symmetry	polyeder	CShM
HP-6	D <sub>6h</sub>	hexagon	33.226
PPY-6	C <sub>5v</sub>	pentagonal pyramide	22.287
OC-6	O <sub>h</sub>	octaeder	1.479
TPR-6	D <sub>3h</sub>	trigonal prisma	9.914
JPPY-6	C <sub>5v</sub>	Johnson pentagonal pyramide J2	26.101

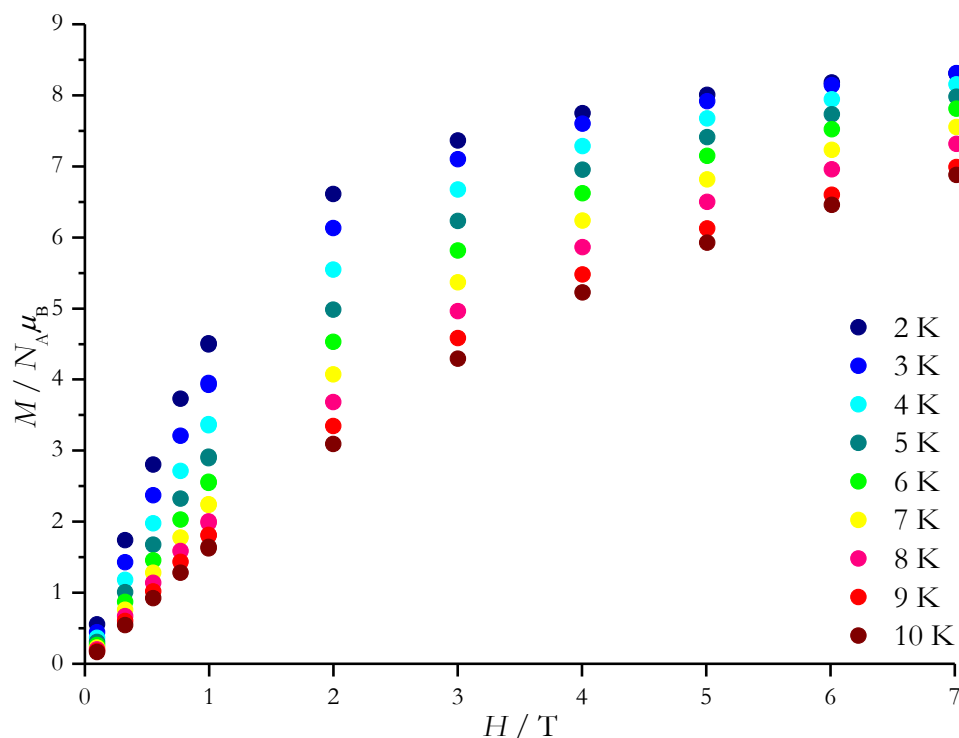
**Table S 11.** Calculated values for Continuous Shape Measurements for Fe3 of **4bu-[Fe<sub>3</sub>Fe]**.

abbreviation	symmetry	polyeder	CShM
HP-6	D <sub>6h</sub>	hexagon	32.532
PPY-6	C <sub>5v</sub>	pentagonal pyramide	22.098
OC-6	O <sub>h</sub>	octaeder	1.410
TPR-6	D <sub>3h</sub>	trigonal prisma	10.103
JPPY-6	C <sub>5v</sub>	Johnson pentagonal pyramide J2	25.908

**Table S 12.** Calculated values for Continuous Shape Measurements for Fe4 of **4bu-[Fe<sub>3</sub>Fe]**.

abbreviation	symmetry	polyeder	CShM
HP-6	D <sub>6h</sub>	hexagon	32.839
PPY-6	C <sub>5v</sub>	pentagonal pyramide	21.879
OC-6	O <sub>h</sub>	octaeder	1.539
TPR-6	D <sub>3h</sub>	trigonal prisma	10.036
JPPY-6	C <sub>5v</sub>	Johnson pentagonal pyramide J2	25.577

## 6.2.1.6. Evaluation of magnetic data


 Figure S 20. Magnetization measurement of  $4\text{bu-}[\text{Fe}_3\text{Fe}]$  at 2-10 K.

The Equation S1 and S2 can be taken from the PHI User Manual v3 (Nicholas Chilton).

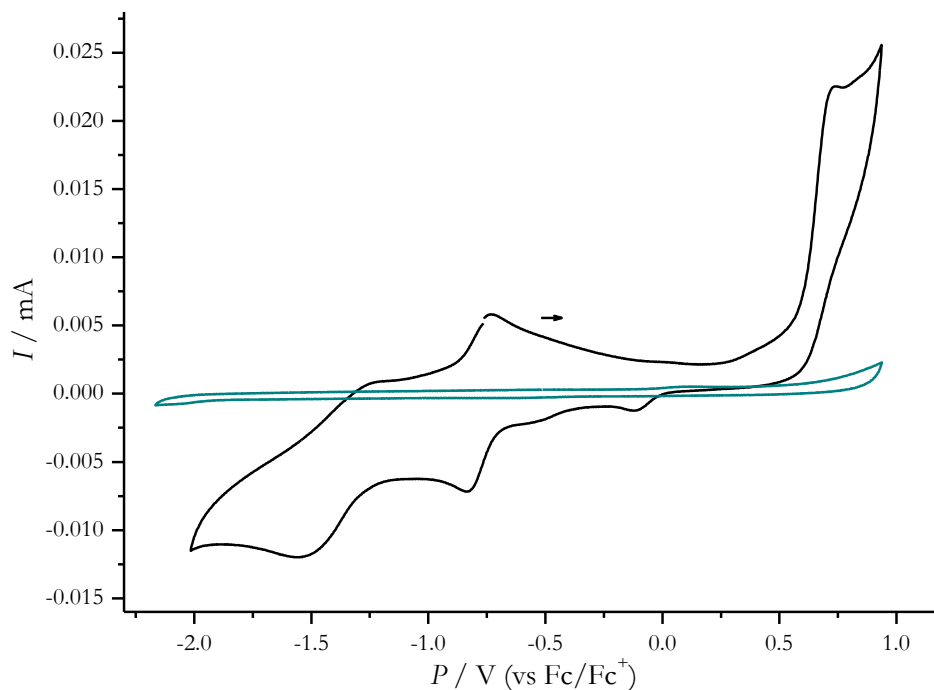
$$\chi_{zj} = \frac{\chi_{\text{TIP}}}{1 - \left( \frac{zJ}{N_A \mu_B^2} \right) \chi_{\text{TIP}}} \quad (\text{S1})$$

$$\chi_{\text{TIP}} = \chi_{\text{calc}} + \text{TIP} \quad (\text{S2})$$

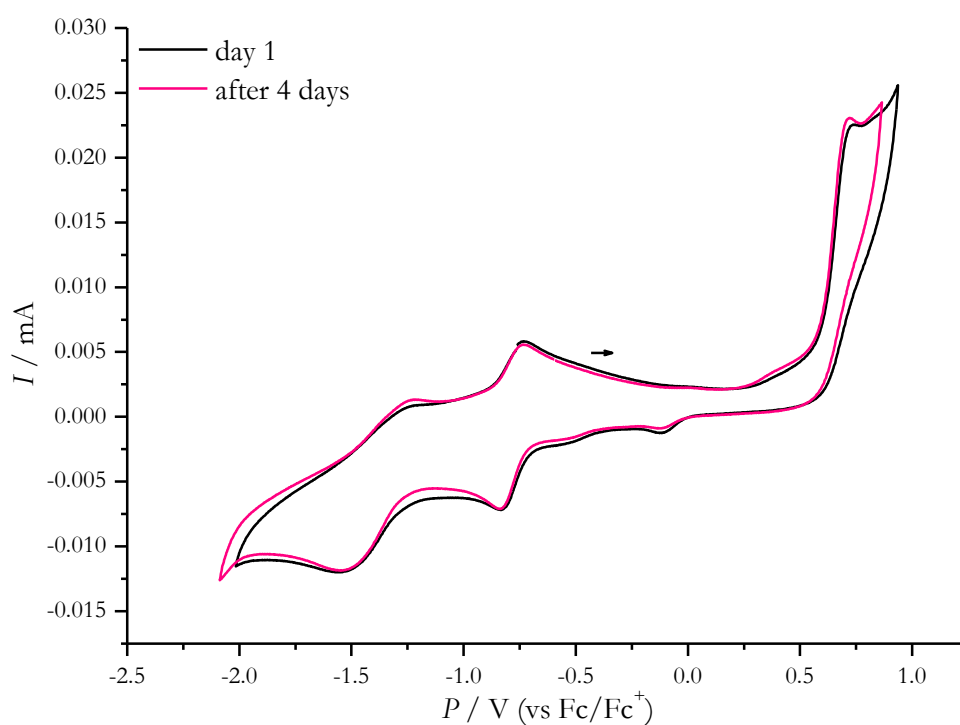
The error residuals and uncertainties are calculated using the sum of squares approach as shown in Equation S3 for the magnetization and susceptibility. If multiple data sets like the susceptibility and magnetization data are simultaneously calculated, the total residual is calculated as the product of the individual sum of squares errors for each data set.

$$\text{Residual} = \left[ \sum_{i=1}^{\text{points}} (M_{\text{exp}} - M_{\text{calc}})^2 \right] \left[ \sum_{i=1}^{\text{points}} (\chi_{\text{exp}} - \chi_{\text{calc}})^2 \right] \quad (\text{S3})$$

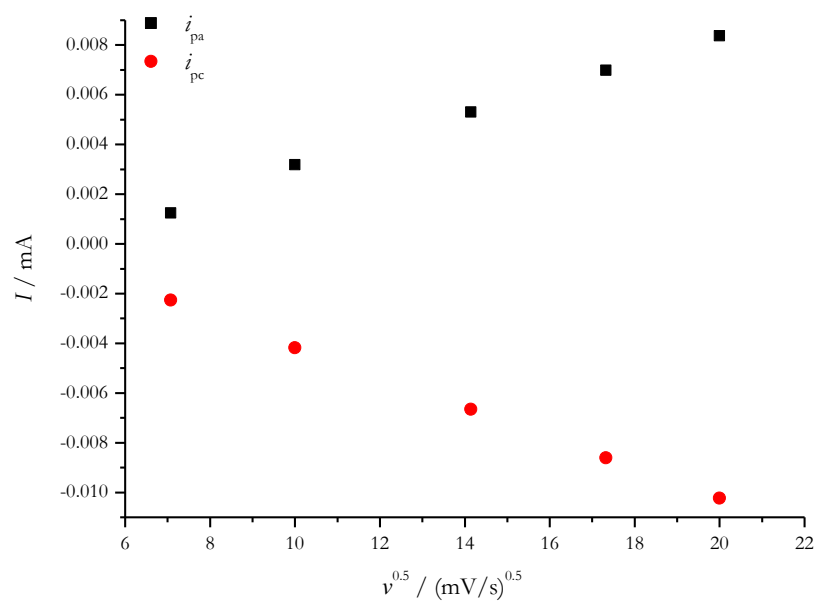
## 6.2.1.7. Cyclic voltammetry



**Figure S 21.** Cyclic voltammogram of **tBu-[Fe<sub>3</sub>Fe]** including the blank solvent window of dimethylformamide with a concentration of 100 mM of the conducting salt tetrabutylammonium hexafluorophosphate.

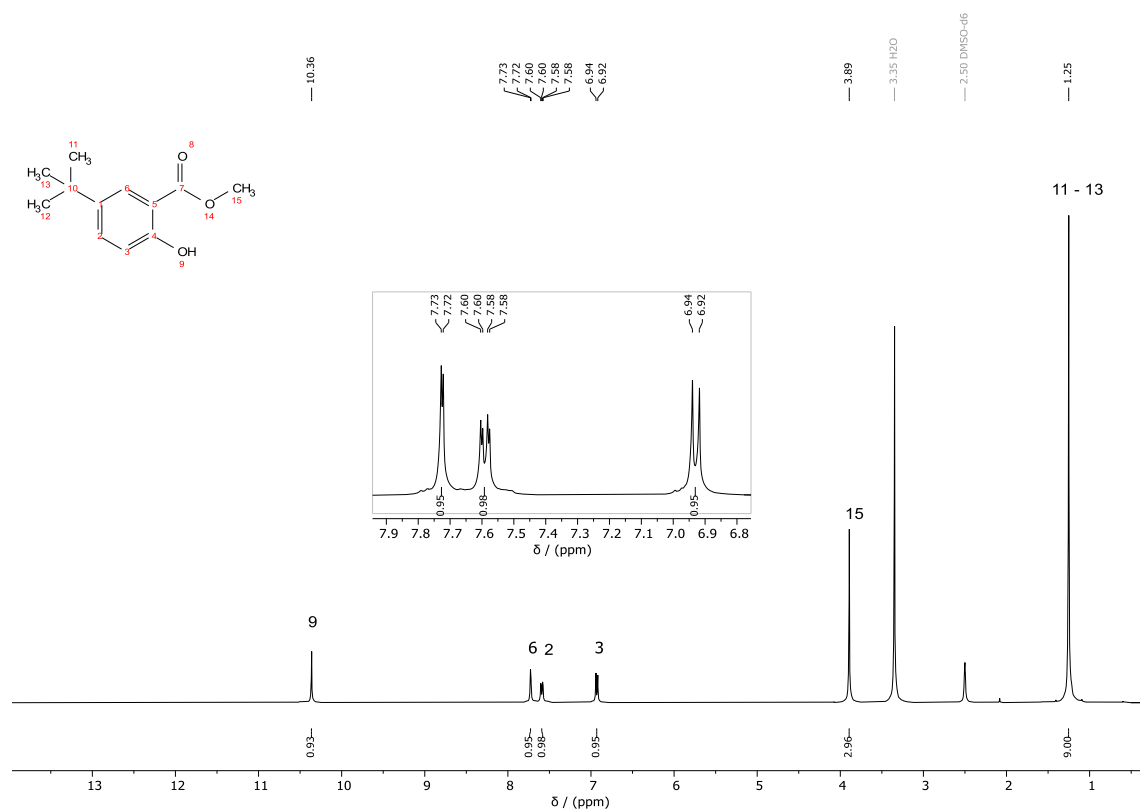
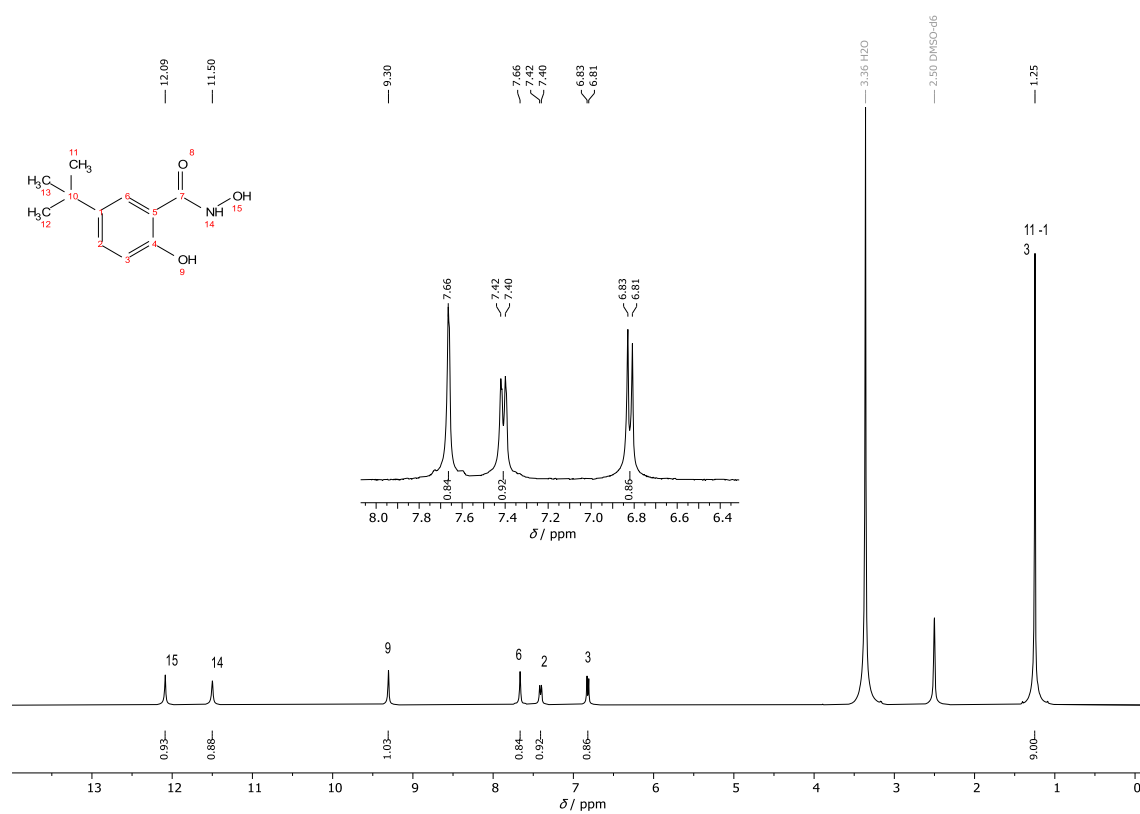


**Figure S 22.** Cyclic voltammogram of **tBu-[Fe<sub>3</sub>Fe]** of a freshly prepared solution and after 4 days in the solution of dimethylformamide with a concentration of 100 mM of the conducting salt tetrabutylammonium hexafluorophosphate.

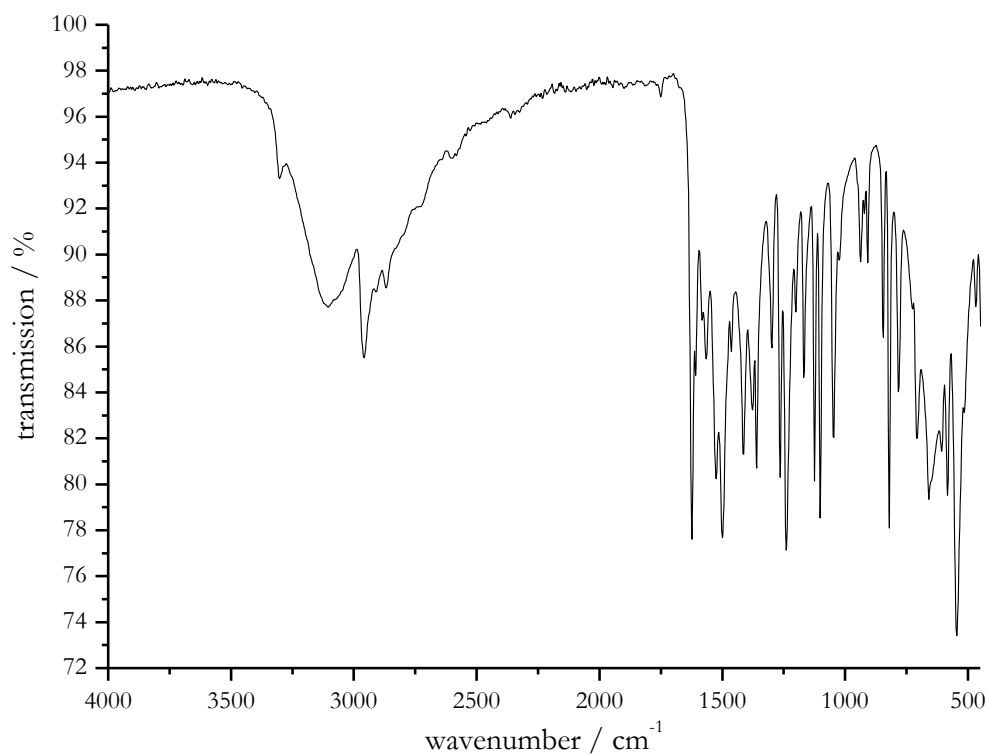


**Figure S 23.** Peak currents ( $I$ ) for different scan rates against the root of the respective scan rate ( $v^{0.5}$ ) shows a linear progression of **4bu-[Fe<sub>3</sub>Fe]**.

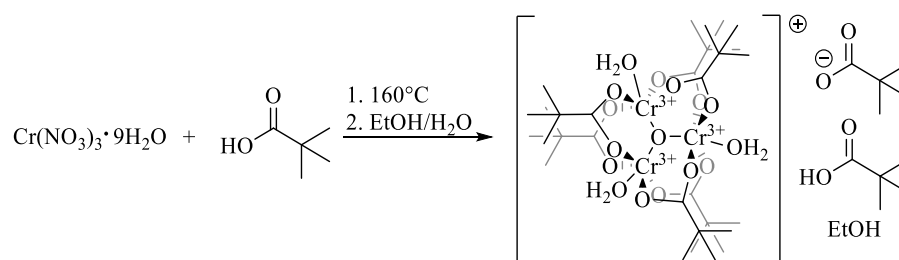
## 6.2.1.8. NMR spectra

Figure S 24. <sup>1</sup>H-NMR of 5-*tert*-butylmethyl salicylate.Figure S 25. <sup>1</sup>H-NMR of 5-*tert*-butylsalicylhydroxamic acid.

## 6.2.1.9. IR spectra


 Figure S 26. Infrared spectra of 5-*tert*-butylsalicylhydroxamic acid (REN-ANLX-001).

## 6.2.2. Supporting information for Chapter 4.1.2.2.

 6.2.2.1. Synthesis of chromium pivalate ( $\text{Cr}_3\text{O}(\text{O}_2\text{Ctert-butyl})_6(\text{H}_2\text{O})_3(\text{O}_2\text{Ctert-butyl})\text{HO}_2\text{Ctert-butyl}$ )




**Ansatz REN-ANL-178:**

compound	$M / \frac{\text{g}}{\text{mol}}$	$m / \text{g}$	$n / \text{mmol}$	$V / \text{mL}$	eq.
$\text{Cr}(\text{NO}_3)_3 \cdot 9\text{H}_2\text{O}$	400.15	10.19	25	-	1
tert-butyl COOH	102.13	25.40	250	-	10
EtOH	-	-	-	70	-
H <sub>2</sub> O	-	-	-	30	-

**Procedure**<sup>[11]</sup>

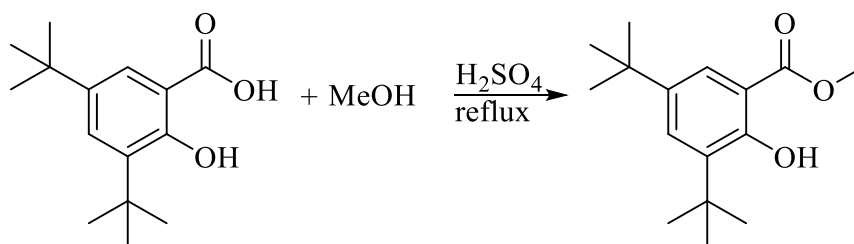
Chromium pivalate was prepared by using a modified procedure from the literature. Chromium(III) nitrate nona aqua (10.19 g, 25 mmol, 1 eq.) and pivalic acid (25.40 g, 250 mmol, 10 eq.) were heated in an open conical flask until no brown nitrogen oxide gases were forming anymore. The green solution was allowed to cool whereby a green precipitate crystallized. This precipitate was recrystallized from a 7:3 mixture of ethanol and deionized water. The hot solution was filtered and was allowed to slowly evaporate under ambient conditions. Chromium(III) pivalate crystals formed after 1-2 days and were collected by filtration.

**Analytcs**

**yield**  $m = 3.8 \text{ g}$  (10 mmol, 40% of theory (based on one chromium))

**IR** ( $\tilde{\nu} / \text{cm}^{-1}$ ) = 2960, 2928, 2905, 2868, 1608, 1532, 1485, 1458, 1429, 1383, 1362, 1293, 1228, 1046, 1031, 939, 903, 864, 786, 768, 674, 665, 618, 526, 468.

**ESI-MS**  $m/z = \text{theo: } [\text{M}]^+ 853.279, \text{exp: } 853.2323$

6.2.2.2. Synthesis of 3,5-di-*tert*-butylsalicylate

## REN-ANL-168:

compound	$M / \frac{\text{g}}{\text{mol}}$	$m / \text{g}$	$n / \text{mmol}$	$V / \text{mL}$	eq.
3,5-di- <i>tert</i> -butylsalicylic acid	250.43	10	40	-	1.0
methanol	32.04	-	-	140	-
sulfuric acid	98.08	-	-	16	-

Procedure<sup>[12]</sup>

3,5-Di-*tert*-butylsalicylic acid (10 g, 40 mmol, 1eq.) was dissolved in 140 mL methanol under stirring. 16 mL sulfuric acid were added under cooling in an ice bath. The solution was heated under reflux for 5 days. After cooling, colorless needles precipitate. The colorless needles were filtered and dried in air. This crude product was used for the next synthesis without further purification.

## Analytic

yield  $m = 9.08 \text{ g}$  (34 mmol 86 % of theory)

$^1\text{H-NMR}$  (400 MHz, DMSO- $d_6$ ,  $\delta / \text{ppm}$ ): 11.40 (s, 1H, H-8), 7.66 (d,  $J = 2.3 \text{ Hz}$ , 1H, H-6), 7.52 (d,  $J = 2.3 \text{ Hz}$ , 1H, H-2), 3.91 (s, 3H, H-11), 1.38 (s, 9H, H-17, H-18, H-19), 1.26 (s, 9H, H-13, H-14, H-15).

$\text{IR}$  ( $\tilde{\nu} / \text{cm}^{-1}$ ) = 3370  $\nu(\text{O-H})$ , 2955  $\nu(\text{CH}_3)$ , 2908, 2869, 1670  $\nu(\text{C=O})$ , 1600  $\nu(\text{C=C})$ , 1242  $\nu(\text{C-O-C})$ , 1178  $\delta(\text{O-CH}_3)$ , 1115  $\delta(\text{C-H arom.})$ , 1036  $\nu(\text{C-O-C})$ , 895  $\delta(\text{C-H arom.})$ .

6.2.2.3. Synthesis of 3,5-di-*tert*-butylsalicylhydroxamic acid

## REN-ANL-170:

compound	$M / \frac{\text{g}}{\text{mol}}$	$m / \text{g}$	$n / \text{mmol}$	$V / \text{mL}$	eq.
3,5-di- <i>tert</i> -butylsalicylate	264.36	5.12	19	-	1.0
NH <sub>2</sub> OH·HCl	69.49	3.85	55	-	3.0
KOH	56.11	7.16	128	-	7.0
Methanol	32.04	-	-	45	-

## Procedure

Potassium hydroxide (7.16 g, 128 mmol, 7.0 eq) and hydroxylamine hydrochloride (3.85 g, 55 mmol, 3.0 eq.) were dissolved separately in 15 mL methanol each under argon atmosphere. The potassium hydroxide solution was added to the hydroxylamine hydrochloride solution, resulting in the precipitation of potassium chloride. Potassium chloride was filtered under argon atmosphere. The hydroxylamine solution was added to a suspension of 3,5-di-*tert*-butyl salicylate (5.12 g, 19 mmol, 1.0 eq.) in 15 mL methanol. The suspension was stirred under argon atmosphere at room temperature for 2 days. Methanol was removed by distillation under reduced pressure. The resulting oil was dissolved in 20 mL of water to give a slightly brownish solution. The pH was adjusted to a value of 5 with 1 M HCl, which caused a colorless precipitate to form. The precipitate was filtered and dried in air. The colorless precipitate was purified by flash chromatography (SiO<sub>2</sub>, EtO<sub>2</sub>/DCM/MeOH in 0.15 % NH<sub>3</sub>-solution (4:4:0.15), R<sub>F</sub> = 0.46). A slightly reddish solid was obtained.

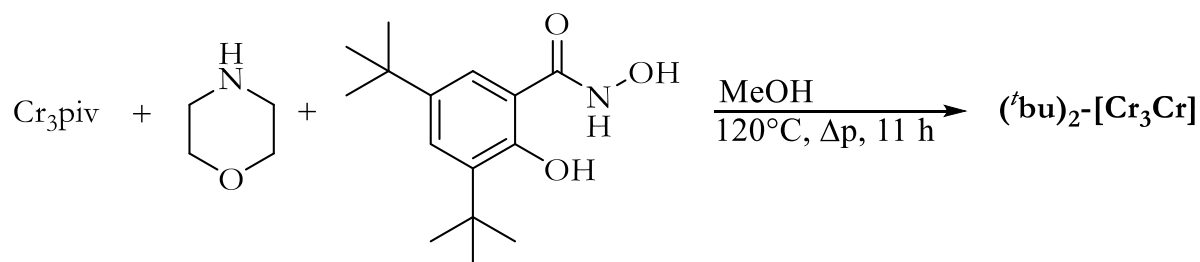
## Analytics

yield  $m = 2.70$  mg (10 mmol, 54 % of theory)

IR ( $\tilde{\nu} / \text{cm}^{-1}$ ) = 3248 (m), 3082 (m), 3013 (m), 2954 (s), 2909 (m), 2870 (m), 1629 (s), 1589 (s), 1525 (m), 1478 (m), 1456 (s), 1434 (s), 1391 (s), 1362 (s), 1339 (m), 1327 (m), 1280 (s), 1251 (s), 1218 (m), 1201 (s), 1154 (s), 1131 (m), 1037 (s), 950 (m), 930 (m), 909 (m), 886 (m), 830 (m), 818 (s), 789 (s), 749 (s), 724 (s), 636 (s), 530 (m), 512 (s), 458 (s).

<sup>1</sup>H-NMR (400 MHz, DMSO-d<sub>6</sub>,  $\delta / \text{ppm}$ ): 13.22 (s, 1H,H-8), 11.71 (s, 1H,H-17), 9.34 (s, 1H,H-19), 7.51 (d,  $J = 2.3$  Hz, 1H,H-6), 7.34 (d,  $J = 2.3$  Hz, 1H,H-2), 1.36 (s, 9H,H-14,H-15,H-16), 1.25 (s, 9H,H-11,H-12,H-13).

ESI-MS  $m/z = \text{theo: } [M+H]^+ 266.1751, \text{exp: } 266.1757; \text{theo: } [M+Na]^+ 288.157, \text{exp: } 288.1573.$

6.2.2.4. Synthesis of [9-MC-3] ( $(^t\text{bu})_2\text{-[Cr}_3\text{Cr]}$ )

## REN-ANL-171-26:

compound	$M / \frac{\text{g}}{\text{mol}}$	$m / \text{g}$	$n / \text{mmol}$	$V / \text{mL}$	eq.
$\text{Cr}_3\text{piv}$ (values for one Cr(III) ion)	1103.19	63	0.2	-	1.0 (for one Cr(III) ion)
3,5-di- <i>tert</i> -butylsalicylic hydroxamic acid	265.35	53	0.2	-	1.0
morpholine	87.12	-	1.1	0.1	5.7

## Procedure

$\text{Cr}_3\text{piv}$  (63 mg, 0.2 mmol, 1 eq. (for one chromium(III) ion)), 3,5-di-*tert*-butylsalicylic hydroxamic acid (53 mg, 0.2 mmol, 1 eq.) and 0.1 mL morpholine (1.1 mmol, 5.7 eq.) were dissolved in MeOH (15 ml) and heated at  $120^\circ\text{C}$  in a Teflon-lined autoclave for 11 hours. The solution was allowed to cool to room temperature and crystals were collected after 2-3 weeks *via* slow evaporation.

## Analytic

yield  $m = 7$  mg (0.004 mmol per Cr, 10% of theory)

IR ( $\tilde{\nu} / \text{cm}^{-1}$ ) = 2954 (m), 2904 (m), 2867 (m), 1607 (m), 1576 (s), 1557 (m), 1538 (m), 1485 (m), 1457 (w), 1424 (s), 1391 (s), 1361 (s), 1291 (m), 1230 (s), 1200 (w), 1172 (w), 1119 (m), 1090 (w), 1047 (w), 1032 (w), 1003 (s), 950 (w), 880 (s), 833 (s), 788 (s), 765 (m), 740 (s), 681 (w), 616 (s), 559 (m), 547 (s), 501 (m), 480 (s), 456 (s).

ESI-MS  $m/z = \text{theo: [M+H]}^+ 1560.591, \text{exp: } 1560.590$ ; (see Table S 19 for detailed evaluation)

X-ray analysis (see Table S 13)

## 6.2.2.5. Structure determination

Table S 13. Crystallographic data of complex  $(\text{tbu})_2\text{-[Cr}_3\text{Cr]}$ .

	$(\text{tbu})_2\text{-[Cr}_3\text{Cr]}$
	REN-ANL-171-26
empirical formula	$\text{C}_{72}\text{H}_{114}\text{Cr}_4\text{N}_6\text{O}_{18}$
formula weight g/mol	1559.712
overall formula	$\text{C}_{146}\text{H}_{236}\text{Cr}_8\text{N}_{12}\text{O}_{38}$
overall formula g/mol	3183.45
crystal size / mm	not measured
crystal system	triclinic
space group	P-1
unit cell dimensions	
$a/\text{Å}$	14.6945(3)
$b/\text{Å}$	21.0629(5)
$c/\text{Å}$	27.2248(6)
$\alpha/^\circ$	87.446(2)
$\beta/^\circ$	88.657(2)
$\gamma/^\circ$	81.410(2)
volume/ $\text{Å}^3$	8322.3(3)
cell formula units Z	2
density $\rho_{\text{calc}} / \text{g cm}^{-3}$	1.270
$\mu / \text{mm}^{-1}$	0.575
F(000)	3384
temperature / K	173
device type	STOE STADIVARI
radiation	Mo-K $\alpha$
independent reflexes	$1.823 < \theta < 31.004$
index ranges	$-21 < h < 21$
	$-30 < k < 30$
	$-39 < l < 39$
collected reflections	152507
independent reflections	152513
completeness	0.876
max. and min. transmission	1.0000 and 0.2531
$R_{\text{int}}$	0.0399
$R_{\text{sigma}}$	0.0553
data/restraints/parameters	46557 / 198 / 2050
goodness-of-fit on $F^2$	0.921
$^a R_1 [I > 2\sigma(I)]$	0.0452
$^b wR_2 [I > 2\sigma(I)]$	0.1138
$R_1 [\text{all data}]$	0.0637
$wR_2 [\text{all data}]$	0.1192

$$^a R_1 = \Sigma(|F_o| - |F_c|) / \Sigma|F_o|, \quad ^b wR_2 = [\Sigma[w(F_o^2 - F_c^2)^2] / \Sigma[w(F_o^2)^2]]^{1/2}, \quad w = 1 / [\sigma^2(F_o^2) + (ap)^2 + bp], \quad p = [\max(F_o^2, 0) + 2F_c^2] / 3.$$

**Table S 14.** Selected bond length of (fbu)<sub>2</sub>-[Cr<sub>3</sub>Cr].

chromium(III) ion	donor atom	bond length	chromium(III) ion	donor atom	bond length
<b>Cr1</b>	O3	1.9727(12)	<b>Cr5</b>	O23	1.9664(12)
	O6	1.9669(12)		O26	1.9671(12)
	O9	1.9629(13)		O29	1.9687(12)
	O10	1.9739(13)		O30	1.9615(13)
	O12	1.9687(13)		O32	1.9656(13)
	O14	1.9741(13)		O34	1.9690(13)
<b>Cr2</b>	O1	1.9095(13)	<b>Cr6</b>	O21	1.9063(12)
	O8	1.9461(12)		O28	1.9483(13)
	O9	2.0252(13)		O29	2.0313(12)
	O11	1.9959(13)		O31	2.0102(13)
	N1	1.9805(15)		N7	1.9794(15)
	N4	2.1255(17)		N10	2.1325(16)
<b>Cr3</b>	O2	1.9492(12)	<b>Cr7</b>	O22	1.9549(13)
	O3	2.0256(12)		O23	2.0178(13)
	O4	1.9135(12)		O24	1.9075(13)
	O13	2.0063(13)		O33	1.9971(13)
	N2	1.9843(14)		N8	1.9941(15)
	N5	2.1222(15)		N11	2.1219(16)
<b>Cr4</b>	O5	1.9499(13)	<b>Cr8</b>	O25	1.9456(13)
	O6	2.0174(12)		O26	2.0319(13)
	O7	1.9064(13)		O27	1.9111(13)
	O15	2.0034(14)		O35	1.9954(13)
	N3	1.9920(16)		N9	1.9853(15)
	N6	2.1154(17)		N12	2.1312(15)

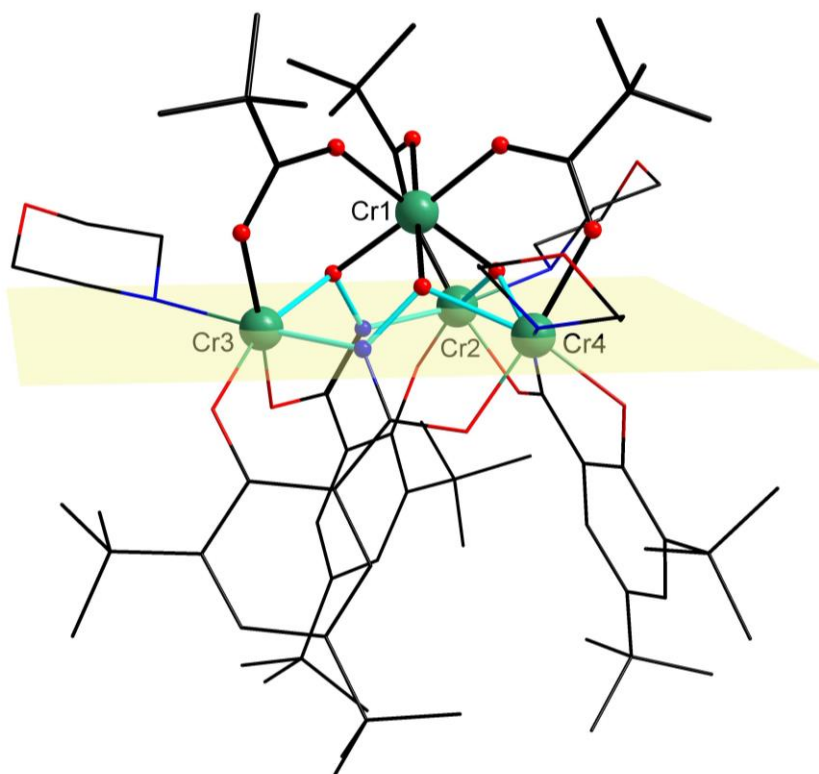


**Figure S 27.** Schematic representation of structure as a “side-on” view with out of plane coordination of iron(III) guest ion Cr1 of  $(t\text{bu})_2\text{-}[\text{Cr}_3\text{Cr}]$  and Cr2-Cr3-Cr4 plane (yellow). Hydrogen atoms are omitted for clarity. Color code: chromium(III) ions green, oxygen red, nitrogen blue, carbon black.

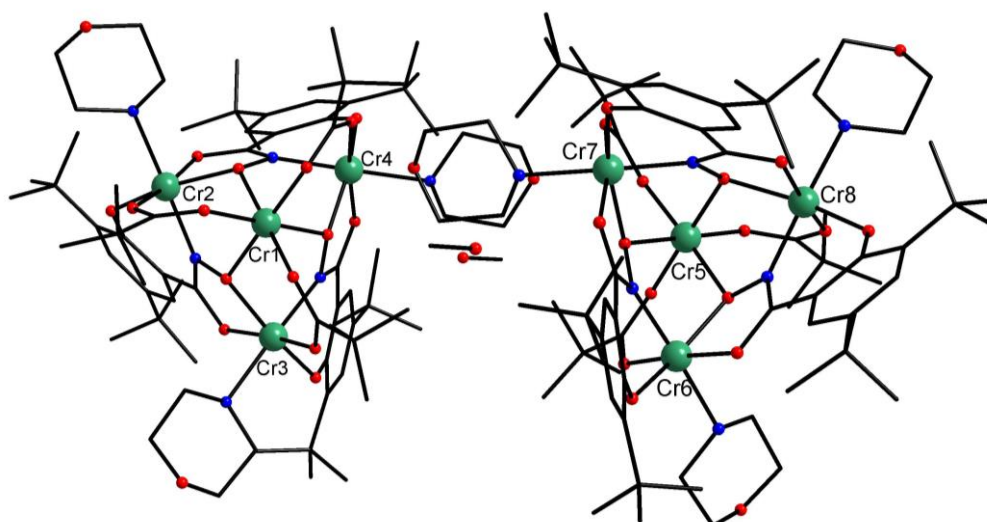


**Figure S 28.** Schematic representation the two molecules in the asymmetric unit of  $(t\text{bu})_2\text{-}[\text{Cr}_3\text{Cr}]$ . Hydrogen atoms are omitted for clarity.

**Table S 15.** Selected angles of ring ions Cr2, Cr3 and Cr4 of  $(t\text{bu})_2\text{-}[\text{Cr}_3\text{Cr}]$  for molecule a).

atoms	angles
-------	--------

N1 Cr2 O9	83.10(6)°
N2 Cr3 O3	83.10(5)°
N3 Cr4 O6	83.81(6)°

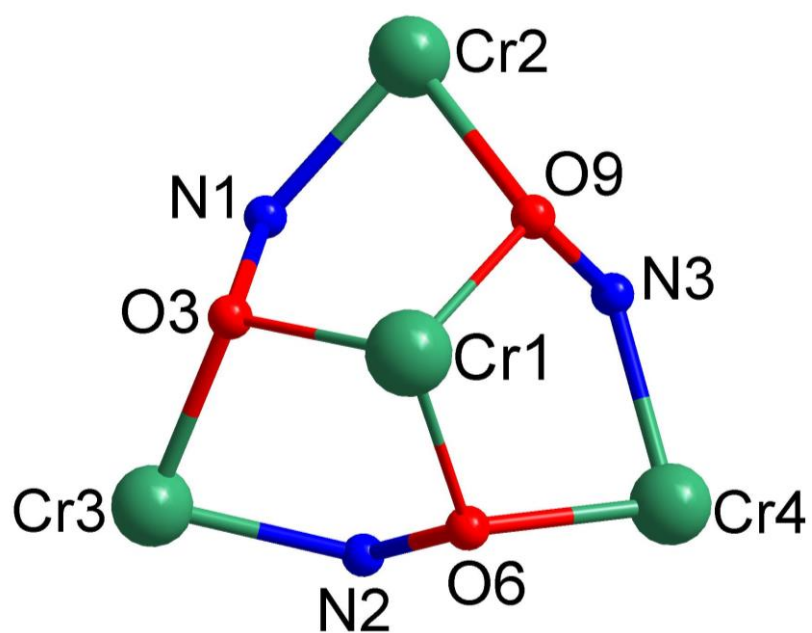


**Figure S 29.** Schematical representation of repeating unit of  $(fBu)_2-[Cr_3Cr]$ . Color code of atoms: oxygen red, nitrogen blue, carbon black, chromium(III) ion green.



6.2.2.6. Continuous Shape Measurements of (**bu**)<sub>2</sub>-[Cr<sub>3</sub>Cr]**Table S 16.** Calculated deviations from ideal polyhedra for Cr1, Cr2, Cr3 and Cr4 of (**bu**)<sub>2</sub>-[Cr<sub>3</sub>Cr] via Continuous Shape Measurements.

Polyhedron <sup>a</sup>	Cr1	Cr2	Cr3	Cr4
HP-6	33.115	31.564	31.429	31.936
PPY-6	30.013	21.917	22.309	23.072
OC-6	0.015	1.237	1.136	0.967
TPR-6	16.343	11.726	11.407	11.925
JPPY-6	33.525	25.519	25.846	26.662

<sup>a</sup> abbreviations: HP-6 hexagon (D<sub>6h</sub>); PPY-6 pentagonal pyramid (C<sub>5v</sub>); OC-6 octahedron (O<sub>h</sub>); TPR-6 trigonal prism (D<sub>3h</sub>); JPPY-6 Johnson pentagonal pyramid J2 (C<sub>5v</sub>)

**Table S 17.** Calculated deviations from ideal polyhedra for Cr5, Cr6, Cr7 and Cr8 of (**bu**)<sub>2</sub>-[Cr<sub>3</sub>Cr] via Continuous Shape Measurements.

Polyhedron <sup>a</sup>	Cr5	Cr6	Cr7	Cr8
HP-6	33.183	31.364	32.277	31.337
PPY-6	29.413	22.181	22.500	21.899
OC-6	0.035	1.160	1.125	1.237
TPR-6	16.023	11.601	11.556	11.479
JPPY-6	33.130	25.670	26.153	25.409

<sup>a</sup> abbreviations: HP-6 hexagon (D<sub>6h</sub>); PPY-6 pentagonal pyramid (C<sub>5v</sub>); OC-6 octahedron (O<sub>h</sub>); TPR-6 trigonal prism (D<sub>3h</sub>); JPPY-6 Johnson pentagonal pyramid J2 (C<sub>5v</sub>)

comparison to [Cr<sub>3</sub>Cr]**Table S 18.** Summarized calculated deviations from ideal polyhedra (SHAPE values) of [Cr<sub>3</sub>Cr] and (**bu**)<sub>2</sub>-[Cr<sub>3</sub>Cr].

structure	guest ion	ring metal ion	ring metal ion	ring metal ion	average
[Cr <sub>3</sub> Cr]	0.015	1.237	1.136	0.967	1.113
molecule a) 'di-bu-[Cr <sub>3</sub> Cr]	0.043	0.732	1.275	1.176	1.061
molecule b) 'di-bu-[Cr <sub>3</sub> Cr]	0.035	1.160	1.125	1.237	1.174
	average 0.039				average 1.118

## 6.2.2.7. Magnetic evaluation of data

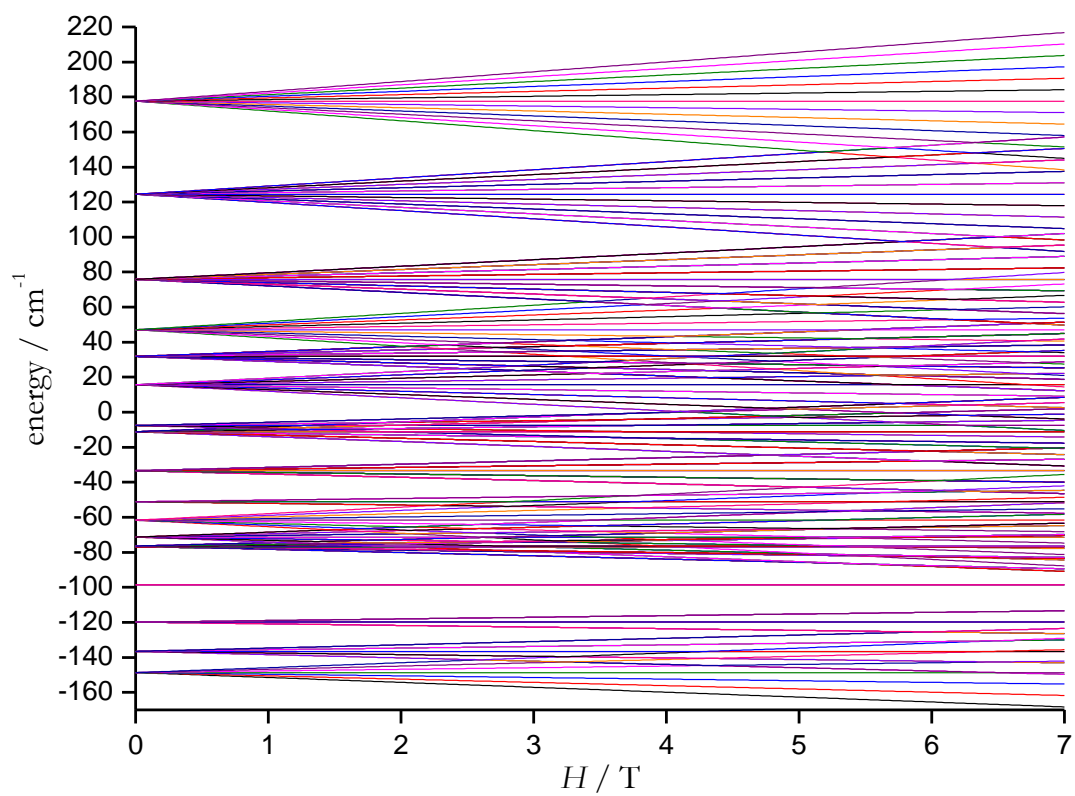


Figure S 30. Simulated Zeeman splitting field dependence of the different spin states of (fbu)<sub>2</sub>-[Cr<sub>3</sub>Cr].

## 6.2.2.8. Electrospray ionization mass spectrometry (ESI)

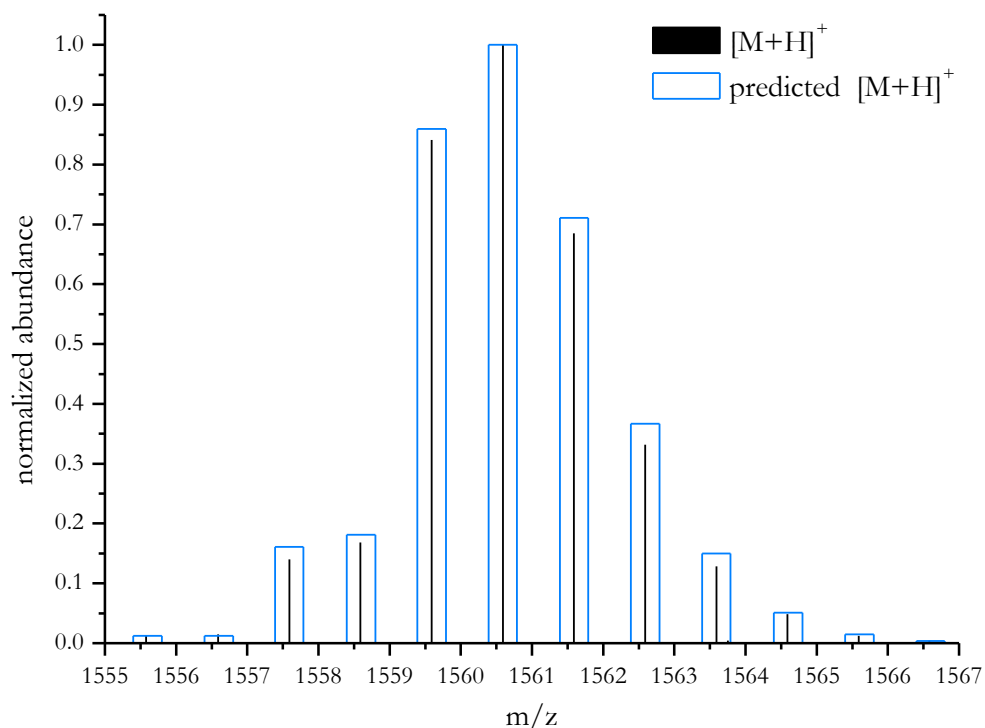


Figure S 31. Normalized abundance from electrospray ionization mass spectrum with zoom-in of isotope pattern of  $(bu)_2-[Cr_3Cr]+H^+$ . Measurement black, prediction blue box.

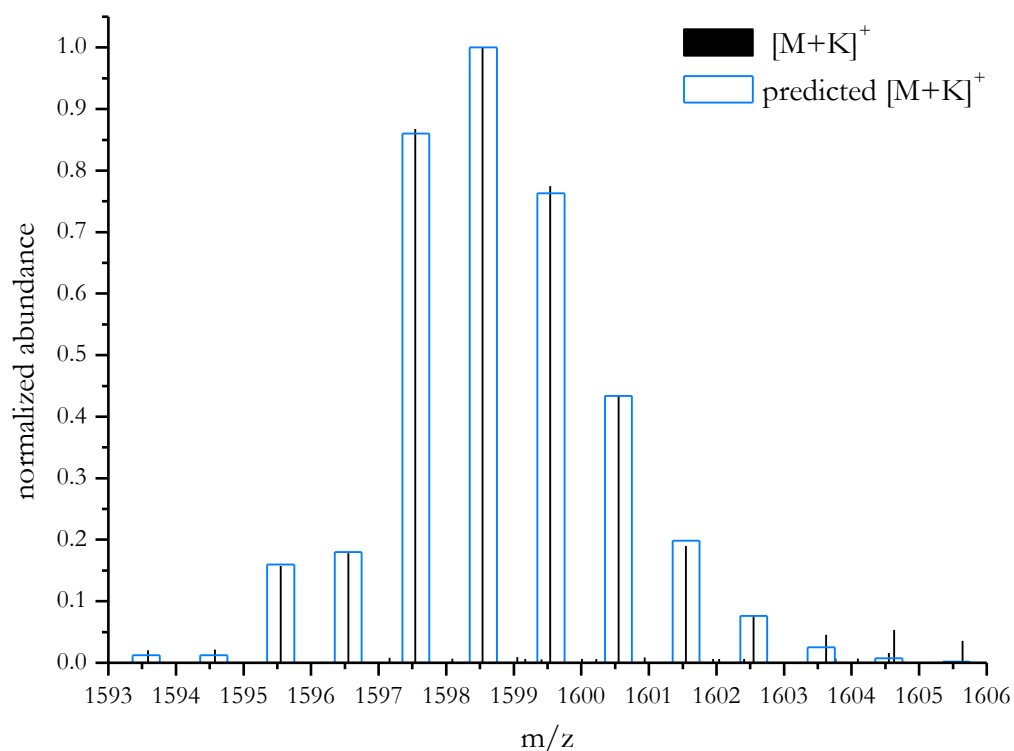
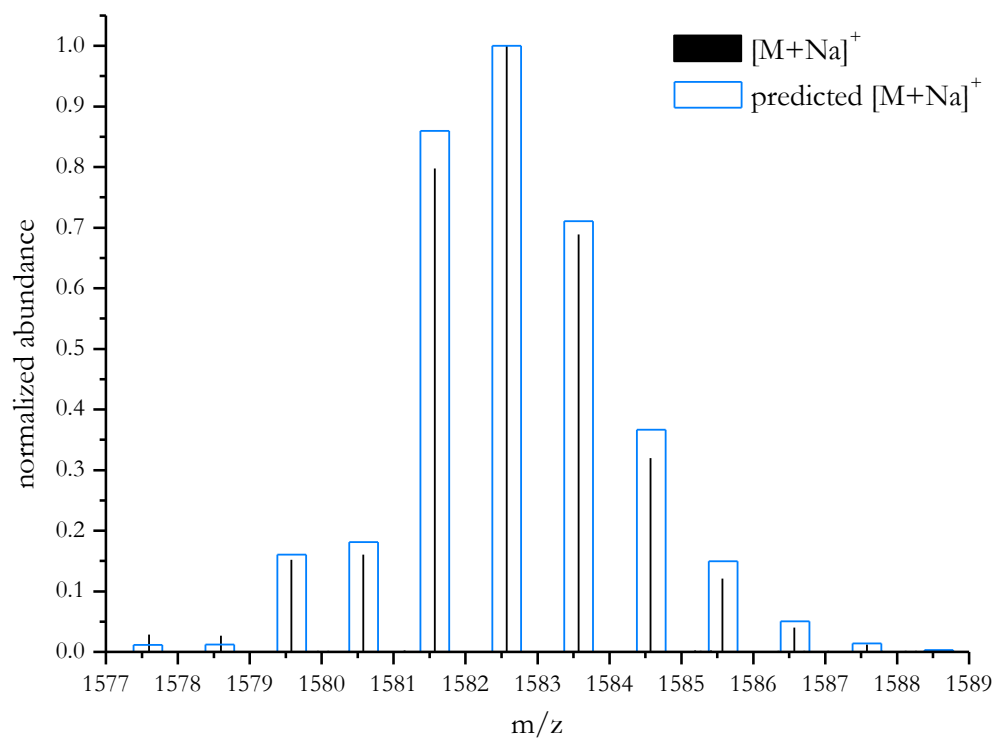
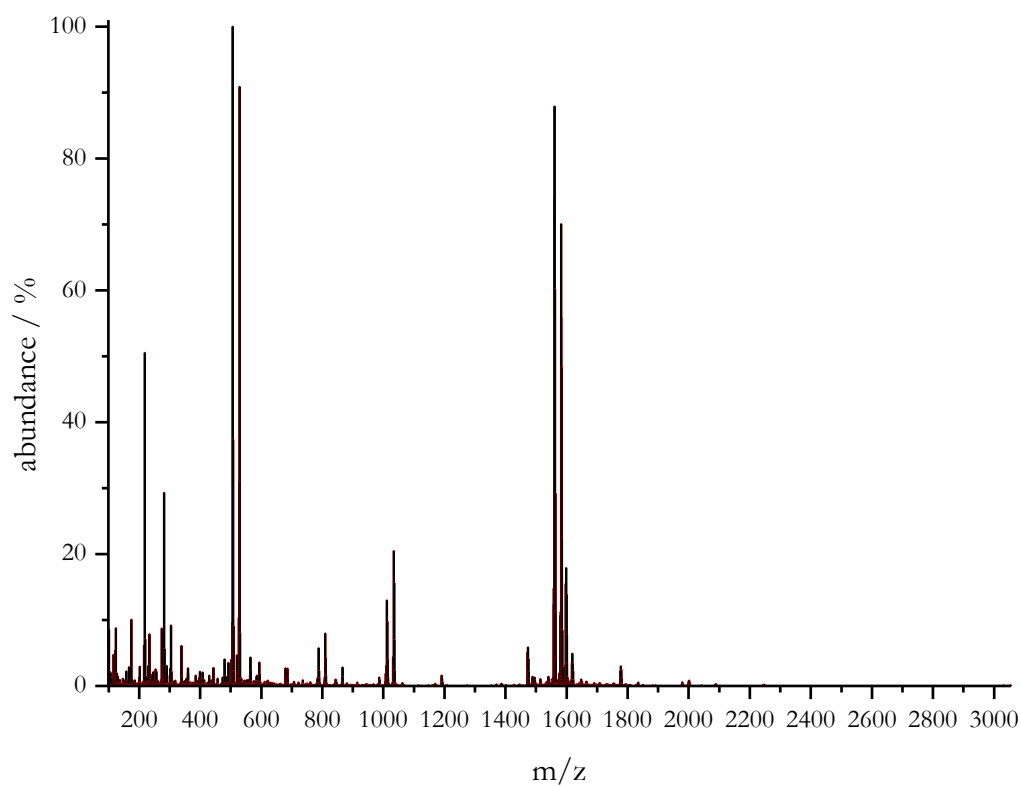


Figure S 32. Normalized abundance from electrospray ionization mass spectrum with zoom-in of isotope pattern of  $(bu)_2-[Cr_3Cr]+K^+$ . Measurement black, prediction blue box.



**Figure S 33.** Normalized abundance from electrospray ionization mass spectrum with zoom-in of isotope pattern of  $(\text{bu})_2\text{-[Cr}_3\text{Cr]}+\text{Na}^+$ . Measurement black, prediction blue box.



**Figure S 34.** Electrospray ionization mass spectrum of  $(\text{bu})_2\text{-[Cr}_3\text{Cr]}$ . Fragment at 506 m/z is observed independently from the ligand, metal ion, base, or co-ligands.

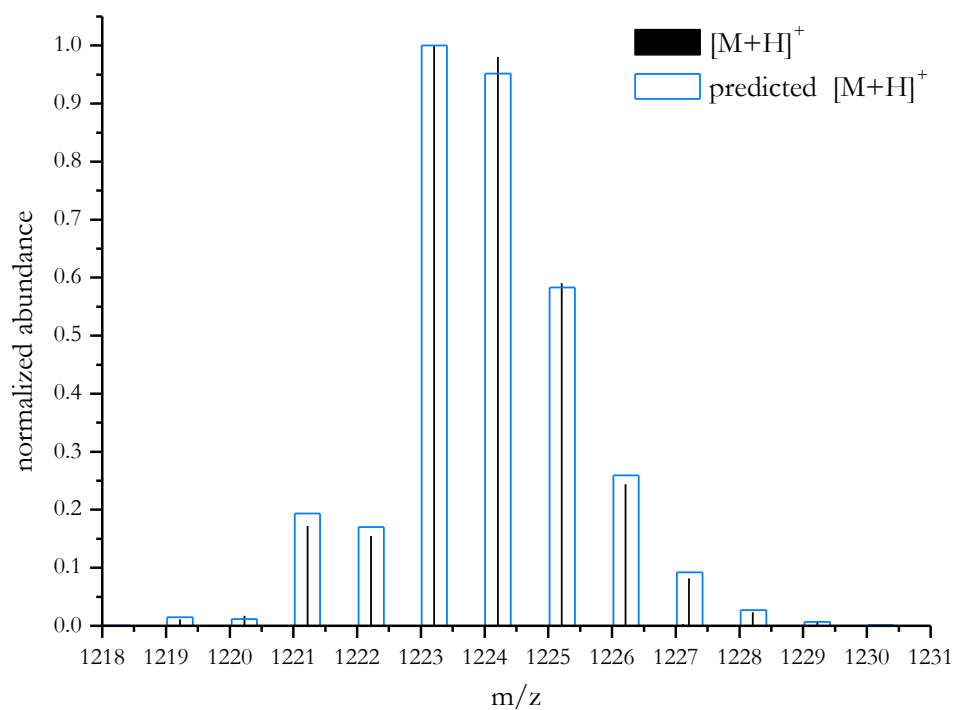


**Figure S 35.** Normalized abundance from electrospray ionization mass spectrum with zoom-in of isotope pattern of  $[\text{Cr}_3\text{Cr}]^+\text{H}^+$ . Measurement black, prediction blue box.

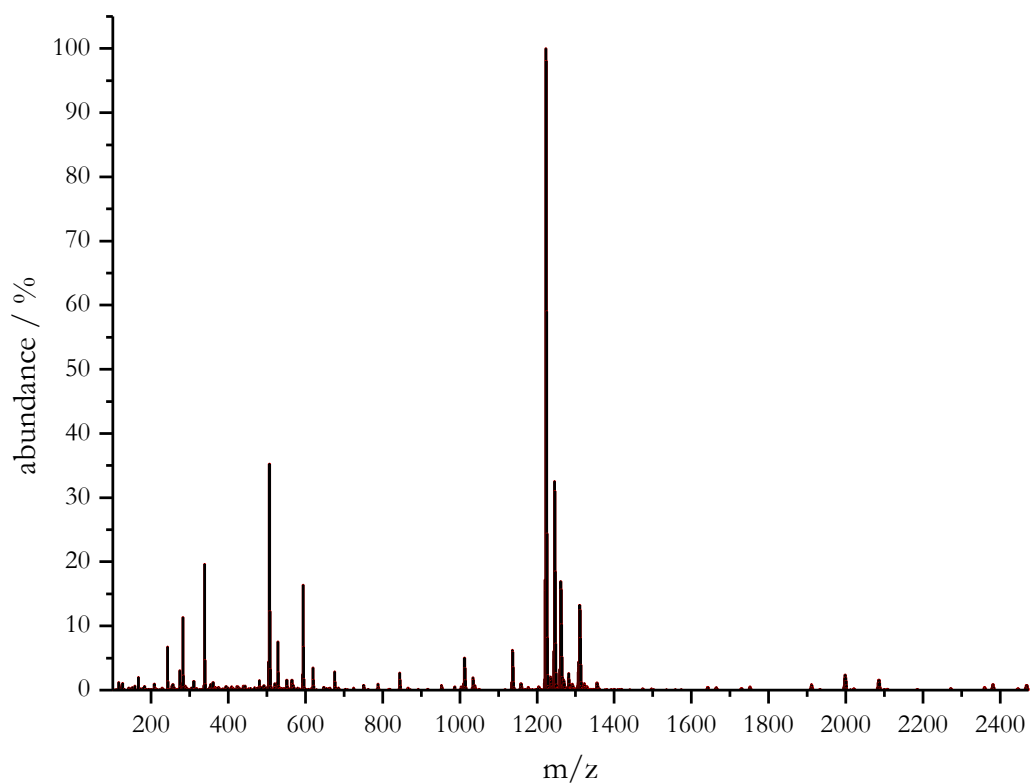


**Figure S 36.** Electrospray ionization mass spectrum of  $[\text{Cr}_3\text{Cr}]$ . Fragment at 506 m/z is observed independently from the ligand, metal ion, base, or co-ligands.

**Table S 19.** Summarized measured and predicted values for  $(\text{bu})_2\text{-[Cr}_3\text{Cr]}$ . For the measured spectra only data above 1% detection are considered. Prediction tool of Mestre Nova always sets highest signal to 100% for each ion ( $\text{H}^+$ ,  $\text{Na}^+$ ,  $\text{K}^+$ ) as adduct ( $\text{C}_{72}\text{H}_{114}\text{Cr}_4\text{N}_6\text{O}_{18}$ ).

measured m/z	rel. abundance / %	predicted m/z	rel. abundance / %
1555.583	1.16	1555.600	1.21
1556.588	1.32	1556.602	1.26
1557.590	12.33	1557.594	16.10
1558.592	14.79	1558.596	18.15
1559.588	73.97	1559.590	85.98
<b>1560.590</b>	<b>87.92</b>	<b>1560.591</b>	<b>100.00</b>
1561.591	60.22	1561.592	71.11
1562.591	29.19	1562.594	36.70
1563.593	11.30	1563.595	15.00
1564.590	4.28	1564.596	5.09
1565.590	1.09	1565.598	1.48
1577.602	2.01	1577.581	1.21
1578.602	1.87	1578.584	1.26
1579.576	10.67	1579.576	16.10
1580.575	11.25	1580.578	18.15
1581.571	55.90	1581.572	85.99
<b>1582.572</b>	<b>70.07</b>	<b>1582.573</b>	<b>100.00</b>
1583.573	48.28	1583.574	71.10
1584.574	22.42	1584.575	36.70
1585.574	8.46	1585.577	15.00
1586.575	2.82	1586.578	5.09
1595.548	2.81	1595.550	15.98
1596.551	3.18	1596.552	18.00
1597.543	15.52	1597.546	86.02
<b>1598.544</b>	<b>17.89</b>	<b>1598.547</b>	<b>100.00</b>
1599.544	13.86	1599.548	76.31
1600.545	7.77	1600.549	43.35
1601.548	3.40	1601.550	19.88

**Table S 20.** Summarized measured and predicted values for  $[\text{Cr}_3\text{Cr}] + \text{H}^+$ . For the measured spectra only data above 1% detection are considered. Prediction tool of Mestre Nova always sets highest signal to 100% for each ion as adduct ( $\text{C}_{48}\text{H}_{66}\text{Cr}_4\text{N}_6\text{O}_{18}$ ).

measured m/z	rel. abundance	predicted m/z	rel. abundance
1219.222	1.13	1219.224	1.47
1220.233	1.71	1220.226	1.15
1221.216	17.23	1221.218	19.34
1222.217	15.46	1222.220	17.03
<b>1223.212</b>	<b>100.00</b>	<b>1223.214</b>	<b>100.00</b>
1224.213	98.08	1224.215	95.18
1225.214	59.02	1225.216	58.32
1226.214	24.39	1226.217	25.95
1227.215	8.16	1227.218	9.23
1228.215	2.32	1228.219	2.73
1226.214	24.39	1226.217	25.95

## 6.2.2.9. Cyclic voltammetry

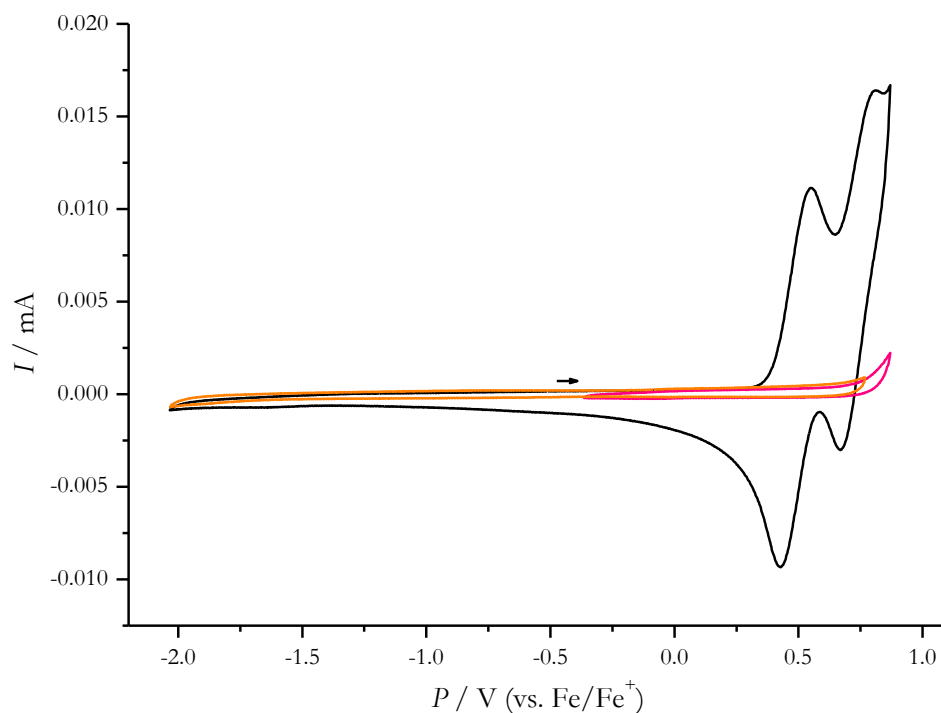


**Figure S 37.** Cyclic voltammogram of  $(\text{tBu})_2\text{-[Cr}_3\text{Cr]}$  including the blank solvent window of tetrahydrofuran with a concentration of 100 mM of the conducting salt tetrabutylammonium hexafluorophosphate.

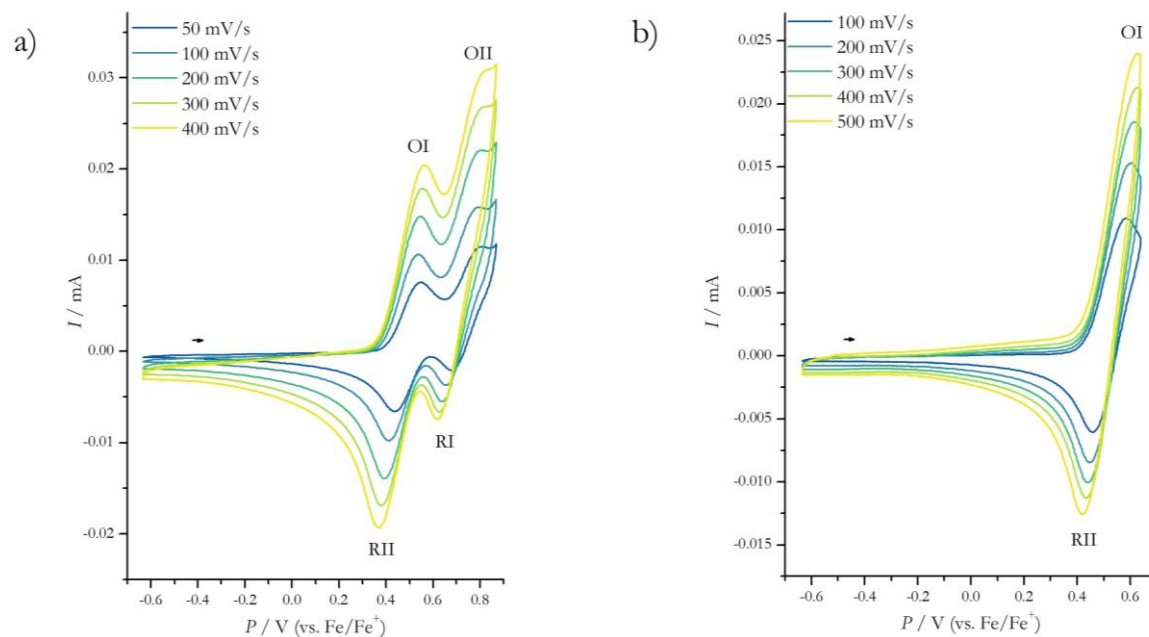


**Figure S 38.** a) Cyclic voltammogram of  $(\text{tBu})_2\text{-[Cr}_3\text{Cr]}$  measurement in the cathodic region with the complete redox pairs OI-RII and OII-RI; b) Cyclic voltammogram of  $(\text{tBu})_2\text{-[Cr}_3\text{Cr]}$  measurement in the anodic region with the redox pair OI-RII.



## 6.2.2.10. NMR spectra

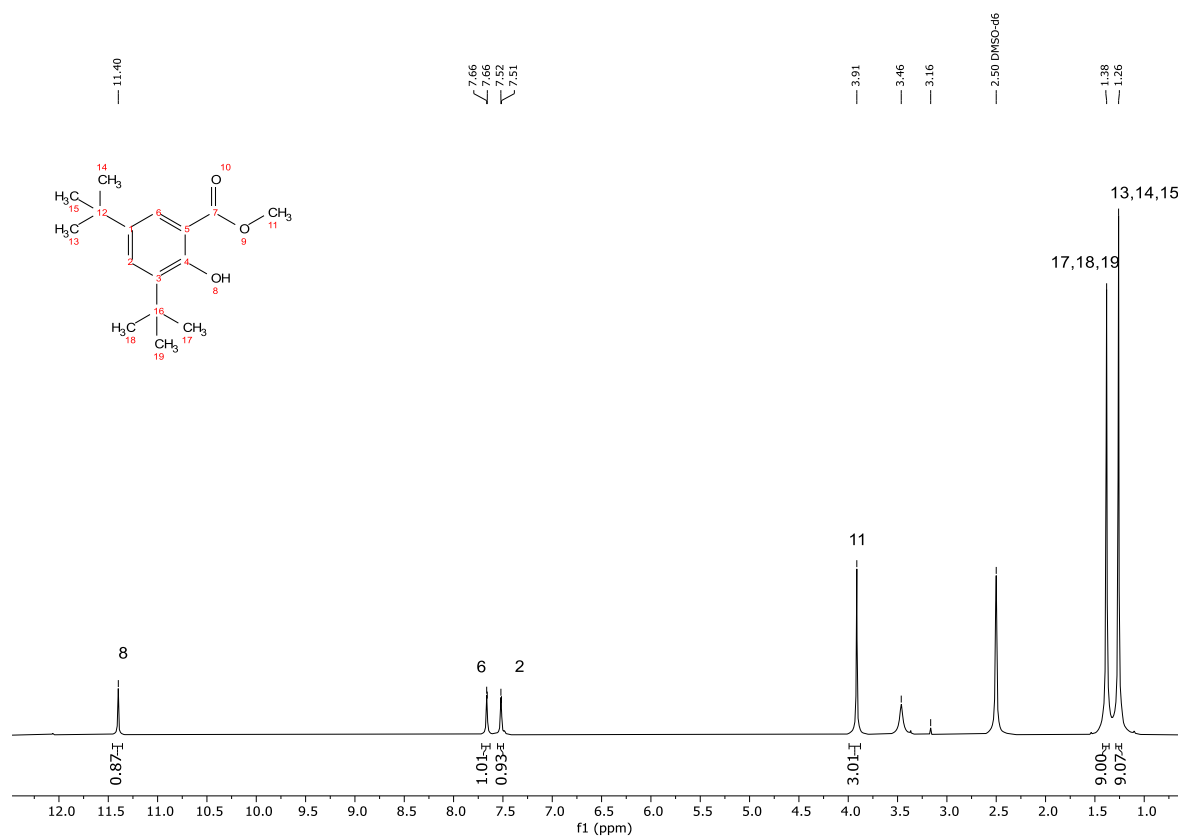


**Figure S 39.**  $^1\text{H-NMR}$  of 3,5-di-*tert*-butylsalicylate.

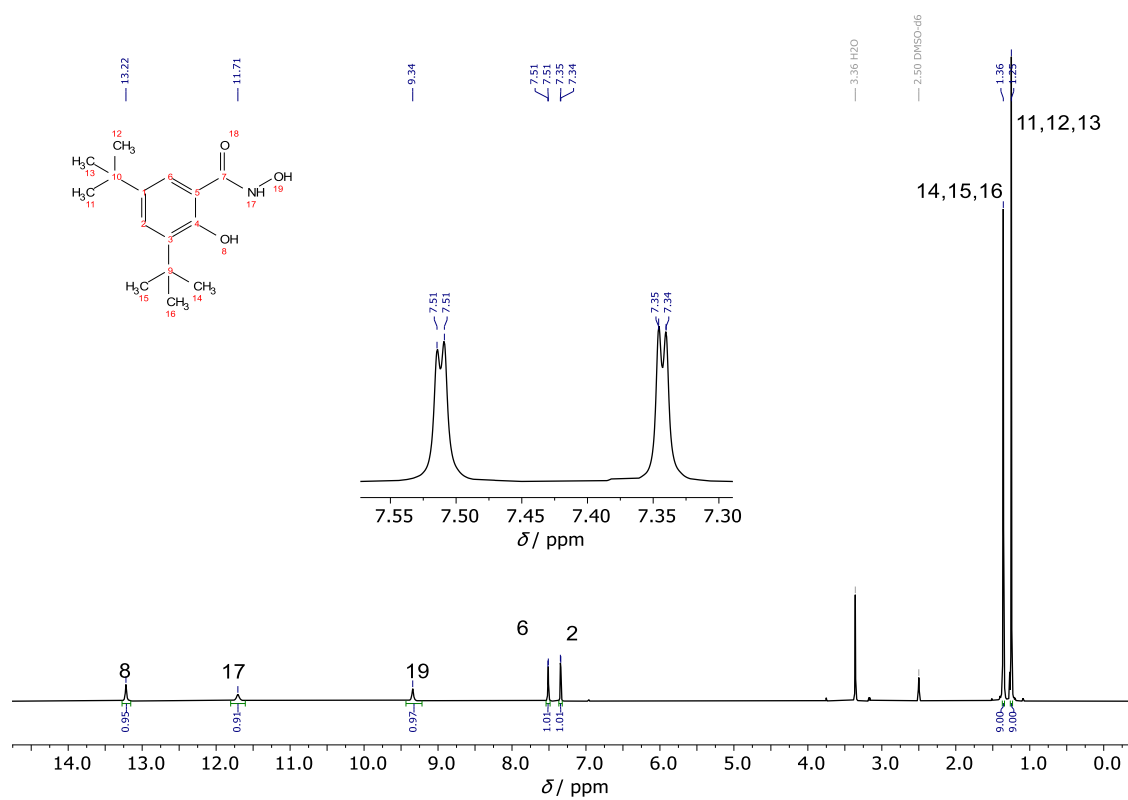


**Figure S 40.**  $^1\text{H-NMR}$  of 3,5-di-*tert*-butylsalicylhydroxamic acid.

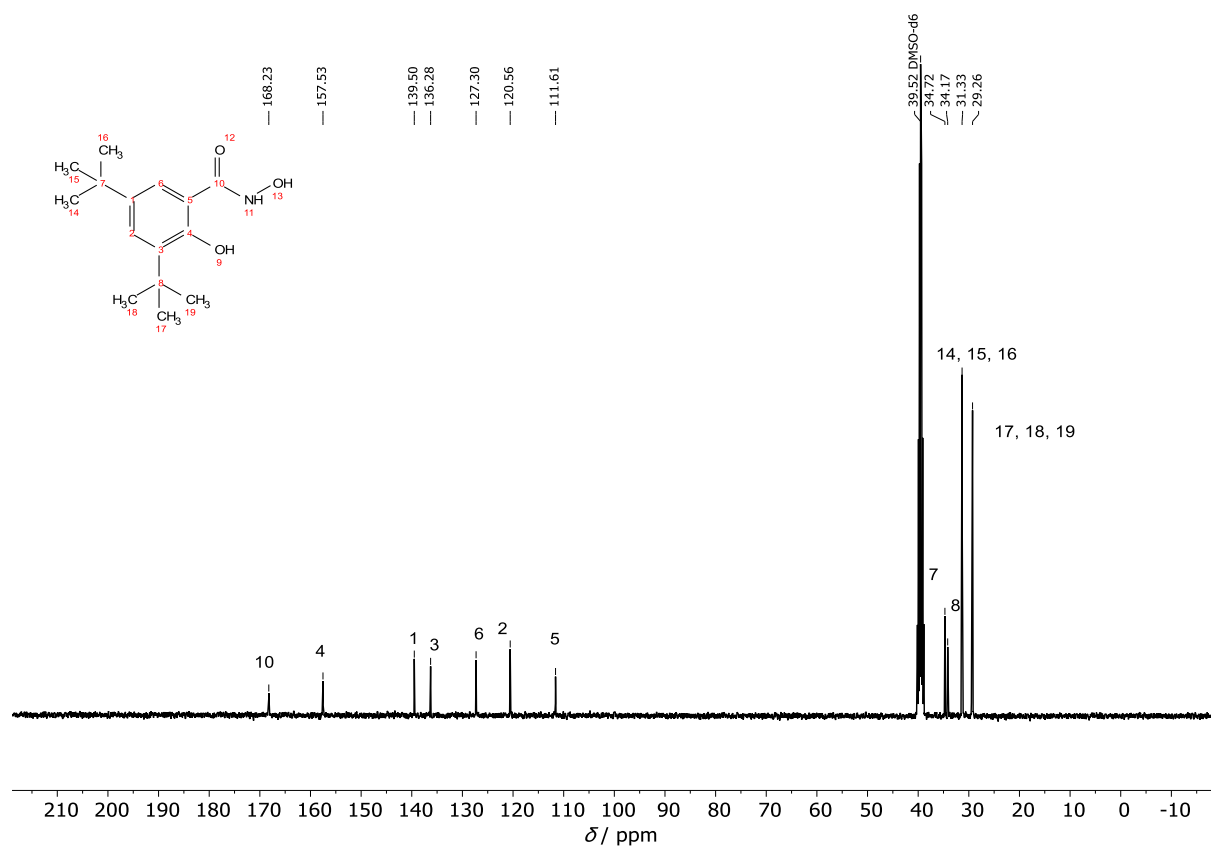


Figure S 41.  $^{13}\text{C}$ -NMR of 3,5-di-*tert*-butylsalicylhydroxamic acid.

## 6.2.2.11. Infrared spectra

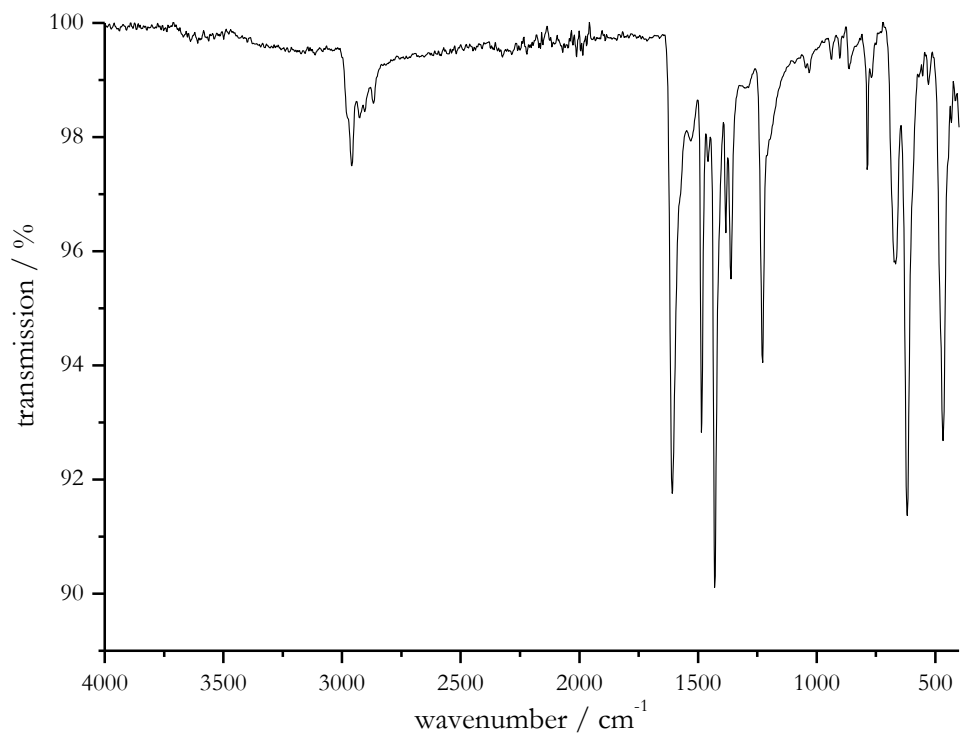


Figure S 42. Infrared spectrum of chromium(III) pivalate Cr<sub>3</sub>piv (REN-ANL-178).

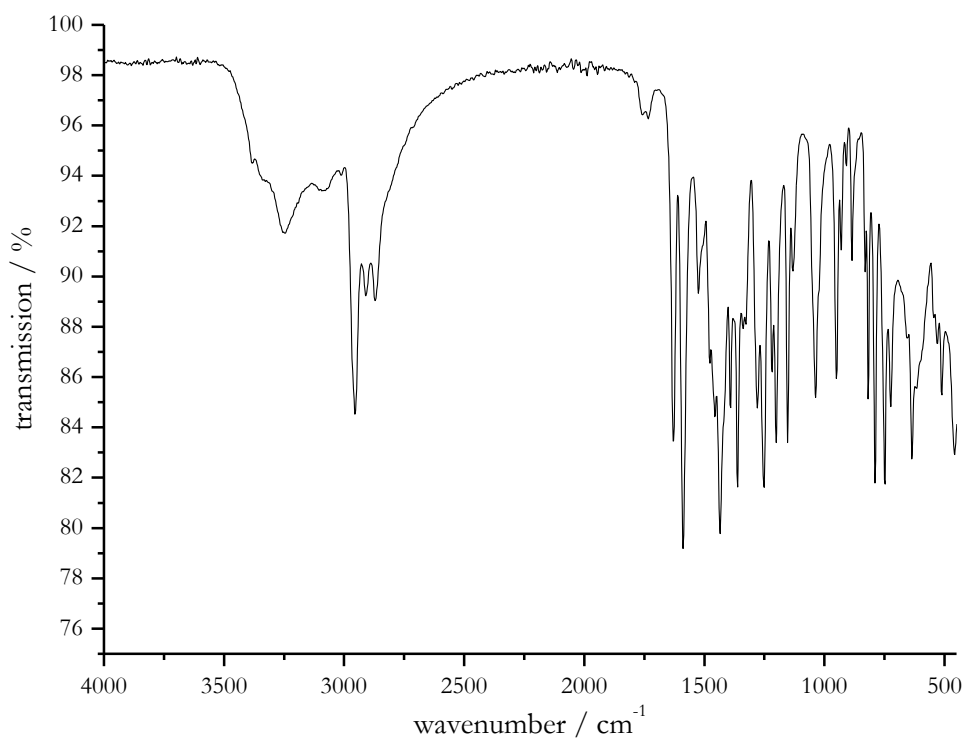
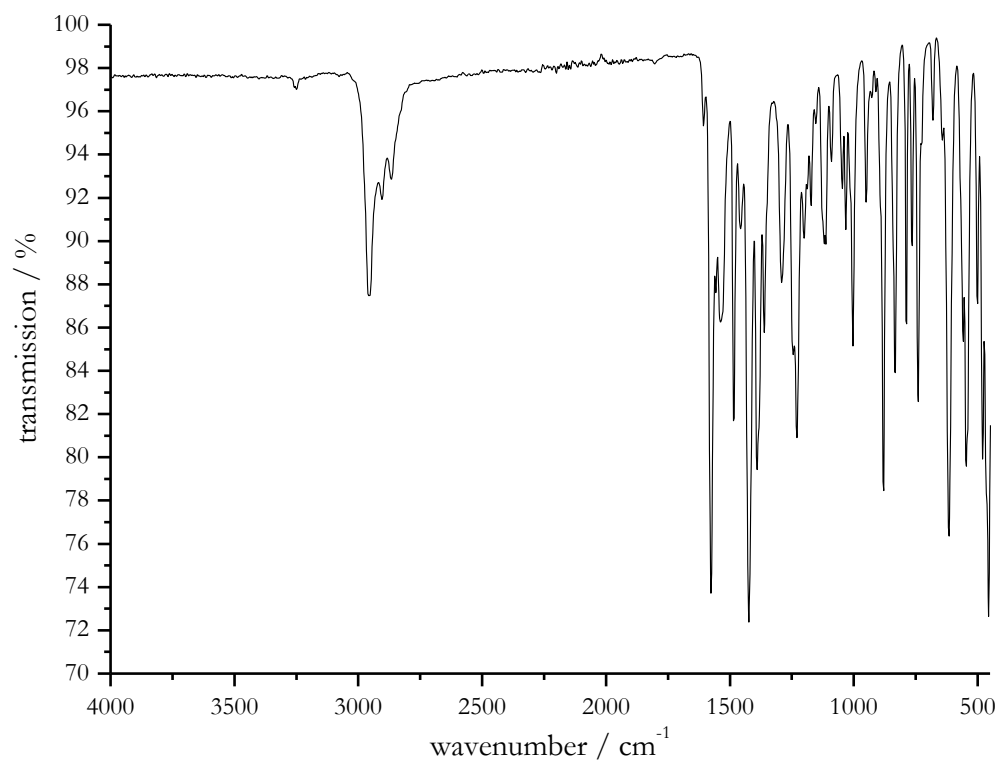
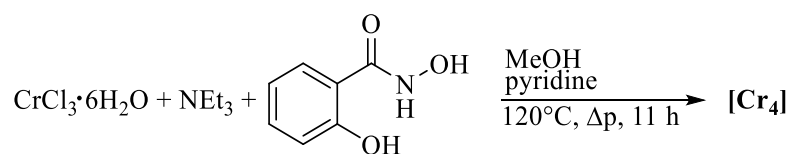


Figure S 43. Infrared spectrum of 3,5-di-*tert*-butyl salicylhydroxamic acid.



**Figure S 44.** Infrared spectrum of **(tBu)<sub>2</sub>-[Cr<sub>3</sub>Cr]** (REN-ANL-179-25).

## 6.3. Supporting information for Chapter 4.1.3.

6.3.1. Synthesis of vacant ShiH<sub>3</sub> [Cr<sub>4</sub>]

REN-ANL-195-28:

compound	$M / \frac{\text{g}}{\text{mol}}$	$m / \text{mg}$	$n / \text{mmol}$	$V / \text{mL}$	eq.
CrCl <sub>3</sub> · 6 H <sub>2</sub> O	266.41	106	0.4	-	1
ShiH <sub>3</sub>	153.14	63	0.4	-	1
NEt <sub>3</sub>	101.19	-	1.2	0.16	3
methanol	32.04	-	-	18.00	-
pyridine	79.10	-	-	2.00	-

**Procedure**

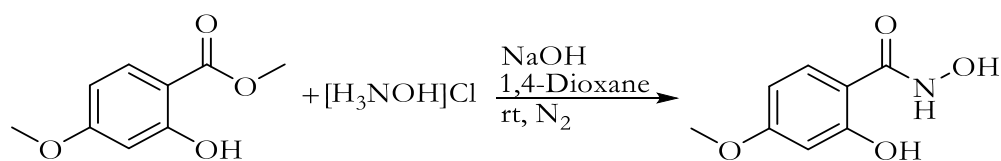
Salicylhydroxamic acid (63 mg, 0.4 mmol, 1 eq.) and triethylamine (0.16 mL, 1.2 mmol, 3 eq.) were stirred in 10 mL methanol. Chromium(III) chloride hexahydrate (106 mg, 0.4 mmol, 1 eq.) was dissolved in 2 mL methanol and added, resulting in the precipitation of a lot of gray precipitate. 2 mL pyridine were added to the suspension which was stirred at room temperature for 15 minutes and transferred to a Teflon vessel, rinsed with 6 mL of methanol and heated in an autoclave reactor at 120°C for 11 hours. After cooling, the reaction solution is centrifuged, filtered and the solvent is slowly evaporated, obtaining brown crystals on the rim of the vials after 2 weeks.

**Analytic**

**yield**  $m$  = 5-10 crystals (not possible to weight)

**X-ray** analysis (see Table S 21)

## 6.3.2. Synthesis of 4-methoxy salicylhydroxamic acid



## Ansatz REN-TF-004:

compound	$M / \frac{\text{g}}{\text{mol}}$	$m / \text{g}$	$n / \text{mmol}$	$V / \text{mL}$	eq.
methyl 4-methoxysalicylate	182.17	5.14	28		1.0
$\text{NH}_2\text{OH}\cdot\text{HCl}$	69.49	3.00	43	-	1.5
$\text{NaOH}$	40.00	3.97	99	-	3.5
$\text{H}_2\text{O}$	18.01	-	-	50	-
1,4-dioxane	88.11	-	-	15	-
dichloromethane	84.93	-	-	20	-

Procedure<sup>[8]</sup>

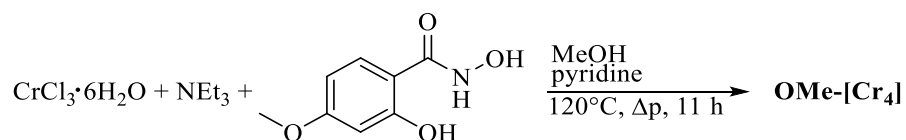
Under nitrogen atmosphere hydroxylamine hydrochloride (3.00 g, 43 mmol, 1.5eq.) and sodium hydroxide (3.97 g, 99 mmol, 3.5 eq.) were dissolved separately in 25 mL degassed water each. The sodium hydroxide solution was added to the hydroxylamine hydrochloride solution. Methyl 4-methoxysalicylate (5.14 g, 28 mmol, 1.0 eq.) dissolved in 15 mL 1,4-dioxane was added. A colorless solution was stirred over night with an attached argon balloon. The solution was concentrated to half of the volume under reduced pressure. A pH = 5 was achieved by addition of 1M HCl while a colorless precipitate formed. This precipitate was filtered, washed with 20 mL dichloromethane and dried under reduced pressure. 4-methoxy-salicylhydroxamic acid was isolated as a colorless powder.

## Analytic

yield  $m = 4.32 \text{ g}$  (24 mmol, 85 % of theory)

$^1\text{H-NMR}$  (400 MHz,  $\text{DMSO-d}_6$ ,  $\delta / \text{ppm}$ ): 12.73 (s, 1H,H-11), 11.33 (s, 1H,H-10), 9.23 (s, 1H,H-9), 7.61 (d,  $J = 8.6 \text{ Hz}$ , 1H,H-3), 6.44 (m, 2H,H-1,H-6), 3.76 (s, 3H, H-13).

$\text{IR}$  ( $\tilde{\nu}/\text{cm}^{-1}$ ): 3277 (s), 2984 (m), 2953 (m), 2849 (m), 2615 (m), 1641 (s), 1602 (s), 1536 (s), 1497 (m), 1465 (m), 1442 (s), 1359 (s), 1342 (s), 1262 (s), 1239 (m), 1202 (s), 1169 (s), 1153 (s), 1108 (s), 1013 (m), 959 (s), 888 (s), 836 (s), 807 (s), 758 (m), 693 (m), 624 (s), 596 (m), 573 (s), 519 (m), 468 (m), 450 (m).

6.3.3. Synthesis of vacant OMe-[Cr<sub>4</sub>]

## REN-ANL-185-28:

compound	$M / \frac{\text{g}}{\text{mol}}$	$m / \text{mg}$	$n / \text{mmol}$	$V / \text{mL}$	eq.
CrCl <sub>3</sub> · 6 H <sub>2</sub> O	266.41	53	0.2	-	1
OMe-ShiH <sub>3</sub>	183.163	37	0.2	-	1
NEt <sub>3</sub> ( $\rho = 0.73 \text{ g} \cdot \text{cm}^{-3}$ )	101.19	-	0.6	0.08	3
methanol	32.04	-	-	18.00	-
pyridine	79.10	-	-	2.00	-

## Procedure

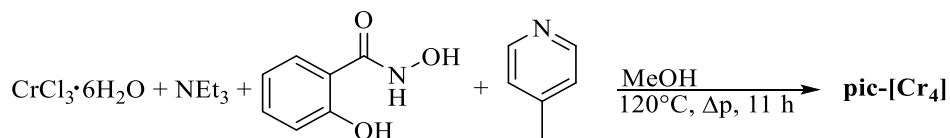
4-methoxysalicylhydroxamic acid (37 mg, 0.2 mmol, 1 eq.) and triethylamine (0.08 mL, 0.6 mmol, 3 eq.) were stirred in 10 mL methanol. Chromium(III) chloride hexahydrate (53 mg, 0.2 mmol, 1 eq.) was dissolved in 2 mL methanol and added, resulting in the precipitation of a lot of gray precipitate. 2 mL pyridine were added to the suspension which was stirred at room temperature for 15 minutes and transferred to a Teflon vessel and rinsed with 6 mL of methanol, heated in an autoclave reactor at 120°C for 11 hours. After cooling, the reaction solution is centrifuged, filtered and the solvent is slowly evaporated, obtaining brown crystals on the rim of the vials after 4 weeks.

## Analytic

yield  $m = 10$ -15 crystals (not possible to weight)

IR ( $\tilde{\nu} / \text{cm}^{-1}$ ) = 2920 (s), 2851 (s), 1733 (w), 1601 (m), 1562 (m), 1503 (m), 1485 (m), 1446 (s), 1421 (m), 1378 (m), 1345 (m), 1325 (m), 1286 (m), 1263 (m), 1214 (s), 1150 (s), 1103 (s), 1064 (s), 1045(s), 974 (m), 958 (m), 908 (m), 879 (m), 826 (m), 761 (m), 748 (m), 692 (s), 672 (s), 641 (s), 615 (s), 594(m), 571 (m), 528 (m), 473 (s), 451 (s).

X-ray analysis (see Table S 21)

6.3.4. Synthesis of pic-[Cr<sub>4</sub>]

## Ansatz REN-ANLX-44-22:

compound	$M / \frac{\text{g}}{\text{mol}}$	$m / \text{mg}$	$n / \text{mmol}$	$V / \text{mL}$	eq.
CrCl <sub>3</sub> · 6 H <sub>2</sub> O	266.41	106	0.4	-	1
ShiH <sub>3</sub>	153.14	63	0.4	-	1
NEt <sub>3</sub>	101.19	-	1.2	0.16	3
methanol	32.04	-	-	18.00	-
γ-picoline	93.13			2.00	

## Procedure

Salicylhydroxamic acid (63 mg, 0.4 mmol, 1 eq.) and triethylamine (0.16 mL, 1.2 mmol, 3 eq.) were stirred in 10 mL methanol. Chromium(III) chloride hexahydrate (106 mg, 0.4 mmol, 1 eq.) was dissolved in 2 mL methanol and added, resulting in the precipitation of a lot of gray precipitate. 2 mL γ-picoline were added to the suspension which was stirred at room temperature for 15 minutes and transferred to a Teflon vessel, rinsed with 6 mL of methanol and heated in an autoclave reactor at 120°C for 11 hours. After cooling, the reaction solution is centrifuged, filtered and the solvent is slowly evaporated, obtaining brown crystals on the rim of the vials after 3 days.

## Analytic

yield  $m = 35$  mg (0.022 mmol per Cr, 22% based on chromium(III) ions)

IR ( $\tilde{\nu} / \text{cm}^{-1}$ ) = 3626 (w,br), 3345 (w,br), 3042 (w), 1621 (m), 1593 (s), 1563 (m), 1503 (s), 1470 (m), 1439 (s), 1390 (m), 1321 (s), 1265 (s), 1230 (m), 1211 (m), 1155 (m), 1100 (m), 1067 (m), 1029 (s), 996 (m), 923 (s), 905 (s), 861 (s), 815 (s), 755 (s), 721 (m), 680 (m), 666 (s), 637 (m), 607 (m), 550 (m), 522 (m), 493 (s), 460 (s).

ESI-MS  $m/z$  (see Table S 29)

EA C<sub>76</sub>H<sub>73</sub>ClCr<sub>4</sub>N<sub>12</sub>O<sub>12</sub> · 5.4 H<sub>2</sub>O (including additional H<sub>2</sub>O) theoretical: C 54.10, H 5.01, N 9.96; found: C 4.11, H 5.03, N 9.99.

X-ray analysis (see Table S 22 Fehler! Verweisquelle konnte nicht gefunden werden.)



## 6.3.5. Synthesis of 3-hydroxy-2-naphthylhydroxamic acid (Nha)



## Ansatz REN-ANLX-50:

compound	$M / \frac{g}{mol}$	$m / g$	$n / mmol$	$V / mL$	eq.
methyl 3-hydroxy-2-naphthoate	202.21	10.00	4.9	-	1.0
$NH_2OH \cdot HCl$	69.49	6.50	9.3	-	1.9
KOH	56.11	7.84	14.0	-	2.8
MeOH	-	-	-	280	-

Procedure<sup>[13]</sup>

Hydroxylamine hydrochloride (6.50 g, 93 mmol, 1.9 eq.) and potassium hydroxide (7.84 g, 140 mmol, 2.8 eq.) were dissolved in 60 mL and 40 mL methanol separately. The potassium hydroxide solution was added to the hydroxylamine hydrochloride solution under cooling with an ice bath while potassium chloride precipitates. Methyl 3-hydroxy-2-naphthoate (10.00 g, 49 mmol, 1.0 eq.) dissolved in 160 mL methanol was added. The yellow suspension was stirred for 5 h with an attached argon balloon. The brown precipitate was filtered and recrystallized from a 1.25 M acetic acid/water solution. In the fridge a brown precipitate crystallized. The precipitate was filtered and recrystallized twice analog to above. 3-hydroxy-2-naphthylhydroxamic acid was isolated as beige needles.

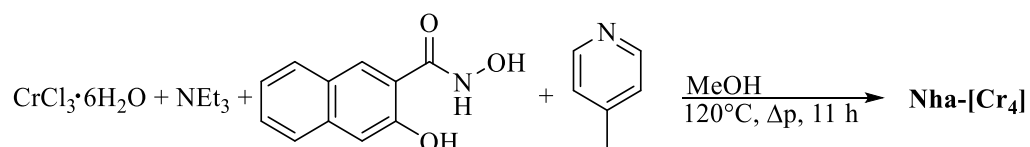
## Analytic

yield  $m = 1.53$  g (0.75 mmol, 15% of theory)

**$^1H$ -NMR** (400 MHz, DMSO- $d_6$ ,  $\delta$  / ppm): 11.51 (s, 2H), 9.46 (s, 1H), 8.31 (s, 1H), 7.83 (d,  $J = 7.1$  Hz, 1H), 7.73 (d,  $J = 7.3$  Hz, 1H), 7.48 (ddd,  $J = 8.2, 6.8, 1.3$  Hz, 1H), 7.33 (ddd,  $J = 8.1, 6.8, 1.2$  Hz, 1H), 7.27 (s, 1H).

**IR** ( $\tilde{\nu}/cm^{-1}$ ): 3272 (s), 3050 (s), 2784(m), 2125(w), 1928(w), 1837(w), 1627 (s), 1568 (m), 1530 (s), 1495 (m), 1456 (m), 1384 (m), 1354(s), 1339 (m), 1311 (s), 1261 (m), 1202(s), 1169(s), 1138 (s), 1087 (s), 1047 (s), 1015 (m), 950 (s), 918 (s), 876 (s), 855(s), 792(m), 768(m), 752 (m), 735 (m), 588 (s), 558(s), 529 (s), 482 (s), 474 (s), 446 (s), 429(s).

**ESI-MS**  $m/z =$  theo:  $[M+H]^+$  204.0655, exp: 204.0660.

6.3.6. Synthesis of Nha-[Cr<sub>4</sub>]

## Ansatz REN-ANLX-56-24:

compound	$M / \frac{\text{g}}{\text{mol}}$	$m / \text{mg}$	$n / \text{mmol}$	$V / \text{mL}$	eq.
CrCl <sub>3</sub> · 6 H <sub>2</sub> O	266.41	133	0.5	-	1
nha	203,20	101	0.5	-	1
NEt <sub>3</sub>	101.19	-	1.2	0.20	3
methanol	32.04	-	-	18.00	-
γ-picoline	93.13	-	-	2.00	-

## Procedure

Salicylhydroxamic acid (63 mg, 0.4 mmol, 1 eq.) and triethylamine (0.16 mL, 1.2 mmol, 3 eq.) were stirred in 10 mL methanol. Chromium(III) chloride hexahydrate (106 mg, 0.4 mmol, 1 eq.) was dissolved in 2 mL methanol and added, resulting in the precipitation of a lot of gray precipitate. 2 mL γ-picoline were added to the suspension which was stirred at room temperature for 15 minutes and transferred to a Teflon vessel and rinsed with 6 mL of methanol, heated in an autoclave reactor at 120°C for 11 hours. After cooling, the reaction solution is centrifuged, filtered and the solvent is slowly evaporated, obtaining brown crystals on the rim of the vials after 3 days.

## Analytic

yield  $m = 10 \text{ mg}$  (purity is still under investigation, X-Ray analysis still pending)

ESI-MS  $m/z$  (see Table S 31)

6.3.7. Structure determination of [Cr<sub>4</sub>]and OMe-[Cr<sub>4</sub>]Table S 21 Crystallographic data of complexes [Cr<sub>4</sub>]and OMe-[Cr<sub>4</sub>].

	[Cr <sub>4</sub> ]	OMe-[Cr <sub>4</sub> ]
	REN-ANL-195-28	REN-ANL-185-28
empirical formula	C <sub>68</sub> H <sub>57</sub> Cr <sub>4</sub> N <sub>12</sub> O <sub>12</sub> Cl	C <sub>72</sub> H <sub>64</sub> Cr <sub>4</sub> N <sub>12</sub> O <sub>16</sub> Cl
formula weight g/mol	1477.710	1596.806
overall formula	C <sub>73</sub> H <sub>77</sub> ClCr <sub>4</sub> N <sub>12</sub> O <sub>17</sub>	C <sub>79.75</sub> H <sub>96.25</sub> ClCr <sub>4</sub> N <sub>12</sub> O <sub>23.75</sub>
overall formula g/mol	1637.91	1846.38
crystal size / mm	0.23 x 0.14 x 0.06	0.2 x 0.119 x 0.032
crystal system	triclinic	triclinic
space group	P-1	P-1
unit cell dimensions		
<i>a</i> / Å	14.6096(11)	11.8438(4)
<i>b</i> / Å	15.0827(12)	18.0784(7)
<i>c</i> / Å	17.6266(14)	21.1735(7)
$\alpha$ /°	79.775(6)	105.364(3)
$\beta$ /°	84.519(6)	94.898(3)
$\gamma$ /°	76.005(6)	100.516(3)
volume/ Å <sup>3</sup>	3703.3(5)	4255.2(3)
cell formula units Z	2	2
density $\rho_{\text{calc}}$ / g cm <sup>-3</sup>	1.469	1.441
$\mu$ / mm <sup>-1</sup>	0.684	0.610
F(000)	1696	1924
temperature / K	120	120
device type	STOE STADIVARI	STOE STADIVARI
radiation	Mo-K $\alpha$	Mo-K $\alpha$
independent reflexes	1.685 < $\theta$ < 30.939	1.771 < $\theta$ < 31.104
index ranges	-20 < <i>h</i> < 21	-16 < <i>h</i> < 17
	-21 < <i>k</i> < 21	-25 < <i>k</i> < 26
	-24 < <i>l</i> < 25	-30 < <i>l</i> < 24
collected reflections	47005	97297
independent reflections	47005	110879
completeness	0.864	0.873
max. and min. transmission	0.9637 and 0.0478	0.9655 and 0.0217
<i>R</i> <sub>int</sub>	0.1265	?
<i>R</i> <sub>sigma</sub>	0.1244	0.1399
data/restraints/parameters	20312 / 3 / 976	97297 / 42 / 1137
goodness-of-fit on <i>F</i> <sup>2</sup>	1.080	1.075
<sup>a</sup> <i>R</i> <sub>1</sub> [ <i>I</i> > 2 $\sigma$ ( <i>I</i> )]	0.1077	0.2112
<sup>b</sup> <i>wR</i> <sub>2</sub> [ <i>I</i> > 2 $\sigma$ ( <i>I</i> )]	0.2768	0.4399
<i>R</i> <sub>1</sub> [all data]	0.1435	0.2817
<i>wR</i> <sub>2</sub> [all data]	0.3164	0.4970

$$^a R_1 = \Sigma(| |F_o| - |F_c| |) / \Sigma |F_o|, \quad ^b wR_2 = [\Sigma[w(F_o^2 - F_c^2)^2] / \Sigma[w(F_o^2)^2]]^{1/2}, \quad w = 1 / [\sigma^2(F_o^2) + (ap)^2 + bp], \quad p = [\max(F_o^2, 0) + 2F_c^2] / 3.$$

6.3.8. Structure determination of pic-[Cr<sub>4</sub>]Table S 22 Crystallographic data of complex pic-[Cr<sub>4</sub>] from block and plate shaped crystals.

	pic-[Cr <sub>4</sub> ] block	pic-[Cr <sub>4</sub> ] plate
	REN-ANLX-043-27	REN-ANLX-043-27
empirical formula	C <sub>76</sub> H <sub>73</sub> ClCr <sub>4</sub> N <sub>12</sub> O <sub>12</sub>	C <sub>76</sub> H <sub>73</sub> ClCr <sub>4</sub> N <sub>12</sub> O <sub>12</sub>
formula weight g/mol	1588.278	1588.278
overall formula	C <sub>83</sub> H <sub>101</sub> ClCr <sub>4</sub> N <sub>12</sub> O <sub>19</sub>	C <sub>152</sub> H <sub>161</sub> Cl <sub>2</sub> Cr <sub>8</sub> N <sub>24</sub> O <sub>32.50</sub>
overall formula g/mol	1814.20	3330.94
crystal size / mm	0.185 x 0.112 x 0.066	0.09 x 0.06 x 0.016
crystal system	triclinic	triclinic
space group	P1	P1
unit cell dimensions		
<i>a</i> / Å	12.5299(3)	12.1574(4)
<i>b</i> / Å	13.1913(3)	13.2654(5)
<i>c</i> / Å	13.6818(3)	26.2873(9)
$\alpha$ / °	94.113(2)	92.281(3)
$\beta$ / °	90.648(2)	91.104(3)
$\gamma$ / °	109.111(2)	110.758(3)
volume / Å <sup>3</sup>	2129.81(9)	3958.6(3)
cell formula units Z	1	1
density $\rho_{\text{calc}}$ / g cm <sup>-3</sup>	1.414	1.397
$\mu$ / mm <sup>-1</sup>	0.604	0.641
F(000)	948	1727
temperature / K	120	120
device type	STOE STADIVARI	STOE STADIVARI
radiation	Mo-K $\alpha$	Mo-K $\alpha$
independent reflexes	2.413 < $\theta$ < 31.006	2.316 < $\theta$ < 30.993
index ranges	-17 < h < 17	-17 < h < 17
	-19 < k < 16	-17 < k < 18
	-19 < l < 19	-35 < l < 37
collected reflections	46912	73404
independent reflections	17548	38406
completeness	0.646	0.761
max. and min. transmission	0.8330 and 0.7446	0.9474 and 0.7883
$R_{\text{int}}$	0.0307	0.0912
$R_{\text{sigma}}$	0.0592	0.2611
data/restraints/parameters	17548 / 443 / 1254	38406 / 93 / 2004
goodness-of-fit on F <sup>2</sup>	0.910	0.867
<sup>a</sup> R <sub>1</sub> [ <i>I</i> > 2 $\sigma$ ( <i>I</i> )]	0.0330	0.0718
<sup>b</sup> wR <sub>2</sub> [ <i>I</i> > 2 $\sigma$ ( <i>I</i> )]	0.0739	0.1765
R <sub>1</sub> [all data]	0.0421	0.1338
wR <sub>2</sub> [all data]	0.0755	0.1929

$${}^a R_1 = \Sigma(|F_o| - |F_c|) / \Sigma|F_o|, {}^b wR_2 = [\Sigma[w(F_o^2 - F_c^2)^2] / \Sigma[w(F_o^2)^2]]^{1/2}, w = 1 / [\sigma^2(F_o^2) + (ap)^2 + bp], p = [\max(F_o^2, 0) + 2F_c^2] / 3.$$

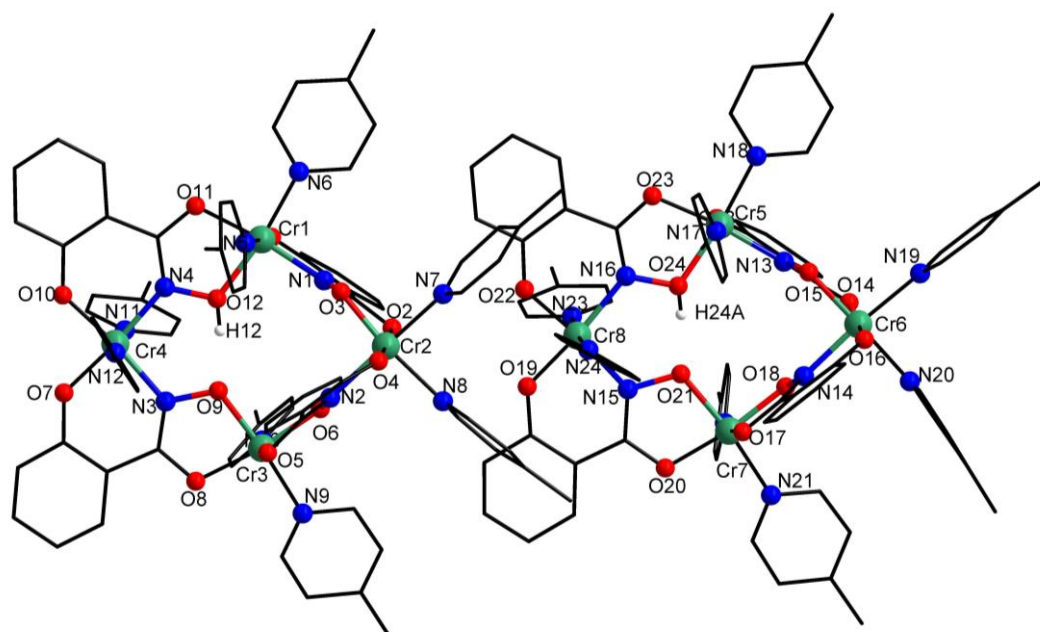


**Figure S 45.** Packing of molecules of **pic-[Cr<sub>4</sub>]**. Hydrogen atoms (except for H12,H24A) and the two chloride counter ions are omitted for clarity. Color code: chromium(III) ions green, oxygen red, nitrogen blue, carbon black.

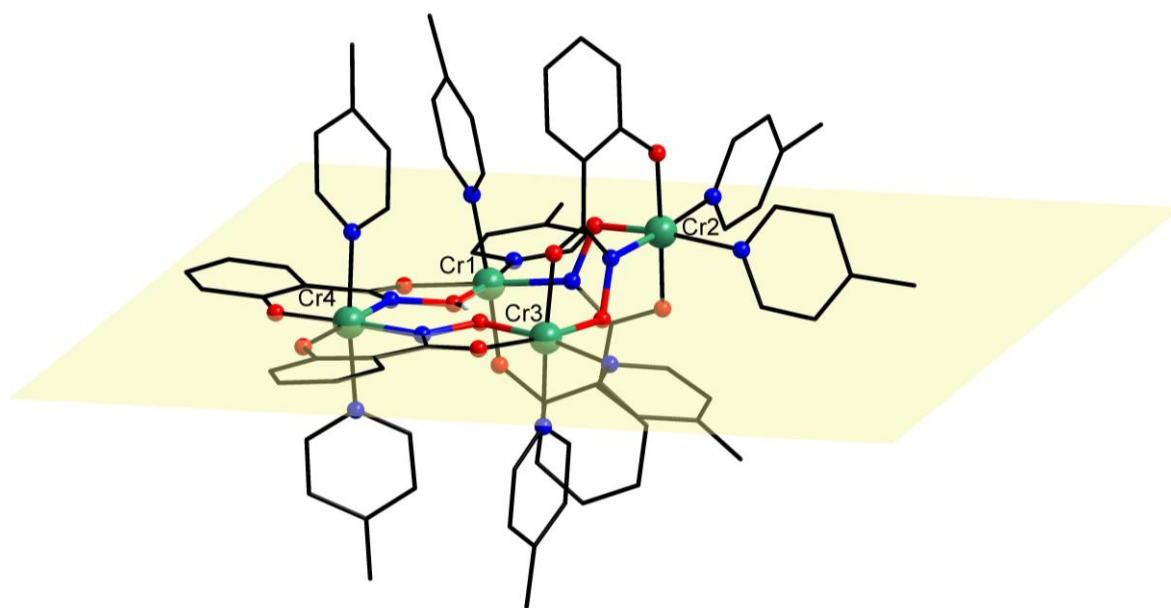


**Figure S 46.** Schematic representation of structure of **pic-[Cr<sub>4</sub>]** as a "side-on" view with out of plane coordination of Cr2 ion of plane through Cr1-Cr3-Cr4 (yellow). Hydrogen atoms are omitted for clarity. Color code: chromium(III) ions green, oxygen red, nitrogen blue, carbon black.

## 6.3.9. Continuous Shape Measurements

**Table S 23.** Calculated deviations from ideal polyhedra for Cr1, Cr2, Cr3 and Cr4 *via* Continuous Shape Measurements [Cr<sub>4</sub>].

Polyhedron <sup>a</sup>	Cr1 <i>cis</i>	Cr2 <i>cis</i>	Cr3 <i>cis</i>	Cr4 <i>trans</i>
HP-6	31.540	32.344	31.563	32.327
PPY-6	27.503	27.458	26.379	28.097
OC-6	0.442	0.402	0.666	0.347
TPR-6	15.357	15.102	14.231	14.449
JPPY-6	31.605	31.312	30.550	31.086

<sup>a</sup> abbreviations: HP-6 hexagon (D<sub>6h</sub>); PPY-6 pentagonal pyramid (C<sub>5v</sub>); OC-6 octahedron (O<sub>h</sub>); TPR-6 trigonal prism (D<sub>3h</sub>); JPPY-6 Johnson pentagonal pyramid J2 (C<sub>5v</sub>)

**Table S 24.** Calculated deviations from ideal polyhedra for Cr1, Cr2, Cr3 and Cr4 *via* Continuous Shape Measurements OMe-[Cr<sub>4</sub>].

Polyhedron <sup>a</sup>	Cr1 <i>cis</i>	Cr2 <i>cis</i>	Cr3 <i>cis</i>	Cr4 <i>trans</i>
HP-6	31.540	32.344	31.563	32.327
PPY-6	27.503	27.458	26.379	28.097
OC-6	0.442	0.402	0.666	0.347
TPR-6	15.357	15.102	14.231	14.449
JPPY-6	31.605	31.312	30.550	31.086

<sup>a</sup> abbreviations: HP-6 hexagon (D<sub>6h</sub>); PPY-6 pentagonal pyramid (C<sub>5v</sub>); OC-6 octahedron (O<sub>h</sub>); TPR-6 trigonal prism (D<sub>3h</sub>); JPPY-6 Johnson pentagonal pyramid J2 (C<sub>5v</sub>)

**Table S 25.** Calculated deviations from ideal polyhedra for Cr1, Cr2, Cr3 and Cr4 *via* Continuous Shape Measurements of molecule a) of pic-[Cr<sub>4</sub>] (plate morphology).

Polyhedron <sup>a</sup>	Cr1	Cr2	Cr3	Cr4
HP-6	31.918	31.972	30.054	32.172
PPY-6	28.263	26.197	27.138	26.856
OC-6	0.376	0.606	0.663	0.527
TPR-6	15.803	14.839	14.396	13.602
JPPY-6	32.287	30.466	30.630	29.887

<sup>a</sup> abbreviations: HP-6 hexagon (D<sub>6h</sub>); PPY-6 pentagonal pyramid (C<sub>5v</sub>); OC-6 octahedron (O<sub>h</sub>); TPR-6 trigonal prism (D<sub>3h</sub>); JPPY-6 Johnson pentagonal pyramid J2 (C<sub>5v</sub>)

**Table S 26.** Calculated deviations from ideal polyhedra for Cr1, Cr2, Cr3 and Cr4 *via* Continuous Shape Measurements of molecule b) of pic-[Cr<sub>4</sub>] (plate morphology).

Polyhedron <sup>a</sup>	Cr5	Cr6	Cr7	Cr8
HP-6	31.283	31.484	31.429	32.176
PPY-6	27.383	26.684	26.425	27.271
OC-6	0.495	0.494	0.674	0.413
TPR-6	14.862	14.247	13.649	13.984
JPPY-6	31.348	29.916	30.490	30.278

<sup>a</sup> abbreviations: HP-6 hexagon (D<sub>6h</sub>); PPY-6 pentagonal pyramid (C<sub>5v</sub>); OC-6 octahedron (O<sub>h</sub>); TPR-6 trigonal prism (D<sub>3h</sub>); JPPY-6 Johnson pentagonal pyramid J2 (C<sub>5v</sub>)

**Table S 27.** Calculated deviations from ideal polyhedra for Cr1, Cr2, Cr3 and Cr4 *via* Continuous Shape Measurements of **pic-[Cr<sub>4</sub>]** (block morphology).

<b>Polyhedron<sup>a</sup></b>	<b>Cr1</b>	<b>Cr2</b>	<b>Cr3</b>	<b>Cr4</b>
<b>HP-6</b>	31.137	30.527	30.683	32.151
<b>PPY-6</b>	27.362	26.443	26.868	27.417
<b>OC-6</b>	0.438	0.503	0.611	0.491
<b>TPR-6</b>	14.717	14.592	14.470	13.976
<b>JPPY-6</b>	31.309	29.727	30.782	30.378

<sup>a</sup> abbreviations: HP-6 hexagon (D<sub>6h</sub>); PPY-6 pentagonal pyramid (C<sub>5v</sub>); OC-6 octahedron (O<sub>h</sub>); TPR-6 trigonal prism (D<sub>3h</sub>); JPPY-6 Johnson pentagonal pyramid J2 (C<sub>5v</sub>)

### 6.3.10. Evaluation of magnetic data

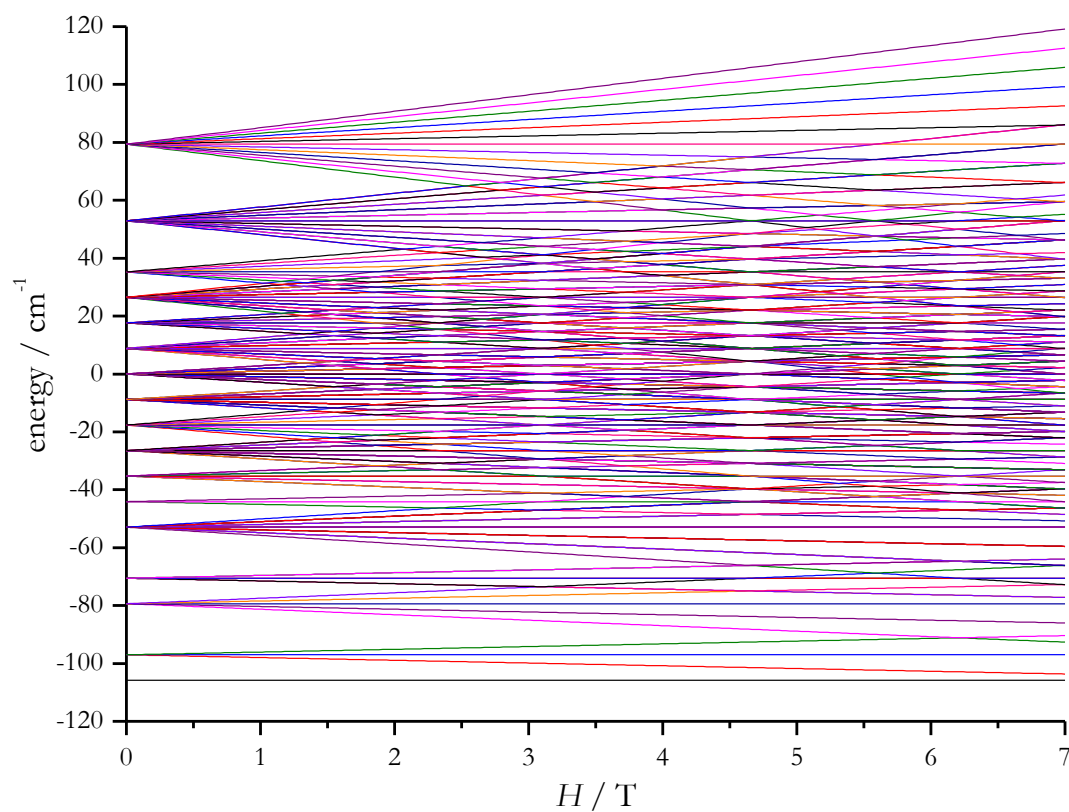
The fitting of magnetization and susceptibility data with two competing coupling constants  $J_1$  and  $J_2$  are summarized in Table S 28.

**Table S 28.** Calculated values for two competing coupling constants  $J_1$  and  $J_2$  of **pic-[Cr<sub>4</sub>]** (with program PHI<sup>®</sup>).

	$g$	$J_1$	$J_2$	$R$
parameters	$2.0444 \pm 0.0004$	$-2.68 \pm 0.01$	$-5.37 \pm 0.01$	$0.4 \cdot 10^{-4}$

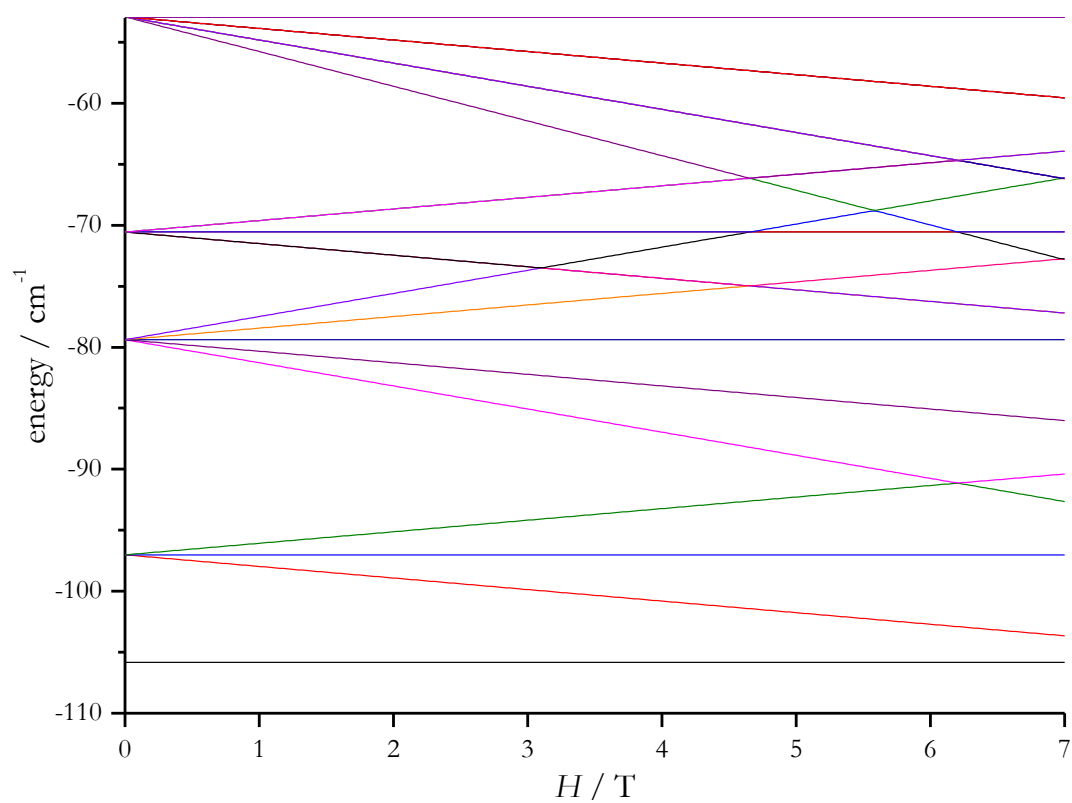
#### Zeeman splitting (simulated)

Figure S 47 shows the simulation of the Zeeman splitting for **pic-[Cr<sub>4</sub>]** with only one coupling constant  $J_1$ . A Zoom-in of lowest lying states is shown in Figure S 48.



**Figure S 47.** Simulated Zeeman splitting field dependence of the different spin states of **pic-[Cr<sub>4</sub>]**.





**Figure S 48.** Zoom-in of lowest lying states of simulated Zeeman splitting field dependence of the different spin states of  $\text{pic-}[\text{Cr}_4]$ .

## 6.3.11. Electrospray Ionization mass spectrometry (ESI)

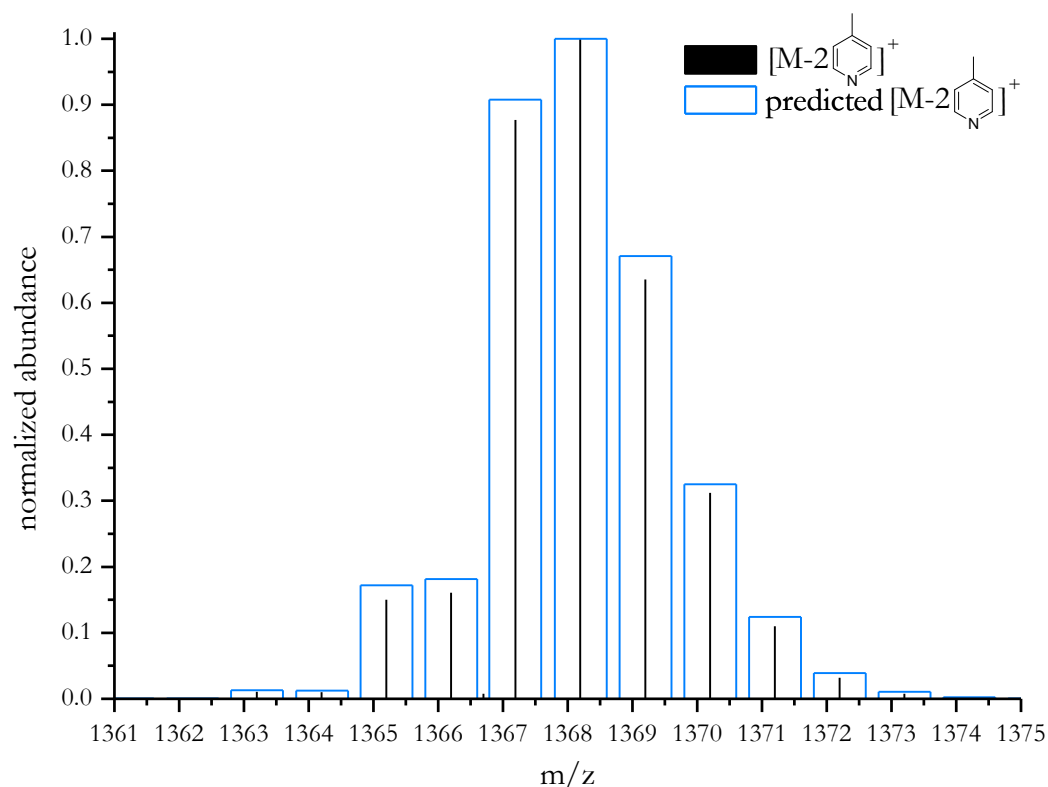


**Figure S 49.** Normalized abundance from electrospray ionization mass spectrum with zoom-in of isotope pattern of **pic-[Cr<sub>4</sub>]** [M-2- $\gamma$ -picoline]<sup>+</sup>. Measurement black, prediction blue box.

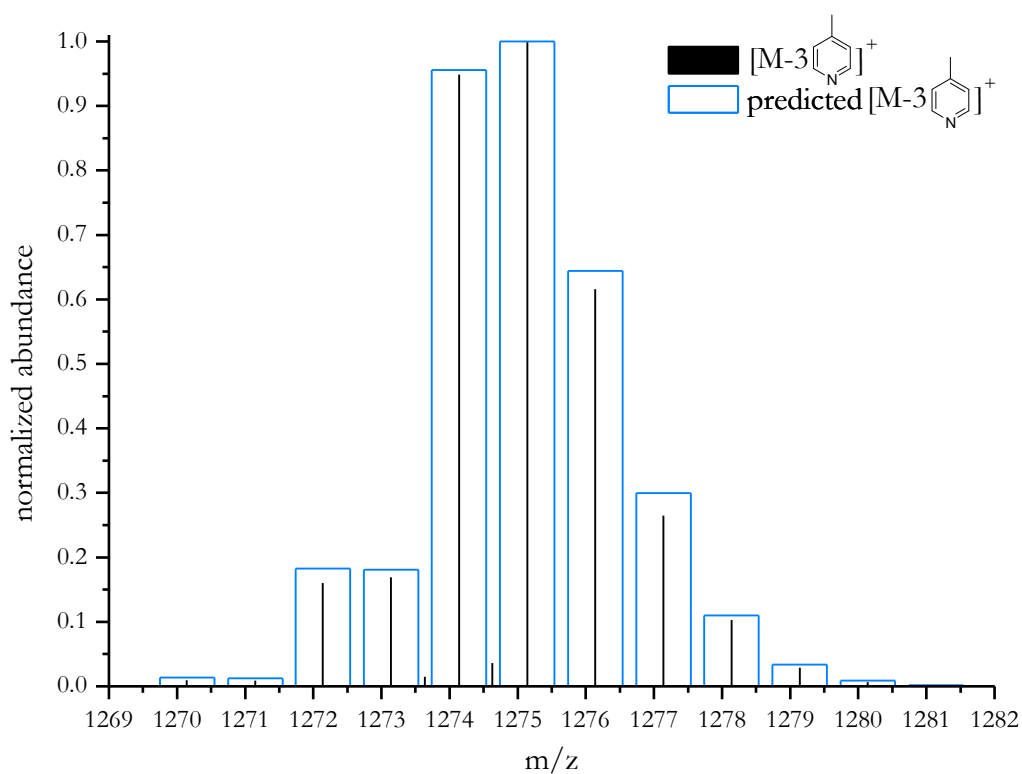


**Figure S 50.** Normalized abundance from electrospray ionization mass spectrum with zoom-in of isotope pattern of **pic-[Cr<sub>4</sub>]** [M-3- $\gamma$ -picoline]<sup>+</sup>. Measurement black, prediction blue box.

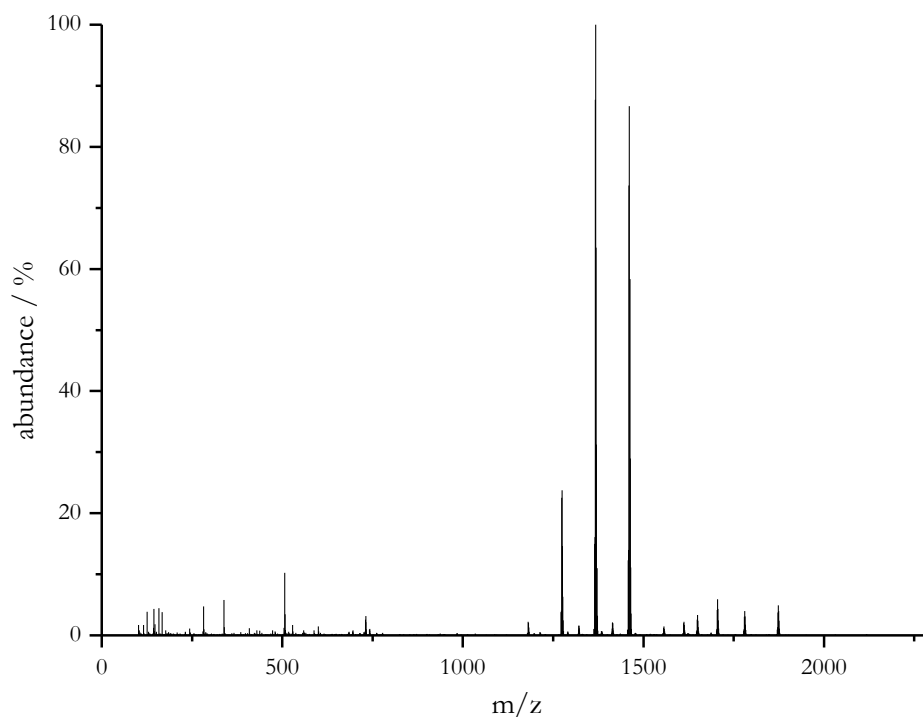


**Figure S 51.** Electrospray ionization mass spectrum of **pic-[Cr<sub>4</sub>]**. Fragment at 506 m/z is observed independently from the ligand, metal ion, base, or co-ligands (275°C).

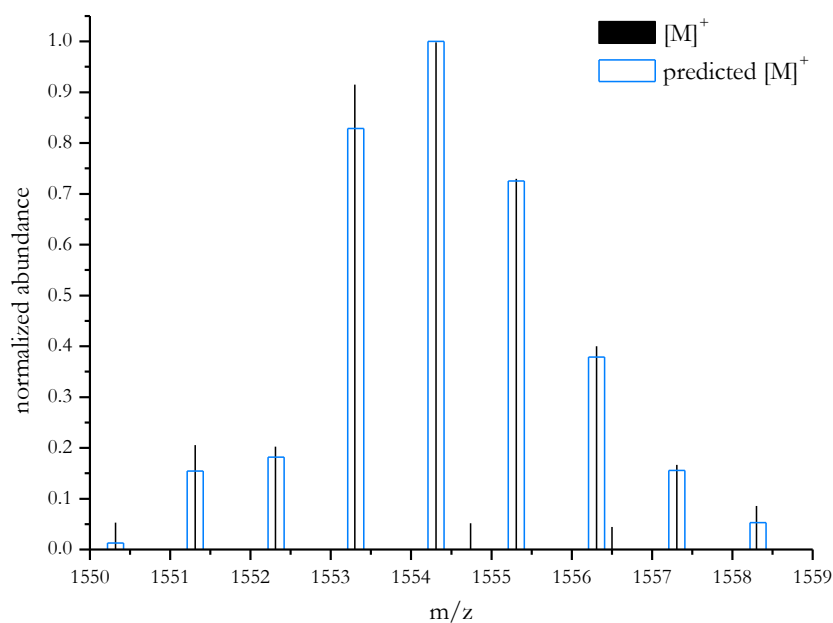


**Figure S 52** Normalized abundance from electrospray ionization mass spectrum with zoom-in of isotope pattern of **pic-[Cr<sub>4</sub>]<sup>+</sup>** at 100°C. Measurement black, prediction blue box.

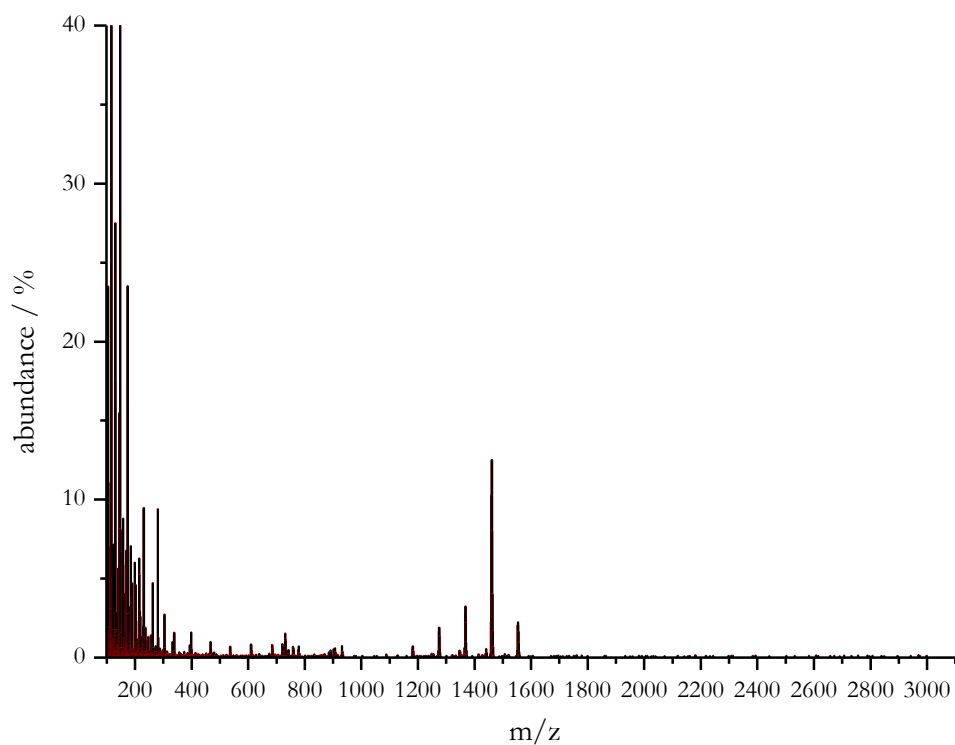


**Figure S 53.** Electrospray ionization mass spectrum of **pic-[Cr<sub>4</sub>]** (100°C).

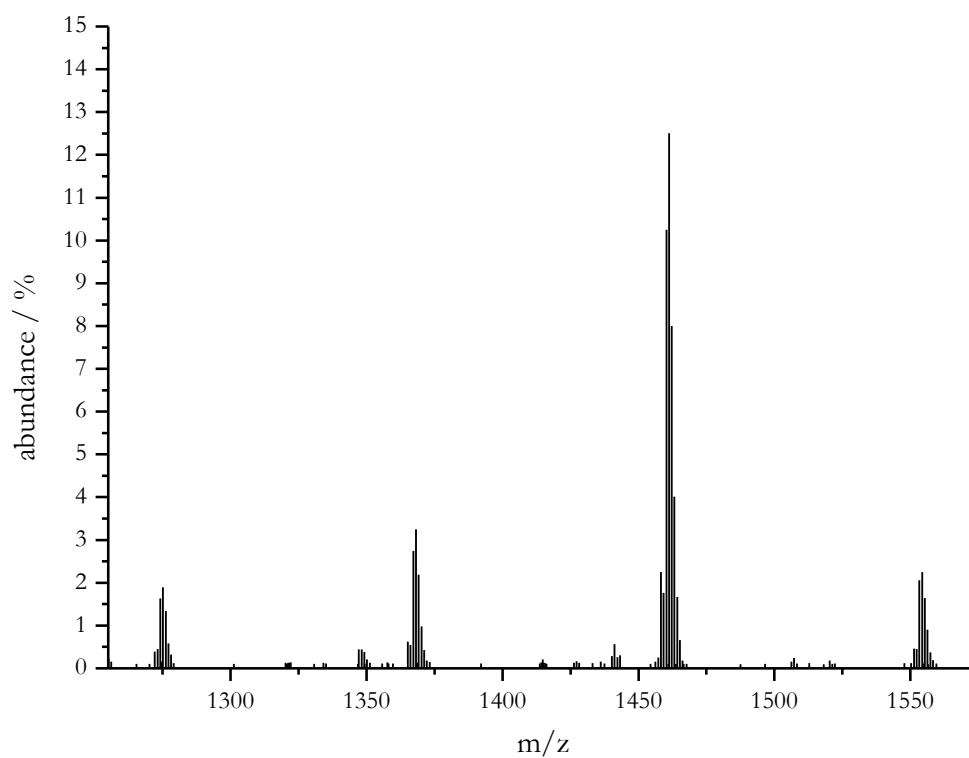


**Figure S 54.** Electrospray ionization mass spectrum zoom-in of **pic-[Cr<sub>4</sub>]** (100°C).

**Table S 29.** Summarized measured and predicted values for **pic-[Cr<sub>4</sub>]** for ESI spectra at 275°C. Because the complex **pic-[Cr<sub>4</sub>]** is positively charged, one proton was subtracted for the prediction. prediction tool, will add this proton for calculation. For the measured spectra only data above 1% detection are considered. Prediction tool of Mestre Nova always sets highest signal to 100% for each ion as adduct (C<sub>70</sub>H<sub>65</sub>Cr<sub>4</sub>N<sub>11</sub>O<sub>12</sub> (-1  $\gamma$ -picoline), (C<sub>64</sub>H<sub>58</sub>Cr<sub>4</sub>N<sub>10</sub>O<sub>12</sub> (-2  $\gamma$ -picoline)),(C<sub>58</sub>H<sub>51</sub>Cr<sub>4</sub>N<sub>9</sub>O<sub>12</sub> (-3  $\gamma$ -picoline))

measured m/z	rel. abundance / %	predicted m/z	rel. abundance / %
1272.139	3.81	1272.141	18.26
1273.140	4.02	1273.143	18.06
1274.135	22.55	1274.136	95.56
<b>1275.136</b>	<b>23.78</b>	<b>1275.137</b>	<b>100.00</b>
1276.137	14.64	1276.138	64.41
1277.138	6.30	1277.139	29.98
1278.137	2.44	1278.140	11.01
1365.197	15.00	1365.199	17.21
1366.199	16.10	1366.201	18.12
1367.193	87.71	1367.194	90.80
<b>1368.194</b>	<b>100.00</b>	<b>1368.195</b>	<b>100.00</b>
1369.196	63.52	1369.196	67.07
1370.197	31.22	1370.198	32.49
1371.198	11.01	1371.199	12.40
1372.198	3.21	1372.200	3.91
1458.255	12.31	1458.257	16.26
1459.257	13.98	1459.259	18.17
1460.251	73.66	1460.252	86.60
<b>1461.252</b>	<b>86.66</b>	<b>1461.253</b>	<b>100.00</b>
1462.254	58.35	1462.254	69.77
1463.255	28.98	1463.256	35.12
1464.256	11.11	1464.257	13.92
1465.257	3.54	1465.258	4.55

**Table S 30.** Summarized measured and predicted values for **pic-[Cr<sub>4</sub>]** for ESI spectra at 100°C. Because the complex **pic-[Cr<sub>4</sub>]** is positively charged, one proton was subtracted for the prediction. prediction tool, will add this proton for calculation. Prediction tool of Mestre Nova always sets highest signal to 100% for each ion as adduct (C<sub>76</sub>H<sub>72</sub>Cr<sub>4</sub>N<sub>12</sub>O<sub>12</sub>).

measured m/z	rel. abundance / %	predicted m/z	rel. abundance / %
1551.311	0.46	1551.315	15.42
1552.312	0.46	1552.317	18.20
1553.304	2.06	1553.310	82.88
<b>1554.308</b>	<b>2.25</b>	<b>1554.311</b>	<b>100.00</b>
1555.310	1.64	1555.312	72.51
1556.311	0.90	1556.314	37.88
1557.315	0.10	1557.315	15.56
1558.299	0.37	1558.316	5.27

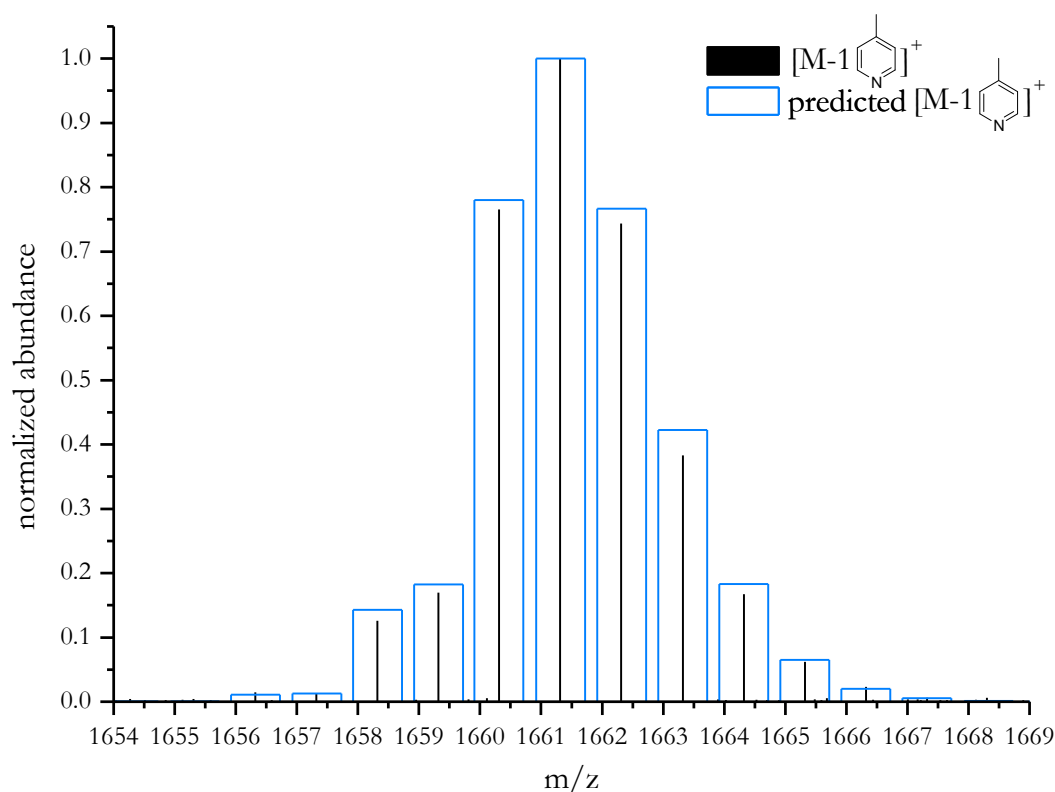


**Figure S 55.** Normalized abundance from electrospray ionization mass spectrum with zoom-in of isotope pattern of **Nha-[Cr<sub>4</sub>] [M-1- $\gamma$ -picoline]<sup>+</sup>** at 275°C. Measurement black, prediction blue box.

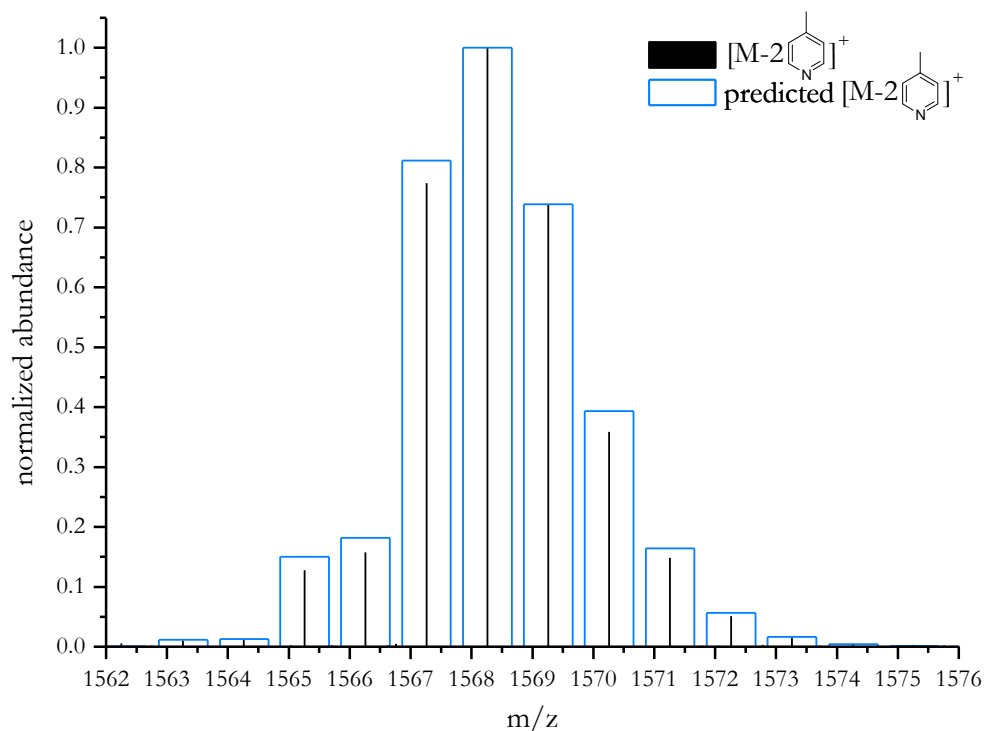


**Figure S 56.** Normalized abundance from electrospray ionization mass spectrum with zoom-in of isotope pattern of **Nha-[Cr<sub>4</sub>] [M-2- $\gamma$ -picoline]<sup>+</sup>** at 275°C. Measurement black, prediction blue box.

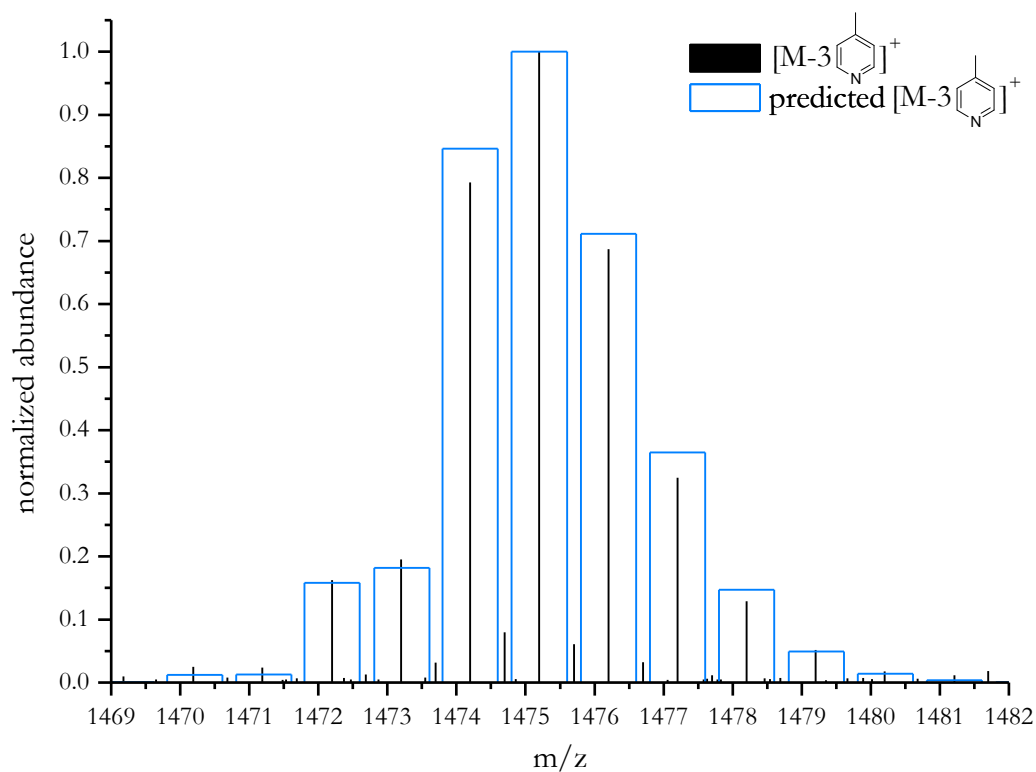


**Figure S 57.** Normalized abundance from electrospray ionization mass spectrum with zoom-in of isotope pattern of **Nha-[Cr<sub>4</sub>] [M-3- $\gamma$ -picoline]<sup>+</sup>** at 275°C. Measurement black, prediction blue box.

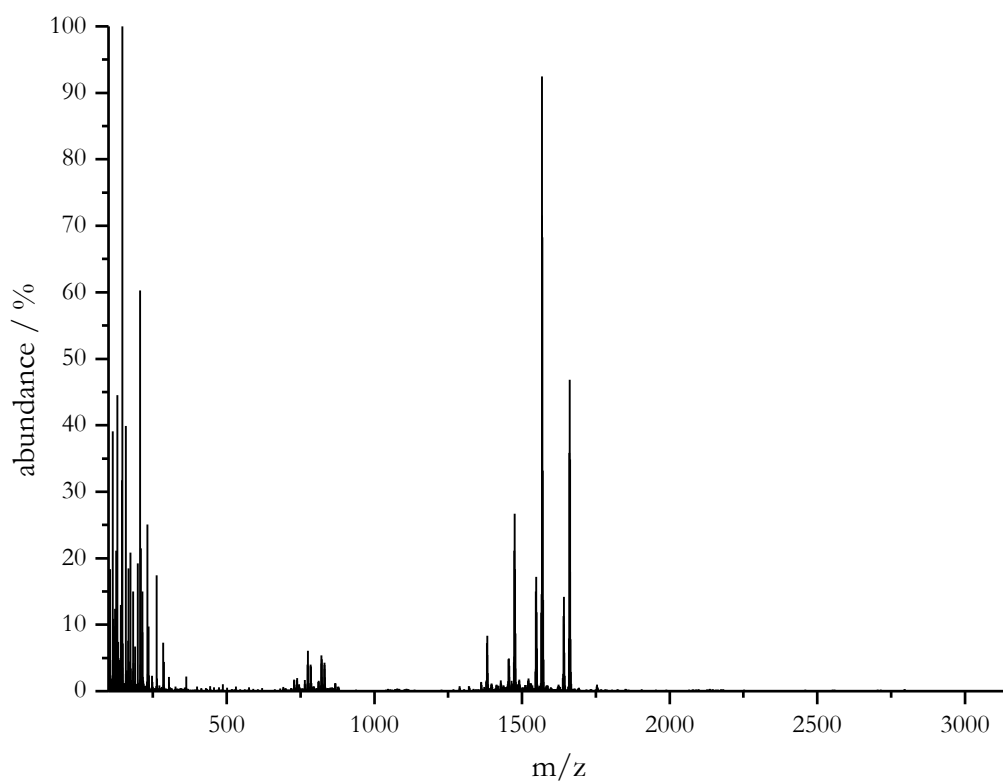


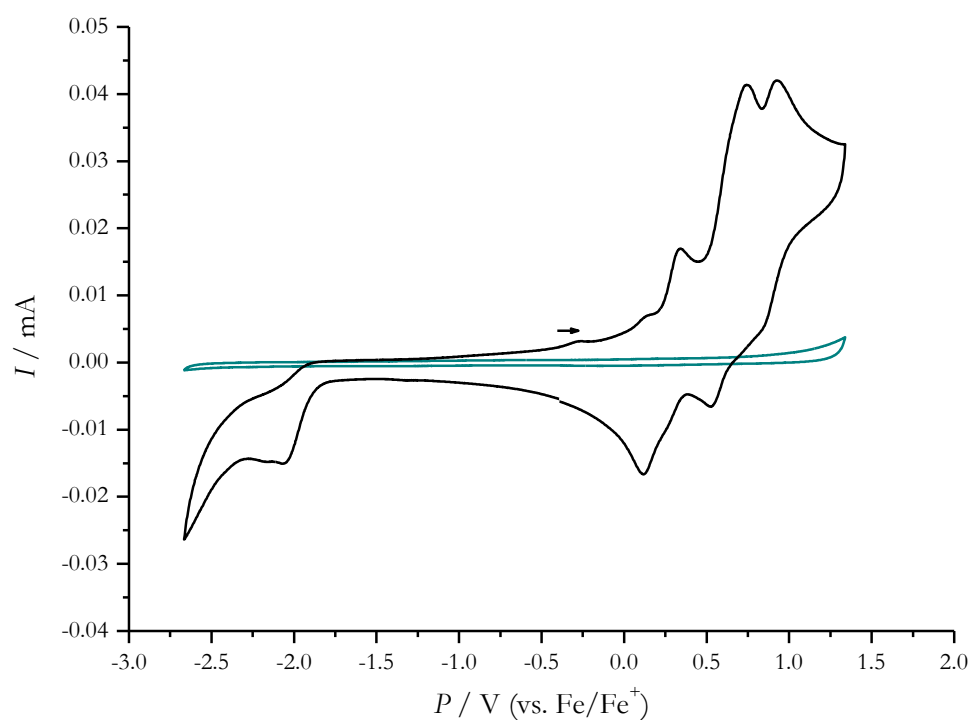
**Figure S 58.** Electrospray ionization mass spectrum of **Nha-[Cr<sub>4</sub>] (275 °C)**.

**Table S 31.** Summarized measured and predicted values for **Nha-[Cr<sub>4</sub>]** for ESI spectra at 275°C. Because the complex **Nha-[Cr<sub>4</sub>]** is positively charged, one proton was subtracted for the prediction. prediction tool, will add this proton for calculation. For the measured spectra only data above 1% detection are considered. Prediction tool of MestReNova always sets highest signal to 100% for each ion as adduct ((C<sub>86</sub>H<sub>73</sub>Cr<sub>4</sub>N<sub>11</sub>O<sub>12</sub>)-1  $\gamma$ -picoline), ((C<sub>80</sub>H<sub>66</sub>Cr<sub>4</sub>N<sub>10</sub>O<sub>12</sub>)-2  $\gamma$ -picoline)),((C<sub>74</sub>H<sub>59</sub>Cr<sub>4</sub>N<sub>9</sub>O<sub>12</sub>)-3  $\gamma$ -picoline)).

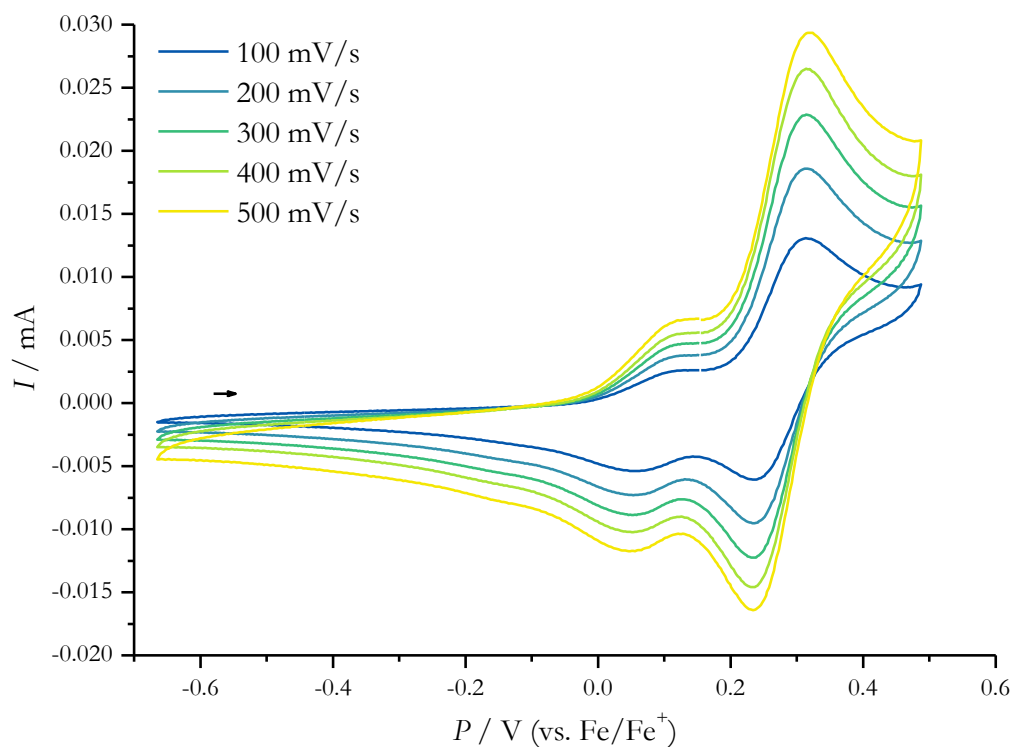
measured m/z	rel. abundance / %	predicted m/z	rel. abundance / %
1658.316	5.91	1658.319	14.31
1659.317	7.93	1659.321	18.22
1660.313	35.87	1660.315	78.03
<b>1661.315</b>	<b>46.85</b>	<b>1661.316</b>	<b>100.00</b>
1662.315	34.84	1662.318	76.66
1663.317	17.95	1663.319	42.26
1664.317	7.84	1664.320	18.29
1665.320	2.92	1665.322	6.52
1666.317	1.09	1666.323	1.98
1564.269	1.20	1564.269	1.27
1565.262	11.80	1565.262	15.03
1566.264	14.58	1566.264	18.21
1567.257	71.57	1567.257	81.16
<b>1568.258</b>	<b>92.49</b>	<b>1568.258</b>	<b>100.00</b>
1569.260	68.29	1569.260	73.90
1570.261	33.19	1570.261	39.32
1571.262	13.72	1571.262	16.44
1572.264	4.75	1572.264	5.67
1472.200	4.33	1472.204	15.83
1473.202	5.21	1473.206	18.18
1474.698	2.12	1474.199	84.66
<b>1475.199</b>	<b>26.68</b>	<b>1475.200</b>	<b>100.00</b>
1476.199	18.33	1476.201	71.15
1477.199	8.66	1477.203	36.50
1478.202	3.43	1478.204	14.73
1479.200	1.37	1479.205	4.90



## 6.3.12. Cyclic voltammetry



**Figure S 59.** Cyclic voltammogram of **pic-[Cr<sub>4</sub>]** including the blank solvent window of acetonitrile with a concentration of 100 mM of the conducting salt tetrabutylammonium hexafluorophosphate.

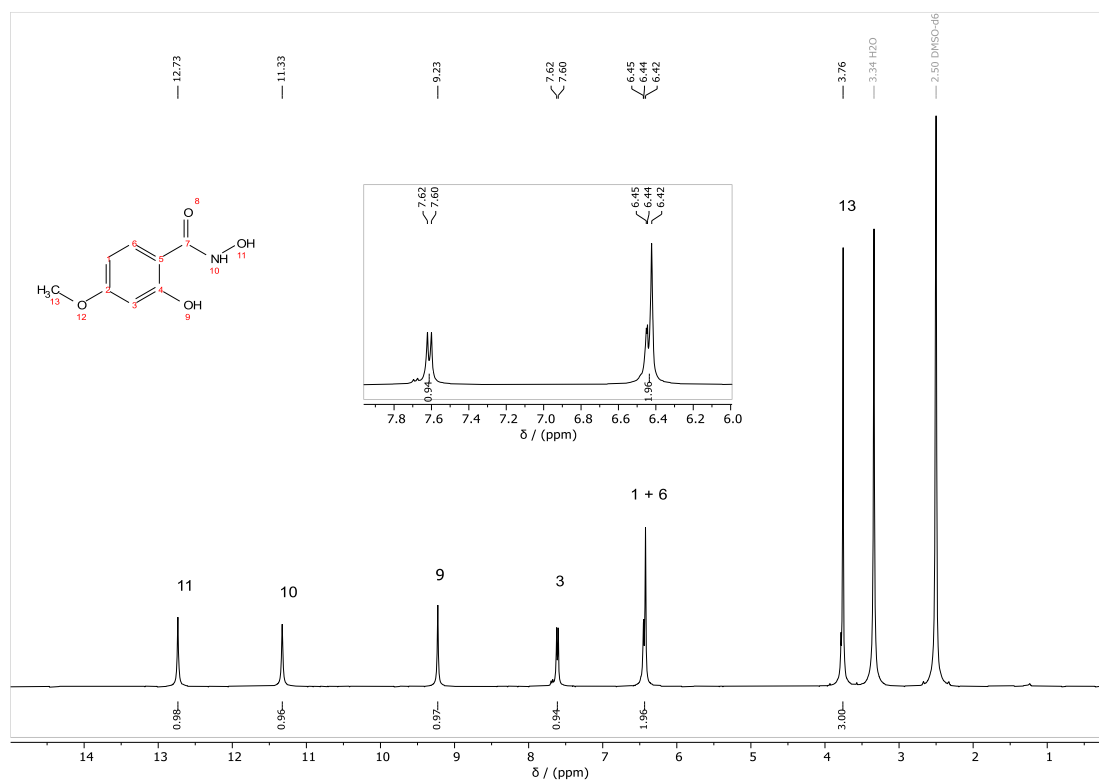
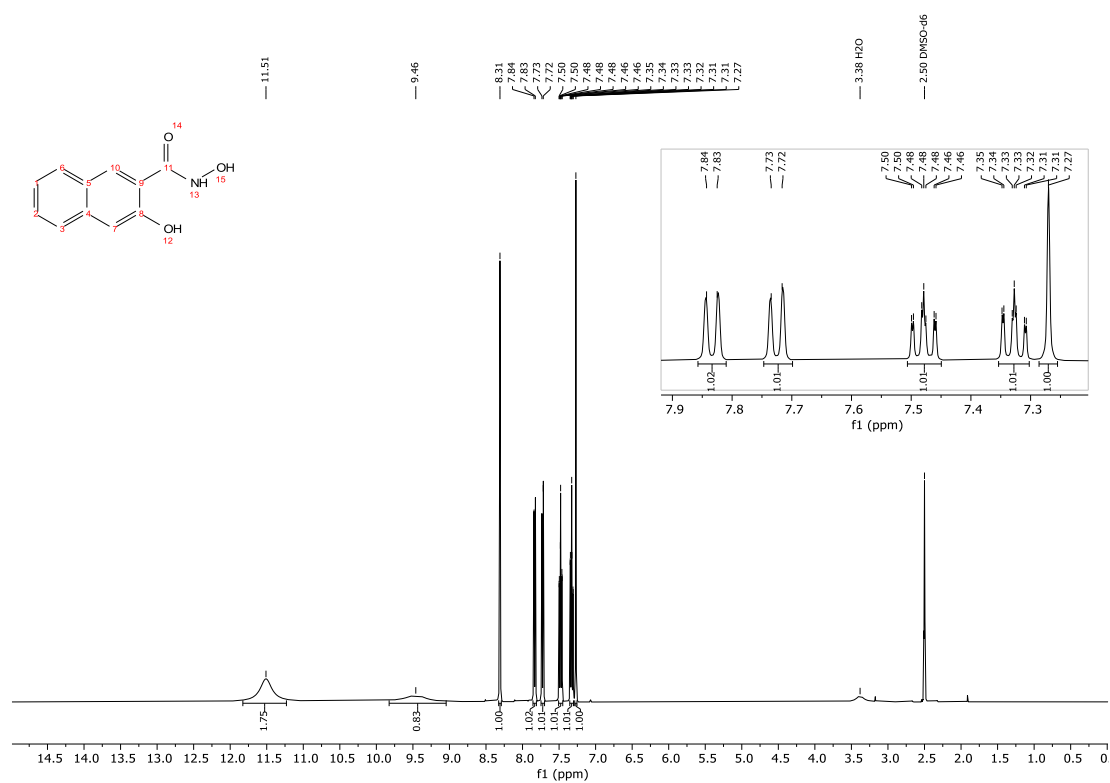


**Figure S 60.** Scan rate study of OII-RII redox pair of **pic-[Cr<sub>4</sub>]**.

**Table S 32.** Values of peak potentials  $E_p$  (anodic, index a; cathodic, index c), half-step potentials  $E_{1/2}$ , and potential for the cyclic voltammogram of **pic-[Cr<sub>4</sub>]**.

<b>Scan rate</b>	<b><math>E_{pa} / \text{V}</math></b>	<b><math>E_{pc} / \text{V}</math></b>
100 mV/s	0.31	0.24
200 mV/s	0.31	0.23
300 mV/s	0.31	0.23
400 mV/s	0.31	0.23
500 mV/s	0.31	0.23

## 6.3.13. NMR

Figure S 61.  $^1\text{H-NMR}$  of 4-methoxy salicylhydroxamic acid.Figure S 62.  $^1\text{H-NMR}$  of 3-hydroxy-2-naphthylhydroxamic acid.

### 6.3.14. Infrared spectra

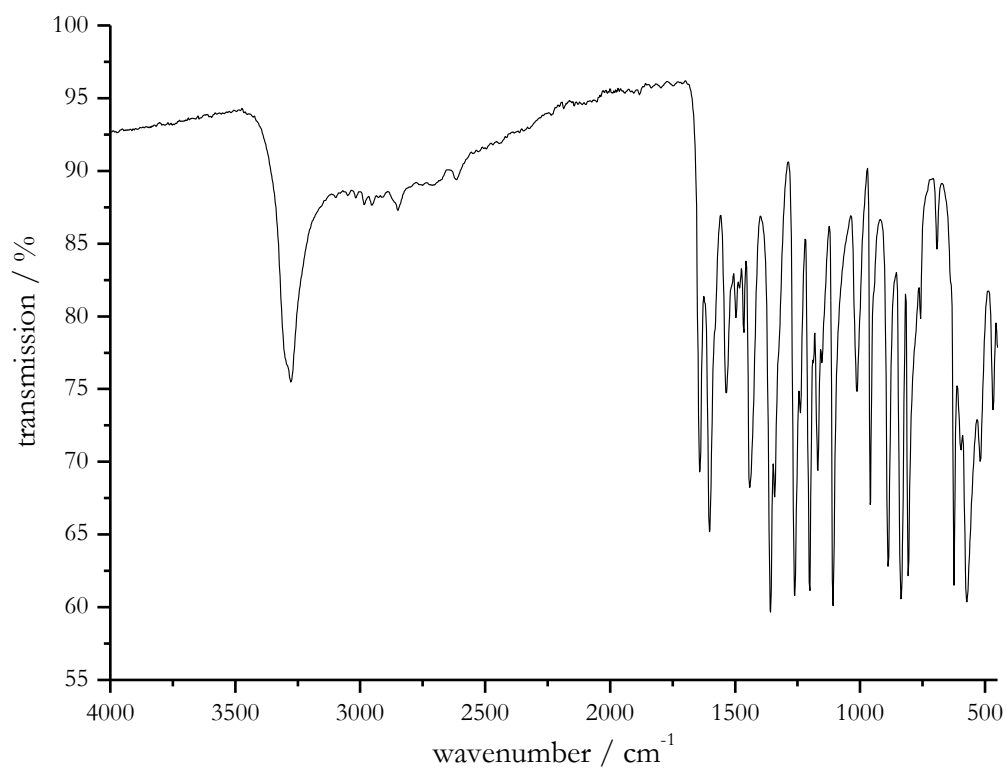


Figure S 63. Infrared spectrum of 4-methoxy salicylhydroxamic acid (REN-TF-004).

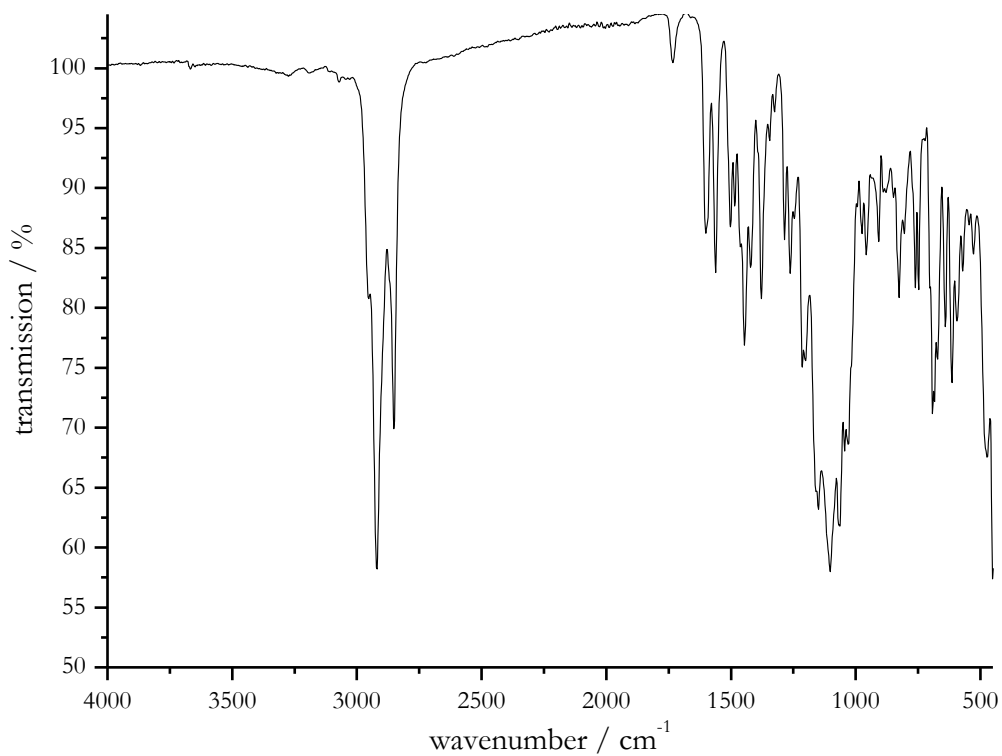


Figure S 64. Infrared spectrum of OMe-[Cr<sub>4</sub>] (REN-ANL-195-25).

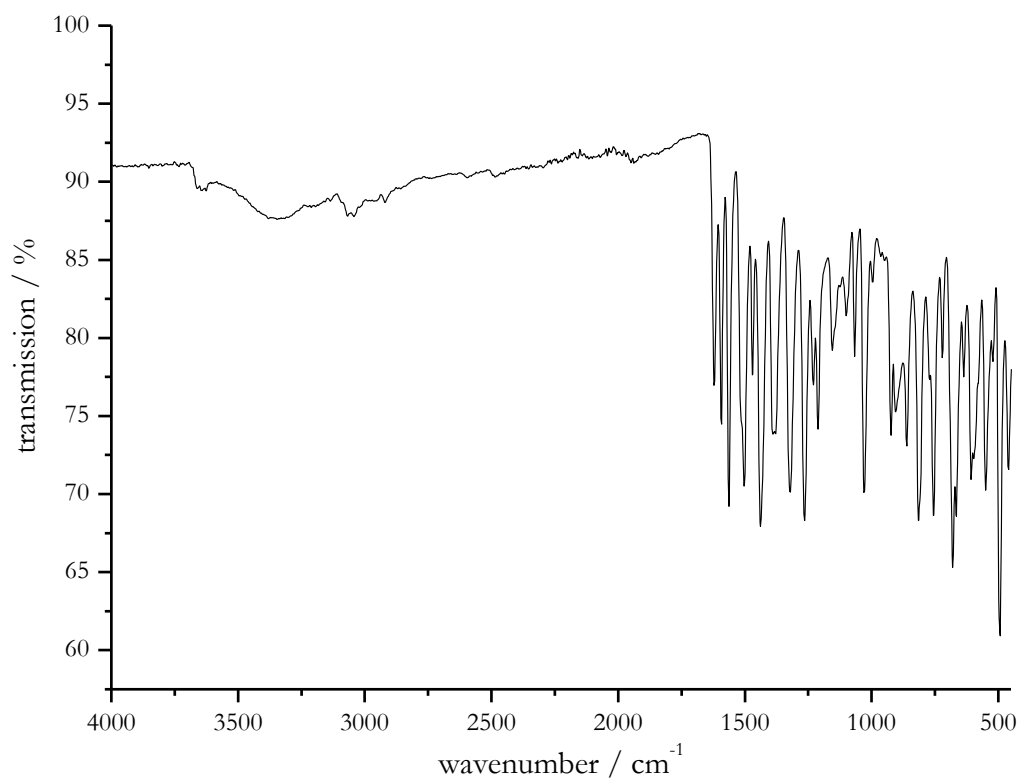


Figure S 65. Infrared spectrum of **pic-[Cr<sub>4</sub>]** (REN-ANLX-044-24).

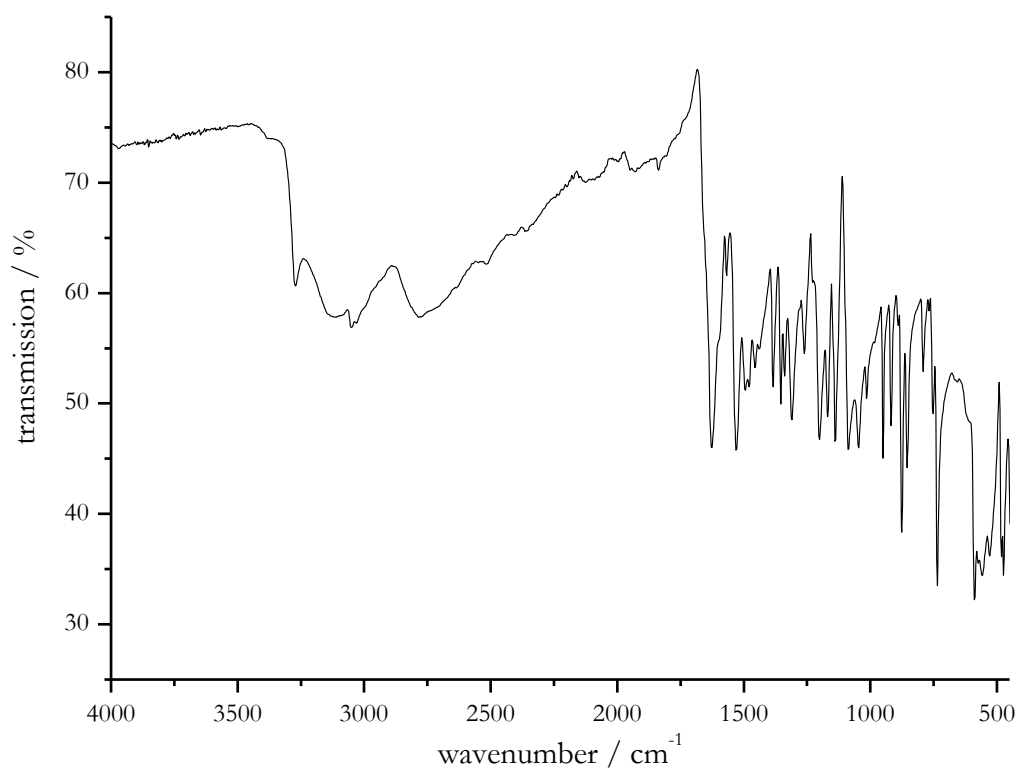
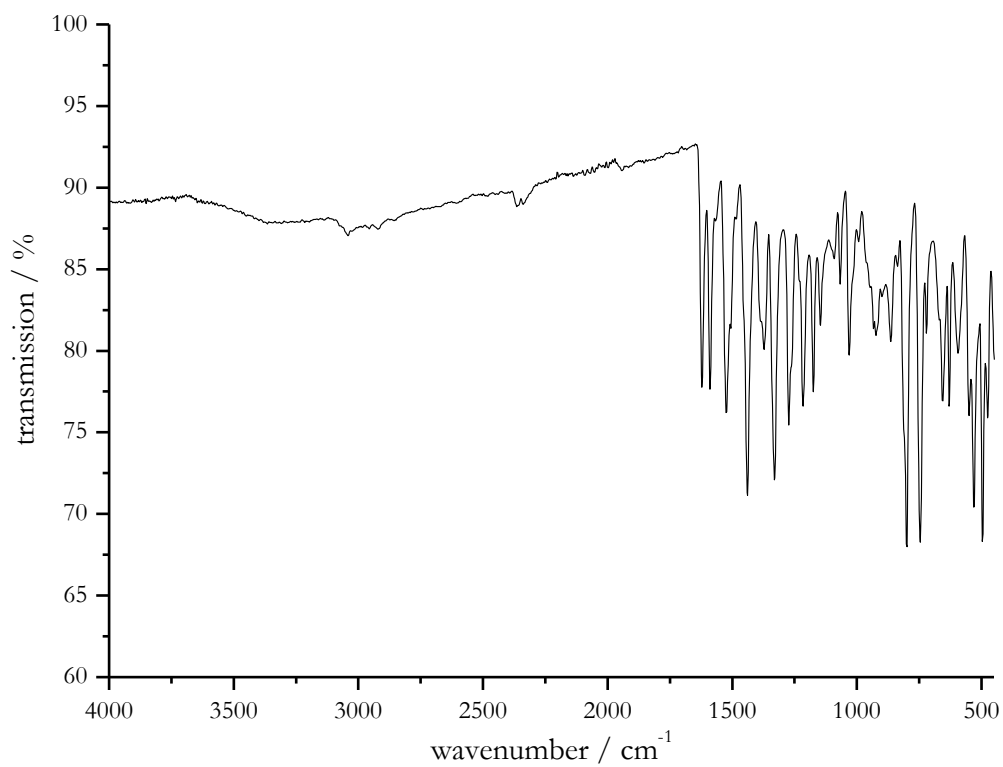


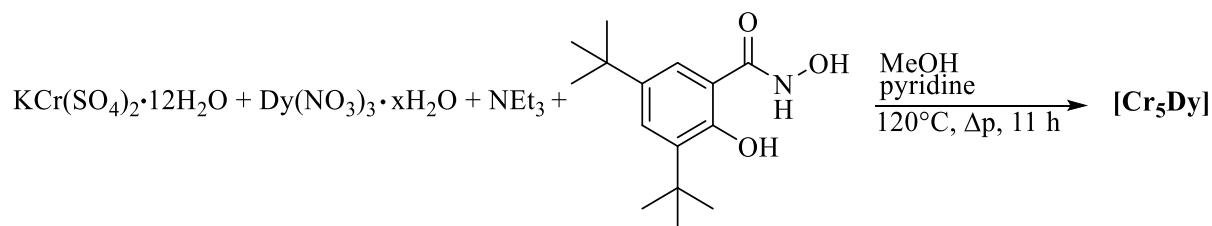
Figure S 66. Infrared spectrum of **Nha** (REN-ANLX-50).



**Figure S 67.** Infrared spectrum of **Nha-[Cr<sub>4</sub>]** (REN-ANLX-056-24).

## 6.4. Supporting information for Chapter 4.2.1.

### 6.4.2.1. Synthesis of [Cr<sub>5</sub>Dy] [15-MC-5] metallacrown



Ansatz REN-ANL-176-22n:

compound	$M / \frac{\text{g}}{\text{mol}}$	$m / \text{mg}$	$n / \text{mmol}$	$V / \text{mL}$	eq.
3,5-di- <i>tert</i> -butyl-salicylhydroxamic acid	265.35	53	0.20	-	4
Dy(NO <sub>3</sub> ) <sub>3</sub> xH <sub>2</sub> O	348.51 (anhydrous)	30	0.05	-	1
KCr(SO <sub>4</sub> ) <sub>2</sub> ·12H <sub>2</sub> O	499.25	100	0.20	-	4
NEt <sub>3</sub>	101.19	-	0.60	0.08	12
MeOH	32.04	-	-	15.00	-
pyridine	79.10	-	-	2.00	-

#### Procedure

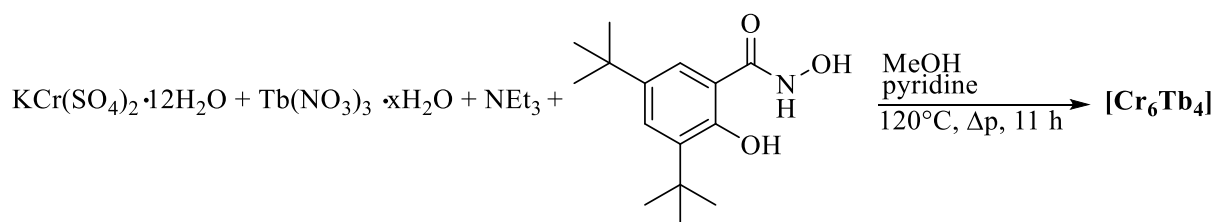
3,5-Di-*tert*-butyl-salicylhydroxamic acid (53 mg, 0.2 mmol, 4 eq.) and dysprosium(III)nitrate (30 mg, 0.05 mmol, 1 eq.) were stirred in 10 mL methanol. Potassium chromium(III) sulfate dodecahydrate (100 mg, 0.2 mmol, 4 eq.) and 2 mL pyridine were added, resulting in a purple suspension. Triethylamine (0.08 mL, 0.6 mmol, 12 eq.) was added dropwise while a grey precipitate formed. The suspension was stirred at room temperature for 15 minutes and transferred to a Teflon vessel, rinsed with 5 mL of methanol, and heated in an autoclave reactor at 120°C for 11 hours. After cooling, the reaction solution was centrifuged, filtered and the solvent was slowly evaporated, obtaining brown crystals after 5 weeks.

#### Analytic

yield  $m = 3 \text{ mg}$  (0.002 mmol per Cr, 5% of theory)

**IR ( $\tilde{\nu}/\text{cm}^{-1}$ ):** 2952 (s), 2904 (w), 2868 (w), 1607 (m), 1563 (m), 1509 (s), 1487 (w), 1447 (m), 1423 (s), 1384 (s), 1359 (m), 1307 (m), 1257 (s), 1226 (m), 1200 (m), 1151 (m), 1125 (s), 1069 (s), 1045 (s), 1017 (w), 970 (m), 889 (w), 834(s), 786 (w), 746 (s), 694 (s), 640 (m), 586 (s), 553 (s), 495 (m), 454 (s), 440 (s), 414 (s).

**X-ray analysis** (see Table S 33Fehler! Verweisquelle konnte nicht gefunden werden.)

6.4.2.2. Synthesis of [Cr<sub>6</sub>Tb<sub>4</sub>]

## Ansatz REN-ANLX-37-28:

compound	$M / \frac{\text{g}}{\text{mol}}$	$m / \text{mg}$	$n / \text{mmol}$	$V / \text{mL}$	eq.
3,5-di- <i>tert</i> -butyl-salicylhydroxamic acid	265.35	53	0.20	-	4
Tb(NO <sub>3</sub> ) <sub>3</sub> · xH <sub>2</sub> O	453.03 (with 6 H <sub>2</sub> O)	30	0.05	-	1
KCr(SO <sub>4</sub> ) <sub>2</sub> · 12H <sub>2</sub> O	499.25	100	0.20	-	4
NEt <sub>3</sub>	101.19	-	0.60	0.08	12
MeOH	32.04	-	-	15.00	-
pyridine	79.10	-	-	2.00	-

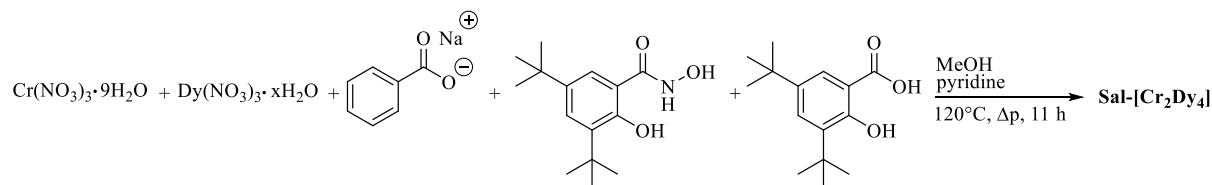
## Procedure

3,5-Di-*tert*-butyl-salicylhydroxamic acid (53 mg, 0.2 mmol, 4 eq.) and terbium(III)nitrate (30 mg, 0.05 mmol, 1 eq.) were stirred in 10 mL methanol. Potassium chromium(III) sulfate dodecahydrate (100 mg, 0.2 mmol, 4 eq.) and 2 mL pyridine were added, resulting in a purple suspension. Triethylamine (0.08 mL, 0.6 mmol, 12 eq.) was added dropwise while a grey precipitate formed. The suspension was stirred at room temperature for 15 minutes and transferred to a Teflon vessel, rinsed with 5 mL of methanol, and heated in an autoclave reactor at 120°C for 11 hours. After cooling, the reaction solution was centrifuged, filtered and the solvent was slowly evaporated, obtaining brown crystals after 6 days.

## Analytic

X-ray analysis (see Table S 33 Fehler! Verweisquelle konnte nicht gefunden werden.)



6.4.2.3. Synthesis of Sal-[Cr<sub>2</sub>Dy<sub>4</sub>] with 3,5-di-*tert*-butyl salicylhydroxamate

## Ansatz REN-ANL-150-22:

compound	$M / \frac{\text{g}}{\text{mol}}$	$m / \text{mg}$	$n / \text{mmol}$	$V / \text{mL}$	eq.
3,5-di- <i>tert</i> -butyl-salicylhydroxamic acid / 3,5-di- <i>tert</i> -butyl-salicylic acid (3:1)	265.35 / 250.34	78	0.2 (based on hydroxamic acid)	-	2
Na benzoate	144.11	86	0.6	-	6
Dy(NO <sub>3</sub> ) <sub>3</sub> ·xH <sub>2</sub> O	348.51 (anhydrous)	46	0.1	-	1
Cr(NO <sub>3</sub> ) <sub>3</sub> ·9H <sub>2</sub> O	400.15	80	0.2	-	2
Pyridin	79.10	-	-	2.00	-
MeOH	-	-	-	15.00	-

## Procedure

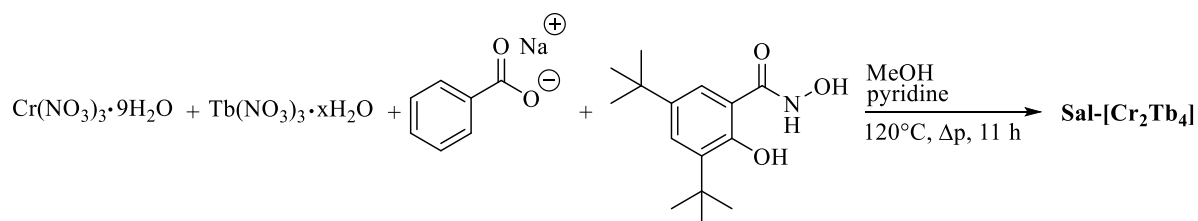
3,5-Di-*tert*-butyl-salicylhydroxamic acid (including 3,5-di-*tert*-butyl-salicylic acid) (78 mg, 0.2 mmol, 2 eq.) and dysprosium(III)nitrate (46 mg, 0.1 mmol, 1 eq.) were stirred in 10 mL methanol. Chromium(III) nitrate nonahydrate (80 mg, 0.2 mmol, 2 eq.) and sodium benzoate (86 mg, 0.6 mmol, 6 eq.) were added and stirred for five minutes. 2 mL pyridine were added, and the suspension was stirred at room temperature for 15 minutes and transferred to a Teflon vessel, rinsed with 5 mL of methanol, and heated in an autoclave reactor at 120°C for 11 hours. After cooling, the reaction solution was filtered and the solvent was slowly evaporated, obtaining brown crystals after 4 weeks.

## Analytic

yield  $m = 10$  mg (0.004 mmol per Cr, 4% of theory)

IR ( $\tilde{\nu}/\text{cm}^{-1}$ ): 2952 (m), 2905 (w), 2868 (s), 1597 (m), 1561 (m), 1537 (m), 1515 (m), 1489 (m), 1462 (m), 1446 (m), 1414 (s), 1392 (s), 1361 (m), 1306 (m), 1277 (m), 1254 (s), 1220 (m), 1200 (m), 1176 (m), 1151 (m), 1126 (m), 1069 (m), 1045 (m), 1025 (m), 1019 (m), 963 (m), 930 (m), 890 (m), 835 (s), 819 (m), 786 (m), 747 (s), 718 (s), 692 (s), 680 (m), 641 (m), 598 (m), 550 (s), 493 (m), 478 (m), 453 (m), 442 (m), 421 (m).

X-ray analysis (see Table S 34 Fehler! Verweisquelle konnte nicht gefunden werden.)

6.4.2.4. Synthesis of Sal-[Cr<sub>2</sub>Tb<sub>4</sub>] with 3,5-di-*tert*-butyl salicylhydroxamate

## Ansatz REN-ANL-177-25:

compound	$M / \frac{\text{g}}{\text{mol}}$	$m / \text{mg}$	$n / \text{mmol}$	$V / \text{mL}$	eq.
3,5-di- <i>tert</i> -butyl-salicylhydroxamic acid	265.35	53	0.20	-	4
Na benzoate	144.11	86	0.60	-	6
Tb(NO <sub>3</sub> ) <sub>3</sub> xH <sub>2</sub> O	453.03 (with 6 H <sub>2</sub> O)	30	0.05	-	1
Cr(NO <sub>3</sub> ) <sub>3</sub> ·9H <sub>2</sub> O	400.15	100	0.20	-	4
Pyridin	79.10	-	-	2.00	-
MeOH	-	-	-	15.00	-

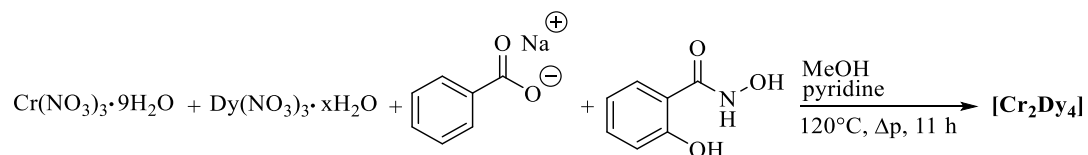
## Procedure

3,5-Di-*tert*-butyl-salicylhydroxamic acid (53 mg, 0.2 mmol, 4 eq.) and terbium(III)nitrato (30 mg, 0.05 mmol, 1 eq.) were stirred in 10 mL methanol. Chromium(III) nitrate nonahydrate (100 mg, 0.2 mmol, 4 eq.) and sodium benzoate (86 mg, 0.6 mmol, 6 eq.) were added and stirred for five minutes. 2 mL pyridine were added, and the suspension was stirred at room temperature for 15 minutes and transferred to a Teflon vessel, rinsed with 5 mL of methanol, and heated in an autoclave reactor at 120°C for 11 hours. After cooling, the reaction solution was filtered and the solvent was slowly evaporated, obtaining brown crystals after 3 weeks.

## Analytic

yield  $m = 9 \text{ mg}$  (0.003 mmol per Cr, 8% of theory)

X-ray analysis (see Table S 34 Fehler! Verweisquelle konnte nicht gefunden werden.)

6.4.2.5. Synthesis of  $[\text{Cr}_2\text{Dy}_4] \text{ShiH}_3$ 

## Ansatz REN-ANL-200-26:

compound	$M / \frac{\text{g}}{\text{mol}}$	$m / \text{mg}$	$n / \text{mmol}$	$V / \text{mL}$	eq.
salicylhydroxamic acid	153.14	62	0.4	-	4
Na benzoate	144.11	172	1.2	-	6
$\text{Dy}(\text{NO}_3)_3 \cdot x\text{H}_2\text{O}$ (anhydrous)	348.51	92	0.1	-	1
$\text{Cr}(\text{NO}_3)_3 \cdot 9\text{H}_2\text{O}$	400.15	160	0.4	-	4
Pyridin	79.10	-	-	2.00	-
MeOH	-	-	-	15.00	-

## Procedure

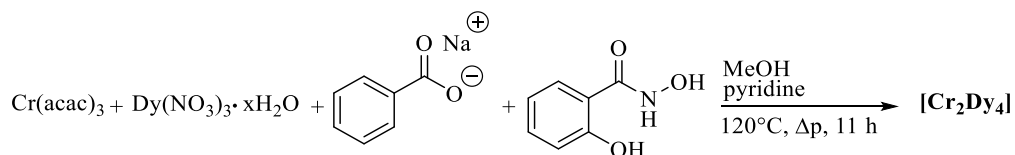
Salicylhydroxamic acid (62 mg, 0.4 mmol, 4 eq.) and dysprosium(III)nitrate (92 mg, 0.1 mmol, 1 eq.) were stirred in 10 mL methanol. 2 mL Pyridine were added, chromium(III) nitrate nonahydrate (160 mg, 0.4 mmol, 4 eq.) and sodium benzoate (172 mg, 1.2 mmol, 6 eq.) were added together and the suspension was stirred at room temperature for 10 minutes and transferred to a Teflon vessel, rinsed with 5 mL of methanol, and heated in an autoclave reactor at 120°C for 11 hours. After cooling, the reaction solution was filtered and the solvent was slowly evaporated, obtaining crystals after 4 weeks.

## Analytic

yield  $m = 15 \text{ mg}$  (0.006 mmol per Cr, 3% of theory)

**IR** ( $\tilde{\nu}/\text{cm}^{-1}$ ): 3066 (w), 1605 (w), 1594 (s), 1563 (s), 1513 (m), 1498 (m), 1487 (m), 1446 (s), 1381 (s), 1321 (s), 1264 (s), 1216 (m), 1154 (m), 1099, 1068 (w), 1044 (s), 1015 (m), 956 (w), 918 (m), 860 (m), 827 (m), 755 (s), 689 (s), 677 (s), 640 (s), 605 (s), 527 (m), 455 (m), 436 (m).

**X-ray** analysis (see Table S 36 **Fehler! Verweisquelle konnte nicht gefunden werden.**)

6.4.2.6. Synthesis of  $[\text{Cr}_2\text{Dy}_4] \text{ShiH}_3$ 

## Ansatz REN-ANL-164-26:

compound	$M / \frac{\text{g}}{\text{mol}}$	$m / \text{mg}$	$n / \text{mmol}$	$V / \text{mL}$	eq.
salicylhydroxamic acid	153.14	31	0.2	-	2
Benzoic acid	122.12	73	0.6	-	6
$\text{Dy}(\text{NO}_3)_3 \cdot x\text{H}_2\text{O}$	348.51 (anhydrous)	46	0.1	-	1
$\text{Cr}(\text{acac})_3$	349.32	70	0.2	-	2
Pyridin	79.10	-	-	2.00	-
MeOH	-	-	-	15.00	-

## Procedure

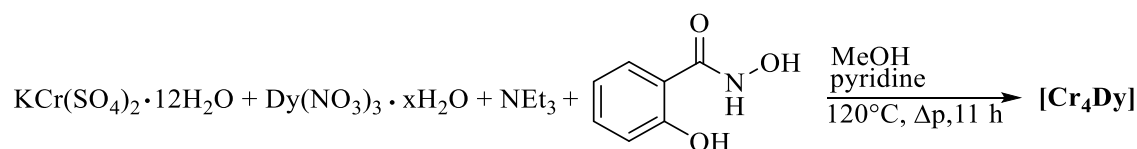
Salicylhydroxamic acid (31 mg, 0.4 mmol, 2 eq.), dysprosium(III)nitrate (46 mg, 0.1 mmol, 1 eq.), chromium acetylacetonate (70 mg, 0.2 mmol, 2 eq.), and benzoic acid (73 mg, 0.6 mmol, 6 eq.), were stirred in 10 mL methanol. 2 mL Pyridine were added, and the suspension was transferred to a Teflon vessel, rinsed with 5 mL of methanol, and heated in an autoclave reactor at 120°C for 11 hours. After cooling, the reaction solution was filtered and the solvent was slowly evaporated, obtaining crystals after 3 weeks.

## Analytic

yield  $m = 10$  mg (0.004 mmol per Cr, 4% of theory)

**IR** ( $\tilde{\nu}/\text{cm}^{-1}$ ): 3065 (w), 1702 (w), 1595 (s), 1566, 1517, 1488 (m), 1446 (s), 1392 (s), 1315 (s), 1262 (s), 1216 (s), 1156 (m), 1099 (m), 1069 (m), 1025 (m), 921 (s), 861 (m), 823 (w), 755 (s), 719 (s), 691 (s), 673 (s), 641 (m), 604 (m), 581 (m), 546 (w), 464 (s).

**X-ray** analysis (see Table S 36 **Fehler! Verweisquelle konnte nicht gefunden werden.**)

6.4.2.7. Synthesis of [Cr<sub>4</sub>Dy] [12-MC-4]metallacrown

## Ansatz REN-ANL-201-27:

compound	$M / \frac{\text{g}}{\text{mol}}$	$m / \text{mg}$	$n / \text{mmol}$	$V / \text{mL}$	eq.
ShiH <sub>3</sub>	153.19	106	0.7	-	7
Dy(NO <sub>3</sub> ) <sub>3</sub> xH <sub>2</sub> O		60	0.1	-	1
Cr(SO <sub>4</sub> ) <sub>2</sub> K 12H <sub>2</sub> O	499.25	200	0.4	-	4
Pyridin	79.10	-	-	2.00	-
NEt <sub>3</sub>	101.19	-	1.2	0.16	12
MeOH	-	-	-	15.00	-

## Procedure

Salicylhydroxamic acid (106 mg, 0.7 mmol, 7 eq.) and dysprosium(III)nitrate (60 mg, 0.1 mmol, 1 eq.) were stirred in 10 mL methanol. 2 mL Pyridine and potassium chromium(III) sulfate dodecahydrate (200 mg, 0.4 mmol, 4 eq.) were added, resulting in a purple suspension. Triethylamine (0.16 mL, 1.2 mmol, 12 eq.) was added dropwise while a grey precipitate formed. The suspension was stirred at room temperature for 15 minutes and transferred to a Teflon vessel, rinsed with 5 mL of methanol, and heated in an autoclave reactor at 120°C for 11 hours. After cooling, the reaction solution is centrifuged, filtered and the solvent was slowly evaporated, obtaining brown crystals after 2-4 weeks.

## Analytic

yield  $m = 20 \text{ mg}$  (0.012 mmol per Cr, 12% of theory)

**IR** ( $\tilde{\nu}/\text{cm}^{-1}$ ): 3068 (br), 1599 (m), 1569 (s), 1520 (m), 1486 (m), 1470 (m), 1438 (m), 1379 (m), 1310 (m), 1244 (m), 1217 (m), 1154 (w), 1097 (w), 1070 (w), 1032 (m), 935 (s), 916 (m), 855 (w), 826 (w), 751 (s), 689 (m), 667 (s), 639 (s), 597 (s), 526 (m), 479 (s), 456 (s), 437 (m), 408 (s).

**X-ray** analysis (see Table S 37 **Fehler! Verweisquelle konnte nicht gefunden werden.**)

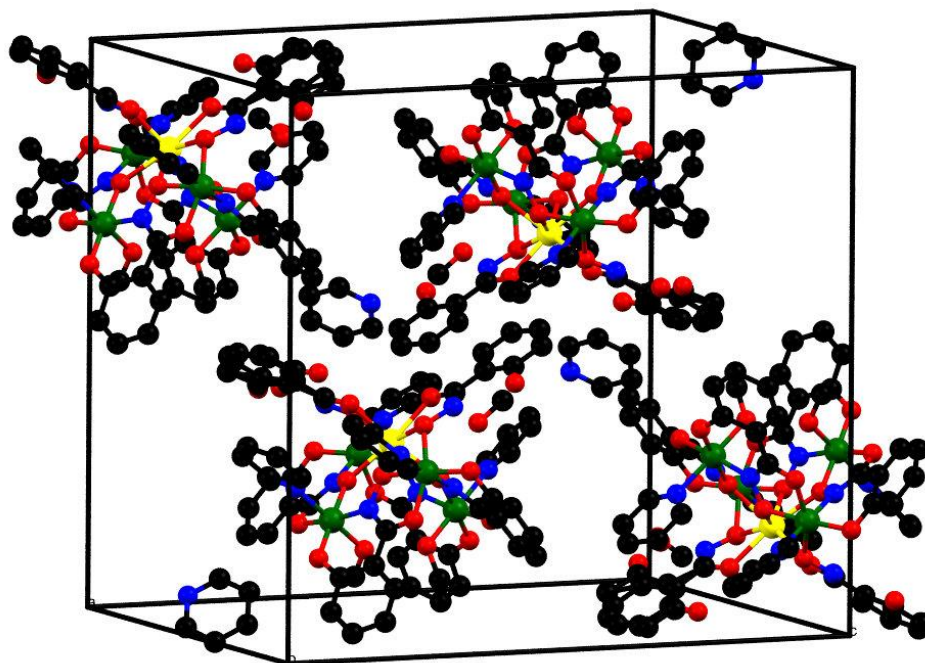


**Figure S 68.** Crystal packing of complex including solvent molecules (MeOH, H<sub>2</sub>O, pyridine) of [Cr<sub>4</sub>Dy]. Hydrogen atoms are omitted for clarity. Color code: dysprosium(III) ions, chromium(III) ions green, oxygen red, nitrogen blue, carbon grey.

6.4.2.8. Structure determination of [Cr<sub>5</sub>Dy] and [Cr<sub>6</sub>Tb<sub>4</sub>]Table S 33. Crystallographic data of complex [Cr<sub>5</sub>Dy] and [Cr<sub>6</sub>Tb<sub>4</sub>].

	[Cr <sub>5</sub> Dy]	[Cr <sub>6</sub> Tb <sub>4</sub> ]
	REN-ANL-176-22n	REN-ANLX-037-28
empirical formula	C <sub>115</sub> H <sub>140</sub> Cr <sub>5</sub> DyN <sub>14</sub> O <sub>22</sub> S	C <sub>222</sub> H <sub>296</sub> N <sub>20</sub> O <sub>40</sub> Tb <sub>4</sub>
formula weight g/mol	2524.630	4517.876
overall formula	C <sub>127</sub> H <sub>154</sub> Cr <sub>5</sub> DyN <sub>16</sub> O <sub>25</sub> S	C <sub>237.20</sub> H <sub>317.60</sub> Cr <sub>6</sub> N <sub>22.80</sub> O <sub>42</sub> Tb <sub>4</sub>
overall formula g/mol	2759.21	5108.00
crystal size / mm	0.14 x 0.067 x 0.025	0.145 x 0.068 x 0.015
crystal system	monoclinic	monoclinic
space group	C12/c1	C12/c1
unit cell dimensions		
<i>a</i> / Å	42.2769(12)	28.1757(10)
<i>b</i> / Å	24.2813(5)	35.6765(9)
<i>c</i> / Å	39.7212(12)	26.2075(9)
$\alpha$ / °	90	90
$\beta$ / °	130.888(2)	93.755(3)
$\gamma$ / °	90	90
volume / Å <sup>3</sup>	30825.7(16)	26287.5(15)
cell formula units Z	8	4
density $\rho_{\text{calc}}$ / g cm <sup>-3</sup>	1.189	1.291
$\mu$ / mm <sup>-1</sup>	0.896	1.367
F(000)	1144	10562
temperature / K	120	293(2)
device type	STOE STADIVARI	STOE STADIVARI
radiation	Mo-K $\alpha$	Mo-K $\alpha$
independent reflexes	1.674 < $\theta$ < 29.183	2.395 < $\theta$ < 30.000
index ranges	-56 < <i>h</i> < 44	-38 < <i>h</i> < 33
	-24 < <i>k</i> < 29	-34 < <i>k</i> < 49
	-43 < <i>l</i> < 51	-36 < <i>l</i> < 35
collected reflections	94940	88230
independent reflections	94940	33009
completeness	0.766	0.861
max. and min. transmission	0.9953 and 0.1891	0.9578 and 0.4497
$R_{\text{int}}$	0.1141	0.1652
$R_{\text{sigma}}$	0.2474	0.4616
data/restraints/parameters	31935 / 211 / 1570	33009 / 183 / 1501
goodness-of-fit on $F^2$	0.914	0.638
<sup>a</sup> $R_1$ [ $I > 2\sigma(I)$ ]	0.0776	0.0562
<sup>b</sup> $wR_2$ [ $I > 2\sigma(I)$ ]	0.1826	0.1109
$R_1$ [all data]	0.1889	0.2323
$wR_2$ [all data]	0.2170	0.1386

$$^a R_1 = \Sigma(| |F_o| - |F_c| |) / \Sigma |F_o|, \quad ^b wR_2 = [\Sigma[w(F_o^2 - F_c^2)^2] / \Sigma[w(F_o^2)^2]]^{1/2}, \quad w = 1 / [\sigma^2(F_o^2) + (ap)^2 + bp], \quad p = [\max(F_o^2, 0) + 2F_c^2] / 3.$$

### 6.4.2.9. Structure determination of Sal-[Cr<sub>4</sub>Dy<sub>2</sub>] and Sal-[Cr<sub>4</sub>Tb<sub>2</sub>] including 3,5-di-*tert*-butylsalicylhydroxate and corresponding acid

**Table S 34.** Crystallographic data of complexes Sal-[Cr<sub>4</sub>Dy<sub>2</sub>] and Sal-[Cr<sub>4</sub>Tb<sub>2</sub>].

	Sal-[Cr <sub>4</sub> Dy <sub>2</sub> ]	Sal-[Cr <sub>4</sub> Tb <sub>2</sub> ]
	REN-ANL-150-22	REN-ANL-177-25
empirical formula	C <sub>136</sub> H <sub>166</sub> Cr <sub>4</sub> Dy <sub>2</sub> N <sub>10</sub> O <sub>24</sub>	C <sub>164</sub> H <sub>203</sub> Cr <sub>4</sub> N <sub>12</sub> O <sub>28</sub> Tb <sub>2</sub>
formula weight g/mol	2858.828	3314.096
overall formula	C <sub>139</sub> H <sub>178.06</sub> Cr <sub>4</sub> Dy <sub>2</sub> N <sub>10</sub> O <sub>27</sub>	C <sub>177</sub> H <sub>227</sub> Cr <sub>4</sub> N <sub>14</sub> O <sub>31</sub> Tb <sub>2</sub>
overall formula g/mol	2953.96	3572.55
crystal size / mm	0.29 x 0.247 x 0.19	0.085 x 0.053 x 0.033
crystal system	triclinic	triclinic
space group	P-1	P-1
unit cell dimensions		
<i>a</i> / Å	15.5590(5)	16.9324(5)
<i>b</i> / Å	15.7147(5)	17.1612(5)
<i>c</i> / Å	16.3709(5)	18.3585(5)
$\alpha$ / °	93.868(2)	77.735(2)
$\beta$ / °	98.364(2)	72.193(2)
$\gamma$ / °	108.786(2)	67.912(2)
volume / Å <sup>3</sup>	3721.2(2)	4677.5(2)
cell formula units Z	1	1
density $\rho_{\text{calc}}$ / g cm <sup>-3</sup>	1.318	1.268
$\mu$ / mm <sup>-1</sup>	1.341	1.039
F(000)	1526	1861
temperature / K	120(2)	120
device type	STOE STADIVARI	STOE STADIVARI
radiation	Mo-K $\alpha$	Mo-K $\alpha$
independent reflexes	2.051 < $\theta$ < 30.716	1.835 < $\theta$ < 31.003
index ranges	-21 < h < 21	-22 < h < 22
	-21 < k < 19	-19 < k < 24
	-23 < l < 23	-25 < l < 26
collected reflections	58647	57342
independent reflections	20236	57342
completeness	0.874	0.866
max. and min. transmission	0.8309 and 0.3704	0.9719 and 0.1189
$R_{\text{int}}$	0.0262	0.0670
$R_{\text{sigma}}$	0.0342	0.0968
data/restraints/parameters	20236 / 510 / 1128	25854 / 279 / 1269
goodness-of-fit on F <sup>2</sup>	1.057	0.925
<sup>a</sup> R <sub>1</sub> [ <i>I</i> > 2 $\sigma$ ( <i>I</i> )]	0.0470	0.0771
<sup>b</sup> wR <sub>2</sub> [ <i>I</i> > 2 $\sigma$ ( <i>I</i> )]	0.1253	0.1971
R <sub>1</sub> [all data]	0.0663	0.1422
wR <sub>2</sub> [all data]	0.1372	0.2341

$$^a R_1 = \Sigma(|F_o| - |F_c|) / \Sigma|F_o|, \quad ^b wR_2 = [\Sigma[w(F_o^2 - F_c^2)^2] / \Sigma[w(F_o^2)^2]]^{1/2}, \quad w = 1 / [\sigma^2(F_o^2) + (ap)^2 + bp], \quad p = [\max(F_o^2, 0) + 2F_c^2] / 3.$$



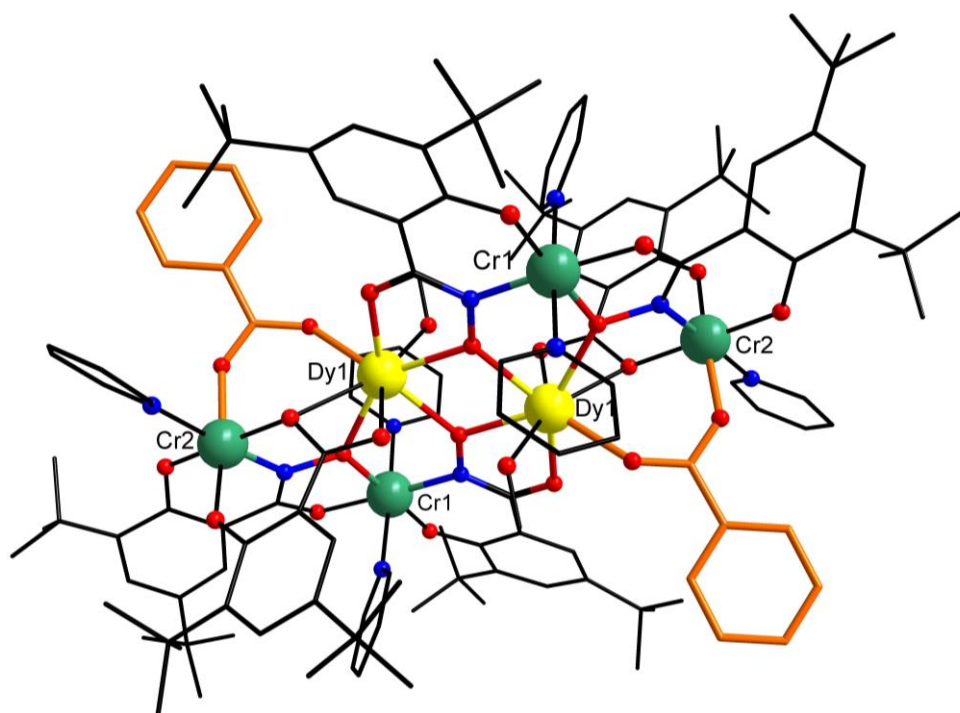


**Figure S 69.** Schematic representation of the molecular structure of  $[\text{Cr}^{\text{III}}_4\text{Dy}^{\text{III}}_2(\mu_2\text{-OOCPh})_2(\text{MeOH})_2(\text{py})_6(\text{di-buShi}^3\text{-})_4(\text{di-buSal}^2\text{-})_2]$  with emphasized coordination mode of benzoate co-ligand (orange, side view) Hydrogen atoms non-coordinated solvent molecules are omitted for clarity are omitted for clarity. Color code: chromium(III) ions green, dysprosium(III) ion yellow, hydrogen atom white, oxygen red, nitrogen blue, carbon black.

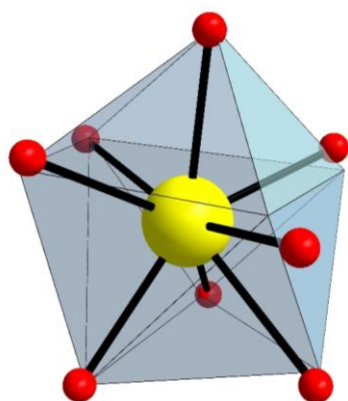


**Figure S 70.** Schematic representation of the ideal coordination polyhedron of the Dy1 of **Sal-[Cr<sub>4</sub>Dy<sub>2</sub>]** for an octahedral symmetry. Color code of atoms: oxygen red, chromium(III) ion green.

**Table S 35.** Calculated deviations from ideal polyhedra for guest ion Dy1 *via* Continuous Shape Measurements.

Polyhedra	CShM
Octagon $D_{8h}$	33.73698
Heptagonal pyramid $C_{7v}$	22.07723
Hexagonal bipyramid $D_{6h}$	16.06394
Cube $O_h$	12.07750
Square antiprism $D_{4d}$	3.87470
<b>Triangular dodecahedron <math>D_{2d}</math></b>	<b>1.56019</b>
Johnson gyrobifastigium J26 $D_{2d}$	12.09568
Johnson elongated triangular bipyramid J14 $D_{3h}$	27.95561
Biaugmented trigonal prism J50 $C_{2v}$	3.88824
Biaugmented trigonal prism $C_{2v}$	3.15843
Snub diphenoid J84 $D_{2d}$	3.85843
Triakis tetrahedron $T_d$	12.72495
Elongated trigonal bipyramid $D_{3h}$	23.28035

6.4.2.10. Structure determination [Cr<sub>4</sub>Dy<sub>2</sub>]Table S 36. Crystallographic data of complex [Cr<sub>4</sub>Dy<sub>2</sub>].

	[Cr <sub>4</sub> Dy <sub>2</sub> ]	[Cr <sub>4</sub> Dy <sub>2</sub> ]
	REN-ANL-164-26	REN-ANL-200-26
empirical formula	C <sub>100</sub> H <sub>76</sub> Cr <sub>4</sub> Dy <sub>2</sub> N <sub>12</sub> O <sub>26</sub>	C <sub>100</sub> H <sub>76</sub> Cr <sub>4</sub> Dy <sub>2</sub> N <sub>12</sub> O <sub>26</sub>
formula weight g/mol	2396.120	2396.120
overall formula	C <sub>112</sub> H <sub>96</sub> Cr <sub>4</sub> Dy <sub>2</sub> N <sub>14</sub> O <sub>28</sub>	C <sub>112</sub> H <sub>96</sub> Cr <sub>4</sub> Dy <sub>2</sub> N <sub>14</sub> O <sub>28</sub>
overall formula g/mol	2619.02	2619.02
crystal size / mm	0.084 x 0.042 x 0.015	0.1 x 0.057 x 0.03
crystal system	monoclinic	monoclinic
space group	C12/c1	C12/c1
unit cell dimensions		
<i>a</i> / Å	35.0082(16)	34.9265(14)
<i>b</i> / Å	19.3804(7)	19.4348(7)
<i>c</i> / Å	17.9218(8)	17.9161(6)
$\alpha$ / °	90	90
$\beta$ / °	92.106(4)	92.358(3)
$\gamma$ / °	90	90
volume / Å <sup>3</sup>	12151.2(9)	12151.0(8)
cell formula units Z	4	4
density $\rho_{\text{calc}}$ / g cm <sup>-3</sup>	1.432	1.432
$\mu$ / mm <sup>-1</sup>	1.634	9.931
F(000)	5272	5272
temperature / K	120	120
device type	STOE STADIVARI	STOE IPDS 2T
radiation	Mo-K $\alpha$	CuK $\alpha$
independent reflexes	1.639 < $\theta$ < 29.750	2.532 < $\theta$ < 59.999
index ranges	-45 < <i>h</i> < 47	-39 < <i>h</i> < 39
	-26 < <i>k</i> < 26	-21 < <i>k</i> < 21
	-19 < <i>l</i> < 24	-20 < <i>l</i> < 18
collected reflections	44367	27667
independent reflections	44367	10836
completeness	0.894	0.999
max. and min. transmission	0.9926 and 0.0270	0.6103 and 0.1758
$R_{\text{int}}$	0.2436	0.1436
$R_{\text{sigma}}$	0.6392	0.1181
data/restraints/parameters	15486 / 6 / 724	9018 / 66 / 724
goodness-of-fit on $F^2$	0.706	1.050
$^a R_1$ [ $I > 2\sigma(I)$ ]	0.0522	0.1567
$^b wR_2$ [ $I > 2\sigma(I)$ ]	0.1246	0.4109
$R_1$ [all data]	0.2326	0.2221
$wR_2$ [all data]	0.1456	0.5146

$$^a R_1 = \Sigma(|F_o| - |F_c|) / \Sigma|F_o|, \quad ^b wR_2 = [\Sigma[w(F_o^2 - F_c^2)^2] / \Sigma[w(F_o^2)^2]]^{1/2}, \quad w = 1 / [\sigma^2(F_o^2) + (ap)^2 + bp], \quad p = [\max(F_o^2, 0) + 2F_c^2] / 3.$$

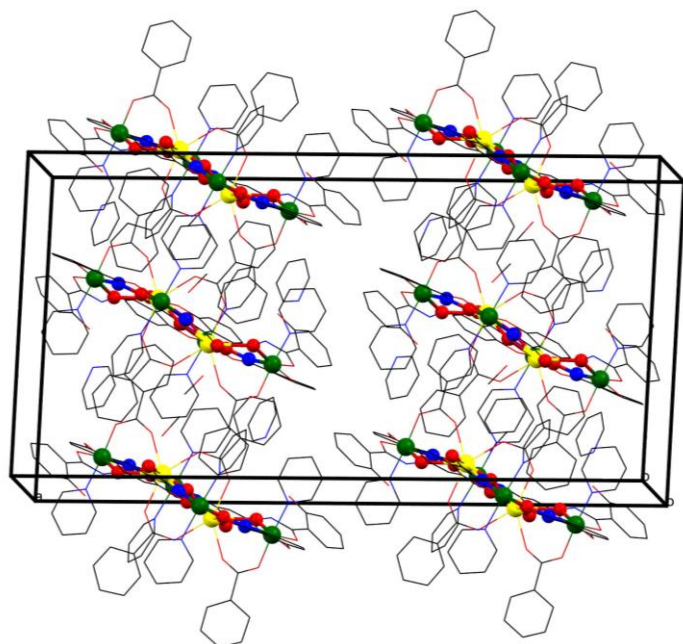


Figure S 71. Packing of [Cr<sub>4</sub>Dy<sub>2</sub>] within cell unit.

6.4.2.11. Structure determination [ $\text{Cr}_4\text{Dy}$ ]Table S 37. Crystallographic data of complex of [ $\text{Cr}_4\text{Dy}$ ] and [ $\text{Cr}_4\text{Ho}$ ].

	[ $\text{Cr}_4\text{Ho}$ ]	[ $\text{Cr}_4\text{Dy}$ ]
	REN-ANLX-015-28 [12-MC-4]	REN-ANL-204-28 [12-MC-4]
empirical formula	$\text{C}_{64}\text{H}_{55}\text{Cr}_4\text{HoN}_{10}\text{O}_{20}$	$\text{C}_{64}\text{H}_{55}\text{Cr}_4\text{DyN}_{10}\text{O}_{20}$
formula weight g/mol	1656.052	1655.051
overall formula	$\text{C}_{284}\text{H}_{272}\text{Cr}_{16}\text{Ho}_4\text{N}_{44}\text{O}_{88}$	$\text{C}_{140}\text{H}_{132}\text{Cr}_8\text{Dy}_2\text{N}_{22}\text{O}_{44}$
overall formula g/mol	7201.16	3567.67
crystal size / mm	0.27 x 0.18 x 0.08	0.12 x 0.07 x 0.03
crystal system	monoclinic	monoclinic
space group	P121/n1	P121/n1
unit cell dimensions		
$a/\text{\AA}$	15.2700(3)	15.2611(6)
$b/\text{\AA}$	22.1971(3)	22.2129(6)
$c/\text{\AA}$	22.9837(4)	22.9307(9)
$\alpha/^\circ$	90	90
$\beta/^\circ$	101.3290(10)	101.387(3)
$\gamma/^\circ$	90	90
volume/ $\text{\AA}^3$	7638.5(2)	7620.3(5)
cell formula units Z	1	2
density $\rho_{\text{calc}}/\text{g cm}^{-3}$	1.565	1.555
$\mu/\text{mm}^{-1}$	1.655	1.601
F(000)	364	3604
temperature / K	120	120.0
device type	STOE STADIVARI	STOE STADIVARI
radiation	Mo-K $\alpha$	Mo-K $\alpha$
independent reflexes	1.807 < $\theta$ < 29.863	2.045 < $\theta$ < 29.732
index ranges	-21 < h < 21	-19 < h < 21
	-31 < k < 30	-28 < k < 30
	-27 < l < 31	-31 < l < 25
collected reflections	99065	55472
independent reflections	20553	19335
completeness	0.934	0.892
max. and min. transmission	0.8710 and 0.0406	0.9221 and 0.7272
$R_{\text{int}}$	0.0661	0.0852
$R_{\text{sigma}}$	0.0731	0.1922
data/restraints/parameters	20553 / 269 / 1056	19335 / 238 / 1044
goodness-of-fit on F <sup>2</sup>	0.964	0.645
$^aR_1 [I > 2\sigma(I)]$	0.0513	0.0470
$^b wR_2 [I > 2\sigma(I)]$	0.1363	0.0990
$R_1[\text{all data}]$	0.0803	0.1180
$wR_2[\text{all data}]$	0.1436	0.1084

$$^aR_1 = \Sigma(|F_o| - |F_c|) / \Sigma|F_o|, \quad ^b wR_2 = [\Sigma[w(F_o^2 - F_c^2)^2] / \Sigma[w(F_o^2)^2]]^{1/2}, \quad w = 1/[\sigma^2(F_o^2) + (ap)^2 + bp], \quad p = [\max(F_o^2, 0) + 2F_c^2]/3.$$

## 6.4.2.12. Continuous Shape Measurements

**Table S 38.** Calculated deviations from ideal polyhedra for Cr1, Cr2, Cr3, Cr4 and Cr5 *via* Continuous Shape Measurements of [Cr<sub>5</sub>Dy] [15-MC-5].

Polyhedron <sup>a</sup>	Cr1	Cr2	Cr3	Cr4	Cr5
HP-6	31.26646	32.20298	30.99254	31.78619	31.24153
PPY-6	26.49317	27.52992	27.71404	27.74002	27.47751
OC-6	0.43029	0.38789	0.36611	0.38321	0.42933
TPR-6	13.60831	14.78111	14.84244	15.74616	14.46011
JPPY-6	30.06875	30.93751	31.12936	31.44570	31.02437

<sup>a</sup> abbreviations: HP-6 hexagon (D<sub>6h</sub>); PPY-6 pentagonal pyramid (C<sub>5v</sub>); OC-6 octahedron (O<sub>h</sub>); TPR-6 trigonal prism (D<sub>3h</sub>); JPPY-6 Johnson pentagonal pyramid J2 (C<sub>5v</sub>)

**Table S 39.** Calculated deviations from ideal polyhedra for Cr1, Cr2, Cr3 *via* Continuous Shape Measurements of [Cr<sub>6</sub>Tb<sub>4</sub>] cluster.

Polyhedron <sup>a</sup>	Cr1	Cr2	Cr3
HP-6	31.129	30.867	32.276
PPY-6	25.855	25.499	26.251
OC-6	0.537	0.532	0.536
TPR-6	12.822	13.528	13.603
JPPY-6	29.406	29.024	29.960

<sup>a</sup> abbreviations: HP-6 hexagon (D<sub>6h</sub>); PPY-6 pentagonal pyramid (C<sub>5v</sub>); OC-6 octahedron (O<sub>h</sub>); TPR-6 trigonal prism (D<sub>3h</sub>); JPPY-6 Johnson pentagonal pyramid J2 (C<sub>5v</sub>)

**Table S 40.** Calculated deviations from ideal polyhedra for Tb1, Tb2 *via* Continuous Shape Measurements of [Cr<sub>6</sub>Tb<sub>4</sub>].

	OP-8	HPY-8	HBPY-8	CU-8	SAPR-8	TDD-8	JGBF-8	JETBPY-8	JBTPR-8	BTPR-8	JSD-8	TT-8	ETBPY-8
Tb1	32.03 9	19.63 4	11.93 9	11.40 3	5.353	3.635	8.967	23.10 8	4.013	3.592	4.642	11.98 8	19.71 7
Tb2	33.04 3	21.50 8	16.51 4	14.24 2	5.267	3.579	13.61 4	23.80 1	3.553	2.846	5.205	14.87 8	20.44 3

abbreviations: OP-8 octagon (D<sub>8h</sub>), HPY-8 heptagonal pyramid (C<sub>7v</sub>), HBPY-8 hexagonal bipyramid (D<sub>6h</sub>), CU-8 cube (O<sub>h</sub>), SAPR-8 square antiprism (D<sub>4d</sub>), TDD-8 triangular dodecahedron (D<sub>2d</sub>), JGBF-8 Johnson gyrobifastigium J26 (D<sub>2d</sub>), JETBPY-8 Johnson elongated triangular bipyramid J14 (D<sub>3h</sub>), JBTPR-8 biaugmented trigonal prism J50 (C<sub>2v</sub>), BTPR-8 biaugmented trigonal prism (C<sub>2v</sub>), JSD-8 snub diphenoic J84 (D<sub>2d</sub>), TT-8 Triakis tetrahedron (T<sub>d</sub>), ETBPY-8 elongated trigonal bipyramid (D<sub>3h</sub>).

**Table S 41.** Calculated deviations from ideal polyhedra for Cr1 and Cr2 *via* Continuous Shape Measurements of [Cr<sub>4</sub>Dy<sub>2</sub>].

Polyhedron <sup>a</sup>	Cr1	Cr2
HP-6	31.266	31.785
PPY-6	27.342	27.605
OC-6	0.321	0.359
TPR-6	14.411	15.247
JPPY-6	31.053	30.803

<sup>a</sup> abbreviations: HP-6 hexagon (D<sub>6h</sub>); PPY-6 pentagonal pyramid (C<sub>5v</sub>); OC-6 octahedron (O<sub>h</sub>); TPR-6 trigonal prism (D<sub>3h</sub>); JPPY-6 Johnson pentagonal pyramid J2 (C<sub>5v</sub>).

**Table S 42.** Calculated values for Continuous Shape Measurements for the guest metal ion Dy1 of [Cr<sub>4</sub>Dy<sub>2</sub>].

OP-8	HPY-8	HBPY-8	CU-8	SAPR-8	TDD-8	JGBF-8
31.069	31.806	22.289	16.025	10.117	2.246	0.767
JETBPY-8	JBTPR-8	BTPR-8	JSD-8	TT-8	ETBPY-8	
<b>28.528</b>	2.599	1.965	3.083	10.825	24.325	

abbreviations: OP-8 octagon ( $D_{8h}$ ), HPY-8 heptagonal pyramid ( $C_{7v}$ ), HBPY-8 hexagonal bipyramid ( $D_{6h}$ ), CU-8 cube ( $O_h$ ), SAPR-8 square antiprism ( $D_{4d}$ ), TDD-8 triangular dodecahedron ( $D_{2d}$ ), JGBF-8 Johnson gyrobifastigium J26 ( $D_{2d}$ ), JETBPY-8 Johnson elongated triangular bipyramid J14 ( $D_{3h}$ ), JBTPR-8 biaugmented trigonal prism J50 ( $C_{2v}$ ), BTPR-8 biaugmented trigonal prism ( $C_{2v}$ ), JSD-8 snub diphenoid J84 ( $D_{2d}$ ), TT-8 Triakis tetrahedron ( $T_d$ ), ETBPY-8 elongated trigonal bipyramid ( $D_{3h}$ ).

**Table S 43.** Calculated values for Continuous Shape Measurements for the ring metal ions Cr1, Cr2, Cr3, and Cr4 of [Cr<sub>4</sub>Dy].

Polyhedron <sup>a</sup>	Cr1	Cr2	Cr3	Cr4
HP-6	31.413	30.871	31.286	30.880
PPY-6	25.435	27.247	25.188	27.395
<b>OC-6</b>	0.882	0.482	0.954	0.471
TPR-6	12.808	14.117	13.438	14.256
JPPY-6	29.623	30.767	28.663	30.861

**Table S 44.** Calculated values for Continuous Shape Measurements for the guest metal ion Dy1 of [Cr<sub>4</sub>Dy].

OP-8	HPY-8	HBPY-8	CU-8	SAPR-8	TDD-8	JGBF-8
31.069	24.127	13.440	10.714	3.673	2.389	10.643
JETBPY-8	JBTPR-8	BTPR-8	JSD-8	TT-8	ETBPY-8	
23.617	2.674	2.438	3.148	11.509	20.075	

abbreviations: OP-8 octagon ( $D_{8h}$ ), HPY-8 heptagonal pyramid ( $C_{7v}$ ), HBPY-8 hexagonal bipyramid ( $D_{6h}$ ), CU-8 cube ( $O_h$ ), SAPR-8 square antiprism ( $D_{4d}$ ), TDD-8 triangular dodecahedron ( $D_{2d}$ ), JGBF-8 Johnson gyrobifastigium J26 ( $D_{2d}$ ), JETBPY-8 Johnson elongated triangular bipyramid J14 ( $D_{3h}$ ), JBTPR-8 biaugmented trigonal prism J50 ( $C_{2v}$ ), BTPR-8 biaugmented trigonal prism ( $C_{2v}$ ), JSD-8 snub diphenoid J84 ( $D_{2d}$ ), TT-8 Triakis tetrahedron ( $T_d$ ), ETBPY-8 elongated trigonal bipyramid ( $D_{3h}$ ).

## 6.4.2.13. Evaluation of magnetic data

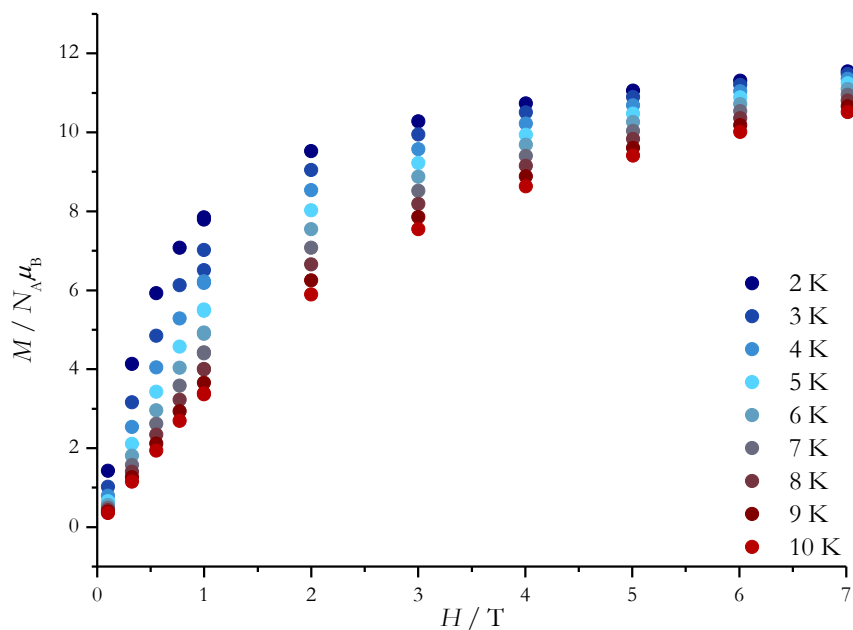


Figure S 72. Magnetization  $M$  plotted against the field strength  $H$  in a temperature range of 2-10 K of  $[\text{Cr}_5\text{Dy}]$ .

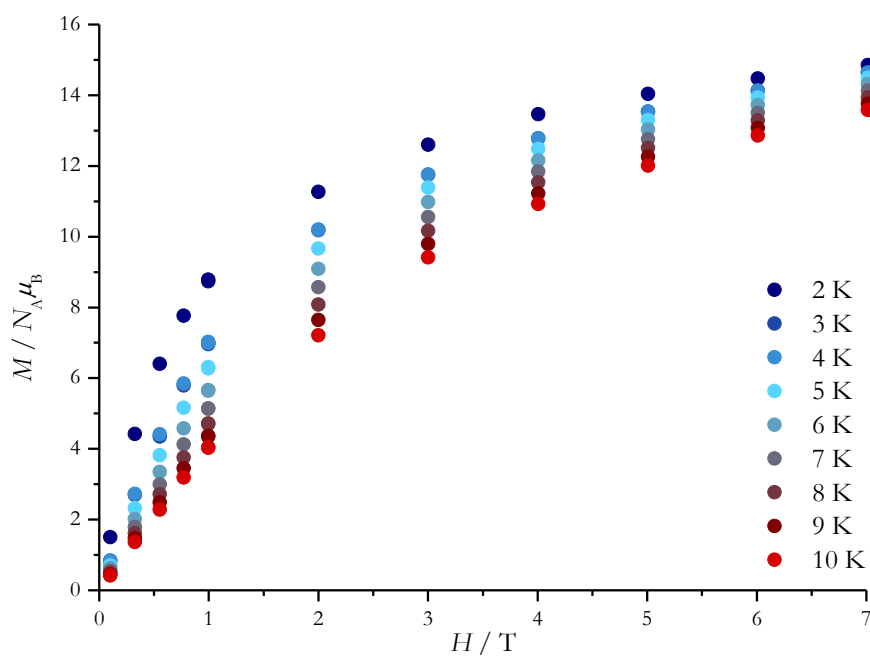


Figure S 73. Magnetization  $M$  plotted against the field strength  $H$  in a temperature range of 2-10 K of  $[\text{Cr}_4\text{Dy}_2]$ .

### 6.4.2.14. Infrared spectra

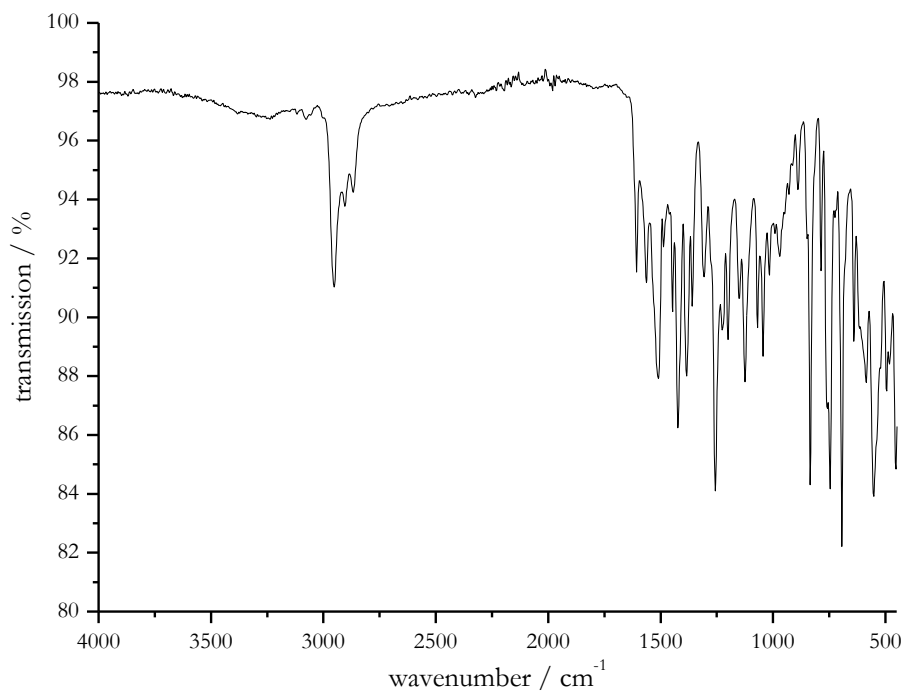


Figure S 74. Infrared spectrum of  $[\text{Cr}_5\text{Dy}]$ .

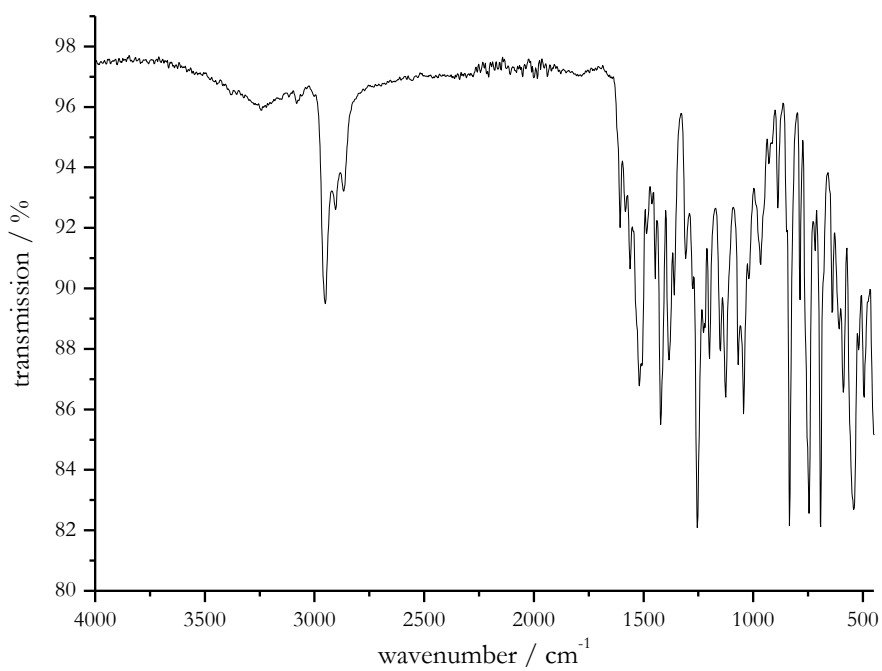


Figure S 75. Infrared spectrum of  $[\text{Cr}_6\text{Tb}_4]$ .



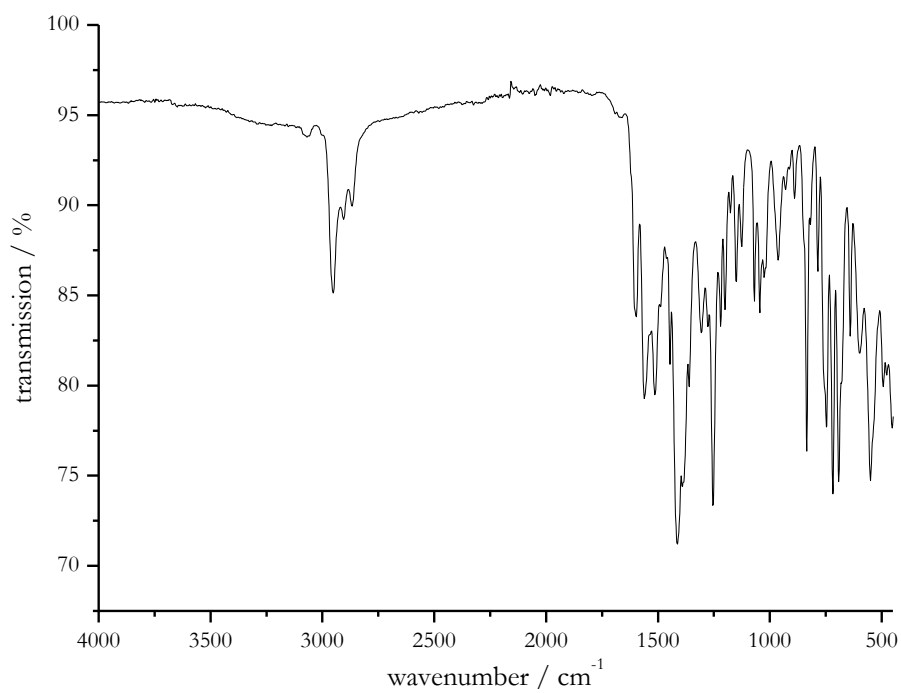


Figure S 76. Infrared spectrum of sal-[Cr<sub>4</sub>Dy<sub>2</sub>].

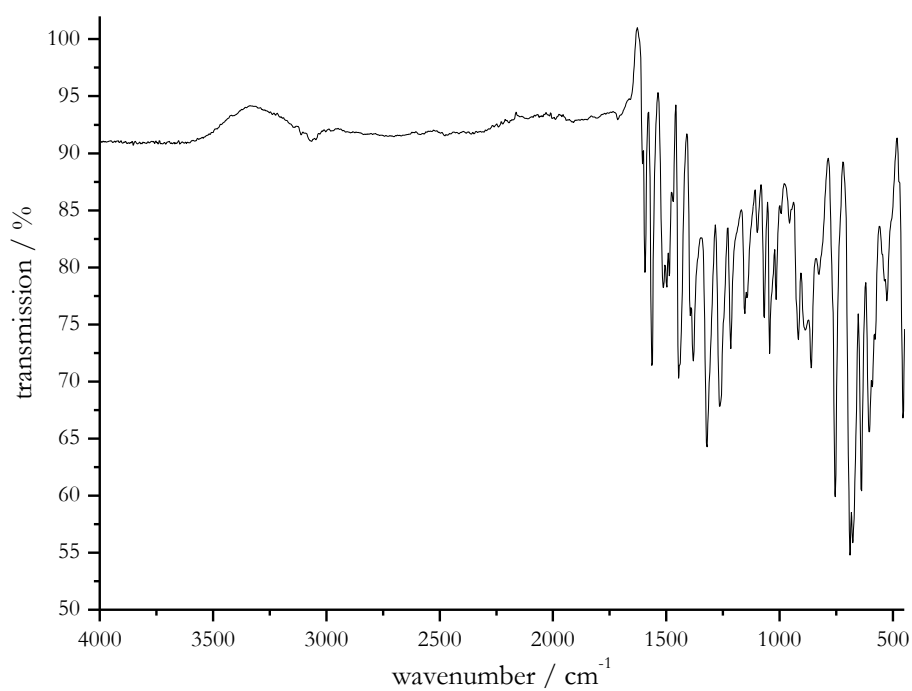
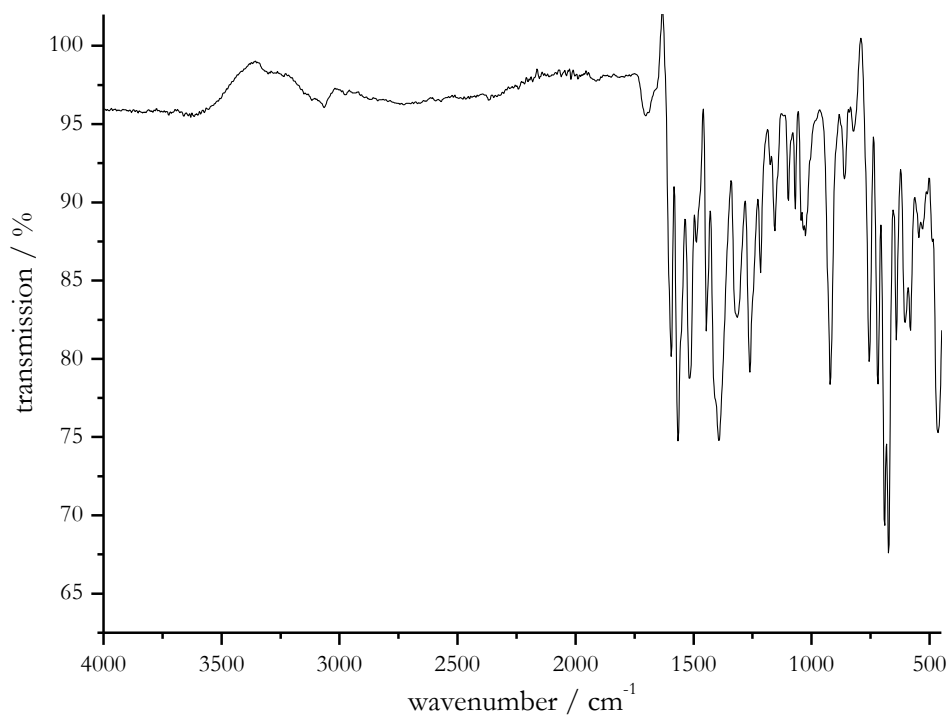
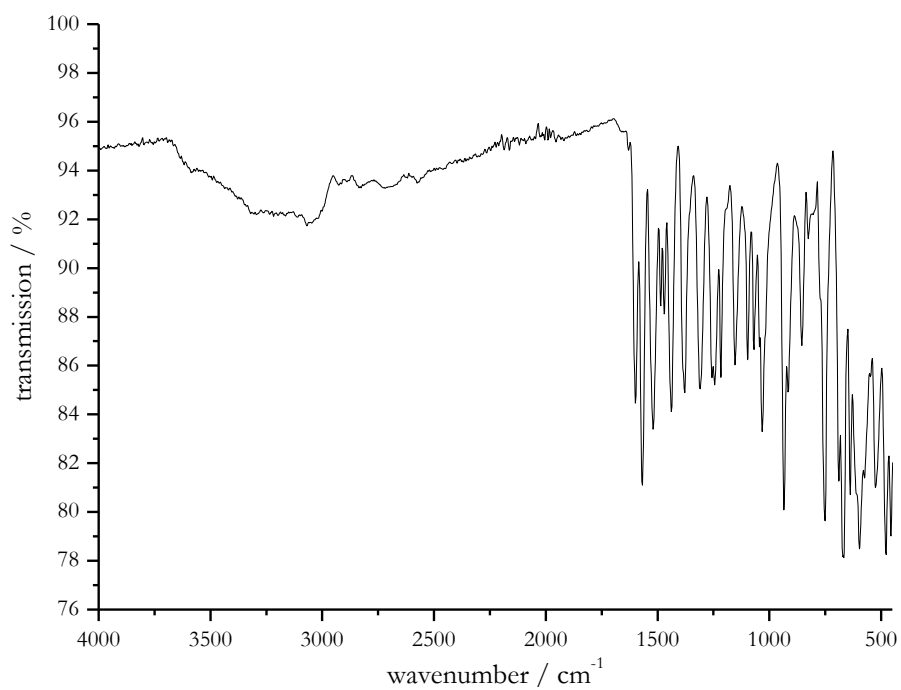


Figure S 77. Infrared spectrum of [Cr<sub>4</sub>Dy<sub>2</sub>] (synthesis with Cr(NO<sub>3</sub>)<sub>3</sub> as reactant).



**Figure S 78.** Infrared spectrum of **[Cr<sub>4</sub>Dy<sub>2</sub>]** (synthesis with Cr(acac)<sub>3</sub> as reactant).



**Figure S 79.** Infrared spectrum of **[Cr<sub>4</sub>Dy]**.

## 6.5. General procedure of solvothermal synthesis

Figure S 80 shows a simplified schematic of an autoclave reactor. This is composed of a stainless-steel autoclave into which a Teflon vessel with reaction solution is placed. The autoclaves are tightly closed and heated to the desired temperature in an oven with a cooling unit. A valve prevents excessive pressure from the gaseous solvent. The reactants were stirred in an appropriate solvent (MeOH, MeCN, EtOH) vials at ambient conditions. The reaction mixtures were transferred to the Teflon vessel and heated in the autoclave reactors in the oven as described before. After cooling, the reaction suspension was filtered, and the filtrate was filled into vials. The vials with perforated lids were left in air to allow the reaction solutions to evaporate.

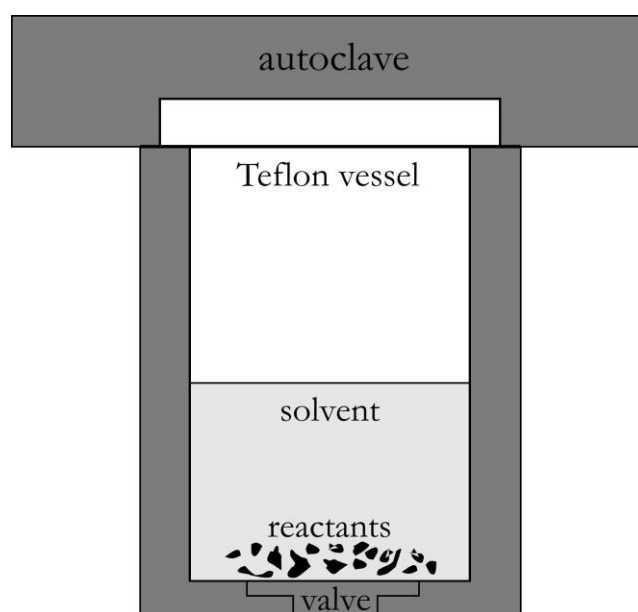


**Figure S 80.** Schematic diagram of the autoclave reactor for solvothermal synthesis in this thesis.

## 7. Instrumental part

### 7.1. General

The chemicals and solvents used were purchased from Abcr, Acros, Alfa Aesar, Deutero, Fluka, Fischer Scientific, Merck/Sigma Aldrich, Roth, and TCI without further purification. Anhydrous and degassed acetonitrile, tetrahydrofuran, and dimethylformamide were purchased from Acros (including Acros Seal) and used for CV measurements.

### 7.2. Infrared spectroscopy

Infrared transmission spectra were recorded using a Bruker ALPHAII ATR-IR instrument at room temperature, analyzed using the program OPUS and plotted using Origin 7.5.

### 7.3. X-Ray analysis

X-ray diffraction of a single crystal were performed on a STOE IPDS 2T by Dr. Dieter Schollmeyer and on a STOE STADIVARI by Dr. Luca Carrella at the Department of Chemistry at Johannes Gutenberg University in Mainz. The solution of the crystal structures was performed by Dr. Luca Carrella using ShelXT<sup>[2]</sup> and ShelXL<sup>[3]</sup> in combination with Olex 2<sup>[4]</sup>. The programs Mercury 2020.1 and Diamond 3 were used for the visualization.

### 7.4. Continous Shape Measurement

Continuous shape Measurements were performed using the SHAPE 2.1 program (Version March 2013), which will be abbreviated as CShMs in this thesis.<sup>[14–18]</sup>

### 7.5. NMR spectroscopy

All NMR spectra (compound dissolved in deuterated solvent) were measured using Bruker DRX 400 ( $\nu(^1\text{H}) = 400.13 \text{ MHz}$ ), Avance III HD 300 ( $\nu(^1\text{H}) = 400 \text{ MHz}$ ,  $\nu(^{13}\text{C}) = 100.1 \text{ MHz}$ ); Avance II 400 ( $\nu(^1\text{H}) = 400.13 \text{ MHz}$ ,  $\nu(\text{C } 13) = 100.1 \text{ MHz}$ ). All deuterated solvents were purchased from Deutero. The spectra were evaluated by the program MestReNova 14.0.1-23559 from the company Mestrelab Research.

### 7.6. ESI mass spectrometry

HRMS analysis were performed on Agilent 6200 series TOF/6500 series Q-TOF (11.0.203.0) with 0.1  $\mu\text{L}$  of injected solution volume (Acq. Mode: ESI\_pos\_ACN\_above1000.m) by Dr. Christopher Kampf at Johannes Gutenberg University Mainz (Department of Chemistry).

### 7.7. Cyclic voltammetry

The PGSTAT 204 potentiostat from Autolab was used for all cyclovoltammetric measurements, and the TSC 1600 closed with built-in platinum counter electrode as a vessel wall from *rhd* instruments was used as the measuring cell. A glass carbon electrode was used as the working electrode (polished after each completed series of measurements using an aluminum(III) oxide polishing paste with a grain size of 0.05  $\mu\text{m}$  from Buehler on a microfiber cloth). Excess polishing paste was rinsed off for one minute in an ultrasonic bath. A silver pseudo reference electrode was used as the reference electrode. Since the potential that develops is dependent on the solution composition, a spatula tip of ferrocene was added after each series of measurements and all measurements were referenced to ferrocene/ferrocenium. Even more accurate referencing would be possible by simultaneously measuring the potential of ferrocene/ferrocenium with the analyte solution, provided there are no waves of analyte in the same potential range. If corrosion of the silver wire was evident, it was also polished and cleaned for one minute in an ultrasonic bath. The platinum crucible of the measuring cell was polished with a cotton swab and polishing paste if contamination was suspected, and then washed with copious amounts of distilled water and acetonitrile. In general, after each series of measurements and, if necessary, after polishing the electrodes, the measuring cell was disassembled and thoroughly cleaned individually with distilled water and acetonitrile. The measuring cell was then dried in individual parts at 60 °C for at least one hour and placed hot in the glove box for the next measurement. Unless otherwise noted, analyte solutions with the concentration of about  $10^{-3}$  mol/L were used for the measurements. Tetrabutylammonium hexafluorophosphate at the concentration of 0.1 mol/L was used as the conducting electrolyte. Acetonitrile (purity of >99.9%), dimethylformamide (purity of >99.8%), and tetrahydrofuran (purity of >99.85%, without stabilizer) in extra dry and oxygen-free form from Thermo Fisher Scientific were used as solvents. Dimethylformamide was stored cold.

For measurements, open circuit voltage was chosen as the starting potential. Measurements were performed at room temperature between 21 °C to 25 °C. The second to fourth measurement runs were used for evaluation, depending on the measurement. Biologic's EC-Lab software was used to determine the maxima, and to calculate integrals and the regression lines. In images of cyclovoltammograms, the direction of potential change is indicated by arrows.

### 7.8. SQUID magnetometry

The magnetic measurements were conducted on a Quantum Design MPMS XL Squid magnetometer. To avoid alignment effects, the samples were fixed in a gelatin capsule with eicosane (except for [Cr<sub>3</sub>Cr] without anisotropy). Magnetic susceptibility measurements were made in a temperature range of a temperature range of 2-300 K under an applied magnetic field of 0.1 T. The in-phase and out-of-phase susceptibility was measured in an oscillating magnetic field of magnetic field of 3 Oe in a frequency range of 1-1399.25 Hz.

### 7.9. Elemental Analysis

The elemental analysis was performed by Brigitte Müller and Nadine Schenke at the Department of Chemistry at the Johannes Gutenberg University on an Elementar vario EL Cube.

## 8. References

- [1] A. Ghirri, J. van Tol, I. Vitorica-Yrezabal, G. A. Timco, R. E. P. Winpenny, *Dalton Trans.* 2015, 44, 14027–14033.
- [2] G. M. Sheldrick, *Acta Crystallogr. Sect. Found. Adv.* 2015, 71, 3–8.
- [3] G. M. Sheldrick, *Acta Crystallogr. Sect. C Struct. Chem.* 2015, 71, 3–8.
- [4] O. V. Dolomanov, L. J. Bourhis, R. J. Gildea, J. a. K. Howard, H. Puschmann, *J. Appl. Crystallogr.* 2009, 42, 339–341.
- [5] O. Kahn, *Molecular Magnetism*, VCH, New York, NY, 1993.
- [6] N. F. Chilton, R. P. Anderson, L. D. Turner, A. Soncini, K. S. Murray, *J. Comput. Chem.* 2013, 34, 1164–1175.
- [7] Sheetal, K. Nehra, R. Kaushal, S. Arora, D. Kaur, R. Kaushal, *Russ. J. Gen. Chem.* 2016, 86, 154–160.
- [8] L. J. Völker, *Molekularer Magnetismus Metallakronen-basierter Komplexverbindungen*, Johannes Gutenberg-Universität Mainz, 2018.
- [9] M. E. Zwaagstra, H. Timmerman, M. Tamura, T. Tohma, Y. Wada, K. Onogi, M.-Q. Zhang, *J. Med. Chem.* 1997, 40, 1075–1089.
- [10] G. Zvilichovsky, *J. Org. Chem.* 1969, 34, 486–489.
- [11] A. Ghirri, J. van Tol, I. Vitorica-Yrezabal, G. A. Timco, R. E. P. Winpenny, *Dalton Trans.* 2015, 44, 14027–14033.
- [12] K. Schwetlick, *Organikum*, Wiley-VCH, Weinheim [u.a.], 2015.
- [13] D. Coucouvanis, *Inorganic Syntheses: Volume 33*, Wiley, New York Chichester, 2002.
- [14] D. Casanova, P. Alemany, *Phys. Chem. Chem. Phys.* 2010, 12, 15523–15529.
- [15] A. Ruiz-Martínez, D. Casanova, S. Alvarez, *Dalton Trans.* 2008, 0, 2583–2591.
- [16] J. Cirera, E. Ruiz, S. Alvarez, *Chem. – Eur. J.* 2006, 12, 3162–3167.
- [17] D. Casanova, J. Cirera, M. Llunell, P. Alemany, D. Avnir, S. Alvarez, *J. Am. Chem. Soc.* 2004, 126, 1755–1763.
- [18] M. Pinsky, D. Avnir, *Inorg. Chem.* 1998, 37, 5575–5582.